Bulk and Nanostructured Metal Halides and Chalcogenides: Synthesis, Optical, Dielectric, and Thermoelectric Properties

A Thesis

Submitted for the Degree of

Doctor of Philosophy

by

Paribesh Acharyya

New Chemistry Unit
Jawaharlal Nehru Centre for Advanced Scientific Research
(A Deemed University)
Bangalore – 560 064, India

May 2022

Dedicated to Mr. Arunava Saha

DECLARATION

I hereby declare that this thesis entitled "**Bulk and Nanostructured Metal Halides and Chalcogenides: Synthesis, Optical, Dielectric, and Thermoelectric Properties**" is a result of studies carried out by me at the New Chemistry Unit, Jawaharlal Nehru Centre for Advanced Scientific Research, Bangalore, India, under the supervision of **Prof. Kanishka Biswas**. This work has not been submitted elsewhere for the award of any degree or diploma.

In keeping with the general practices of reporting scientific observations, due acknowledgements have been made wherever the work described is based on the findings of other investigators in a collaborative pursuit. Any omission which might have occurred by oversight or error in judgement is regretted.

Bangalore, India
17 May 2022

Paribesh Acharyya

CERTIFICATE

I hereby certify that the work described in this thesis titled "**Bulk and Nanostructured Metal Halides and Chalcogenides: Synthesis, Optical, Dielectric, and Thermoelectric Properties**" has been carried out by Mr. Paribesh Acharyya at New Chemistry Unit, Jawaharlal Nehru Centre for Advanced Scientific Research, Bangalore, India under my supervision and that it has not been submitted elsewhere for the award of any degree or diploma.

Kanishk Bis

Bangalore, India
17 May 2022

Prof. Kanishka Biswas
(Research Supervisor)

ACKNOWLEDGEMENTS

Completion of my Ph.D. thesis necessitated a lot of guidance and supports from many people. I take this opportunity to mention a few of them. However, my sincere thanks extend to everyone who has played a role in making this dream a reality.

Firstly, my research supervisor, Prof. Kanishka Biswas for constant guidance throughout my Ph.D. career and giving me the freedom to carry out and express my scientific thoughts. His inputs in both scientific and non-scientific problems (like how to make better presentations, how to write grant proposals etc.) have led to me become a much well-prepared researcher.

My beloved lab mates: Dr. Satya, Dr. Manoj, Dr. Ananya, Dr. Subhajit, Dr. Manisha, Dr. Provas, Dr. Tanmoy, Dr. Suresh, Dr. Shidaling, Dr. Kaushik, Dr. Prabir, Dr. Archana, Dr. R. K. Gopal, Dr. Jayita, Dr. Ekashmi, Subarna, Dr. Abdul, Dr. Anuradha, Dr. Manjunatha, Dr. Moinak, Arka, Sushmita, Krishnendu, Debattam, Riddhimoy, Animesh Bhui, Anustoop, Vaishali, Animesh Das, Subhajit, Aditya, Ivy, Anupama, Aman, Pavan and Prema for their cheerful company and keeping a healthy competitive spirit in the lab.

I would like to thank Bharat Ratna Prof. C. N. R. Rao, FRS for his words of encouragements. I also thank him for providing the infrastructure and facilities to carry out my research work.

I would like to thank Prof. Subi Jacob George, NCU chair for all the departmental instrument facilities.

I would like to thank Prof. Umesh V. Waghmare, Prof. Swapan K. Pati, Prof. A. Sundaresan, Prof. Ajay Soni, Prof. Sarit S. Agasti, Prof. S. K. Prasad, Dr. Koushik Pal, Prof. Dirtha Sanyal, Dr. David J. Voneshen, Dr. Martin Etter, Dr. Pralok K Samanta, Dr. Juhi Pandey, Dr. Raju K. Biswas, Mr. Kewal Singh Rana, Dr. Premkumar Yanda, Ms. Raagya Arora, Dr. Dipti Swain, Dr. Pragnya Satapathy for the fruitful scientific collaborations and all the insightful discussions. I have learnt a lot whenever we had meeting or discussion with them.

I would like to thank all the funding agencies like DST and Synchrotron facilities at DESY-Germany and Photon Factory, KEK, Japan, for carrying out collaborative studies on temperature-dependent X-ray diffraction. Without their support, it would have never been possible to conduct research.

I am thankful to all my course instructors: Prof. Kanishka Biswas, Prof. Sebastian C. Peter, Prof. Sarit S. Agasti and Prof. A. Sundaresan, whose courses have been extremely helpful.

Constant assistance and a friendly nature of the technical staff helped me doing my experiments smoothly. Here, I would like to acknowledge Mrs. Usha, Mr. Vasu, Mr. Anil, Mr. Rahul, Dr. Jay Ghatak, Mr. Mahesh, Mr. Shiva, Mr. Kanan, Mr. N. Kishore, Mr. M. Gowda, Mr. Dileep, Mr. Srinivas and others.

I thank all the staff members associated with Academic, Admin, NCU, ICMS, Library, Hostel, Mess, Security, Utility, Gardening, Cleaning, Dhanvantari and other department.

I would like to thank UGC for the research fellowship.

I would like to thank my friends from JNCASR without whom, life at JNC would never be so meaningful: Arunava, Risov, Sanchita, Swadhin, Souvik, Sudeep, Rajib, Debu.

I thank all my seniors, and juniors in JNCASR. Their help and advice made my academic and non-academic life a memorable and comfortable one here at JNC.

I would like to acknowledge my childhood, school, college, and university friends who left an everlasting impression on me.

The various sports groups I have been associated with in JNCASR.

Lastly, I would like to acknowledge my parents and family. Without their unconditional love and support, all my efforts would have gone to vain.

PREFACE

Metal halides and chalcogenides are the important classes of materials with a rich structural diversity and plethora of diverse properties. In my Ph.D. thesis, I have implemented different synthetic route for synthesis of various metal halides and chalcogenides in the form of bulk, single crystal and nanostructures. I have studied their various properties, gained an in-depth understanding of the structure-property relationship. Finally, I have probed their applicability in different fields, such as optical, magnetic, and dielectric responses of metal halides, and thermoelectric application for metal chalcogenides. Apart from the present introductory part (**Part 1**), my thesis work is divided into six parts.

Part 2 of my thesis involves the synthesis and optical properties of layered 2D Pb-based metal halide-based perovskites nanostructures. In **Chapter 2.1,** we have discussed the single pot solution-based transformation to tetragonal 2D $CsPb_2Br_5$ nanosheets (NSs) from orthorhombic 3D $CsPbBr_3$ nanocrystals (NCs). In spite of having indirect band gap, as synthesized $CsPb_2Br_5$ nanosheets show bright green luminescence band. We investigated the origin of the luminescence property of $CsPb_2Br_5$, which was arising from the amorphous lead bromide ammonium complexes present at the surface of this material. In **Chapter 2.2,** we have discussed the formation of $Cs_2PbI_2Cl_2$ NCs using benzoyl halides and studied the optical properties. We have also shown the chemical transformation of 2D $Cs_2PbI_2Cl_2$ to 3D $CsPbBr_3$ and 0D Cs_4PbCl_6 for the first time. Furthermore, Mn^{2+} was inserted as a dopant in $Cs_2PbI_2Cl_2$ NCs and investigated the optical properties.

Part 3 of my thesis offers the synthesis and photoluminescence (PL) blinking properties of 2D NSs of layered perovskites. In **Chapter 3.1**, we have synthesized the 2D NSs and NCs of $Cs_3Bi_2I_6Cl_3$ by hot-injection method. The 2D NSs and NCs of $Cs_3Bi_2I_6Cl_3$ showed distinct optical properties. Finally, the super-resolution fluorescence microscopy was employed to investigate the single-particle PL properties of 2D NSs and NCs of $Cs_3Bi_2I_6Cl_3$, both of which showed luminescence at green region along with the localized blinking events at millisecond time scale. In **Chapter 3.2,** we have demonstrated the low-temperature colloidal synthesis of free-standing ultrathin NPLs of $Cs_3Bi_2I_9$ and studied their optical properties. We have studied the single-particle fluorescence properties of $Cs_3Bi_2I_9$ NPLs by super-resolution fluorescence microscopy.

Part 4 involves the thermal conductivity studies of Bridgman grown large single crystal of layered metal halide perovskites. In **Chapter 4.1,** we have demonstrated intrinsically ultralow lattice thermal conductivity (κ_L) of ~ 0.37-0.28 W/mK in the 295-523 K temperature range in a single crystal of layered Ruddlesden-Popper (RP) perovskite, $Cs_2PbI_2Cl_2$. The damped acoustic phonon modes and strong acoustic-optical phonon mode coupling resulted in an ultralow κ_L value in all-inorganic 2D RP perovskite, $Cs_2PbI_2Cl_2$. In **Chapter 4.2,** we have studied the thermal conductivity of $Cs_3Bi_2I_6Cl_3$. Surprisingly single crystal exhibits glass-like thermal conductivity in the temperature range of 2-400 K. The presence of high anharmonicity, soft vibration of selective sublattices and local distortion in the Bi-octahedra in $Cs_3Bi_2I_6Cl_3$ are the primary reasons for the glass-like thermal conductivity. In **Chapter 4.3**, we have the discussed the thermal transport properties of 0D $Cs_3Bi_2I_9$ bulk ingot.

Part 5 involves the dielectric, magnetic, and thermochromic properties of complex metal halides. In **Chapter 5.1,** we have demonstrated a broadband colossal dielectric constant (CDC) with a low dielectric loss in superionic bulk $RbAg_4I_5$. Fluctuation in the dipole moments associated with movement of Ag^+ clusters results in CDC in $RbAg_4I_5$. In **Chapter 5.2,** we have synthesised polycrystalline layered metal halide, $RbSn_2Br_5$, and its mixed halide counterparts, $RbSn_2Br_3Cl_2$ and $RbSn_2Br_4I$ by mechanochemistry and studied their optical properties. In **Chapter 5.3**, polycrystalline $Rb_2CuCl_2Br_2$ were synthesized by mechanochemistry, and their optical and magnetic properties have been investigated. In **Chapter 5.4**, we have demonstrated the thermochromic properties of mechanochemically synthesized $(Ag_{1-x}Cu_x)_2HgI_4$ samples (where $0 \leq x \leq 1$).

Part 6 involves the synthesis and thermoelectric (TE) properties of germanium telluride (GeTe)-based materials. In **Chapter 6.1** we have demonstrated high TE performance, and high mechanical stability in Sb doped GeTe-rich $(GeTe)_{1-2x}(SnSe)_x(SnS)_x$ system. Initially, the addition of SnSe and SnS in GeTe reduces the κ_{latt} due to phonon scattering. Further, introduction of Sb doping introduces additional phonon scattering center and optimizes the *p*-type carrier concentration. As a result, 10 mol % Sb-doped $(GeTe)_{0.95}(SnSe)_{0.025}(SnS)_{0.025}$ sample exhibits ultralow κ_{lat} of ~ 0.34 W/mK accompanied by the zT of ~1.9 at 710 K. Moreover, the measured Vickers microhardness value of high-performance sample is ~194 H_V, higher than pristine GeTe (~145 H_V). Motivated by the high zT and enhanced mechanical stability, we have

constructed single-leg based TE device and achieved a high output power of ~ 150 mW for the temperature difference of 462 K, for 10 mol % Sb-doped $(GeTe)_{0.95}(SnSe)_{0.025}(SnS)_{0.025}$ sample. In **Chapter 6.2,** we unraveled the role of Hg and Sb doping in GeTe system with a record high TE performance. The enhanced Seebeck coefficient in Hg doped GeTe system arises due the valence band convergence and low κ_{lat} is mainly attributed due to the presence of HgTe nanoprecipitates. The co-doped samples introduce a localized electronic state near the Fermi level which boost the Seebeck coefficient. The enhanced power factor and low thermal conductivity in $Ge_{0.87}Hg_{0.05}Sb_{0.08}Te$ leads to peak zT of 2.6 at 723 K. Furthermore, we have constructed single leg TE device of $Ge_{0.87}Hg_{0.05}Sb_{0.08}Te$ sample and obtained a high output power of 160 mW for the temperature difference of 464 K.

In **Part 7**, I have summarized thesis and provided a brief outlook into the future directions in developing new and efficient metal halides and chalcogenides materials for various applications. To summarize, the initial part of my thesis involved the synthesis and detailed optical properties of various nanostructures of metal halide perovskites with vast structural diversity **(Part 2 and 3)**. Then, we have studied the thermal transport properties of low dimensional metal halide perovskites single crystals and presented an in-depth understanding of the origin of low thermal conductivity (**Part 4**). I have also explored the mechanochemical synthetic route to synthesize complex metal halides and studied their different physical properties (e.g., optical, dielectric, and magnetic properties) in **Part 5**. Finally, we have demonstrated how low κ_{lat} and electronic structure modulation can be beneficial in realizing high TE performance in GeTe-based systems (**Part 6**).

TABLE OF CONTENTS

Part 1

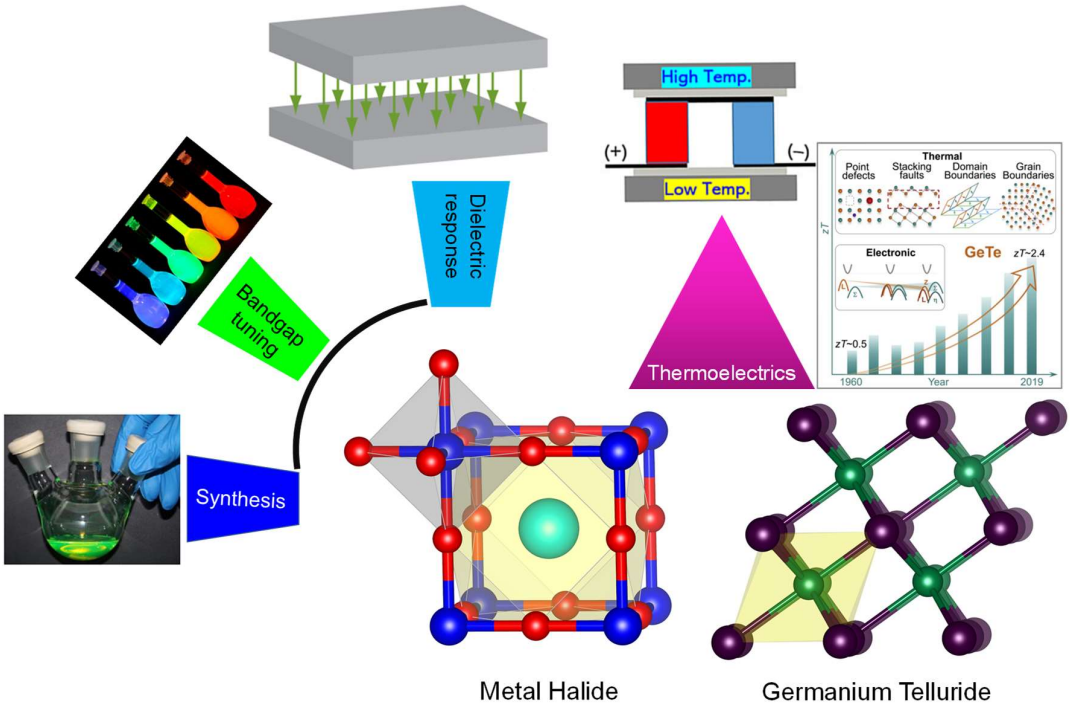

A Brief Introduction to Metal Halides and Metal Chalcogenides

Part 1

A Brief Introduction to Metal Halides and Metal Chalcogenides[†]

Summary

Metal halide perovskites and metal chalcogenides have appeared as an exciting class of materials for diverse applications. Three-dimensional (3D) halide perovskites have experienced extraordinary rapid progress and attained momentous attention from the worldwide scientific community owing to their distinct variety of properties and prospective multifunctional applications in the field of photovoltaic and optoelectronic devices. In contrast, all-inorganic two-dimensional (2D) layered halide perovskites are relatively new and gained significant attention in last few years. In the initial part of this chapter, I have discussed about the synthesis, structural diversity and different application of metal halides. On the other hand, metal chalcogenides having a vast compositional variety as well as diverse crystal structures exhibit remarkable physical and chemical properties, which designate them as emerging candidates for thermoelectric applications. Thermoelectric materials which can convert heat energy to electricity rely on crystalline inorganic solid-state compounds exhibiting low phonon transport (i.e. low thermal conductivity) without much inhibiting the electrical transport. Crystalline materials with low lattice thermal conductivity (κ_{lat}) provide an attractive paradigm as it helps in simplifying the complex interrelated thermoelectric parameters and allows us to focus largely on improving the electronic properties. Later part of this chapter highlights a brief introduction of heavy metal chalcogenides followed by their unique chemistry and bonding and their potential applications. Last part of this chapter is focused on a general methods for characterizations and properties measurements.

[†]*A part of this chapter is published in* **P. Acharyya,** K. Kundu, and K. Biswas, *Nanoscale* 2020, **12**, 21094-21117 (Review) and **P. Acharyya**, D. Sarkar, P. Dutta, and K. Biswas, Comprehensive Inorganic Chemistry III, Elsevier. *submitted* (Book Chapter), Ed. by Ram Seshadri & Serena Corr.

1.1 Introduction to metal halides

Metal halides have gained increasing attention over the past few year.[1, 2] Among these, metal halide perovskites, ABX_3 (where, A, B and X are the organic/inorganic monovalent cation, divalent metal cation and halide ions, respectively) with three-dimensional (3D) structure are most studied.[3, 4] 3D perovskites exhibit astonishing range of properties, for instance, high absorption coefficients, band gap tunability, wide emissive range, high photoluminescence quantum yield (PLQY), long diffusion lengths, high charge-carrier mobilities and ferroelectric domains.[2-14] In consideration of these versatile properties, a rapid advancement was accomplished towards the energy conversion applications, such as, in perovskite solar cells (PSCs) and light-emitting devices (LEDs).[10, 15, 16] The power conversion efficiency (PCE) of PSCs and the external quantum efficiency (EQE) of LEDs devices have been improved promptly from 3.8% to ~25% and 1% to ~21%, respectively, within few years.[4, 17-28] Furthermore, the halide perovskites have recently gained extensive attention in photocatalysis owing to their unique crystal structure, broad absorption range, and suitable charge-transport properties.[29-31] Mention must be made that the structural distortion and stability of 3D hybrid and all-inorganic analogues are governed by the well-known Goldschmidt tolerance factor (t) and the octahedral factor (μ):

$$t = \frac{r_A + r_X}{\sqrt{2}(r_B + r_X)}$$

$$\mu = {r_B}/{r_X}$$

Where r_A, r_B and r_X are the radii of the A-site cation, B-site cation and halide ion, respectively. The stability of 3D perovskite structures is generally predicted by these two parameters, t and μ, which lie in the range of $0.8 < t < 1$ and $0.442 < \mu < 0.895$, respectively.[3, 4, 32, 33] Recently, Bartel et al. reported a new tolerance factor, which anticipated the stability of perovskites probably better compare to the extensively used Goldschmidt tolerance factor.[34]

Despite versatile exploitation, the intrinsic instabilities of 3D perovskite halides during exposure in light, heat, and moisture together with the presence of toxic lead (Pb)

limit their future progress in real-world commercialization and application.[35, 36] To address some of these concerns and also to create structural diversity, layered two-dimensional (2D) hybrid perovskites were first appeared as a novel class of materials with outstanding layer-dependent tunable optical properties, generation of stable excitons at room temperature, large exciton binding energy originating from the quantum and dielectric confinement effects in conjunction with the improved environmental stability and photostability.[37-41] The 2D layered structures are formed by the corner-sharing of $[BX_6]^{4-}$ metal halide octahedra, and the layers are isolated by the large organic cations.[38, 39] The 2D structure can be derived from their 3D structure by cutting through a definite crystallographic plane (e.g., <100>, <110> or <111>) which is discussed later in detail.[40] The 2D perovskites also hold worthy prospect for solar cell and optoelectronic applications.[40, 42, 43] Recently, a PCE value of 12.52% was accomplished in the layered Ruddlesden-Popper hybrid perovskite-based solar cells.[37] While the hybrid 2D perovskites have showed good progress,[39, 41] the all-inorganic layered 2D perovskites seems to be a fast growing field and recently it is gaining tremendous momentum. In the case of traditional 3D perovskites, the all-inorganic halides generally displayed better thermal stability, reduced moisture sensitivity, and minor defect concentration compared to the hybrid perovskites. This resulted in the intrinsically stable all-inorganic perovskites with favorable optical properties, including high PL intensity, tunable emission, narrower line-widths, high PLQY and wide color gamut.[44-46]

1.1.1 Crystal structures

A conventional 3D halide perovskite is represented as ABX_3. The BX_3 unit forms the corner sharing network of BX_6 octahedra and A is located within the cuboctahedral cavity (AX_{12} polyhedron).[47] The set of A, B or X atoms which may adopt the perovskite structures that depends upon the ionic radii of the corresponding ions, which satisfy the Goldschmidt's Tolerance Factor.[34, 48, 49] The 2D perovskites can be considered as slicing of the 3D perovskite structure along specific crystallographic direction.[33, 50] Typically ⟨100⟩- and ⟨111⟩ slicing of the 3D ABX_3 perovskites are well-known members of all-inorganic 2D halide perovskites family as shown in Figure 1.1. Please note that the dimensionality discussed here is referred to the connectivity of corner sharing BX_6

octahedra in the crystal structure. The reduction of dimensionality significantly influences the electronic structure and physical properties of metal halide perovskites (discussed later).

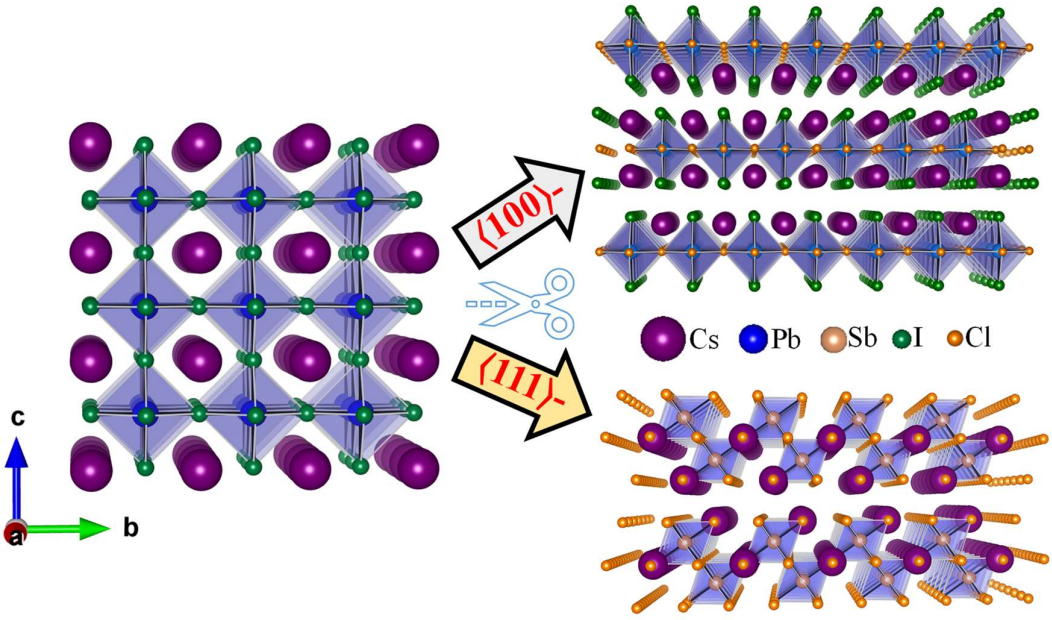

Figure 1.1. *Schematic representation of cuts along the ⟨100⟩, and ⟨111⟩-directions of the parent 3D perovskite structure that give rise to the families of 2D layered perovskites.*

Ruddlesden-Popper (RP) perovskite halides

The 2D layered RP phase of perovskite halide are obtained by the ordered removal of B cation along ⟨100⟩-direction, which possess a general formula of $A_{n+1}B_nX_{3n+1}$ (Figure 1. 2a).[33] RP phase can be visualized as two AX type rock-salt type layers are sandwiched between *n* numbers of ABX_3 perovskite layers along the *c*-axis and stabilized in such a manner that these layers are offset by one octahedral unit.[51] The simplest member of this series is A_2BX_4 (RP phase, $n = 1$), which adopts the famous K_2NiF_4-type structure (space group *I*4/*mmm*).[52]

The RP phase is well-known in hybrid perovskites family, as there are diverse choice of A cation, while for all-inorganic perovskites, a few RP phases were reported so far.[37, 39, 53-56] Recently, mixed halide (B = Sn, Pb) RP phases have been synthesized.[56, 57] Li et al. synthesized single crystal of $Cs_2SnI_2Cl_2$ and $Cs_2PbI_2Cl_2$ by solid state method

and their structures have been represented in Figures 1.2a-c.[56, 57] The 2D layer is formed by the corner sharing $[BI_2Cl_4]^{4-}$ octahedra (B = Pb or Sn), where I^- ions occupy the out of plane site and Cl^- ions occupy in plane site serving as bridging ligands. Cs^+ ions counterbalance the charges of the 2D layers. The size of A cation and other halide composition failed to stabilize the RP structure, which explain the uniqueness of these compositions.[56] $Rb_2CdI_2Cl_2$ also adopts similar 2D layered RP structure.[58]

There are few transition metal based RP halides (n = 1 and 2) have been reported so far. The RP phases for n = 1 are A_2MCl_4 (A = Cs, Rb and M = Cd, Mn) and $Rb_3M_2Cl_7$ for n = 2 (M = Cd and Mn) but an in-depth investigation is required to understand the properties of these materials.[59-61] Yamaura's group reported a new double-layered mixed halide perovskite, $Cs_3Cu_2Cl_4Br_3$.[62] The structure is formed by double layers of $Cu_2Cl_4Br_3$ with distorted octahedra, $CuCl_4Br_2$ and structure is similar to the $Sr_3Ti_2O_7$ (RP phase n = 2).

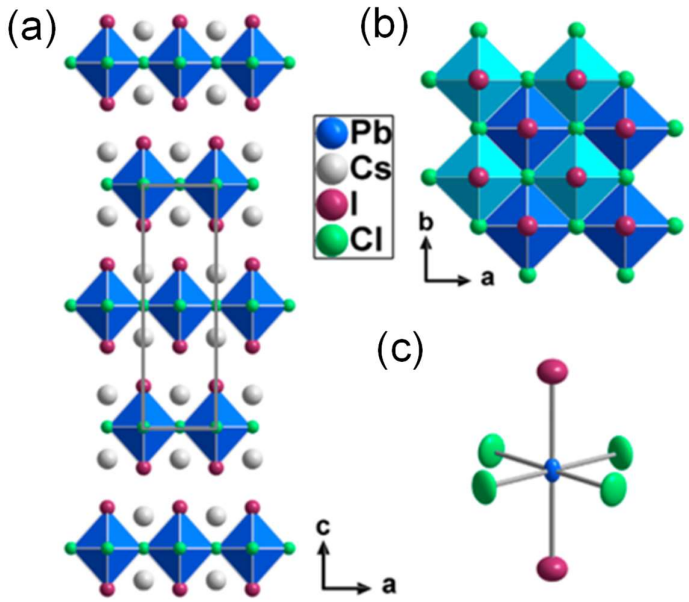

Figure 1.2. *(a) Ruddlesden-Popper (RP) perovskites with general formula: $A_{n+1}B_nX_{3n+1}$, can be obtained by cutting along the ⟨100⟩-direction of the parent 3D ABX_3 structure. Crystal structure of $Cs_2PbI_2Cl_2$ which adopts the K_2NiF_4-type structure (RP phase, n = 1), side view (unit cell outlined in gray); (b) top-down view (Cs^+ are hidden and the adjacent perovskite slabs are in different color to depict the relative stacking of layers with (1/2, 1/2) displacement); and (c) the elongated $[PbI_2Cl_4]$ octahedral unit. Selective*

bond length: Pb-Cl (2.8193(4) Å), Pb-I (3.171(2) Å), and Cs-I (3.781(3) Å). Reproduced from ref. 56 ©American Chemical Society for (a, b, c).

⟨111⟩-Oriented perovskite halides

The ⟨111⟩-oriented perovskite with general formula of $A_{n+1}B_nX_{3n+3}$ is the richest subgroup of all-inorganic 2D halide perovskites. The bilayer structures (n = 2) are stabilized by the trivalent metal ions like $Bi^{3+}$and Sb^{3+}, where B-sites are occupied by the trivalent cation and vacancy at a ratio of 2:1 resulting in a $A_3B_2X_9$ structure ($A_3B_2[V]_1X_9$; where V denotes vacancy). In these perovskites, the vacancies are ordered along the <111> direction, and as a result, the 2D bilayers of corner connected BX_6 octahedra are formed, e.g. $Cs_3Sb_2I_9$.[63] Interestingly, $A_3Bi_2I_9$ can adopt both 2D and 0D crystal structures depends upon the sizes of A cations, which are demonstrated in Figure 1.3a.[64-67] $Rb_3Bi_2I_9$ adopts 2D layered structure crystalized in monoclinic phase (space group *P*21/*n*). Replacing Rb^+ with the larger Cs^+ at the A cation site tends to form the dimer, where BiI_6 octahedra fused together to form face sharing $Bi_2I_9^{3-}$ dimer. These dimers are electronically isolated from each other, and making them a 0D crystal structure of $Cs_3Bi_2I_9$ (space group P*6₃/mmc*), Figure 1.3a.[68] Both the $Cs_3Sb_2I_9$ and $Rb_3Sb_2I_9$ form a 2D layered structure,[69] and similarly, $Cs_3Bi_2Br_9$, $Rb_3Sb_2Br_9$, $Cs_3Sb_2Br_9$, and $Cs_3Sb_2Cl_9$ form 2D layered structure.[70-72]

The dimensionality of 0D $Cs_3Bi_2I_9$ can be increased by halide mixing, which can modify the electronic structure and the physical properties. Mixing neighbouring halides (Br-I, Br-Cl) alters the optical band gap with similar structure as in case of 2D $Cs_3Bi_2I_6Br_3$.[73] Whereas, mixing halides with larger variation of ionic radii (Cl-I) lead to a new 2D structure. $Cs_3Bi_2I_6Cl_3$ is the newest member of ⟨111⟩-oriented perovskites, which adopts the crystal structure similar to $Cs_3Bi_2Br_9$, where I atoms situated at the apical position and Cl atom at the bridging positions.[74] The presence of Cl atom at bridging positions leads to the structural transformation from 0D $Cs_3Bi_2I_9$ to 2D $Cs_3Bi_2I_6Cl_3$, as exemplified in Figure 1.3b.

The vacancy site of $A_3B_2X_9$ can be lowered to 25% by mixing bivalent cations, resulting in a ⟨111⟩-oriented triple-layered (n = 3) perovskite, $A_4[B^{2+}(B^{3+})_2]X_{12}$.[75] Solis-Ibarra's group reported triple layered ⟨111⟩-oriented perovskites, which is also the first mixed metal halide layered perovskites.[76] $Cs_4CuSb_2Cl_{12}$ crystallized in monoclinic crystal

system (space group *C*2/*m*), where the layered is formed by the alternative corner sharing $CuCl_6$ and $SbCl_6$ octahedra, as illustrated in Figure 1.3c. The structure is a stretched version of $Cs_3Sb_2Cl_9$, where $CuCl_6$ octahedra is introduced between the layers of $SbCl_6$.[76] Both the octahedra are distorted significantly with a large discrepancy in Cu-Cl axial and equatorial bond in $CuCl_6$ octahedra, which is characterized by the Jahn-Teller distortion of Cu^{2+} ions. Similarly, Mn^{2+} and Cd^{2+} can also stabilize this triple-layered ⟨111⟩-oriented perovskites.[77, 78] Recently, Solis-Ibarra's group have discovered a series of new ⟨111⟩-oriented layered perovskites viz., $Cs_4CdSb_2Cl_{12}$, $Rb_4MnSb_2Cl_{12}$, $Rb_4CuSb_2Cl_{12}$, $Cs_4MnBi_2Cl_{12}$, and $Cs_4CdBi_2Cl_{12}$ by combined theoretical and experimental methods.[79]

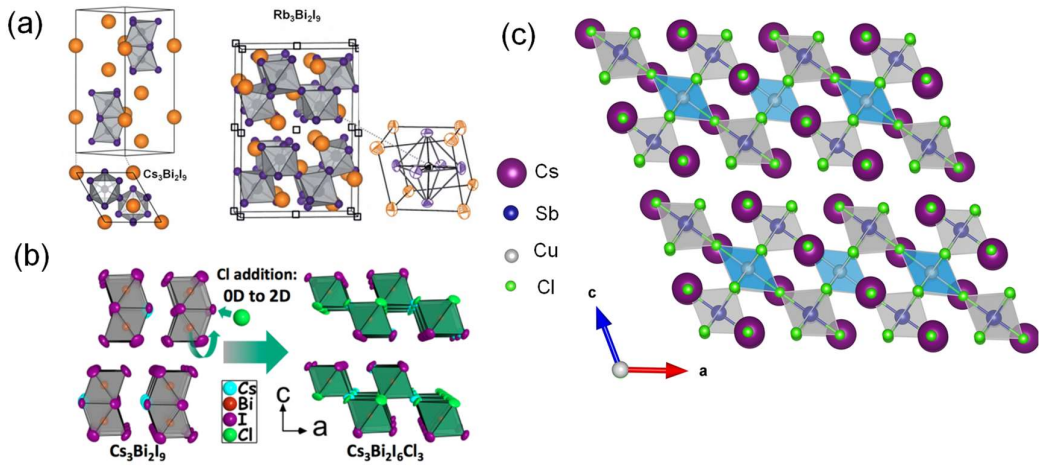

Figure 1.3. *(a) Crystal structures of 0D $Cs_3Bi_2I_9$ and 2D $Rb_3Bi_2I_9$. (b) Cl- addition to 0D $Cs_3Bi_2I_9$ leads to 2D $Cs_3Bi_2I_6Cl_3$ structure. (c) Crystal structures of $Cs_4CuSb_2Cl_{12}$ Reproduced from ref. 67 ©American Chemical Society for (a), and Reproduced from ref. 74 ©American Chemical Society for (b).*

Perovskite-like 2D structures

APb_2Br_5 (A = Cs, Rb) is often defined in the category of 2D perovskite-like structure, which crystalized in tetragonal phase (space group *I*4/*mcm*).[75] The crystal structure is generally described as the layered structure connected by the $[Pb_2Br_5]^-$ polyhedral, which are separated by the layers of A^+ ions, as shown in Figure 1.4. $CsPb_2Br_5$ is considered as thermodynamically stable structure than its 3D counterpart. The structure formation can be expressed

$$CsPbBr_3\ (3D) + PbBr_2 \rightarrow CsPb_2Br_5\ (2D)$$

This formation can be described as breaking of corner sharing $PbBr_6$ octahedrons along *c*-direction and formation of $PbBr_8$ capped-triangular prisms layer along *ab*-direction.[80, 81] $CsBi_3I_{10}$ is well-known layered structure, which is similar to the BiI_3 but these layers are partially broken between the layers due to the presence of Cs^+ similar to 0D $Cs_3Bi_2I_9$.[82-85] The crystal structure of $CsBi_3I_{10}$ classified as quasi-2D layered structure.

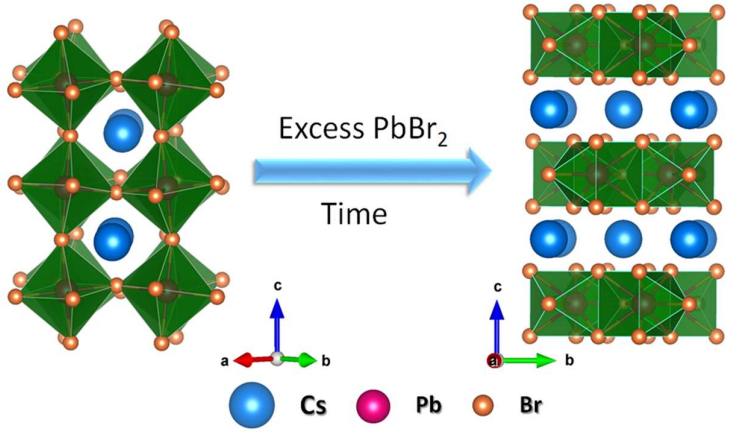

Figure 1.4. *(a) Transformation of orthorhombic $CsPbBr_3$ to tetragonal $CsPb_2Br_5$ crystal structures.*

Complex metal halides

$RbAg_4I_5$ is a well-known metal halide prototypical superionic conductor with very high ionic conductivity of ~ 0.2 S/cm at room temperature.[86] The room temperature superionic phase (α-phase) has a complex cubic crystal structure with four $RbAg_4I_5$ unit in the unit cell.[87-89] Three types of crystallographically nonequivalent sites are present for Ag^+: one eight-fold (Ag-c sites) and two 24-fold sets (Ag-I and Ag-II sites). The superionicity in $RbAg_4I_5$ arises from the fast diffusion of Ag^+ (diffusion coefficient ~ 10^{-6} $cm^2\ s^{-1}$) in a β-Mn type rigid iodide sublattice.[87-91] The iodide substructure contains 56 iodide tetrahedra in which 16 Ag^+ are randomly distributed in the interstitial positions. The tetrahedral framework is arranged in such a fashion that they create a network of passageways for the diffusions of Ag^+. The room temperature cubic α-phase of $RbAg_4I_5$ is preceded by

two structural phase transitions with decreasing temperature: a weakly first order α → β phase transition at 209 K and a first order β → γ phase transition at 121 K (Figure 1.5a).[88, 92-95] Remarkably, the iodide substructure remains almost intact, suffering only minor distortions to accommodate the partial ordering of Ag^+ at specific sites, across all these phase transitions.[88] The partial ordering of Ag^+ in the β phase restricts the movement of Ag^+ along the crystallographic *c*-axis, which decreases the ionic conductivity. Interestingly, Ag^+ remains partially disordered in the lowest temperature γ phase; however, the Ag^+ ionic diffusion occurs only within isolated clusters.[89]

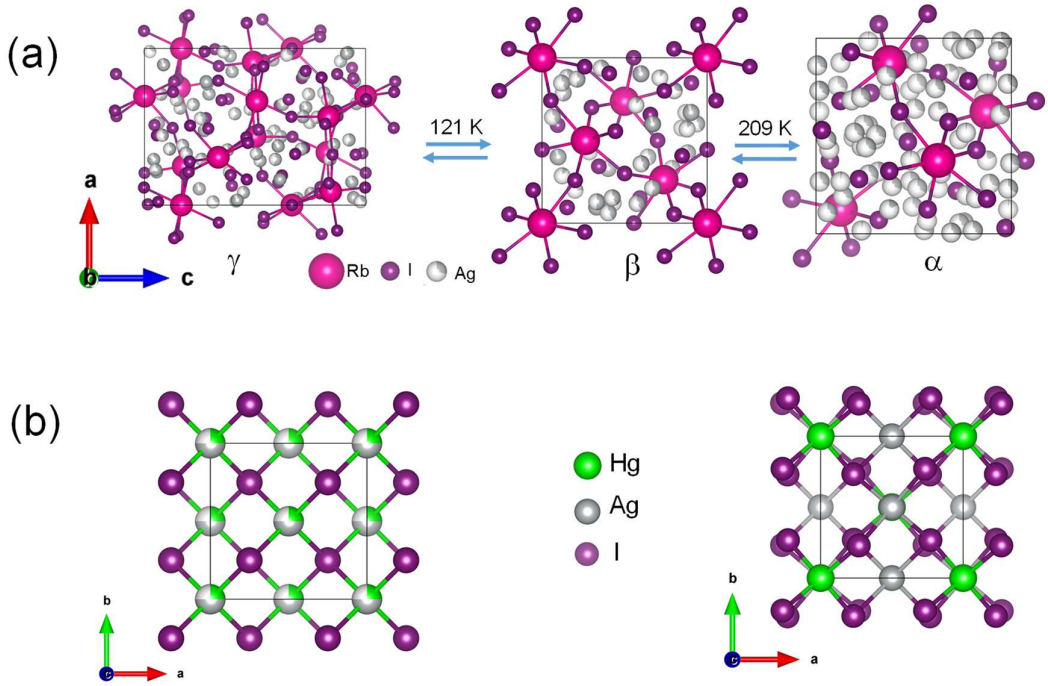

Figure 1.5. *(a) Crystal structure of $RbAg_4I_5$ at different temperature. (b) Crystal structure of α-Ag_2HgI_4 (left), and β -Ag_2HgI_4 (right).*

Another important class of complex metal halides is inorganic thermochromic materials (Ag_2HgI_4 and Cu_2HgI_4). β-Ag_2HgI_4 and β-Cu_2HgI_4 have a body-centered tetragonal crystal structure with space groups *I*-4 and *I*-42*m,* respectively, at ambient temperature, in which Hg and I form covalently bonded corner sharing tetrahedra at the corners as well as in the middle of the unit cell. Ag^+ cations occupy the tetrahedral voids

(Figure 1.5b).[96-98] These structures can be derived from chalcopyrite ($Cu_2Fe_2S_4$) by re-arranging four Ag/Cu and two Hg atoms over the eight cationic sites.[96] β-Ag_2HgI_4 further undergoes a phase transition from tetragonal to cubic structures at 50 °C where the cubic structure is of the disordered cubic zinc blend type (space group; *F4-3m*).[96, 99] In the cubic phase, the cations (Hg^{2+} and Ag^{+}) randomly occupy the tetrahedral voids within an anionic (I^{-}) rigid face centered cubic sublattice (Figure 1.5b).[96] The rapid hopping of the Ag^{+} within these tetrahedral voids enables this α-cubic to show superionicity at high temperatures. On the other hand, Cu_2HgI_4 also exhibits equivalent cubic crystal structure above 70 °C. They are isomorphous in nature, and the formation of the solid solution is preferred due to the similar lattice constant.[100]

1.1.2 Synthesis

This section has discussed the development of the foremost synthetic approach of metal halides.

Solution-based synthesis and chemical transformation

In view of the quantum confinement effect and higher exciton binding energy of 2D all-inorganic perovskite halides, substantial attempts have been dedicated toward synthesizing all-inorganic 2D perovskites in the last few years. Till date, two well-known procedures are consistently implemented to prepare perovskite nanostructures, a) the hot-injection[101] and b) the ligand-assisted reprecipitation (LARP) or anti-solvent recrystallization approaches.[102] These processes typically involve the dissolution of precursor salts at a specific stoichiometric ratio in a suitable solvent followed by induced crystallizations. In the hot-injection method, the pre-heated cation precursor (e.g. Cs-oleate) is swiftly injected into the pre-dissolved precursor salts in an organic solvent (e.g. 1-octadecene, ODE) containing the capping ligands [e.g. oleic acid (OA), oleylamine (OAm) etc.] at elevated temperature.[1] In contrast, the LARP or anti-solvent recrystallization method involves the dissolution of precursor salts in polar solvents [e.g. *N,N*-dimethylformamide (DMF), dimethyl sulfoxide (DMSO) etc.] and its subsequent injection into an immiscible or anti-solvent (e.g. toluene, hexane etc.) containing the ligands under vigorous stirring at room temperature.[103] The schemes of two representative

synthetic methods implemented for the preparation of perovskite nanostructures are displayed in Figures 1.6a-b.

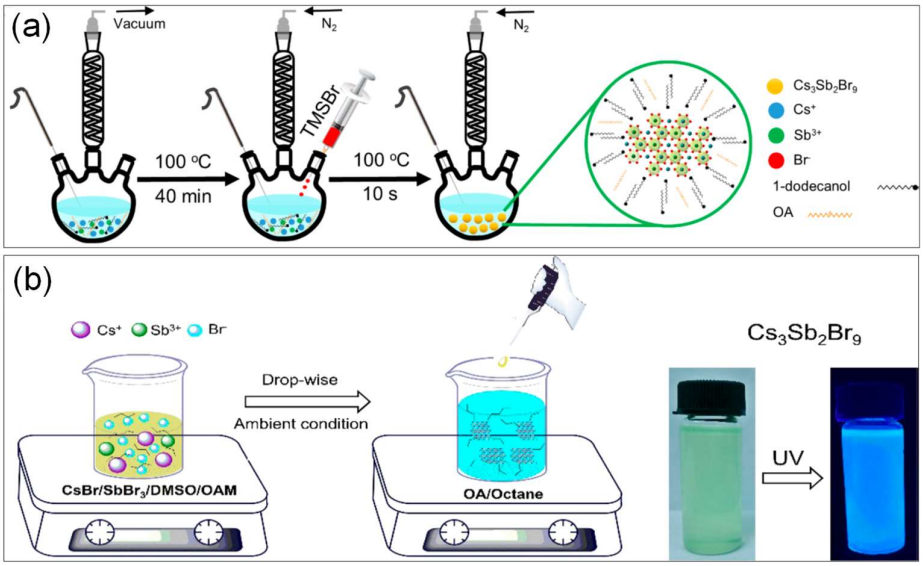

Figure 1.6. *(a) Schematic representation of the reaction system and the hot-injection synthetic route for $Cs_3Sb_2Br_9$ nanocrystals (NCs) in 1-dodecanol solvent by injecting trimethylsilyl bromide (TMSBr) as halide precursor. (b) Schematic representation of the reaction system for modified ligand-assisted reprecipitation (m-LARP) approach for the synthesis of $Cs_3Sb_2Br_9$ quantum dots (QDs). Representative images of a colloidal $Cs_3Sb_2Br_9$ QD solution with and without 365 nm UV light excitation. Reproduced from ref. 102 ©American Chemical Society for (a) and Reproduced from ref. 101 ©American Chemical Society for (b).*

In 2017, Nag and co-workers[104] reported the first colloidal synthesis of 2D $Cs_3Sb_2I_9$ and $Rb_3Sb_2I_9$ by the hot-injection approach. The $Cs_3Sb_2I_9$ nanocrystals (NCs) were synthesized by rapidly injecting the pre-heated (at 100 ^{0}C) Cs-oleate precursor solution into a reaction mixture containing Sb precursor salt, octanoic acid, OAm, and ODE at two different temperatures (i.e., 180 ^{0}C and 230 ^{0}C). The final product was collected by quenching the reaction mixture in an ice bath followed by centrifugation. The morphology of the $Cs_3Sb_2I_9$ NCs was altered by changing the reaction temperatures. At 180 ^{0}C, the orange-coloured nanoplatelet (NPL)-type morphology was formed with an average length of 27 ± 3 nm and a breadth of 14 ± 3 nm. In contrast, the red-colored nanorods (NRs) were achieved at 230 ^{0}C with an average length and diameter of 655 ±

20 nm and 46 ± 4 nm, respectively. The schematic depiction of the morphology tuning as a function of the reaction temperature is presented in Figure 1.7a. For the synthesis of $Rb_3Sb_2I_9$ NCs, a similar procedure was implemented using Rb-oleate precursor solution, in which a nearly spherical-type morphology was attained with an average diameter of 7.5 ± 2 nm and 17 ± 3 nm at 180 ^{0}C and 230 ^{0}C, respectively. The representative TEM image has been shown in Figure 1.7b. Afterward, Nag and co-workers synthesized the colloidal NCs of $A_3Bi_2I_9$ (A = Cs, Rb) by implementing the hot-injection scheme.[65]

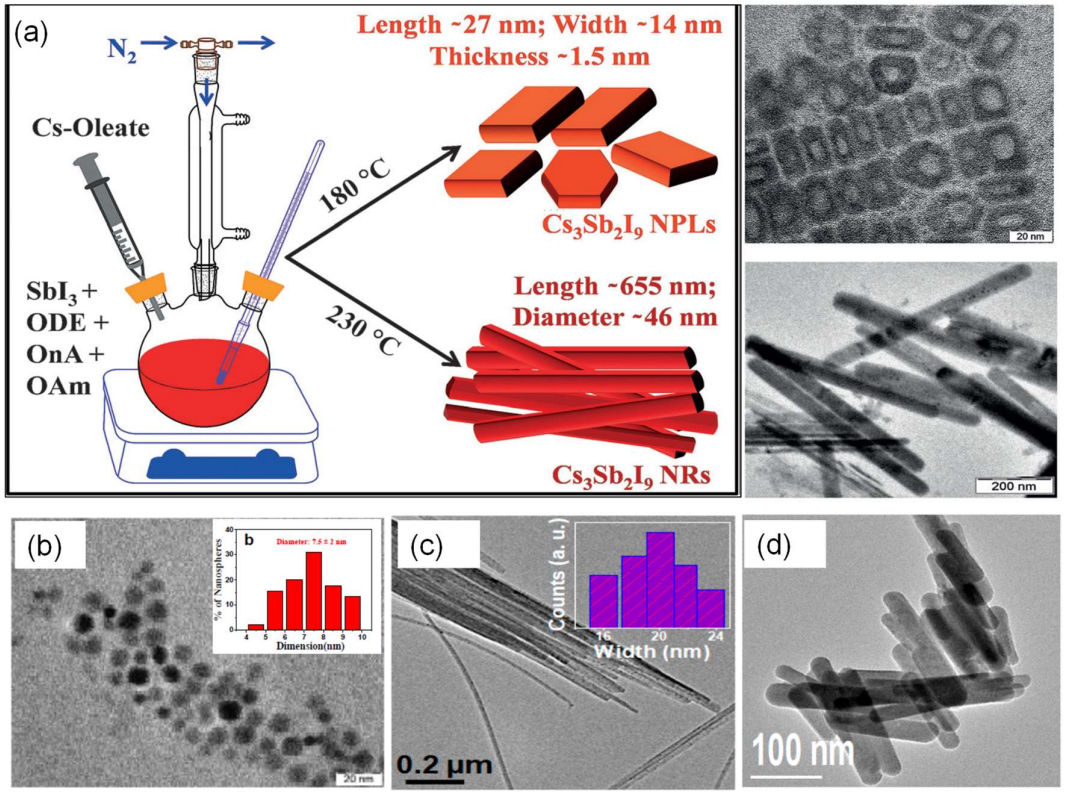

Figure 1.7. *(a) Schematic representations of the synthesis of $Cs_3Sb_2I_9$ nanoplatelets (NPLs) and nanorods (NRs). ODE = 1-octadecene, OnA = octanoic acid, OAm = oleylamine. TEM images of (b) $Rb_3Sb_2I_9$ nanocrystals (NCs) with size distribution histogram, (c) $Cs_3Sb_2Cl_9$ nanowires (NWs) with width distribution histogram, (d) $Cs_3Sb_2Cl_9$ nanorods (NRs), Reproduced from ref. 104 ©Wiley-VCH for (a, b), Reproduced from ref. 105 ©American Chemical Society for (c, d),*

The Cs-oleate or Rb-oleate precursor solution was injected into the Bi-precursor solution in ODE at 180 ^{0}C that also comprised OA and OAm. Finally, isopropanol was used as an

anti-solvent to precipitate the desired NCs with an estimated yield of 60-70%. A quasi-spherical type of morphology was obtained with an average diameter of 5 ± 1 nm and 4.5 ± 1 nm for $Cs_3Bi_2I_9$ and $Rb_3Bi_2I_9$ NCs, respectively. In the same year, Acharya and co-workers synthesized uniform $Cs_3Sb_2Cl_9$ nanowires (NWs).[105] In this reaction scheme, Cs-oleate was swiftly added in a solution of $SbCl_3$ in ODE containing a mixture of capping ligands, OA and hexadecylammonium chloride (HDA·HCl) under N_2 atmosphere at 170 °C. The NWs was collected after addition of *t*-butanol in the reaction flask, followed by the centrifugation, which had a length of 3.4 ± 0.6 μm and a diameter of ~20 ±6 nm. Interestingly, the $Cs_3Sb_2Cl_9$ NRs with an average length and diameter of 165 ± 12 and 20 ± 5 nm, respectively were obtained by the same reaction conditions of NWs, apart from the use of OAm instead of hexadecylamine (HDA). The TEM images of $Cs_3Sb_2Cl_9$ NWs and NRs have been exemplified in Figures 1.7c,d.

Balakrishnan and Kamat have reported ligand (i.e., dodecyl dimethylammonium bromide, DDAB) induced chemical transformation of 2D NSs of $CsPb_2Br_5$ from cubic $CsPbBr_3$ NCs.[106] The reaction scheme is directed through the formation of stable $[Pb_2Br_5]^-$ from the initial $[PbBr_3]^-$ complex after the addition of DDAB in pre-synthesized $CsPbBr_3$ NCs, which is shown below:

$$nCsPbBr_3 + DDA^+ \rightarrow (n-x)CsPbBr_3 + xDDA^+[PbBr_3]^- + xCs^+$$

$$2xDDA^+[PbBr_3]^- + xCs^+ \rightarrow x[CsPb_2Br_5] + xDDA^+Br^- + xDDA^+$$

Zhang et al. synthesized brightly luminescent $Cs_3Sb_2Br_9$ QDs at room temperature (RT) using a modified LARP approach.[101] In a representative synthesis route, DMF or DMSO was utilized as "good" solvent to dissolve the CsBr, $SbBr_3$ and OAm, forming a clear precursor solution. Subsequently, a fixed amount of precursor solution was dropped under vigorous stirring into a solution of octane and OA, which recognized as "poor" solvent for the precursor ions. Figure 1.6b shows the schematic illustrations of the LARP technique employed for the synthesis of $Cs_3Sb_2Br_9$ QDs along with the optical images of the as-synthesized solution with and without UV light irradiation. A highly supersaturated state was achieved instantaneously and prompted fast recrystallization. This method was successfully established to produce QDs with an average diameter of 3.07 ± 0.6 nm. In

the same year, Yang et al. reported a facile method to synthesize $Cs_3Bi_2X_9$ (X = Cl, Br, I) NCs at RT.[107] A fixed amount of CsX and BiX_3 at a molar ratio of 3:2 was dissolved in DMSO and subsequently added dropwise into either toluene (for $Cs_3Bi_2I_9$) or isopropanol (for $Cs_3Bi_2Br_9$) or acetone (for $Cs_3Bi_2Cl_9$) under vigorous stirring. For the fabrication of OA-capped NCs, a certain amount of precursor solution was injected into the mixed solution of isopropanol and OA. A quasi-spherical shape with an average diameter of 6 nm was achieved for the $Cs_3Bi_2Br_9$ NCs. Afterward, the synthesis of $Cs_3Bi_2Br_9$ QDs was accompanied by initially dissolving CsBr and $BiBr_3$ in DMSO with the addition of OAm. Then, the controlled crystallization of QDs was successfully achieved by the drop wise addition of the precursor solution into the mixed solution of antisolvent, ethanol and OA. For comparison, toluene was also used as the antisolvent, however, the as-synthesized QDs in toluene was not stable in ambient conditions. An average diameter of 3.88 nm was accomplished for the $Cs_3Bi_2Br_9$ QDs.[108]

The anti-solvent recrystallization strategy was implemented by our group to synthesize micrometer-sized particles of $Cs_2PbI_2Cl_2$, where the precursor solution of CsI and $PbCl_2$ (2:1 molar ratio) in mixed solvents of DMF and DMSO (2:1, v/v) was injected into toluene under vigorous stirring.[109]

Solid-state synthesis

Solid-state reaction is a common synthesis method to obtain polycrystalline and single crystalline material from solid reagents. For the reaction to occur usually a very high temperature is employed. Factors that affect solid-state reaction are chemical and morphological properties of the reagents including the reactivity, surface area, and free energy change with the solid-state reaction, and other reaction conditions, such as the temperature, pressure, and the environment of the reaction. The advantage of solid-state reaction method includes the simplicity and large-scale production.[110]

Metal halides and chalcogenides known to date have been synthesized by sealed-tube reactions in vacuum (10^{-3} - 10^{-5} Torr) at high-temperature. In high temperature vacuum sealed tube melting reaction, appropriate quantities of starting materials (mostly in their elemental form) are heated above the melting point of the desired product in absence of air, followed by cooling of the subsequent reaction mixture at a specific

cooling speed depending upon material's nature (congruent/incongruent). Products of the reactions are generally thermodynamically stable polycrystalline or single-crystalline ingots.

For single and highly oriented crystals, one of the common approaches is to use the vertical Bridgman technique.[111] The core principle behind the Bridgman method is the directional solidifying of the compounds by translating the compound from a hot zone where it has been kept above the melting temperature to a cold zone of the furnace, which is below the melting temperature of the compound. Initially, the polycrystalline material in high vacuum-sealed ampoule is melted fully in the hot zone and then slowly translated towards the cold zone with a speed of ~1 mm/hr. Single crystal generally starts to grow along a certain direction once it starts to solidify from the pointed portion of the tapered ampoule. Sometimes a seed of the single crystal with a specific orientation is kept at the bottom of the crucible from where the crystal growth starts.

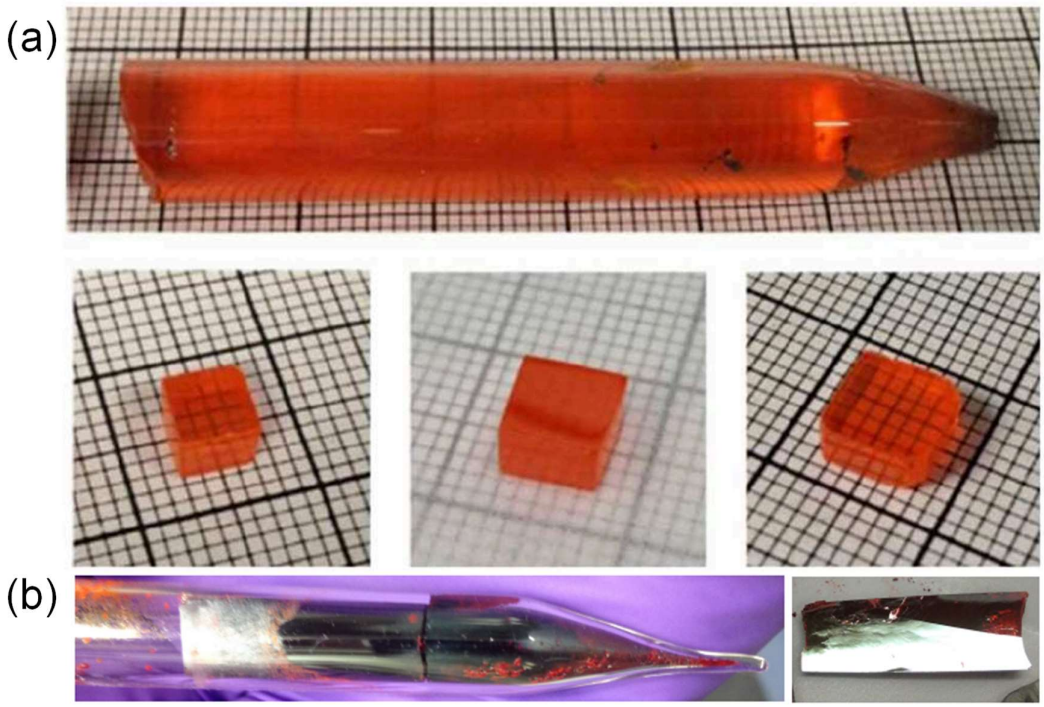

Figure 1.8. *Bridgman method grown (a) $CsPbBr_3$ and (b) $Cs_3Bi_2I_6Cl_3$ single crystal. Reproduced from Ref. 114 ©Nature Publishing Group for (a). Reproduced from ref. 74 ©American Chemical Society for (b).*

Halide perovskite single crystal was first grown by gradually cooling the temperature of saturated solution from the aqueous acid solution.[112] In the crystallization process, slowing down the cooling rate normally leads to larger single crystals with fewer seed crystals and higher quality single crystals with fewer defects, which enables larger crystals dimensional sizes, smoother morphology, and better optoelectronic performance.[113] Similar to the controlled cooling processes, perovskite single crystals can also be grown from all-solid raw materials by the traditional high temperature Bridgman method.[56, 74] Despite the long amount of time and high energy consumption involved, raising temperature above solid's melting point is suitable for raw materials with low solubility, like all-inorganic perovskite. This method was always used to grow large-sized $CsPbBr_3$ (Figure 1.8a),[114] $Cs_2PbI_2Cl_2$,[56, 115] and $Cs_3Bi_2I_6Cl_3$[74] (Figure 1.8b) single crystals. My thesis involves the use of both furnace melting and Bridgman technique for material synthesis.

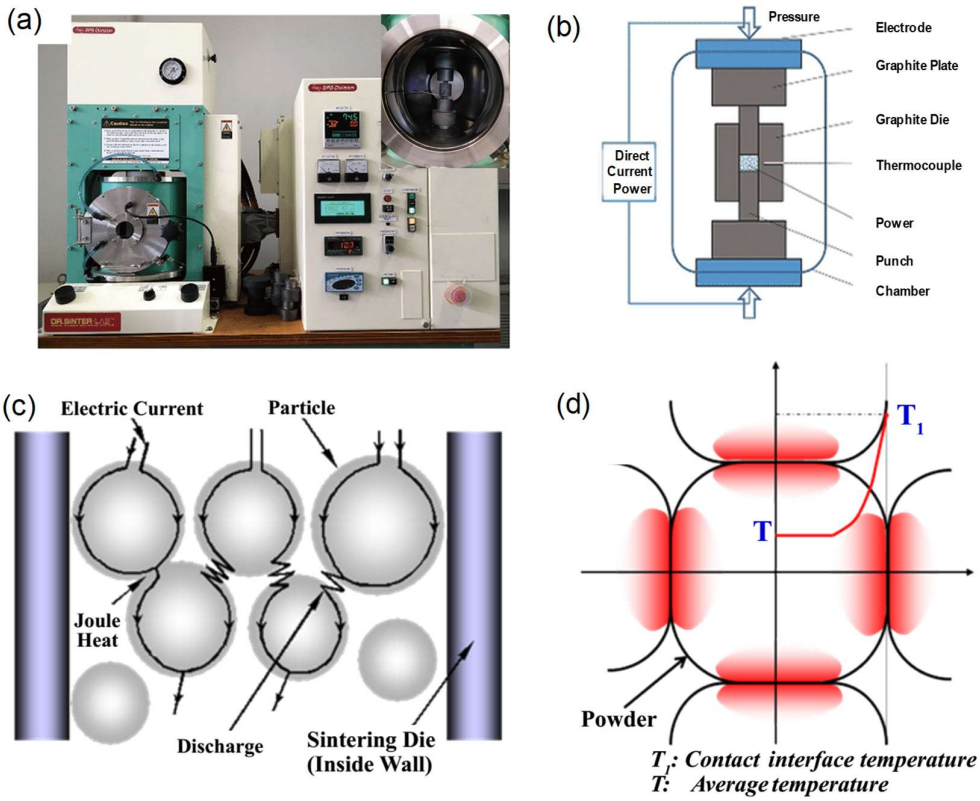

Figure 1.9. *(a) Photograph of SPS-211Lx instrument. The inset image shows sitering chamber. (b) Schematic illustration of a spark plasma sintering equipment.*

(c) Possible electric current path through powder particles inside the die. (d) The temperature image on powder particles surface. Contact surface temperature (T_1) differs significantly from average temperature (T).[116]

The Spark plasma sintering (SPS) is a newly developed technique for the syntheses and processing of thermoelectric materials employing ON-OFF pulse DC voltage/ current (Figure 1.9).[116-118] This is considered an energy-saving sintering technology due to its short processing time and small number of processing steps. The SPS process is based on the electrical spark discharge phenomenon. Application of high energy, low voltage spark pulse (spark discharge) momentarily produces a local high-temperature state (several to ten thousand degrees) in the gap between the particles of material *via* Joule heating (Figure 1.9c, d). This results in vaporization and melting of the powder particles' surfaces and the formation of constricted shapes or "necks" around the contact area between the particles. These constricted shapes gradually develop and plastic transformation progresses during sintering, resulting in a sintered material with density of ≥ 97%. By application of voltage and current repeatedly with this ON-OFF, the discharge point and the Joule heating point (locally high-temperature generation field) move throughout the sample, resulting in less power consumption and efficient sintering. Since only the surface temperature of the particles rises rapidly by self-heating, particle growth of the starting powder materials is controlled. Therefore, a precision sintered compact is manufactured in a shorter time. At the same time, bulk fabrication of particles with an amorphous structure and crystalline nanostructure formation are now possible without changing their characteristics. Vaporization, melting, and sintering are completed in short periods of approximately 5-20 minutes, including temperature rise and holding times.

In order to prepare high performance thermoelectric materials, spark plasma sintering (SPS) of the melt grown ingots in SPS-211Lx, Fuji Electronic Industrial Co., Ltd (Figure 1.9a). The SPS process and geometrical configuration of the punches, mould and powder are illustrated in Figure 1.9. Powders to be consolidated, are placed in a die and heated by applying the electric current. The melt grown ingots were first ground into fine powders using a mortar and pestle to reduce the grains size in an inert glove box. This powder was then pressed into cylindrical shape by SPS method (SPS-211Lx, Fuji

Electronic Industrial Co., Ltd.) at specific temperature and pressure under vacuum (Figure 1.9a). Highly dense (≥ 98% of theoretical density) disk-shaped pellets with ~ 10 mm diameter and ~ 10 mm thickness were obtained.

Solid-state mechanochemical synthesis has appeared as an innovative way for the synthesis of metal halides, which holds several advantages over the solution-phase synthesis methods, such as intrinsically reduced toxicity by overcoming the use of organic solvents along with the rapidity, reproducibility, and improved control over the stoichiometry of final products.[119] Biswas' group[120] first executed the mechanochemical synthesis to prepare a scalable quantity of bulk powder of $CsPb_2Br_5$ and $CsPb_2Cl_5$ with 2D crystal structures.[120] In this method, an appropriate molar ratio of the starting precursors were mixed and ground mechanically in a mortar and pestle in a N_2-filled glove bag for 2 hours. The post-synthetic transformations of $CsPbBr_3$ to $CsPb_2Br_5$ was also achieved by the solid-state mechanochemical grinding with requisite quantity of $CsPbBr_3$ with $PbBr_2$.[120] Later on, our group,[109, 121] Singhal et al.,[122] and Ajjouri et al.[123] executed this method to synthesize a series of 2D materials, for example, $Cs_3Bi_2I_9$, $Cs_2PbI_2Cl_2$, $Cs_4CuSb_2Cl_{12}$, and $A_3Bi_2X_9$ ($A = K^+, Rb^+, Cs^+$; $X = I^-, Br^-, Cl^-$), respectively. Solis-Ibarra and co-workers also synthesized several <111>-oriented layered double perovskites ($Cs_4CdSb_2Cl_{12}$, $Rb_4MnSb_2Cl_{12}$, $Rb_4CuSb_2Cl_{12}$, $Cs_4MnBi_2Cl_{12}$, $Cs_4CdBi_2Cl_{12}$, and $Cs_4Mn_{1-x}Cu_xSb_2Cl_{12}$, x = 0-1) by precipitating from the solution of corresponding metal halides and metal oxides in hot concentrated hydrohalic acid.[77, 79] Recently, Cai et al. reported the colloidal synthesis of $Cs_4CuSb_2Cl_{12}$ NCs for the first time by hot-injection route with average diameter of ~ 12.5 nm.[124]

1.1.3 Optical properties

Recently, 2D layered halide perovskites have received enormous attention thanks to their fascinating optical properties, such as band tunability, emission line-width, bright color emission, PLQY, photostability, and excitonic features,[41, 125] which are beneficial for optoelectronic applications. In this chapter, we highlight the recent progress associated with the optical properties of metal halides.

Kanatzidis and co-workers first synthesized a 2D layered RP phase of all-inorganic $Cs_2PbI_2Cl_2$.[56] The bulk $Cs_2PbI_2Cl_2$ revealed a sharp absorption edge at 3.04 eV

with a small kink like feature, which mainly ascribed to an excitonic absorption. From the temperature-dependent PL study, a broad PL emission was appeared with decreasing the temperature and associated with the self-trapped excited state. Afterward, Manna and co-workers synthesized the NCs of $Cs_2PbI_2Cl_2$, which exhibited a narrow excitonic absorption around 400 nm (~3.1 eV).[126] A considerably broad PL was evidenced for the as-synthesized NCs with a weak PL quantum yield. At the same time, Kanatzidis and co-workers focused their attention to the development of Pb-free all-inorganic perovskites with low-dimensional structures.[57] 2D RP phase of $Cs_2SnCl_2I_2$ was also synthesized, which showed a direct band gap of 2.62 eV. Additionally, a series of $Cs_{4-x}Rb_xSn_3Cl_8I_2$ solid solutions (where, x = 0→2) displayed similar band gap behaviours, signifying unperturbed impact of cation mixing (Cs/Rb) on the band gaps.[57] An emission near to the band edge of $Cs_2SnCl_2I_2$ was identified at around 510 nm. Recently, Kovalenko and co-workers synthesized a new Pb-free material, $Cs_8Sn_6Br_{13}I_7$ in the form of orange needles, which showed an optical band edge of 2.23 eV.[127]

Recently, a layer-dependent band gap of all-inorganic RP phases (for example, $Cs_2PbI_2Cl_2$, $Cs_2SnCl_2I_2$, and Cs_2PbI_4) was calculated theoretically.[128, 129] With increasing the number of layers, the estimated band gaps were reduced. These 2D RP phases displayed strong anisotropic absorption features. Moreover, the theoretically estimated exciton-binding energy of monolayer of 2D Cs_2PbI_4 was found to be larger (181.70 meV) than that of conventional 3D $CsPbI_3$ (59.12 meV). Later on, it was verified that the RP phase of Cs_2PbX_4 was unstable and challenging to attain the pure phase during solid-state synthesis.[56]

The UV-Vis spectrum of single crystals of layered $CsPb_2Br_5$ exhibited only one absorption edge at 370 nm with an estimated band gap of 3.35 eV.[130] The colloidal suspension of 2D $CsPb_2Br_5$ nanoplatelets exhibited a sharp excitonic peak in absorption spectrum, which displayed green light emission under irradiation of 365 nm UV light. The nanoplatelets solution of $CsPb_2Br_5$ was characterized by a symmetric PL emission peak at 512 nm with a narrow line width of 12 nm and the absolute PL quantum yield (PLQY) of ~87% in toluene solution.[131] The PL emission of as-synthesized nanoplatelets with halide mixing (i.e., $CsPb_2Br_{5-x}Cl_x$ or $CsPb_2Br_{5-x}I_x$) exhibited narrow and bright emission color from blue to red and successfully covered the entire visible spectral

regions, as shown in Figure 1.10a. Further, Figure 1.10b reveals the color alteration of colloidal suspension with the gradual halide exchange from Br-to-Cl and Br-to-I, respectively in $CsPb_2Br_5$. A range of 20-90% of PLQY was obtained for the halide-exchanged NPLs solutions.[131] Subsequently, Tang et al. synthesized $CsPb_2Br_5$ microplates with a narrow PL line width of 20 nm, where the emission peak centered at ~528 nm.[132] Later on, the optical properties of NWs and NSs of $CsPb_2Br_5$ was reported by Ruan et al.[133] The absorption peaks of NWs and NSs were found at ~512 and 515 nm with the PL emission peaks centered at 525 and 529 nm, respectively. Interestingly, the PLQY of NWs (~9.9%) was found to be higher than the NSs (~1.0%) at an excitation wavelength of 450 nm. The scalable quantity of $CsPb_2Br_5$ and $CsPb_2Cl_5$ bulk powders was also synthesized by our group,[120] which showed an optical band edges at 537 nm (2.30 eV) and 418 nm (2.97 eV), respectively. Solid-state PL spectra of $CsPb_2Br_5$ showed band edge emission at 540 nm with a low energy peak at 590 nm, whereas a band edge emission at 446 nm was evidenced for $CsPb_2Cl_5$ associated with a low intense additional lower energy peak appears at ~500 nm.[120]

Bi (III) and Sb (III) were implemented to replace Pb in 3D halide perovskite, which formed low-dimensional $A_3B_2X_9$-type of stoichiometry due to their higher oxidation state. These materials with reduced dimensions exhibited intriguing optical properties. In 2015, Seshadri and co-workers explored the optical band gaps of several Bi-based halides, $A_3Bi_2I_9$ (A = K, Rb, Cs).[67] The experimental band edges were found at ~2 eV for all three materials. The steepness of absorption edge was greater for the layered structures ($A_3Bi_2I_9$, A = K, Rb) than that of $Cs_3Bi_2I_9$ structure having isolated anions. The calculated band structures also revealed the direct band gap for the layered Rb and K-based ternary bismuth iodides, whereas $Cs_3Bi_2I_9$ showed an indirect band gap. However, a previous report established a relationship between the estimated band gap of several $A_3B_2X_9$ materials (A = K, Rb, Cs; B = Bi, Sb; X = Br, I) and their melting point (T_m), and average atomic number (Z_{av}).[134] Recently, Creutz et al. reported the layered and dimer

modifications of $Cs_3Bi_2I_9$, in which the dimer modification has lower extinction coefficient compared to the layered form in the visible range.[135]

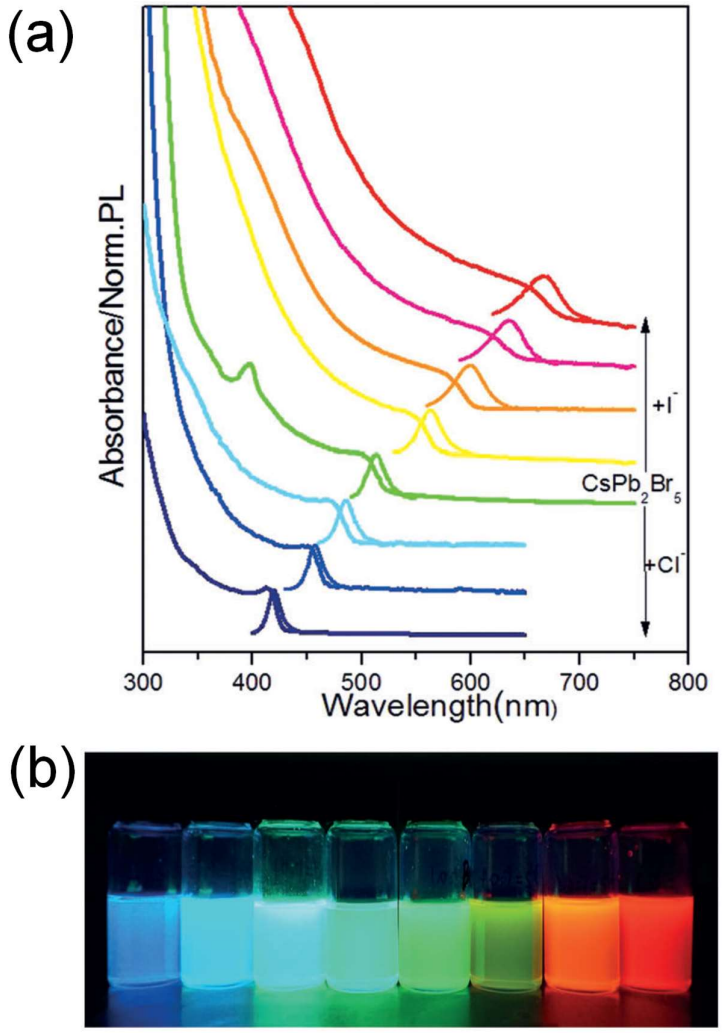

Figure 1.10. *(a) Evolution of the optical absorption (left) and photoluminescence, PL (right) spectra of $CsPb_2Br_5$ nanoplatelets with increasing quantities of anion-exchange of I^- and Cl^-, respectively. (b) Photograph of $CsPb_2Br_5$ nanoplatelets under the irradiation of a 365 nm UV lamp. Reproduced from ref. 131 ©Wiley-VCH for (a, b).*

The absorption peak was appeared at 550 nm with a sharp band edge in layered $Cs_3Bi_2I_9$, while it was blue-shifted to 492 nm in case of the dimer modification with a broad inclined tail. The band dispersion and bonding character of these materials were discussed from

the DFT calculations, which exhibited a predominant contribution of halide np and Bi 6s orbitals to the valence-band maxima, and the conduction-band minima originated from the Bi 6p orbitals. The theoretical calculations predicted a considerably smaller bandgap of layered polymorph (~1.9 eV) compared to its dimer analogue (~2.3 eV), which corroborated well with the experimental observations. Although no PL emission from $Cs_3Bi_2I_9$ was detected at room temperature; at cryogenic temperature of 5 K, the emission was successfully perceived, in which the two structural polymorphs showed markedly diverse emission spectra. The layered polymorph displayed a reasonably sharp emission peak at 605 nm (~2.05 eV) with a line width of ~ 85 meV. Conversely, a broad PL emission centered at 643 nm (~1.93 eV) with a line width of ~ 200 meV was detected for the dimer polymorph.[135]

Interestingly, for the 0D dimer structure of colloidal $Cs_3Bi_2I_9$ NCs, a dual emission peak at 2.66 and 2.28 eV was evidenced, which was originated from the de-excitation through the electronic band gap and from the excitonic emission, respectively.[65] On the contrary, the as-synthesized colloidal NCs of $Rb_3Bi_2I_9$ with 2D layered structure did not display any quantifiable PL at room temperature due to the presence of the deep defect states in the band-gap region. Liang et al. reported a material with composition of $CsBi_3I_{10}$, which possessed a layered crystal structure.[83] A high absorption coefficient of $\sim 10^5$ cm^{-1} in visible light and an appropriate direct optical bandgap of 1.78 eV were obtained for $CsBi_3I_{10}$ thin film, which has potential as light absorber in solar cells.

Recently Seshadri's group witnessed a dramatic variations in the optical properties for the solid solution of $Cs_3Bi_2(Cl_{1-x}I_x)_9$.[136] A shift of absorption edges toward the lower energy associated with the peak widening was evidenced with increase in the occupancy of I atoms, which was further supported by the observed color changes from yellow to orange.

In order to gain an in-depth insight into the optical properties of halide perovskites at the single particle level, advanced spectroscopic techniques, such as super-resolution fluorescence microscopy is extensively employed earlier for microcrystals and NCs of 3D halide perovskites.[4] The PL intermittency with time, i.e., random discrete jumps in intensity between bright (ON) and dark (OFF) levels, is termed as "blinking" or "flickering", which existed owing to the repetitive recombinations of photogenerated

charge carriers or excitons through radiative and non-radiative pathways.[137-141] Figure 1.11a represents PL flickering and blinking of single $CsPbBr_3$ perovskite nanocrystals. The blinking behaviour of pure $CsPbBr_3$ and mixed $CsPbBr_3$/CdS systems has been shown in Figures 1.11b-c, in which pure $CsPbBr_3$ QDs spend most of their time in low-emissivity OFF state and show only short bursts toward high-emissivity ON state. This single particle PL studies also suitable to disclose the photostability and photooxidation of perovskites under investigation. At present, such studies are mostly limited to 3D Pb-based halide perovskites. However, the recent emergence of 2D Pb-free perovskites and their fascinating optical properties prompted us to investigate the PL blinking properties in various nanostructures of all-inorganic halide perovskites.

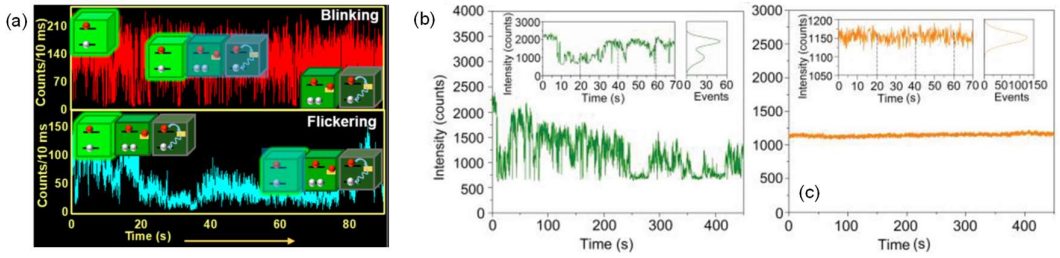

Figure 1.11. *(a) Photoluminescence flickering and blinking of single $CsPbBr_3$ perovskite nanocrystals. (b-c) Blinking behavior of pure $CsPbBr_3$ and obtained $CsPbBr_3$/CdS. b) pure $CsPbBr_3$ QDs spend most of their time in low-emissivity OFF state and show only short bursts toward high-emissivity ON state and have formed "blinking" phenomenon of QDs. c) $CsPbBr_3$/CdS QDs exhibit a distinct nonblinking feature and keep ON state nearly 450 s with no twinkle state. The insets in (b) and (c) show the PL intensity time trace in 70 s and PL intensity distribution of pure $CsPbBr_3$ (green curve) and $CsPbBr_3$/CdS (orange curve), respectively, indicating the ON and OFF states. Reproduced from ref. 137 ©American Chemical Society for(a), Reproduced from ref. 141 ©Wiley-VCH for (b, c),*

1.1.4. Thermochromic properties

Thermochromism is the reversible change in the color of a compound when it is heated or cooled. For inorganic compounds this transition is most often due to a change in

crystalline phase, to a change in ligand geometry, or to a change in number of molecules of solvent in the coordination sphere.[142]

In the first systematic investigation of thermochromism (1871), Houston examined a number of solids by heating them on copper strips over a Bunsen burner and reported only those compounds whose color change was fully reversible.[143] Red or reddish compounds which darkened or turned black were copper ferrocyanide, antimony sulfide, iron oxide, copper iodide, mercury sulfide, lead chromate, lead oxide, and potassium dichromate; orange compounds which turned to red or dark red were arsenic sulfide, mercury oxide, lead iodide, ferric oxalate; yellow compounds which turned to orange or orange-red were mercury sulfate, barium chromate, stannic sulfide, and arsenic sulfide; green compounds included silver iodide, which turned yellow then orange, and iodide of mercury, which changed to orange then red then brownish red. Not entirely reversible changes were those of zinc oxide, which turned a light yellowish green, and tin oxide, which went from white to green and even to orange and red-orange, returning on cooling to a greenish white.

The structure of Ag_2HgI_4 has been studied as a function of temperature by means of X-ray diffraction, specific heat measurements, and determinations of electrical conductivity as well as by magnetic susceptibility and by visual color changes. The variation in these properties may be correlated with the thermochromic color transitions. Ketelaar[24] has found the low-temperature (β) forms of both Ag_2HgI_4 and Cu_2HgI_4 to be isomorphous and tetragonal (pseudo-cubic) and the α modifications to be cubic. Silver and mercury can occupy the same lattice points, but not all the lattice points are occupied. The silver ions are much more mobile than the mercury ions. Specific heats begin to show anomalies at 37° C though the phase transition from the β to the α form is reported at 50.7 ± 0.2° C. Ketelaar proposes that a continuous order-disorder transition occurs over a considerable range of temperature.[24] Electrical conductivity begins to increase rapidly at about 40° C. Diffuse reflectance spectroscopy (DRS) has been used to measure the thermochromic transition temperature of Cu_2HgI_4, Ag_2HgI_4, and AgI.

Table 1.1. *Metal halide thermochromic compounds*[143]

Compounds	Transition temperature (°C)	Colour change on heating
HgI_2	127	red to yellow
AgI	147	yellow to red brown
Ag_2HgI_4	50.7	yellow to orange
Cu_2HgI_4	71	red to brown black
Tl_2HgI_4	116.5	orange to red

Ag_2HgI_4 turns red as the temperature is increased from 25 to 155° C. The color change is most pronounced from 25 to 55° C, but darkening continues as the temperature is increased. Similarly for Cu_2HgI_4, the color change is from red to black in the 25-85° C interval.

Measurements of the magnetic susceptibility of Cu_2Hgl_4, Ag_2HgI_4, and Tl_2HgI_4 show no discontinuity in magnetic properties at the thermochromic transition temperature.[144] This is consistent with an order-disorder mechanism involving a motion of metal ions during a continuous transformation process, with no change in electron configuration. Measurements of electrical conductivity of Ag_2HgI_4, Cu_2HgI_4, and their eutectoid show a sharp increase in conductivity at the transition point between the β and α structures corresponding to the thermochromic color changes.[143]

Recently, Hybrid halide perovskites exhibits thermochromic behaviour.[145] The yellow color of hybrid perovskites heated to a different temperature to observe the chromatic variation (Figure 1.12a). The color of the thermochromic ink changes from yellow to orange when the temperature reaches 60 °C. In these conditions, the solubility changes together with the initial formation of a fine precipitate. The second chromatic variation from orange to bright red occurs when the temperature is increased further to 90 °C. Finally, when the temperature reaches 120 °C, the color of the mixture turns gradually from dark red to black. To investigate the optical properties of the perovskite

inks, three mixtures were heated to different temperatures (60, 90, and 120 °C) and the colored powders were filtered and collected. Figure 1.12b shows the absorption spectra of the powders. The extrapolated edges of absorption spectra are 597 nm for the sample heated at 60 °C, 615 nm at 90 °C, and 651 nm at 120 °C. The absorption red shift induced by the increment of the temperature confirms the chromatic variation of the samples.

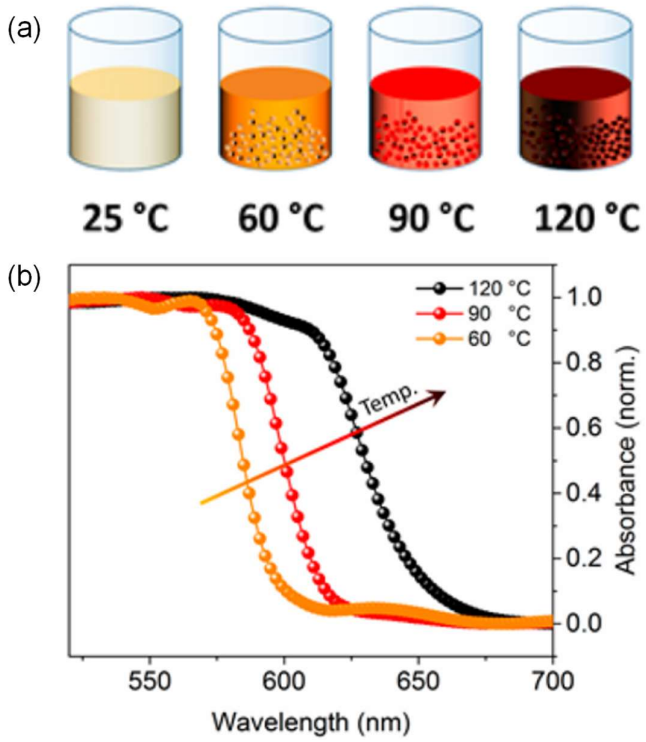

Figure 1.12. *(a) schematic representation of the perovskite thermchromics at 25, 60, 90, 120 °C. (b) Absorption spectra of the precipitated solids collected from the respective inks. Reproduced from ref. 145©American Chemical Society for(a, b).*

1.1.5. Dielectric properties

Dielectric materials ideally have zero *dc* electrical conductivity. Dielectric properties may be defined from the behaviour of the material in a parallel plate capacitor.[110] This is a pair of conducting plates, parallel to one another and separated by a distance, *d*, that is small compared with the linear dimensions of the plates, Figure 1.13a. With a vacuum between the plates, the capacitance C_0 is defined as

$$C_0 = \frac{\varepsilon_0 A}{d}$$

where ε_0 is the *permittivity of free space*, 8.854×10^{-12} F/m, and A is the area of the plates. Since ε_0 is constant, the capacitance depends only on the dimensions A and d of the capacitor. On applying a potential difference, V, between the plates, a quantity of charge, Q_0, is stored on them, given by

$$Q_0 = C_0 V$$

If a dielectric substance is now placed between the plates and the same V is applied, the amount of charge stored increases to Q_1 and the capacitance increases to C_1. This is because the effect of V is to cause a small polarisation of the valence electron charge clouds, although no long range of motion of ions or electrons should occur. The polarisation disappears when V is removed. The *dielectric constant* or *relative permittivity*, ε, of the dielectric is related to the increase in capacitance by

$$\varepsilon' = \frac{C_1}{C_0}$$

The magnitude of ε depends on the degree of polarisation that can occur. For air, $\varepsilon' = 1$. For most ionic solids such as Al_2O_3 and NaCl, $\varepsilon' = 5$–10. For ferroelectric materials such as $BaTiO_3$, $\varepsilon' = 10^3$–10^4.[110]

The response of a material to an applied field is described using three terms: *permittivity*, *polarisability* and *dielectric susceptibility*, which essentially represent the same phenomena but are defined in different ways. Dielectric susceptibility is the same as (relative) permittivity after subtraction of the contribution from the permittivity of free space, i.e.

$$\varepsilon_0 \chi = \varepsilon_0 \varepsilon' - \varepsilon_0; \chi = (\varepsilon' - 1)$$

whereas polarisability, α, is a measure of the dipole moment, p, created in response to E_0, Figure 1.13b. *Polarisation* is then the summation of all the individual dipole moments that are created, i.e.

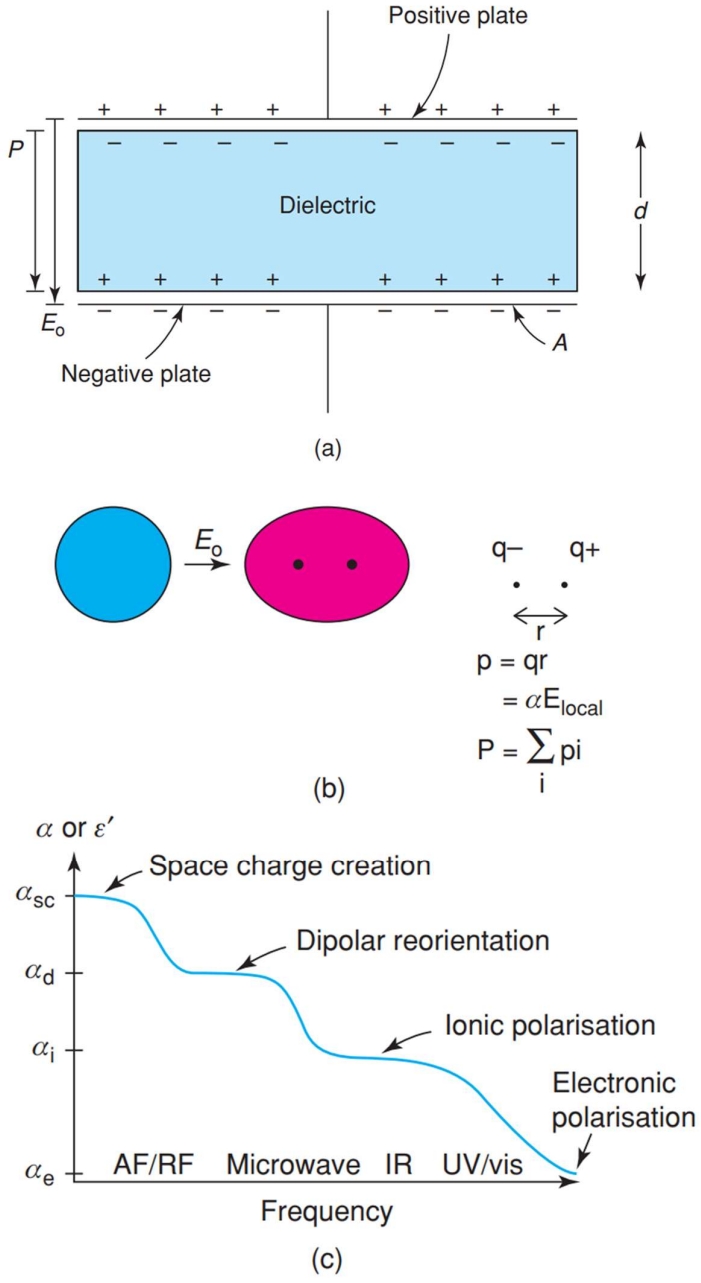

Figure 1.13. *(a) Dielectric material between the plates of a parallel plate capacitor, (b) creation of induced dipoles in an electric field and (c) frequency dependence of polarisability and permittivity. (adapted from Ref. [110])*

$$P = \sum_i p_i = \sum_i \alpha_i E_{local,i}$$

where there are *i* dipoles per unit volume. The terms ε, α and χ do not generally have fixed values for a particular material but are dependent on the measuring frequency, unless measurements are made under *dc* conditions. This is because different processes contribute to dipole moment creation and reorientation, which operate on different timescales, as shown schematically in Figure 1.13c. At the highest frequencies, in the UV/vis region, small displacements of the electronic charge clouds on individual atoms may occur, giving a difference in the centre of gravity of the electronic charge distribution from that of the positive nucleus, this is the *electronic polarisability*, α_e. With decreasing frequency, small displacements of individual atoms or ions are possible, as shown by the familiar peaks in IR/Raman spectra, which are associated with specific vibrational modes. At these frequencies, *ionic polarisability*, α_i, is detected. At still lower frequencies, molecular motions, rotations, and dipole reorientations occur in the microwave region leading to the *orientational polarisability*, α_D.[110]

Materials with ultrahigh dielectric constants and a low value of dielectric loss are important for energy storage and electronic devices.[146-151] Traditionally, high dielectric constant is found in ferroelectric complex oxides, but they exhibit high dielectric loss as well.[152-157] Superionic metal halides exhibit colossal dielectric constant due to high *ionic polarisability.*

1.1.6. Magnetic properties

Recently 2D transition metal halides with intrinsic magnetism have drawn pronounced attention due to their possible applications in spintronic devices.[158, 159] In addition, these compounds are enriched with different interesting magnetic states, which include ferromagnetic (FM), antiferromagnetic (AFM), skyrmion and quantum spin liquid.[160, 161] One can also able to form hetero-structure interfaces by incorporating these 2D magnetic materials into the other functional devices.[158, 159] Among the 2D transition metal halides, perovskite magnetic halides are comparatively less studied.[162] In general 2D RP phase is adopted in K_2NiF_4 structure, where NiF_2 layers are separated by two KF layers. The intra-

layer interactions are FM in nature, whereas the inter-layer interactions are AFM type.[163] Most of the members of this system are ordered magnetically at low temperatures. For example, both 2D Rb_2MnCl_4 and Cs_2MnCl_4 undergo AFM transition at around T_N = 55 K.[164] On the other hand, the $Rb_2CuCl_{4-x}Br_x$ (x = 0, 1, 2) compounds have much lower transition temperature, T_N = 13.7 K to 17.2 K.[163] Super-exchange interaction between transition metal ions via halogen played the vital role behind the observed magnetism.

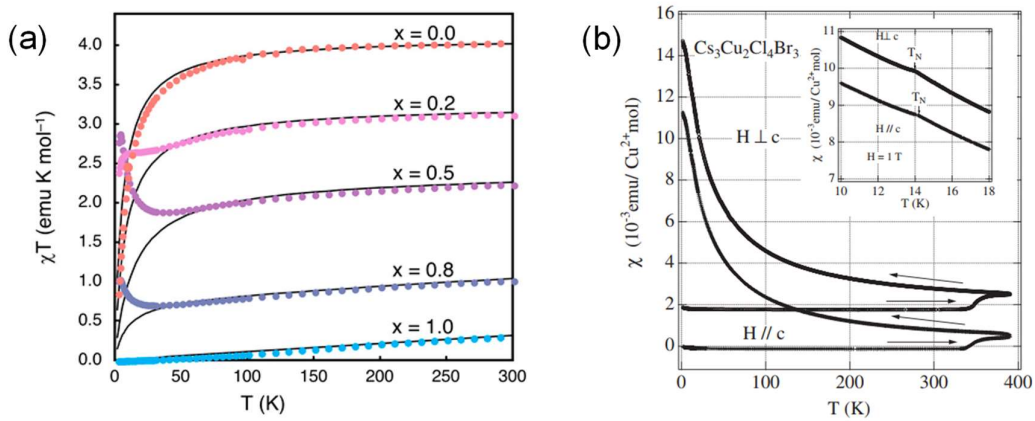

Figure 1.14. *(a) Temperature dependence of the magnetic susceptibility-temperature product (χT) for $Cs_4Mn_{1-x}Cu_xSb_2Cl_{12}$ (from top to bottom x = 0.0, 0.2, 0.5, 0.8, 1.0). Solid lines represent the best fit of the data. (b) Temperature dependence of magnetic susceptibility of $Cs_3Cu_2Cl_4Br_3$. The plot for magnetic field H ⊥ c is shifted vertically by 2 x 10^{-3} emu Cu^{2+} mol. Arrows denote the directions of temperature change. The inset shows the enlargement of susceptibility near the magnetic phase transition temperature of the heated crystal. Reproduced from ref. 77 ©American Chemical Society for (a) and Reproduced from ref. 62 ©Physical Society of Japan for (b).*

It is worth mentioning that the transition metal based layered halide double perovskites (⟨111⟩-oriented, n = 3) with nominal composition, $Cs_4Mn_{1-x}Cu_xSb_2Cl_{12}$ ($0 \leq x \leq 1$) have certain important magnetic properties.[77] The layered $Cs_4MnSb_2Cl_{12}$ compound is AFM in nature. Whereas Pauli paramagnetic behavior is observed in the case of $Cs_4CuSb_2Cl_{12}$, as shown in Figure 1.14a. This type of paramagnetic behavior is an indication to the delocalization of thermally excited charge carriers present in the system. This is also in line with the metallic nature of the $Cs_4CuSb_2Cl_{12}$ compound.[77] The $Cs_3Cu_2Cl_4Br_3$ with double-layered perovskite structure is a new addition to this magnetic

halide system.[62] It has two layers of $Cu_2Cl_4Br_3$ with elongated $CuCl_4Br_2$ octahedra (see details in structure section). Like $Rb_2CuCl_{4-x}Br_x$ (x = 0, 1, 2) materials, $Cs_3Cu_2Cl_4Br_3$ also undergoes an AFM transition at around 14 K, which is demonstrated in Figure 1.14b (inset). Spin singlet state with a large value of excitation gap is observed in $Cs_3Cu_2Cl_4Br_3$, which arises due to the dimerization between the two $Cu_2Cl_4Br_3$ layers. In addition to the AFM transition, $Cs_3Cu_2Cl_4Br_3$ has a structural phase transition at around 330 K and this transition is related to the order-disorder transition of Cu^{2+} orbitals, as shown in Figure 1.14b.[62]

1.1.7. Thermal transport properties

Although the influence of the lattice vibrations on the optoelectronic properties of halide perovskites has been studied,[9, 69, 165] the thermal transport and thermoelectrics properties of these compounds have gained significant attention recently.[166] The thermometric efficiency of a material can be designated by the thermoelectric Figure of merit, $zT = (\sigma S^2/\kappa)T$, where T, σ, S, and κ denote the absolute temperature, electrical conductivity, Seebeck coefficient, and thermal conductivity, respectively (brief discussion in subsequent part). The progress of efficient thermoelectric materials can be accomplished by the concurrent improvement in power factor (σS^2) and reduction in κ.[167-169]

Recently, few experimental and theoretical studies were appeared on the investigation of thermal properties of halide perovskites, mostly based on the organic-inorganic hybrid analogues,[170-175] where thermal conductivity was expectedly low due to their soft lattice structure.[166] The investigation of thermoelectric properties in all-inorganic perovskites is limited over the 3D crystal structure. Lee et al. reported the thermal properties of several perovskites NWs (such as, $CsSnI_3$, $CsPbBr_3$ and $CsPbI_3$), which showed ultralow thermal conductivity in the range of 0.38-0.45 W/mK (Figure 1.15a) and zT of ~ 0.11 for $CsSnI_3$ at room temperature (Figure 1.15b).[176] Further, the zT was improved (0.14 ± 0.01 at 345 K) *via* optimization of the Cl doping in $CsSnI_{3-x}Cl_x$ thin film.[177] Recently, Kanatzidis' group have reported the ultralow thermal conductivity of $CsSnX_3$ (X = Br, I) as shown in Figure 1.15c which was ascribed to the dynamic cation off-centering with the distortion of SnX_6 octahedra and attained zT of ~0.15 at 550 K for $CsSnI_3$ (Figure 1.15d).[178] This is the highest experimental reported zT value among the

family of all-inorganic halide perovskites, but this value is significantly low compared to the state of art thermoelectric materials due to the electrically resistive nature of halide perovskites.[166] 2D metal chalcogenide are potential thermoelectric materials owing to their anisotropic crystal structure and low thermal conductivity.[179-182] Thus, 2D halide perovskites may be a potential contender for future low thermal conductive material and thermoelectrics. The thermal conductivity of 2D $CsPb_2Br_5$ films was measured to be ~0.33 ± 0.02 W/mK.[183]

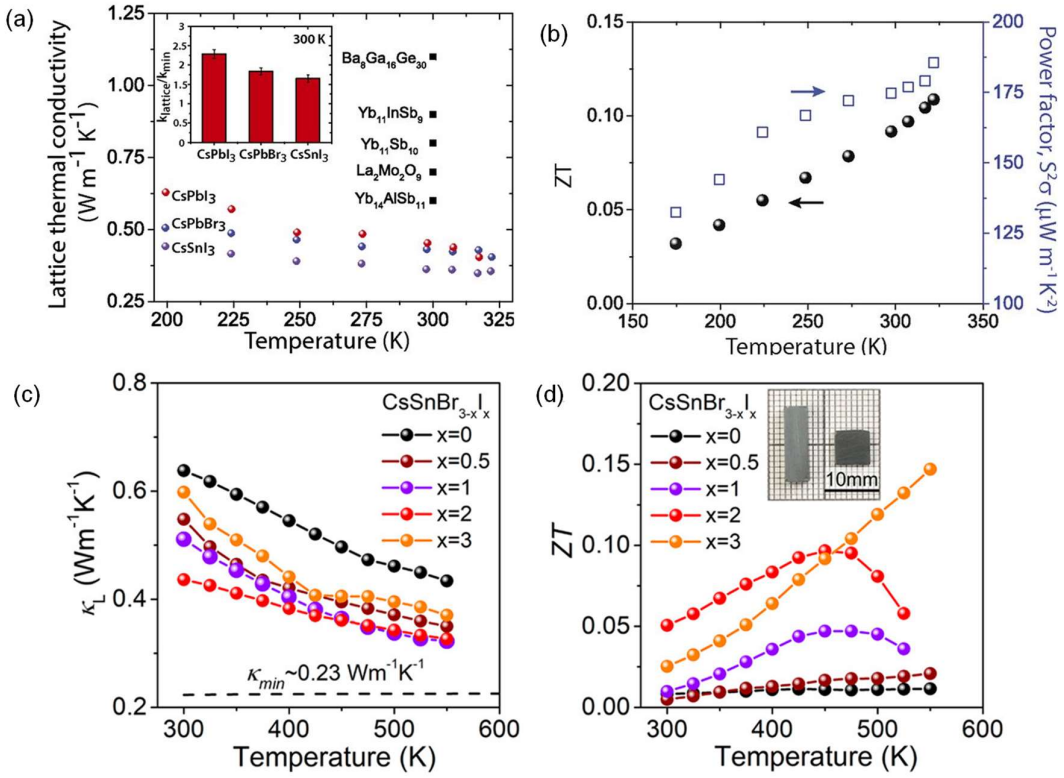

Figure 1.15. *(a) Comparison between inorganic perovskites and other single crystals with ultralow thermal conductivity materials, (Inset) Ratio of lattice thermal conductivity to the minimum thermal conductivity for AIHP NWs. (b) Figure of merit ZT (black dots) and power factor (blue squares) obtained from the exact same single $CsSnI_3$ NW. Temperature variation of (c) lattice thermal conductivity (κ_{lat}) and (d) ZT for $CsSnBr_{3-x}I_x$ (x = 0–3). Reproduced from ref. 176© Proceedings of the National Academy of Sciences for (a, b), Reproduced from ref. 178©American Chemical Society for (c, d).*

1.2. Introduction to metal chalcogenides

Metal chalcogenides constitute one of the most important classes in the field of chemistry, exhibiting rich compositional and structural diversity on parity with oxides and organic compounds. Chalcogenides are compounds that contain at least one chalcogen atom (Q = S/ Se/ Te) in a chemically reduced state compared to its elemental form. Chalcogenides bear few chemical resemblances to oxides, but there are also big dissimilarities in chemical character and physical properties among them which are significant enough to warrant a separate treatment of the chalcogenides as a distinct class of materials. These differences must, of course, originate from the differences between the oxygen atom on the one hand and the atoms of S, Se, Te on the other. Some important differences in the atomic properties of oxygen and the chalcogen are:[184]

(a) The chalcogen atoms are larger (and also heavier) than oxygen atoms.

(b) The chalcogens are less electronegative than oxygen.

(c) The chalcogens have d orbitals of accessible energy (3d for S, 4d for Se and 5d for Te), while oxygen has not.

(d) The metal-to-chalcogen bonds are more covalent than metal-to-oxygen bonds (consequence of (b)).

(e) The metal-to-chalcogen bonds often involve the d orbitals of the chalcogen, while this is not possible for the bonding to oxygen (consequence of (c)).

(f) The chalcogenides are more polarizable than oxide ions (consequence of (a) and (c)).

One of the most striking differences between oxides and chalcogenides is the facile ability of the chalcogen to form stable Q−Q bonds: catenation. For instance, there are many allotropes of sulfur, owing to the ability of sulfur to form chains of singly bonded atoms. This catenation is also observed in metal chalcogenides, for example, in pyrite where S-S (S_2^{2-}) units are found. Similarly, selenides and tellurides also exhibit Q-Q bonding as in Se_2^{2-} and Te_2^{2-} units of pyrite-type structures but in contrast with sulfides, they can form solid-state structures that contain Q_n rings or chains with $n > 2$ as exemplified by Se_5 moiety in Nb_2Se_9[185] and Te_6 group in $Re_6Te_{16}Cl_6$[186]. In general, as we move from sulfides to selenides to tellurides, the degree of covalent bonding, delocalization of electrons and metallic behaviour increase, and the importance of long

range Q-Q interactions (*i.e.*, less than single bond) increases.[187] Te-Te single bonds are ca. 275 pm in length, but in a large number of telluride compounds, Te-Te bonds with distances intermediate between single bonds and van der Waals interactions (ca. 420 pm) exist. These bonds are energetically weak but are structurally important; they also manifest as Te···Te interlayer interactions that essentially stabilize the structures of layered tellurides such as $TaIrTe_4$ and $NbIrTe_4$.[188]

Besides, catenation can produce stable complex polychalcogenide anions (Q_x^{2-}, where x is up to 7 or 8). These anions serve as reactive building blocks for molecules and solid-state materials. Chalcogenides are similar to oxides in that there are as many chalcoanions, particularly with the main-group and early-transition metal atoms (e.g. $[PS_4]^{3-}$, $[P_2S_7]^{4-}$, $[SiS_4]^{4-}$, $[GeS_4]^{4-}$, $[MoS_4]^{2-}$, $[VS_4]^{3-}$ etc.), as there are oxyanions (e.g. $[PO_4]^{3-}$, $[P_2O_7]^{4-}$, $[SiO_4]^{4-}$, $[Si_2O_7]^{6-}$, $[MoO_4]^{2-}$, $[VO_4]^{3-}$ etc.). In fact, chalcogens can form many other chalcoanions which do not have analogous oxyanions, few examples being $[P_2Se_6]^{4-}$, $[P_3Se_7]^{3-}$, $[P_2Se_8]^{2-}$, $[P_8Se_{18}]^{6-}$, $[GeS_4]^{4-}$, $[GeSe_5]^{4-}$, $[Ge_2Se_6]^{6-}$ etc.[189-191] Metal oxides are usually ionic in character, and they resemble fluorides more than they do chalcogenides. For instance, dioxides such as VO_2, CrO_2, and MnO_2 crystallize in a rutile-type (TiO_2) structure similar to the corresponding fluorides *viz.* VF_2, CrF_2 and MnF_2. On the other hand, while VS_2 and CrS_2 are not known, MnS_2 has a pyrite-type structure characterized by S_2^{2-} units, which is rarely found in oxides. Similarly, $MnSe_2$ and $MnTe_2$ also crystallize in pyrite-type structures. It is noteworthy that although Mn metal atoms have octahedral coordination in both MnO_2 and MnQ_2, the overall structures are significantly different. Besides, layered structures are very common among metal dichalcogenides but seldom found among oxides. The structures of most oxides are well represented by models that treat atoms as hard, charged spheres with ionic radii specific to a given element. The constant-radius approximation is, however, not accurate for metal chalcogenides because of their more covalent character.[187] Some of the important distinctions between metal oxides and metal chalcogenides are summarized in Table 1.2.

Table 1.2. *Some important distinctions between metal oxides and metal chalcogenides.*

Feature	Oxides	Chalcogenides
Close packing	Usually	Sometimes
Octahedral/tetrahedral metal-coordination	Yes	Usually
Trigonal prismatic metal-coordination	Very rarely	Groups 5 and 6
Layered structures	Rarely	Usually
Q-Q bonds	Peroxides	Common
Bonding	Ionic	Covalent

Metal chalcogenides are central to many important technologies. They exhibit a broad range of chemical and physical properties associated with diverse scientific phenomena and enable a plethora of applications.[192-199] For example, CdTe and $CuInSe_2$ are high-performing materials for thin-film solar photovoltaics; PbTe, GeTe and $Bi_2Te_{3-x}Se_x$ are the champion thermoelectric materials; Co(Ni)/Mo/S composites are the best available catalysts for hydro-desulphurization of crude oil; $Ge_2Sb_2Te_5$ is a high density memory material; CdHgTe is the key infrared detector material in night-vision cameras etc.

Metal chalcogenides are at the cutting edge of many research areas. Some examples include nonlinear optics,[200] optical information storage,[201] photovoltaic energy conversion,[202] thermoelectric energy conversion,[197, 203, 204] radiation detectors,[205] thin-film electronics,[206] spintronics,[207] fast-ion conductivity,[208] rechargeable batteries,[209] catalysis,[210] novel magnetism,[211] unconventional superconductivity[212] and science in two dimensions.[198, 213] In the recent times, the scientific community has witnessed sensational discoveries pertinent to metal chalcogenides such as quantum spin Hall effect,[214] topological insulators,[215-218] topological crystalline insulators,[219, 220] non-saturating magnetoresistance[221] and many others which will have huge implications, especially in the fields of spintronics and (opto) electronics. We are currently in the midst of an impressive expansion in solid-state chemistry of chalcogenide with emphasis on the synthesis of materials with new compositions and structures on the one hand, and

exploration of their novel properties on the other. Most of the aforementioned applications and phenomena are associated with chalcogenides of transition metals and main group p-block metals. The following sections will briefly discuss about the thermoelectric application.

1.2.1. Metal chalcogenides based high-performance thermoelectrics

In this part we will discuss about the thermoelectric application of metal chalcogenides. First, we will briefly discuss about what do we mean by thermoelectrics and its relevance in the present scenario, followed by important parameters to optimize to obtain high thermoelectric performance.

1.2.1.1. Thermoelectrics

The advent of technological modernization and improvement in the standard of living has coincided with the burgeoning increase in energy consumption, bulk of which are fulfilled using rapidly dwindling non-renewable energy resources. Overcoming such energy dilemma led to exploration of alternative sustainable energy sources, and thermoelectricity is being increasingly viewed as an essential piece to this energy puzzle.[204, 222-225] Thermoelectric material which can generate electricity through a temperature gradient directly (Figure 1.16a), is a clean energy conversion process, whose performance is guided by its Figure of merit zT[226] (discussed earlier please see section 1.9).Quest for high performing thermoelectric materials have traditionally relied on either improving the power factor (σS^2) or decreasing the thermal conductivity (κ).

While the phenomenon of thermoelectricity is already 200 years old, as Seebeck first observed it in 1821, the Figure of merit equation was defined much later in 1911, with first generation thermoelectric devices having $zT \sim 1.0$ being furnished only in 1950s and 1960s.[227, 228] This followed by a period of relatively stagnant improvement in this field until 1990s, after which following the new ideas brought forward by Hicks and Dresselhaus, significant breakthroughs have been achieved in this field. The last couple of decades oversaw second and third generation of thermoelectric materials with

efficiency exceeding 15% and is largely due to our improved understanding of the electrical and phonon transport properties.[228]

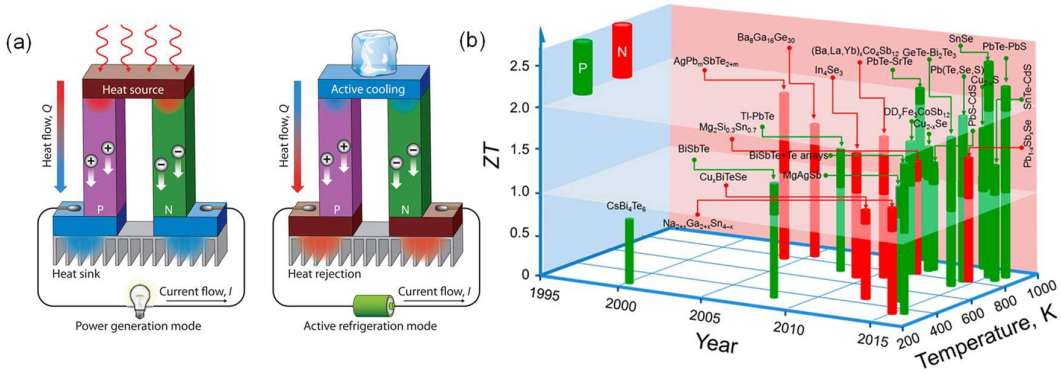

Figure 1.16. *(a) Schematic illustrations of a thermoelectric (TE) module for active power generation-Seebeck effect (left) and refrigeration-Peltier effect (right). (b) TE* ***Figure****-of-merit* (*zT*) *as a function of temperature and year illustrating important milestones. (b) Reproduced from ref. 168©American Chemical Society.*

Electronic band engineering approaches such as band flattening,[229] band convergence,[230, 231] introduction of resonant levels,[232, 233] mobility and carrier concentration engineering,[234, 235] quantum confinement[236] etc. has been successfully applied to improve the power factor of a thermoelectric material. While on the other hand, phonon suppressing techniques like point defect/alloy scattering,[237, 238] introduction of nano-precipitates,[239, 240] all-scale hierarchical architectures[241, 242] and intrinsic phonon scattering techniques[243] etc. are also being employed efficiently. The present approaches to engineer high performance thermoelectric material revolve around the simultaneous optimization of both electronic and phonon transport.[224, 244] With the help of the advanced approaches, rational designing of several state-of-the-art thermoelectric materials have been possible which includes $Bi_{2-x}Sb_xTe_3$,[240, 245, 246] PbTe,[233, 241, 247] SnTe,[230, 237, 248] GeTe,[249-252] SnSe,[180, 253-256] clathrates and skutterudites,[257-259] half-heuslers,[260, 261] $Cu_{2-x}Se$[262, 263] etc., most of which has peak zT values > 2 at high temperatures (Figure 1.16b).

Despite of having made such progress in achieving high thermoelectric Figure of merit, the potential application of these materials in thermoelectric energy generators

(TEGs) have somewhat been restricted due to their poor energy conversion efficiency. The power generation efficiency, η, of TEGs is given by:[204]

$$\eta = \frac{T_h - T_c}{T_h} \frac{\sqrt{1+Z\bar{T}}-1}{\sqrt{1+Z\bar{T}}+\frac{T_c}{T_h}} = \varepsilon \frac{\sqrt{1+Z\bar{T}}-1}{\sqrt{1+Z\bar{T}}+\frac{T_c}{T_h}}$$

where, T_h, T_c and $\bar{T}$ denotes temperatures of the hot-side, cold-side and average temperature of T_h and T_c respectively. $Z\bar{T}$ of a material is defined as:[204]

$$Z\bar{T} = \frac{\int_{T_c}^{T_h} ZT \, dT}{T_h - T_c}$$

The above equation indicates that if a high zT value is achieved over a wide range of temperature, a high average zT ($Z\bar{T}$) can be obtained, and as a consequence an efficient thermoelectric material can be furnished.

1.2.1.2. Strategies to improve thermoelectric Figure of merit

From the above mentioned zT equation, it is clear that improving zT can also be achieved by improving the power factor (σS^2) of a material and reduce the thermal conductivity. Power factor (σS^2) is a purely electronic property, governed by materials' electronic structure and scattering mechanism. Strategies to enhance power factor include: a) engineering of carrier-concentration (n_H) through chemical doping,[264] b) enhancement of the effective carrier mass (m^*) and Seebeck coefficient (S) via the convergence of multiple valence/conduction band extrema,[231, 232, 265] or distortion of the density of states near Fermi level by resonance impurity levels,[233, 248, 266, 267] and c) enhancement of carrier mobility (μ) by modulation-doping.[268, 269] Here, I will summarize the most recent approaches of designing high-performance Thermoelectric materials.

Carrier concentration optimization

The fundamental challenge of designing high zT thermoelectric materials is strong interdependence of σ, S and κ through carrier concentration, n (Figure 1.17) which can be

optimized by controlling the doping level. The maximum *zT* value arises in the carrier concentration range of 10^{19}-10^{21} cm^{-3}, which falls in between metals and semiconductors - that is concentration typically found in heavily doped semiconductors (i.e. degenerate semiconductor).[270] However, carrier concentration (n_H) increases rapidly with rising temperature, following the power law of $T^{3/2}$. Although conventional doping is effective to tune room temperature carrier optimization, it is difficult to achieve optimum carrier concentration at high temperature. Thus, the maximum theoretical *zT* cannot be fully realized at every working temperature. An effective solution to this issue is the use of functionally graded doping, by integrating two or multiple segments with dissimilar n_H. The modifications to the conventional doping method to include temperature-dependent doping behaviour are helpful to acquire larger average *zT* values which are especially important for technological applications.

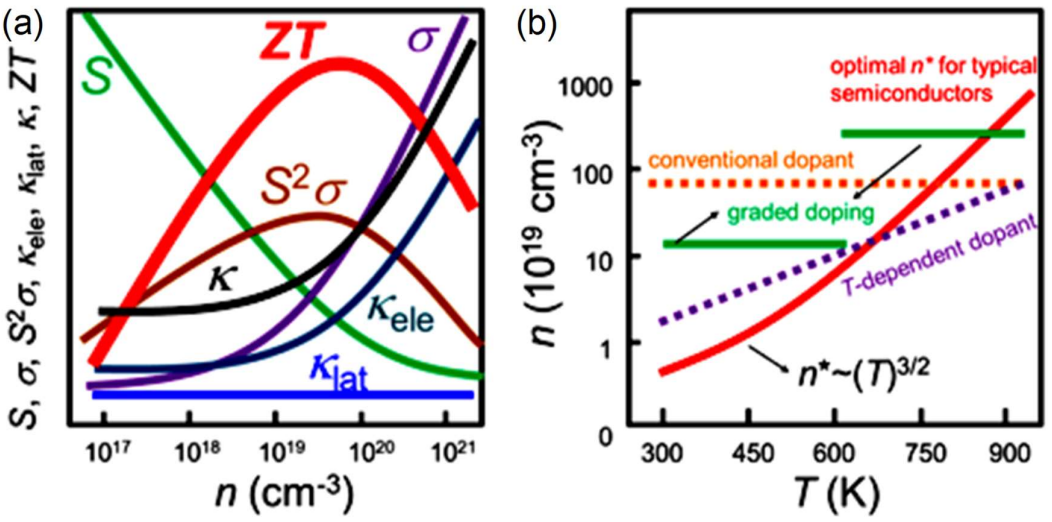

Figure 1.17. *(a) Schematic diagram showing the dependence of ZT (~zT) and its parameters (electrical conductivity σ, Seebeck coefficient S, power factor $S^2\sigma$, electronic thermal conductivity κ_{el}, lattice thermal conductivity κ_{lat} and total thermal conductivity, κ) on carrier concentration n. (b) Strategies for stabilizing the optimal carrier concentration. Reproduced from ref. 168© 2016 American Chemical Society.*

Resonance level

The concept of resonance level was first proposed in 1950.[271] Resonance level originates from the coupling between electrons of a dilute impurity with those of the valence or

conduction band of the host solid near its Fermi level.[272] Thus, resonance dopant creates an excess density of states near the valence or the conduction band edge of the host compound (Figure 1.18a) and results in higher effective mass, m^* and thereby enhances Seebeck coefficient, according to Mott expression.[197]

$$S = \frac{\pi^2}{3}\frac{k_B}{q}\,k_B T\left\{\frac{d[ln(\sigma(E))]}{dE}\right\}_{E=E_F}$$

$$= \frac{\pi^2}{3}\frac{k_B}{q}\,k_B T\left\{\frac{1}{n_H}\frac{dn_H(E)}{dE} + \frac{1}{\mu}\frac{d\mu(E)}{dE}\right\}_{E=E_F}$$

Here, $\sigma(E)$ is the electrical conductivity determined as a function of the band filling or Fermi energy, E_F ($\sigma(e) = n_H(E)q\mu(E)$) and $n_H(E)$ ($n_H(E) = g(E)f(E)$), the carrier density at the energy level, E (here q is the carrier charge, and $\mu(E)$ is the mobility as a function of energy, $f(E)$ is the Fermi function, $g(E)$ is density of state).

When electronic scattering is independent of energy, $\sigma(E)$ is just proportional to the density of states (DOS) at E. Based on the above expression it is clear that the system with rapid change in DOS near E_F is expected to have large Seebeck. Pisarenko plot represents the dependence of Seebeck on carrier concentration. A significantly higher S value than what a Pisarenko plot gives the indication of resonance level formation (Figure 1.18b).[233] Group-III (mainly Al, In and Tl) dopants form resonance level in PbTe.[272] Heremans, *et. al.*, demonstrated experimentally that Tl doping improves S of PbTe by resonance level formation and thereby achieved the double value of zT, as seen in Figure 1.18c.[233]

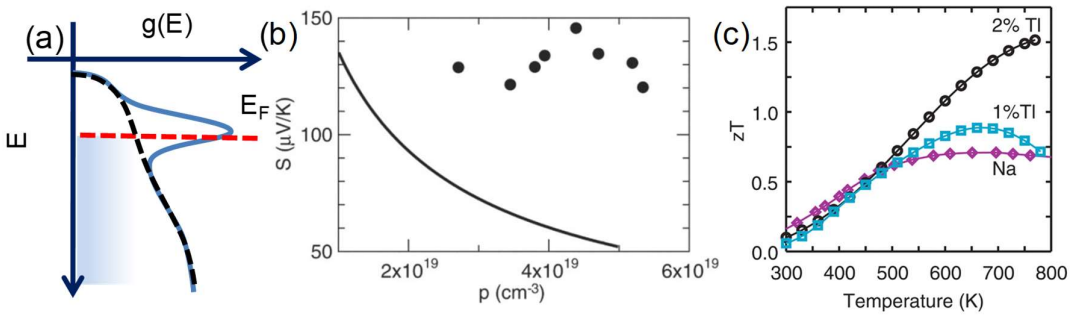

Figure 1.18. *(a) Schematic diagram of resonance level in the valence band. Schematic diagram of density of state (DOS) of the valence band of pristine sample (dotted black line). Tl-doped PbTe shows asymmetric distortion of DOS (blue line) near Fermi level.*

(b) Pisarenko relation of Seebeck coefficient vs hole concentration, p for PbTe (solid line) at 300 K compared to the results on Tl-PbTe sample. Significantly large S value in Tl-doped PbTe confirmed the presence of resonance level. (c) The temperature dependent zT values for $Tl_{0.02}Pb_{0.98}Te$ (black circles) and $Tl_{0.01}Pb_{0.99}Te$ (blue squares) compared to that of a reference sample of Na-PbTe (purple diamonds).

Electronic band convergence

Multiple pockets in valence or conduction band extreme give rise to high Seebeck coefficient because these valleys (separate pockets of Fermi surface with the same energy) have the effect of producing large effective mass (m^*) without explicitly reducing μ, as seen in the following equation:[231, 232, 265]

$$m^* = N_V^{2/3} m_b^*$$

Where N_V represents orbital degeneracy and m_b^* represents single valley density of state effective mass of degenerate valleys. Thus, effective doping to energetically align the electronic bands for a higher degree of band degeneracy lies at the core of the band-convergence scheme. The aim is to enhance the Seebeck coefficient without substantially degrading the σ. When the system is heavily doped, overall effective mass can be enhanced through carrier redistribution to multiple valleys, thus results in high Seebeck coefficient. Since carrier mobility will be unaffected in this process, valence band convergence gives rise to significantly high σS^2 and zT in carrier optimized system.

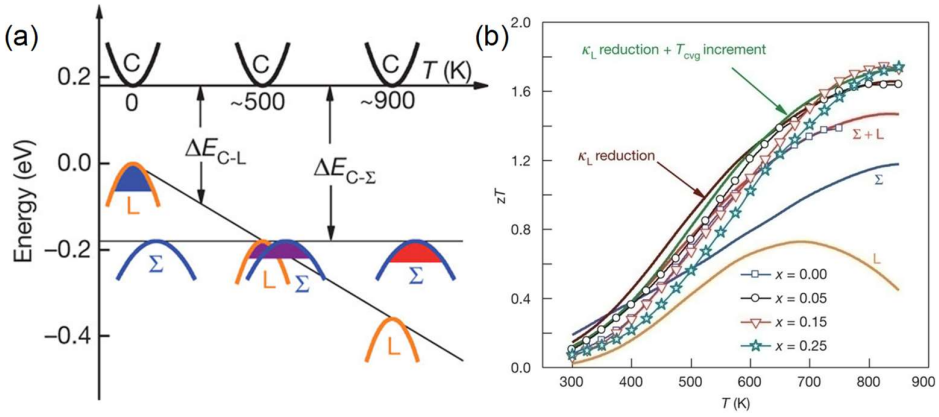

Figure 1.19. *(a) Relative energy of the valence bands in $PbTe_{0.85}Se_{0.15}$. At, 500 K the two valence bands converge, resulting in contributions from both the L and Σ bands in the*

transport properties. (b) Temperature dependent zT of p-PbTe$_{1-x}$Se$_x$ materials doped with 2 atom % Na. Reproduced from ref. 231 ©Nature Publishing Group.

Pei et al. have demonstrated the band convergence of at least 12 valleys in doped PbTe$_{1-x}$Se$_x$ alloys, leading to an extraordinarily high *zT* value of 1.8 at about 850 K, as seen in Figure 1.19.[231] Alloying Se reduces the energy difference between the *L* and *Σ* bands of the PbTe making the two bands effectively converged. Hence enhancement in N_V from 4 (for *L* band) to 12 (for *Σ* band) results in an increase in m^* and Seebeck coefficient. A similar result was observed in PbTe, after it was alloyed with wide band gap chalcogenides (MgTe, CaTe, BaTe).[242]

Recently, an innovative strategy of slight-symmetry reduction has been adopted to realize band convergence in GeTe. Detailed electronic structure analysis of GeTe demonstrate that rhombohedral distortion of GeTe along the [111] crystallographic direction (along the L point of BZ) splits up the 4 L pockets of cubic GeTe ($Fm\bar{3}m$) into 3 L + 1 Z pockets in rhombohedral GeTe (*R3m)* and 12 Σ pockets of cubic GeTe into 6 Σ + 6 η pockets in rhombohedral GeTe.[273, 274] Thus manipulation of the degree of the rhombohedral distortion (also referred as slight symmetry reduction) can result in band convergence of L and Σ bands. In a recent report by Li et al., it has been shown that slight symmetry reduction of cubic GeTe towards rhombohedral symmetry by Pb and Bi doping causes an effective valence band (L and Σ bands) convergence, resulting in a high zT of ~2.4 in rhombohedral phase of Pb and Bi codoped GeTe at 600 K.[273, 274]

Reduction of the lattice thermal conductivity

One of the customary approaches to high performance thermoelectrics is by reducing the thermal conductivity of the solids.[275] In general, for solids, total thermal conductivity (κ_{tot}) mainly constitutes of three parts, *viz.*, the electronic thermal conductivity (κ_{el}), the lattice thermal conductivity (κ_{lat}), and the bipolar thermal conductivity (κ_b). With the aid of Wiedemann–Franz–Lorenz law, $\kappa_{el} = L\sigma T$, for the electronic thermal conductivity, *zT* can be re-written as $zT = \frac{S^2}{L}\left[\frac{1}{1+\frac{\kappa_{lat}+\kappa_b}{\kappa_{el}}}\right]$. Here, *L* is the Lorenz number, and the values mostly lie in the range of 1.6 to 2.5 × 10^{-8} V^2 K^{-2}. Materials exhibiting low κ_{lat}, and low κ_b is

paramount in order to achieve high TE performance, while a high κ_{el} leads to a high power factor.[197] Contributions from κ_b comes only at elevated temperatures and in very narrow-gap semiconductors, being almost negligible in room temperature conditions. Thus, exploring new strategies to maximize the suppression of κ_{lat} is crucial for a better TE performance.

Phonons are the quantized normal modes of atomic vibrations in a periodic lattice. We will consider here crystalline solids in which well-defined phonon modes exist and carries thermal energy. Considering kinetic theory within Boltzmann transport equation, κ_L of a solid can be written as[276]:

$$\kappa_L = \frac{1}{3}\int_0^{\omega_{max}} C(\omega)v(\omega)l_{ph}(\omega)\, d\omega$$

where $C(\omega)$ is the spectral volumetric heat capacity, $v(\omega)$ is the phonon group velocity and $l_{ph}(\omega)$ is the phonon mean free path. A typical temperature dependent κ_L of a crystalline semiconductor is shown in Figure 1.20a. At low temperature, three-phonon scattering or Umklapp scattering strength is low so that l_{ph} often reaches the characteristic length-scale of the material. At low temperature, κ_L follows the temperature dependence of C_v and increases with temperature as $\sim T^3$.[277] At high temperature, C_v becomes constant to the Dulong-Petit value and κ_L decreases with increasing temperature following T^{-1} temperature dependence due to Umklapp scattering.[277] This results in a peak in temperature dependent κ_L (Figure 1.20a), which also strongly depends on the disorder and grain-boundary present in the materials.

Thermal transport in amorphous materials and glasses, however, is distinctly different from the crystalline solids. Apart from the much lower value of thermal conductivity in amorphous materials and glasses, its temperature dependence is also different between these two categories of materials. Comparison of typical temperature dependence of thermal conductivity in a crystalline insulator (α-quartz) and amorphous material (vitreous silica) is shown in Figure 1.20b.[278] Unlike in crystalline materials, thermal conductivity in amorphous materials and glasses increases following T^2

temperature dependence at low temperature, followed by a plateau region of nearly constant values and then slowly increases towards the 'glass limit'.[279, 280] The goal is then to further suppress κ_L in these materials with various strategies and reach the 'glass limit' without significantly suppressing the charge carrier mobility. We should also mention that, although rare, some crystalline materials like $Ba_8Ga_{16}Ge_{30}$[281] and $Bi_4O_4SeCl_2$[282] show typical glass like temperature dependent κ_L. However, κ_L cannot be arbitrarily low in a crystalline solid – its lowest attainable value is generally referred as minimum lattice thermal conductivity κ_{min}, which is an important parameter which guide material design principles for high-performance thermoelectric materials.

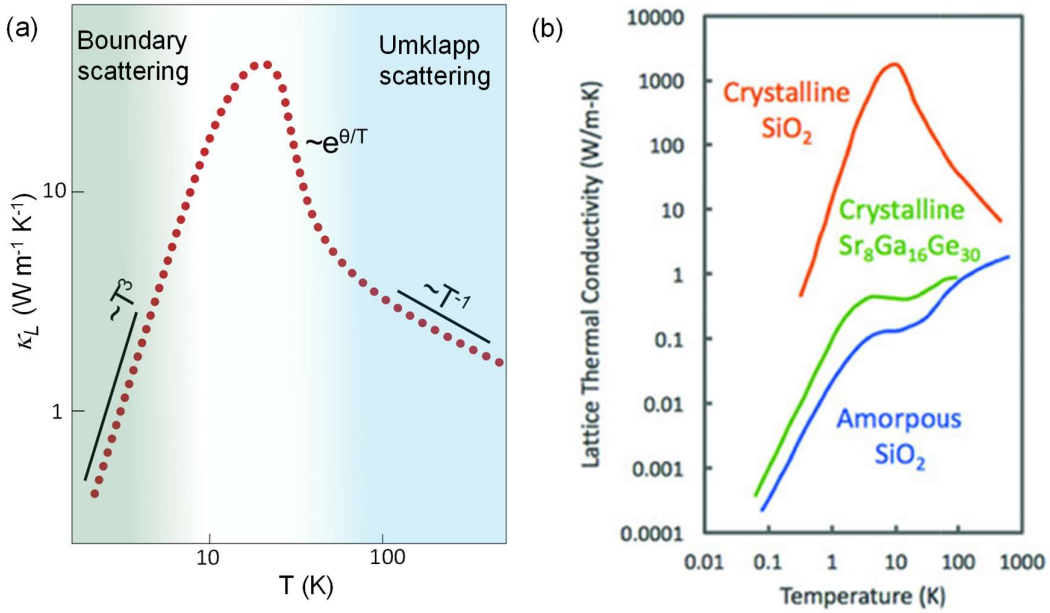

Figure 1.20. *(a) The schematic shows typical temperature dependent κ_L in a crystalline solid and various scattering mechanisms operating in different temperature regimes. (b) Typical temperature dependence of κ_L in a crystalline (α-quartz) and an amorphous solid (vitreous-silica). Reproduced from ref. 280 ©Wiley-VCH for (b).*

For bulk materials, $\kappa_{lat} = \frac{1}{3} C_V v_g^2 \tau$, provides proper description to the lattice thermal conductivity. Thus, to minimize the κ_{lat}, one has to engineer materials which decrease the specific heat (C_V), the group velocity (v_g) or the phonon relaxation time (τ). Typically, in thermoelectrics, the phonon relaxation time is the most focused variable to

tweak and achieve desirable κ_{lat} via extrinsically introducing 0D point defects, 1D dislocations or 2D grain boundaries or fine precipitates (Figure 1.21). Each of these defects enhances the phonon-scattering process and decreases the relaxation time (τ) and thereby decreasing the κ_{lat}.[283] Each of the aforementioned processes has their own frequency (ω) dependence. For example, the 0D point defects scatters the high frequency phonons ($\tau_{PD} \sim \omega^{-4}$); 1D dislocation scatters the mid frequency phonons ($\tau_{DC} \sim \omega^{-3}$ for dislocation cores and $\tau_{DS} \sim \omega^{-1}$ for dislocation strains); 2D interface scattering originating from grain boundaries or precipitates are effective for the low frequency phonons ($\tau_{inter} \sim \omega^{0}$).[283] The Umklapp process[284] which is ubiquitous has a relaxation time, $\tau_U \sim \omega^{-2}$, thus being effective in scattering the phonons of all frequencies. Callaway devised a phenomenological model considering all the contributions arising from the microstructural effects on phonon scattering at various length scales.[285] The model which is given as,[285, 286]

$$\kappa_{lat} = \frac{k_B}{2\pi^2 v_g}\left(\frac{k_B T}{\hbar}\right)^3 \int_0^{\theta_{D/T}} \tau_C(x) \frac{x^4 e^4}{(e^x-1)^2} dx$$

acts as a guide to quantitatively access the contributions arising from each micro-structural effect. k_B in equation corresponds to Boltzmann's constant; $\hbar$, T and τ_C denotes Plank's constant, absolute temperature and total relaxation time respectively. τ_C corresponds to the individual relaxation time via the relation $\tau_C^{-1} = \tau_U^{-1} + \tau_{PD}^{-1} + \tau_{DS}^{-1} + \tau_{DC}^{-1} + \tau_{inter}^{-1} + \ldots$, where τ_U, τ_{PD}, τ_{DS}, τ_{DC} and τ_{inter} corresponds to relaxation times arising from the contributions of Umklapp scattering, point defects, dislocation strain, dislocation cores and interface scattering respectively.

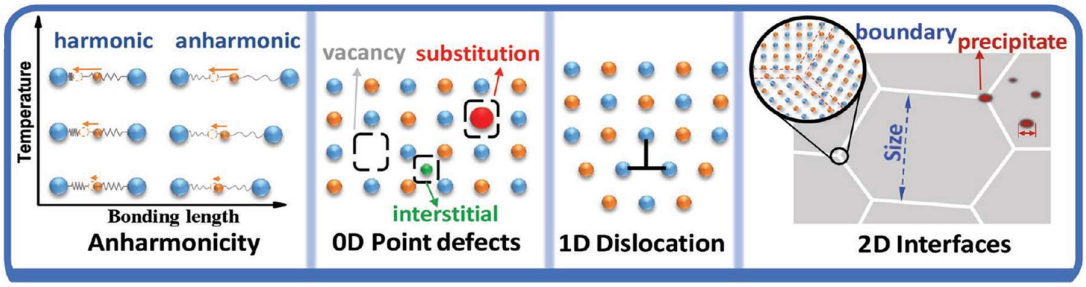

Figure 1.21. *A simple schematic to explain the various routes to suppress κ_{lat} in the crystal system. Reproduced with permission from ref. 283 © Wiley-VCH.*

Apart from the extrinsic approaches to reduce the thermal conductivity, rational unearthing of materials with intrinsically low lattice thermal conductivity is an intriguing and efficient prospect. Since electrons and phonons propagate within the same sublattice, suppressing the phonon transport also handicaps the electron mobility. Thus materials with innate κ_{lat} offer an independent control to achieve high TE performances without having to compromise on the electrical mobility which is beneficial in maintaining high power factor.[243]

1.2.1.3. Germanium telluride: A potential thermoelectric material

In recent years, plenty of new materials have been identified with satisfactory TE properties. TE materials which are used for mid-temperature (500–800 K) power conversion, are particularly interesting since the major share of the waste heat in industry and automobile exhaust is within this range.[287] Lead chalcogenides, such as PbTe and other lead chalcogenides has been raised to the peak *via* synergistic effect of band engineering (resonance levels formation, band convergence and bands alignment)[233] and nano/microstructure manipulation in all scaled hierarchical architectures.[241] However, environmental concern about Pb, has slowed down the progress of its mass-market application. Hence, the solid-state chemist and TE community demand discovery of Pb-free high performance TE materials.

Recntly, germanium telluride (GeTe) and it derivatives from IV-VI semiconducting metal chalcogenides family is recently emerging as potential alternative of PbTe.[249, 250] Although GeTe-based thermoelectric is known since 1960,[288] recent years have witnessed tremendous improvement in thermoelectric performance ($zT > 2$) of various GeTe-based materials which is mainly originating from better under-standing of its crystal-electronic structure as well as lattice dynamics.[252, 289, 290] In order to gain a better insight into the structure-properties correlation of GeTe, we must understand the nature of chemical bonding, crystal structure and phase transition of GeTe in-details.

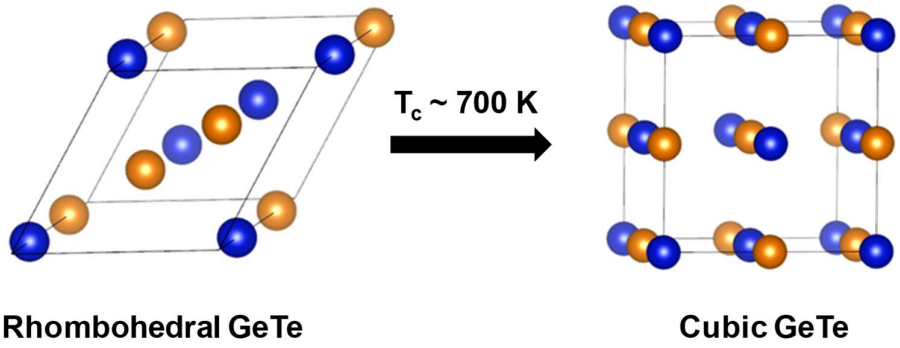

Figure 1.22. *Rhombohedral to a cubic structural phase transition in GeTe (blue and yellow atoms are Ge and Te, respectively).*

1.2.1.4. Crystal structure

GeTe has rocksalt crystal structure (space group $Fm\bar{3}m$ with a lattice constant of a = 6.009 Å, β phase), similar to lead chalcogenides (PbX; X= S/Se/Te) only at high temperature (>700 K).[252] Below 700 K, GeTe undergoes a structural distortion along [111] direction of cubic structure and adopts rhombohedral structure ($R3m$ with the lattice parameters of a = b = 4.164 Å and c = 10.690 Å, α phase) (Figure 1.22). Although similar structural distortion is also observed in semimetal Sb and Bi, GeTe is ferroelectric because of the presence of two different atoms (Ge and Te) with different electronegativity making the bonding polar. At room temperature, the crystal structure of PbTe and SnTe is cubic, whereas GeTe crystallizes in the less symmetric rhombohedral crystal structure. This anomaly mainly governs by the presence of the ns^2 lone pair on the cation.[252]

The relative displacement of Ge and Te sublattice along the [111] direction make GeTe ferroelectric near room temperature. This distortion changes the angle α = 88.35º from ideal angle of 90º between the axes in the face-centered cubic unit cell.[252]

1.2.1.5 Thermoelectric properties

Electronic transport

GeTe is rich with naturally formed and thermodynamically stable Ge-vacancies which drives the system to be intrinsically off-stoichiometric along with naturally occurring Ge

precipitations in the matrix.[291] These thermodynamically favourable Ge vacancies makes pristine GeTe to be highly p-type with a very high carrier concentration of ~10^{21} cm^{-3}. The high concentration of Ge vacancies results in high electrical conductivity of ~ 8000 S/cm and moderate Seebeck coefficient of ~32 μV/K in GeTe at room temperature (Figure 1.23a).[290] Interesting, GeTe exhibits higher S values compared to that of SnTe although both the materials possesses similar carrier concentration. Further, GeTe exhibits exceptionally high power factor (~ 50 μW/cmK^2) compared to other TE materials from IV-VI family, especially PbTe (~30 μW/cmK^2) and SnTe (~20 μW/cmK^2) which can be understood by analysing their electronic structure.[290]

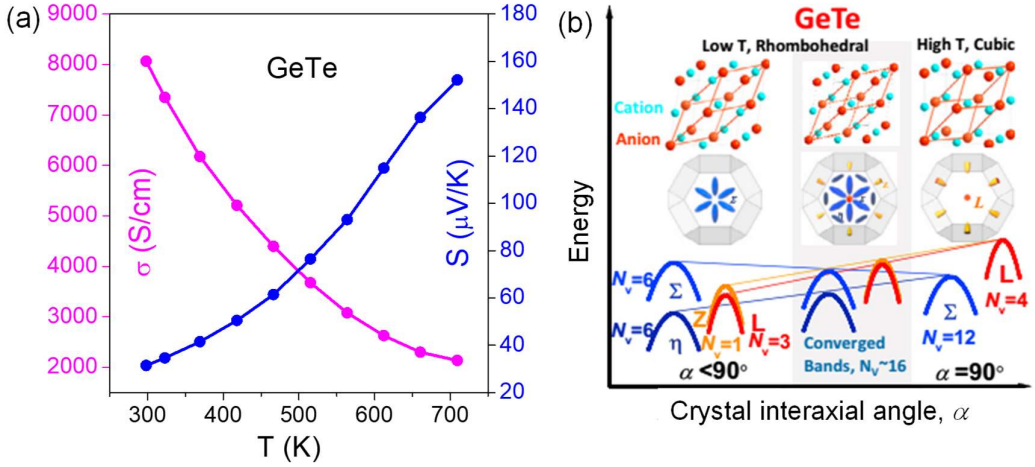

Figure 1.23. *(a) Temperature dependent electrical conductivity and Seebeck Coefficient of GeTe. (b) Schematic energy diagram of the evolution of the electronic structure of GeTe from the rhombohedral phase cubic to depending on interaxial angle. Reproduced from ref 273 ©Elsevier for(b).*

Both SnTe and PbTe possess rock-salt NaCl structure (*Fm-3m*) with valence band maxima occurring at L in Brillouin zone. Electronic structure calculations of GeTe have been demonstrated that 8 half-valleys at L band (4 equivalent L band) in cubic GeTe (*Fm-3m*) splited into 6 half-valleys at L- point (3 equivalent L band) and 2 half-valleys at Z-point (1 equivalent Z band) in rhombohedral GeTe phase (*R3m*), while 12 full valleys of Σ–band in *Fm-3m* splited into 6 along Σ and rest 6 full valleys along η-line (Figure 1. 23b).[273] Notably, valence band maximum at L-point in cubic GeTe shifts to heavy Σ–

band in rhombohedral GeTe during phase-transition. As a result, heavier effective mass carriers of Σ–band are dominated in transport properties in rhombohedral GeTe at room temperature, which, in fact, led to the unconventional enhancement in power factor in GeTe, unlike PbTe and SnTe. Further, GeTe has relatively low energy difference (~ 0.23 eV) between the heavy hole Σ band and light hole *L* band, and the energy offset decreases with increasing temperature which results in the increasing contribution of the lower lying valance band in electronic transport.[273] A part of my thesis (**part 6**) is involves understanding structure-property relationship and enhanced the thermoelectric performance of GeTe by using aforementioned strategies and improving its thermoelectric performance.

Thermal conductivity

Wdowik et al provide clear insight into the lattice dynamics of GeTe (both the phases α & β) together with inelastic neutron scattering experiments and density functional theory calculation.[292] To understand the thermal transport of both rhombohedral and cubic GeTe, it is important to examine phonon dispersions of both the phases. Phonon dispersion for *α*-GeTe at Γ point exhibits six vibrational modes namely 3 acoustic modes, 2 transverse optical modes (TO) and one longitudinal optical mode (LO) (Figure 1.24a). Both A_1 (non-degenerate) and E (doubly degenerate) modes for rhombohedral GeTe (*α*-GeTe) are Raman and IR active owing to the absence of inversion symmetry in the structure. Whereas, phonon-dispersion of the high-symmetry rocksalt structure of GeTe (*β* phase) provide the evidence for the presence of several soft phonon modes mainly TO components which are responsible for the symmetry change at the phase transition (Figure 1.24b).[292] Notably, phonon dispersion of cubic GeTe exhibits several imaginary modes in the Brillouin Zone which is the one of the reason for the absence of cubic GeTe at ambient condition, whereas rhombohedral phase exhibits real modes. β phase exhibits local distortions similar to Peierls distortion, which result in three shorter (2.86 Å) and three longer (3.25 Å) Ge-Te bonds.[293]

GeTe is much more resistant to heat conduction compared to another polycrystalline thermoelectric compounds with a strong mass disorder like InSb (InSb,

κ_{lat} ~ 16 W/m.K; GeTe, κ_{lat} ~3 W/ m.K, Figure 1.24c).[294] Here, chemical bonding plays an important role. Softer bonding in GeTe compared to InSb leads to decrease in the speed of sound and the lattice thermal conductivity. Octahedral coordination in GeTe results in softer bonding compared to that of InSb (tetrahedral bonding) which leads to the decrease in the average sound velocity in GeTe (1900 m/s) compared to InSb (2300 m/s), thereby lower lattice thermal conductivity in GeTe. Moreover, the strong anharmonic interaction between soft ferroelectric transverse optic mode and longitudinal acoustic modes cause sudden decrease in lattice thermal conductivity of GeTe near the phase transition (Figure 1.24c).[295] This soft-phonon mode mediated phase transition temperature can be decreased to room temperature from 700 K through proper doping/alloying,[296] which can bring down the lattice thermal conductivity of GeTe to its minimum value (κ_{min} ~ 0.3 W/mK), thus can improve thermoelectric performance of GeTe near room temperature. κ_{lat} of GeTe can be further decreased by employing convention strategies like alloying and nanostructuring in order to improve its TE performance.[252, 290]

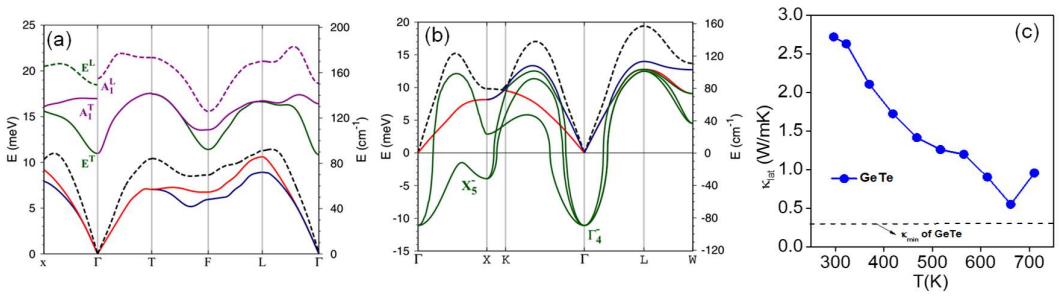

Figure 1.24. *Phonon dispersion plot of (a) rhombohedral and (b) cubic GeTe. Solid and dashed lines represent transverse (T) and longitudinal (L) modes, respectively. (c) Temperature dependent lattice thermal conductivity of GeTe showing sudden drop near the phase transition. Reproduced from ref 292 ©American Physical Society for (a, b).*

1.2.2. Synthesis

We have used solid state melting reaction for the synthesis of metal chalcogenides (as discussed in halide section) followed by SPS to obtain high dense (~98% of theoretical density) pellet for thermoelectric measurement.

1.3. Characterization techniques

Here we discuss the general principle of the technique in brief. Specific measurements are discussed in each chapter.

1.3.1. Powder X-ray diffraction (PXRD)

Powder X-ray diffraction is the most commonly used technique in solid state inorganic chemistry and has many uses from analysis and assessing phase purity to determine the structure. In this thesis, lab source X- ray have been used for structural characterization. In the laboratory, X-rays are generated in a cathode tube. In this technique, a tungsten filament was heated to produce electrons and electron beam was then accelerated towards an anode by applying a voltage (~ 30 - 40 kV). When electrons have sufficient energy to dislodge inner shell electrons of the target material, characteristic X-ray spectra are produced. These spectra consist of several components, the most common being Kα and Kβ. Kα consists, in part, of Kα_1 and Kα_2. Kα_1 has a slightly shorter wavelength and twice intensity than Kα_2. The specific wavelengths are characteristic of the target material (Cu, Fe, Mo, Cr). Cu is the most common target material use for laboratory X-ray. To produce monochromatic X-rays, it is required filtering out K$_\beta$ radiation by foils or crystal monochromators. For Cu radiation, a sheet of Ni foil is a very effective filter, but it is difficult to remove Kα_2 from Kα_1 because of close wavelength. The filtering process in laboratory X-ray leads to a reduction in intensity and hence it is difficult to detect low-intensity peaks in laboratory X-ray diffraction. In addition, it is difficult to distinguish peak splitting when peaks appear closely.

X-ray diffraction obeys Bragg's law, which states that constructive interference would occur if the path difference between the X-rays scattered from parallel planes were an integer number of the wavelength of radiation. If the planes of atoms, separated by a distance d, make an angle θ with the incident beam, then the path difference would be $2d\sin\theta$. So, for constructive interference, the Braggs law must be satisfied

$$i.e. \quad n\lambda = 2d\sin\theta, \; n = 1, 2, 3,$$

λ= wavelength of the X-ray radiation

In this thesis, room-temperature PXRD experiments on the samples are carried out using Bruker D8 diffractometer and Rigaku SmartLab SE.

1.3.2. Raman spectroscopy

Raman spectroscopy is one of the vibrational spectroscopic techniques used to provide information on molecular vibrations and crystal structures. This technique is based on inelastic scattering of monochromatic light. A change in the molecular polarizability with respect to the vibronic coordinate is required for a molecule to exhibit Raman effect. Normally, a laser source Nd-YAG with a fixed wavelength of 532 nm, an Argon ion laser source at 514 nm or He-Ne laser at 633 nm are used as light source. The laser light interacts with molecular vibrations, phonons or other excitations in the system, resulting in the energy of the laser photons being shifted up or down. The shift in energy gives information about the vibrational modes in the system. Low temperature Raman spectroscopic measurements were carried out on pellet shaped samples using Horiba Jobin-Yvon LabRAM HR evolution Raman spectrometer with 1800 gr/mm and Peltier cooled CCD detector.

1.3.3. Transmission electron microscope (TEM)

TEM is one of the important tools in material science for characterization of the microscopic structure of materials. A TEM image represents a two-dimensional projection of a three-dimensional object. TEM operates on the same basic principles as the light microscope, however, uses electrons as “light source” that makes it possible to get a resolution of about thousand times better than a visible light microscope. Instead of glass lenses focusing the light in the light microscope, the TEM uses electromagnetic lenses to focus the electrons into a very thin beam. The electron beam then travels through the specimen you want to study. When the electron beam passes through an ultra-thin specimen, it gets absorbed or diffracted through the specimen. Some of the electrons are scattered and disappear from the beam depending on the density of the material present on the focused region. A “shadow image” is formed by the interaction of the electrons transmitted through the specimen focused onto a fluorescent screen or a photographic film or by a sensor such as a charge-coupled device (CCD). TEM study allows to focus

electron beam to any part of specimen and electron diffraction data from a different area of the specimen can give us more details about the accurate local structure of the sample. The details of TEM instrument where used are given in the respective chapter.

1.3.4. Field emission scanning electron microscope (FESEM)

A FESEM is used to visualize topographic details of the sample surface. Similar to TEM, FESEM microscope also uses electrons as a light source. Electrons are ejected from a field emission source and accelerated in a high electrical field gradient. These electrons (termed as primary electrons) produce a narrow scan beam within the high vacuum column, which bombards the sample material. The incident electrons cause emission of electrons from the sample due to elastic and inelastic scattering. The angle and velocity of these secondary electrons produced by inelastic collision of accelerated electrons with sample atoms relate to the surface structure of the object. High-energy electrons those are produced by an elastic collision of a primary electrons with atom's nucleus of the sample are termed as backscattered electrons (BSE). Larger atoms (with a high atomic number, *Z*) have a higher chance of producing elastic collisions because of their greater cross-sectional area. Thus, a "brighter" BSE intensity correlates with higher average *Z* in the sample, and "dark" areas have lower average *Z*. BSE images are very helpful for obtaining high-resolution compositional maps of a sample. The details of FESEM instrument where used are given in the respective chapter.

1.3.5. Energy dispersive X-ray analysis (EDX)

EDX is an analytical technique used for elemental composition analysis of the sample. EDX makes use of the X-ray spectrum emitted by a solid sample bombarded with a focused beam of electrons. For EDX analysis, an X-ray detector is generally integrated with FESEM instrument. Its characterization capabilities are due in large part to the fundamental principle that each element has a unique atomic structure allowing a unique set of peaks on its electromagnetic emission spectrum. In my Ph.D., FESEM images in back scattered electron (BSE) mode and normal mode were taken using ZEISS Gemini attached to JEOL (JEM2100PLUS) FESEM instrument.

1.3.6. Positron annihilation spectroscopy (PAS)

PAS is a non-destructive nuclear solid state technique commonly used for defects and voids study in materials. It is a powerful technique to study open volume defects like dislocation, agglomerates, and vacancies at ppm concentration. Positrons (e^+) is an antiparticle of the electron (e^-) having exactly equal rest-mass of the electron (511 keV) but with a positive charge. One can obtain positrons from the β^+ decay of radioactive isotopes such as ^{22}Na, ^{64}Cu, and ^{58}Co. In my work, ^{22}NaCl has been used as positron source. Positrons injected from a radioactive source get thermalized within 1-10 ps and annihilate with a nearby electron inside the material, normally (379 out of 380 cases) emitting two exactly opposite 511 keV gamma rays, in the center of mass frame.

The experimental details about the positron annihilation spectroscopy have been given in the relevant chapter.

1.3.7. Optical spectroscopy and microscopy

UV-Vis-NIR absorption spectroscopy

Absorption spectroscopy refers to the spectroscopic technique that measures the absorption of an incident radiation as a function of wavelength, when radiation passes through a material under study. UV-Vis-NIR absorption spectroscopy is one of the most common techniques to characterize the NCs from ultraviolet to infrared spectral region. Semiconducting materials have discrete valence and conduction band which are separated by a band gap instead of continuous band as bulk semiconductors. Upon excitation with photons electronic transition can take place from the valence band to the conduction band and the position of the transition in the absorption spectrum gives the estimation of the band gap. The change in absorption edge indicates the change in band gap of the NCs as a function of size, shape and composition. When light is passed through an absorbing medium, a small portion of the light is absorbed by the medium. The absorption (A) is governed by Beer-Lambert's law, as following:

$$A = -\log_{10}\frac{I}{I_0} = \varepsilon c l$$

where, I_0 and I = Intensity of incident and transmitted light

ε = Molar extinction coefficient, expressed in $Lmol^{-1}cm^{-1}$

c = Molar concentration (mol/L)

l = Optical path length (cm), defined by the length of the absorbing medium

Transmittance (T) is defined as, $T = I/I_0$. Another important term is optical density (OD), which is defined as, $OD = \log_{10}(1/T)$. Transmittance and optical density account for both absorption and scattering of light when it travels through a medium, whereas, absorption accounts only for the absorption of light.

Diffuse reflectance spectroscopy

In my thesis work, the diffuse reflectance method has been used for the determination of band gap of the solid powdered materials. Diffuse reflectance is an excellent sampling tool for powdered crystalline materials. When light shines onto a powder sample, two types of reflections can occur. Some of the light undergoes specular reflection at the powder surface. Diffuse reflection happens when radiation penetrates into the sample and then emerges at all the angles after suffering multiple reflections and refractions by sample particles. A diffuse reflection accessory is designed to minimize the specular component. To estimate optical energy difference between the valence band and conduction band, optical diffuse reflectance measurements have been done with finely ground powder at room temperature. Absorption (α/Λ) data were estimated from reflectance data using Kubelka−Munk equation:

$$\alpha/\Lambda=(1-R)^2/(2R)$$

where R is the reflectance, α and Λ are the absorption and scattering coefficients, respectively. The energy band gaps were derived from α/Λ vs E (eV) plots. Electronic absorption spectroscopy is also performed in the solution phase and compared with solid state spectra. In my thesis work, we have collected the absorption data using FT-IR Bruker IFS 66V/S spectrometer and Perkin-Elmer Lambda 900, UV/Vis/NIR spectrometer.

Photoluminescence

Luminescence is nothing but the emission of light. It occurs via transition of an electron from an excited state to lower energy state (generally the ground state). Luminescence spectroscopy can have three major branches: fluorescence spectroscopy, phosphorescence spectroscopy and chemiluminescence spectroscopy. Fluorescence and phosphorescence are also categorized as either photoluminescence (PL) or electroluminescence (EL), depending on the excitation procedure. Mechanism of PL is commonly described with the help of Jablonski diagram as shown in Figure 1.25. A simple schematic diagram of a spectrophotometer for photoluminescence measurement is presented in Figure 1.26. In my thesis work, we have collected the emission spectra using PerkinElmer LS 55 luminescence spectrometer in the solid state and in solution phase at different excitation wavelengths.

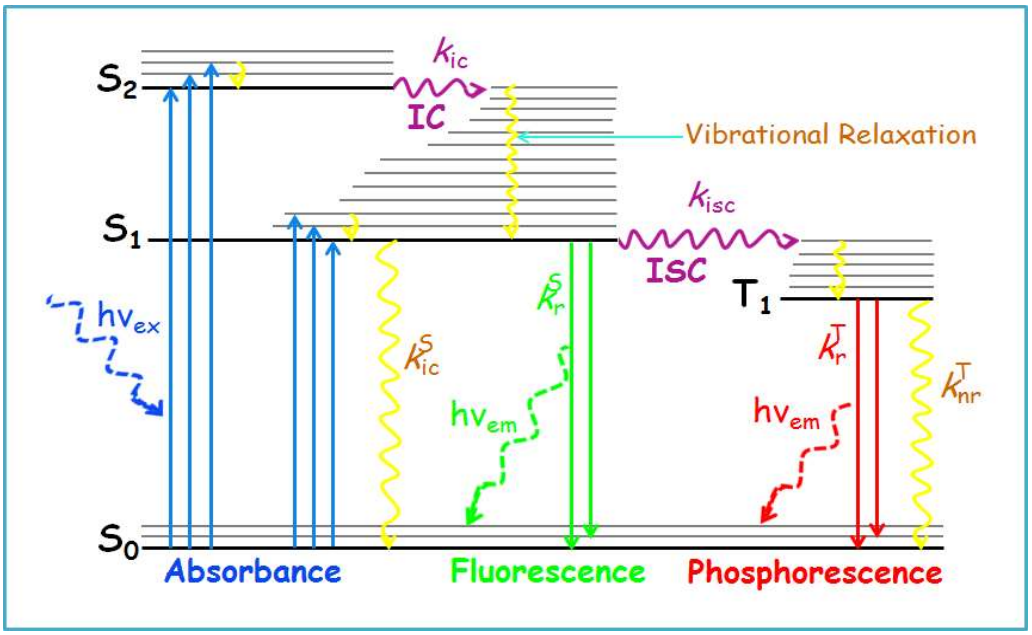

Figure 1.25. *A typical Jablonski diagram is a simplified representation of the electronic energy levels, emphasizing different de-excitation processes via which an excited electron can come down to the ground state by emitting light. S and T denote singlet and triplet states respectively, while, IC is internal conversion and ISC is intersystem crossing.*[297]

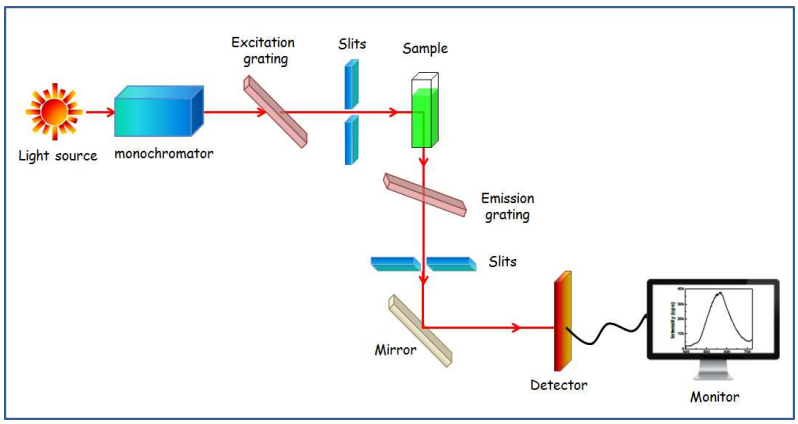

Figure 1.26. *Schematic illustration of a simplified spectrofluorometer showing the main components and working principle of the instrument.*

1.3.8 Super-resolved fluorescence microscopy

In my thesis work, the super-resolved fluorescence microscopy was employed in collaboration with Prof. Sarit S. Agasti. In general samples were dispersed in toluene and dried over a cover-slip for imaging. Brightfield images were captured first using lower magnification objective (EC plan-Neofluar 10×/0.3 M27) and the resulted image showed a distribution of tiny NPLs. The fluorescence images of the same crystals revealed the photoluminescent properties of the materials. Next, we further investigated the properties of these materials after looking at higher magnification objective (Alpha Plan-Apochromat100×/1.46 Oil DIC M27 Elyra) using high energy laser for excitation.

1.3.9 Atomic force microscopy (AFM)

AFM is a method to see a surface morphology as well as surface roughness in its full, three-dimensional glory of nano to micrometer sized materials. AFM provides important information regarding the height profile of the sample. Typically, AFM consists of a cantilever with a sharp tip whose radius is in the order of nanometers. In proximity of a sample surface, forces between the tip and the sample lead to a deflection of the cantilever according to the Hooke's law and this deflection is measured using a laser spot reflected from the top surface of the cantilever into an array of photodiodes. The AFM can be operated in various modes, depending on the application and the primary imaging modes

including static (also called contact) mode and dynamic (noncontact or tapping) mode. In static mode, the cantilever is dragged across the surface of the sample and the contours of the surface are directly measured using the deflection of the cantilever. In the dynamic mode, the cantilever is externally oscillated at or close to its fundamental resonance frequency or in a harmonic. The oscillation amplitude, phase and resonance frequency are modified by tip sample interaction forces. These changes in oscillation with respect to the external reference oscillation provide information about the sample's characteristics. The major advantage of AFM over other microscopic technique is the fact that AFM provides a three-dimensional surface profile instead of a two dimensional projection of the sample. The working principle of a typical AFM is described in Figure 1.27. In my thesis work we have used Bruker Innova Microscope in tapping mode with 10 nm diameter containing antimony doped Silicon tip.

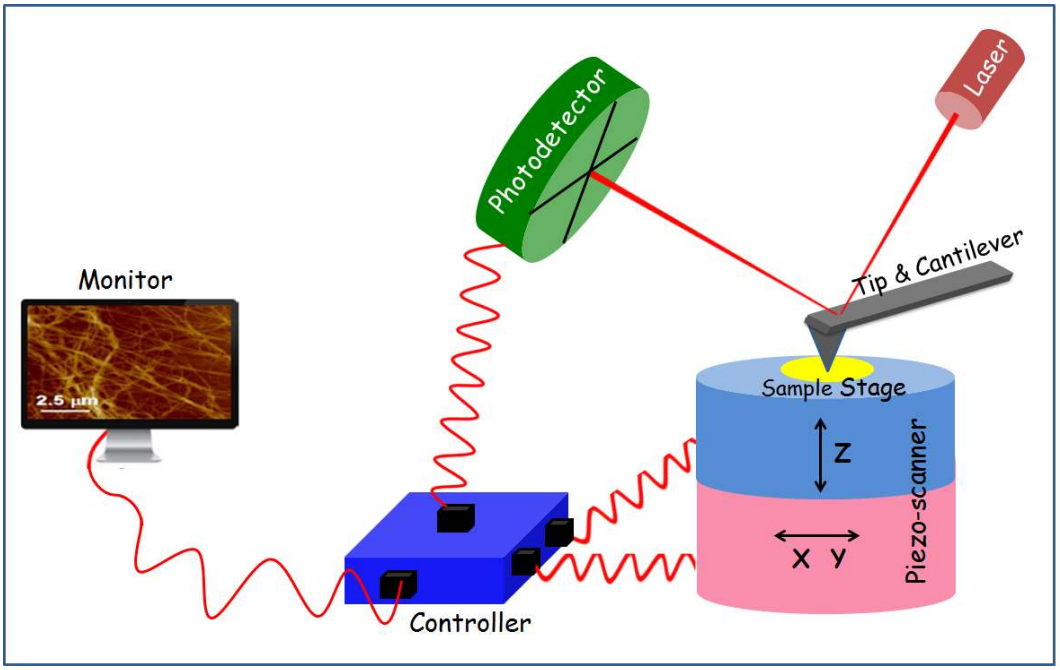

Figure 1.27. *Simplified schematic representation of an atomic force microscope (AFM) showing the main components and working principles of the instrument.*

1.3.10. Thermogravimetric analysis (TGA) and differential scanning calorimetry (DSC)

Thermogravimetric analysis or thermal gravimetric analysis (TGA) is a method of thermal analysis in which the mass of a sample is measured over time as the temperature changes. This measurement provides information about physical phenomena, such as phase transitions, absorption, adsorption and desorption; as well as chemical phenomena including chemisorptions, thermal decomposition, and solid-gas reactions. TGA experiments were carried out using a 2 STAR TGA instrument. The temperature range has been given in the relevant chapter.

DSC is a thermo-analytical technique in which the difference in the amount of heat required to increase the temperature of a sample and reference is measured as a function of temperature. Both the sample and reference are maintained at nearly the same temperature throughout the experiment. The basic principle underlying this technique is that when the sample undergoes any physical transformation such as phase transition, melting etc, amount of heat flow required to maintain both of them at the same temperature will be different. When the amount of heat required for the sample is lesser than the reference, the process is termed as exothermic. Endothermic process requires a higher amount of heat flow to maintain the temperature. By observing the difference in heat flow between the sample and reference, differential scanning calorimeters are able to measure the amount of heat absorbed or released during such transitions. DSC data were collected using TA INSTRUMENT Differential Scanning Calorimeter (DSC Q2000) in N_2 atmosphere. The temperature range has been given in the relevant chapter.

1.3.11. X-ray pair distribution function (PDF)

Pair distribution function (PDF) analysis is a powerful technique for probing atomic-scale disorder that cannot be detected using traditional diffraction methods.[298] Unlike other crystallographic methods, PDF analysis is a total scattering technique, which means that both Bragg and diffuse scattering are included. The PDF reveals both the long-range periodic structure (Bragg reflections) and the local structure imperfections (diffuse component of the diffraction pattern).[298]

Temperature dependent X-ray PDF data was collected using finely ground powder in beamline P02.1, PETRA III, DESY, Hamburg. Synchrotron beam of fixed energy (energies are given at respective chapters) and spot size 0.5 X 0.5 mm^2 was used to collect data.[299] From the coherent part $I^{coh}(Q)$ of the measured total diffracted intensity of the material, the total scattering structure function, S(Q), is obtained as

$$S\,(Q) = \frac{I^{coh}(Q) - \sum C_i |f_i(Q)|^2}{|\sum C_i f_i(Q)|^2} + 1$$

where the coherent intensity is corrected for background and other experimental effects and normalized by the flux and number of atoms in the sample. Here c_i and f_i are the atomic concentration and X-ray atomic form factor, respectively, for the atomic species of type i. The momentum transfer, Q, is given by:

$$Q = 4\pi \sin\theta/\lambda$$

Via Fourier-transforming the expression Q[S(Q)−1], we obtain:

$$G(r) = \frac{2}{\pi}\int_0^\infty Q[S(Q) - 1]\, sin\, Q\,(r) dQ$$

Where G(r) is the atomic pair distribution function, which is also defined as:

$$G(r) = 4\pi r[\rho(r) - \rho_0]$$

Where ρ_0 is the average atomic number density, ρ(r) is the atomic pair density, and r is a radial distance. The function G(r) gives information about the number of atoms in a spherical shell of unit thickness at a distance r from a reference atom. Finally, the experimental G(r) can be compared and refined against the theoretical G(r) from a structural model, given by:

$$G(r) = 4\pi r \rho_0 = \frac{1}{r}\sum_v \sum_\mu \frac{f(0)_v f(0)_\mu}{\langle f(0)\rangle^2}\, \delta(r - r_{v\mu})$$

2D image plate data was collected using a Perkin-Elmer detector which was processed using Fit2D or DAWNSci[300] software to obtain the scattering intensities *S*(Q) in the Q-space. The pair distribution *G*(r) was then obtained by Fourier transformation of the scattering structure function *F*(Q) = Q[*S*(Q) - 1] using PDFgetX2[301] or PDFgetX3[302] software. Finally, the modeling and refinement of *G*(r) was done using the software PDFgui.[303]

1.3.12 Dielectric spectroscopy

The dielectric constant is an important electrical property of a material. The dielectric constant can be measured by using two electrodes on opposite sides of the sample pellet as in a parallel plate capacitor. Electrical contacts are made using copper wires attached with silver paste on either side of the sample. We have used PELCO high-performance silver paste which has less dielectric noise and is effective at wide range of temperatures. In my thesis work, we have used Solartron 1260A impedance analyser dielectric properties measurement. Temperature and frequency dependent dielectric permittivity (ε) of the studied sample was measured by an Impedance Analyzer (Solartron SI 1260) attached to a 4 K closed cycle refrigerator (Advanced Research Systems, Inc.). A Lakeshore 335 temperature controller was used to control the temperature of the system and measure the temperature. A polished thin rectangular-shaped sample was used for this dielectric measurement. Thin layer of silver paste on either side of the two polished surfaces was used as electrodes.

The obtained dielectric constant is a complex quantity and is given by:

$$\varepsilon_r = \varepsilon_r' - i\varepsilon_r''$$

$$loss = tan\delta = \varepsilon_r''/\varepsilon_r'$$

here ε_r' and ε_r'' are the real and imaginary parts of the dielectric constant, respectively. The dielectric loss is also known as dissipation factor. From the capacitance data, the dielectric constant is obtained by using the relation, $\varepsilon_r' = Cd/\varepsilon_o A$ where, ε_o is the permittivity of free space (8.854×10^{-12} F.m^{-1}), A is the area of the parallel electrodes, and d is the distance between the electrodes or thickness of the sample.

1.3.13. Electronic transport measurement

The power factor of the zT expression depends on the product of the Seebeck coefficient and the electrical conductivity. The Seebeck coefficient is the ratio of a resulting electric field gradient to an applied temperature gradient. In a typical measurement, the temperature is varied around a constant average temperature and the slope of the voltage (V) *vs.* temperature difference (ΔT) curve gives the Seebeck coefficient (the slope method) or just $V/\Delta T$ is measured (single point measurement). Either a specific temperature difference is stabilized before each measurement (steady-state), which takes longer, or measurements are conducted continuously while the temperature difference is varied slowly (quasi- steady-state). Little difference was found between steady-state and quasi-steady-state measurements when good thermal and electrical contact is ensured. The employed temperature difference should be kept small, but too small will lead to decreased accuracy. Usually, 4 - 20 K (or 2 - 10 K) is appropriate for the full temperature span.

In the present thesis, temperature dependent Seebeck coefficient measurement has been done using the most popular commercial instruments ULVAC ZEM 3 RIKO using off-axis 4-point geometry under low-pressure helium (He) atmosphere (Figure 1.28a). In the off-axis, 4-point geometry, the thermocouples, and voltage leads are pressed against the sides of the sample (Figure 1.28b). The instrument uses slope method to extract the Seebeck coefficient from steady-state measurements. In the slope method, the measured raw data is corrected for constant offset voltages by using the slope of several (ΔT, V) points for extracting the Seebeck coefficient. The typical sample for measurement has a rectangular shape with the dimensions of ~ 2 mm × 2 mm × 8 mm and ΔT values 5, 10, 15 K have been used in the measurement. The error in the measurement is ~ 5%. In a typical measurement, the sample is set in a vertical position between the upper and lower electrode blocks in the heating furnace. For temperature dependent measurement, the sample was first heated to a specified temperature using an infrared (IR) furnace. Thereafter a temperature gradient across the sample was created by heating the lower part of it by a heater. Seebeck coefficient is measured by measuring the upper and lower temperatures T_1 and T_2 with the thermocouples pressed against the side of the sample,

followed by measurement of voltage (ΔV) between the same wires on one side of the thermocouple.[304]

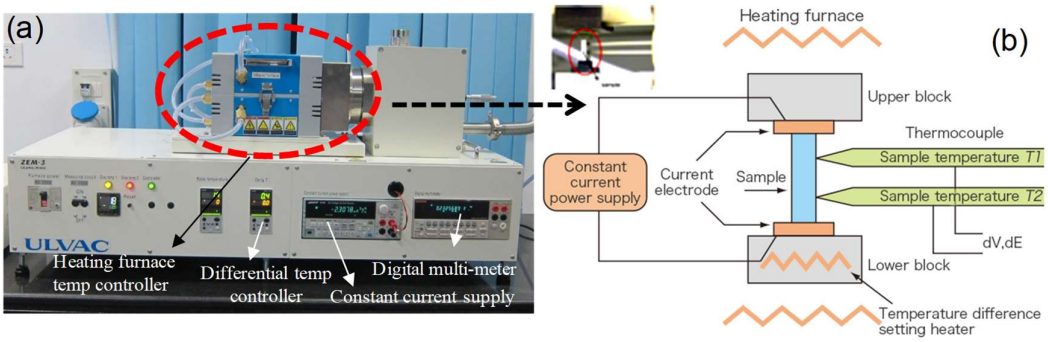

Figure 1.28. *(a) Photograph of sample-chamber in ULVAC-ZEM3 apparatus. (b) Schematic of UlVAC-ZEM 3 four-probe measurement system.*

The electrical conductivity, σ is measured using the four-probe method. Temperature dependent σ has been measured concurrently during Seebeck measurement in ULVAC ZEM 3 RIKO. For the measurement, a constant current I is applied to both ends of the sample to measure the voltage V between the thermocouples. By knowing resistance of sample, R ($R = V/I$), we can calculate σ from resistivity (ρ) of the sample using following equations:

$$\rho = R \times \frac{A}{l}$$

$$\sigma = \frac{1}{\rho}$$

where A is sample cross section and l is the distance between probes.

1.3.14. Hall effect

The Hall effect describes the behavior of the free carriers in a semiconductor when an electric and a magnetic field is applied along the perpendicular direction.[305] Thus, measurement of the Hall voltage is used to determine the type of charge carrier present in the system, the free carrier density and the carrier mobility. When a current-carrying semiconductor is kept in a magnetic field, the charge carriers of the semiconductor

experience a force in a direction perpendicular to both the magnetic field and the current. At equilibrium, a voltage appears at the semiconductor edges. The ratio of the induced voltage to the product of the current density (I/t, where I is applied current and t is sample thickness), n_H is charge carrier density, and the applied magnetic field (B) is defined as Hall coefficient (R_H) as shown in the equation:

$$R_H = \frac{Vt}{IB}$$

$$n_H = \frac{1}{R_H e}$$

where, e is the charge of an electron (1.602×10^{-19} C). In this thesis Hall measurement has been done in an inhouse equipment developed by Excel instrument. We have used a four-contact Hall-bar geometry and a varying magnetic field up for the measurements.

1.3.15 Thermal conductivity

The flash diffusivity method most frequently is used for the determination of thermal conductivity (κ) of material. Non-contact, non-destructive, easy sample preparation, applicability for a wide range of diffusivity values with excellent accuracy and reproducibility makes this method more advantageous than direct method. In the flash diffusivity method, the thermal conductivity is calculated as $\kappa = DC_p\rho$, where D is thermal diffusivity, ρ is density, and C_p is the constant pressure heat capacity. In this method, the sample is mounted on a carrier system, which is located in a furnace. After the sample reaches a predetermined temperature, a short heat pulse from a pulsed laser is applied to one side of a thin sample, resulting in homogeneous heating. The relative temperature increase on the rear face of the sample is then measured as a function of time by an IR detector. The temperature will rise to a maximum, after which it will decay. The time for the temperature to increase to half-maximum, $t_{1/2}$, is used to calculate the thermal diffusivity using the following equation:

$$D = 0.1388 \times \frac{l^2}{t_{1/2}}$$

where D is thermal diffusivity in cm^2/sec, l is the thickness.[306]

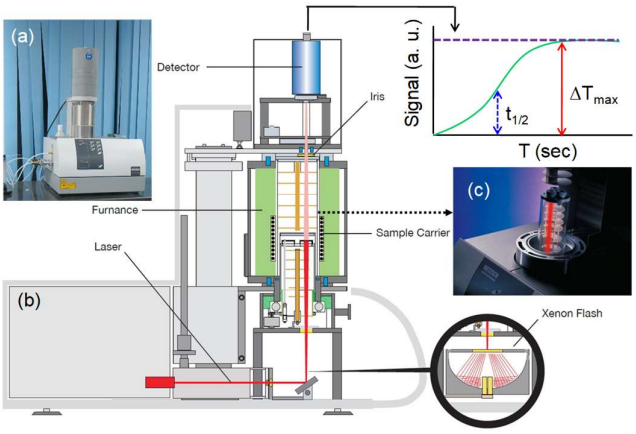

Figure 1.29. *(a) Photograph of NETZSCH LFA-457 instrument. (b) and (c) Schematic of LFA- 457 diffusivity measurement apparatus.*

In this thesis, temperature dependent thermal transport measurement (300-1373 K) has been done using the most popular NETZSCH LFA-457 instrument in N_2 atmosphere (Figure 1.29). The samples were coated with a thin layer of graphite (~ 5 μm) in order to enhance the absorption of laser energy and emission of IR radiation to the detector. It also increases the signal to noise ratio. The error for the κ measurement is ~ 5%. The samples were placed inside SiC sample holder to mount on carrier system (Figure 1. 29c). A Nd-Glass pulsed laser source of wavelength 1054 nm has been used for all the measurement. To measure the increased temperature on the rear face of the sample a liquid N_2 cooled InSb IR detector has been used. The density (ρ) was determined using the dimensions and mass of the sample and C_p, was derived indirectly using a standard sample (pyroceram). The thermal diffusivity data were analyzed using a Cowan model with pulse correction to account for heat losses on the sample faces.[307]

The low temperature (2-300 K) thermal conductivity was measured using Physical Property Measurement System (PPMS), Quantum Design (DynaCool) in Thermal Transport option (TTO) over the temperature range 1.9-390 K. The TTO system measures thermal conductivity κ by applying heat from the heater shoe in order to create a user-specified temperature differential between the two thermometer shoes. The TTO system dynamically models the thermal response of the sample to the low-frequency, square-

wave heat pulse, thus expediting data acquisition. TTO can then calculate thermal conductivity directly from the applied heater power, resulting ΔT, and sample geometry. The thermal and electrical connections for an idealized TTO sample are shown in Figure 1.30a. For clarity, the sample is shown mounted in the four probe geometry. The four basic physical elements are illustrated: the sample, the epoxy bonds that adhere the leads to the sample, the copper leads, and the heater and thermometer shoe assemblies that screw down onto the leads. For thermal conductivity and Seebeck coefficient measurements, heat is applied to one end of the sample by running current through the heater (Q+/-). The temperatures T_{hot} and T_{cold} are measured at the thermometer shoes. Heat exits the sample to the cold foot. Time traces of ΔT and ΔV during the heat pulse are illustrated in Figure 1.30b.

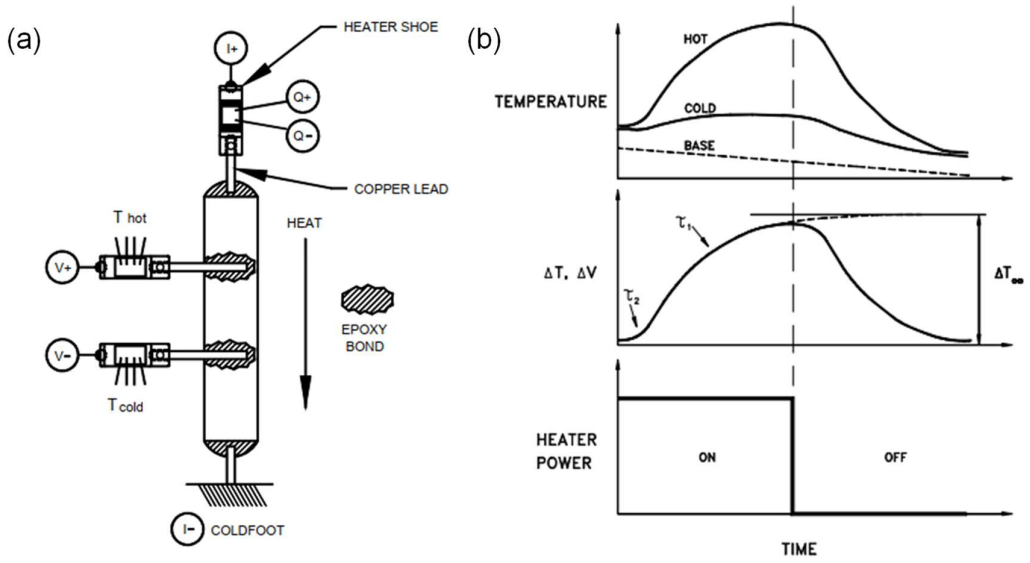

Figure 1.30. *(a) Thermal and electrical connections for an idealized sample. (b) Heat pulse and temperature and voltage response at hot and cold thermometer shoes in an idealized sample. Top panel: time trace of hot and cold thermometers during an idealized heat pulse; middle panel: corresponding temperature ΔT and voltage ΔV differentials across the sample, indicating thermal time constants τ_1 and τ_2 and the estimate of the asymptotic differential ΔT_{∞},; bottom panel: heater power during square-wave heat pulse. (adapted from Ref. [308])*

Heat capacity

The Quantum Design Heat Capacity option measures the heat capacity at constant pressure

$$C_p = (\frac{dQ}{dT})_p$$

As with other techniques for measuring heat capacity, the Quantum Design Heat Capacity option controls the heat added to and removed from a sample while monitoring the resulting change in temperature. During a measurement, a known amount of heat is applied at constant power for a fixed time, and then this heating period is followed by a cooling period of the same duration. A platform heater and platform thermometer are attached to the bottom side of the sample platform (see Figure 1.31).

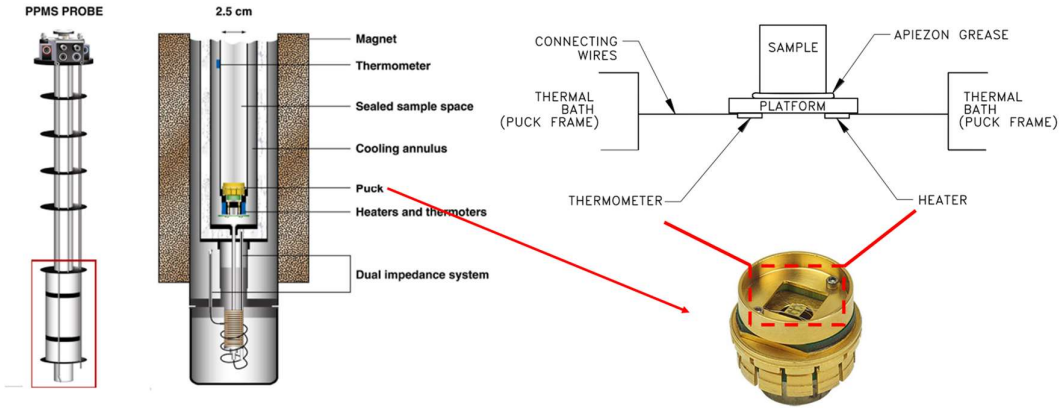

Figure 1.31. *Left. Detailed view of the sample chamber of PPMS probe. Right. Heat capacity puck along with the schematic diagram of the sample stage. (adapted from Ref.* [309]*)*

1.4. Fabrication of single leg thermoelectric device

A thermoelectric material can be combined with metal electrodes to form a thermoelectric element to measure its power-generating properties. The thermoelement here were prepared using powder metallurgy processes to create stacked Cu/Fe/powdered TE material/Fe/Cu structures. The powders were charged into a graphite die such that the thickness of each electrode layer was 0.3 mm, and that of the thermoelectric material layer

was 7.7 mm. The powder layers were consolidated into thermoelement using Spark Plasma Sintering at ~ 773 K and a pressure of 50 MPa in vacuum for 5 min.

Power generating properties and thermoelectric conversion efficiency of the fabricated thermoelement has been measured using mini-PEM module testing system (Advance Riko, Figure 1.32a).[310] This system was used to conduct the current load tests of the thermo-elements with large temperature gradients. A schematic of the experimental apparatus is shown in Figure 1.32b. The thermo-element was sandwiched between Cu blocks; the upper block contained a heating element and the lower block functioned as an isothermal heat sink with an integrated flow calorimeter. High temperature part can reach up to 600 °C (standard specifications), while low temperature part is cooled with water flow. Thermocouples were used to monitor the temperatures of the upper (T_h) and lower (T_c) Cu foils. A DC supply was connected to either end of the TE element. The conversion efficiency is evaluated from current dependency of power generation measured with four-probe method and heat flow measured with heat flow meter.

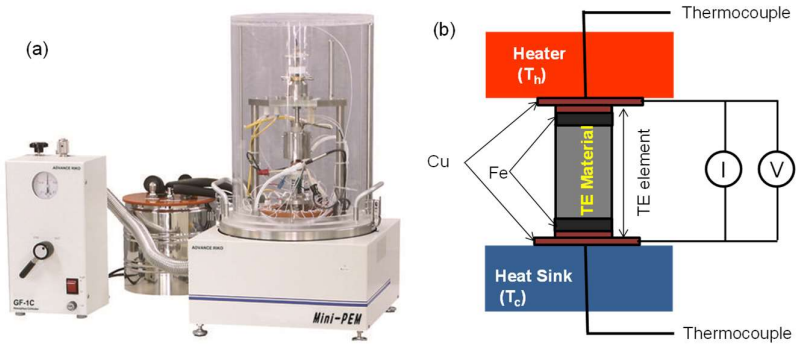

Figure 1.32. *(a) Photograph of Mini-PEM instrument. (b) Schematic diagram of the mounted thermoelement in the Mini-PEM test system.*

1.5. Scope of the thesis

Metal halides and chalcogenides are the most important classes of materials with a rich structural diversity and plethora of diverse application. In my Ph.D. work, we have implemented different synthetic route such as hot injection method for synthesis of monodispersed nanocrystals, Bridgman method to grow large single crystals, mechanochemical grinding to synthesize bulk powder of complex metal halides, high

temperature melting reaction to grow high quality polycrystal metal chalcogenides. Further we have studied their properties, gained an in-depth understanding of their diverse structure, and established their structure-property relationship. Finally, we have probed their applicability in diverse fields, such as optical blinking and magnetic properties along with the dielectric response in metal halides, while thermoelectric application for metal chalcogenides. Apart from the present introductory part (**Part 1**), my thesis work is divided into six parts (2-7), containing two chapters for each of the parts 2, 3, and 6; three chapters for part 4. Part 5 includes four chapters, while the last part (**Part 7**) provides a summarized future outlook.

Part 2 of my thesis involves the synthesis and characterization of 2D Pb-based metal halide-based perovskites. In **Chapter 2.1,** we have discussed the single pot solution-based transformation tetragonal 2D $CsPb_2Br_5$ nanosheets (NSs) from orthorhombic 3D $CsPbBr_3$ nanocrystals (NCs). Density functional theoretical (DFT) calculation of electronic structure demonstrate the direct band gap nature in 3D $CsPbBr_3$, while 2D $CsPb_2Br_5$ NSs exhibit indirect band gap and thus not expected to show the photoluminescence (PL). In spite of having indirect band gap, as synthesized $CsPb_2Br_5$ nanosheets show bright green luminescence with a blue shift of the PL spectra with respect to that of the $CsPbBr_3$ NCs. We investigated the origin of the luminescence property of $CsPb_2Br_5$, which was arising from the different amorphous lead bromide ammonium complexes present at the surface of this material, but not from the indirect band gap $CsPb_2Br_5$. In **Chapter 2.2,** we have discussed the formation of 2D nanoplates (NPs) of Ruddlesden-Popper (RP) phase of $Cs_2PbI_2Cl_2$ using benzoyl halides as halide source and subsequently, studied the optical properties of these synthesized samples both at cryogenic and room temperatures. We have also shown the chemical transformation of 2D RP phase of $Cs_2PbI_2Cl_2$ to 3D $CsPbBr_3$ and 0D Cs_4PbCl_6 by adding $PbBr_2$ and $MnCl_2$ in solution at room temperature, respectively for the first time. Furthermore, Mn^{2+} was inserted as a dopant (up to 5 mol %) with partial replacement of Pb^{2+} in $Cs_2PbI_2Cl_2$ NCs and investigated the optical properties. The Mn^{2+} doping in the $Cs_2PbI_2Cl_2$ NCs shows additional dopant emission band at 585 nm with prolonged lifetime in millisecond scale.

Part 3 of my thesis offers the synthesis and PL blinking properties of 2D nanostructures of layered perovskites. In **Chapter 3.1**, we have synthesized the 2D NSs

and small NCs of $Cs_3Bi_2I_6Cl_3$ by hot-injection method for the first time. The 2D NSs and NCs of $Cs_3Bi_2I_6Cl_3$ showed distinct optical properties and excitonic recombination dynamics, while at cryogenic temperature activation of shallow trap states was evidenced. Finally, the fluorescence microscopy was employed to investigate the single-particle PL properties of 2D NSs and NCs of $Cs_3Bi_2I_6Cl_3$, both of which showed luminescence at green region along with the localized blinking events at millisecond time scale. In **Chapter 3.2,** we have demonstrated the low-temperature colloidal synthesis of free-standing ultrathin (∼1.78 nm) few-layer (∼2 layers) NPLs (300-600 nm lateral dimension) of $Cs_3Bi_2I_9$ and studied their optical properties. We have also synthesized NSs (0.6-1.5 μm) and NCs of layered $Cs_3Bi_2I_9$ by varying the reaction temperature and subsequently, provided intriguing chemical insight to the formation mechanism. Further, bulk powder and crystalline ingot of $Cs_3Bi_2I_9$ have also been synthesized by mechanochemistry, liquid-assisted grinding (LAG), and vacuum-sealed tube melting reaction. In ultrathin NPLs, the optical property is controlled by lower energy states associated with the local intrinsic electronic structure of the edges of the perovskite layers. We have studied the single-particle fluorescence properties of $Cs_3Bi_2I_9$ NPLs was also investigated by super-resolution fluorescence microscopy, which revealed that the luminescence intensity of the NPLs is homogeneous and in the far-red region; importantly, the fluorescence blinking was in the millisecond time scale. The dispersive nature of the blinking kinetics indicated the existence of surface defects present on the large surface of the NPLs that trapped excitons, leading to nonradiative recombination. These trapping sites could alternatively be activated and deactivated by incident photons.

Part 4 involves the thermal conductivity studies of layered metal halide perovskite single crystals. In **Chapter 4.1,** we have demonstrated intrinsically ultralow lattice thermal conductivity (κ_L) of ~ 0.37-0.28 W/mK in the 295-523 K temperature range in a single crystal of layered Ruddlesden-Popper (RP) perovskite, $Cs_2PbI_2Cl_2$, synthesized by Bridgman method. We have measured an anisotropic ultralow κ_L along perpendicular and parallel to the Bridgman growth direction. An intriguing lattice dynamics in $Cs_2PbI_2Cl_2$ is noticed due to its anisotropic chemical bonding with co-existing mixed ionic (weak) and covalent (strong) bonding. The damped acoustic phonon modes and strong acoustic-optical phonon mode coupling resulted in an ultralow κ_L value

in all-inorganic 2D RP perovskite, $Cs_2PbI_2Cl_2$. In **Chapter 4.2,** we have studied the thermal conductivity of $Cs_3Bi_2I_6Cl_3$. Surprisingly single crystal of exhibits ultralow and glass-like thermal conductivity in the temperature range of 2-400. The presence of local distortion in the Bi-octahedra makes the $Cs_3Bi_2I_6Cl_3$ a highly disorder system, which is the primary reason for the glass-like thermal conductivity. While in **Chapter 4.3**, we have the discussed the thermal transport properties of 0D $Cs_3Bi_2I_9$ polycrystal samples which exhibits thermal conductivity similar to the typically crystalline materials.

Part 5 involves the dielectric, magnetic, and thermochromic properties of complex metal halides. In **Chapter 5.1,** we have demonstrated a broadband colossal dielectric constant (CDC) with a low dielectric loss in superionic $RbAg_4I_5$, which is synthesized by a facile solvent-free mechanochemical synthesis at room temperature. The presence of two structural phase transitions with decreasing temperature: α (cubic, space group $P4_332$) → β (rhombohedral, space group $R32$) at 209 K and β → γ (trigonal, space group P321) at 121 K was confirmed *via* temperature dependent powder X-ray diffraction (PXRD) and differential scanning calorimetry (DSC). The temperature dependent positron annihilation lifetime (PAL) spectroscopy and coincidence Doppler broadening (CDB) spectra evidence the presence of charged vacancies associated with the diffusion of Ag^+. We have shown that ε' increases by 10^2 order in magnitude as $RbAg_4I_5$ goes through the γ → β superionic phase transition from the low temperature side and ε' reaches a giant value of ~ 6.4 x 10^8 at 0.1 Hz in the room temperature superionic α phase. The molecular dynamics (MD) simulation showed charge density fluctuation within Ag^+ clusters because of intercluster Ag^+ diffusion. This causes fluctuation in the instantaneous dipole moments associated with Ag^+ clusters and results in the experimentally observed CDC in the room temperature superionic phase of $RbAg_4I_5$. In **Chapter 5.2,** we have presented all-solid state mechanochemical synthesis of 2D layered Pb-free metal halide, $RbSn_2Br_5$, and its mixed halide counterparts, $RbSn_2Br_3Cl_2$ and $RbSn_2Br_4I$. The Raman spectral investigation of as-synthesized powders displayed distinct modes at low frequency regions corresponding to the Sn-Br bond vibrations from 2D polymeric $[Sn_2Br_5]_n^{n-}$ layer units. We have studied the optical properties of as-synthesized materials by solid-state UV-Vis absorption and PL spectroscopic techniques, which showed an optical band gap of ~3.20 eV along with a PL emission centered at ~2.51 eV. We have

extended the investigation to explore the optical properties and charge-carrier recombination dynamics both at 298 K and 77 K using toluene-dispersed solution of $RbSn_2Br_5$ after prolonged ultrasonication. The excitonic recombinations occurred through the band-edge states and intrinsic defect sites (shallow states) at both temperature with average life-times in the range of few nanoseconds. The optical band gap (2.68-3.36 eV) and PL emission (2.31 eV to 2.58 eV) were further tuned by adjusting the halide composition in $RbSn_2Br_5$ by synthesizing $RbSn_2Br_3Cl_2$ and $RbSn_2Br_4I$. Finally, the dielectric measurement of $RbSn_2Br_5$ was carried out as a function of temperature (4-300 K). In **Chapter 5.3**, bulk polycrystalline powders of Pb-free RP-type phase of $Rb_2CuCl_2Br_2$ were synthesized by liquid-assisted mechanochemical grinding and their optical and magnetic properties have been investigated. The optical properties and carrier recombination dynamics of $Rb_2CuCl_2Br_2$ at both room-temperature and cryogenic temperature (77 K) are studied thoroughly. A red-shifted dual emission with enhanced intensity was evidenced at 77 K in comparison to the room-temperature emission. Finally, the magnetic measurement of $Rb_2CuCl_2Br_2$ showed a paramagnetic to antiferromagnetic (AFM) transition at ~16.1 K. In **Chapter 5.4**, we have discussed the thermochromic properties of as synthesized $(Ag_{1-x}Cu_x)_2HgI_4$ (where $0 \leq x \leq 1$). Temperature dependent solid state diffuse reflectance spectroscopy confirmed the thermochromic behavior of these materials. Differential scanning calorimetry (DSC) shows that the phase transition temperature passes through a minimum at 36 °C when $x = 0.5$ in $(Ag_{1-x}Cu_x)_2HgI_4$. A noticeable red shift in the PL spectra is detected with increase in the Cu content in $(Ag_{1-x}Cu_x)_2HgI_4$ and falls within the two extremities (i.e., $x = 0$ and 1).

Part 6 involves the thermoelectric performance of germanium telluride. In **Chapter 6.1** we have demonstrated an ultralow κ_{lat}, high thermoelectric performance, and high mechanical stability in Sb doped GeTe-rich $(GeTe)_{1-2x}(SnSe)_x(SnS)_x$ system. The realization of ultralow κ_{lat} and high zT is achieved *via* two successive stages. Initially, the addition of SnSe and SnS (each of 2.5 mol%) in GeTe reduces the κ_{latt} due to phonon scattering because of enhanced point defects and microstructures. Further, introduction of Sb doping introduces additional phonon scattering center and optimizes the *p*-type carrier concentration. As a result, 10 mol % Sb-doped $(GeTe)_{0.95}(SnSe)_{0.025}(SnS)_{0.025}$ sample exhibits ultralow κ_{lat} of ~ 0.34 W/mK accompanied by the zT of ~1.9 at 710 K.

The ultralow κ_{lat} is attributed due to the phonon scattering in Sb-doped $(GeTe)_{1-2x}(SnSe)_x(SnS)_x$ primarily by (a) excess solid solution point defects and (b) grain boundaries and micron size precipitates, thereby κ_{lat} reaches nearly to the κ_{min} of GeTe (0.3 W/m.K). Moreover, the measured Vickers microhardness (mechanical stability) value of high-performance sample is ~194 H_V, that is higher compared to pristine GeTe (~145 H_V). Motivated by the high zT and enhanced mechanical stability, we have constructed single-leg based thermoelectric device and achieved a high output power, ~ 150 mW for the temperature difference of 462 K, for 10 mol % Sb-doped $(GeTe)_{0.95}(SnSe)_{0.025}(SnS)_{0.025}$ sample. In **Chapter 6.2,** we unraveled the role of Hg and Sb doping in GeTe system with a record high thermoelectric performance. The role of Hg and Sb are distinct but complementary in terms of modulating the electronic structure and scatter the heat carrying acoustic phonon modes. The enhanced Seebeck coefficient in Hg doped GeTe system arises due the valance band convergence and low κ_{lat} is mainly attributed due to the presence of HgTe nano precipitates, confirmed by microscopic analysis. With the additional Sb doping to tune the carrier concentration of the Hg doped GeTe system. The co-doped samples introduce a resonance level near the fermi level which boost the Seebeck coefficient and power factor. The enhanced power factor and low thermal conductivity in $Ge_{0.87}Hg_{0.05}Sb_{0.08}Te$ leads to peak zT of 2.6 at 723 K. Furthermore, we have studied TE power generating properties of the single leg TE device of $Ge_{0.87}Hg_{0.05}Sb_{0.08}Te$ sample and obtained a high output power of 160 mW for the temperature difference of 464 K.

In **Part 7**, I have summarized all the chapters and provided a brief outlook into the future directions in developing new and efficient materials for various application.

1.6. References

1. L. Protesescu, S. Yakunin, M. I. Bodnarchuk, F. Krieg, R. Caputo, C. H. Hendon, R. X. Yang, A. Walsh and M. V. Kovalenko, *Nano Lett.*, 2015, **15**, 3692.

2. Q. A. Akkerman, G. Rainò, M. V. Kovalenko and L. Manna, *Nat. Mater.*, 2018, **17**, 394.

3. J. Shamsi, A. S. Urban, M. Imran, L. De Trizio and L. Manna, *Chem. Rev.*, 2019, **119**, 3296.

4. L. Chouhan, S. Ghimire, C. Subrahmanyam, T. Miyasaka and V. Biju, *Chem. Soc. Rev.*, 2020, **49**, 2869.

5. S. D. Stranks, G. E. Eperon, G. Grancini, C. Menelaou, M. J. P. Alcocer, T. Leijtens, L. M. Herz, A. Petrozza and H. J. Snaith, *Science*, 2013, **342**, 341.

6. G. Xing, N. Mathews, S. S. Lim, N. Yantara, X. Liu, D. Sabba, M. Grätzel, S. Mhaisalkar and T. C. Sum, *Nat. Mater.*, 2014, **13**, 476.

7. W.-Q. Liao, Y. Zhang, C.-L. Hu, J.-G. Mao, H.-Y. Ye, P.-F. Li, S. D. Huang and R.-G. Xiong, *Nat. Commun.*, 2015, **6**, 7338.

8. T. M. Brenner, D. A. Egger, L. Kronik, G. Hodes and D. Cahen, *Nat. Rev. Mater.*, 2016, **1**, 15007.

9. J. S. Manser, J. A. Christians and P. V. Kamat, *Chem. Rev.*, 2016, **116**, 12956.

10. W. Zhang, G. E. Eperon and H. J. Snaith, *Nat. Energy*, 2016, **1**, 16048.

11. W. Li, Z. Wang, F. Deschler, S. Gao, R. H. Friend and A. K. Cheetham, *Nat. Rev. Mater.*, 2017, **2**, 16099.

12. J. Huang, Y. Yuan, Y. Shao and Y. Yan, *Nat. Rev. Mater.*, 2017, **2**, 17042.

13. L. M. Herz, *ACS Energy Lett.*, 2017, **2**, 1539.

14. Y. Fu, H. Zhu, J. Chen, M. P. Hautzinger, X. Y. Zhu and S. Jin, *Nat. Rev. Mater.*, 2019, **4**, 169.

15. M. A. Green, A. Ho-Baillie and H. J. Snaith, *Nat. Photonics*, 2014, **8**, 506.

16. S. D. Stranks and H. J. Snaith, *Nat. Nanotechnol*, 2015, **10**, 391.

17. A. Kojima, K. Teshima, Y. Shirai and T. Miyasaka, *J. Am. Chem. Soc.*, 2009, **131**, 6050.

18. H.-S. Kim, C.-R. Lee, J.-H. Im, K.-B. Lee, T. Moehl, A. Marchioro, S.-J. Moon, R. Humphry-Baker, J.-H. Yum, J. E. Moser, M. Grätzel and N.-G. Park, *Sci. Rep.*, 2012, **2**, 591.

19. D. Luo, W. Yang, Z. Wang, A. Sadhanala, Q. Hu, R. Su, R. Shivanna, G. F. Trindade, J. F. Watts, Z. Xu, T. Liu, K. Chen, F. Ye, P. Wu, L. Zhao, J. Wu, Y. Tu, Y. Zhang, X. Yang, W. Zhang, R. H. Friend, Q. Gong, H. J. Snaith and R. Zhu, *Science*, 2018, **360**, 1442.

20. J. Tong, Z. Song, D. H. Kim, X. Chen, C. Chen, A. F. Palmstrom, P. F. Ndione, M. O. Reese, S. P. Dunfield, O. G. Reid, J. Liu, F. Zhang, S. P. Harvey, Z. Li, S. T. Christensen, G. Teeter, D. Zhao, M. M. Al-Jassim, M. F. A. M. van Hest, M. C. Beard, S. E. Shaheen, J. J. Berry, Y. Yan and K. Zhu, *Science*, 2019, **364**, 475.

21. G. E. Eperon, M. T. Hörantner and H. J. Snaith, *Nat. Rev. Chem.*, 2017, **1**, 0095.

22. N. J. Jeon, H. Na, E. H. Jung, T.-Y. Yang, Y. G. Lee, G. Kim, H.-W. Shin, S. Il Seok, J. Lee and J. Seo, *Nat. Energy*, 2018, **3**, 682.

23. X. Zheng, Y. Hou, C. Bao, J. Yin, F. Yuan, Z. Huang, K. Song, J. Liu, J. Troughton, N. Gasparini, C. Zhou, Y. Lin, D.-J. Xue, B. Chen, A. K. Johnston, N. Wei, M. N. Hedhili, M. Wei, A. Y. Alsalloum, P. Maity, B. Turedi, C. Yang, D. Baran, T. D. Anthopoulos, Y. Han, Z.-H. Lu, O. F. Mohammed, F. Gao, E. H. Sargent and O. M. Bakr, *Nat. Energy*, 2020, **5**, 131.

24. J. A. A. Ketelaar, *Trans. Faraday Soc.*, 1938, **34**, 874.

25. K. Lin, J. Xing, L. N. Quan, F. P. G. de Arquer, X. Gong, J. Lu, L. Xie, W. Zhao, D. Zhang, C. Yan, W. Li, X. Liu, Y. Lu, J. Kirman, E. H. Sargent, Q. Xiong and Z. Wei, *Nature*, 2018, **562**, 245.

26. Y. Cao, N. Wang, H. Tian, J. Guo, Y. Wei, H. Chen, Y. Miao, W. Zou, K. Pan, Y. He, H. Cao, Y. Ke, M. Xu, Y. Wang, M. Yang, K. Du, Z. Fu, D. Kong, D. Dai, Y. Jin, G. Li, H. Li, Q. Peng, J. Wang and W. Huang, *Nature*, 2018, **562**, 249.

27. T. Chiba, Y. Hayashi, H. Ebe, K. Hoshi, J. Sato, S. Sato, Y.-J. Pu, S. Ohisa and J. Kido, *Nat. Photonics*, 2018, **12**, 681.

28. W. Xu, Q. Hu, S. Bai, C. Bao, Y. Miao, Z. Yuan, T. Borzda, A. J. Barker, E. Tyukalova, Z. Hu, M. Kawecki, H. Wang, Z. Yan, X. Liu, X. Shi, K. Uvdal, M. Fahlman, W. Zhang, M. Duchamp, J.-M. Liu, A. Petrozza, J. Wang, L.-M. Liu, W. Huang and F. Gao, *Nat. Photonics*, 2019, **13**, 418.

29. H. Huang, B. Pradhan, J. Hofkens, M. B. J. Roeffaers and J. A. Steele, *ACS Energy Lett.*, 2020, **5**, 1107.

30. J. Liang, D. Chen, X. Yao, K. Zhang, F. Qu, L. Qin, Y. Huang and J. Li, *Small*, 2020, **16**, 1903398.

31. S. Shyamal and N. Pradhan, *J. Phys. Chem. Lett.*, 2020, **11**, 6921.

32. W. Travis, E. N. K. Glover, H. Bronstein, D. O. Scanlon and R. G. Palgrave, *Chem. Sci.*, 2016, **7**, 4548.

33. B. Saparov and D. B. Mitzi, *Chem. Rev.*, 2016, **116**, 4558.

34. C. J. Bartel, C. Sutton, B. R. Goldsmith, R. Ouyang, C. B. Musgrave, L. M. Ghiringhelli and M. Scheffler, *Sci. Adv.*, 2019, **5**, eaav0693.

35. Y. Rong, Y. Hu, A. Mei, H. Tan, M. I. Saidaminov, S. I. Seok, M. D. McGehee, E. H. Sargent and H. Han, *Science*, 2018, **361**, eaat8235.

36. J.-P. Correa-Baena, M. Saliba, T. Buonassisi, M. Grätzel, A. Abate, W. Tress and A. Hagfeldt, *Science*, 2017, **358**, 739.

37. H. Tsai, W. Nie, J.-C. Blancon, C. C. Stoumpos, R. Asadpour, B. Harutyunyan, A. J. Neukirch, R. Verduzco, J. J. Crochet, S. Tretiak, L. Pedesseau, J. Even, M. A. Alam, G. Gupta, J. Lou, P. M. Ajayan, M. J. Bedzyk, M. G. Kanatzidis and A. D. Mohite, *Nature*, 2016, **536**, 312.

38. L. Etgar, *Energy Environ. Sci.*, 2018, **11**, 234.

39. L. Mao, C. C. Stoumpos and M. G. Kanatzidis, *J. Am. Chem. Soc.*, 2019, **141**, 1171.

40. I. C. Smith, E. T. Hoke, D. Solis-Ibarra, M. D. McGehee and H. I. Karunadasa, *Angew. Chem. Int. Ed.*, 2014, **53**, 11232.

41. M. D. Smith, B. A. Connor and H. I. Karunadasa, *Chem. Rev.*, 2019, **119**, 3104.

42. D. H. Cao, C. C. Stoumpos, O. K. Farha, J. T. Hupp and M. G. Kanatzidis, *J. Am. Chem. Soc.*, 2015, **137**, 7843.

43. L. Pedesseau, D. Sapori, B. Traore, R. Robles, H.-H. Fang, M. A. Loi, H. Tsai, W. Nie, J.-C. Blancon, A. Neukirch, S. Tretiak, A. D. Mohite, C. Katan, J. Even and M. Kepenekian, *ACS Nano*, 2016, **10**, 9776.

44. X. Li, F. Cao, D. Yu, J. Chen, Z. Sun, Y. Shen, Y. Zhu, L. Wang, Y. Wei, Y. Wu and H. Zeng, *Small*, 2017, **13**, 1603996.

45. M. B. Faheem, B. Khan, C. Feng, M. U. Farooq, F. Raziq, Y. Xiao and Y. Li, *ACS Energy Lett.*, 2020, **5**, 290.

46. J. Liang, X. Han, J.-H. Yang, B. Zhang, Q. Fang, J. Zhang, Q. Ai, M. M. Ogle, T. Terlier, A. A. Martí and J. Lou, *Adv. Mater.*, 2019, **31**, 1903448.

47. R. H. Mitchell, M. D. Welch and A. R. Chakhmouradian, *Mineral. Mag.*, 2017, **81**, 411.

48. V. M. Goldschmidt, *Naturwissenschaften*, 1926, **14**, 477.

49. Q. A. Akkerman, A. L. Abdelhady and L. Manna, *J. Phys. Chem. Lett.*, 2018, **9**, 2326.

50. E. R. Dohner, A. Jaffe, L. R. Bradshaw and H. I. Karunadasa, *J. Am. Chem. Soc.*, 2014, **136**, 13154.

51. F. Zhang, H. Lu, J. Tong, J. J. Berry, M. C. Beard and K. Zhu, *Energy Environ. Sci.*, 2020, **13**, 1154.

52. S. N. Ruddlesden and P. Popper, *Acta Crystallographica*, 1958, **11**, 54.

53. X. Gao, X. Zhang, W. Yin, H. Wang, Y. Hu, Q. Zhang, Z. Shi, V. L. Colvin, W. W. Yu and Y. Zhang, *Adv. Sci.*, 2019, **6**, 1900941.

54. C. C. Stoumpos, D. H. Cao, D. J. Clark, J. Young, J. M. Rondinelli, J. I. Jang, J. T. Hupp and M. G. Kanatzidis, *Chem. Mater.*, 2016, **28**, 2852.

55. C. C. Stoumpos, C. M. M. Soe, H. Tsai, W. Nie, J.-C. Blancon, D. H. Cao, F. Liu, B. Traoré, C. Katan, J. Even, A. D. Mohite and M. G. Kanatzidis, *Chem*, 2017, **2**, 427.

56. J. Li, Q. Yu, Y. He, C. C. Stoumpos, G. Niu, G. G. Trimarchi, H. Guo, G. Dong, D. Wang, L. Wang and M. G. Kanatzidis, *J. Am. Chem. Soc.*, 2018, **140**, 11085.

57. J. Li, C. C. Stoumpos, G. G. Trimarchi, I. Chung, L. Mao, M. Chen, M. R. Wasielewski, L. Wang and M. G. Kanatzidis, *Chem. Mater.*, 2018, **30**, 4847.

58. X. Li, S. Wang, S. Zhao, L. Li, Y. Li, B. Zhao, Y. Shen, Z. Wu, P. Shan and J. Luo, *Chem. Eur. J.*, 2018, **24**, 9243.

59. M. H. Brooker and J. Wang, *Journal of Raman Spectroscopy*, 1992, **23**, 471.

60. J. Makovsky, A. Zodkevitz and Z. H. Kalman, *J. Cryst. Growth*, 1971, **11**, 99.

61. A. G. Ageev, A. N. Vtyurin, A. S. Krylov and A. D. Shefer, *Crystallogr. Rep*, 1998, **43**, 53.

62. F. Yamada, T. Ono, H. Tanaka and J.-i. Yamaura, *J. Phys. Soc. Jpn.*, 2007, **76**, 014708.

63. B. Saparov, F. Hong, J.-P. Sun, H.-S. Duan, W. Meng, S. Cameron, I. G. Hill, Y. Yan and D. B. Mitzi, *Chem. Mater.*, 2015, **27**, 5622.

64. M. I. Saidaminov, O. F. Mohammed and O. M. Bakr, *ACS Energy Lett.*, 2017, **2**, 889.

65. J. Pal, A. Bhunia, S. Chakraborty, S. Manna, S. Das, A. Dewan, S. Datta and A. Nag, *J. Phys. Chem. C*, 2018, **122**, 10643.

66. Q. Fan, G. V. Biesold-McGee, J. Ma, Q. Xu, S. Pan, J. Peng and Z. Lin, *Angew. Chem. Int. Ed.*, 2020, **59**, 1030.

67. A. J. Lehner, D. H. Fabini, H. A. Evans, C.-A. Hébert, S. R. Smock, J. Hu, H. Wang, J. W. Zwanziger, M. L. Chabinyc and R. Seshadri, *Chem. Mater.*, 2015, **27**, 7137.

68. F. Giustino and H. J. Snaith, *ACS Energy Lett.*, 2016, **1**, 1233.

69. K. M. McCall, C. C. Stoumpos, S. S. Kostina, M. G. Kanatzidis and B. W. Wessels, *Chem. Mater.*, 2017, **29**, 4129.

70. E. Y. Peresh, V. I. Sidei, O. V. Zubaka and I. P. Stercho, *Inorg. Mater.*, 2011, **47**, 208.

71. Z. Ma, Z. Shi, D. Yang, F. Zhang, S. Li, L. Wang, D. Wu, Y. Zhang, G. Na, L. Zhang, X. Li, Y. Zhang and C. Shan, *ACS Energy Lett.*, 2020, **5**, 385.

72. I. Stercho, A. Pogodin, O. Kokhan, I. Barchiy, A. Fedorchuk, I. Kityk and Piaseck, Michal, *Chem. Met. Alloys*, 2017, **10**, 113.

73. T. L. Hodgkins, C. N. Savory, K. K. Bass, B. L. Seckman, D. O. Scanlon, P. I. Djurovich, M. E. Thompson and B. C. Melot, *Chem. Commun.*, 2019, **55**, 3164.

74. K. M. McCall, C. C. Stoumpos, O. Y. Kontsevoi, G. C. B. Alexander, B. W. Wessels and M. G. Kanatzidis, *Chem. Mater.*, 2019, **31**, 2644.

75. Q. A. Akkerman and L. Manna, *ACS Energy Lett.*, 2020, **5**, 604.

76. B. Vargas, E. Ramos, E. Pérez-Gutiérrez, J. C. Alonso and D. Solis-Ibarra, *J. Am. Chem. Soc.*, 2017, **139**, 9116.

77. B. Vargas, R. Torres-Cadena, J. Rodríguez-Hernández, M. Gembicky, H. Xie, J. Jiménez-Mier, Y.-S. Liu, E. Menéndez-Proupin, K. R. Dunbar, N. Lopez, P. Olalde-Velasco and D. Solis-Ibarra, *Chem. Mater.*, 2018, **30**, 5315.

78. Y.-P. Lin, S. Hu, B. Xia, K.-Q. Fan, L.-K. Gong, J.-T. Kong, X.-Y. Huang, Z. Xiao and K.-Z. Du, *J. Phys. Chem. Lett.*, 2019, **10**, 5219.

79. B. Vargas, R. Torres-Cadena, D. T. Reyes-Castillo, J. Rodríguez-Hernández, M. Gembicky, E. Menéndez-Proupin and D. Solis-Ibarra, *Chem. Mater.*, 2020, **32**, 424.

80. P. Acharyya, P. Pal, P. K. Samanta, A. Sarkar, S. K. Pati and K. Biswas, *Nanoscale*, 2019, **11**, 4001.

81. G. Li, H. Wang, Z. Zhu, Y. Chang, T. Zhang, Z. Song and Y. Jiang, *Chem. Commun.*, 2016, **52**, 11296.

82. X.-W. Tong, Z.-X. Zhang, D. Wang, L.-B. Luo, C. Xie and Y.-C. Wu, *J. Mater. Chem. C*, 2019, **7**, 863.

83. G.-X. Liang, X.-Y. Chen, Z.-H. Chen, H.-B. Lan, Z.-H. Zheng, P. Fan, X.-Q. Tian, J.-Y. Duan, Y.-D. Wei and Z.-H. Su, *J. Phys. Chem. C*, 2019, **123**, 27423.

84. S. Ge, X. Guan, Y. Wang, C.-H. Lin, Y. Cui, Y. Huang, X. Zhang, R. Zhang, X. Yang and T. Wu, *Adv. Funct. Mater.*, 2020, **30**, 2002110.

85. M. B. Johansson, H. Zhu and E. M. J. Johansson, *J. Phys. Chem. Lett.*, 2016, **7**, 3467.

86. B. B. Owens and G. R. Argue, *Science*, 1967, **157**, 308.

87. S. Geller, *Science*, 1967, **157**, 310.

88. S. Geller, *Phys. Rev. B: Condens. Matter Mater. Phys.*, 1976, **14**, 4345.

89. K. Funke, R. D. Banhatti, D. Wilmer, R. Dinnebier, A. Fitch and M. Jansen, *J. Phys. Chem. A*, 2006, **110**, 3010.

90. H. Looser, M. Mali, J. Roos and D. Brinkmann, *Solid State Ion.*, 1983, **9–10**, 1237.

91. G. G. Bentle, *J. Appl. Phys.*, 1968, **39**, 4036.

92. F. L. Lederman, M. B. Salamon and H. Peisl, *Solid State Commun.*, 1976, **19**, 147.

93. D. Brinkmann, W. Freudenreich, H. Arend and J. Roos, *Solid State Commun.*, 1978, **27**, 133.

94. D. A. Gallagher and M. V. Klein, *Phys. Rev. B: Condens. Matter Mater. Phys.*, 1979, **19**, 4282.

95. R. Vargas and G. W. Coronel, *Solid State Ion.*, 1995, **81**, 69.

96. S. Hull and D. A. Keen, *J. Phys. Condens. Matter*, 2000, **12**, 3751.

97. K. W. Browall, J. S. Kasper and H. Wiedemeier, *J. Solid State Chem.*, 1974, **10**, 20.

98. S. Hull and D. A. Keen, *J. Phys. Condens. Matter*, 2001, **13**, 5597.

99. A. M. Sukeshini and K. Hariharan, *Solid State Commun.*, 1991, **78**, 85.

100. L. Suchow and P. H. Keck, *J. Am. Chem. Soc.*, 1953, **75**, 518.

101. J. Zhang, Y. Yang, H. Deng, U. Farooq, X. Yang, J. Khan, J. Tang and H. Song, *ACS Nano*, 2017, **11**, 9294.

102. M.-M. Yao, C.-H. Jiang, J.-S. Yao, K.-H. Wang, C. Chen, Y.-C. Yin, B.-S. Zhu, T. Chen and H.-B. Yao, *Inorg. Chem.*, 2019, **58**, 11807.

103. F. Zhang, H. Zhong, C. Chen, X.-g. Wu, X. Hu, H. Huang, J. Han, B. Zou and Y. Dong, *ACS Nano*, 2015, **9**, 4533.

104. J. Pal, S. Manna, A. Mondal, S. Das, K. V. Adarsh and A. Nag, *Angew. Chem. Int. Ed.*, 2017, **56**, 14187.

105. B. Pradhan, G. S. Kumar, S. Sain, A. Dalui, U. K. Ghorai, S. K. Pradhan and S. Acharya, *Chem. Mater.*, 2018, **30**, 2135.

106. S. K. Balakrishnan and P. V. Kamat, *Chem. Mater.*, 2018, **30**, 74.

107. B. Yang, J. Chen, F. Hong, X. Mao, K. Zheng, S. Yang, Y. Li, T. Pullerits, W. Deng and K. Han, *Angew. Chem. Int. Ed.*, 2017, **56**, 12471.

108. M. Leng, Y. Yang, K. Zeng, Z. Chen, Z. Tan, S. Li, J. Li, B. Xu, D. Li, M. P. Hautzinger, Y. Fu, T. Zhai, L. Xu, G. Niu, S. Jin and J. Tang, *Adv. Funct. Mater.*, 2018, **28**, 1704446.

109. P. Acharyya, K. Maji, K. Kundu and K. Biswas, *ACS Appl. Nano Mater.*, 2020, **3**, 877.

110. A. R. West, *Solid state chemistry and its applications*, John Wiley & Sons, 2014.

111. P. W. Bridgman, *Proc. Am. Acad. Arts Sci.*, 1925, **60**, 305.

112. C. C. Stoumpos, C. D. Malliakas and M. G. Kanatzidis, *Inorg. Chem.*, 2013, **52**, 9019.

113. L. Yin, H. Wu, W. Pan, B. Yang, P. Li, J. Luo, G. Niu and J. Tang, *Adv. Opt. Mater.*, 2019, **7**, 1900491.

114. Y. He, L. Matei, H. J. Jung, K. M. McCall, M. Chen, C. C. Stoumpos, Z. Liu, J. A. Peters, D. Y. Chung, B. W. Wessels, M. R. Wasielewski, V. P. Dravid, A. Burger and M. G. Kanatzidis, *Nat. Commun.*, 2018, **9**, 1609.

115. P. Acharyya, T. Ghosh, K. Pal, K. Kundu, K. Singh Rana, J. Pandey, A. Soni, U. V. Waghmare and K. Biswas, *J. Am. Chem. Soc.*, 2020, **142**, 15595.

116. G. J. Xie, *Powder Metall. Min.*, 2013, **2**, e109.

117. Z. A. Munir, U. Anselmi-Tamburini and M. Ohyanagi, *J. Mater. Sci.*, 2006, **41**, 763.

118. O. Guillon, J. Gonzalez-Julian, B. Dargatz, T. Kessel, G. Schierning, J. Räthel and M. Herrmann, *Adv. Eng. Mater.*, 2014, **16**, 830.

119. F. Palazon, Y. El Ajjouri and H. J. Bolink, *Adv. Energy Mater.*, 2020, **10**, 1902499.

120. P. Pal, S. Saha, A. Banik, A. Sarkar and K. Biswas, *Chem. Eur. J.*, 2018, **24**, 1811.

121. A. Sarkar, P. Acharyya, R. Sasmal, P. Pal, S. S. Agasti and K. Biswas, *Inorg. Chem.*, 2018, **57**, 15558.

122. N. Singhal, R. Chakraborty, P. Ghosh and A. Nag, *Chem. Asian J.*, 2018, **13**, 2085.

123. Y. El Ajjouri, V. S. Chirvony, N. Vassilyeva, M. Sessolo, F. Palazon and H. J. Bolink, *J. Mater. Chem. C*, 2019, **7**, 6236.

124. T. Cai, W. Shi, S. Hwang, K. Kobbekaduwa, Y. Nagaoka, H. Yang, K. Hills-Kimball, H. Zhu, J. Wang, Z. Wang, Y. Liu, D. Su, J. Gao and O. Chen, *J. Am. Chem. Soc.*, 2020, **142**, 11927.

125. D. Marongiu, M. Saba, F. Quochi, A. Mura and G. Bongiovanni, *J. Mater. Chem. C*, 2019, **7**, 12006.

126. Q. A. Akkerman, E. Bladt, U. Petralanda, Z. Dang, E. Sartori, D. Baranov, A. L. Abdelhady, I. Infante, S. Bals and L. Manna, *Chem. Mater.*, 2019, **31**, 2182.

127. O. Nazarenko, M. R. Kotyrba, S. Yakunin, M. Wörle, B. M. Benin, G. Rainò, F. Krumeich, M. Kepenekian, J. Even, C. Katan and M. V. Kovalenko, *Chem. Mater.*, 2019, **31**, 2121.

128. Z. Xu, M. Chen and S. F. Liu, *J. Phys. Chem. C*, 2019, **123**, 27978.

129. Y.-F. Ding, Q.-Q. Zhao, Z.-L. Yu, Y.-Q. Zhao, B. Liu, P.-B. He, H. Zhou, K. Li, S.-F. Yin and M.-Q. Cai, *J. Mater. Chem. C*, 2019, **7**, 7433.

130. I. Dursun, M. De Bastiani, B. Turedi, B. Alamer, A. Shkurenko, J. Yin, A. M. El-Zohry, I. Gereige, A. AlSaggaf, O. F. Mohammed, M. Eddaoudi and O. M. Bakr, *ChemSusChem*, 2017, **10**, 3746.

131. K.-H. Wang, L. Wu, L. Li, H.-B. Yao, H.-S. Qian and S.-H. Yu, *Angew. Chem. Int. Ed.*, 2016, **55**, 8328.

132. X. Tang, Z. Hu, W. Yuan, W. Hu, H. Shao, D. Han, J. Zheng, J. Hao, Z. Zang, J. Du, Y. Leng, L. Fang and M. Zhou, *Adv. Opt. Mater.*, 2017, **5**, 1600788.

133. L. Ruan, W. Shen, A. Wang, A. Xiang and Z. Deng, *J. Phys. Chem. Lett.*, 2017, **8**, 3853.

134. E. Y. Peresh, V. I. Sidei, N. I. Gaborets, O. V. Zubaka, I. P. Stercho and I. E. Barchii, *Inorg. Mater.*, 2014, **50**, 101.

135. S. E. Creutz, H. Liu, M. E. Kaiser, X. Li and D. R. Gamelin, *Chem. Mater.*, 2019, **31**, 4685.

136. E. E. Morgan, L. Mao, S. M. L. Teicher, G. Wu and R. Seshadri, *Inorg. Chem.*, 2020, **59**, 3387.

137. S. Seth, T. Ahmed and A. Samanta, *J. Phys. Chem. Lett.*, 2018, **9**, 7007.

138. T. Ahmed, S. Seth and A. Samanta, *ACS Nano*, 2019, **13**, 13537.

139. A. Halder, N. Pathoor, A. Chowdhury and S. K. Sarkar, *J. Phys. Chem. C*, 2018, **122**, 15133.

140. C. Galland, Y. Ghosh, A. Steinbrück, M. Sykora, J. A. Hollingsworth, V. I. Klimov and H. Htoon, *Nature*, 2011, **479**, 203.

141. X. Tang, J. Yang, S. Li, Z. Liu, Z. Hu, J. Hao, J. Du, Y. Leng, H. Qin, X. Lin, Y. Lin, Y. Tian, M. Zhou and Q. Xiong, *Adv. Sci.*, 2019, **6**, 1900412.

142. J. H. Day, *Chem. Rev.*, 1963, **63**, 65.

143. J. H. Day, *Chem. Rev.*, 1968, **68**, 649.

144. R. Asmussen and P. Andersen, *Acta Chem. Scand.*, 1958, **12**, 939.

145. M. De Bastiani, M. I. Saidaminov, I. Dursun, L. Sinatra, W. Peng, U. Buttner, O. F. Mohammed and O. M. Bakr, *Chem. Mater.*, 2017, **29**, 3367.

146. A. I. Kingon, J. P. Maria and S. K. Streiffer, *Nature*, 2000, **406**, 1032.

147. Y. Wang, W. Jie, C. Yang, X. Wei and J. Hao, *Adv. Funct. Mater.*, 2019, **29**, 1808118.

148. K. Yim, Y. Yong, J. Lee, K. Lee, H. H. Nahm, J. Yoo, C. Lee, C. Seong Hwang and S. Han, *NPG Asia Mater.*, 2015, **7**, e190.

149. X. Hao, *J. Adv. Dielectr.*, 2013, **03**, 1330001.

150. F. Palumbo, C. Wen, S. Lombardo, S. Pazos, F. Aguirre, M. Eizenberg, F. Hui and M. Lanza, *Adv. Funct. Mater.*, 2020, **30**, 1900657.

151. J. I. Roscow, C. R. Bowen and D. P. Almond, *ACS Energy Lett.*, 2017, **2**, 2264.

152. B. G. Kim, S. M. Cho, T. Y. Kim and H. M. Jang, *Phys. Rev. Lett.*, 2001, **86**, 3404.

153. C. Pecharromán, F. Esteban-Betegón, J. F. Bartolomé, S. López-Esteban and J. S. Moya, *Adv. Mater.*, 2001, **13**, 1541.

154. Y. Yan, J. E. Zhou, D. Maurya, Y. U. Wang and S. Priya, *Nat. Commun.*, 2016, **7**, 13089.

155. J. Yu, T. Ishikawa, Y. Arai, S. Yoda, M. Itoh and Y. Saita, *Appl. Phys. Lett.*, 2005, **87**, 252904.

156. Z. Wang, X. M. Chen, L. Ni and X. Q. Liu, *Appl. Phys. Lett.*, 2007, **90**, 022904.

157. J. H. Haeni, P. Irvin, W. Chang, R. Uecker, P. Reiche, Y. L. Li, S. Choudhury, W. Tian, M. E. Hawley and B. Craigo, *Nature*, 2004, **430**, 758.

158. K. F. Mak, J. Shan and D. C. Ralph, *Nat. Rev. Phys.*, 2019, **1**, 646.

159. K. S. Burch, D. Mandrus and J.-G. Park, *Nature*, 2018, **563**, 47.

160. N. Sivadas, S. Okamoto, X. Xu, C. J. Fennie and D. Xiao, *Nano Lett.*, 2018, **18**, 7658.

161. Q. Tong, F. Liu, J. Xiao and W. Yao, *Nano Lett.*, 2018, **18**, 7194.

162. L. J. De Jongh, P. Bloembergen and J. H. P. Colpa, *Physica*, 1972, **58**, 305.

163. H. T. Witteveen, *Physica*, 1974, **71**, 204.

164. A. Epstein, E. Gurewitz, J. Makovsky and H. Shaked, *Phys. Rev. B*, 1970, **2**, 3703.

165. A. D. Wright, C. Verdi, R. L. Milot, G. E. Eperon, M. A. Pérez-Osorio, H. J. Snaith, F. Giustino, M. B. Johnston and L. M. Herz, *Nat. Commun.*, 2016, **7**, 11755.

166. M. A. Haque, S. Kee, D. R. Villalva, W.-L. Ong and D. Baran, *Adv. Sci.*, 2020, **7**, 1903389.

167. L.-D. Zhao, V. P. Dravid and M. G. Kanatzidis, *Energy Environ. Sci.*, 2014, **7**, 251.

168. G. Tan, L.-D. Zhao and M. G. Kanatzidis, *Chem. Rev.*, 2016, **116**, 12123.

169. J. R. Sootsman, D. Y. Chung and M. G. Kanatzidis, *Angew. Chem. Int. Ed.*, 2009, **48**, 8616.

170. G. A. Elbaz, W.-L. Ong, E. A. Doud, P. Kim, D. W. Paley, X. Roy and J. A. Malen, *Nano Lett.*, 2017, **17**, 5734.

171. H. Ma, C. Li, Y. Ma, H. Wang, Z. W. Rouse, Z. Zhang, C. Slebodnick, A. Alatas, S. P. Baker, J. J. Urban and Z. Tian, *Phys. Rev. Lett.*, 2019, **123**, 155901.

172. B. Li, Y. Kawakita, Y. Liu, M. Wang, M. Matsuura, K. Shibata, S. Ohira-Kawamura, T. Yamada, S. Lin, K. Nakajima and S. Liu, *Nat. Commun.*, 2017, **8**, 16086.

173. Y. Wang, R. Lin, P. Zhu, Q. Zheng, Q. Wang, D. Li and J. Zhu, *Nano Lett.*, 2018, **18**, 2772.

174. S.-Y. Yue, X. Zhang, G. Qin, J. Yang and M. Hu, *Phys. Rev. B*, 2016, **94**, 115427.

175. A. Giri, A. Z. Chen, A. Mattoni, K. Aryana, D. Zhang, X. Hu, S.-H. Lee, J. J. Choi and P. E. Hopkins, *Nano Lett.*, 2020, **20**, 3331.

176. W. Lee, H. Li, A. B. Wong, D. Zhang, M. Lai, Y. Yu, Q. Kong, E. Lin, J. J. Urban, J. C. Grossman and P. Yang, *Proc. Natl. Acad. Sci. U. S. A.*, 2017, **114**, 8693.

177. T. Liu, X. Zhao, J. Li, Z. Liu, F. Liscio, S. Milita, B. C. Schroeder and O. Fenwick, *Nat. Commun.*, 2019, **10**, 5750.

178. H. Xie, S. Hao, J. Bao, T. J. Slade, G. J. Snyder, C. Wolverton and M. G. Kanatzidis, *J. Am. Chem. Soc.*, 2020, **142**, 9553.

179. Y. Xia, K. Pal, J. He, V. Ozoliņš and C. Wolverton, *Phys. Rev. Lett.*, 2020, **124**, 065901.

180. L.-D. Zhao, G. Tan, S. Hao, J. He, Y. Pei, H. Chi, H. Wang, S. Gong, H. Xu, V. P. Dravid, C. Uher, G. J. Snyder, C. Wolverton and M. G. Kanatzidis, *Science*, 2016, **351**, 141.

181. S. Roychowdhury, T. Ghosh, R. Arora, U. V. Waghmare and K. Biswas, *Angew. Chem. Int. Ed.*, 2018, **57**, 15167.

182. S. Chandra and K. Biswas, *J. Am. Chem. Soc.*, 2019, **141**, 6141.

183. T. Haeger, M. Wilmes, R. Heiderhoff and T. Riedl, *J. Phys. Chem. Lett.*, 2019, **10**, 3019.

184. F. Jellinek, *React. Solids*, 1988, **5**, 323.

185. A. Meerschaut, L. Guemas, R. Berger and J. Rouxel, *Acta Crystallogr., Sect. B: Struct. Sci.*, 1979, **35**, 1747.

186. Y. V. Mironov, M. A. Pell and J. A. Ibers, *Angew. Chem. Int. Ed. Engl.*, 1996, **35**, 2854.

187. T. Weber, R. Prins and R. A. van Santen, *Transition metal sulphides: chemistry and catalysis*, Springer Science & Business Media, 1998.

188. A. Mar, S. Jobic and J. A. Ibers, *J. Am. Chem. Soc.*, 1992, **114**, 8963.

189. S. Dehnen and M. Melullis, *Coord. Chem. Rev.*, 2007, **251**, 1259.

190. M. G. Kanatzidis, *Curr. Opin. Solid State Mater. Sci.*, 1997, **2**, 139.

191. M. G. Kanatzidis, *Inorg. Chem.*, 2017, **56**, 3158.

192. M. K. Jana and C. N. R. Rao, *Phil. Trans. R. Soc. A*, 2016, **374**, 20150318.

193. M. Chhowalla, H. S. Shin, G. Eda, L.-J. Li, K. P. Loh and H. Zhang, *Nat. Chem.*, 2013, **5**, 263.

194. C. N. R. Rao, U. Maitra and U. V. Waghmare, *Chem. Phys. Lett.*, 2014, **609**, 172.

195. C. N. R. Rao, H. S. S. Ramakrishna Matte and U. Maitra, *Angew. Chem. Int. Ed.*, 2013, **52**, 13162.

196. Q. Si, R. Yu and E. Abrahams, *Nat. Rev. Mater.*, 2016, **1**, 16017.

197. J. R. Sootsman, D. Y. Chung and M. G. Kanatzidis, *Angew. Chem. Int. Ed.*, 2009, **48**, 8616.

198. Q. H. Wang, K. Kalantar-Zadeh, A. Kis, J. N. Coleman and M. S. Strano, *Nat. Nanotechnol.*, 2012, **7**, 699.

199. G. Eda, T. Fujita, H. Yamaguchi, D. Voiry, M. Chen and M. Chhowalla, *ACS Nano*, 2012, **6**, 7311.

200. H. Lin, L. Chen, L.-J. Zhou and L.-M. Wu, *J. Am. Chem. Soc.*, 2013, **135**, 12914.

201. S. Hudgens and B. Johnson, *MRS Bull.*, 2004, **29**, 829.

202. S. C. Riha, B. A. Parkinson and A. L. Prieto, *J. Am. Chem. Soc.*, 2009, **131**, 12054.

203. Z. Lai, Y. Chen, C. Tan, X. Zhang and H. Zhang, *Chem*, 2016, **1**, 59.

204. X.-L. Shi, J. Zou and Z.-G. Chen, *Chem. Rev.*, 2020, **120**, 7399.

205. A. Rogalski, *Rep. Prog. Phys.*, 2005, **68**, 2267.

206. B. Radisavljevic, A. Radenovic, J. Brivio, V. Giacometti and A. Kis, *Nat. Nanotechnol.*, 2011, **6**, 147.

207. J. J. Cha, J. R. Williams, D. Kong, S. Meister, H. Peng, A. J. Bestwick, P. Gallagher, D. Goldhaber-Gordon and Y. Cui, *Nano Lett.*, 2010, **10**, 1076.

208. N. Kamaya, K. Homma, Y. Yamakawa, M. Hirayama, R. Kanno, M. Yonemura, T. Kamiyama, Y. Kato, S. Hama, K. Kawamoto and A. Mitsui, *Nat. Mater.*, 2011, **10**, 682.

209. F. Cheng, J. Liang, Z. Tao and J. Chen, *Adv. Mater.*, 2011, **23**, 1695.

210. D. Merki and X. Hu, *Energy Environ. Sci.*, 2011, **4**, 3878.

211. J. M. Caron, J. R. Neilson, D. C. Miller, K. Arpino, A. Llobet and T. M. McQueen, *Phys. Rev. B*, 2012, **85**, 180405.

212. S. Medvedev, T. M. McQueen, I. A. Troyan, T. Palasyuk, M. I. Eremets, R. J. Cava, S. Naghavi, F. Casper, V. Ksenofontov, G. Wortmann and C. Felser, *Nat. Mater.*, 2009, **8**, 630.

213. H. S. S. Ramakrishna Matte, A. Gomathi, A. K. Manna, D. J. Late, R. Datta, S. K. Pati and C. N. R. Rao, *Angew. Chem. Int. Ed.*, 2010, **49**, 4059.

214. M. König, S. Wiedmann, C. Brüne, A. Roth, H. Buhmann, L. W. Molenkamp, X.-L. Qi and S.-C. Zhang, *Science*, 2007, **318**, 766.

215. D. Hsieh, Y. Xia, D. Qian, L. Wray, J. H. Dil, F. Meier, J. Osterwalder, L. Patthey, J. G. Checkelsky, N. P. Ong, A. V. Fedorov, H. Lin, A. Bansil, D. Grauer, Y. S. Hor, R. J. Cava and M. Z. Hasan, *Nature*, 2009, **460**, 1101.

216. D. Kong and Y. Cui, *Nat. Chem.*, 2011, **3**, 845.

217. L. Müchler, F. Casper, B. Yan, S. Chadov and C. Felser, *Phys. Status Solidi RRL*, 2013, **7**, 91.

218. Y. Xia, D. Qian, D. Hsieh, L. Wray, A. Pal, H. Lin, A. Bansil, D. Grauer, Y. S. Hor, R. J. Cava and M. Z. Hasan, *Nat. Phys.*, 2009, **5**, 398.

219. L. Fu, *Phys. Rev. Lett.*, 2011, **106**, 106802.

220. T. H. Hsieh, H. Lin, J. Liu, W. Duan, A. Bansil and L. Fu, *Nat. Commun.*, 2012, **3**, 982.

221. M. N. Ali, J. Xiong, S. Flynn, J. Tao, Q. D. Gibson, L. M. Schoop, T. Liang, N. Haldolaarachchige, M. Hirschberger, N. P. Ong and R. J. Cava, *Nature*, 2014, **514**, 205.

222. G. Tan, L.-D. Zhao and M. G. Kanatzidis, *Chem. Rev.*, 2016, **116**, 12123.

223. B. Jiang, Y. Yu, J. Cui, X. Liu, L. Xie, J. Liao, Q. Zhang, Y. Huang, S. Ning, B. Jia, B. Zhu, S. Bai, L. Chen, S. J. Pennycook and J. He, *Science*, 2021, **371**, 830.

224. S. Roychowdhury, T. Ghosh, R. Arora, M. Samanta, L. Xie, N. K. Singh, A. Soni, J. He, U. V. Waghmare and K. Biswas, *Science*, 2021, **371**, 722.

225. Y. Xiao and L.-D. Zhao, *Science*, 2020, **367**, 1196.

226. M. Dutta, T. Ghosh and K. Biswas, *APL Mater.*, 2020, **8**, 040910.

227. C. Goupil, H. Ouerdane, K. Zabrocki, W. Seifert, N. F. Hinsche and E. Müller, *Thermodynamics and thermoelectricity*, 2016, 1.

228. L.-D. Zhao, V. P. Dravid and M. G. Kanatzidis, *Energy Environ. Sci.*, 2014, **7**, 251.

229. Y. Xiao, H. Wu, J. Cui, D. Wang, L. Fu, Y. Zhang, Y. Chen, J. He, S. J. Pennycook and L.-D. Zhao, *Energy Environ. Sci.*, 2018, **11**, 2486.

230. D. Sarkar, T. Ghosh, A. Banik, S. Roychowdhury, D. Sanyal and K. Biswas, *Angew. Chem. Int. Ed.*, 2020, **59**, 11115.

231. Y. Pei, X. Shi, A. LaLonde, H. Wang, L. Chen and G. J. Snyder, *Nature*, 2011, **473**, 66.

232. A. Banik, U. S. Shenoy, S. Saha, U. V. Waghmare and K. Biswas, *J. Am. Chem. Soc.*, 2016, **138**, 13068.

233. J. P. Heremans, V. Jovovic, E. S. Toberer, A. Saramat, K. Kurosaki, A. Charoenphakdee, S. Yamanaka and G. J. Snyder, *Science*, 2008, **321**, 554.

234. J. M. Hodges, S. Hao, J. A. Grovogui, X. Zhang, T. P. Bailey, X. Li, Z. Gan, Y.-Y. Hu, C. Uher, V. P. Dravid, C. Wolverton and M. G. Kanatzidis, *J. Am. Chem. Soc.*, 2018, **140**, 18115.

235. Y. Qin, Y. Xiao and L.-D. Zhao, *APL Mater.*, 2020, **8**, 010901.

236. T. C. Harman, P. J. Taylor, M. P. Walsh and B. E. LaForge, *Science*, 2002, **297**, 2229.

237. S. Roychowdhury, R. K. Biswas, M. Dutta, S. K. Pati and K. Biswas, *ACS Energy Lett.*, 2019, **4**, 1658.

238. L. Fu, M. Yin, D. Wu, W. Li, D. Feng, L. Huang and J. He, *Energy Environ. Sci.*, 2017, **10**, 2030.

239. K. Biswas, J. He, Q. Zhang, G. Wang, C. Uher, V. P. Dravid and M. G. Kanatzidis, *Nat. Chem.*, 2011, **3**, 160.

240. B. Poudel, Q. Hao, Y. Ma, Y. Lan, A. Minnich, B. Yu, X. Yan, D. Wang, A. Muto, D. Vashaee, X. Chen, J. Liu, M. S. Dresselhaus, G. Chen and Z. Ren, *Science*, 2008, **320**, 634.

241. K. Biswas, J. He, I. D. Blum, C.-I. Wu, T. P. Hogan, D. N. Seidman, V. P. Dravid and M. G. Kanatzidis, *Nature*, 2012, **489**, 414.

242. L. D. Zhao, H. J. Wu, S. Q. Hao, C. I. Wu, X. Y. Zhou, K. Biswas, J. Q. He, T. P. Hogan, C. Uher, C. Wolverton, V. P. Dravid and M. G. Kanatzidis, *Energy Environ. Sci.*, 2013, **6**, 3346.

243. M. K. Jana and K. Biswas, *ACS Energy Lett.*, 2018, **3**, 1315.

244. Y. Xiao, H. Wu, W. Li, M. Yin, Y. Pei, Y. Zhang, L. Fu, Y. Chen, S. J. Pennycook, L. Huang, J. He and L.-D. Zhao, *J. Am. Chem. Soc.*, 2017, **139**, 18732.

245. S. I. Kim, K. H. Lee, H. A. Mun, H. S. Kim, S. W. Hwang, J. W. Roh, D. J. Yang, W. H. Shin, X. S. Li, Y. H. Lee, G. J. Snyder and S. W. Kim, *Science*, 2015, **348**, 109.

246. Z. Xu, H. Wu, T. Zhu, C. Fu, X. Liu, L. Hu, J. He, J. He and X. Zhao, *NPG Asia Mater.*, 2016, **8**, e302.

247. Y. Xiao and L.-D. Zhao, *NPJ Quantum Mater.*, 2018, **3**, 55.

248. Q. Zhang, B. Liao, Y. Lan, K. Lukas, W. Liu, K. Esfarjani, C. Opeil, D. Broido, G. Chen and Z. Ren, *Proc. Natl. Acad. Sci. U. S. A.*, 2013, **110**, 13261.

249. P. Acharyya, S. Roychowdhury, M. Samanta and K. Biswas, *J. Am. Chem. Soc.*, 2020, **142**, 20502.

250. M. Samanta and K. Biswas, *J. Am. Chem. Soc.*, 2017, **139**, 9382.

251. C. Zhou, H. Lin, Y. Tian, Z. Yuan, R. Clark, B. Chen, L. J. van de Burgt, J. C. Wang, Y. Zhou, K. Hanson, Q. J. Meisner, J. Neu, T. Besara, T. Siegrist, E. Lambers, P. Djurovich and B. Ma, *Chem. Sci.*, 2018, **9**, 586.

252. S. Roychowdhury, M. Samanta, S. Perumal and K. Biswas, *Chem. Mater.*, 2018, **30**, 5799.

253. S. Chandra and K. Biswas, *J. Am. Chem. Soc.*, 2019, **141**, 6141.

254. C. Chang, M. Wu, D. He, Y. Pei, C.-F. Wu, X. Wu, H. Yu, F. Zhu, K. Wang, Y. Chen, L. Huang, J.-F. Li, J. He and L.-D. Zhao, *Science*, 2018, **360**, 778.

255. L.-D. Zhao, S.-H. Lo, Y. Zhang, H. Sun, G. Tan, C. Uher, C. Wolverton, V. P. Dravid and M. G. Kanatzidis, *Nature*, 2014, **508**, 373.

256. S. Chandra, A. Banik and K. Biswas, *ACS Energy Lett.*, 2018, **3**, 1153.

257. M. S. Ikeda, H. Euchner, X. Yan, P. Tomeš, A. Prokofiev, L. Prochaska, G. Lientschnig, R. Svagera, S. Hartmann, E. Gati, M. Lang and S. Paschen, *Nat. Commun.*, 2019, **10**, 887.

258. X. Shi, J. Yang, J. R. Salvador, M. Chi, J. Y. Cho, H. Wang, S. Bai, J. Yang, W. Zhang and L. Chen, *J. Am. Chem. Soc.*, 2011, **133**, 7837.

259. Y. Tang, Z. M. Gibbs, L. A. Agapito, G. Li, H. S. Kim, M. B. Nardelli, S. Curtarolo and G. J. Snyder, *Nat. Mater.*, 2015, **14**, 1223.

260. C. Fu, T. Zhu, Y. Liu, H. Xie and X. Zhao, *Energy Environ. Sci.*, 2015, **8**, 216.

261. C. Fu, S. Bai, Y. Liu, Y. Tang, L. Chen, X. Zhao and T. Zhu, *Nat. Commun.*, 2015, **6**, 8144.

262. H. Liu, X. Yuan, P. Lu, X. Shi, F. Xu, Y. He, Y. Tang, S. Bai, W. Zhang, L. Chen, Y. Lin, L. Shi, H. Lin, X. Gao, X. Zhang, H. Chi and C. Uher, *Adv. Mater.*, 2013, **25**, 6607.

263. A. A. Olvera, N. A. Moroz, P. Sahoo, P. Ren, T. P. Bailey, A. A. Page, C. Uher and P. F. P. Poudeu, *Energy Environ. Sci.*, 2017, **10**, 1668.

264. Y. Pei, A. D. LaLonde, N. A. Heinz, X. Shi, S. Iwanaga, H. Wang, L. Chen and G. J. Snyder, *Adv. Mater.*, 2011, **23**, 5674.

265. Z. Zheng, X. Su, R. Deng, C. Stoumpos, H. Xie, W. Liu, Y. Yan, S. Hao, C. Uher, C. Wolverton, M. G. Kanatzidis and X. Tang, *J. Am. Chem. Soc.*, 2018, **140**, 2673.

266. C. M. Jaworski, V. Kulbachinskii and J. P. Heremans, *Phys. Rev. B*, 2009, **80**, 233201.

267. L. Wu, X. Li, S. Wang, T. Zhang, J. Yang, W. Zhang, L. Chen and J. Yang, *NPG Asia Mater.*, 2017, **9**, e343.

268. T. Berry, C. Fu, G. Auffermann, G. H. Fecher, W. Schnelle, F. Serrano-Sanchez, Y. Yue, H. Liang and C. Felser, *Chem. Mater.*, 2017, **29**, 7042.

269. M. Samanta, M. Dutta and K. Biswas, in *Advances in the Chemistry and Physics of Materials*, WORLD SCIENTIFIC, 2019, pp. 350.

270. G. J. Snyder and E. S. Toberer, *Nat. Mater.*, 2008, **7**, 105.

271. J. Korringa and A. N. Gerritsen, *Physica*, 1953, **19**, 457.

272. Y. I. Ravich and S. A. Nemov, *Semiconductors*, 2002, **36**, 1.

273. J. Li, X. Zhang, Z. Chen, S. Lin, W. Li, J. Shen, I. T. Witting, A. Faghaninia, Y. Chen, A. Jain, L. Chen, G. J. Snyder and Y. Pei, *Joule*, 2018, **2**, 976.

274. S. Roychowdhury and K. Biswas, *Chem*, 2018, **4**, 939.

275. T. Zhu, Y. Liu, C. Fu, J. P. Heremans, J. G. Snyder and X. Zhao, *Adv. Mater.*, 2017, **29**, 1605884.

276. T. M. Tritt, *Thermal conductivity: theory, properties, and applications*, Springer Science & Business Media, 2005.

277. N. W. Ashcroft and N. D. Mermin, *Solid state physics*, holt, rinehart and winston, new york London, 1976.

278. D. G. Cahill and R. O. Pohl, *Sol. State Commun.*, 1989, **70**, 927.

279. W.-X. Zhou, Y. Cheng, K.-Q. Chen, G. Xie, T. Wang and G. Zhang, *Adv. Funct. Mater.*, 2020, **30**, 1903829.

280. M. Beekman and D. G. Cahill, *Cryst. Res. Technol.*, 2017, **52**, 1700114.

281. M. A. Avila, K. Suekuni, K. Umeo, H. Fukuoka, S. Yamanaka and T. Takabatake, *Phys. Rev. B*, 2006, **74**, 125109.

282. D. Gibson Quinn, T. Zhao, M. Daniels Luke, C. Walker Helen, R. Daou, S. Hébert, M. Zanella, S. Dyer Matthew, B. Claridge John, B. Slater, W. Gaultois Michael, F. Corà, J. Alaria and J. Rosseinsky Matthew, *Science*, 2021, **373**, 1017.

283. Z. Chen, X. Zhang and Y. Pei, *Adv. Mater.*, 2018, **30**, 1705617.

284. J. P. Heremans, *Nat. Phys.*, 2015, **11**, 990.

285. J. Callaway, *Phys. Rev.*, 1959, **113**, 1046.

286. J. He, S. N. Girard, M. G. Kanatzidis and V. P. Dravid, *Adv. Funct. Mater.*, 2010, **20**, 764.

287. J. Yang and T. Caillat, *MRS Bulletin*, 2006, **31**, 224.

288. F. D. Rosi, J. P. Dismukes and E. F. Hockings, *Electr. Eng.*, 1960, **79**, 450.

289. S. Duan, W. Xue, H. Yao, X. Wang, C. Wang, S. Li, Z. Zhang, L. Yin, X. Bao, L. Huang, X. Wang, C. Chen, J. Sui, Y. Chen, J. Mao, F. Cao, Y. Wang and Q. Zhang, *Adv. Energy Mater.*, 2022, **12**, 2103385.

290. S. Perumal, S. Roychowdhury and K. Biswas, *J. Mater. Chem. C*, 2016, **4**, 7520.

291. X. Zhang, J. Li, X. Wang, Z. Chen, J. Mao, Y. Chen and Y. Pei, *J. Am. Chem. Soc.*, 2018, **140**, 15883.

292. U. D. Wdowik, K. Parlinski, S. Rols and T. Chatterji, *Phys. Rev. B*, 2014, **89**, 224306.

293. Z. Sun, J. Zhou, H.-K. Mao and R. Ahuja, *Proc. Natl. Acad. Sci. U. S. A.*, 2012, **109**, 5948.

294. S. Lee, K. Esfarjani, T. Luo, J. Zhou, Z. Tian and G. Chen, *Nat. Commun.*, 2014, **5**, 3525.

295. E. F. Steigmeier and G. Harbeke, *Solid State Commun.*, 1970, **8**, 1275.

296. Z. Liu, J. Sun, J. Mao, H. Zhu, W. Ren, J. Zhou, Z. Wang, D. J. Singh, J. Sui, C.-W. Chu and Z. Ren, *Proc. Natl. Acad. Sci. U. S. A.*, 2018, **115**, 5332.

297. J. R. Lakowicz, *Principles of fluorescence spectroscopy*, Springer, 2006.

298. T. Egami and S. J. Billinge, *Underneath the Bragg peaks: structural analysis of complex materials*, Elsevier, 2003.

299. A.-C. Dippel, H.-P. Liermann, J. T. Delitz, P. Walter, H. Schulte-Schrepping, O. H. Seeck and H. Franz, *J. Synchrotron Rad.*, 2015, **22**, 675.

300. M. Basham, J. Filik, M. T. Wharmby, P. C. Y. Chang, B. El Kassaby, M. Gerring, J. Aishima, K. Levik, B. C. A. Pulford, I. Sikharulidze, D. Sneddon, M. Webber, S. S. Dhesi, F. Maccherozzi, O. Svensson, S. Brockhauser, G. Naray and A. W. Ashton, *J. Synchrotron Rad.*, 2015, **22**, 853.

301. X. Qiu, J. W. Thompson and S. J. L. Billinge, *J. Appl. Crystallogr.*, 2004, **37**, 678.

302. P. Juhas, T. Davis, C. L. Farrow and S. J. L. Billinge, *J. Appl. Crystallogr.*, 2013, **46**, 560.

303. C. L. Farrow, P. Juhas, J. W. Liu, D. Bryndin, E. S. Božin, J. Bloch, P. Th and S. J. L. Billinge, *J. Phys: Condens. Matter*, 2007, **19**, 335219.

304. ULVACZEM3RIKO, *Seebeck-Coefficient and Eleectric-Resistance-Measuring-System Manual*, 2012.

305. E. H. Hall, *Am. J. Math.*, 1879, **2**, 287.

306. W. J. Parker, R. J. Jenkins, C. P. Butler and G. L. Abbott, *J. Appl. Phys.*, 1961, **32**, 1679.

307. R. D. Cowan, *J. Appl. Phys.*, 1963, **34**, 926.

308. *Physical Property Measurement System - TTO Option - User's Manual (Quantum Design).*

309. *Physical Property Measurement System - Heat Capacity Option - User's Manual (Quantum Design).*

310. H. Kunioka, A. Yamamoto, T. Iida and H. Obara, *Appl. Phys. Express*, 2017, **10**, 095801.

PART 2

Synthesis and Optical Properties of 2D Layered Perovskite Halide Nanostructures

Chapter 2.1

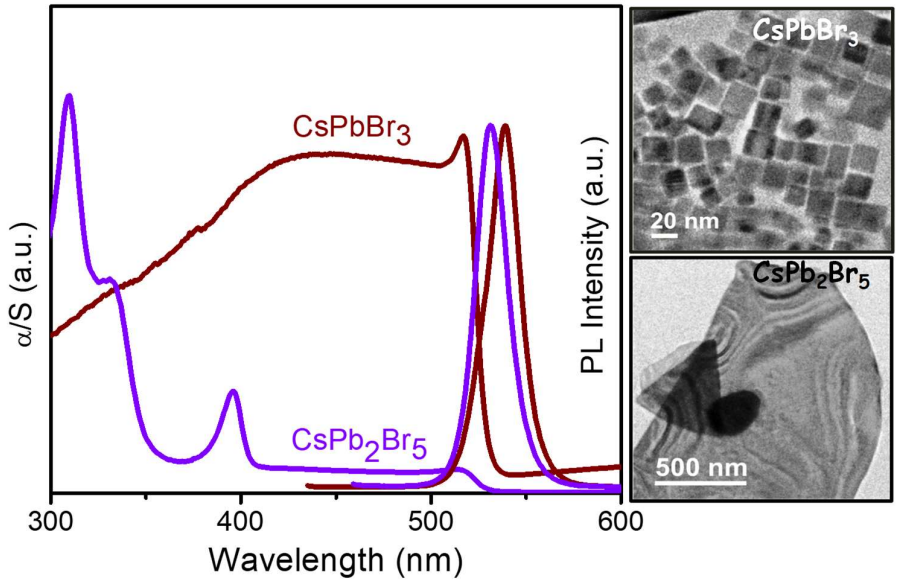

Single Pot Synthesis of Indirect Band Gap 2D $CsPb_2Br_5$ Nanosheets From Direct Band Gap 3D $CsPbBr_3$ Nanocrystals and the Origin of their Luminescence Properties

Chapter 2.1

Single Pot Synthesis of Indirect Band Gap 2D $CsPb_2Br_5$ Nanosheets from Direct Band Gap 3D $CsPbBr_3$ Nanocrystals and the Origin of their Luminescence Properties[†]

Summary

Two-dimensional (2D) perovskites recently attracted significant interest due to their unique and novel optoelectronic properties. $CsPb_2Br_5$, a 2D inorganic perovskite halide, is an indirect band gap semiconductor, thereby it is not supposed to be luminescent. However, fundamental understanding of the origin of its luminescence property is still lacking as there are contradictory literatures present concerning its luminescence property. In this chapter, we demonstrate the single pot solution based transformation of 2D $CsPb_2Br_5$ nanosheets from the nanocrystals of 3D $CsPbBr_3$ and investigated the origin of its luminescent properties by detailed experiments and density functional theoretical (DFT) calculations. The photoluminescence of $CsPb_2Br_5$ originates from the different amorphous lead bromide ammonium complexes those are present at the surface of the nanosheets. We have also highlighted the formation mechanism of 2D nanosheets from 3D $CsPbBr_3$ nanocrystals. These combined theoretical and experimental studies offer significant insights to the optical property and formation mechanism of 2D $CsPb_2Br_5$ perovskites.

[†]**P. Acharyya,** P. Pal, P. K. Samanta, A. Sarkar, S. K. Pati and K. Biswas. *Nanoscale*, 2019, **11**, 4001-4007.

2.1.1. Introduction

The boundless quests for efficient optoelectronic materials have pushed the scientific community to investigate the new and simple synthesis and study the optical properties of perovskite halides in the last decade. Perovskite halides being quite inexpensive and easy to process via solution have found immense interest for having potential applications in photovoltaics, lasers, light-emitting diodes and photodetectors.[1-5] Moreover, a reduction in the dimensionality of the perovskite halides can result in quantum confinement, diminished dielectric screening, increased lattice relaxation, improved exciton binding energy, lower fluorescence decay time, higher absorption cross-section and notable optical nonlinearity with respect to their bulk counterparts.[3, 4]

In recent years, two dimensional (2D) hybrid halide perovskites[6] such as Ruddlesden-Popper[7-9] and Dion-Jacobson[10] phases become a subject of intense investigations for their structural diversity, tunability of covalent organic molecules and optoelectronic applications. Organic-inorganic hybrid halide perovskites are not so suitable for application due to stability issues at this moment. Hence, all-inorganic metal halide perovskites can be an alternative due to their promising properties and superior stability at ambient conditions.[11] Lead-based halide perovskites have created a sensation with their astonishing optoelectronic properties since these are defect-tolerant in nature[5, 12] for an instance Mn-doped $CsPbBr_3$ is useful for white LED applications.[13-15] Novel synthetic strategies have been employed to prepare all inorganic lead halide perovskites,[16] such as $CsPbBr_3$ nanocrystals with 3D connectivity have been obtained by the solution phase transformation from the 0D Cs_4PbX_6.[16-18] Among the alkali metal lead halides, one of the emerging materials is $CsPb_2Br_5$ which has a two dimensional (2D) layered structure in which Cs ion is sandwiched in between $[Pb_2Br_5]^-$ polyhedrons (Figure 2.1.1a).[19] $CsPb_2Br_5$ is considered as a secondary metastable material which is formed by nonstoichiometric material transfer, or structural rearrangement from its 3D counterpart.[20-22] Recently, 2D $CsPb_2Br_5$ has been synthesized via solution based methods[23, 24] and mechanochemistry.[25] Previous reports have shown that metastable $CsPb_2Br_5$ was formed along with 3D $CsPbBr_3$ with highly luminescent properties.[22, 26, 27] Furthermore, $CsPb_2Br_5$ nanoplatelets showed significant photoluminescent properties, which are advantageous for further optoelectronic applications.[24, 26-28] The presence of

$CsPb_2Br_5$ increases the stability to $CsPbBr_3$ which enhance the color tunability and solar cell efficiency.[29, 30] However, first-principles calculation revealed that $CsPb_2Br_5$ with an indirect band gap is theoretically unable to exhibit luminescence.[19, 31] Kamat and co-workers have reported post synthetic transformation of 3D $CsPbBr_3$ to 2D $CsPb_2Br_5$, where ligands have passivated the defect sites of 3D $CsPbBr_3$ to generate the 3D/2D interfaces.[32] They have demonstrated that lead bromide complex in the system could be the main source of the luminescence of $CsPb_2Br_5$. These contradictory results reported in recent report [24, 31, 32] stimulate us to find out the single pot colloidal phase transformation mechanism of 3D $CsPbBr_3$ to 2D $CsPb_2Br_5$ and the origin of its luminescence property of $CsPb_2Br_5$.

In this chapter, we demonstrate the single pot solution-based transformation tetragonal 2D $CsPb_2Br_5$ nanosheets from orthorhombic 3D $CsPbBr_3$ nanocrystals in the presence of oleylamine, oleic acid and excess $PbBr_2$ at 200 ^oC. Density functional theoretical (DFT) calculation of electronic structure demonstrate the direct band gap nature in 3D $CsPbBr_3$, while 2D $CsPb_2Br_5$ nanosheets exhibit indirect band gap thus not expected to show the photoluminescence. In spite of the having indirect band gap, as synthesized $CsPb_2Br_5$ nanosheets show bright green luminescence with a blue shift of the PL spectra with respect to that of the $CsPbBr_3$ nanocrystals. We investigate the origin of the luminescence property of $CsPb_2Br_5$, which was arising from the different amorphous lead bromide ammonium complexes present at the surface of this material, but not from the indirect band gap $CsPb_2Br_5$. These amorphous complexes are undetectable in X-ray diffraction studies but they show significant photoluminescence in optical spectroscopy.

2.1.2. Methods

Reagents. Caesium carbonate (Cs_2CO_3, 99.9%, Sigma Aldrich), oleic acid (OA, tech. 90%, Sigma Aldrich), oleylamine (OAm, tech. 70%, Sigma Aldrich), lead bromide ($PbBr_2$, 99.9%, Sigma Aldrich), 1-octadecene (ODE, tech. 90%, Sigma Aldrich), and toluene (AR, 99.0%, SDFCL) were used for the solution phase syntheses without further purification.

Synthesis of Cs-oleate. 20 mL ODE and 410 mg (1.26 mmol) Cs_2CO_3 were taken in a 50 mL three necked round bottom flask and heated at 120 °C in vacuum for 1 hour to get a homogeneous solution. 1.30 mL of OA was added and the solution was kept for another 30 minutes at the same conditions. Then under a nitrogen atmosphere, the temperature was increased up to 150 °C and kept for few minutes to get a clear Cs-oleate solution. This Cs-oleate solution was stored at room temperature under nitrogen atmosphere for further use.

Synthesis of colloidal $CsPbBr_3$ and $CsPb_2Br_5$. 10 mL ODE and 138 mg $PbBr_2$ were added into a 25 mL three neck flask. The solution mixture was heated to 120 ºC for 1h. Under a nitrogen atmosphere, oleic acid (1 mL) and oleylamine (1 mL) were added to the solution mixture and heated to 200 ºC until all $PbBr_2$ got dissolved. Cs-oleate (0.4 mL) was injected into the flask and reaction was terminated at certain time interval: immediately, 2 min, 3 min, 5 min, 10 min, 20 min, and 30 min by dipping the reaction flask into an ice bath. The crude product was centrifuged in toluene at 8000 rpm for 10 min, washed several times with hot toluene and used for further studies.

Powder X-ray diffraction (PXRD) patterns of the samples were collected using CuKα (λ=1.5406 Å) radiation on a Bruker D8 diffractometer at room temperature.

Field emission scanning electron microscopy (FESEM) experiments were performed using NOVANANO SEM 600 (FEI, Germany) operated at 15 kV. EDAX compositional analysis was performed during FESEM imaging.

Thermal gravimetric analysis (TGA) was performed by using a 2 STAR TGA instrument. Samples were heated at a rate of 5 °C min^{-1} in N_2 atmosphere (40 mL min^{-1}) throughout a temperature range of 30–500 °C.

Atomic force microscopy (AFM) was performed on a Bruker Innova Microscope in tapping mode with 10 nm diameter containing antimony doped Silicon tip.

Transmission electron microscopy (TEM) images of the as synthesized materials were taken using a JEOL (JEM3010) TEM instrument (300 kV accelerating voltage) fitted with

a Gatan CCD camera and also with a FEI TECNAI G2 20 STWIN TEM instrument (operating at 200 kV).

Optical spectroscopy. To estimate the optical band gap, diffuse reflectance measurements were carried out in the range of λ = 250 to 800 nm by using a Perkin-Elmer Lambda 900 UV/Vis/near-IR spectrometer in reflectance mode. Absorption (α/S) data were calculated from reflectance data by using the Kubelka–Munk equation: $\alpha/S = (1-R)^2/(2R)$, in which R is the reflectance, α and S are the absorption and scattering coefficients respectively. The energy band gaps were derived from α/S *vs.* E (nm) plots.

The emission spectra were recorded on Perkin Elmer LS 55 Luminescence Spectrometer in solid state. The luminescence spectra of solid powders were recorded at different excitation wavelengths.

Computational details. The DFT calculation are done in collaboration with Prof. S. K. Pati, JNCASR, India. DFT calculations were carried out using Generalized Gradient Approximation (GGA) for the exchange–correlation energy functional in the version of Perdew, Burke and Ernzerhof (PBE) and ultrasoft pseudopotentials. Plane-wave basis set cut offs for the wave functions and charge density were set at 40 Ry and 320 Ry, respectively. The crystal structures were fully relaxed until the total force on each atom was less than 0.05 eV/Å. A uniform grid of 4×4×2 *k*-mesh in the Brillouin zone was used for relaxing crystal structures of $PbBr_2$, $CsPbBr_3$ and $CsPb_2Br_5$. Experimentally predicted lattice parameters for $PbBr_2$ (Orthorhombic: a = 4.71 Å, b = 8.02 Å, and c = 9.48 Å)[33], $CsPbBr_3$ (Orthorhombic: a = 8.21 Å, b = 8.26 Å, and c=11.76 Å)[34] and $CsPb_2Br_5$ (Tetragonal: a = b = 8.49 Å, and c = 15.20 Å)[19] were considered in our DFT calculation. The electronic band structures for $CsPbBr_3$ and $CsPb_2Br_5$ were calculated using 6×6×4 *k*-mesh in the Brillouin zone. All the DFT calculations were performed using PWSCF v.5.0.2 code, as implemented in the Quantum ESPRESSO package.[35]

2.1.3. Results and Discussion

2D $CsPb_2Br_5$ nanosheets (NSs) were synthesized by the solution based hot-injection method at 200 °C by adding pre-synthesized Cs-oleate in the $PbBr_2$-oleic acid and

oleylamine mixture. The 3D $CsPbBr_3$ was obtained by quenching the reaction mixture immediately after the addition of Cs-oleate, whereas pure 2D $CsPb_2Br_5$ was produced when the reaction was continued for 20 minutes. While the reaction mixtures were quenched at different time (2, 3, 5 and 10 minutes) after addition of Cs-oleate the products were the mixtures of $CsPbBr_3$-$CsPb_2Br_5$ (Figure 2.1.1b).

The powder X-ray diffraction (PXRD) pattern (Figure 2.1.1b) demonstrated that the synthesized $CsPb_2Br_5$ (PDF # 25-0211) was crystalline having tetragonal phase with space group *I4/mcm*. The tetragonal phase of $CsPb_2Br_5$ exhibits a sandwiched structure consisting of layers containing $[Pb_2Br_5]^-$ polyhedrons and intercalated Cs^+ ions. In the $[Pb_2Br_5]^-$ layers (Figure 2.1.1a) Pb^{2+} ions coordinates with eight Br^- forming an elongated polyhedron.[31]

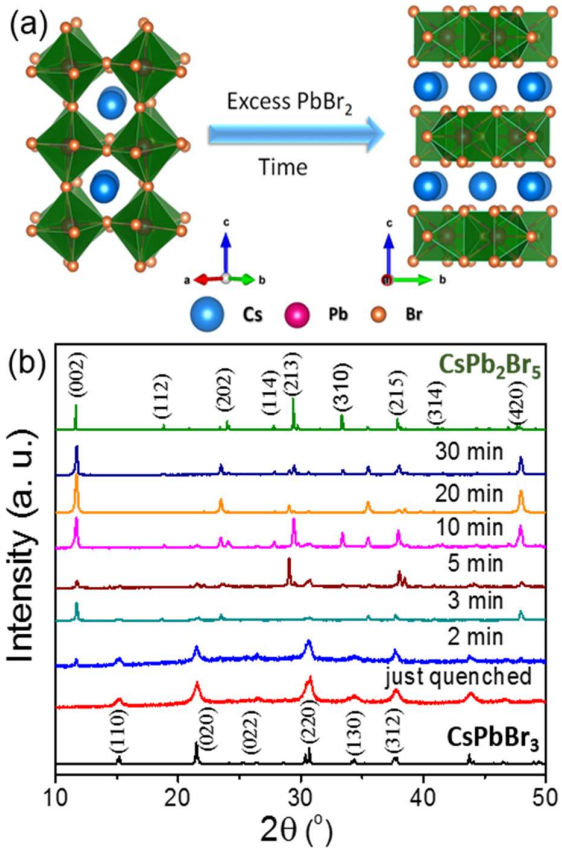

Figure 2.1.1. *(a) Transformation of orthorhombic $CsPbBr_3$ to tetragonal $CsPb_2Br_5$ (crystal structures), (b) PXRD patterns of $CsPbBr_3$, $CsPb_2Br_5$ and mixed $CsPbBr_3$-$CsPb_2Br_5$ at different time interval of the reaction.*

The peak that appears at 2θ = 11.66° is assigned to the (002) plane for the layered 2D $CsPb_2Br_5$, which is the characteristic peak of a layered compound. While the PXRD of immediately quenched reaction is well matched with the orthorhombic 3D $CsPbBr_3$ (space group *Pbnm*) perovskite structure (PDF # 74-2251). The crystal structure of $CsPbBr_3$ is based on the corner-shared $PbBr_6^{4-}$ octahedra and the Cs^+ cations are embedded into the cuboctahedra voids (Figure 2.1.1a). The PXRD patterns of the samples obtained in different reaction times (2-30 mins) show the clear single pot transformation of $CsPbBr_3$ to $CsPb_2Br_5$ (Figure 2.1.1b).

The characteristic diffraction peaks for (202) and (220) planes for the $CsPbBr_3$ were diminished and the peak for (002) plane for $CsPb_2Br_5$ were enhanced with increasing the reaction time. All the peaks for the $CsPbBr_3$ were disappeared completely and pure $CsPb_2Br_5$ product was formed after 20 minutes, which indicated the conversion of strained 3D $CsPbBr_3$ to layered 2D $CsPb_2Br_5$. It was verified by the controlled reaction that at lower temperatures (e.g. 150 °C and 180 °C) even for longer reaction time spans (e.g. 1 hr) or with the absence of capping agents, full conversion of 2D $CsPb_2Br_5$ was not complete. Hence, high temperature and the presence of long chain ammonium capping agents were required to facilitate the relaxation of the strain in the 3D structure which enabled to form the 2D structure. In the light of these results, we assume that at the high temperature, the kinetic motion of embedded Cs^+ ions increase and the presence of capping agents and excess $PbBr_2$ help to dissociate the interconnected 3D network of $PbBr_6^-$ octahedrons. The $[Pb_2Br_5]^-$ layered framework is energetically favorable at high temperatures when the excess $PbBr_2$ is present in solution.[31] Our density functional theoretical (DFT) calculation predicted that formation of $CsPb_2Br_5$ from $CsPbBr_3$ and $PbBr_2$ (equation 1) is favorable and the formation energy was calculated as -6.92 kcal/mol.

$$\text{Formation energy} = E_{CsPb_2Br_5} - E_{CsPbBr_3} - E_{PbBr_2} \qquad (1)$$

The free cations are easily placed in between the $[Pb_2Br_5]^-$ layers to maintain the charge balance. Initially, the kinetically stable 3D $CsPbBr_3$ perovskite formed in solution. Further, with increasing reaction time and in presence of excess $PbBr_2$, 3D $CsPbBr_3$

rearrange into thermodynamically stable 2D $CsPb_2Br_5$. We can write the transformation as:

$$CsPbBr_3 + PbBr_2 \longrightarrow CsPb_2Br_5 \qquad (2)$$

We observed morphological changes in the overall transformation of $CsPbBr_3$ to $CsPb_2Br_5$ by transmission electron microscopy (TEM) analysis.

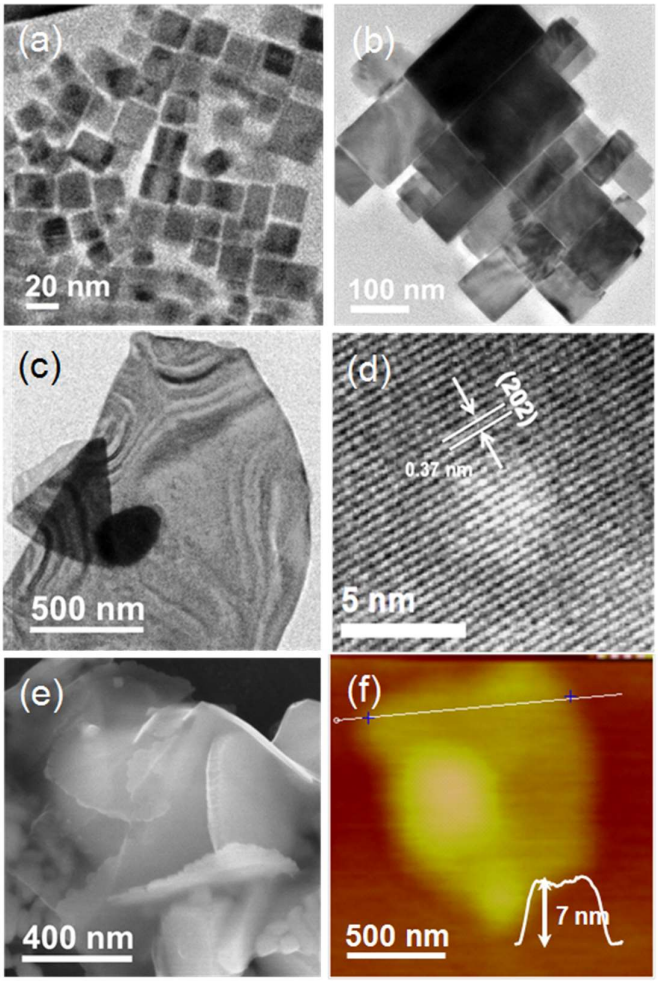

Figure 2.1.2. *(a) TEM image of the $CsPbBr_3$ nanocrystals after immediate quenching of reaction. (b) TEM image of the sample after 5 min of reaction which contain mixture of $CsPbBr_3$ and $CsPb_2Br_5$. (c) TEM image of $CsPb_2Br_5$ nanosheets obtained after 20 min of reaction. (d) HRTEM image with lattice plane (202) of $CsPb_2Br_5$ nanosheets. (e) FESEM image of the $CsPb_2Br_5$ nanosheets. (f) AFM image and height profile (inset) of the $CsPb_2Br_5$ nanosheets.*

At initial stage of reaction (just quenched), small square shaped monodispersed nanocrystals $CsPbBr_3$ with size of ~20 nm was formed (Figure 2.1.2a and Figure 2.1.3a, b). At 3 minutes, the formations of polydispersed nanocrystals (NCs) with different sizes ranging from 50 to 200 nm were observed (Figure 2.1.3c). Those NCs were too close to each other and tend to form large plate shaped structure when the reaction was quenched after 5 mins (Figure 2.1.2b and 2.1.3d). Nanoplates (NPLs) with few NCs were observed when the reaction was quenched after 10 mins (Figure 2.1.3e) and finally NSs were formed after 20 mins (Figure 2.1.2c and 2.1.3f).

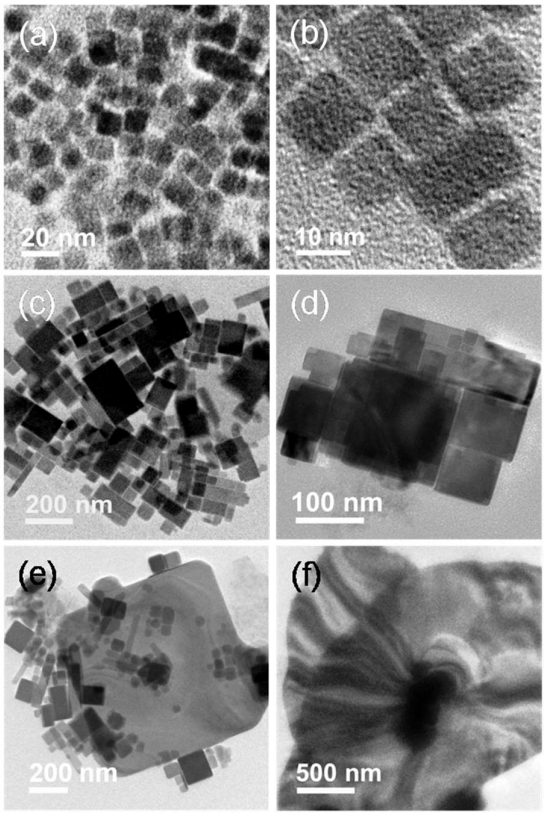

***Figure 2.1.3**. (a) and (b) TEM images of the nanocrystals after immediate quenching of reaction mixture, (c) and (d) TEM image of the nanocrystals obtained after 3 and 5 min of reactions respectively, contain mixture of $CsPbBr_3$ and $CsPb_2Br_5$, (e) TEM image of $CsPb_2Br_5$ nanoplate along with small nanocrystals obtains in 10 mins of reaction, (f) TEM image of the $CsPb_2Br_5$ nanosheets in 20 mins.*

The HRTEM image of sample obtained after 5 minutes clearly showed the lateral attachment of smaller NCs to form the larger nanoplate type structure (Figure 2.1.4).[36] A similar observation was noticed for the formation of $CsPbBr_3$ nanoplates with higher order structure.[37] The NPLs $CsPb_2Br_5$ has been grown further probably due to Ostwald ripening resulting in the formation of large nanosheets (NSs) with lateral dimension of few microns (Figure 2.1.2c). Those NSs are single crystalline in nature with the lattice fringes of 0.37 nm representing of (202) planes (Figure 2.1.2d). The lateral dimension of 2D nanosheets were measured to be 1-2 μm by field emission scanning electron microscopy (FESEM) (Figure 2.1.2e). The thickness of 7-8 nm of the $CsPb_2Br_5$ NSs was measured by atomic force microscopy (Figure 2.1.2f). The amorphous nature of the lead halide amine complexes was further confirmed by a TEM study of the controlled reaction. The diffused pattern in electron diffraction (ED) signifies the amorphous complexes.

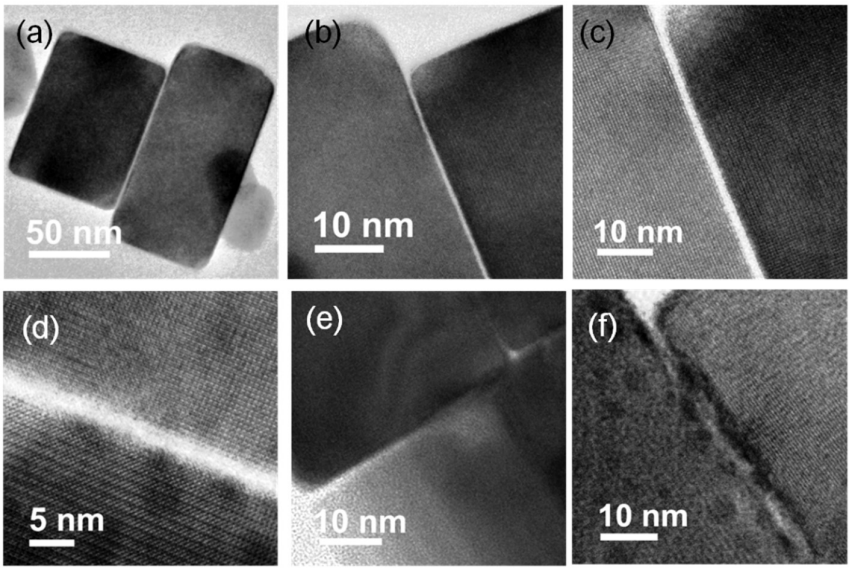

Figure 2.1.4 *(a) and (b) TEM images of the nanocrystals (NCs) in 3 mins, (c) and (d) TEM/HRTEM images of the nanocrystals in 3 mins contains NCs close to each other, (e) TEM image of square shaped $CsPbBr_3$ NCs along with $CsPb_2Br_5$, after 5 mins, (f) HRTEM image clearly shows that the lateral attachment of NCs to form the larger nanoplate type structure.*

The optical absorption and emission spectra of as-synthesized materials at different reaction times were shown in Figure 2.1.5a and 2.1.5b, respectively. The 3D perovskite (just quenched sample) shows an optical absorption edge at 530 nm (2.34 eV,

Figure 2.1.5a) and an intense photoluminescence (PL) band at 540 nm when excited at 400 nm. The products formed in 2, 3, and 5 minutes of reaction spans also show similarly intense PL spectra (slightly higher wavelength, Figure 2.1.5b). The PL spectra exhibit a shoulder peak at 533 nm, which was supposed to be arising for the presence of dual phase of $CsPbBr_3$-$CsPb_2Br_5$ (Figure 2.1.5b). The XRD pattern also emphasized for the presence of both $CsPbBr_3$ and $CsPb_2Br_5$. The intense and sharp PL spectra of 3D $CsPbBr_3$ which have direct band gap could be attributed to the nano grain size, strong electron-hole coulombic interaction and low trap state density.[11] Althought, the absorption edge of the product formed after 20 minutes persistent at the same position compared to that of its 3D counterpart (just quenched) but shows extremely low intensity (Figure 2.1.5a). The

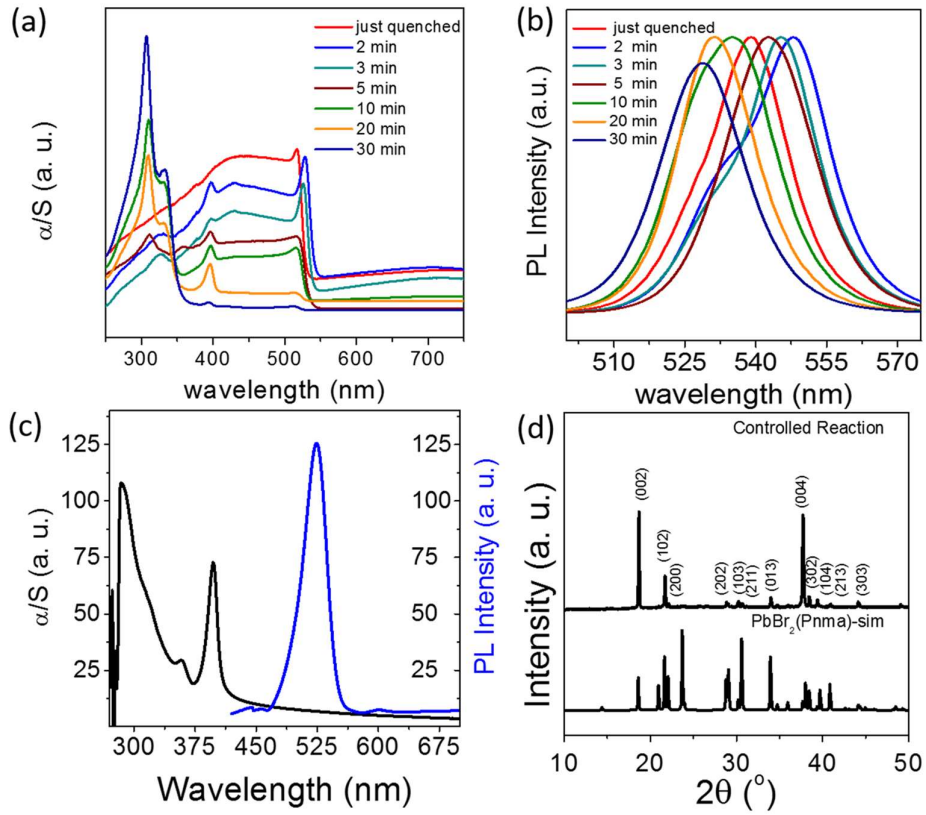

Figure 2.1.5 *(a) Solid-state UV/Vis absorption (α/S) spectra of synthesized materials in different time of the reaction. (b) Solid-state PL spectra of synthesized materials in different time of the reaction. (c) Solid-state UV/Vis absorption (α/S) (black) and PL (blue) spectra of synthesized materials in controlled reaction in absence of Cs-oleate. (d) Powder XRD pattern of control reaction.*

product formed at 20 min reaction show an intense PL spectrum around 531 nm when excited at 410 nm (Figure 2.1.5b). The PL peak of product obtained after 20 min of the reaction is blue shifted compared to that of the just quenched product. Previously it was reported that the 2D $CsPb_2Br_5$ or mixture of $CsPbBr_3$ and $CsPb_2Br_5$ materials showed sharp photoluminescence properties and the luminescence properties arose mainly from the presence of 3-D/2-D interfaces.[22, 32] Interestingly, Jiang et al. reported 2D $CsPb_2Br_5$ of possessing large indirect bandgap and being PL inactive.[31] Our computational results also demonstrated that 3D $CsPbBr_3$ showed a direct band gap with a value of 2.03 eV at the Γ point, whereas, 2D $CsPb_2Br_5$ showed an indirect band gap of 3.06 eV (VBM and CBM are found at X point, Γ point, respectively, see the Figure 2.1.6) which indicates that the emission would not come from this material.

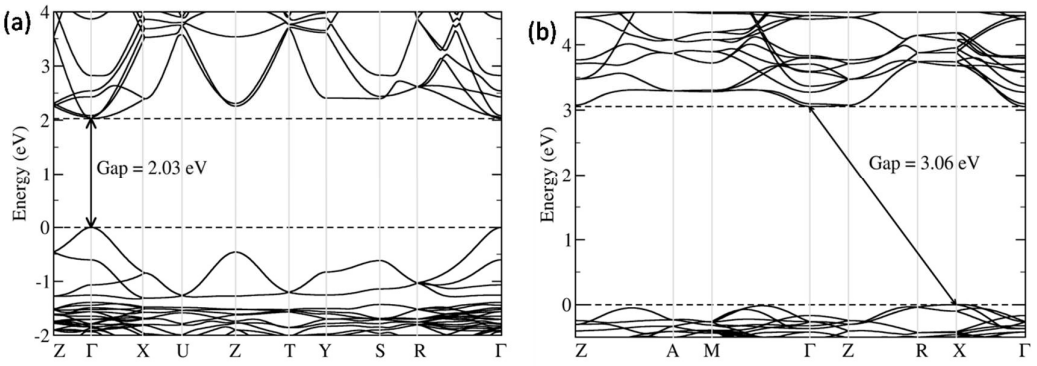

Figure 2.1.6. *The electronic band structure of (a) orthorhombic $CsPbBr_3$ and (b) tetragonal $CsPb_2Br_5$.*

Thus, it is an interesting topic of conflicting interpretations. In order to find out the causes of the emission for $CsPb_2Br_5$, controlled reaction was carried out in absence of Cs-oleate without changing the reaction conditions as stated before for the synthesis of $CsPb_2Br_5$. Several absorption bands (315, 356 and 398 nm) were observed for the controlled product (Figure 2.1.5c) and the PXRD pattern of the product matched well with the orthorhombic phase of $PbBr_2$ (PDF # 84-1181) (Figure 2.1.5d). The synthesized $PbBr_2$ showed a PL band at 525 nm when excited at 400 nm (Figure 2.1.5c). This result indicates that excess $PbBr_2$ or some of its other derivative (discussed below) present along with $CsPb_2Br_5$ showed the PL band.

While analyzing the full range of the optical absorption spectra (250-750 nm), we observed that the material just after quenching showed absorption spectrum with single absorption maxima appearing at 517 nm which belonged to the conventional band edge absorption of $CsPbBr_3$ (Figure 2.1.5a). Each of the materials synthesized in 2, 3 and 5 minutes were showing another two absorption peaks, one appearing at 395 nm and the other appearing close to 320 nm. $CsPb_2Br_5$ formed at higher reaction times (20 and 30 minutes) which also showed three absorption maxima in the absorption spectrum (Figure 2.1.5a). With the increasing reaction time, the intensity of the band edge absorption of $CsPbBr_3$ decreases, while the higher energy absorption peak (320 nm) increased which split into two peaks at 334 and 309 nm (Figure 2.1.5a). The high energy absorption peak (320 nm) appeared for the formation $PbBr_3^-$ according to earlier reports.[38, 39] The $PbBr_3^-$ was partially converted to $PbBr_4^{2-}$ with increase in the reaction time due to the presence of high concentration of bromide ions, coming from $PbBr_2$, which actually provides the absorption band at 334 nm.[38] The excess free $PbBr_2$ in the reaction system reacted with soluble [$PbBr_3^-$] [ammonium $^+$] complex and a nonstoichiometric transfer of materials led to the formation of [$Pb_2Br_5^-$] [ammonium $^+$] complex which is a more stable phase. The excess $PbBr_2$ facilitated the conversion of the $PbBr_3^-$ to $Pb_2Br_5^-$, and provided more intense absorption peak at 309 nm.[39, 40] Halide complexes of heavy metal ions (Pb^{2+}, Sn^{2+}, Sb^{3+} and Bi^{3+}) with ns^2 electron pair are known to show low energy metal centered *s* to *p* transition and high energy ligand-to-metal charge transfer (LMCT) where ligand-electrons were transferred from the filled *p*-orbitals to the empty *p*-orbitals of the metal.[38] The absorption bands in range of 300-400 nm observed here are attributed to the metal centered *s* to *p* absorption in lead bromide based ammonium complexes. Hence, the origin of the luminescence property of $CsPb_2Br_5$ due to the different lead bromide amine complexes which are present in the reaction mixture along with the desired product.

While PXRD shows the pure tetragonal phase of the nanosheets of $CsPb_2Br_5$, surface of the nanosheets may possess amorphous ammonium complexes $PbBr_4^{2-}$ and $Pb_2Br_5^-$. In the TGA studies, 7% weight loss occurred in the temperature range of 25-375 ^oC due to the removal of capped alkyl amines. While at high temperatures, ~15% weight loss occurred due to the sublimation of $PbBr_2$ (Figure 2.1.7a).[41] An FTIR study of the synthesized material show two sharp bands at 1456 and 1377 cm^{-1} along with a broad

band at 3450 cm^{-1} due to the presence of ammonium cations (Figure 2.1.7b).[42] Thus, different amorphous lead halide amine complexes were present on the surface of $CsPb_2Br_5$ which were undetectable in PXRD, but could only be detected via spectroscopic techniques.

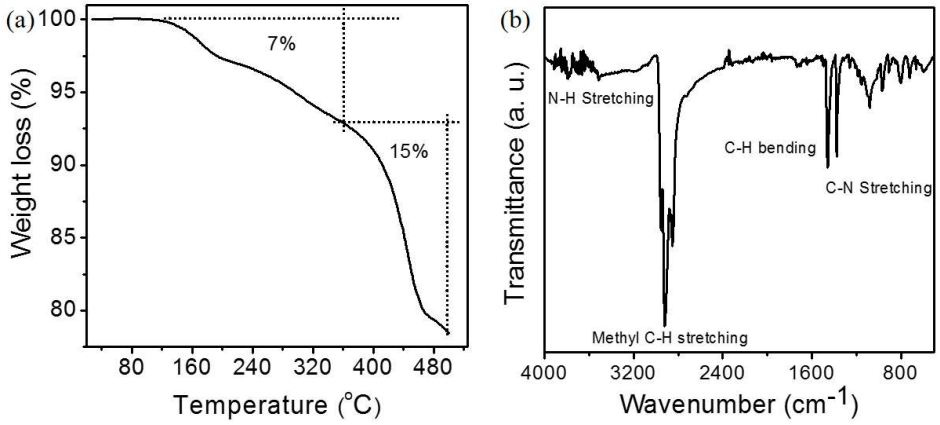

Figure 2.1.7 (a) TGA curve and (b) FTIR spectra of as-synthesized $CsPb_2Br_5$.

2.1.4. Conclusions

Nanosheets of 2D $CsPb_2Br_5$ has been synthesized *via* single pot solution based transformation of 3D $CsPbBr_3$ nanocrystals. High temperatures and presence of long chain ammonium ligands assist to break down the three dimensional networks of $CsPbBr_3$ and re-organize into 2D slab structures of $CsPb_2Br_5$ in presence of excess $PbBr_2$. DFT calculations of electronic structure of $CsPb_2Br_5$ demonstrated that it possesses indirect band gap of 3.06 eV in between VBM and CBM at X point and Γ point, respectively, thereby it should not show luminescence. The surface of $CsPb_2Br_5$ contains amorphous ammonium complexes of $PbBr_4^{2-}$ and $Pb_2Br_5^{-}$ which are responsible for the photoluminescence of nanosheets of $CsPb_2Br_5$. These amorphous complexes are undetectable by PXRD but could be detected via optical spectroscopic techniques due to strong metal centered *s* to *p* absorption band and corresponding luminescence.

2.1.5. References

1. D. B. Mitzi, C. A. Feild, W. T. A. Harrison and A. M. Guloy, *Nature*, 1994, **369**, 467.

2. S. D. Stranks and H. J. Snaith, *Nat. Nanotech.*, 2015, **10**, 391.

3. I. C. Smith, M. D. Smith, A. Jaffe, Y. Lin and H. I. Karunadasa, *Chem. Mater.*, 2017, **29**, 1868.

4. J. S. Manser, J. A. Christians and P. V. Kamat, *Chem. Rev.*, 2016, **116**, 12956.

5. A. Swarnkar, V. K. Ravi and A. Nag, *ACS Energy Lett.*, 2017, **2**, 1089.

6. L. Dou, A. B. Wong, Y. Yu, M. Lai, N. Kornienko, S. W. Eaton, A. Fu, C. G. Bischak, J. Ma, T. Ding, N. S. Ginsberg, L.-W. Wang, A. P. Alivisatos and P. Yang, *Science*, 2015, **349**, 1518.

7. C. C. Stoumpos, D. H. Cao, D. J. Clark, J. Young, J. M. Rondinelli, J. I. Jang, J. T. Hupp and M. G. Kanatzidis, *Chem. Mater.*, 2016, **28**, 2852.

8. C. C. Stoumpos, C. M. M. Soe, H. Tsai, W. Nie, J.-C. Blancon, D. H. Cao, F. Liu, B. Traoré, C. Katan, J. Even, A. D. Mohite and M. G. Kanatzidis, *Chem*, 2017, **2**, 427.

9. H. Tsai, W. Nie, J.-C. Blancon, C. C. Stoumpos, R. Asadpour, B. Harutyunyan, A. J. Neukirch, R. Verduzco, J. J. Crochet, S. Tretiak, L. Pedesseau, J. Even, M. A. Alam, G. Gupta, J. Lou, P. M. Ajayan, M. J. Bedzyk, M. G. Kanatzidis and A. D. Mohite, *Nature*, 2016, **536**, 312.

10. L. Mao, W. Ke, L. Pedesseau, Y. Wu, C. Katan, J. Even, M. R. Wasielewski, C. C. Stoumpos and M. G. Kanatzidis, *J. Am. Chem. Soc.*, 2018, **140**, 3775.

11. J. Liang, J. Liu and Z. Jin, *Solar RRL*, 2017, **1**, 1700086.

12. Q. A. Akkerman, G. Rainò, M. V. Kovalenko and L. Manna, *Nat. Mater.*, 2018, **17**, 394.

13. W. J. Mir, M. Jagadeeswararao, S. Das and A. Nag, *ACS Energy Lett.*, 2017, **2**, 537.

14. D. Parobek, Y. Dong, T. Qiao and D. H. Son, *Chem. Mater.*, 2018, **30**, 2939.

15. A. K. Guria, S. K. Dutta, S. D. Adhikari and N. Pradhan, *ACS Energy Lett.*, 2017, **2**, 1014.

16. D. Yang, M. Cao, Q. Zhong, P. Li, X. Zhang and Q. Zhang, *J. Mater. Chem. C*, 2019, **7**, 757.

17. L. Wu, H. Hu, Y. Xu, S. Jiang, M. Chen, Q. Zhong, D. Yang, Q. Liu, Y. Zhao, B. Sun, Q. Zhang and Y. Yin, *Nano Lett.*, 2017, **17**, 5799.

18. Q. A. Akkerman, S. Park, E. Radicchi, F. Nunzi, E. Mosconi, F. De Angelis, R. Brescia, P. Rastogi, M. Prato and L. Manna, *Nano Lett.*, 2017, **17**, 1924.

19. I. Dursun, M. De Bastiani, B. Turedi, B. Alamer, A. Shkurenko, J. Yin, M. El-Zohry Ahmed, I. Gereige, A. AlSaggaf, F. Mohammed Omar, M. Eddaoudi and M. Bakr Osman, *ChemSusChem*, 2017, **10**, 3746.

20. C. C. Stoumpos, C. D. Malliakas and M. G. Kanatzidis, *Inorg. Chem.*, 2013, **52**, 9019.

21. D. M. Trots and S. V. Myagkota, *J. Phys. Chem. Solids*, 2008, **69**, 2520.

22. X. Zhang, B. Xu, J. Zhang, Y. Gao, Y. Zheng, K. Wang and W. Sun Xiao, *Adv. Funct. Mater.*, 2016, **26**, 4595.

23. X. Tang, Z. Hu, W. Yuan, W. Hu, H. Shao, D. Han, J. Zheng, J. Hao, Z. Zang, J. Du, Y. Leng, L. Fang and M. Zhou, *Adv. Optical Mater.*, 2016, **5**, 1600788.

24. K.-H. Wang, L. Wu, L. Li, H.-B. Yao, H.-S. Qian and S.-H. Yu, *Angew. Chem. Int. Ed.*, 2016, **55**, 8328.

25. P. Pal, S. Saha, A. Banik, A. Sarkar and K. Biswas, *Chem. Eur. J.*, 2018, **24**, 1811.

26. L. Ruan, J. Lin, W. Shen and Z. Deng, *Nanoscale*, 2018, **10**, 7658.

27. C. Han, C. Li, Z. Zang, M. Wang, K. Sun, X. Tang and J. Du, *Photonics Res.*, 2017, **5**, 473.

28. W. Shen, L. Ruan, Z. Shen and Z. Deng, *Chem. Commun.*, 2018, **54**, 2804.

29. P. Song, B. Qiao, D. Song, Z. Liang, D. Gao, J. Cao, Z. Shen, Z. Xu and S. Zhao, *J. Alloys Compd.*, 2018, **767**, 98.

30. X. Zhang, Z. Jin, J. Zhang, D. Bai, H. Bian, K. Wang, J. Sun, Q. Wang and S. F. Liu, *ACS Appl. Mater. Interfaces*, 2018, **10**, 7145.

31. G. Li, H. Wang, Z. Zhu, Y. Chang, T. Zhang, Z. Song and Y. Jiang, *Chem. Commun.*, 2016, **52**, 11296.

32. S. K. Balakrishnan and P. V. Kamat, *Chem. Mater.*, 2018, **30**, 74.

33. W. Nieuwenkamp and J. M. Bijvoet, *Z. Kristallogr.*, 1932, **84**, 49.

34. J. Yin, P. Maity, M. De Bastiani, I. Dursun, O. M. Bakr, J.-L. Bredas and O. F. Mohammed, *Sci. Adv.*, 2017, **3**, e1701793.

35. S. B. P. Giannozzi, N. Bonini, M. Calandra, R. Car, C. Cavazzoni, D. Ceresoli,, M. C. G. L. Chiarotti, I. Dabo, A. Dal Corso, S. Fabris, G. Fratesi, S. de, R. G. Gironcoli, U. Gerstmann, C. Gougoussis, A. Kokalj, M. Lazzeri, L., N. M. Martin-Samos, F. Mauri, R. Mazzarello, S. Paolini, A. Pasquarello, L., C. S. Paulatto, S. Scandolo, G. Sclauzero, A. P. Seitsonen, A. Smogunov, P. and R. M. W. Umari, *J. Phys.: Condens. Matter*, 2009, **21**, 395502.

36. Y. Tong, B. J. Bohn, E. Bladt, K. Wang, P. Müller-Buschbaum, S. Bals, A. S. Urban, L. Polavarapu and J. Feldmann, *Angew. Chem. Int. Ed.*, 2017, **56**, 13887.

37. Y. Bekenstein, B. A. Koscher, S. W. Eaton, P. Yang and A. P. Alivisatos, *J. Am. Chem. Soc.*, 2015, **137**, 16008.

38. K. Oldenburg, A. Vogler and Z. Naturforsch., *B: J. Chem. Sci.* , 1993, **48**, 1519.

39. S. J. Yoon, K. G. Stamplecoskie and P. V. Kamat, *J. Phys. Chem. Lett.*, 2016, **7**, 1368.

40. K. Nitsch, M. Dusek, M. Nikl, K. Polak and M. Rodova, *Prog. Cryst. Growth Charact. Mater.*, 1995, **30**, 1.

41. Y. Liu, Z. Yang, D. Cui, X. Ren, J. Sun, X. Liu, J. Zhang, Q. Wei, H. Fan, F. Yu, X. Zhang, C. Zhao and S. Liu, *Adv. Mater.*, 2015, **27**, 5176.

42. J. Pal, S. Manna, A. Mondal, S. Das, K. V. Adarsh and A. Nag, *Angew. Chem. Int. Ed.*, 2017, **56**, 14187.

Chapter 2.2

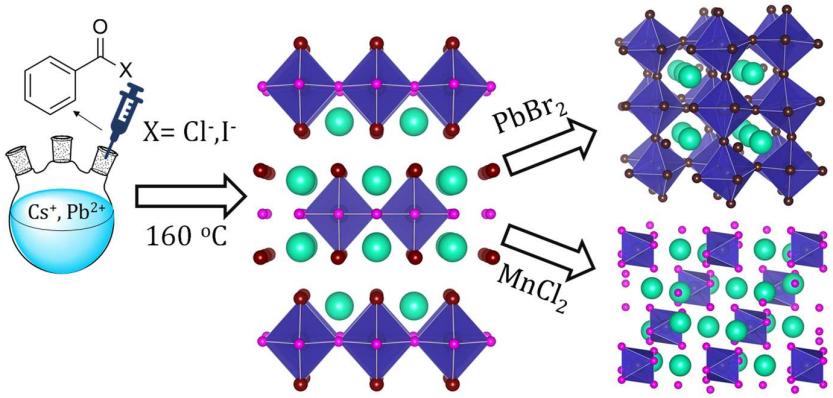

Synthesis, Chemical Transformation and Optical Properties of 2D Nanoplates and Scaled-Up Bulk Polycrystals of Ruddlesden-Popper, $Cs_2PbI_2Cl_2$

Chapter 2.2

Synthesis, Chemical Transformation and Optical Properties of 2D Nanoplates and Scaled-Up Bulk Polycrystals of Ruddlesden-Popper, $Cs_2PbI_2Cl_2$[†]

Summary

Two-dimensional (2D) layered Ruddlesden-Popper (RP) phases of halide perovskite offer exotic properties and interesting structure, which make them suitable candidate for solar photovoltaics, light emitting diode (LED) and photodetector applications. Simple and scaled-up synthesis, chemical transformations, doping and stability are the important steps towards the applications. In this chapter, all-inorganic RP phase of $Cs_2PbI_2Cl_2$ was synthesized via a facile hot-injection method using benzoyl halides as halide sources. Different morphologies in the form of 2D nanoplates (NPLs) and small nanocrystals (NCs) were obtained by changing the concentration of capping agents (i.e., oleic acid and oleylamine) in solution. The excitonic absorption peak was appeared for NPLs and NCs, which is the characteristic feature of 2D halide perovskites. Further, the scalable quantity (~1 g) of bulk powder and micrometer-sized particles of $Cs_2PbI_2Cl_2$ were synthesized via liquid assisted mechanochemical grinding and anti-solvent method, respectively. We have performed post-synthetic chemical transformation to synthesize three-dimensional (3D) $CsPbBr_3$ disk-shaped particles and zero-dimensional (0D) Cs_4PbCl_6 NCs from the presynthesized RP $Cs_2PbI_2Cl_2$ NCs in solution and studied their optical properties. Finally, doping of Mn^{2+} was carried out in $Cs_2PbI_2Cl_2$ NCs, which demonstrated a typical feature of Mn^{2+} dopant emission along with host emission properties. Low-temperature (77 K) photoluminescence (PL) spectra reveal red-shifted and line-width broadening emission along with longer PL lifetime for both undoped and Mn-doped NCs compared to room temperature PL. Further, the temperature-dependent PL spectra and thermogravimetric analysis (TGA) revealed excellent thermal stability of $Cs_2PbI_2Cl_2$. This work offers an insight for exploration of synthesis process, post-synthetic chemical transformation, and dopant insertion in all-inorganic 2D RP perovskites.

[†]**P. Acharyya,** K. Maji, K. Kundu and K. Biswas. *ACS Appl. Nano Mater.,* 2020, **3**, 877-886.

2.2.1. Introduction

Low-dimensional perovskite halides like Ruddlesden-Popper (RP),[1-3] and Dion-Jacobson (DJ) [4] phases are regarded as the new frontier that justify remarkable recognition for solar photovoltaics and photodetectors.[5] Recently, in the hybrid RP perovskite halides, different large organic cations introduced along the crystallographic planes at the A-site of ABX_3 wedges.[6] The represented chemical formula of RP phase is $A_{n-1}A'_2B_nX_{3n+1}$, where A′ and A signify organic cations between diverse layers and small cations in the voids of the layers, respectively, whereas B and X denote to the usual bivalent metal cations and halides, respectively. The number of metal halide monolayer sheets in between the insulating A′ organic layers is indicated as *n*.[2] Noteworthy advancement has been comprehended in the field of 2D RP lead halide perovskites, mostly aiming on the hybrid organic-inorganic compounds with elongated organic chains.[7, 8] However, presence of the long organic chains in the spacing layer of hybrid organic-inorganic RP phases provide negligible electronic coupling between inorganic perovskite layers.[9, 10] Thus, introducing an inorganic layer at the expense of a long organic spacing layer will offer reasonable interaction between the adjacent layers, which may result in the superior chemical and thermal stability,[11, 12] and exciting properties that are distinct from both the electronically uncoupled hybrid layered phases and 3D conventional perovskites.[3] Fully inorganic RP halide perovskites are rarely explored so far.[13-16] The generic formula to represent Cs-Pb-X based all-inorganic RP phase can be written as $Cs_{n+1}Pb_nX_{3n+1}$, in which the n layers of $CsPbX_3$ unit are separated by an extra CsX layer.[3] Recently, all-inorganic mixed halide RP phases have been reported,[13-15] which possess single-layer RP structure (n = 1), as shown in Figure 2.2.1a. The synthetic strategies reported by Manna's group used PbX_2 as halide precursors,[14] whereas Pradhan's group used oleylamine-HCl and oleic acid-HI as halide sources for the synthesis of all-inorganic RP $Cs_2PbI_2Cl_2$.[15] Previously, Manna and co-workers pointed out the limitation of using PbX_2 during the synthesis of 3D $APbX_3$, which was overcome by introducing benzoyl halides as halide precursors instead of PbX_2.[17] The introduction of benzoyl halides offers a halide-rich environment and, simultaneously, due to their strong reactivity, a proficient protonation of oleylamine ligand takes place to produce oleylammonium ions, which gives rise to the formation of lead halide-terminated surfaces.[17]

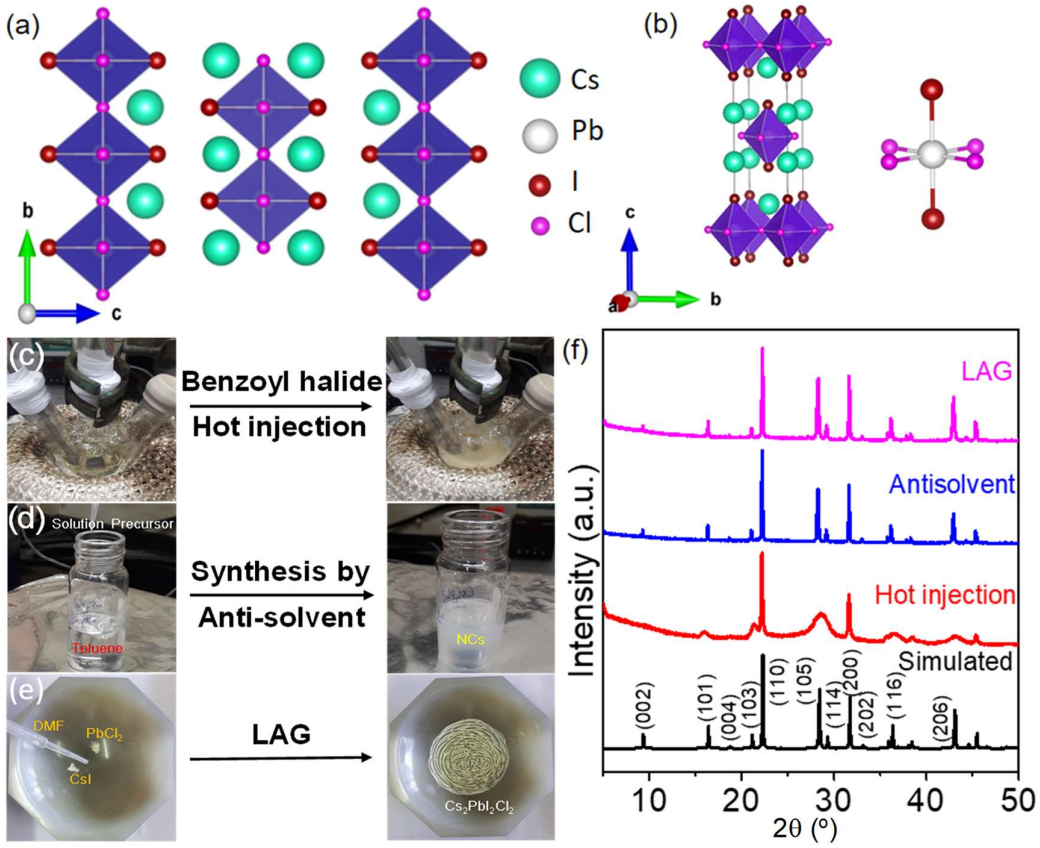

Figure 2.2.1. *(a) Crystal structure of $Cs_2PbI_2Cl_2$. (b) Unit cell of $Cs_2PbI_2Cl_2$. Photograph of (c) hot injection, (d) antisolvent, and (e) liquid assisted grinding (LAG) synthesis of $Cs_2PbI_2Cl_2$. (f) PXRD patterns of $Cs_2PbI_2Cl_2$, obtained by hot-injection method, antisolvent method, and LAG.*

In this chapter, the 2D nanoplates (NPs) of Ruddlesden-Popper (RP) phase of $Cs_2PbI_2Cl_2$ were synthesized by a single pot solution-based method using benzoyl halides as halide source and subsequently, the optical properties of these synthesized samples were investigated both in cryogenic and room temperatures. We have obtained the small nanocrystals (NCs) of $Cs_2PbI_2Cl_2$ when the capping agent concentration was increased during hot-injection reaction. Moreover, scalable quantity of bulk powder and micron-sized particles of $Cs_2PbI_2Cl_2$ were synthesized *via* liquid assisted mechanochemical grinding and anti-solvent method, respectively. We have also shown the chemical transformation of 2D RP phase of $Cs_2PbI_2Cl_2$ to 3D $CsPbBr_3$ and 0D Cs_4PbCl_6 by adding

$PbBr_2$ and $MnCl_2$ in solution at room temperature, respectively for the first time. Furthermore, we have inserted Mn^{2+} as a dopant (up to 5 mol %) with partial replacement of Pb^{2+} in $Cs_2PbI_2Cl_2$ NCs and studied the optical properties. Mn^{2+} doping in the $Cs_2PbI_2Cl_2$ NCs shows an extra emission band at 585 nm with delayed lifetime. Thus, in this report, new synthesis of all-inorganic halide RP compound both in nano and bulk phases, post-synthetic chemical transformation and Mn^{2+} doping along with their detailed optical property and thermal stability have been investigated. Notably, these thermally stable nano-dimensional RP phases and their optical properties at cryogenic as well as ambient temperatures offer potential applications in the versatile fields of optoelectronics such as in solar photovoltaics, photodetectors and LED.

2.2.2. Methods

Reagents. Cesium (I) iodide (CsI, 99.9%, Sigma Aldrich), lead (II) chloride ($PbCl_2$, 99.9%, Sigma Aldrich), lead (II) bromide ($PbBr_2$, 99.99%, Sigma Aldrich), cesium carbonate (Cs_2CO_3, 99.9%, Sigma Aldrich), lead (II) acetate trihydrate ($Pb(OAc)_2{\cdot}3H_2O$, 99.9%, Sigma Aldrich), manganese (II) acetate ($Mn(OAc)_2$, > 98% Sigma Aldrich), benzoyl chloride (PhCOCl, 99%, Sigma Aldrich), manganese (II) chloride ($MnCl_2$, >99%, Sigma Aldrich), potassium iodide (KI, 99%, Sigma Aldrich), oleic acid (OA, technical grade, 90%), oleylamine (OAm, technical grade, 90%), 1-octadecene (ODE, technical grade, 90%), toluene, hexane, *N,N*-dimethyl formamide (DMF), dimethyl sulfoxide (DMSO), and ethanol (EtOH) were used without any further purification.

Synthesis of benzoyl iodide from benzoyl chloride. For the synthesis of benzoyl iodide, 3.5 g of potassium iodide and 1.5 mL of benzoyl chloride were mixed in a 20 mL vial at ambient condition. The reaction mixture was stirred for overnight at 80 ^oC on a hot plate. The red colour solution was cooled to room temperature and diluted by 5 mL of ODE solvent. The solution was then collected after centrifuge at 4000 rpm for 5 minutes. The reaction scheme is shown in Scheme 2.2.1A. The formation of benzoyl iodide was confirmed by ^1H NMR spectroscopy (Figure 2.2.2).

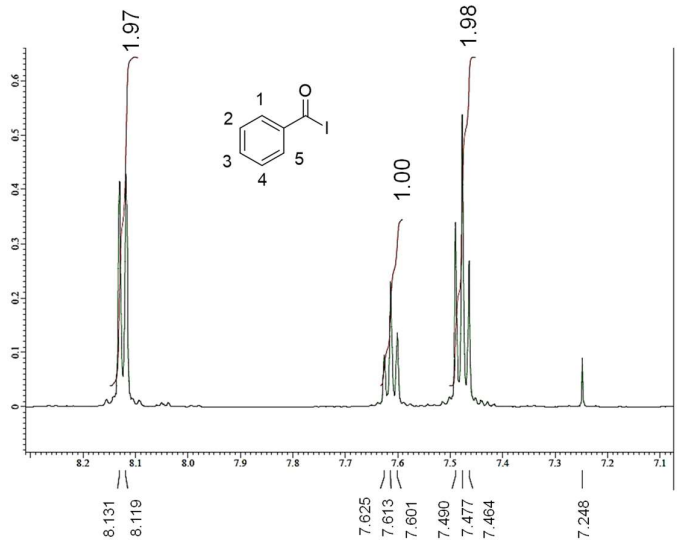

Figure 2.2.2. *^{1}H NMR spectra of benzoyl iodide in $CDCl_3$ solvent.*

Synthesis of colloidal $Cs_2PbI_2Cl_2$. In a typical synthesis, 65.2 mg (0.2 mmol) cesium carbonate, 76 mg (0.2 mmol) lead acetate trihydrate and 5 mL ODE were loaded into 25 mL of three-necked round bottom flask in Schlenk line. 0.5 mL of OA and OAm were added for nanoplate synthesis, whereas 1 mL of OA and OAm were added for nanocrystal and dried under vacuum for 2 hours at 130 ℃ along with magnetic stirring. Subsequently, the temperature was increased to 160 ℃ under N_2 atmosphere and 1:1 mixture of benzoyl chloride and benzoyl iodide were injected swiftly into the reaction flask. The reaction mixture became milky white within a few seconds, and then the flask was kept at room temperature to cool slowly. Then, the $Cs_2PbI_2Cl_2$ nanostructures (~10 mg) were collected by centrifuging at 8000 rpm for 10 minutes followed by washing with toluene (10 mL each time) for 2-3 times. The details of the reaction scheme are shown in Scheme 2.2.1B.

Post-synthetic transformation of 2D $Cs_2PbI_2Cl_2$ to 3D $CsPbBr_3$. At first, precursor solution of $PbBr_2$ was prepared by taking 183.5 mg (0.5 mmol) of $PbBr_2$ and 5 mL ODE in a three necked round bottom flask in the Schlenk line. 0.5 mL of each OA and OAm were added at N_2 atmosphere and increase the temperature to 120 ºC and kept until all $PbBr_2$ dissolve. Then, the temperature of the precursor solution was decreased to room

temperature and toluene dispersed $Cs_2PbI_2Cl_2$ was injected swiftly. Within one-minute greenish yellow coloured $CsPbBr_3$ NCs were started to form and then the solution was centrifuged at 9000 rpm for 10 minutes. The synthesized $CsPbBr_3$ NCs were washed 2-3 times by toluene.

Post-synthetic transformation of 2D $Cs_2PbI_2Cl_2$ to 0D Cs_4PbCl_6. Similarly, precursor solution of $MnCl_2$ was prepared by taking 63 mg (0.5 mmol) $MnCl_2$ and 5 mL ODE and loaded in a three necked round bottom flask in Schlenk line. 0.5 mL OA and 0.5 mL OAm were added at N_2 atmosphere and raised the temperature to 120 ºC to dissolve all $MnCl_2$. Then, the temperature of the black coloured $MnCl_2$ solution precursor was decreased to room temperature and toluene dispersed $Cs_2PbI_2Cl_2$ was injected swiftly. After 5 minutes the whole solution was collected and centrifuged at 9000 rpm for 10 minutes. The synthesized Cs_4PbCl_6 NCs were washed 2-3 times by toluene. The details of the post-synthetic transformation scheme are shown in Scheme 2.2.1C.

Synthesis of Mn doped $Cs_2PbI_2Cl_2$. In a typical synthesis of $Cs_2Pb_{0.95}Mn_{0.05}I_2Cl_2$, 65.2 mg (0.2 mmol) cesium carbonate, 72.1 mg (0.19 mmol) lead acetate trihydrate, 1.73 mg (0.01 mmol) magnesium acetate and 5 mL ODE were loaded into 25 mL of three-necked round bottom flask in Schlenk line. 1 mL OA and 1 mL OAm were added and dried under vacuum for 2 hours at 130 ℃ along with magnetic stirring. Subsequently, the temperature was increased to 160 ℃ under N_2 atmosphere and 1:1 mixture of benzoyl chloride and benzoyl iodide were injected swiftly and let the flask to cool to room temperature slowly. Then the as-synthesized Mn doped $Cs_2PbI_2Cl_2$ nanoplates were collected by centrifuging at 8000 rpm for 10 min and washing with toluene 2-3 times.

Synthesis of $Cs_2PbI_2Cl_2$ by liquid assisted grinding (LAG). In a typical synthesis, 113.6 mg, 0.5 mmol of CsI and 117.38 mg, 0.25 mmol of $PbCl_2$ were taken in a stoichiometry ratio in a mortar pestle and few drops of organic solvents (EtOH/ DMF) were added in two different reactions. The mixtures were ground mechanically for about 2 hours in a N_2 filled glove bag. After 2 hours, pure phase of $Cs_2PbI_2Cl_2$ was formed,

when DMF solvent was used. The details of the liquid assisted grinding (LAG) are shown in Scheme 2.2.1D.

Synthesis of $Cs_2PbI_2Cl_2$ by anti-solvent reprecipitation method. For the synthesis of colloidal $Cs_2PbI_2Cl_2$, CsI and $PbCl_2$ were taken as 2:1 molar ratio and dissolved in 2:1 volume ratio of DMSO and DMF to form precursor solution. Typically, 52 mg (0.2 mmol) of CsI and 27.8 mg (0.1 mmol) of $PbCl_2$ were dissolved in a mixture of 2 mL DMSO and 1 mL DMF to form total 3 mL of precursor solution. Then 200 µL of precursor solution was injected into 5 mL of toluene under vigorous stirring of few minutes. Then the solution was centrifuged at 8000 rpm for 10 minutes and washed by toluene for 2-3 times. The details of anti-solvent reaction scheme are shown in Scheme 2.2.1E.

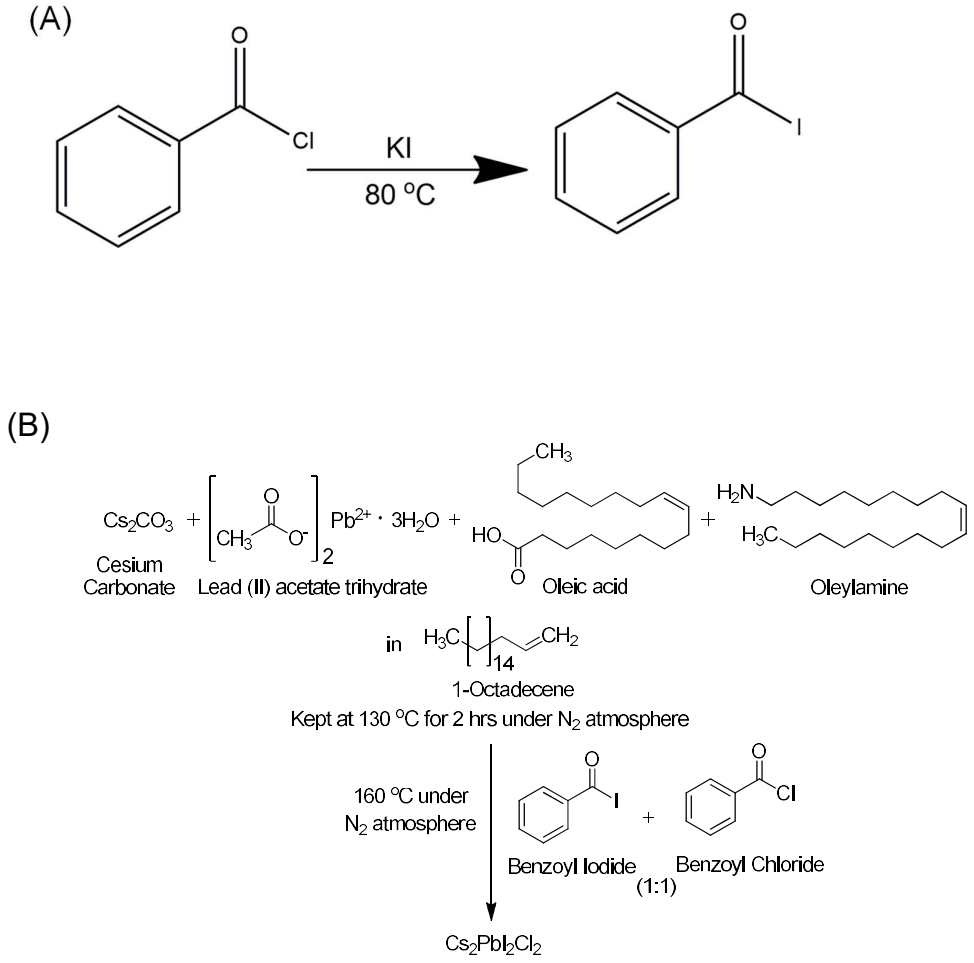

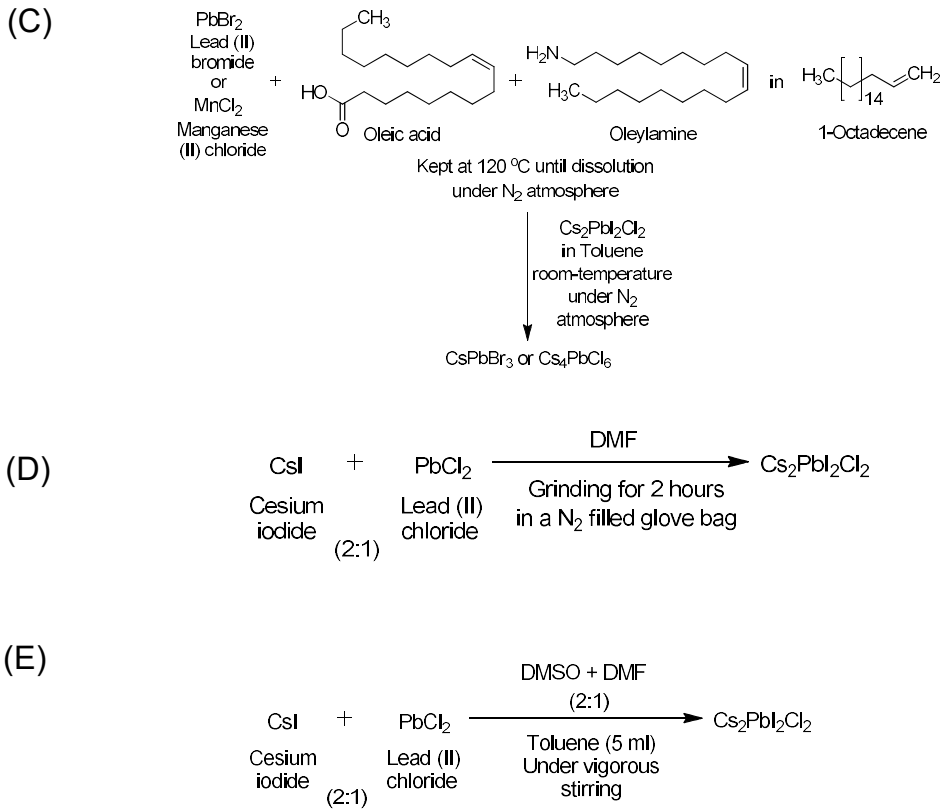

Scheme 2.2.1. *Synthesis schemes of (A) benzoyl iodide, and 2D all-inorganic RP $Cs_2PbI_2Cl_2$ by (B) hot-injection method, (C) its post-synthetic chemical transformation to 3D $CsPbBr_3$ and 0D Cs_4PbCl_6, (D) liquid assisted grinding (LAG), and (E) anti-solvent methods.*

Powder X-ray diffraction (PXRD). The PXRD measurement was carried out by Bruker D8 diffractometer with Cu Kα (λ = 1.5406 Å) radiation.

Transmission electron microscopy (TEM). The TEM measurement was performed using a JEOL (JEM3010) TEM instrument (300 kV accelerating voltage) fitted with a Gatan CCD camera.

Field emission scanning electron microscopy (FESEM). FESEM images were acquired by a Tescan-Mira 3 LMH.

Electronic absorption spectroscopy. Electronic absorption spectroscopy of NPLs and NCs was performed in solution phase by PerkinElmer, Lambda-900 UV/ Vis/ near-IR spectrometer. Diffuse reflectance measurements were carried out in the range of 250 to 800 nm to estimate the optical band gap in the solid-state sample. The emission spectra were recorded on Perkin Elmer LS 55 Luminescence spectrometer in solid state and solution phase at room temperature. Low-temperature PL measurements were performed using Edinburgh FLS1000 spectrofluorometer and excited with EPLED-340 (wavelength 340 nm ± 10 nm) at 77 K using a vacuum liquid-nitrogen cryostat.

Fluorescence life-time and quantum yield measurements. A Horiba Delta Flex time-correlated single-photon-counting (TCSPC) instrument was employed to acquire time-resolved decay plots in which a 373 nm nano-LED was used as the light source with 1 MHz of pulse repetition rate. Ludox AS40 colloidal silica (Sigma-Aldrich) was utilized as scatterer to accumulate the instrument response function (IRF). The instrumental full-width at half maximum (FWHM) together with detector response was found to be 0.2 ns for the 373 nm LED light source. The collection of the excited state decay of synthesized samples was performed by choosing a fixed emission wavelength. For 590 nm of emission wavelength, a 355 nm spectra LED light source was used. The decay was fitted by using IBH software (DAS6). The average lifetime (τ_{avg}) values of NCs were calculated by following equation; $\langle \tau_{avg} \rangle = \sum_i {A_i \tau_i^2}/{A_i \tau_i}$ where, A_i and τ_i are the fraction of the ith component and decay time, respectively. The absolute photoluminescence quantum yield (PLQY) values were measured using Edinburgh FLS1000 spectrofluorometer with a calibrated integrating sphere (λ_{ex} = 380 nm). Samples were prepared in glass substrates by drop casting the solution and subsequently, inserted in the sample holder for PLQY measurement.

Thermogravimetric analysis (TGA). Thermogravimetric analysis was carried out using a 2 STAR TGA instrument, in which the samples were heated in N_2 atmosphere (40 mL min^{-1}) at a rate of 5 °C min^{-1} in the temperature range of 50-800 °C.

Elemental analysis. Perkin-Elmer Optima 7000DV Inductively Coupled Plasma-Atomic Emission Spectroscopy (ICP-AES) instrument was employed to measure the amount of Pb, and Mn present in $Cs_2Pb_{1-x}Mn_xI_2Cl_2$ nanoplates. The standard solutions were prepared with ICP standards of Pb and Mn (1000 mg L^{-1}, Sigma-Aldrich). Samples were dissolved in concentrated nitric acid to acquire the Pb^{2+} and Mn^{2+} ion concentration.

Nuclear magnetic resonance (NMR). ^1H spectra were recorded on a GEOL-600 Fourier transformation spectrometer with 600 MHz. The chemical shifts (δ) are reported in parts per million (ppm) with respect to trimethylsilyl (TMS). Short notations used are d for doublet, t for triplet and m for multiplet.

2.2.3. Results and Discussion

A solution-based approach was used for the synthesis of 2D nanoplates (NPLs) and nanocrystals (NCs) of $Cs_2PbI_2Cl_2$. Initially, cesium carbonate and lead acetate were dissolved in 1-octadecene (ODE), oleic acid (OA) and oleylamine (OAm) at 130 ºC under inert atmosphere in a three-necked round bottom flask. Subsequently, benzoyl halides were swiftly injected into the reaction flask at 160 ºC. The as-synthesized product (~10 mg) was thoroughly washed with hot toluene (10 mL each time) for 2-3 times and used for further characterization.

To synthesize the pure phase of $Cs_2PbI_2Cl_2$, various reaction conditions were attempted. For example, at first, the reaction flask was kept for one hour for the formation of Cs- and Pb-oleate and then benzoyl halides were swiftly injected at three different temperature of 150 ºC, 160 ºC and 200 ºC. We observed that the product was nearly pure at 160 ºC, while Cs_4PbCl_6 was also formed along with $Cs_2PbI_2Cl_2$ phase at other temperatures. Then, we have varied the reaction time for the first step, i.e. the formation of Cs-oleate and Pb-oleate from cesium carbonate and lead acetate. We observed that maintaining the first step of the reaction for 2 hours at 130 ºC followed by injection of benzoyl halide at 160 ºC was the ideal condition for the synthesis of pure all-inorganic RP phase of $Cs_2PbI_2Cl_2$ (Figure 2.2.1c). The morphologies of the final products are NPLs and NCs depending upon the amount of the OA and OAm. Hence, temperature, reaction

time and concentration of capping agent play crucial role to synthesize pure phase of $Cs_2PbI_2Cl_2$.

Further, we have synthesized micron-sized particles of $Cs_2PbI_2Cl_2$ by anti-solvent method at room temperature (Figure 2.2.1d, and Scheme 2.2.1E). In a typical synthesis, CsI and $PbCl_2$ were dissolved in DMSO and DMF solvents. Then, the solution was injected swiftly to toluene at room temperature, which leads to immediate formation of $CsPbI_2Cl_2$ micron-sized particles. We have also synthesized bulk powders of $Cs_2PbI_2Cl_2$ by liquid assisted mechanochemical grinding (LAG) in DMF and EtOH solvents, starting with stoichiometric ratio of CsI and $PbCl_2$ as precursors at room temperature, which can yield gram scale (~ 1 g) quantities of $Cs_2PbI_2Cl_2$ (Figure 2.2.1e, and Scheme 2.2.1D). In presence of EtOH solvent, impurity phases were detected from the PXRD pattern, which appear from the unreacted $PbCl_2$. On the other hand, the pure phase of $Cs_2PbI_2Cl_2$ was obtained using DMF solvent (Figure 2.2.1e).

PXRD patterns of NCs and NPLs, agglomerated micro particles and the bulk powders synthesized by hot injection, anti-solvent and LAG methods, respectively have been indexed based on the pure phase of tetragonal $Cs_2PbI_2Cl_2$ (space group I*4/mmm*), as shown in Figure 2.2.1f. $Cs_2PbI_2Cl_2$ adopts K_2NiF_4 structure that is n = 1 in the $Cs_{n+1}Pb_nX_{3n+1}$ RP phase. The 2D layers were formed by corner sharing $PbI_2Cl_4^{4-}$ octahedra, in which I^- ions occupy axial sites whereas Cl^- ions occupy the equatorial sites. A unit cell and individual octahedron were shown in Figure 2.2.1b. The monovalent Cs^+ cations are distributed in between the layer of the structure (Figures 2.2.1a, b).

Transmission electron microscopic (TEM) images of the sample, synthesized by using 0.5 mL of OA and OAm confirmed the formation of the NPLs with the average size of 500 nm (Figures 2.2.3a, b), whereas NCs with an average size of 17.4 ± 0.5 nm were formed when 1 mL of OA and OAm were used (Figures 2.2.3d, e). The *d*- spacing values for NPLs and NCs were measured as 0.935 nm and 0.54 nm, which indicated the (002) and (101) planes of $Cs_2PbI_2Cl_2$, respectively, as shown in the HRTEM (Figure 2.2.3c and 2.2.3f, respectively). The selected area electron diffraction (SAED) pattern confirmed the formation of tetragonal crystal structure and single crystalline nature (inset of Figures 2.2.3c and 2.2.3f). Lower concentration of the capping agent (OA and OAm) favors the formation of large NPLs, while at higher concentration of capping agent leads to small

sized NCs, which indicate that the concentration of the capping agent plays a critical role in controlling the size of $Cs_2PbI_2Cl_2$ nanostructures.

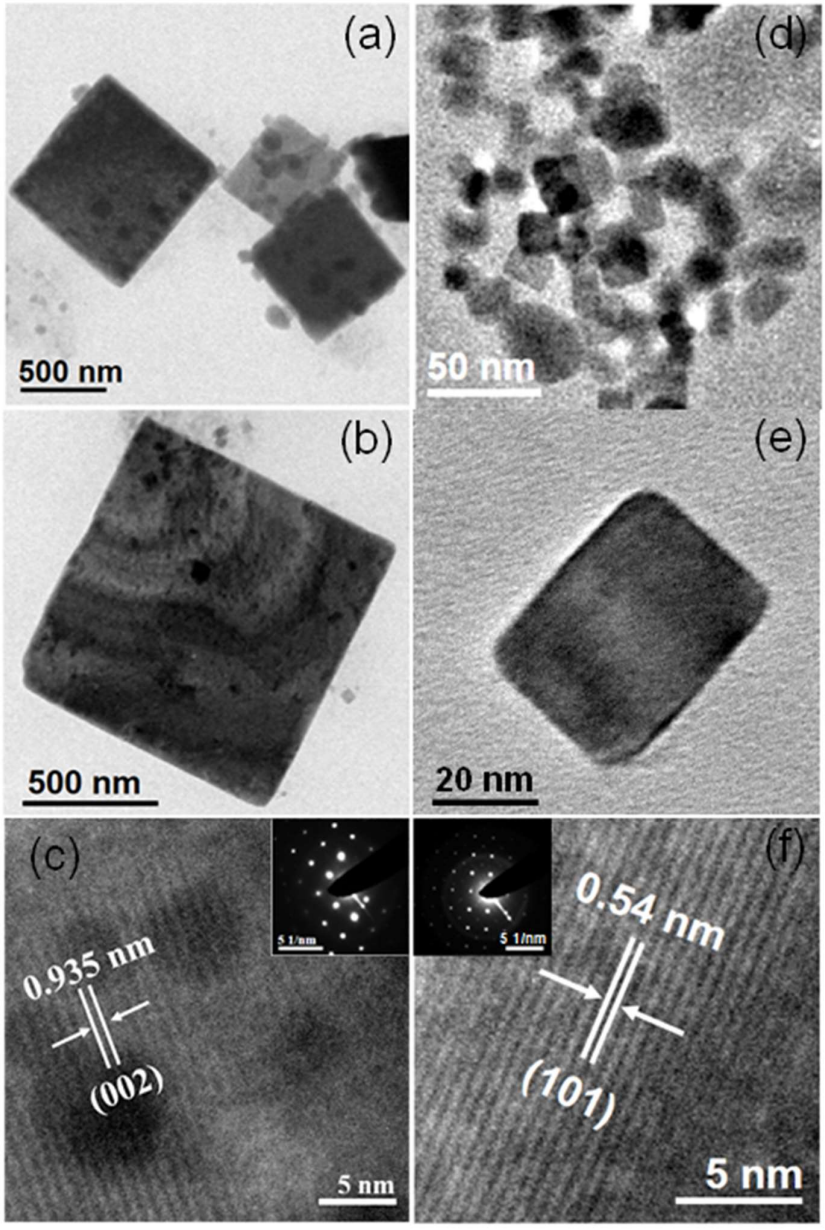

Figure 2.2.3. *TEM images of (a, b) $Cs_2PbI_2Cl_2$ NPLs and (d, e) $Cs_2PbI_2Cl_2$ NCs. HRTEM images and SAED patterns (insets) of (c) $Cs_2PbI_2Cl_2$ NPLs and (f) $Cs_2PbI_2Cl_2$ NCs.*

Strong binding of the capping agents at their higher concentration prevents the growth of the NCs and results in smaller sized NCs. Conversely, these NCs grow more along the *ac*-plane at lower concentration of capping agent and lead to the formation of larger NPLs.[18]

Optical properties of these materials were investigated *via* electronic absorption and photoluminescence (PL) spectroscopy at room temperature (Figure 2.2.4). The excitonic absorption peaks were appeared at 414 nm, 415 nm and 419 nm for NPLs, NCs and agglomerated micro particles, respectively (Figures 2.2.4a-c). Excitonic peak feature is the characteristics of 2D perovskite halides.[30] The photoluminescence study shows a PL peak around 425 nm, when excited at 380 nm for $Cs_2PbI_2Cl_2$ NCs, NPLs and agglomerate microparticles (Figures 2.2.4a-c, respectively). However, the intensity of the PL emission of agglomerated microparticles synthesized by anti-solvent method can be enhanced with adding extra surfactant (OAm). The enhancement of the PL emission by OAm may be due to partial passivation of the trap states.[19] Optical properties of bulk $Cs_2PbI_2Cl_2$ powder was measured by solid state diffuse reflectance spectroscopy (Figure 2.2.4d). Sharp adsorption edge with excitonic peak around 410 nm was observed for the solid powder sample, which matches well with the optical absorption data of single crystal $Cs_2PbI_2Cl_2$ reported by Kanatzidis group.[13] However, a broad PL band exhibits at 459 nm when excited at 380 nm (Figure 2.2.4d). In the solid-state optical spectra, broadening in PL spectra is mainly attributed to the presence of defects states.[20] The blue shifts of the PL peak of NPLs and NCs compared to bulk powder may be due to the possible quantum confinement phenomena.[19]

To acquire further understandings into the excitonic feature of photogenerated charge carriers of $Cs_2PbI_2Cl_2$ NCs and their dynamics, we performed PL measurement at 77 K. It has been evidenced from Figure 2.2.4e that the PL peak is red-shifted and broadened at 77 K compared to the room temperature PL. The $Cs_2PbI_2Cl_2$ NCs at room temperature unveils narrow band emission at 425 nm. At 77 K, an additional broad-band emission is observed centered at ~440 nm along with the free excitonic (FE) peak at 428 nm (Figure 2.2.4e). The low-temperature PL results imply that the electron-phonon coupling is reasonably strong and exhibit phonon-assisted self-trapped exciton (STE) recombination, which is responsible for the broad PL band.[21] The blue-shifted PL at room

temperature with respect to PL at 77 K is contemplated to arise from the electron-phonon coupling.

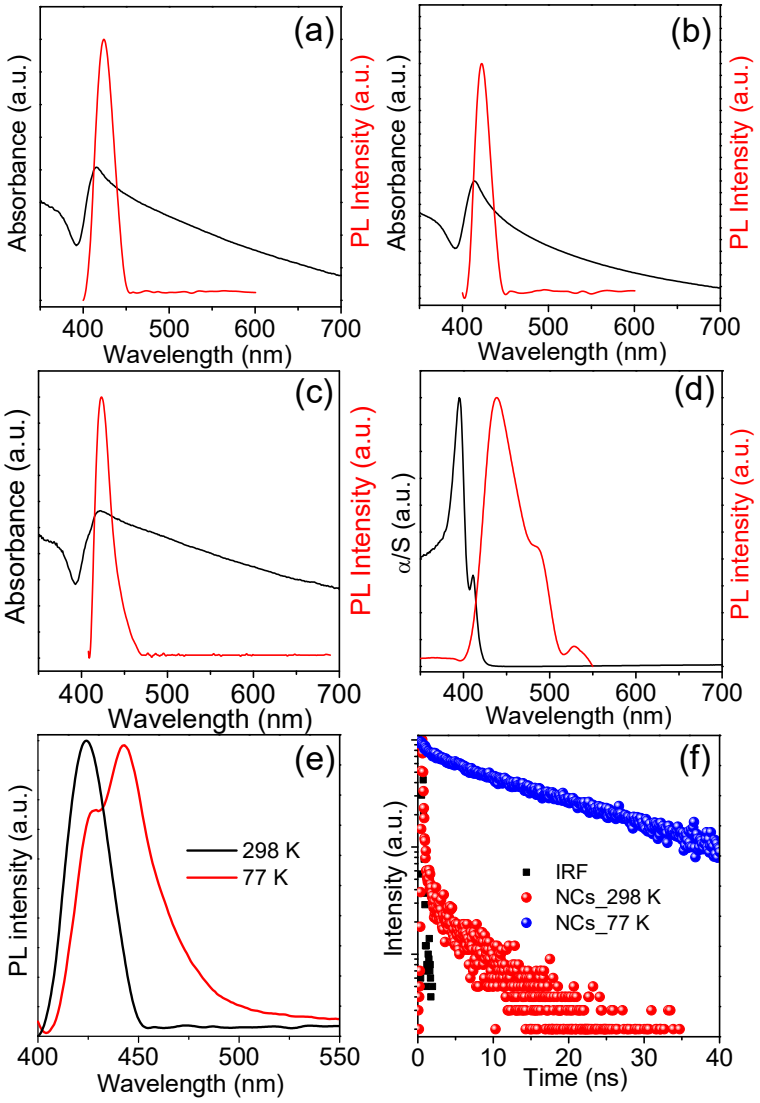

Figure 2.2.4. *Optical absorption (black) and PL (red) spectra of (a) $Cs_2PbI_2Cl_2$ NCs (b) $Cs_2PbI_2Cl_2$ NPLs, and (c) $Cs_2PbI_2Cl_2$ agglomerate microparticles in solution. (d) Solid state electronic absorption (α/S) and PL of bulk powder of $Cs_2PbI_2Cl_2$. (e) PL spectra of $Cs_2PbI_2Cl_2$ NCs at 298 and 77 K. (f) PL decay profile of $Cs_2PbI_2Cl_2$ NCs at 298 and 77 K.*

The STE emission at 77 K is also observed earlier for low-dimensional lead halides.[22] Figure 2.2.4f exemplifies the PL decays of NCs at room temperature, which can be fitted well by bi-exponential function with an average lifetime (τ_{avg}) of 4.39 ns comprised of a long-lived (τ_1 = 4.8 ns) and short-lived components (τ_2 = 0.27 ns) with relative amplitudes of 36% and 64%, respectively. On the other hand, the τ_{avg} of NCs was found to be 20.17 ns at 77 K, involving a long-lived (τ_1 = 20.22 ns) and short-lived components (τ_2 = 1.65 ns) with relative amplitudes of 97% and 3%, respectively. The longer excitonic emission lifetime of the NCs at low temperature might be due to the trapping of excitonic charge carriers at liquid N_2 temperature.[15]

In the ever-growing field of halide perovskites, post-synthetic chemical transformation signifies an innovative strategy to alter the stoichiometry, morphology and optical properties. Recently, Cs_4PbX_6 has been post-synthetically transformed to brightly emitting $CsPbX_3$ NCs by water-triggered reaction or by thermal annealing,[23, 24] whereas thiourea-assisted post-treatment method was established for the synthesis of ultrathin $CsPbX_3$ nanowires (NWs) from $CsPbBr_3$ nanocubes.[25] 3D cubic $CsPbBr_3$ nanocrystals has also been transformed to 2D $CsPb_2Br_5$ nanosheets by addition of excess $PbBr_2$.[26-28] We performed post-synthetic chemical transformation to synthesize 3D $CsPbBr_3$ disk-shaped particles and 0D Cs_4PbCl_6 NCs from pre-synthesized 2D RP $Cs_2PbI_2Cl_2$ NCs at room temperature. Metal halides ($PbBr_2$ or $MnCl_2$) were found to play vital role for these post-synthetic chemical transformation reactions. From 2D $Cs_2PbI_2Cl_2$ to 3D $CsPbBr_3$ transformation, first $PbBr_2$ precursor solution was prepared in 1-octadecene (ODE) solvent in presence of capping agent at 120 ^oC. Then, toluene-dispersed $Cs_2PbI_2Cl_2$ was injected swiftly to $PbBr_2$ solution at room temperature, which led to the immediate formation of strongly green fluorescent $CsPbBr_3$ NCs. Similarly, $MnCl_2$ plays a vital role in the post-synthetic transformation of 0D Cs_4PbCl_6 from 2D $Cs_2PbI_2Cl_2$ at room temperature. The driving force for this transformation to the lower dimensionality may be due to the presence of excess chloride ions from $MnCl_2$, which stabilized the 0D phase of Cs_4PbCl_6.

The transformed nanostructures were further characterized by PXRD. $CsPbBr_3$ exits in two different crystalline phases, i.e. orthorhombic and cubic, which can be distinguished by the characteristic peak around $2\theta = 30^o$.[29, 30] The PXRD pattern of the

transformed $CsPbBr_3$ NCs is well-matched with the diffraction pattern of orthorhombic phase (P*bnm*) (Figure 2.2.5a). The PXRD of Cs_4PbCl_6 NCs can be indexed with its rhombohedral phase (R-*3ch*) (Figure 2.2.5b). TEM of $CsPbBr_3$ shows disk-like morphology of average size of ~ 200 nm (Figure 2.2.5c). The morphology of Cs_4PbCl_6 was well-defined square-type with average size of ~ 20 nm (Figure 2.2.5d). The SAED pattern confirmed that the synthesized $CsPbBr_3$ and Cs_4PbCl_6 were single crystalline in nature (Figures 2.2.5c, d inset). The transformed 3D $CsPbBr_3$ NCs and 0D Cs_4PbCl_6 NCs exhibit different optical properties compared to the 2D $Cs_2PbI_2Cl_2$ NCs. The absorption peak of $CsPbBr_3$ was exhibited at 493 nm, and PL emission peak was noticed at 515 nm, when excited at 480 nm (Figure 2.2.5e). Whereas the emission peak of Cs_4PbCl_6 was observed at 360 nm, when excited at 300 nm (Figure 2.2.5f). Cs_4PbCl_6 has an indirect bandgap, hence the emission of Cs_4PbCl_6 was probably due to the Frenkel excitons, self-trapped by the $PbCl_6^{4-}$ octahedrons, as reported previously.[31]

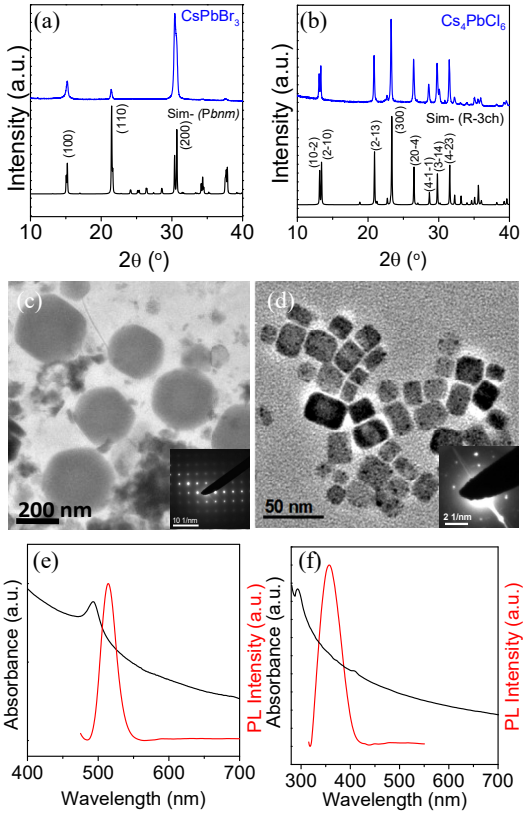

Figure 2.2.5. *PXRD pattern of (a) $CsPbBr_3$ and (b) Cs_4PbCl_6 obtained from the chemical transformation from 2D RP phase of $Cs_2PbI_2Cl_2$. TEM image with SAED pattern (inset)*

of (c) $CsPbBr_3$ and (d) Cs_4PbCl_6. Optical absorption and PL spectra of (e) 3D $CsPbBr_3$ and (f) 0D Cs_4PbCl_6.

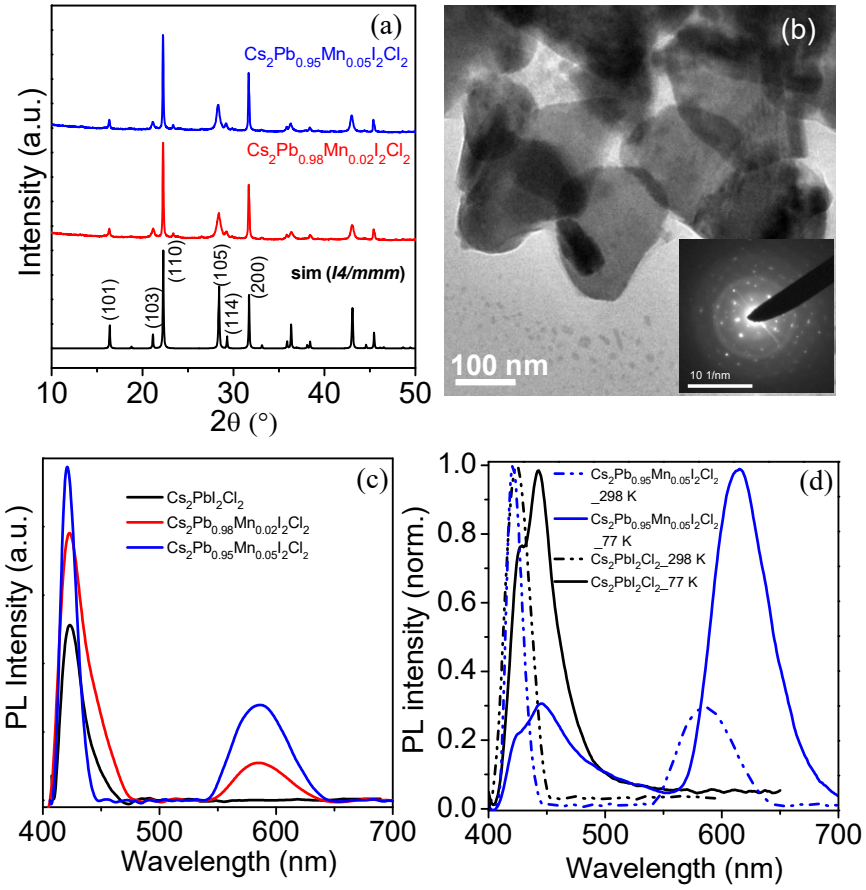

Figure 2.2.6. *(a) PXRD patterns and (b) TEM image with SAED pattern (inset) of $Cs_2Pb_{0.95}Mn_{0.05}I_2Cl_2$. (c) PL spectra of $Cs_2Pb_{1-x}Mn_xI_2Cl_2$ (x =0, 0.02, 0.05). (d) Comparative PL spectra of $Cs_2PbI_2Cl_2$ (black) and $Cs_2Pb_{0.95}Mn_{0.05}I_2Cl_2$ (blue) NCs at 298 and 77 K.*

Furthermore, Mn^{2+} was doped at the Pb^{2+} site of $Cs_2PbI_2Cl_2$ NCs. Exciton energy transfer to Mn^{2+} states depends upon the host band gap and relative position of $^4T_1$ and $^6A_1$ of Mn^{2+}.[32,33] The band gap of $Cs_2PbI_2Cl_2$ is appropriate for the exciton energy transfer of Mn (II) d-d transition. The synthesis of Mn-doped $Cs_2PbI_2Cl_2$ was carried out in a similar hot-injection method. In a typical synthesis, cesium carbonate, lead acetate, and manganese acetate were dissolved in ODE, OA and OAm at 130 ºC under inert

atmosphere in a three-necked round bottom flask followed by the addition of benzoyl halides into the reaction flask at 160 ºC. The as-synthesized product was thoroughly washed with hot toluene for 2-3 times and used for further characterization. The concentration of Mn^{2+} in $Cs_2Pb_{1-x}Mn_xI_2Cl_2$ samples were investigated *via* ICP analysis, which are found to be 2% and 5% (Table 2.2.1). PXRD pattern of $Cs_2Pb_{1-x}Mn_xI_2Cl_2$ could be indexed based on the pure phase of tetragonal $Cs_2PbI_2Cl_2$ structure (space group I*4/mmm*) with the minor higher angle shift in 2θ value, as the ionic radius of Pb^{2+} and Mn^{2+}were 133 pm and 97 pm, respectively (Figures 2.2.6a). The TEM image of $Cs_2Pb_{0.95}Mn_{0.05}I_2Cl_2$ was shown in Figure 2.2.6b, which also showed the plate-type of morphology. SAED pattern confirmed the tetragonal crystal structure with single crystalline nature of $Cs_2Pb_{0.95}Mn_{0.05}I_2Cl_2$ (Figure 2.2.6b inset).

Table 2.2.1. *Elemental analysis of $Cs_2Mn_xPb_{1-x}I_2Cl_2$ by ICP-AES.*

Nominal composition	**Composition from ICP analysis**
$Cs_2Pb_{0.95}Mn_{0.05}I_2Cl_2$	$Cs_2Pb_{0.98}Mn_{0.02}I_2Cl_2$
$Cs_2Pb_{0.9}Mn_{0.1}I_2Cl_2$	$Cs_2Pb_{0.95}Mn_{0.05}I_2Cl_2$

Figure 2.2.6c represents the PL spectra of $Cs_2Pb_{1-x}Mn_xI_2Cl_2$ (where x = 0%, 2 % and 5%) at room temperature. The PL spectra showed strong and broad d-d ($^4T_1$ to $^6A_1$) emission at 585 nm along with the host emission at 422 nm, when excited at 380 nm. Low-temperature PL of $Cs_2Pb_{0.95}Mn_{0.05}I_2Cl_2$ NCs at 77 K also revealed red-shifted and line-width broadened emission peak for both excitonic and dopant emissions in comparison to the room temperature emission (Figure 2.2.6d). The electronic absorption spectra of Mn^{2+} doped sample remained similar as undoped sample as shown in Figure 2.2.7a. To investigate the origin of this emission, photoluminescence excitation (PLE) spectra were recorded at room temperature (Figure 2.2.7b) by monitoring PL at 585 nm.

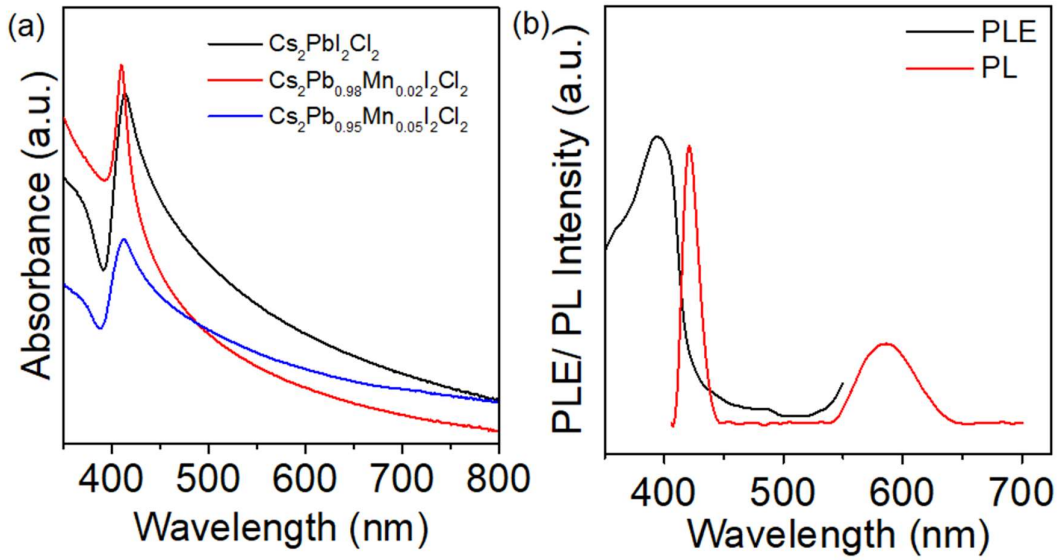

Figure 2.2.7. *(a) Absorption spectra of $Cs_2Pb_{1-x}Mn_xI_2Cl_2$ where x = 0%, 2% and 5 %. (b) PLE and PL spectra of $Cs_2Pb_{0.95}Mn_{0.05}I_2Cl_2$.*

The PLE spectra follow the absorption spectra, which implies that both the emission (exciton and dopant emission) originated from the same absorption. Figure 2.2.8 illustrates the Mn d-d emission decay curves at room temperature and 77 K. The PL decay of $Cs_2Mn_{0.95}Mn_{0.05}I_2Cl_2$ NCs was well-fitted by triexponential function with a lifetime of 1-2 ms, when emission was collected at 590 nm (Figure 2.2.8a and Table 2.2.2) and the lifetime was found to be 1-5 ns, when emission was collected at 430 nm (Figure 2.2.8b and Table 2.2.2), at room temperature. The longer lifetime emission was mainly attributed to the forbidden Mn^{2+} d-d transition. Hence, the forbidden Mn^{2+} emission was sensitized by the host $Cs_2PbI_2Cl_2$ following the energy transfer mechanism, which clearly reveals the successful doping of Mn^{2+} in $Cs_2PbI_2Cl_2$ NCs. The lifetime components for excitonic emissions increased at 77 K compared to room temperature for Mn doped sample.

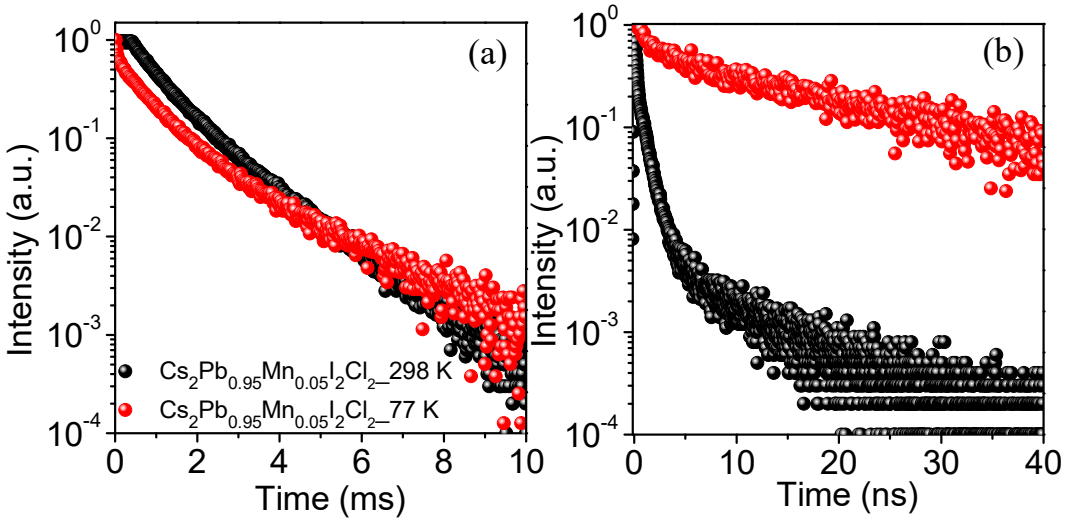

Figure 2.2.8. *Decay profile of $Cs_2Pb_{1-x}Mn_xI_2Cl_2$ NCs, when emission was collected at (a) 590 nm and (b) 430 nm.*

Table 2.2.2. *Lifetime data of $Cs_2Pb_{0.95}Mn_{0.05}I_2Cl_2$ NCs at 298 and 77 K.*

Emission collected	τ_1	τ_2	τ_3	A_1 (%)	A_2 (%)	A_3 (%)
430 nm at 298 K	0.82 ns	6.59 ns	0.32 ns	53.76	10.55	35.69
590 nm at 298 K	0.55 ms	1.05 ms	1.81 ms	17.65	55.87	22.47
430 nm at 77 K	0.80 ns	2.83 ns	20.40 ns	2.66	6.39	90.95
590 nm at 77 K	0.03 ms	0.72 ms	2.11 ms	3.19	55.08	41.73

The dopant emissions from $Cs_2PbI_2Cl_2$ NCs synthesized from the benzoyl halide are similar to that of the earlier synthesized $Cs_2PbI_2Cl_2$ using mixed oleylammonium chlorides and iodides, apart from the number of lifetime components.[15] The additional lifetime component may arise from the probable surface defect states,[17] which further leads to the variation in PL quantum yield (PLQY) values compared to earlier reported Mn^{2+} doped $Cs_2PbI_2Cl_2$ NCs.[15] The absolute PLQY of $Cs_2PbI_2Cl_2$ NCs was found to be 0.02%, whereas 5% Mn-doped $Cs_2PbI_2Cl_2$ NCs showed an enhanced PLQY of 0.97%. Earlier Manna and co-workers also observed similar low PLQY (< 0.1%) of all-inorganic RP phase of lead halide perovskite NCs.[14]

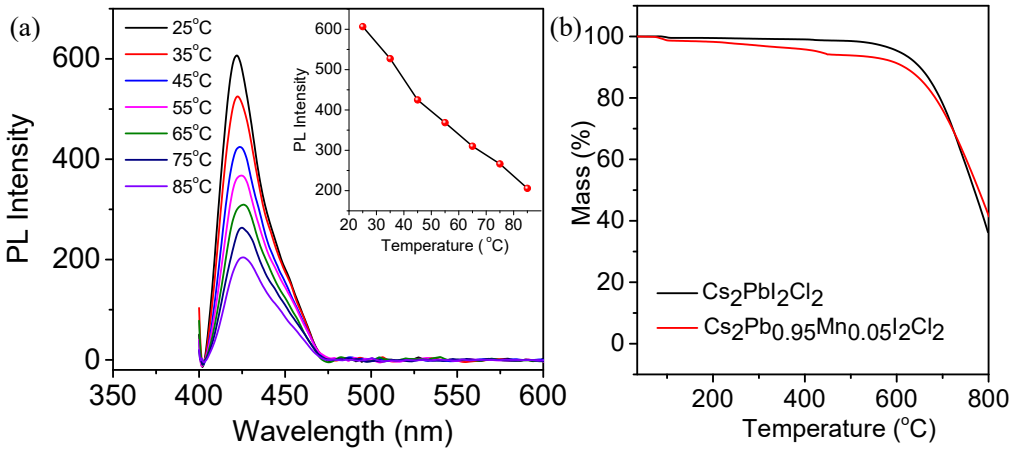

Figure 2.2.9. *(a) Temperature dependent PL of $Cs_2PbI_2Cl_2$ NCs (inset shows PL intensity variation with temperature). (b) TGA profile of $Cs_2Pb_{1-x}Mn_xI_2Cl_2$ NCs, where x = 0% and 5%.*

Finally, the thermal photoluminescence characteristics and thermal stability of $Cs_2PbI_2Cl_2$ NCs have been systematically verified, which are essential for their practical utility. The temperature-dependent PL spectra under 380 nm excitation in the temperature range of 25-85 °C with an interval of 10 °C was recorded (Figure 2.2.9a). The decrease of PL emission intensity with increasing temperature up to 85 °C with respect to its initial PL intensity at 25 °C, as evidenced from the inset of Figure 2.2.9a, might be due to the thermal dissociation of electron-hole pair and consequent diminution of the excitonic

population along with the thermally activated charge carrier trapping.[34, 35] This thermal quenching can be designated by the Arrhenius-type model;[35]

$$I_T = \frac{I_0}{1+A.\exp\left(^{E_B}/_{k_BT}\right)} \qquad (1)$$

Herein, I_0 and I_T are the intensities of the initial and variable temperatures, respectively. The parameters, A and k_B are the pre-exponential coefficient and Boltzmann constant, respectively. Typically, the exciton binding energy reveals the stability of exciton, which is designated as E_B. We found a very good linear relationship between ln (I_0/I_T-1) and $1/k_BT$ based on the correlation coefficient (R^2) of 0.985 at the temperature range of 25 °C to 85 ^{0}C (Figure 2.2.10). The value E_B can be estimated from the linear plot, which is found to be 161.24 meV. The E_B value for 2D RP phase of $Cs_2PbI_2Cl_2$ NCs is found to be comparable with the low-dimensional halides,[35] but much larger than that of the 3D $CsPbX_3$ NCs (~15-50 meV).[34, 36] A higher value of E_B is also an instinctive approximation of the superior thermal stability of $Cs_2PbI_2Cl_2$ than that of the $CsPbX_3$ NCs.[34] Further, both undoped and 5% Mn-doped $Cs_2PbI_2Cl_2$ NCs did not exhibit any noteworthy decomposition even after heating up to 600 °C at inert atmosphere, as evidenced from the thermogravimetric analysis (TGA) plot (Figure 2.2.9b).

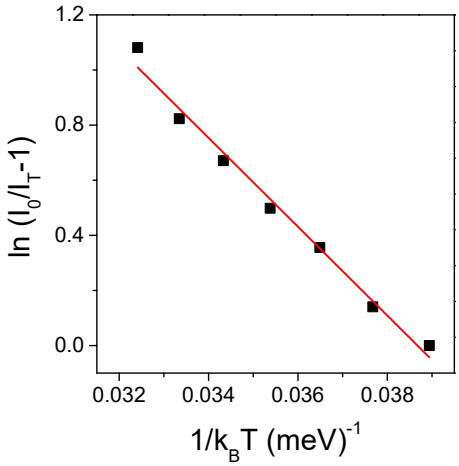

Figure 2.2.10. *The Arrhenius-type plot for the PL intensity variation of $Cs_2PbI_2Cl_2$ NCs with temperature.*

2.2.4. Conclusions

All-inorganic RP phase of 2D $Cs_2PbI_2Cl_2$ was synthesized by the solution based hot-injection method using benzoyl halides as halide precursors. The morphologies of the $Cs_2PbI_2Cl_2$ were varied from NPLs to NCs with varying the concentration of capping agents, wherein a higher concentration of capping agents favours the formation of NCs. Further, the scalable quantity (~ 1 g) of bulk powder and micrometer-sized particles of $Cs_2PbI_2Cl_2$ were synthesized *via* liquid assisted mechanochemical grinding and anti-solvent method, respectively, which is important in terms of application point of view. Optical properties of both NPLs and NCs revealed typical excitonic features related to the 2D layered structure. Further, the post-synthetic transformation to 3D $CsPbBr_3$ and 0D Cs_4PbCl_6 from 2D RP phase was achieved by adding $PbBr_2$ and $MnCl_2$, respectively in the solution at room temperature. Finally, Mn^{2+} was doped at the Pb^{2+} site of $Cs_2PbI_2Cl_2$ NCs, where the successful doping was confirmed by optical property study. The PL spectra exhibited Mn^{2+} d-d ($^4T_1$ to $^6A_1$) emission at 585 nm along with the host emission at 422 nm and the longer life-time further suggests forbidden nature of Mn^{2+} d-d transition. The line widths, peak energies, and lifetimes of PL emissions as a function of temperature were discussed in detail. Low-temperature PL experiments at 77 K for both undoped and Mn-doped NCs suggest strong electron-phonon coupling along with the evolution of phonon-assisted self-trapped exciton. Superior thermal stability was evidenced from the high temperature PL and TGA analysis for RP phase nanostructured samples. These findings result in a prominent advancement toward the synthesis of all-inorganic halide RP compound both in nano and bulk forms, post synthetic chemical transformation, doping and its subsequent effect on the structure-optical property relationships. In summary, flexibility and versatility of our synthetic strategies will permit for the forthcoming advancement of 2D all-inorganic halides in nano-dimensions and could be exploited in the field of solar cells, photodetectors, and optoelectronics.

2.2.5. References

1. C. C. Stoumpos, D. H. Cao, D. J. Clark, J. Young, J. M. Rondinelli, J. I. Jang, J. T. Hupp and M. G. Kanatzidis, *Chem. Mater.*, 2016, **28**, 2852.

2. H. Tsai, W. Nie, J. C. Blancon, C. C. Stoumpos, R. Asadpour, B. Harutyunyan, A. J. Neukirch, R. Verduzco, J. J. Crochet, S. Tretiak, L. Pedesseau, J. Even, M. A. Alam, G. Gupta, J. Lou, P. M. Ajayan, M. J. Bedzyk, M. G. Kanatzidis and A. D. Mohite, *Nature*, 2016, **536**, 312.

3. Y. Yu, D. Zhang and P. Yang, *Nano Lett.*, 2017, **17**, 5489.

4. L. Mao, W. Ke, L. Pedesseau, Y. Wu, C. Katan, J. Even, M. R. Wasielewski, C. C. Stoumpos and M. G. Kanatzidis, *J. Am. Chem. Soc.*, 2018, **140**, 3775.

5. M. I. Saidaminov, O. F. Mohammed and O. M. Bakr, *ACS Energy Lett.*, 2017, **2**, 889.

6. B. Saparov and D. B. Mitzi, *Chem. Rev.*, 2016, **116**, 4558.

7. H. Lin, C. Zhou, Y. Tian, T. Siegrist and B. Ma, *ACS Energy Lett.*, 2018, **3**, 54.

8. L. Mao, C. C. Stoumpos and M. G. Kanatzidis, *J. Am. Chem. Soc.*, 2019, **141**, 1171.

9. L. Dou, A. B. Wong, Y. Yu, M. Lai, N. Kornienko, S. W. Eaton, A. Fu, C. G. Bischak, J. Ma, T. Ding, N. S. Ginsberg, L. W. Wang, A. P. Alivisatos and P. Yang, *Science*, 2015, **349**, 1518.

10. Y. Takeoka, K. Asai, M. Rikukawa and K. Sanui, *Bull. Chem. Soc. Jpn.*, 2006, **79**, 1607.

11. Y. Zhou and Y. Zhao, *Energy Environ. Sci.*, 2019, **12**, 1495.

12. J. Liang, J. Liu and Z. Jin, *Solar RRL*, 2017, **1**, 1700086.

13. J. Li, Q. Yu, Y. He, C. C. Stoumpos, G. Niu, G. G. Trimarchi, H. Guo, G. Dong, D. Wang, L. Wang and M. G. Kanatzidis, *J. Am. Chem. Soc.*, 2018, **140**, 11085.

14. Q. A. Akkerman, E. Bladt, U. Petralanda, Z. Dang, E. Sartori, D. Baranov, A. L. Abdelhady, I. Infante, S. Bals and L. Manna, *Chem. Mater.*, 2019, **31**, 2182.

15. A. Dutta, R. K. Behera, S. Deb, S. Baitalik and N. Pradhan, *J. Phys. Chem. Lett.*, 2019, **10**, 1954.

16. J. Li, C. C. Stoumpos, G. G. Trimarchi, I. Chung, L. Mao, M. Chen, M. R. Wasielewski, L. Wang and M. G. Kanatzidis, *Chem. Mater.*, 2018, **30**, 4847.

17. M. Imran, V. Caligiuri, M. Wang, L. Goldoni, M. Prato, R. Krahne, L. De Trizio and L. Manna, *J. Am. Chem. Soc.*, 2018, **140**, 2656.

18. Z. Liang, S. Zhao, Z. Xu, B. Qiao, P. Song, D. Gao and X. Xu, *ACS Appl. Mater. Interfaces*, 2016, **8**, 28824.

19. B. Yang, J. Chen, F. Hong, X. Mao, K. Zheng, S. Yang, Y. Li, T. Pullerits, W. Deng and K. Han, *Angew. Chem., Int. Ed.*, 2017, **56**, 12471.

20. A. Sarkar, P. Acharyya, R. Sasmal, P. Pal, S. S. Agasti and K. Biswas, *Inorg. Chem.*, 2018, **57**, 15558.

21. K. M. McCall, C. C. Stoumpos, S. S. Kostina, M. G. Kanatzidis and B. W. Wessels, *Chem. Mater.*, 2017, **29**, 4129.

22. R. Gautier, M. Paris and F. Massuyeau, *J. Am. Chem. Soc.*, 2019, **141**, 12619.

23. L. Wu, H. Hu, Y. Xu, S. Jiang, M. Chen, Q. Zhong, D. Yang, Q. Liu, Y. Zhao, B. Sun, Q. Zhang and Y. Yin, *Nano Lett.*, 2017, **17**, 5799.

24. F. Palazon, C. Urso, L. De Trizio, Q. Akkerman, S. Marras, F. Locardi, I. Nelli, M. Ferretti, M. Prato and L. Manna, *ACS Energy Lett.*, 2017, **2**, 2445.

25. P. Li, D. Yang, Y. Tan, M. Cao, Q. Zhong, M. Chen, H. Hu, B. Sun, Y. Xu and Q. Zhang, *ACS Appl. Mater. Interfaces*, 2019, **11**, 3351.

26. S. K. Balakrishnan and P. V. Kamat, *Chem. Mater.*, 2018, **30**, 74.

27. P. Acharyya, P. Pal, P. K. Samanta, A. Sarkar, S. K. Pati and K. Biswas, *Nanoscale*, 2019, **11**, 4001.

28. P. Pal, S. Saha, A. Banik, A. Sarkar and K. Biswas, *Chem. Eur. J.*, 2018, **24**, 1811.

29. J. Song, J. Li, X. Li, L. Xu, Y. Dong and H. Zeng, *Adv. Mater.*, 2015, **27**, 7162.

30. X. Li, Y. Wu, S. Zhang, B. Cai, Y. Gu, J. Song and H. Zeng, *Adv. Funct. Mater.*, 2016, **26**, 2435.

31. Y. Zhang, B. Fan, Y. Liu, H. Li, K. Deng and J. Fan, *Appl. Phys. Lett.*, 2018, **112**, 183101.

32. A. K. Guria, S. K. Dutta, S. D. Adhikari and N. Pradhan, *ACS Energy Lett.*, 2017, **2**, 1014.

33. B. Luo, F. Li, K. Xu, Y. Guo, Y. Liu, Z. Xia and J. Z. Zhang, *J. Mater. Chem. C*, 2019, **7**, 2781.

34. W. Lv, X. Tang, L. Li, L. Xu, M. Li, R. Chen and W. Huang, *J. Phys. Chem. C*, 2019, **123**, 24313.

35. R. Roccanova, A. Yangui, G. Seo, T. D. Creason, Y. Wu, D. Y. Kim, M. H. Du and B. Saparov, *ACS Mater. Lett.*, 2019, **1**, 459.

36. S. M. Lee, C. J. Moon, H. Lim, Y. Lee, M. Y. Choi and J. Bang, *J. Phys. Chem. C*, 2017, **121**, 26054.

PART 3

2D Nanosheets of Layered Perovskite Halides: Synthesis and their Photoluminescence Blinking Properties

Chapter 3.1

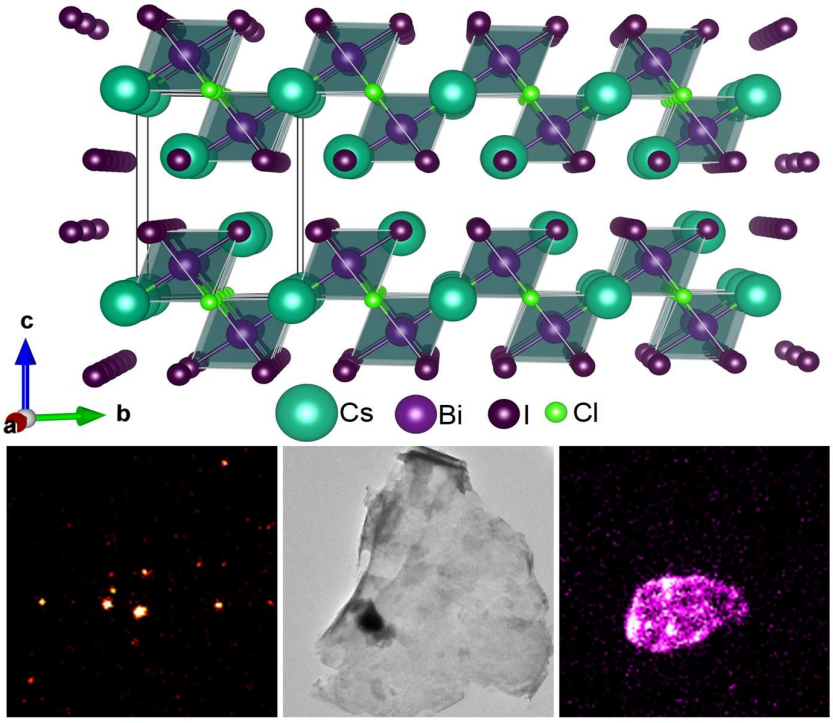

Synthesis and Localized Photoluminescence Blinking of Lead-free 2D Nanostructures of $Cs_3Bi_2I_6Cl_3$

Chapter 3.1

Synthesis and Localized Photoluminescence Blinking of Lead-free 2D Nanostructures of $Cs_3Bi_2I_6Cl_3$[†]

Summary

Two-dimensional (2D) lead-free halide perovskites have produced enormous perception in the field of optoelectronics due to their fascinating optical properties, however, an in-depth understanding on their shape-controlled charge-carrier recombination dynamics is still lacking, which could be resolved by exploring the photoluminescence (PL) blinking behaviour at the single-particle level. In this chapter, we demonstrate, for the first time, the synthesis of nanocrystals (NCs) and 2D nanosheets (NSs) of layered mixed halide, $Cs_3Bi_2I_6Cl_3$, by solution-based method. We applied fluorescence microscopy and super-resolution optical imaging at single-particle level to investigate their morphology-dependent PL properties. Narrow emission line-widths and passivation of non-radiative defects were evidenced for 2D layered nanostructures, whereas the activation of shallow trap states was recognized at 77 K. Interestingly, individual NCs were found to display temporal intermittency (blinking) in PL emission. On the other hand, NS showed temporal PL intensity fluctuations within localized domains of the crystal. In addition, super-resolution optical image of the NS from localization-based method showed spatial inhomogeneity of the PL intensity within perovskite crystal.

[†]K. Kundu,[*] **P. Acharyya,**[*] K. Maji, R. Sasmal, S. S. Agasti, and K. Biswas. *Angew. Chem., Int. Ed.* 2020, **59**, 13093-13100. (**contributed equally*)

3.1.1. Introduction

Low-dimensional ultrathin layered materials have unique advantages over their bulk counterparts in terms of the extended photocarrier life-times and favourable optical responses owing to their spatial confinement effects.[1] Considering these characteristics, a number of prospects for next-generation optoelectronic devices arise for the development of low-dimensional materials beyond conventional three-dimensional (3D) counterparts, which should preserve the fascinating electronic and optical properties, appropriate for these devices.[2] Over the past few years, hybrid organic-inorganic perovskites (e.g., methylammonium lead iodide, $MAPbI_3$) have been exploited as innovative absorber materials for photovoltaic applications with their unique advantages of tunable bandgaps, easy solution processability and efficient charge-transfer processes, for which the power conversion efficiency achieved over 22% till now.[3] Nevertheless, the long-term stability (e.g., moisture sensitivity and thermal stability) and environmental impact (i.e., the toxicity of its Pb content) endure foremost difficulty for their implementation in large-scale application, which possibly lead to dissociation, noticeable defect formation, or mechanical catastrophe.[4] In the meantime, cesium-based all-inorganic perovskites (i.e., $CsPbX_3$) gained growing recognition in the photovoltaic community, thanks to their better thermal stability in comparison to hybrid organic-inorganic analogues.[5, 6] Currently, substantial attempts are being devoted to synthesize and characterize the 2D perovskites due to their improved stability over 3D materials.[4, 7] On the other hand, direct approaches were implemented to eliminate the toxic Pb^{2+} in all-inorganic $APbX_3$-based perovskites by exchanging with other isovalent ions, for example, Sn^{2+} or Ge^{2+} from same-group ns^2 cations, and divalent cations beyond the IVA group (e.g. Ba^{2+} and Sr^{2+}).[8-12] However, all of these attempts were failed to meet the prospect of an ideal solar cell absorber because of their high oxidation tendencies and oversized band gaps.[10, 11, 13] With the purpose of maintaining the chemistry of lone-pair ns^2 state, the trivalent cations from group VA (e.g. Bi^{3+} and Sb^{3+}) have been utilized at the B-site of the perovskite structures as the alternative of Pb^{2+}.[14-17] Nevertheless, in presence of Bi^{3+} or Sb^{3+}, the usual ABX_3 structures with corner sharing BX_6 octahedra are transformed into a stable $A_3B_2X_9$ stoichiometry, which can exist as either bi-octahedral zero-dimensional (0D) face-sharing $(B_2X_9)^{3-}$ clusters or 2D layers with partly corner sharing

BX_6 octahedra.[14-17] In comparison to the 0D phase of $A_3B_2X_9$ materials having low-symmetry induced indirect band gap and inferior hopping-like carrier transport,[14, 16] their 2D analogues are more suitable for photovoltaics, which are expected to show a direct band gap and decent in-layer carrier transport.[14, 16]

Interestingly, most of the widely investigated 2D perovskites were composed of organic cations, which simply function as the insulating barrier or the supporting layer to attain the 2D structure according to the recent reviews by Kanatzidis,[18] and Karunadasa.[19] On the other hand, all-inorganic 2D derivatives are rarely explored in spite of their high intrinsic stability.[20-22] Further, the significance of mixed-halide composition is well-known for their better phase stability,[23, 24] improved optical properties than neat halide composition,[25, 26] along with their potential use in top-cell of tandem devices.[27] Till now, all of these 2D perovskites with mixed halide compositions contain Pb and at present, such Pb-free materials are limited because of the fact that there is slender option of inorganic cations, which can stabilize the desired mixed halide perovskite structure.[28] Recently, Kanatzidis and co-workers synthesized single crystal of $Cs_3Bi_2I_6Cl_3$, the latest member of (111)-oriented mixed halide 2D perovskite, which is comprising of corner-shared $[BiCl_{6/2}I_3]^{3-}$ octahedra by capping the bilayers with I atoms along with Cl atoms occupied at bridging positions and isostructural to $Cs_3Bi_2Br_9$ and α-$Cs_3Sb_2I_9$,[29] as represented in Figure 3.1.1a.

In this chapter, for the first time, the 2D nanosheets (NSs) and small nanocrystals (NCs) of $Cs_3Bi_2I_6Cl_3$ were synthesized by hot-injection method. The temperature-dependent morphological evolution has been conferred from the microscopic and infrared spectroscopic analysis. The nanostructured $Cs_3Bi_2I_6Cl_3$ showed promising environmental and thermal stability as evidenced from the powder X-ray diffraction (PXRD), high-temperature photoluminescence (PL) and thermogravimetric analysis (TGA) studies. The 2D NSs and NCs of $Cs_3Bi_2I_6Cl_3$ showed distinct optical properties and excitonic recombination dynamics, while at cryogenic temperature activation of shallow trap states was evidenced. Finally, fluorescence microscopy was employed to investigate the single-particle PL properties of 2D NSs and NCs of $Cs_3Bi_2I_6Cl_3$, both of which showed luminescence at green region along with the localized blinking events at millisecond time scale. Each NC repeatedly undergoes dynamical fluctuations in PL emission, which

indicates high photostability of the NCs. Super-resolved images created by fitting the blinking events to a Gaussian function depicted a spatially heterogeneous but localized distribution of blinking events within a single NS. We believe that these lead-free 2D nanostructured materials have prominent prospective to turn into a new class of environmentally benign solution-processed 2D semiconductors for ultrathin and flexible optoelectronics.

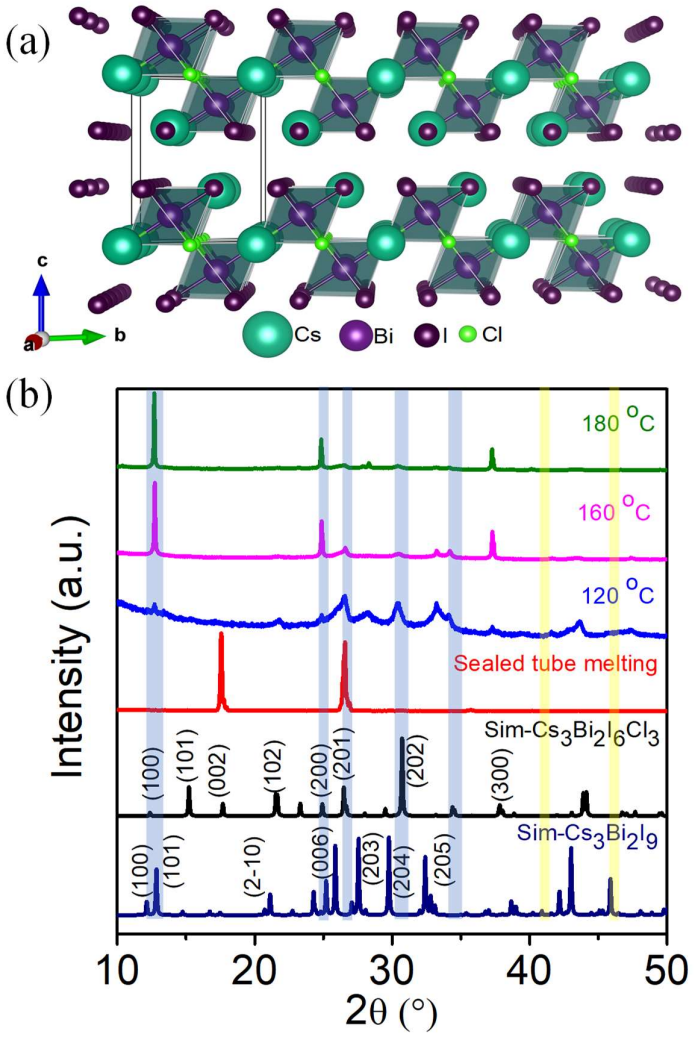

Figure 3.1.1. *(a) Crystal structure of $Cs_3Bi_2I_6Cl_3$, (b) PXRD patterns of $Cs_3Bi_2I_6Cl_3$ obtained by melting reaction and hot injection at different temperatures. The coloured shades indicate the eye guide for the difference in pattern between $Cs_3Bi_2I_9$ and $Cs_3Bi_2I_6Cl_3$.*

3.1.2. Methods

Reagents: Caesium carbonate (Cs_2CO_3, 99.9%, Sigma-Aldrich), bismuth iodide (BiI_3, 99.9%, Sigma-Aldrich), bismuth chloride ($BiCl_3$, 99.9%, Sigma-Aldrich), cesium chloride (CsCl, 99.9%, Sigma-Aldrich), oleic acid (OA, tech. 90%, Sigma-Aldrich), oleylamine (OAm, tech. 70%, Sigma-Aldrich), 1-octadecene (ODE, tech. 90%, Sigma Aldrich), and toluene (AR, 99.0%, SDFCL) were used for the syntheses without further purification.

Synthesis of Cs-Oleate. In a typical synthesis, 410 mg (1.26 mmol) Cs_2CO_3 and 20 mL ODE were taken in a 50 mL 3-necked round-bottom flask and heated at 120 °C with continuous magnetic stirring in vacuum for 1 h to get a homogeneous solution. In the above solution, 1.30 mL of OA was added and the solution was kept for another 30 min at the same condition. The vacuum was replaced with nitrogen atmosphere and kept for 5 min to get a clear Cs-oleate solution. This Cs-oleate solution was stored at room temperature under nitrogen atmosphere for further use.

Synthesis of colloidal $Cs_3Bi_2I_6Cl_3$. In order to synthesize the colloidal $Cs_3Bi_2I_6Cl_3$ nanostructures of different morphologies (NCs, NSs-NCs and NSs), the reactions were carried out by a hot injection method. Typically, 153.3 mg (0.26 mmol) BiI_3, 41 mg (0.13 mg) $BiCl_3$ and 10 ml ODE were taken in a 50 mL 3-necked round-bottom flask, and the flask was degassed at 100 °C for 60 min along with magnetic stirring. 1 mL OA and 1 mL OAm were added to the mixture at 100 °C under N_2 atmosphere to dissolve BiI_3 and $BiCl_3$. Then, temperature of the reaction was raised to 120, 160, and 180 °C for the three separate reactions to produce different morphology nanostructures (NCs, NSs-NCs and NSs). The pre-synthesized Cs-oleate (0.1 M, 0.6 mL) solution in ODE, preheated at 90 °C, was swiftly injected to the reaction mixture at 120, 160, and 180 °C respectively. Within few seconds, the reaction mixture became turbid red, and then the reaction was quenched by dipping the reaction flask into an ice bath. N_2 atmosphere was maintained throughout the reaction process in a Schlenk line. The synthesized $Cs_3Bi_2I_6Cl_3$ nanostructures were then washed with toluene and precipitated by centrifugation at 9000 rpm for 10 min, followed by dispersing the products in toluene for further studies. We

obtained $Cs_3Bi_2I_6Cl_3$ with NCs, NCs-NSs and NSs-like morphology at 120, 160 and 180 ^oC respectively.

Synthesis of crystalline ingot of $Cs_3Bi_2I_6Cl_3$. Crystalline ingot (~500 mg) of $Cs_3Bi_2I_6Cl_3$ was synthesized by reaction of stoichiometric (3:2) amounts of the starting materials CsCl and BiI_3 in quartz ampoules. The tube was sealed under vacuum ($\sim 10^{-6}$ Torr) and the seal tube was placed in a tube furnace, which was heated in 10 h to 750 °C, held for 48 h, then cooled slowly to 300 °C and annealed it for 48 h and cooled to room temperature over 48 h. The resulting polycrystalline $Cs_3Bi_2I_6Cl_3$ ingot was formed.

Powder X-ray diffraction. The powder X-ray Diffraction patterns of all the samples were collected on a Bruker D8 difractometer by using Cu Kα (λ=1.5406 Å) at room temperature.

Electronic absorption spectroscopy: Solid powder - Diffuse reflectance measurement was carried out to estimate the optical band gap in the range of 250 to 800 nm by using Perkin-Elmer Lambda 900 UV/Vis/Near-IR spectrometer in reflectance mode for bulk $Cs_3Bi_2I_6Cl_3$. Absorption (α/S) data were calculated from reflectance data by using the Kubelka-Munk equation: $\alpha/S = (1-R)^2/(2R)$, in which R is the reflectance, α and S are the absorption and scattering coefficients, respectively. The energy band gap was derived from the α/S vs. E (eV) plot. The emission spectra were obtained by using Perkin-Elmer LS 55 Luminescence spectrometer in the solid state. Luminescence spectra of the solid samples were recorded at the different excitation wavelength.

Solution phase - A UV-vis near-IR spectrophotometer (UV-2600, Shimadzu Corporation, Kyoto, Japan) was used to record the absorption spectrum of the perovskite solutions dispersed in toluene. A FluoroMax-4 spectrofluorometer (Horiba JobinYvon Inc.) with a 5 nm slit width was used to record the photoluminescence (PL) spectrum of the perovskite solutions with an excitation wavelength of 450 nm.

Low-temperature photoluminescence (PL) measurements. Low-temperature PL measurements were performed using Edinburgh FLS1000 spectrofluorometer and excited

with EPL-405 (wavelength 405 nm ± 10 nm) at 77 K using a vacuum liquid-nitrogen cryostat.

Fluorescent life-time measurement. The time-correlated single photon counting (TCSPC) method was implemented during the fluorescence life-time measurements using the FluoroCube (Horiba Jobin Yvon, formerly IBH product) with a 405 nm LED excitation source. The TBX-04 picosecond photon-detection module was used to detect the fluorescence signal. The DAS 6 decay analysis software package (HORIBA Jobin Yvon IBH) was used to analyze the fluorescence decay, where the best decay curve fit was achieved by monitoring the reduced χ^2 values and the weighted residuals.

Thermogravimetric analysis. Thermogravimetric analysis (TGA) was performed by using a 2 STAR TGA instrument. Samples were heated at a rate of 5 °C min^{-1} in N_2 atmosphere (40 mL min^{-1}) throughout a temperature range of 30-750 °C.

Transmission electron microscopy. The transmission electron microscopy (TEM) images of the synthesized $Cs_3Bi_2I_6Cl_3$ were taken using a JEOL (JEM3010).

Atomic force microscopy (AFM). AFM image was recorded using JPK NanoWizard II instrument.

Fourier transform infrared spectroscopy (FTIR). FTIR spectra were recorded in the range of 400-4000 cm^{-1} by using a Bruker Optics Alpha-P FTIR spectrophotometer equipped with an attenuated total reflectance (ATR) module.

Raman spectroscopy. Raman spectroscopic measurements of perovskite samples were performed using a Renishaw *InVia* Raman spectrometer with a Leica upright microscope using 785 nm laser excitation sources and a 1200 grooves per mm grating. A silicon standard (520.5 cm^{-1}) was used as a reference to calibrate the Raman instrument before measurements. The spectrum was recorded with an exposure time of 10 sec and five

accumulations. The collection optics was set using a 50X objective. The system was controlled by Renishaw WiRE 4.1 software.

Super-resolved fluorescence imaging. The super-resolved fluorescence imaging is done in collaboration with Prof. Sarit S. Agasti, JNCASR, India. The NCs and NSs were dispersed in toluene to a certain concentration and drop casted to a coverslip to dry out at atmospheric conditions and subjected for fluorescence microscopy using ZEISS ELYRA PS1 system. Bright field and fluorescence images were captured using higher magnification objective (Plan-Apochromat 63x/1.40 Oil DIC M27). The fluorescence microscopy was carried out using structured illumination method (SIM) after excitation using 488 nm laser and appropriate emission filter sets (BP 495-575 + LP 755) and the resulted images showed distribution of NCs and NSs. The laser power density was kept 630 W cm^{-2} for this entire measurement. The recorded images were further processed using Image J for additional adjustment and calculation of dimensions of nanostructures.

The blinking studies were performed by using Alpha Plan-Apochromat 100x/1.46 Oil DIC M27 Elyra objective in TIRF mode. 488 nm laser (12 mW at the objective) was used for excitation and emission was recorded with corresponding emission filter (BP 495-575 + LP 755). Fluorescence blinking events of both NCs and NSs were recorded for 10,000 frames with 40 ms integration time. Electron Multiplication (EM) gain was kept at 100. Image processing was done using ZEN 2.0 software to evaluate the time-trace of PL emission, localization fitting, photon count, localization precision and molecular density diagram of the NC and NSs.

3.1.3. Results and Discussion

The $Cs_3Bi_2I_6Cl_3$ nanostructures were synthesized by the solution based hot-injection method. Typically, appropriate proportions of BiI_3 and $BiCl_3$ were dissolved in 1-octadecene (ODE) along with the oleic acid (OA) and oleylamine (OAm) under an inert atmosphere at 100 ^oC followed by the hot-injection of Cs-oleate into the reaction mixture at different temperatures (120-180 ^oC). This led to the immediate formation of $Cs_3Bi_2I_6Cl_3$ NCs, mixture of NCs-NSs and NSs at 120 ^oC, 160 ^oC and 180 ^oC, respectively. Subsequently, the reaction mixture was ice quenched and then, washed

several times with hot toluene. Additionally, we have synthesized high quality crystalline ingot of $Cs_3Bi_2I_6Cl_3$ by vacuum (~10^{-6} Torr) sealed quartz tube melting reaction at 750 ^oC.

The powder X-ray diffraction (PXRD) patterns of as-synthesized $Cs_3Bi_2I_6Cl_3$ by hot-injection method and sealed tube melting reaction were perfectly matched with the trigonal phase of $Cs_3Bi_2I_6Cl_3$ (space group *P*-3*m*1). The PXRD patterns were also compared with the hexagonal $Cs_3Bi_2I_9$ (space group $P6_3/mmc$), which clearly indicate the formation of pure phase 2D trigonal $Cs_3Bi_2I_6Cl_3$, as illustrated in Figure 3.1.1b. The crystal structure of $Cs_3Bi_2I_6Cl_3$ is 2D layered type similar to the α-$Cs_3Sb_2I_9$, where corner shared octahedra were formed by the $[BiI_3Cl_3]^{3-}$ units (Figure 3.1.1a). The presence of bridging Cl atom in the octahedra unit leads to the 2D structure unlike the 0D molecular phase of $Cs_3Bi_2I_9$.

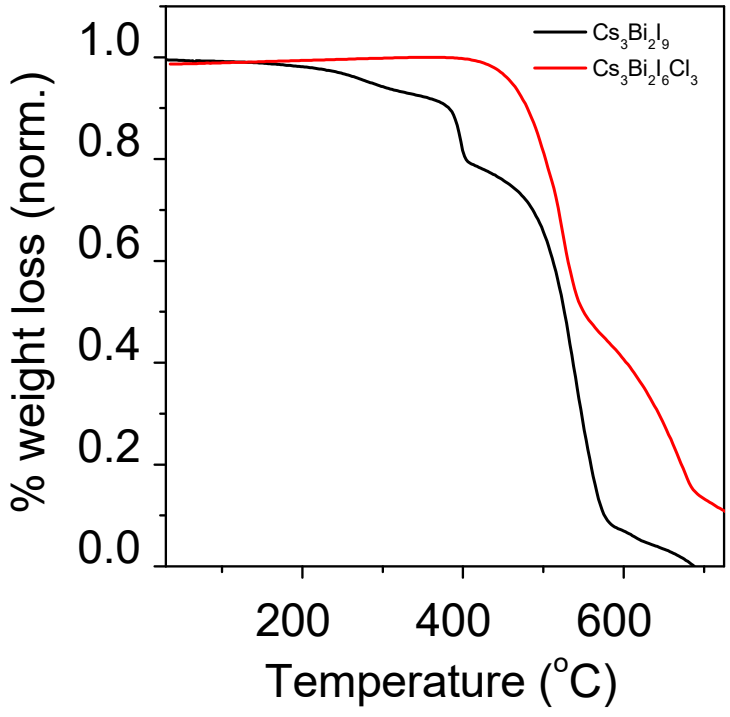

Figure 3.1.2. *Thermogravimetric analysis (TGA) of $Cs_3Bi_2I_6Cl_3$ and $Cs_3Bi_2I_9$ NCs.*

Furthermore, we have compared the thermal stability of 2D layered $Cs_3Bi_2I_6Cl_3$ with earlier reported 0D molecular $Cs_3Bi_2I_9$ (Figure 3.1.2).[30] Interestingly, thermogravimetric analysis (TGA) of $Cs_3Bi_2I_9$ reveals an early weight loss at ~245 °C along with the significant second weight loss at ~370 °C, which is probably due to the decomposition of $Cs_3Bi_2I_9$ to CsI and BiI_3. On the other hand, TGA profile of $Cs_3Bi_2I_6Cl_3$ initially shows a noteworthy weight loss in between 425 to 530 °C, which is probably due to the removal of organic capping ligand and sublimation of BiI_3. This certainly signifies the improved thermal stability of the 2D layered mixed halide counterpart compared to their 0D iodide-based molecular structure. Synthesized 2D nanostructured samples are also stable at ambient conditions since no indication of degradation or new phase is evidenced from the PXRD patterns even after five months (Figure 3.1.3).

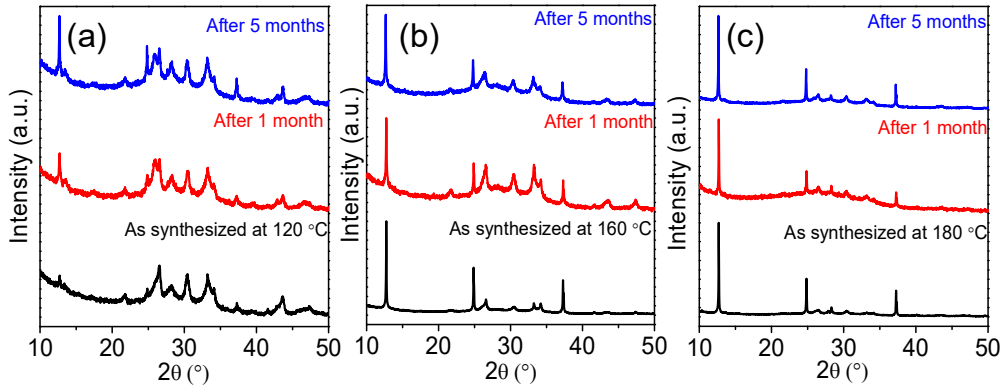

Figure 3.1.3. *PXRD patterns of as synthesized $Cs_3Bi_2I_6Cl_3$ at three different temperatures (a-c) immediate after synthesis (black), after one month (red) and five months (blue).*

The morphologies of the as-synthesized $Cs_3Bi_2I_6Cl_3$ nanostructures were characterized by transmission electron microscopy (TEM). Small NCs with a size of ~ 20 nm were formed, when $Cs_3Bi_2I_6Cl_3$ was synthesised at 120 ºC by the hot-injection method (Figure 3.1.4a). From the high-resolution TEM (HRTEM) image of NCs, the *d*-spacing value of lattice fringe was found to be 0.33 nm, which is denoted to the (201) plane of $Cs_3Bi_2I_6Cl_3$ (Figure 3.1.4b). It is important to mention here that the changes in the morphology were evidenced with increase in reaction temperature from 120 ºC to 180 ºC. Formation of NSs along with NCs were noticed during the intermediate reaction temperature of 160 ºC

(Figure 3.1.4c), whereas at 180 ºC, complete transformation to NSs (with the lateral size of ~5 μm) was evidenced (Figure 3.1.4e). Subsequently, the *d*-spacing value of high temperature samples (at 160 ºC and 180 ºC) was found to be 0.35 nm, which corresponds to the (200) plane, as verified from the HRTEM images (Figures 3.1.4d and f). Further, the AFM analysis (Figure 3.1.5) shows that the measured thickness of the NSs is ~2-4 nm, which resembles with the nearly two to four layers of $Cs_3Bi_2I_6Cl_3$, stacked along the *c*-direction. This confirms the thin 2D nature of the $Cs_3Bi_2I_6Cl_3$ NSs.

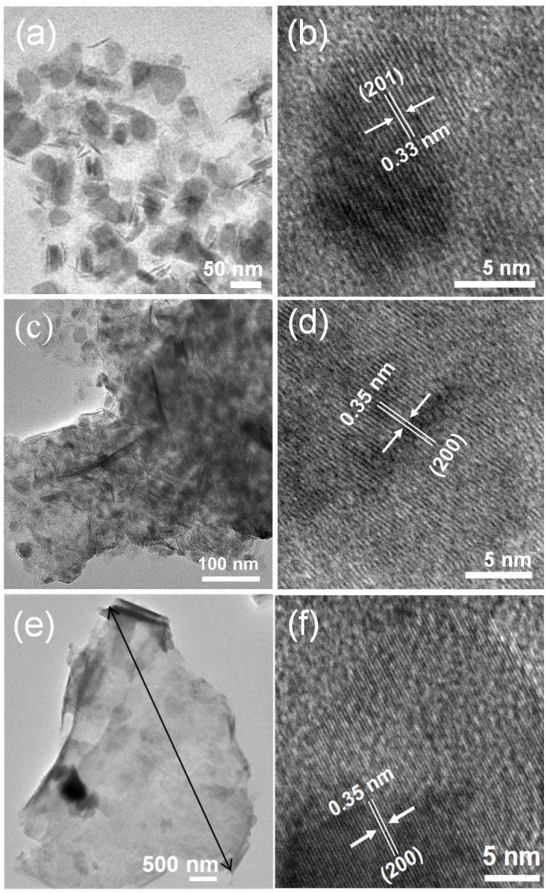

Figure 3.1.4. *(a) TEM image of $Cs_3Bi_2I_6Cl_3$ NCs, (b) HRTEM image with lattice plane (201) of the $Cs_3Bi_2I_6Cl_3$ NCs. (c) TEM images of $Cs_3Bi_2I_6Cl_3$ NCs along with NSs. (d) HRTEM image with lattice plane (200) of the NCs along with NSs (e) TEM image of $Cs_3Bi_2I_6Cl_3$ NSs, where the arrow indicates the lateral dimension of NSs, (f) HRTEM image with lattice plane (200) of the $Cs_3Bi_2I_6Cl_3$ NSs.*

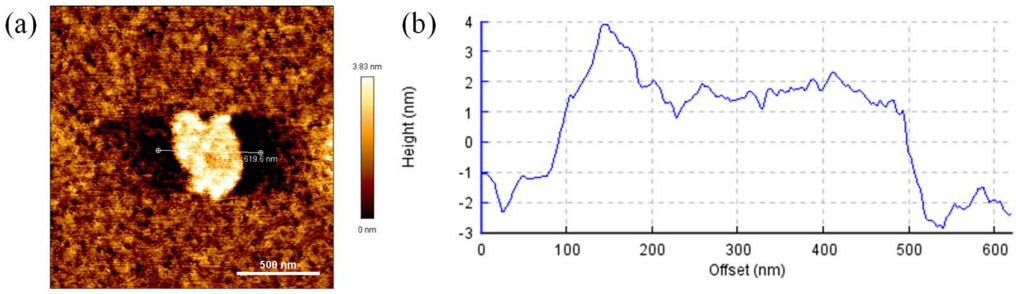

Figure 3.1.5. *(a) AFM image and (b) height profile of the $Cs_3Bi_2I_6Cl_3$ nanosheets (NSs).*

In order to unveil the growth mechanism of the $Cs_3Bi_2I_6Cl_3$ NCs, the Fourier transform infrared spectroscopy (FTIR) was implemented to explore the role of the ligands (OA and OAm) that exist in the surface of NCs as capping agents or stabilizing ligands. The FTIR spectra of as-synthesized $Cs_3Bi_2I_6Cl_3$ at three different reaction temperatures were illustrated in Figure 3.1.6. The $Cs_3Bi_2I_6Cl_3$ NCs synthesized at 120 ºC demonstrate characteristic modes of oleyl group (i.e., $CH_3(CH_2)_7$-CH=CH-$(CH_2)_8$-) from both OA and OAm, for example, peaks at ~2851 and ~2920 cm^{-1} are due to the symmetric and asymmetric -CH_2 stretching modes, respectively, and a weak peak at ~1640 cm^{-1} is due to the $\nu_{C=C}$ stretching mode. Moreover, the spectrum of the NCs shows typical vibrational signatures of the carboxylic acid group ($\nu_{C=O}$) at 1712 cm^{-1} along with the modes at 3175 and 1520 cm^{-1}, which belong to the ν_{N-H} stretching and NH_2 scissoring groups, respectively from the amine moiety. The strong C-H bending modes at 1460 and 1378 cm^{-1} are also noticed, which appeared due to the presence of hydrocarbon chains of both OA and OAm.[31-34] In the FTIR spectrum of the high-temperature synthesized $Cs_3Bi_2I_6Cl_3$ samples (Figure 3.1.6), the vibrational modes belong to the ammonium N-H disappeared, while those from carboxylate moieties were retained, signifying the removal of OAm and retention of OA from the surface. Thus, OA and OAm are attached to the surface of NCs, but the OAm-surface interaction is weaker in comparison to the OA-surface binding. Increase in temperature destabilizes the [X···H-N^+] type of H-bonding interaction and further dissociates the ammonium moiety from the surface of $Cs_3Bi_2I_6Cl_3$, whereas the oleate binding is more robust at the elevated temperatures.[34] The preferential

binding of ligand during the growth of nanostructured $Cs_3Bi_2I_6Cl_3$ apparently involves temperature-dependent dynamics of surface-ligand interaction, in which the morphological evolution with temperature can be termed as a kinetically controlled process. Thus, the change in reaction temperature permits the dynamic solvation with the exchange of ligands on and off the surface of growing nanostructures.[34]

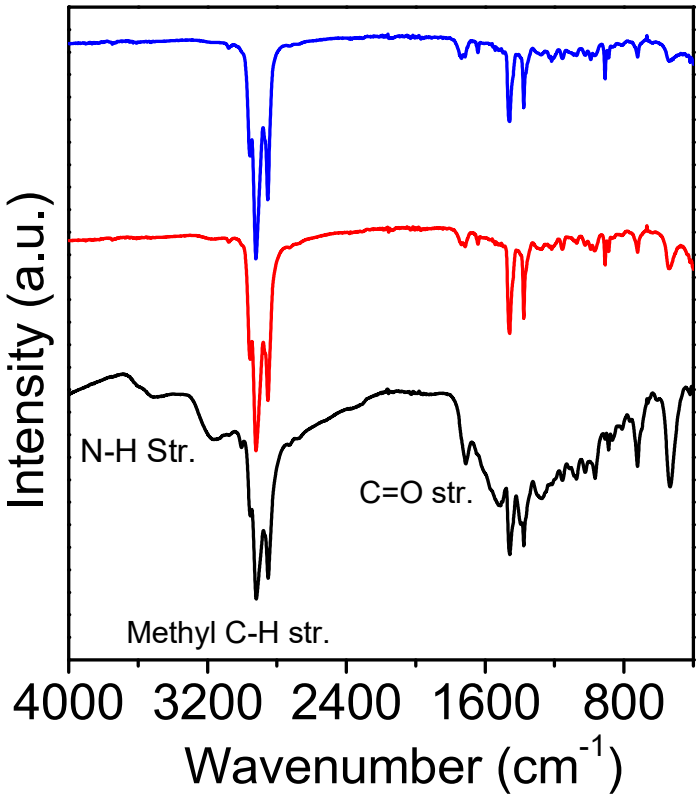

***Figure 3.1.6**. FTIR spectra of $Cs_3Bi_2I_6Cl_3$ NCs synthesized at 120 °C (black spectrum), $Cs_3Bi_2I_6Cl_3$ NSs mixed with NCs synthesized at 160 °C (red spectrum) and $Cs_3Bi_2I_6Cl_3$ NSs synthesized at 180 °C (blue spectrum).*

High temperatures considerably weaken the OAm-surface binding, resulted in the formation of large 2D NSs by lateral oriented attachment type growth of the NCs.[9] Such temperature-controlled morphological transformations was observed earlier in $CsPbBr_3$ perovskite NCs.[35] However, description of the ligand orientations around the surface of NCs would demand additional in-depth modelling and methodical kinetic studies, which

control both the nucleation and crystallization processes during the formation of 2D layered materials.

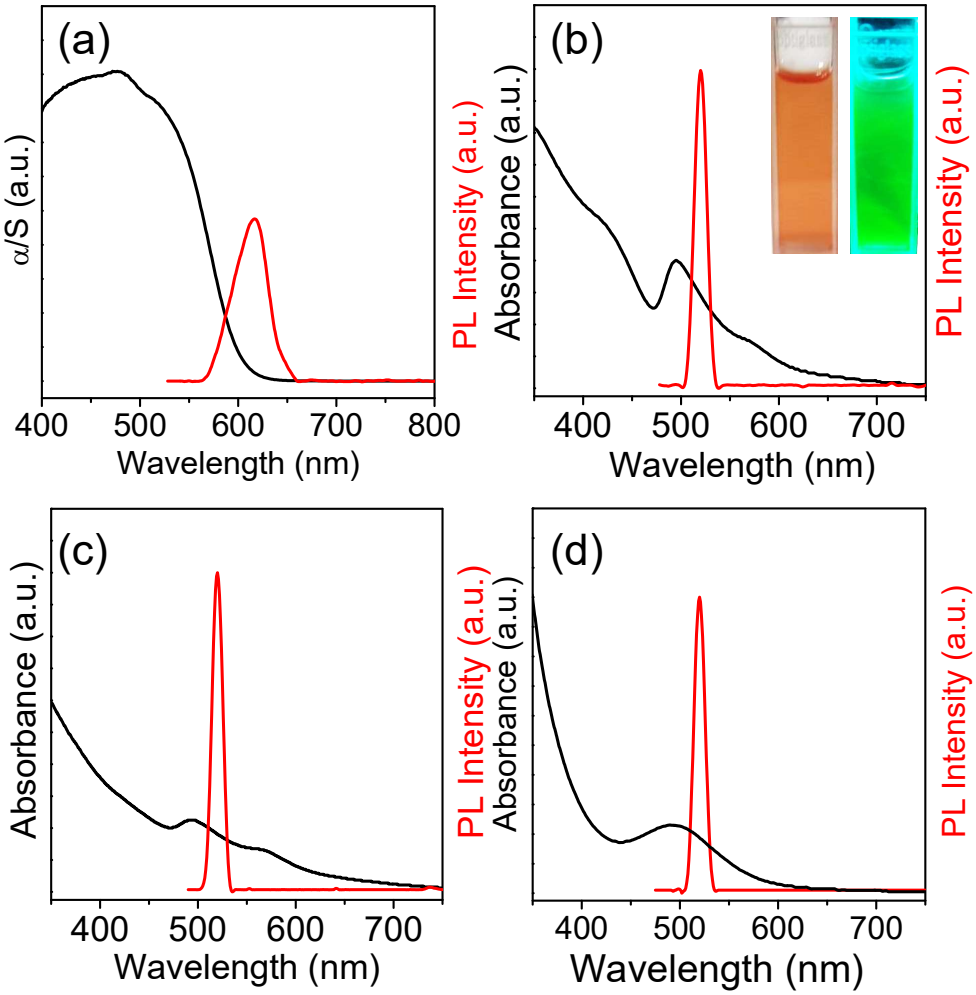

Figure 3.1.7. *Solid-state electronic absorption (α/S) (black) and PL (red) spectra of (a) $Cs_3Bi_2I_6Cl_3$ bulk powders. UV/Vis absorption (black) and PL (red) spectra of (b) $Cs_3Bi_2I_6Cl_3$ NCs, (c) $Cs_3Bi_2I_6Cl_3$ NCs-NSs and (c) $Cs_3Bi_2I_6Cl_3$ NSs measured in solution phase. Inset in (b) the photograph of solution in absence (left) and presence (right) of UV light.*

The optical properties of bulk crystalline ingot of $Cs_3Bi_2I_6Cl_3$ were investigated in the solid state initially and subsequently, compared with the solution phase optical properties of $Cs_3Bi_2I_6Cl_3$ NCs or NSs that dispersed in toluene (Figures 3.1.7a-d). Electronic absorption spectroscopy of the bulk $Cs_3Bi_2I_6Cl_3$ showed an optical absorption edge at 607

nm (2.04 eV), which is comparable to previously reported band gap value for the $Cs_3Bi_2I_6Cl_3$ single crystal. Photoluminescence (PL) measurement reveals a broad emission band of bulk $Cs_3Bi_2I_6Cl_3$ at 615 nm (2.02 eV) in the solid state at the excitation wavelength of 485 nm. The excitonic peaks of all $Cs_3Bi_2I_6Cl_3$ nanostructured samples were appeared at ~ 496 nm (2.50 eV), whereas the emission band emerged at 520 nm (2.38 eV), when excited at 450 nm in the solution phase. The narrow full width at the half maximum (FWHM) of the PL found to be ~13 nm along with the small Stokes shift (0.12 eV), which indicate that the PL emission of $Cs_3Bi_2I_6Cl_3$ samples emerges from the bound excitonic recombination.[36] The narrower and blue-shifted band-edge emission of $Cs_3Bi_2I_6Cl_3$ NCs compared to their bulk counterparts also demonstrate the quantum confinement effect and the superior PL properties of NCs.[22, 36] Further, the sharp emission appeared for all $Cs_3Bi_2I_6Cl_3$ nanostructured samples in comparison to the broad emission peak of reported $Cs_3Bi_2I_9$ nanostructures,[30] which may be due to the 2D structure and the presence of minimal defects or trap states. This observation signifies the passivation effect of the bridged Cl in the 2D analogue, which was not present in the case of 0D molecular $Cs_3Bi_2I_9$.[24, 37]

In order to gain more insight into the excitonic recombination dynamics of 2D $Cs_3Bi_2I_6Cl_3$ nanostructures, time-resolved PL measurements were performed by using time-correlated single photon counting (TCSPC) technique. The PL decays of synthesized $Cs_3Bi_2I_6Cl_3$ nanostructures were fitted by tri-exponential function,[38-40] which are shown in Figure 3.1.8a. The tri-exponential PL decay curves can be represented according to the following equation:[41, 42]

$$A(t) = A_1 \exp\left(-t/\tau_1\right) + A_2 \exp\left(-t/\tau_2\right) + A_3 \exp\left(-t/\tau_3\right) \qquad (1)$$

where, A is the intensity of the emission at given time t. A_1, A_2, A_3 are fitting parameters (i.e., relative amplitude for the different life-time component), and τ_1, τ_2, and τ_3 represent various lifetime component. In addition, the average life-time (τ_{avg}) can be obtained using following equation;[41]

$$\tau_{avg} = {A_1\tau_1^2 + A_2\tau_2^2 + A_3\tau_3^2}\Big/{A_1\tau_1 + A_2\tau_2 + A_3\tau_3} \quad (2)$$

The measured life-time components along with the average life-time (τ_{avg}) values of 2D $Cs_3Bi_2I_6Cl_3$ NCs and NSs at 298 K were provided in Table 3.1.1 and found to be in the comparable range to those of colloidal $Cs_3Sb_2Br_9$, $MA_3Bi_2X_9$ quantum dots (QDs) and $Cs_3Bi_2X_9$ NCs.[42-46] The multi-exponential PL decay for the nanostructured samples indicates towards the radiative (excitonic) and other non-radiative recombination.[47, 48] However, the minor variations between the lifetime components imply temporal fluctuations (e.g. blinking) in the emission of NCs and NSs.

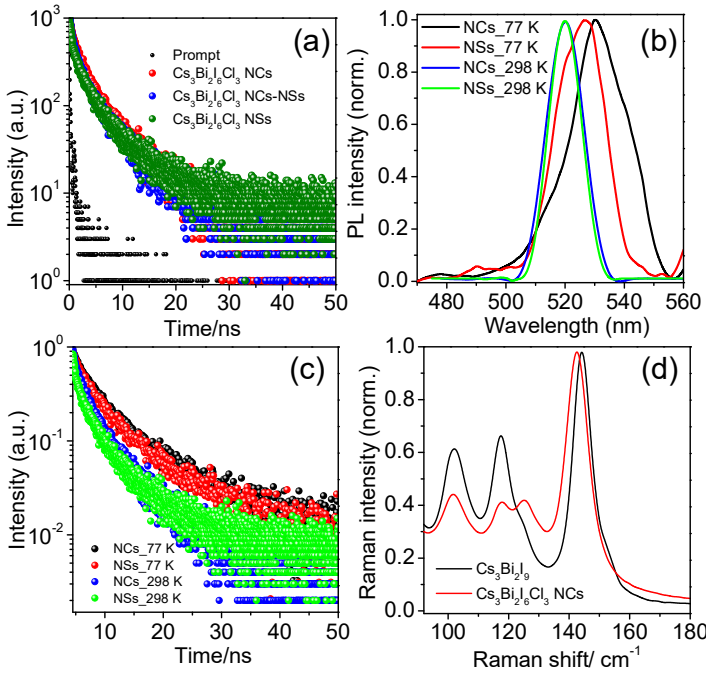

Figure 3.1.8. *(a) Time-resolved photoluminescence (PL) decay curves of $Cs_3Bi_2I_6Cl_3$ NCs, NCs-NSs, and NSs. (b) Comparative PL spectra and (c) time-resolved decay curves of $Cs_3Bi_2I_6Cl_3$ NCs and NSs at two different temperatures (298 and 77 K); and (d) Raman spectra of layered $Cs_3Bi_2I_6Cl_3$ NCs along with the molecular $Cs_3Bi_2I_9$ NCs for comparison under 785 nm laser excitation.*

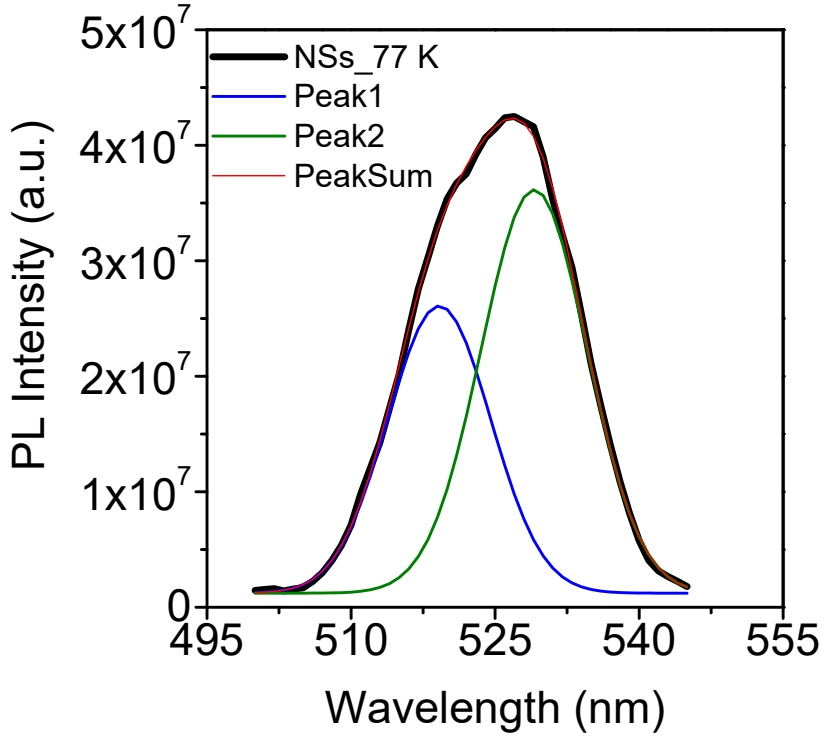

Figure 3.1.9. *Deconvoluted PL spectra of 2D nanosheets (NSs) of $Cs_3Bi_2I_6Cl_3$ at 77 K.*

With the aim of further exploring the mechanism of charge-carrier dynamics in $Cs_3Bi_2I_6Cl_3$ nanostructures, the low-temperature PL studies were carried out at 77 K. The slight red-shifted PL peak (~530 nm) with asymmetric broad feature (Figure 3.1.8b) in both NCs and NSs at 77 K compared to the room temperature PL spectra can be attributed to the activation of shallow trap states at low temperature, which has energy levels close to the band-edge.[49-51] The PL emission broadening at 77 K comprises of multipeak emissions with slight differences in energies (Figure 3.1.9). Interestingly, Kanatzidis and co-workers observed a single broad PL peak for $Cs_3Bi_2I_6Cl_3$ single crystals at 13 K, which was completely quenched at around 80 K.[29] The changes of life-time are fairly mild (Table 3.1.1) between 77 K and room temperature, which indicate again the fluctuation of emission events and existence of shallow trap states.

Table 3.1.1. *Fitted lifetime values using a tri-exponential decay with the relative amplitude of each component and average lifetime of $Cs_3Bi_2I_6Cl_3$ at 298 and 77 K.*

System	τ_1/ns	τ_2/ns	τ_3/ns	A_1	A_2	A_3	τ_{avg}/ns
$Cs_3Bi_2I_6Cl_3$ NCs_298 K	0.512	2.57	7.83	0.16	0.49	0.35	6.055
$Cs_3Bi_2I_6Cl_3$ NCs-NSs_298 K	0.601	2.93	9.17	0.25	0.51	0.24	6.455
$Cs_3Bi_2I_6Cl_3$ NSs _298 K	0.549	2.75	8.76	0.24	0.45	0.31	6.693
$Cs_3Bi_2I_6Cl_3$ NCs_77 K	0.641	2.91	9.37	0.02	0.35	0.63	8.389
$Cs_3Bi_2I_6Cl_3$ NSs_77 K	0.781	3.21	10.08	0.06	0.41	0.53	8.718

Furthermore, the temperature-dependent PL spectra of $Cs_3Bi_2I_6Cl_3$ NCs was investigated by analyzing the PL intensity at the temperature range of 25-85 °C under 450 nm excitation. The diminution of PL intensity with increasing temperature, as evidenced from Figure 3.1.10a, could be due to the thermally activated non-radiative recombination process.[46] This thermally induced PL quenching phenomena can be accomplished by the following equation;[45, 46]

$$I_T = \frac{I_0}{1+A.\exp\left(\frac{-E_B}{k_BT}\right)} \qquad (3)$$

where, I_0, I_T, A and k_B are the PL intensities at initial and variable temperatures, the pre-exponential coefficient and Boltzmann constant, respectively. E_B signifies the exciton binding energy for excitons to obliterate by the non-radiative trap states, in which the larger value is favourable for excitonic stabilization and for proficient PL. The value E_B of $Cs_3Bi_2I_6Cl_3$ NCs is estimated to be 69.90 meV from the linear plot of $ln\ (I_0/I_T - 1)$ and $1/k_BT$ (Figure 3.1.10b), which is comparable with the earlier reported $MA_3Bi_2I_9$ (MA = methylammonium),[52] but larger than that of the 3D $CsPbX_3$ NCs (~15-50 meV).[53, 54] The E_B value of ~70 meV is found to be higher than that of thermal ionization energy (~26 meV), which confirmed the existence of excitons well above the room temperature, and

further emphasized the prospective use of this material in exciton-associated optoelectronic devices.[46, 55]

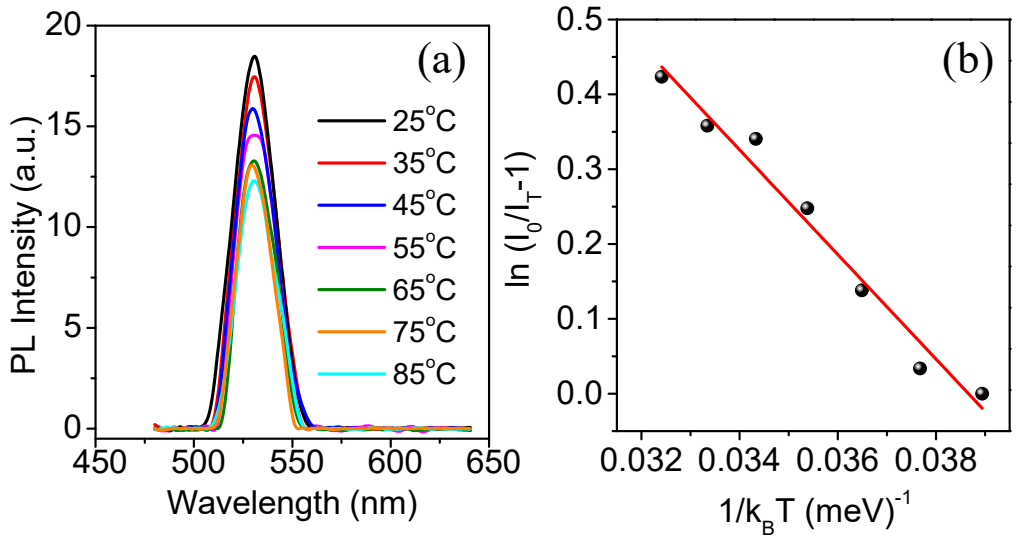

***Figure 3.1.10**. (a) Temperature dependent PL spectra of $Cs_3Bi_2I_6Cl_3$ NCs measured in solution phase. (b) The Arrhenius-type plot for the PL intensity variation of NCs with temperature.*

In order to identify the distinctive vibrational signatures of the mixed halide 2D layered $Cs_3Bi_2I_6Cl_3$ from 0D molecular $Cs_3Bi_2I_9$ structures, the Raman spectroscopic measurements were carried out using 785 nm laser excitation within the wavenumber range of 110-180 cm^{-1} (see Figure 3.1.8d). The principal vibrations in $Cs_3Bi_2I_9$ appear from the strongly bound $[Bi_2I_9]^{3-}$ unit. The stretching Bi-I vibrational signatures are mainly related to the three bridging and six terminal I atoms connected to the two Bi atoms together, which are the key modes in the Raman spectra. The peaks at 144 and 117 cm^{-1} in $Cs_3Bi_2I_9$ are designated to the symmetric terminal Bi-I stretch $A_1'(\nu_1)$ and its antisymmetric fragment $E'(\nu_{10})$, respectively. All the vibrational signatures of parent $Cs_3Bi_2I_9$ are in good agreement with the reported literature by Kanatzidis and co-workers.[56] Moreover, the Raman modes obtained for the 2D $Cs_3Bi_2I_6Cl_3$ NCs are shown in Figure 3.1.8d, which consist of similar vibrational signatures from the parent compound apart from the significant splitting of the antisymmetric terminal Bi-I stretch.

Splitting of the vibrational modes can be anticipated due to the local distortions mainly by the occupation of the different halides (herein, I^- and Cl^-) at the octahedral corners of mixed halide $Cs_3Bi_2I_6Cl_3$. Further, lowering of the crystal symmetry of $Cs_3Bi_2I_6Cl_3$ NCs from $Cs_3Bi_2I_9$ is also believed to be responsible for the mode splitting characteristics of low-energy modes in $Cs_3Bi_2I_6Cl_3$.[57, 58] Interestingly, the characteristic terminal Bi-I stretch at the higher energy side is significantly red-shifted for $Cs_3Bi_2I_6Cl_3$ compared to $Cs_3Bi_2I_9$ NCs, which can be correlated with the polarizability of halides that control the interaction of Cs^+ with the surrounding Bi-X cage.[59, 60] Also, the terminal Bi-I mode of $Cs_3Bi_2I_6Cl_3$ has the common signature of reduced Raman intensity for the layered compounds compared to the modes of $Cs_3Bi_2I_9$,[56] which further correspond to the loss of polarization on this specific mode due to the mixing of halides.[61]

Finally, to acquire a deeper understanding into the nature of emitting states of $Cs_3Bi_2I_6Cl_3$ nanostructures, we examined the PL in single-particle level by employing super-resolution fluorescence microscopy. The temporal fluctuations of PL intensity can be termed as "blinking" or "flickering" in NCs.[62] However, such events were only explored recently in a vast array of samples, for example in conventional 3D perovskite NCs and micrometer-sized crystals of $CsPbBr_3$, $MAPbBr_3$ and $MAPbI_3$ and 2D nanoplates of $Cs_3Bi_2I_9$.[30, 62-69] In this context, our objective was to gain a mechanistic view on the non-radiative processes in 2D layered perovskite nanostructures as a model system with varied morphology (NSs and NCs), which has not been investigated in the past. Particularly, we studied PL blinking by monitoring the characteristics of distinct quenchers in 2D NSs and small NCs. In this chapter, we tried to offer a widespread view of charge-carrier dynamics in a single $Cs_3Bi_2I_6Cl_3$ NC and NS by considering all probable recombination pathways (for example, radiative as well as non-radiative).

Figure 3.1.11a exhibits a distribution of NCs from the bright-field optical image. The PL emission with high signal-to-noise ratio for NCs can be identified from the fluorescence images. The optical responses of $Cs_3Bi_2I_6Cl_3$ NCs were examined using Structured Illumination Microscopy (SIM) based fluorescence imaging (Figure 3.1.11b). Single-molecule localization microscopy was performed on $Cs_3Bi_2I_6Cl_3$ NCs using 488 nm laser excitation, where emission was collected using a band pass filter that transmit emission between 495-575 nm optical window. Under the total internal reflection

fluorescence (TIRF) illumination mode the NCs were imaged with an integration time of 40 *ms*, where a temporal fluctuation in photoluminescence emission was evidenced from the NCs (Figure 3.1.11c).

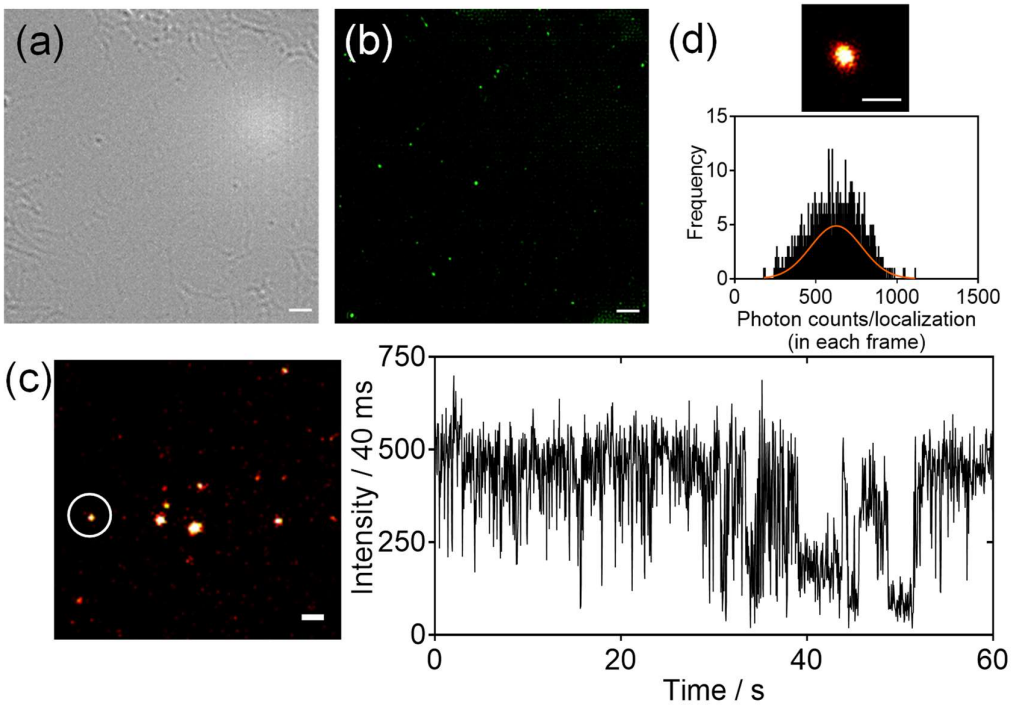

Figure 3.1.11. *Optical microscopy images and blinking behaviour of $Cs_3Bi_2I_6Cl_3$ NCs (a) bright-field image. (b) Fluorescence microscopy image using SIM method shows NCs are fluorescent in nature. (c) (left) Time dependent fluorescence trace analysis shows blinking nature of NC. (right) The time trace was generated from the NC that is circled in the diffraction-limited image. (d) (Upper panel) super resolved image of NC that was reconstructed from localizing the blinking events. (Lower panel) photon counts calculated from the fluorescence blinking of NC with average photon counts for localized point in each frame is ~625. Scale bar 2.5 µm for (a, b), 1 µm for (c), 100 nm for (d).*

This is presumably a consequence of the trap states (e. g. shallow trap) in nanostructured materials.[67, 68] The blinking events of each $Cs_3Bi_2I_6Cl_3$ NCs were recorded for few minutes under continuous illumination. It was evident that each crystal repeatedly undergoes dynamical fluctuations in PL emission, which indicates high photostability of

the NCs. Notably, time trace of individual NC shows that rather than a completely non-emissive or dark state, the NC exhibit a "dim" off state. The blinking pattern of this nature is previously reported for $CsPbBr_3$ NCs.[62, 65, 66, 69] The emission intensities corresponding to the many of these "dim" off states are slightly above the background intensity level. The non-zero off states can be attributed to a fact where the time duration of completely non-emissive off state is much shorter than our experimental integration time and do not exceed more than a few milliseconds. Based on the PL blinking of the NCs, we applied a localization microscopy-based method to reconstruct a super-resolution image of the NC. In this strategy, the emission profile of the emitting object in each frame was fitted to a 2D Gaussian function to determine the precise location of the emitter. The magnified view of a super-resolved NC is represented in the inset of Figure 3.1.11d, from which spatial distribution of the NC emission can be viewed. We collected an average of ~625 photons from each localized point in each frame (Figure 3.1.11d), which accounted for the localization accuracy of ~22 nm (Figure 3.1.12) for the NC. Figure 3.1.13 also illustrates photon counts of a number of $Cs_3Bi_2I_6Cl_3$ NCs.

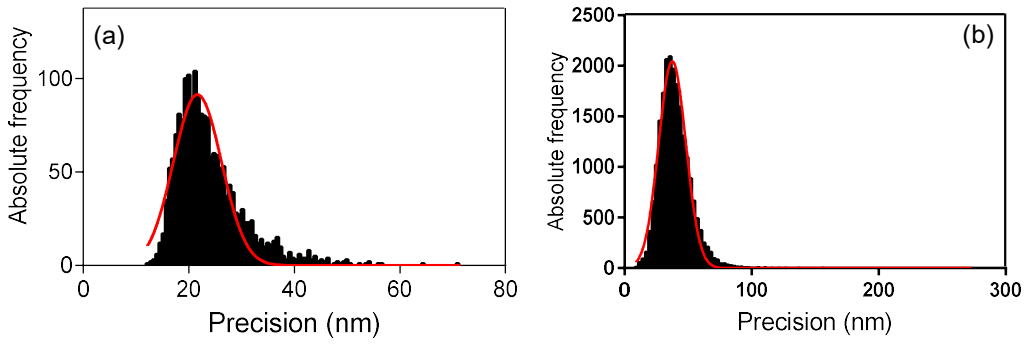

Figure 3.1.12. *Localization precision from Gaussian fitting of the blinking events of the $Cs_3Bi_2I_6Cl_3$ (a) NCs and (b) NSs.*

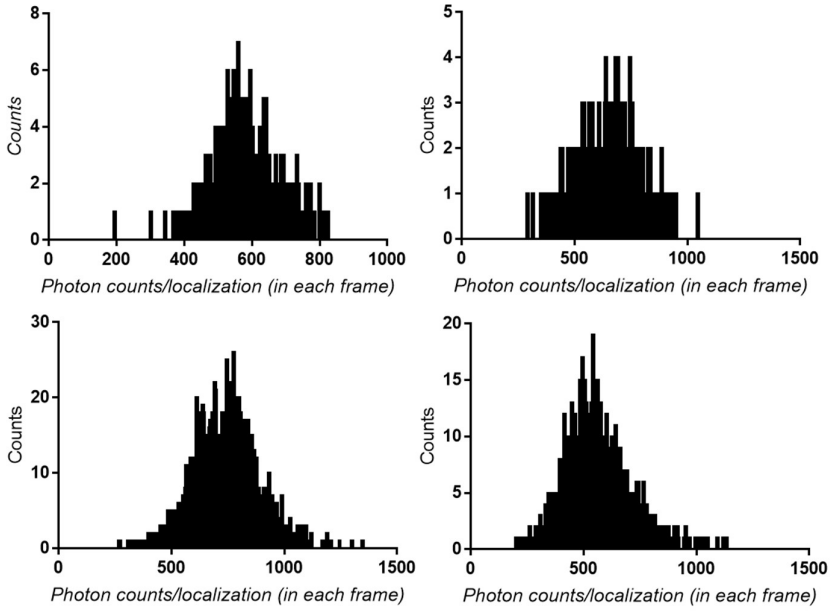

Figure 3.1.13. *Photon counts for several $Cs_3Bi_2I_6Cl_3$ NCs.*

Similarly, we have studied PL blinking properties of $Cs_3Bi_2I_6Cl_3$ NSs. The fluorescence image from SIM showed that there is a large spatial variation of emission intensities within a single NS (Figures 3.1.14a and b). Interestingly, we also found that the local emissive nanodomains within the perovskite NS undergo dynamical fluctuations in emission between multiple intensity levels. where the irregular oscillation in emission intensity occurs on top of some basal emission level. Figure 3.1.14c shows the temporal snapshot of a NS over the continuous imaging time, whereas Figure 3.1.14d shows representative emission intensity traces from two nanodomains within the same NS. Notably, the nature of photoluminescence fluctuation does not allow us to define a clear on, and off-state for the emissive domains as the intensity fluctuations do not follow a typical two-step process with a sharp transition between a distinct on and off state. Similar nature of PL fluctuation in perovskite microcrystals has been observed in a few recent studies, but a clear understanding of their origin is still under investigation.[64, 70-72] There are few possible explanations to this fact: (1) as discussed in the case of NCs, the time duration of completely not-emissive off state could be much shorter than our experimental

integration time. (2) There could be the presence of multiple emissive sites (nanoscopic domains) within the single NS undergoing simultaneous fluorescence fluctuation.

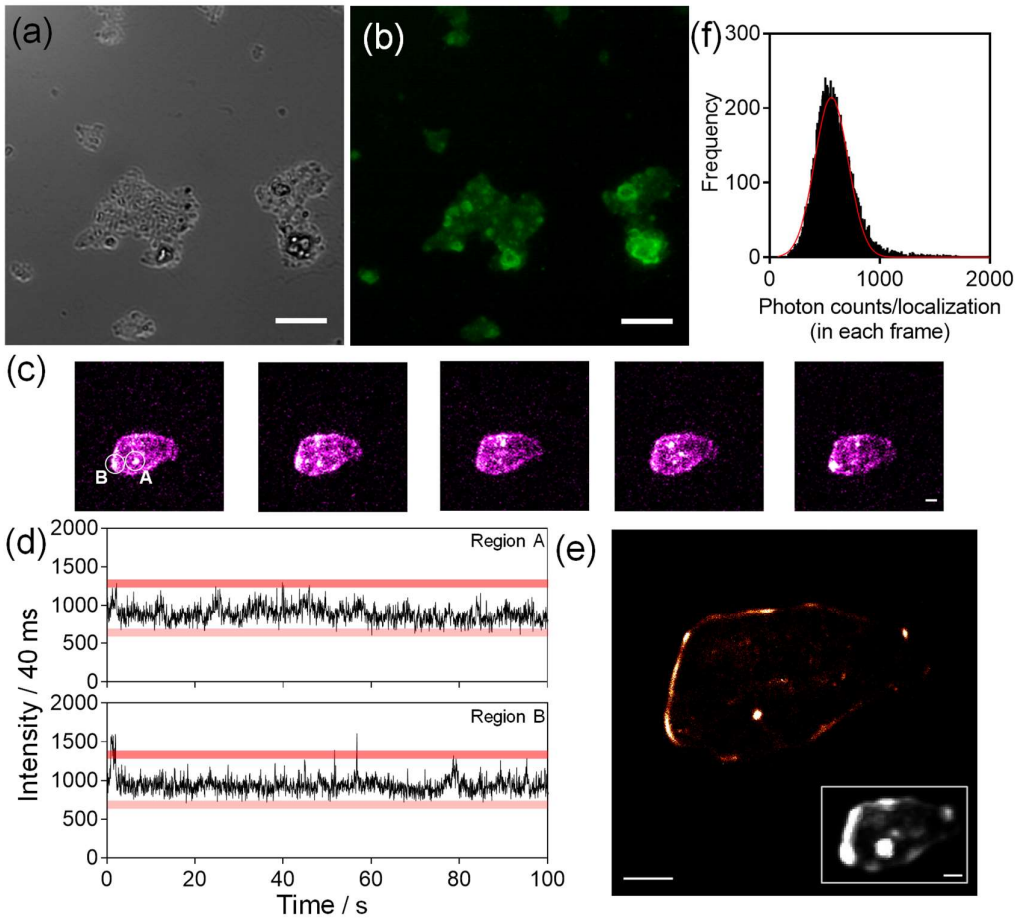

Figure 3.1.14. *Fluorescence microscopy images and blinking behaviour of $Cs_3Bi_2I_6Cl_3$ NSs (a) bright-field image, (b) fluorescence microscopy image (SIM) shows NSs are fluorescent in nature, (c) Temporal snapshots of PL image of a NS over imaging time. d) Time dependent fluorescence trace analysis shows the blinking nature of NS. (e) Super resolved images of NSs that were reconstructed from localizing the blinking events showed localized blinking domains from a single NS. The inset shows the corresponding diffraction-limited image. (f) Photon counts calculated from the fluorescence blinking of NS with average photon counts for localized point in each frame is ~560. The scale bar is 500 nm (a, b); and 1 μm for (c, e).*

These nanoscale domains are difficult to separate as they are smaller than the achievable resolution from the imaging method. Similar to the case of NCs, we applied localization microscopy-based method to reconstruct a super-resolution image of the NS. The magnified view of a super-resolved NS is represented in Figure 3.1.14e, from which spatial distribution of the cluster of the emission sites can be viewed. An average of ~560 photons was collected from each localized point in each frame for the NS (Figure 3.1.14f), that also considered for the localization accuracy of ~ 38 nm (Figure 3.1.12b).

3.1.4. Conclusions

Nanosheets (NSs) and nanocrystals (NCs) of 2D layered all-inorganic mixed halide, $Cs_3Bi_2I_6Cl_3$ were successfully synthesized by hot-injection approach at three different reaction temperatures. Unlike molecular structure of $Cs_3Bi_2I_9$, the presence of bridging Cl atom in $[Bi_2X_9]^{3-}$ of $Cs_3Bi_2I_6Cl_3$ leads to the layered structure. Interestingly, the formation of NCs was evidenced at lower reaction temperature (120 ^oC), whereas the higher temperature (180 ^oC) favoured the formation of 2D NSs. Optical properties studies showed a narrow and blue-shifted band-edge emissions with small Stokes shift for the 2D NSs or NCs compared to that of the bulk form, implying a quantum confined system with bound excitonic recombination. Furthermore, the time-resolved PL analysis indicated the minor variations between the lifetime components, which imply temporal fluctuations in the emission of NCs and NSs. Low-temperature PL study revealed slight red-shifted and broadened PL emission for both the NCs and NSs compared to that in room-temperature, which indicated the activation of shallow trap states at 77 K. Finally, the time-dependent PL imaging studies provided a comprehensive picture of the charge-carrier recombination dynamics in NCs and NSs, which revealed a discrete dynamical fluctuation of emission (i.e. blinking) in nanodomains from these nanostructures.

3.1.5. References

1. J. Song, L. Xu, J. Li, J. Xue, Y. Dong, X. Li and H. Zeng, *Adv. Mater.*, 2016, **28**, 4861.

2. X. Lv, W. Wei, C. Mu, B. Huang and Y. Dai, *J. Mater. Chem. A*, 2018, **6**, 5032.

3. Y. Zhao and K. Zhu, *Chem. Soc. Rev.*, 2016, **45**, 655.

4. M. Pandey, K. W. Jacobsen and K. S. Thygesen, *J. Phys. Chem. Lett.*, 2016, **7**, 4346.

5. A. Swarnkar, A. R. Marshall, E. M. Sanehira, B. D. Chernomordik, D. T. Moore, J. A. Christians, T. Chakrabarti and J. M. Luther, *Science*, 2016, **354**, 92.

6. R. J. Sutton, G. E. Eperon, L. Miranda, E. S. Parrott, B. A. Kamino, J. B. Patel, M. T. Hörantner, M. B. Johnston, A. A. Haghighirad and D. T. Moore, *Adv. Energy Mater.*, 2016, **6**, 1502458.

7. J. Hu, L. Yan and W. You, *Adv. Mater.*, 2018, **30**, 1802041.

8. F. Hao, C. C. Stoumpos, D. H. Cao, R. P. H. Chang and M. G. Kanatzidis, *Nat. Photonics*, 2014, **8**, 489.

9. C. C. Stoumpos, L. Frazer, D. J. Clark, Y. S. Kim, S. H. Rhim, A. J. Freeman, J. B. Ketterson, J. I. Jang and M. G. Kanatzidis, *J. Am. Chem. Soc.*, 2015, **137**, 6804.

10. A. Kumar, K. R. Balasubramaniam, J. Kangsabanik and A. Alam, *Phys. Rev. B*, 2016, **94**, 180105.

11. T. J. Jacobsson, M. Pazoki, A. Hagfeldt and T. Edvinsson, *J. Phys. Chem. C*, 2015, **119**, 25673.

12. W. Ke and M. G. Kanatzidis, *Nat. Commun.*, 2019, **10**, 965.

13. F. Jiang, D. Yang, Y. Jiang, T. Liu, X. Zhao, Y. Ming, B. Luo, F. Qin, J. Fan and H. Han, *J. Am. Chem. Soc.*, 2018, **140**, 1019.

14. A. J. Lehner, D. H. Fabini, H. A. Evans, C.-A. Hébert, S. R. Smock, J. Hu, H. Wang, J. W. Zwanziger, M. L. Chabinyc and R. Seshadri, *Chem. Mater.*, 2015, **27**, 7137.

15. J.-C. Hebig, I. Kuhn, J. Flohre and T. Kirchartz, *ACS Energy Lett.*, 2016, **1**, 309.

16. B. Saparov, F. Hong, J.-P. Sun, H.-S. Duan, W. Meng, S. Cameron, I. G. Hill, Y. Yan and D. B. Mitzi, *Chem. Mater.*, 2015, **27**, 5622.

17. Q. Fan, G. V. Biesold-McGee, J. Ma, Q. Xu, S. Pan, J. Peng and Z. Lin, *Angew. Chem., Int. Ed.*, 2020, **59**, 1030.

18. L. Mao, C. C. Stoumpos and M. G. Kanatzidis, *J. Am. Chem. Soc.*, 2018, **141**, 1171.

19. M. D. Smith, E. J. Crace, A. Jaffe and H. I. Karunadasa, *Annu. Rev. Mater. Res.*, 2018, **48**, 111.

20. Q. A. Akkerman, E. Bladt, U. Petralanda, Z. Dang, E. Sartori, D. Baranov, A. L. Abdelhady, I. Infante, S. Bals and L. Manna, *Chem. Mater.*, 2019, **31**, 2182.

21. A. Dutta, R. K. Behera, S. Deb, S. Baitalik and N. Pradhan, *J. Phys. Chem. Lett.*, 2019, **10**, 1954.

22. J. Pal, S. Manna, A. Mondal, S. Das, K. V. Adarsh and A. Nag, *Angew. Chem., Int. Ed.*, 2017, **56**, 14187.

23. X. Meng, Z. Wang, W. Qian, Z. Zhu, T. Zhang, Y. Bai, C. Hu, S. Xiao, Y. Yang and S. Yang, *J. Phys. Chem. Lett.*, 2019, **10**, 194.

24. G. Paul and A. J. Pal, *J. Phys. Chem. C*, 2019, **123**, 13500.

25. S. Dastidar, D. A. Egger, L. Z. Tan, S. B. Cromer, A. D. Dillon, S. Liu, L. Kronik, A. M. Rappe and A. T. Fafarman, *Nano Lett.*, 2016, **16**, 3563.

26. S. Colella, E. Mosconi, P. Fedeli, A. Listorti, F. Gazza, F. Orlandi, P. Ferro, T. Besagni, A. Rizzo and G. Calestani, *Chem. Mater.*, 2013, **25**, 4613.

27. P. McMeekin David, G. Sadoughi, W. Rehman, E. Eperon Giles, M. Saliba, T. Hörantner Maximilian, A. Haghighirad, N. Sakai, L. Korte, B. Rech, B. Johnston Michael, M. Herz Laura and J. Snaith Henry, *Science*, 2016, **351**, 151.

28. J. Li, C. C. Stoumpos, G. G. Trimarchi, I. Chung, L. Mao, M. Chen, M. R. Wasielewski, L. Wang and M. G. Kanatzidis, *Chem. Mater.*, 2018, **30**, 4847.

29. K. M. McCall, C. C. Stoumpos, O. Y. Kontsevoi, G. C. B. Alexander, B. W. Wessels and M. G. Kanatzidis, *Chem. Mater.*, 2019, **31**, 2644.

30. A. Sarkar, P. Acharyya, R. Sasmal, P. Pal, S. S. Agasti and K. Biswas, *Inorg. Chem.*, 2018, **57**, 15558.

31. H. Yang, Y. Zhang, J. Pan, J. Yin, O. M. Bakr and O. F. Mohammed, *Chem. Mater.*, 2017, **29**, 8978.

32. T. Togashi, M. Nakayama, A. Hashimoto, M. Ishizaki, K. Kanaizuka and M. Kurihara, *Dalton Trans.*, 2018, **47**, 5342.

33. K. Wang, Z. Jin, L. Liang, H. Bian, D. Bai, H. Wang, J. Zhang, Q. Wang and S. Liu, *Nat. Commun.*, 2018, **9**, 4544.

34. A. Pan, B. He, X. Fan, Z. Liu, J. J. Urban, A. P. Alivisatos, L. He and Y. Liu, *ACS Nano*, 2016, **10**, 7943.

35. L. Peng, A. Dutta, R. Xie, W. Yang and N. Pradhan, *ACS Energy Lett.*, 2018, **3**, 2014.

36. Z. Liang, S. Zhao, Z. Xu, B. Qiao, P. Song, D. Gao and X. Xu, *ACS Appl. Mater. Interfaces*, 2016, **8**, 28824.

37. W.-J. Yin, H. Chen, T. Shi, S.-H. Wei and Y. Yan, *Adv. Electron. Mater.*, 2015, **1**, 1500044.

38. F. Meng, X. Liu, X. Cai, Z. Gong, B. Li, W. Xie, M. Li, D. Chen, H.-L. Yip and S.-J. Su, *Nanoscale*, 2019, **11**, 1295.

39. J.-L. Xie, Z.-Q. Huang, B. Wang, W.-J. Chen, W.-X. Lu, X. Liu and J.-L. Song, *Nanoscale*, 2019, **11**, 6719.

40. B. Yang, J. Chen, S. Yang, F. Hong, L. Sun, P. Han, T. Pullerits, W. Deng and K. Han, *Angew. Chem., Int. Ed.*, 2018, **57**, 5359.

41. S. Sun, D. Yuan, Y. Xu, A. Wang and Z. Deng, *ACS Nano*, 2016, **10**, 3648.

42. B. Yang, J. Chen, F. Hong, X. Mao, K. Zheng, S. Yang, Y. Li, T. Pullerits, W. Deng and K. Han, *Angew. Chem., Int. Ed.*, 2017, **56**, 12471.

43. M. Leng, Z. Chen, Y. Yang, Z. Li, K. Zeng, K. Li, G. Niu, Y. He, Q. Zhou and J. Tang, *Angew. Chem., Int. Ed.*, 2016, **55**, 15012.

44. M. Leng, Y. Yang, K. Zeng, Z. Chen, Z. Tan, S. Li, J. Li, B. Xu, D. Li and M. P. Hautzinger, *Adv. Funct. Mater.*, 2018, **28**, 1704446.

45. M. Leng, Y. Yang, Z. Chen, W. Gao, J. Zhang, G. Niu, D. Li, H. Song, J. Zhang and S. Jin, *Nano Lett.*, 2018, **18**, 6076.

46. J. Zhang, Y. Yang, H. Deng, U. Farooq, X. Yang, J. Khan, J. Tang and H. Song, *ACS Nano*, 2017, **11**, 9294.

47. B. R. C. Vale, E. Socie, A. s. Burgos-Caminal, J. Bettini, M. A. Schiavon and J.-E. Moser, *J. Phys. Chem. Lett.*, 2019, **11**, 387.

48. G. Ghosh, B. Jana, S. Sain, A. Ghosh and A. Patra, *Phys. Chem. Chem. Phys.*, 2019, **21**, 19318.

49. F. Zhao, J. Li, X. Gao, X. Qiu, X. Lin, T. He and R. Chen, *J. Phys. Chem. C*, 2019, **123**, 9538.

50. A. A. Lohar, A. Shinde, R. Gahlaut, A. Sagdeo and S. Mahamuni, *J. Phys. Chem. C*, 2018, **122**, 25014.

51. A. Baumann, S. Väth, P. Rieder, M. C. Heiber, K. Tvingstedt and V. Dyakonov, *J. Phys. Chem. Lett.*, 2015, **6**, 2350.

52. B. W. Park, B. Philippe, X. Zhang, H. Rensmo, G. Boschloo and E. M. J. Johansson, *Adv. Mater.*, 2015, **27**, 6806.

53. W. Lv, X. Tang, L. Li, L. Xu, M. Li, R. Chen and W. Huang, *J. Phys. Chem. C*, 2019, **123**, 24313.

54. S. M. Lee, C. J. Moon, H. Lim, Y. Lee, M. Y. Choi and J. Bang, *J. Phys. Chem. C*, 2017, **121**, 26054.

55. B. R. Sutherland and E. H. Sargent, *Nat. Photonics*, 2016, **10**, 295.

56. K. M. McCall, C. C. Stoumpos, S. S. Kostina, M. G. Kanatzidis and B. W. Wessels, *Chem. Mater.*, 2017, **29**, 4129.

57. M. R. Benzigar, S. Joseph, A. V. Baskar, D. H. Park, G. Chandra, S. Umapathy, S. N. Talapaneni and A. Vinu, *Adv. Funct. Mater.*, 2018, **28**, 1803701.

58. R. G. Niemann, A. G. Kontos, D. Palles, E. I. Kamitsos, A. Kaltzoglou, F. Brivio, P. Falaras and P. J. Cameron, *J. Phys. Chem. C*, 2016, **120**, 2509.

59. T. Glaser, C. Müller, M. Sendner, C. Krekeler, O. E. Semonin, T. D. Hull, O. Yaffe, J. S. Owen, W. Kowalsky and A. Pucci, *J. Phys. Chem. Lett.*, 2015, **6**, 2913.

60. M. Ledinský, P. Löper, B. Niesen, J. Holovský, S.-J. Moon, J.-H. Yum, S. De Wolf, A. Fejfar and C. Ballif, *J. Phys. Chem. Lett.*, 2015, **6**, 401.

61. B.-W. Park, S. M. Jain, X. Zhang, A. Hagfeldt, G. Boschloo and T. Edvinsson, *ACS Nano*, 2015, **9**, 2088.

62. S. Seth, T. Ahmed and A. Samanta, *J. Phys. Chem. Lett.*, 2018, **9**, 7007.

63. M. Gerhard, B. Louis, R. Camacho, A. Merdasa, J. Li, A. Kiligaridis, A. Dobrovolsky, J. Hofkens and I. G. Scheblykin, *Nat. Commun.*, 2019, **10**, 1698.

64. N. Pathoor, A. Halder, A. Mukherjee, J. Mahato, S. K. Sarkar and A. Chowdhury, *Angew. Chem., Int. Ed.*, 2018, **57**, 11603.

65. T. Ahmed, S. Seth and A. Samanta, *ACS Nano*, 2019, **13**, 13537.

66. N. A. Gibson, B. A. Koscher, A. P. Alivisatos and S. R. Leone, *J. Phys. Chem. C*, 2018, **122**, 12106.

67. Y. Tian, A. Merdasa, M. Peter, M. Abdellah, K. Zheng, C. S. Ponseca Jr, T. n. Pullerits, A. Yartsev, V. Sundström and I. G. Scheblykin, *Nano Lett.*, 2015, **15**, 1603.

68. S. Seth, N. Mondal, S. Patra and A. Samanta, *J. Phys. Chem. Lett.*, 2016, **7**, 266.

69. A. Swarnkar, R. Chulliyil, V. K. Ravi, M. Irfanullah, A. Chowdhury and A. Nag, *Angew. Chem., Int. Ed.*, 2015, **54**, 15424.

70. Y. Tian, A. Merdasa, E. Unger, M. Abdellah, K. Zheng, S. McKibbin, A. Mikkelsen, T. Pullerits, A. Yartsev and V. Sundstrom, *J. Phys. Chem. Lett.*, 2015, **6**, 4171.

71. A. Halder, N. Pathoor, A. Chowdhury and S. K. Sarkar, *J. Phys. Chem. C*, 2018, **122**, 15133.

72. A. Halder, R. Chulliyil, A. S. Subbiah, T. Khan, S. Chattoraj, A. Chowdhury and S. K. Sarkar, *J. Phys. Chem. Lett.*, 2015, **6**, 3483.

Chapter 3.2

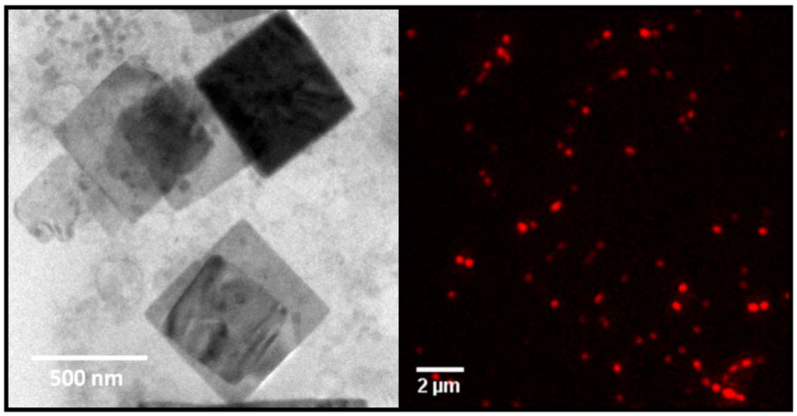

Synthesis of Ultrathin Few-Layer 2D Nanoplates of Halide Perovskite $Cs_3Bi_2I_9$ and Single-Nanoplate Super-Resolved Fluorescence Microscopy

Chapter 3.2

Synthesis of Ultrathin Few-Layer 2D Nanoplates of Halide Perovskite $Cs_3Bi_2I_9$ and Single-Nanoplate Super-Resolved Fluorescence Microscopy[†]

Summary

The discovery of new two-dimensional (2D) perovskite halides has created sensation recently because of their structural diversity and intriguing optical properties. The toxicity of Pb-based perovskite halides led to the development of Pb-free halides. In this chapter, we have demonstrated a one-pot solution-based synthesis of 2D ultrathin (~1.78 nm) few-layer (2–4 layers) nanoplates (300–600 nm lateral dimension), nanosheets (0.6–1.5 μm), and nanocrystals of layered $Cs_3Bi_2I_9$ by varying the reaction temperature from 110 to 180 °C. We have established a mechanistic pathway for the variation of morphology of $Cs_3Bi_2I_9$ with temperature in the presence of organic capping ligands. Further, we have synthesized the bulk powder of $Cs_3Bi_2I_9$ by mechanochemical synthesis and liquid-assisted grinding and crystalline ingot by vacuum-sealed tube melting. 2D nanoplates and bulk $Cs_3Bi_2I_9$ demonstrate optical absorption edge along with excitonic transition. Photoluminescence properties of individual nanoplates were studied by super-resolution fluorescence imaging, which indicated the blinking behavior down to the level of an individual $Cs_3Bi_2I_9$ nanoplate along with its emission at the far-red region and high photostability.

[†] A. Sarkar,[*] **P. Acharyya,**[*] R. Sasmal, P. Pal, S. S. Agasti, and K. Biswas. *Inorg. Chem.,* 2018, **57**, 15558–15565. (**contributed equally*)

3.2.1. Introduction

Metal halide perovskites have experienced extraordinary rapid progress and attained momentous attentions from the worldwide scientific societies owing to their prospective multifunctional applications in the field of photovoltaic and optoelectronic devices.[1] Despite the stimulating advancements, their commercialization still faces severe challenges attributable to the toxicity of lead (Pb) and instability under heat, moisture, and irradiation.[2, 3] Recently, substantial efforts have been devoted to expand this field towards environmentally benign Pb-free alternatives.[4-6] Sn and Ge have been tried as replacements for Pb in perovskite halides,[7, 8] but Sn-perovskites have been reported to possess self-doping effects and more unstable than its Pb-based counterparts,[7] while Ge being an expensive rare metal cannot be used for large scale practical applications. Further, the tendency of Sn^{2+} and Ge^{2+} to oxidize to their respective +4 states by losing the outermost ns^2 electrons affects the stability, transport properties, and carrier mobility of those specific perovskites.[9] Pb^{2+} in the $[MX_6]$ octahedra can also be replaced by stable trivalent and tetravalent cations by keeping the perovskite-type structure intact. Replacing three Pb^{2+} ions with two stable trivalent cations (Sb^{3+}/Bi^{3+}) would transform the 3D connectivity into a 2D layered network by aligning along a particular crystallographic direction.[6] However, the higher size of the monovalent cation at the A site causes every two $[MX_6]$ octahedra to form isolated face sharing bioctahedra, resulting in a 0D structure with the A-site cations occupying the interstitial spaces, which is observed in $Cs_3Bi_2I_9$ (Figure 3.2.1a).[6, 7] Such reduction in the dimensionality of a perovskite structure decreases the band dispersion and raises the effective masses of charge carriers.[10-12] $Cs_3Bi_2I_9$, a bismuth-based inorganic lead-free perovskite halide, is a well-known layered perovskite that has found immense interest for its optical and electronic properties.[13-25] The Bi^{3+} oxidation state being stable because of its inert lone pair effect leads to its long-term durability, potentially better transport properties, and carrier mobility. It is more stable and less toxic than many of its Pb-based counterparts. The layered $Cs_3Bi_2I_9$ perovskite in the form of nanostructures, bulk solid, and single crystals are generally synthesized by spin coating, chemical vapor deposition, Bridgman crystal growth, and others.[13-23] Nonetheless, any simple synthesis without any support or template as well as

the study of the optical properties of the freestanding few-layer ultrathin $Cs_3Bi_2I_9$ 2D nanoplates (NPLs) is still rare.

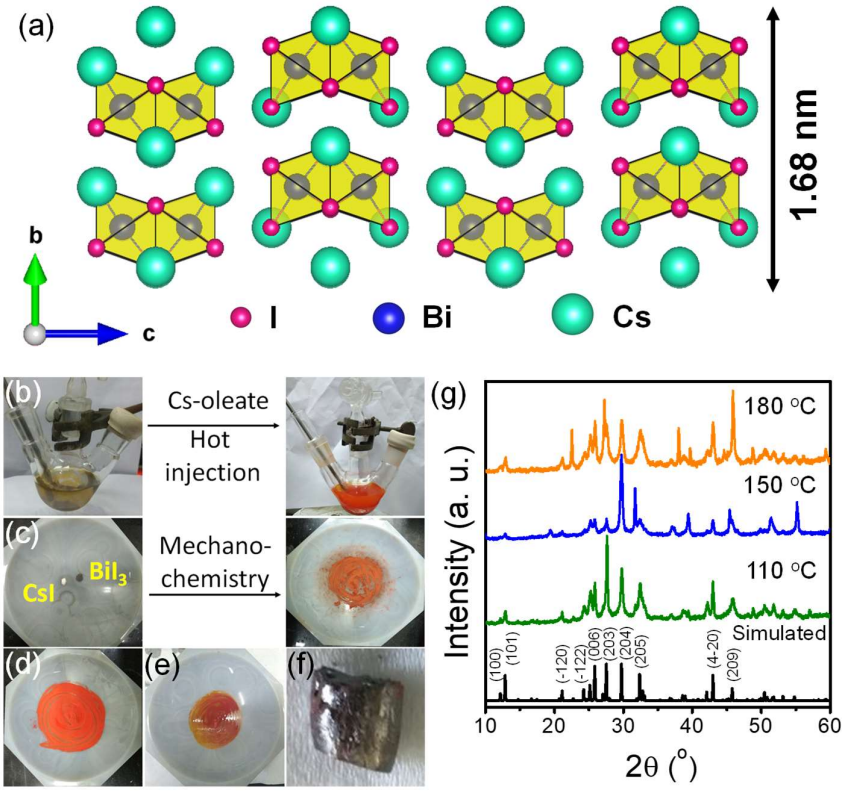

Figure 3.2.1. *(a) Crystal structures of $Cs_3Bi_2I_9$. (b) Photograph of hot injection synthesis of $Cs_3Bi_2I_9$, (c) solid-state mechanochemical synthesis of $Cs_3Bi_2I_9$ from BiI_3 and CsI. Photographs of $Cs_3Bi_2I_9$ synthesized by LAG with (d) ethanol and (e) NMP. (f) Picture of $Cs_3Bi_2I_9$ ingot synthesized by sealed-tube melting reaction. (g) PXRD patterns of $Cs_3Bi_2I_9$ obtained by hot injection at different temperatures*

In this chapter, we have demonstrated the low-temperature colloidal synthesis of free-standing ultrathin (~1.78 nm) few-layer (~2 layers) NPLs (300-600 nm lateral dimension) of $Cs_3Bi_2I_9$ without using any support or template with high yield and reproducibility and studied their optical properties. We have also synthesized nanosheets (NSs; 0.6-1.5 μm) and nanocrystals (NCs) of layered $Cs_3Bi_2I_9$ by varying the reaction temperature and provided intriguing chemical insight to the formation mechanism.

Further, bulk powder and crystalline ingot of $Cs_3Bi_2I_9$ have also been synthesized by mechanochemistry, liquid-assisted grinding (LAG), and vacuum-sealed tube melting

reaction. In ultrathin NPLs, the optical property is controlled by lower energy states associated with the local intrinsic electronic structure of the edges of the perovskite layers. We have studied the single-particle fluorescence properties of $Cs_3Bi_2I_9$ NPLs by super-resolution fluorescence microscopy, which revealed that the luminescence intensity of the NPLs is homogeneous and in the far-red region; importantly, the fluorescence blinking was in the millisecond time scale. The dispersive nature of the blinking kinetics indicated the existence of surface defects present on the large surface of the NPLs that trapped excitons, leading to nonradiative recombination. These trapping sites could alternatively be activated and deactivated by incident photons.

3.2.2. Methods

Reagents. Caesium carbonate (Cs_2CO_3, 99.9%, Sigma-Aldrich), bismuth iodide (BiI_3, 99.9%, Sigma-Aldrich), oleic acid (OA, tech. 90%, Sigma-Aldrich), oleylamine (OAm, tech. 70%, Sigma-Aldrich), 1-octadecene (ODE, tech. 90%, Sigma Aldrich), and toluene (AR, 99.0%, SDFCL) were used for the syntheses without further purification.

Synthesis of Cs-oleate. In a typical synthesis, 410 mg (1.26 mmol) Cs_2CO_3 and 20 mL ODE were taken in a 50 mL 3-neckedround-bottom flask and heated at 120 °C in vacuum for 1 h to get a homogeneous solution. 1.30 mL of OA was added into the above solution, and the solution was kept for another 30 min at the same condition. The vacuum was replaced with nitrogen atmosphere, and temperature was increased up to 150 °C and kept for 5 min to get a clear Cs-oleate solution. This Cs-oleate solution was stored at room temperature under nitrogen atmosphere for further use.

Synthesis of colloidal $Cs_3Bi_2I_9$. In order to synthesize the colloidal $Cs_3Bi_2I_9$ nanostructures of different morphologies (NSs, NPLs and NCs), the reactions were carried out by a hot injection method. 222 mg (0.38 mmol) BiI_3 and 10 ml ODE were taken in a 50 mL 3-necked round-bottom flask, and the flask was degassed at 100°C for 60 min along with magnetic stirring. 1 mL OA and 1 mL OAm were added to the mixture at 100 °C under N_2 atmosphere to dissolve BiI_3. Then, temperature of the reaction was raised to 110, 150, and 180 °C for three separate reactions to produce different

morphology nanostructures. The presynthesized Cs-oleate (0.1 M, 0.6 mL) solution in ODE, preheated at 90 °C, was swiftly injected to the reaction mixture at 110, 150, and 180 °C respectively. Within few seconds, the reaction mixture became turbid red, and then the reaction was quenched by dipping the reaction flask into an ice bath. N_2 atmosphere was maintained throughout the reaction process in a Schlenk line. The synthesized $Cs_3Bi_2I_9$ nanostructures were then washed with tert-butanol and precipitated by centrifugation at 8000 rpm for 10 min, followed by redispersing the products in nonpolar solvents such as toluene for further studies. We obtained $Cs_3Bi_2I_9$ with NSs and NPLs-like morphology at 110 and 150 °C, respectively, whereas at 180 °C, $Cs_3Bi_2I_9$ NCs were formed.

Solid-state mechanochemical synthesis of $Cs_3Bi_2I_9$. In a typical synthesis of bulk powder of $Cs_3Bi_2I_9$, 64.5 mg (0.25 mmol) of CsI and 98.25 mg (0.16 mmol) of BiI_3 were taken in stoichiometric ratios of 3:2 in a mortar pestle, mixed, and ground mechanically for 2h in a N_2-filled glove bag. The physical mixture of CsI and BiI_3 converted from black to deep red in 1 h. The grinding process was still continued for another 1 h to assure pure-phased product.

Synthesis of $Cs_3Bi_2I_9$ by liquid-assisted grinding. In this synthetic process, 64.5 mg (0.25 mmol) of CsI and 98.25 mg (0.16mmol) of BiI_3 were taken in a stoichiometric ratio of 3:2 in a mortar pestle, and few drops of different organic solvents (ethanol, N, N dimethyl formamide, and N-methyl pyrrolinone) were added in three different reactions. The mixtures were ground mechanically for 2 h in a N_2-filled glove bag. The black physical mixture of CsI and BiI_3 converted to bright red for the ethanol-assisted reaction and deep red for N, N-dimethyl formamide (DMF)- and N-methyl-2-pyrrolidone (NMP)-assisted reactions, respectively.

Synthesis of crystalline ingot of $Cs_3Bi_2I_9$. Crystalline ingot (~1 g) of $Cs_3Bi_2I_9$ was synthesized by reaction of stoichiometric (3:2) amounts of the starting materials CsI and BiI_3 in quartz ampoules. The tube was sealed under vacuum (~10^{-6} Torr) and slowly

heated to 923 K. It was then left for a time period of 12 h, followed by slow cooling to room temperature over 8 h.

Powder X-ray diffraction. Powder X-ray diffraction (PXRD) patterns of the samples were collected using Cu Kα (λ = 1.5406 Å) radiation on a Bruker D8 diffractometer at room temperature.

Field-emission scanning electron microscopy. Field-emission scanning electron microscopy (FESEM) experiments were performed using NOVANANO SEM 600 (FEI, Germany) operated at 15 kV. Energy dispersive X-ray (EDAX) compositional analysis was performed during FESEM imaging.

Thermogravimetric analysis. Thermogravimetric analysis (TGA) was performed by using a 2 STAR TGA instrument. Samples were heated at a rate of 5 °C min^{-1} in N_2 atmosphere (40 mL min^{-1}) throughout a temperature range of 30-750 °C. The TGA curve of as synthesized $Cs_3Bi_2I_9$ NPLs has been shown in Figure 3.2.2a. The TGA data shows an initial weight loss of 10% in the temperature range of 50- 410 °C because of the decomposition of the capping agents. Subsequently, the second weight loss of 35% is observed within a temperature range of 410-650 °C because of the decomposition of $Cs_3Bi_2I_9$ into CsI and BiI_3. Evaporation of BiI_3 accounts for the major weight loss.

Atomic force microscopy. Atomic force microscopy (AFM) was performed on a Bruker Innova Microscope in the tapping mode with 10 nm diameter containing an antimony-doped Silicon tip.

Transmission electron microscopy. The transmission electron microscopy (TEM) images of the synthesized $Cs_3Bi_2I_9$ were taken using a JEOL (JEM3010) TEM instrument (300 kV accelerating voltage) fitted with a Gatan CCD camera and also with a FEI TECNlAI G2 20 STWIN TEM instrument (operating at 200 kV).

Electronic absorption spectroscopy. UV-visible absorption spectra were recorded using a PerkinElmer, Lambda-900 UV/vis/near-IR spectrometer. To estimate the optical band gap in the solid-state sample, diffuse reflectance measurements were carried out in the range of λ =250-800 nm by using a PerkinElmer Lambda 900 UV/vis/near-IR spectrometer in the reflectance mode. Absorption (α/S) data were calculated from reflectance data by using the Kubelka-Munk equation: $\alpha/S = (1-R)^2/(2R)$, in which R is the reflectance, α and S are the absorption and scattering coefficients, respectively. The energy band gaps were derived from α/S versus E (nm) plots. Electronic absorption spectroscopy is also performed in the solution phase and compared with solid state spectra. The emission spectra were recorded on PerkinElmer LS 55 luminescence spectrometer in the solid state and in solution phase. Luminescence spectra of were recorded at different excitation wavelengths.

Fluorescent lifetime measurement. Time-resolved decay experiments were recorded on a Horiba Delta Flex time-correlated single-photon-counting instrument. A 373 nm nano-LED with a pulse repetition rate of 1 MHz was used as the light source. The instrument response function was collected by using a scatterer (Ludox AS40 colloidal silica, Sigma-Aldrich). For the 373 nm LED light source, the instrumental full-width at half-maximum including the detector response was 0.2 ns. The excited state decay of the sample was collected by fixing the emission wavelength at a particular wavelength. The decay was fitted using IBH software (DAS6).

Super-Resolved Fluorescence Imaging. $Cs_3Bi_2I_9$ NPLs were dispersed in toluene and dried over a cover-slip for imaging. Brightfield images were captured first using lower magnification objective (EC plan-Neofluar 10×/0.3 M27) and the resulted image showed a distribution of tiny NPLs. The fluorescence images of the same crystals revealed the photoluminescent properties of the materials. Next, we further investigated the properties of these materials after looking at higher magnification objective (Alpha Plan-Apochromat100×/1.46 Oil DIC M27 Elyra) using high energy laser for excitation.

Confocal Microscopy Imaging. Confocal microscopy imaging was done at room temperature using a Zeiss LSM 880 laser scanning confocal microscope. The microscope objective of 63× (NA 1.4) was employed. The sample was prepared by sealing cover slip on top of the glass slide. Laser was used at 488 and 543 nm for excitation. The super-resolved fluorescence imaging and confocal microscopy imaging are done in collaboration with Prof. Sarit S. Agasti, JNCASR, India.

3.2.3. Results and Discussion

A solution-based synthetic approach under an inert atmosphere Schlenk-line was followed here for the synthesis of 2D few-layer NPLs with thickness in the range of 2–3-unit cells (~2 nm) and also for the syntheses of NSs and NC of $Cs_3Bi_2I_9$. Typically, BiI_3 was dissolved in ODE using OA and OAm, followed by hot injection of presynthesized Cs-oleate quickly into the BiI_3 solution at different temperatures (110-180 °C) (Figure 3.2.1b). The orange/red reaction mixture was then quenched by ice-water bath after 10 min of reaction and precipitated by tert-butanol, which was further thoroughly washed with hot toluene several times.

The final products varied in morphologies such as NSs, NPLs, and NCs depending on reaction temperatures that is 110, 150, and 180 °C, respectively. Moreover, we have synthesized bulk powder $Cs_3Bi_2I_9$ by simple mechanochemistry (Figure 3.2.1c)[26] and LAG in three different solvents, namely DMF, NMP, and ethanol (LAG, Figure 3.2.1d-e) with stoichiometric CsI and BiI_3 at room temperature. Further, we have synthesized crystalline ingot (Figure 3.2.1f) of $Cs_3Bi_2I_9$ under vacuum (~10^{-6} Torr) via a sealed quartz tube melting reaction at 650 °C.

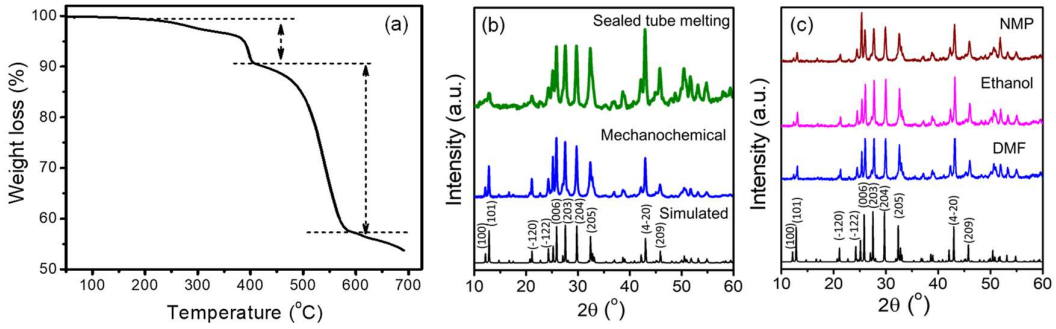

Figure 3.2.2. *(a) TGA curve of as-synthesized NPLs of $Cs_3Bi_2I_9$. PXRD pattern of $Cs_3Bi_2I_9$ synthesized via (b) seal tube melting reaction and mechanochemical process; and (c) liquid assisted grinding (LAG) in different organic solvents (NMP, ethanol and DMF).*

PXRD patterns of NSs, NPLs, and NCs (Figure 3.2.1g) synthesized by the hot injection method, bulk compounds synthesized by mechanical grinding (Figure 3.2.2b) and the solid-state sealed tube melting process (Figure 3.2.2b); and the bulk powders by LAG (Figure 3.2.2c) could be indexed based on the pure-phase hexagonal $Cs_3Bi_2I_9$ (space group $P6_3/mmc$). $Cs_3Bi_2I_9$ possesses 0D connectivity in the structure consisting of two face-sharing $Bi_2I_9^{3-}$ bioctahedra, which are separated by the independent monovalent Cs^+ occupying the interstitial spaces (Figure 3.2.1a). The face-sharing $Bi_2I_9^{3-}$ bioctahedra form the layers which are stacked in crystallographic *b*-axis with the thickness of each layer being 0.84 nm (Figure 3.2.1a). Further, as-synthesized $Cs_3Bi_2I_9$ powders possessed good thermal stability as seen in the TGA (Figure 3.2.2a).

NPL (Figure 3.2.3a, 3.2.4b) and large-area thin NS (Figure 3.2.3e, 3.2.4a) morphologies of $Cs_3Bi_2I_9$ synthesized by the hot injection method at 150 and 110 °C, respectively, were observed in FESEM. 2D NPLs of $Cs_3Bi_2I_9$ possess lateral dimensions of 300-600 nm with a thickness of few nanometres (Figure 3.2.3a). EDAX analysis of $Cs_3Bi_2I_9$ NPLs showed the presence of Cs, Bi, and I being consistent with their stoichiometric ratio (Figure 3.2.4d). Small NCs (Figure 3.2.4c) resulted in the hot injection synthesis at 180 °C, while agglomerated bulk particles with large grain size in the range 0.6-1.5 μm of $Cs_3Bi_2I_9$ were observed in the mechanochemical synthesis and LAG.

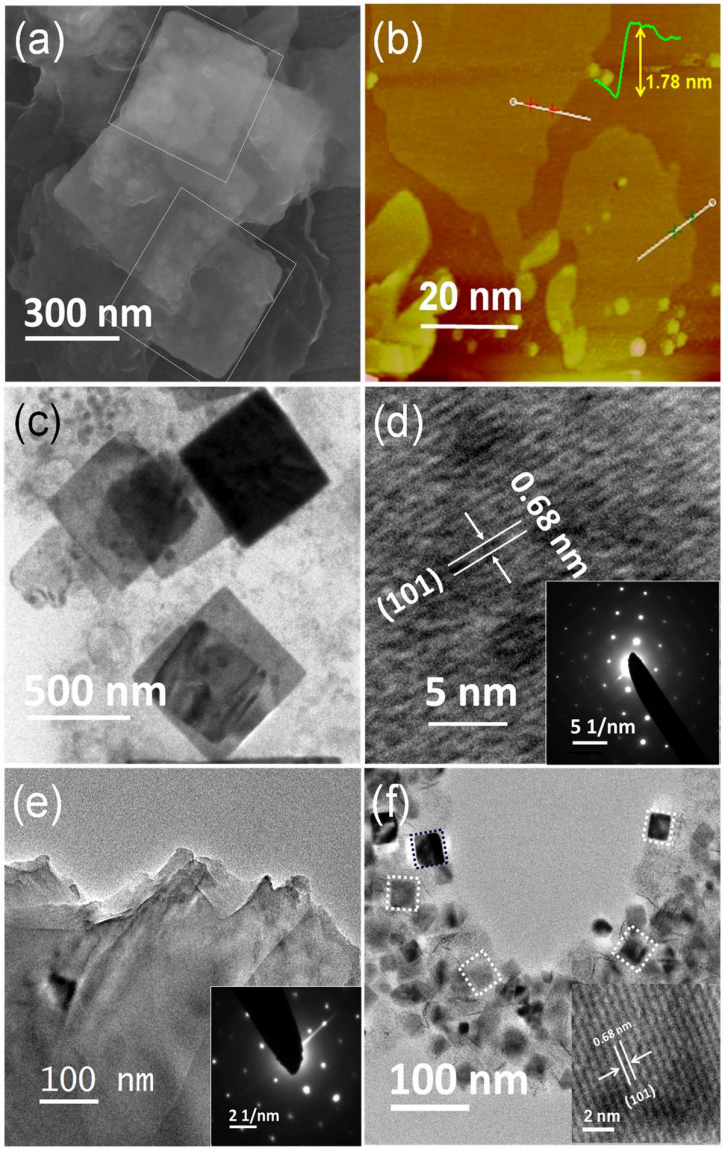

Figure 3.2.3. *(a) FESEM image of the $Cs_3Bi_2I_9$ nanoplates (b) AFM image and height profile (inset) of the $Cs_3Bi_2I_9$ nanoplates (c) TEM image of the $Cs_3Bi_2I_9$ nanoplates (d) HRTEM image with lattice plane (101) and SAED pattern (inset) of the $Cs_3Bi_2I_9$ nanoplates (e) TEM image of $Cs_3Bi_2I_9$ nanosheets, SAED pattern (inset) (f) TEM and HRTEM image (inset) of $Cs_3Bi_2I_9$ nanocrystals.*

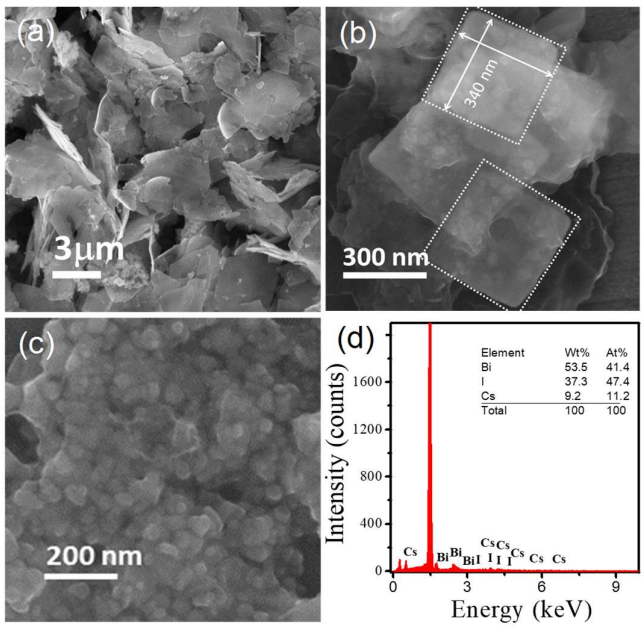

Figure 3.2.4. *FESEM images of the $Cs_3Bi_2I_9$ (a) nanosheets (NSs), (b) nanoplates (NPLs), (c) nanocrystals (NCs) and (d) EDAX spectra of NPLs of $Cs_3Bi_2I_9$.*

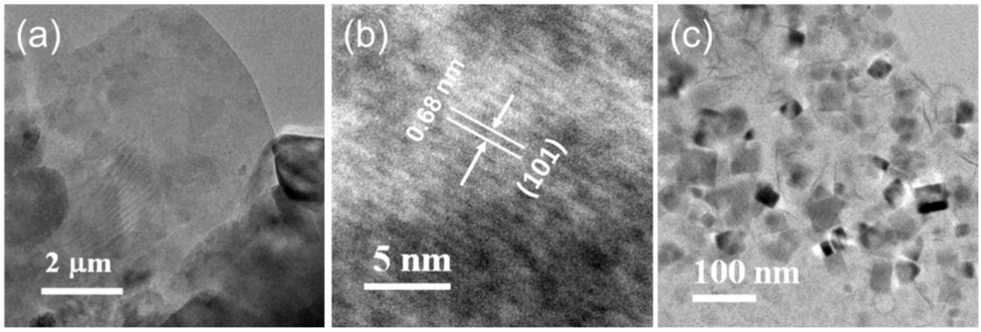

Figure 3.2.5*.(a) TEM and (b) HRTEM images of the $Cs_3Bi_2I_9$ nanosheets (NSs), and (c) TEM images of $Cs_3Bi_2I_9$ nanocrystals (NCs).*

The thickness of the NPLs was measured with AFM to be ~1.78 nm, which matches closely with total thickness of two successive layers (i.e. 1.68 nm) stacked along the crystallographic *b*-direction consisting of face-sharing metal-halide bioctahedral (Figure 3.2.3b).

Transmission electron micrographs of the sample synthesized at 150 °C by hot injection method revealed that the square-shaped ultrathin NPLs (Figure 3.2.3c) possessed lateral dimensions ranging between 300 and 600 nm. The high-resolution TEM (HRTEM) image of a typical ultrathin $Cs_3Bi_2I_9$ NPL demonstrates the lattice fringes with the spacing of 0.68 nm (Figure 3.2.3d) corresponding to the (101) planes of hexagonal $Cs_3Bi_2I_9$. The selected-area electron diffraction (SAED) pattern confirmed that the $Cs_3Bi_2I_9$ NPLs were single crystalline in nature (Figure 3.2.3d inset). Ultrathin NSs synthesized at 110 °C are single crystalline in nature (Figure 3.2.3e inset), possessed lateral dimensions of 2-5 μm, and thickness of few nanometres (Figure 3.2.3e and 3.2.5a). However, the NCs synthesized at 180 °C had dimensions of 30-50 nm (Figure 3.2.3f and 3.2.5c). In the NCs, the d-spacing value was measured as 0.68 nm, which indicated the (101) plane of $Cs_3Bi_2I_9$ (Figure 3.2.3f inset). From the HRTEM analysis, the crystals were shown to have grown along (101) planes for NPLs, NSs, and NCs.[27]

Hot injection at lower temperature favored the formation of large 2D NSs/ NPLs, whereas higher temperature reaction favored the formation of NCs, which indicates that temperature played a critical role in determining the morphology and size of the $Cs_3Bi_2I_9$ nanostructures. Thickness of perovskite NPLs are generally controlled by the concentration of OA in the reaction mixture, where thinner and larger (lateral dimension) NSs/NPLs are resulted at higher OA concentration and NCs are formed with lower OA concentration.[28] We assumed that at low temperature (110 °C), OA binds through the carboxylate group strongly to the selective surface of $Cs_3Bi_2I_9$.[29] Hence, adsorbed OA prevents the growth in the crystallographic *b*-direction and $Cs_3Bi_2I_9$ grows asymmetrically along the *ac*-plane, resulting in large (2-5 μm) NSs with the exposed (101) lattice planes (Figure 3.2.5b). However, at higher temperature (150 °C), the solubility of OA in ODE increases (i.e. effective OA capping agent concentration decreases), which gives rise to the formation of 2D NPLs with lateral dimension of 300-600 nm (Figure 3.2.6). When the reaction was conducted at further higher temperature (180 °C), the surface-ligand interactions were not controlled because of the enhanced solubility of OA in ODE, resulting in the synthesis of NCs (Figures 3.2.5c, 7). A similar temperature-controlled study of the formation of different morphologies was reported for $CsPbBr_3$[27] and wurtzite CdSe.[30]

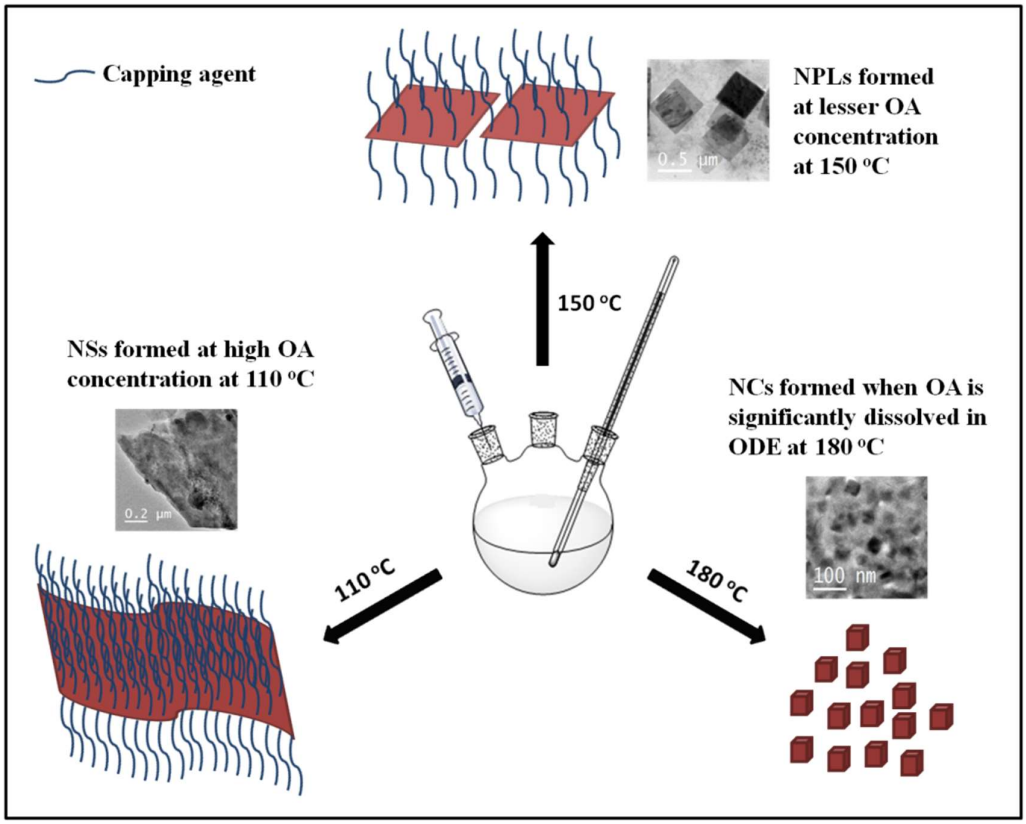

Figure 3.2.6. *Proposed formation mechanism of NSs, NPLs and NCs of $Cs_3Bi_2I_9$.*

We studied the optical properties of $Cs_3Bi_2I_9$ NPLs, NSs, and NCs in the solid state (Figure 3.2.7) Electronic absorption spectroscopy of the $Cs_3Bi_2I_9$ NPLs showed an optical absorption edge at 611 nm (2.03 eV, Figure 3.2.7a). Photoluminescence (PL) studies at the solid state revealed that a broad emission peak (Figure 3.2.7a) was deconvoluted to 623 nm (1.99 eV) and 645 nm (1.93 eV) peaks, when excited at 480 nm (Figure 3.2.8a). These two PL bands are probably due to the direct band gap transition (1.99 eV) and phonon-assisted transition (1.93 eV) in $Cs_3Bi_2I_9$ that are earlier proposed by Zhang et al.,[13] which needed further investigation. However, we observe a prominent peak in absorption spectra of NPLs, NCs, and bulk samples of $Cs_3Bi_2I_9$ around ~2.55 eV (Figure 3.2.7 and Figure 3.2.9), which was proposed to be excitonic transition by recent reports.[19, 23]

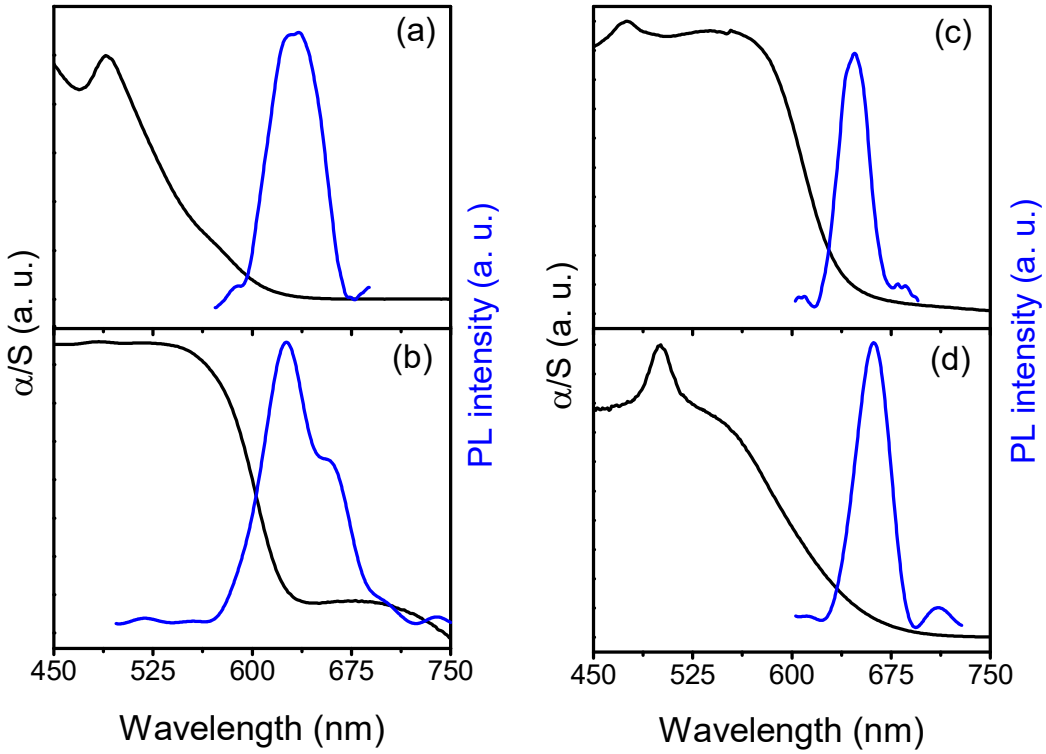

Figure 3.2.7. *Solid-state electronic absorption (α/S) (black) and PL (blue) spectra of (a) $Cs_3Bi_2I_9$ nanoplates, (b) $Cs_3Bi_2I_9$ nanosheets, (c) $Cs_3Bi_2I_9$ nanocrystals, and (d) $Cs_3Bi_2I_9$ bulk powders (mechanochemistry).*

Optical absorption edge for the NSs were observed at 622 nm (1.99 eV) with two distinct PL emissions taking place at 626 nm (1.98 eV) and 659 nm (1.88 eV) respectively similar to NSs, when excited at 465 nm (Figure 3.2.7b and 3.2.8b). This slight red shift of absorption spectra of NSs compared to that of the NPLs can be attributed to the large lateral dimension of NSs. The optical absorption edge for the NCs were observed at 634 nm (1.96 eV) with two PL bands measured at 637 nm (1.95 eV) and 649 nm (1.91 eV) respectively, when excited at 475 nm (Figure 3.2.7c and 3.2.8c). However, the optical absorption edge for the bulk powder synthesized by mechanochemical grinding was found to be at 645 nm (1.92 eV), and two PL peaks appeared at 656 nm (1.89 eV) and 668 nm (1.85 eV), when excited at a wavelength of 460 nm (Figure 3.2.7d and 3.2.8d). The blue shift in electronic absorption spectra of ultrathin NPLs compared to that of bulk powder as well as of NCs due to possible quantum confinement in ultrathin 2D NPLs.

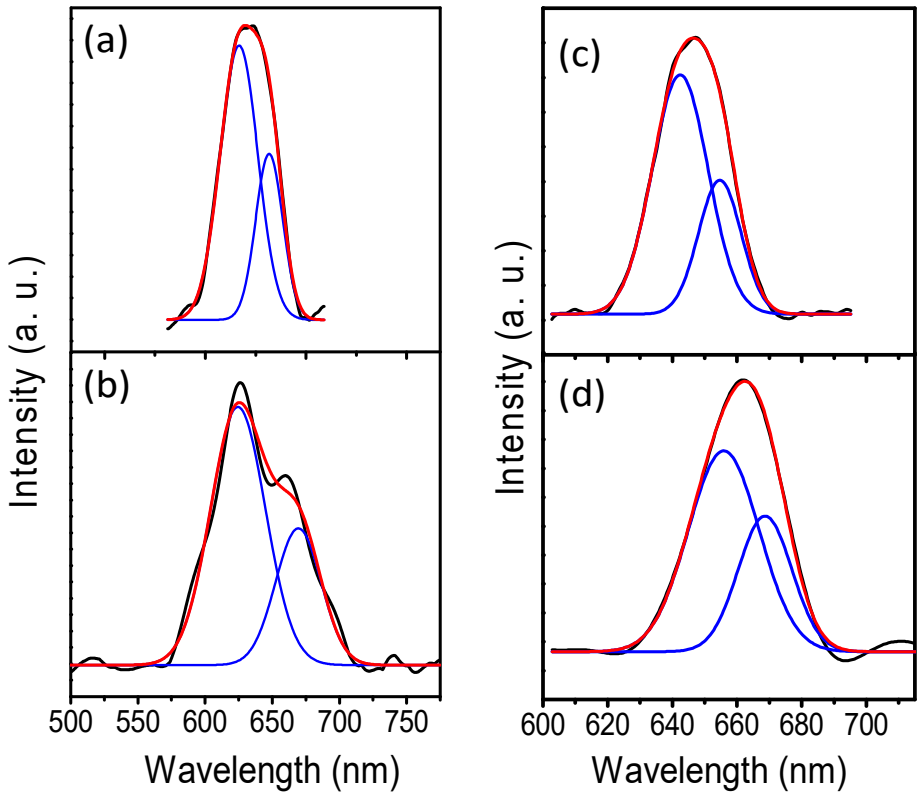

Figure 3.2.8. *(a) Deconvoluted PL spectra of $Cs_3Bi_2I_9$ (a) nanoplates (NPLs), (b) nanosheets (NSs),(c) nanocrystals (NCs) and (d) bulk powder synthesized by mechanical grinding.*

The studies for optical properties were also carried out in the solution phase (Figure 3.2.10). In solution phase absorption spectra, the blue shift of the excitonic peak is prominent for NPLs compared to NCs. The excitonic peak exhibits at 480 nm for NPLs, whereas in case of NCs, the position of this excitonic peak is 497 nm. The blue shift in electronic absorption spectra of ultrathin NPLs compared to that of NCs is probably due to quantum confinement. PL studies in the solution phase revealed that the position of the emission band is at lower wavelength and sharper compared to solid state PL band.

The band positions appeared at 544 nm (Figure 3.2.10a,), 535 nm (Figure 3.2.10c), and 520 nm (Figure 3.2.10e) for NPLs, NSs, and NCs, respectively, when excited at a wavelength of 450 nm. Similar PL emission in lower wavelength in solution phase small NCs by Nag and co-workers.[23] In the solid-state optical spectra, broadening

in emission band is mainly due to the presence of more defect states compared to that in solution. The PL decays of NPLs were well fit by a triexponential function with a short-lived component (τ_1 = 0.3 ns) with relative amplitudes of 25%, a middle component (τ_2 = 0.9 ns) with relative amplitudes of 64%, and a long-lived component (τ_3 = 9.1 ns) with relative amplitudes of 11% (Figure 3.2.11).[31]

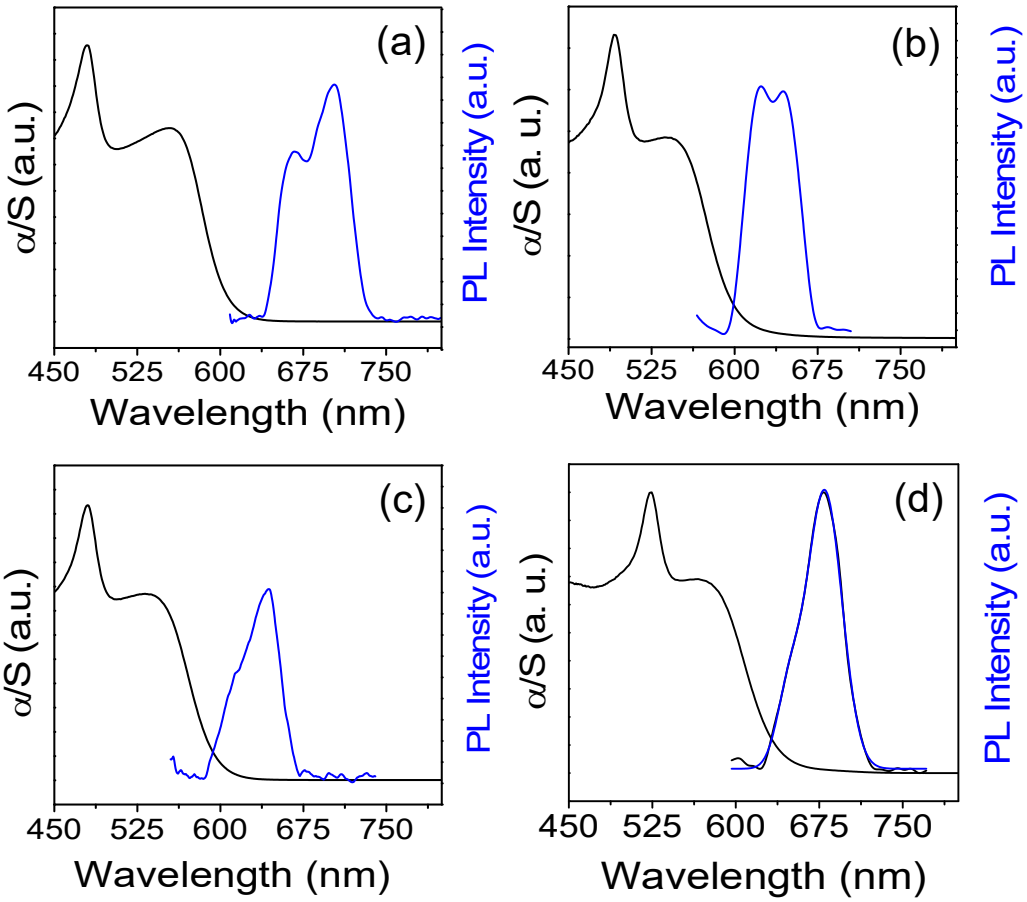

Figure 3.2.9. *Solid state UV/vis absorption (α/S) (black) and PL (blue) spectra of $Cs_3Bi_2I_9$ synthesized via LAG with organic solvents (a) DMF, (b) ethanol and (c) NMP. (d) Solid state UV/vis absorption (α/S) (black) and PL (blue) spectra of crystalline ingot of $Cs_3Bi_2I_9$ synthesized via vacuum sealed tube melting.*

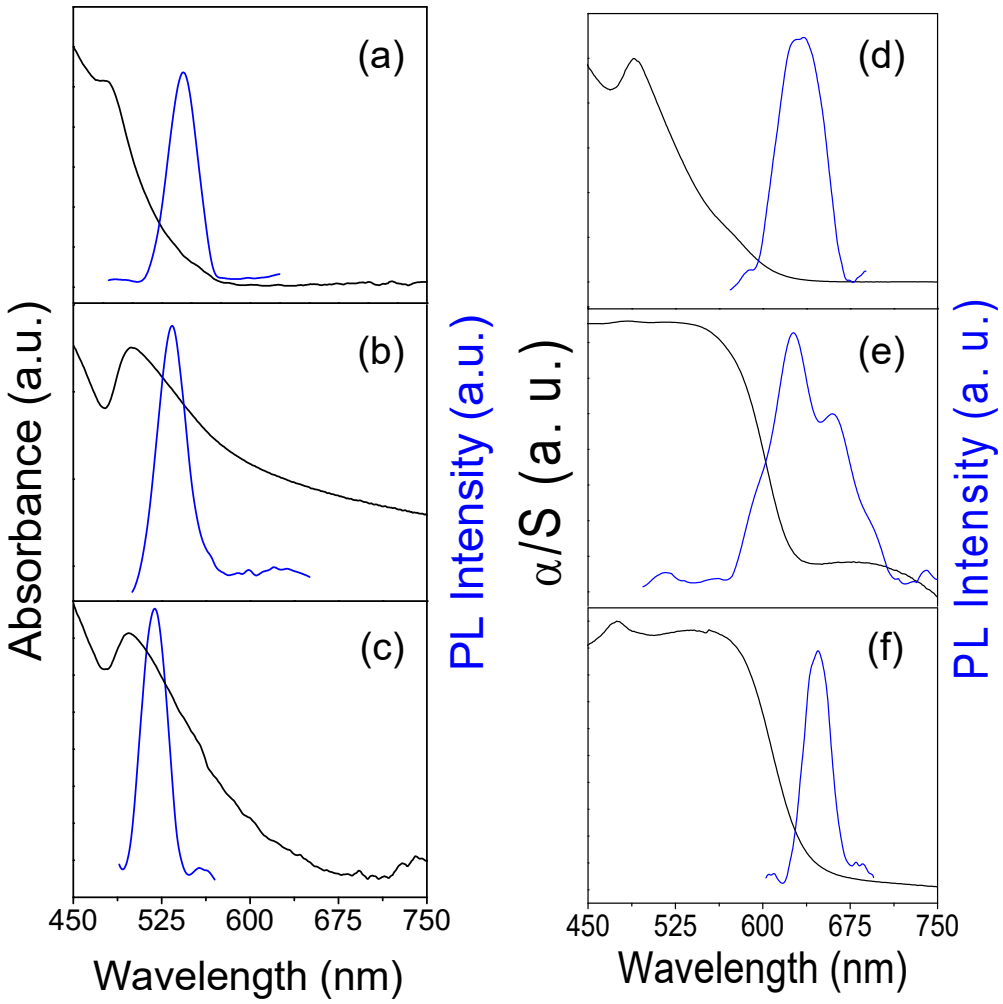

Figure 3.2.10. *Comparison of UV/Vis absorption (black) and PL (blue) spectra of (a) $Cs_3Bi_2I_9$ NPLs, (c) $Cs_3Bi_2I_9$ NSs, (e) $Cs_3Bi_2I_9$ NCs with solid state electronic absorption (α/S) and PL spectra of (b) $Cs_3Bi_2I_9$ NPLs, (d) $Cs_3Bi_2I_9$ NSs, (f) $Cs_3Bi_2I_9$ NCs.*

We have subsequently investigated the PL behavior of individual $Cs_3Bi_2I_9$ NPL via super-resolution fluorescence microscopy. The bright-field optical image (Figure 3.2.12a) showed a distribution of NPLs. Those bright-field images of $Cs_3Bi_2I_9$ NPLs showed that the average diameter of NPLs was around ~450 nm (Figure 3.2.13a), which is supported by TEM and SEM measurements.

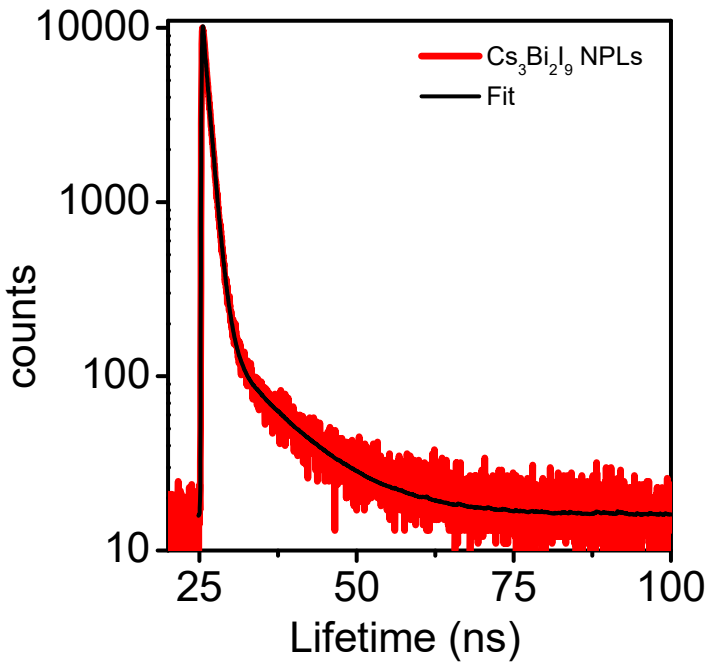

Figure 3.2.11. *PL decay profiles of colloidal $Cs_3Bi_2I_9$ NPLs. The samples were excited at 373 nm and the emission at 540 nm is monitored.*

The fluorescence image (Figure 3.2.12b) of the NPLs revealed the photoluminescent emission with high signal-to-noise ratio. We further investigated the properties of $Cs_3Bi_2I_9$ NPLs under higher magnification objective using high-intensity laser for excitation. Super resolution localization microscopy was initially performed on each $Cs_3Bi_2I_9$ NPL using 488 nm laser excitation, where emission was collected from a band pass emission filter (BP 570-650 + LP 750). In the total internal reflection fluorescence illumination mode, these crystals showed systematic fluorescence ON and OFF behavior because of trap states resulting from surface defects of the material.[32, 33] This blinking of the crystalline material was recorded for few minutes, and it was observed that each crystal repeatedly transformed to its ON and OFF states (Figure 3.2.12d), which indicated high photostability of the NPLs. This was further confirmed by looking at the molecular density profile of any particular crystal blinking region (Figure 3.2.12c-I,ii), which indicated the number of multiple fluorescence blinking events in a particular region. The high fluorescence intensity of the crystalline material was supported by calculating the

photon counts from the blinking events. Photon count was found to be on an average of 400-600 for $Cs_3Bi_2I_9$ NPLs (Figure 3.2.13b).

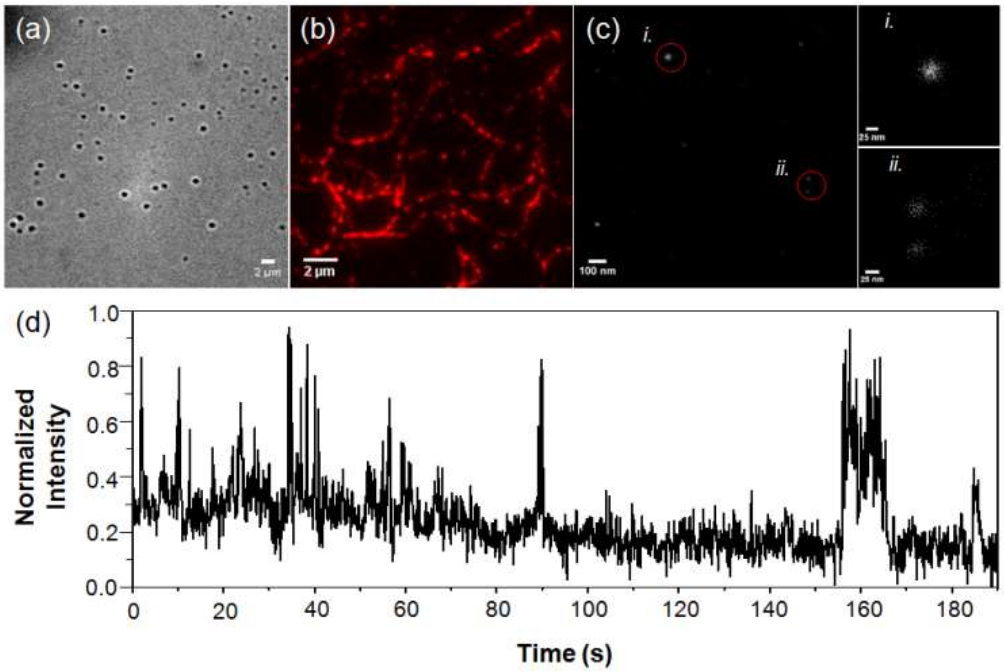

Figure 3.2.12. *Fluorescence microscopy images and blinking behavior of $Cs_3Bi_2I_9$ nanoplatelets: (a) bright-field image, (b) fluorescence microscopy image shows $Cs_3Bi_2I_9$ NPLs are fluorescent in nature, (c) molecular density of individual plate for multiple blinking events of $Cs_3Bi_2I_9$ NPLs after excitation using 488 nm laser (630 W cm^{-2}). Fluorescence blinking events were recorded over 10000 frames with 100 ms exposure time. The zoomed-in region from (c) shows repetitive ON and OFF cycle for each $Cs_3Bi_2I_9$ NPLs (I, ii), and (d) systematic plot of fluorescence ON and OFF of $Cs_3Bi_2I_9$ NPLs upon irradiation with 488 nm laser and collecting the emission from a band pass emission filter set (BP 570-650 + LP 750).*

The photophysical properties of $Cs_3Bi_2I_9$ NPLs were also studied using different off-resonance wavelengths. Upon excitation using 405 nm laser, emission spectra were monitored in two different emission windows (BP 495-575+ LP 750 and BP 570-650 + LP 750). Fluorescence blinking was not observed from $Cs_3Bi_2I_9$ NPLs when it was excited using 405 nm laser, as we do not see any fluorescence emission with this excitation wavelength from the solid sample. Figure 3.2.14a-d are the single NPL fluorescence frames from two emission windows. Subsequently, the fluorescence

blinking properties of the NPLs were also recorded using 560 nm laser (emission filter BP570-650 + LP 750). The NPLs were emitting fluorescence in this excitation and emission window, and the fluorescence ON/OFF switching was observed from this excitation wavelength. In Figure 3.2.14e, it clearly suggests the occurrence of the above phenomenon. In comparison to excitation at 488 nm, the blinking behavior is slightly different and the fluorescence ON time appeared to be higher in the case of excitation at 560 nm (Figure 3.2.14f).

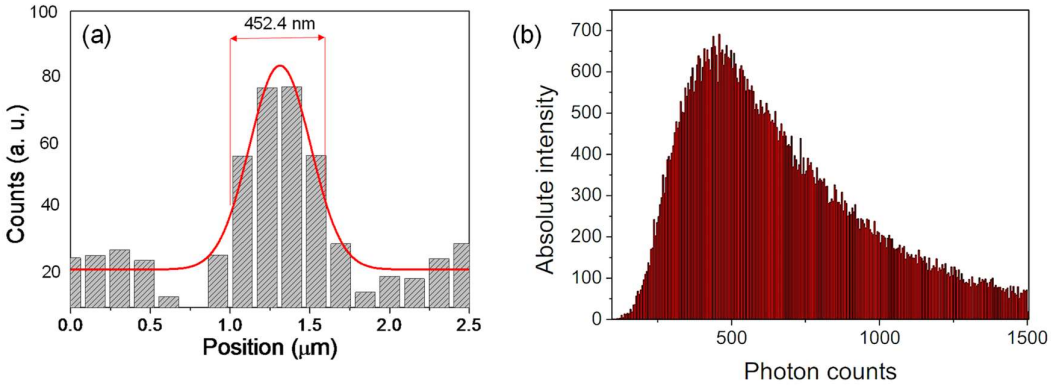

Figure 3.2.13. *(a) Diameter of each $Cs_3Bi_2I_9$ NPL from bright field image. (b) Photon count calculated from super resolution microscopy of $Cs_3Bi_2I_9$ NPLs.*

Further, the fluorescence properties of the NPLs were studied by confocal microscopy at different wavelengths and emission windows. The confocal microscopy images (Figure 3.2.15b,c) showed that $Cs_3Bi_2I_9$ NPLs emit fluorescence upon excitation with both 488 and 543 nm lasers. It is shown in colocalized image of red (excitation at 543) and green (excitation at 488 nm) fluorescence of the sample (Figure 3.2.15f), where red emission can be visualized from the entire NPLs (or clusters of NPLs), but green emission is specially restricted toward the middle of the clusters.

The emission spectra of the NPLs were also recorded from the spectral scanning confocal microscopy images. It was observed that the emission of the NPLs highly depended upon the size of the sample when excited at 488 nm (Figure 3.2.16). The bigger NPL showed high intensity emission at 620 nm. However, for the smaller NPL, the excitation at 488 nm resulted in multiple emission bands at 580, 620, and 670 nm with

similar fluorescence intensity; the 620 nm band is consistent with solid-state PL spectra $Cs_3Bi_2I_9$ NPLs (Figure 3.2.7a), while the other emission bands are observed probably due to the surface defects. On the other hand, excitation at 543 nm gave rise to emission majorly at 620 nm (Figure 3.2.17).

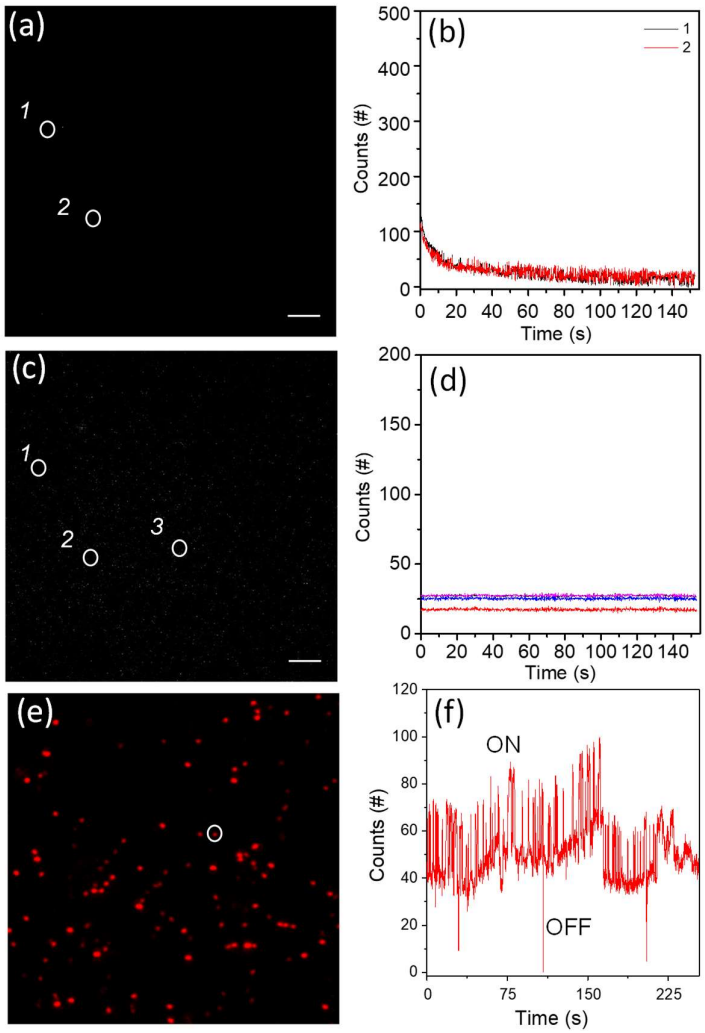

Figure 3.2.14. *Single-molecule blinking analysis of $Cs_3Bi_2I_9$ nanoplates (a) fluorescence images were recorded after excitation using 405 nm laser and emission of nanoplates were monitored in 495-575 nm wavelength, (c) excitation using 405 nm laser and emission of nanoplates were collected in 570-650 nm wavelength, (e) excitation using 560 nm laser and emission of nanoplates were monitored in 570-650 nm wavelength. Arbitrary fluorescence spots were picked to show single nanoplate traces. (b,d)*

Nonemissive/nonblinking nature of nanoplates at 405 excitation and (f) blinking nature of nanoplates at 560 nm excitation. The scale bar is 2.5 μm (a,c,e).

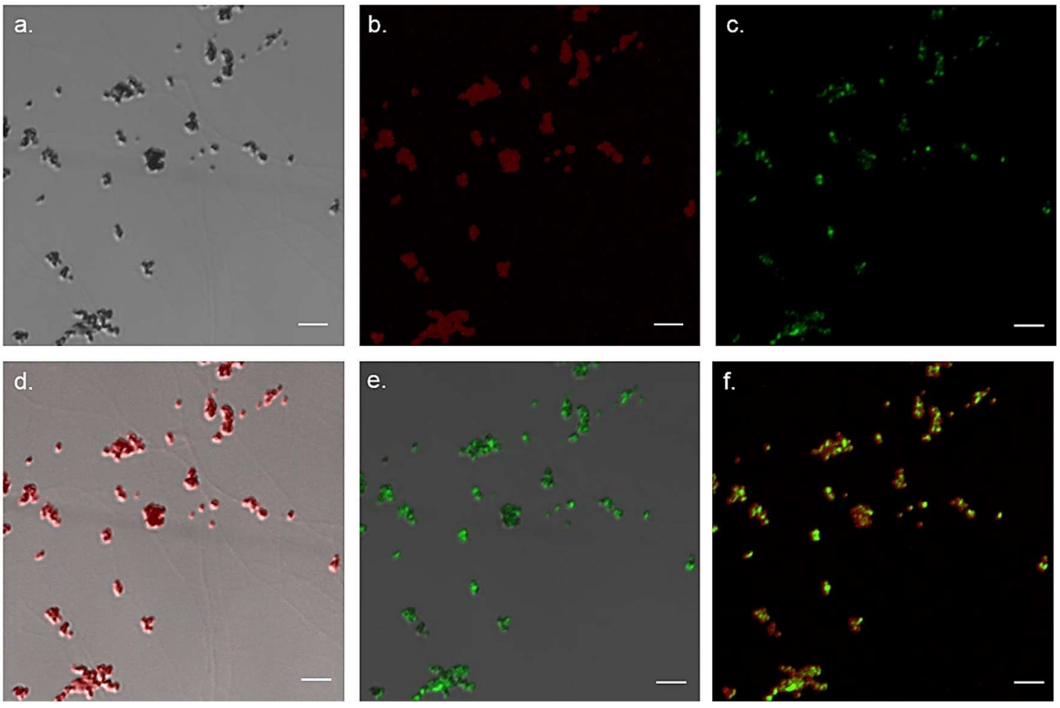

Figure 3.2.15. *Confocal microscopy images of $Cs_3Bi_2I_9$ NPLs upon excitation of 488 and 543 nm lasers. (a) bright field images, (b) fluorescence images after excitation at 543 nm laser (filter set: BP 580-720 nm), (c) fluorescence images after excitation at 488 nm laser (filter set: BP 520-720 nm), (d) co-localized image of bright field and red emission (ex. 543 nm) fluorescence, (e) co-localized image of bright field and green emission (ex. 488 nm) fluorescence, and (f) co-localized image of red and green emissive NPLs. Scale bar 2.5 μm (a-f).*

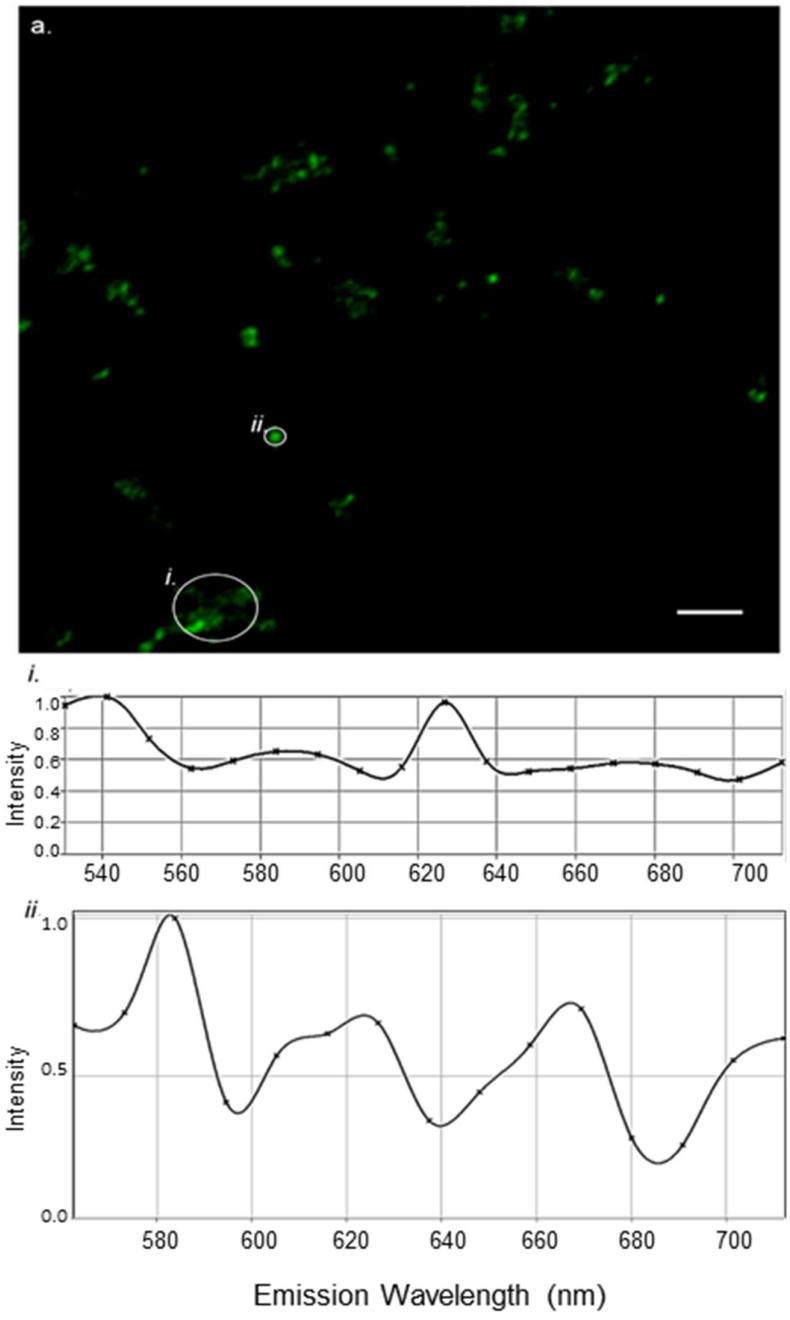

Figure 3.2.16. *Emission spectra of $Cs_3Bi_2I_9$ NPLs upon excitation at 488 nm laser. Scale bar 2.5 μm (a).*

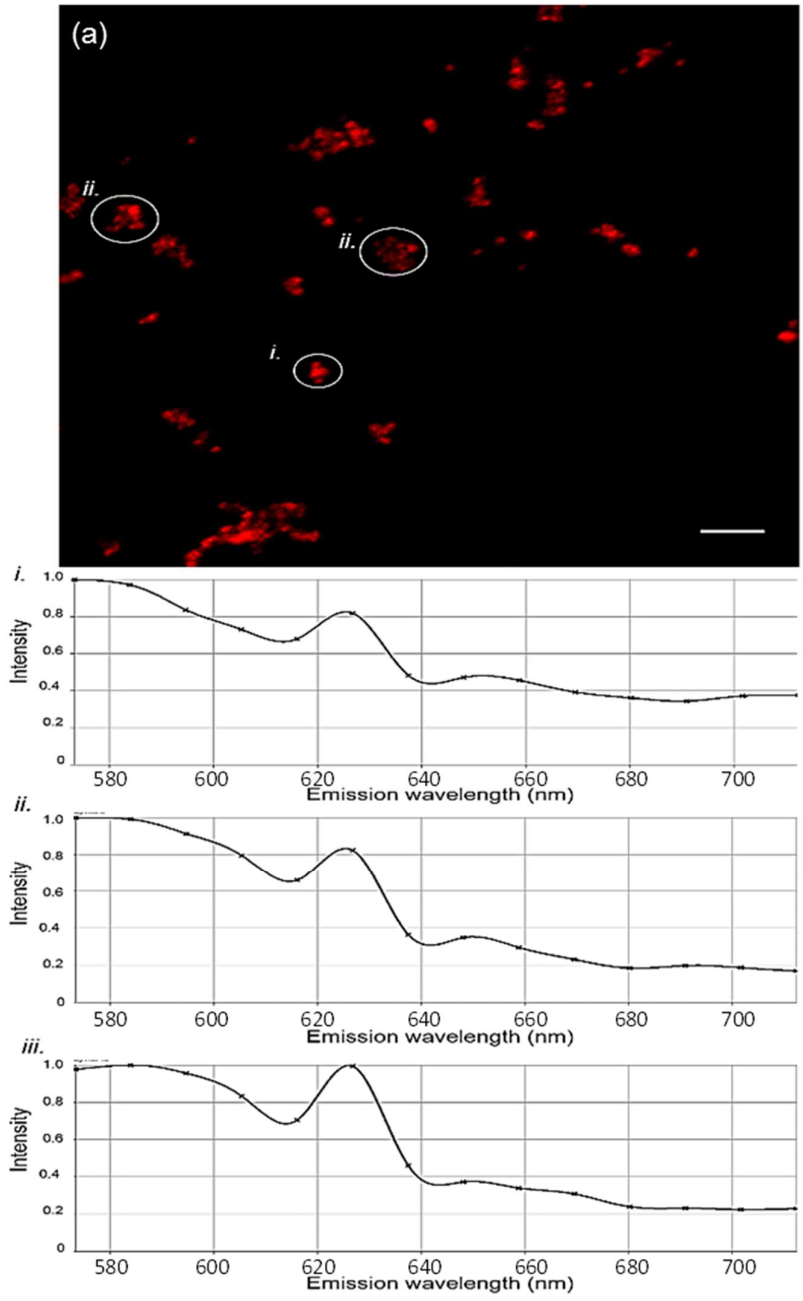

Figure 3.2.17. *Emission spectra of $Cs_3Bi_2I_9$ NPLs upon excitation at 543 nm laser. Scale bar 2.5 μm (a).*

3.2.4. Conclusions

2D ultrathin NPLs of a Pb-free layered $Cs_3Bi_2I_9$ have been synthesized in a one-step hot injection process at 150 °C with good yield. The morphologies of the $Cs_3Bi_2I_9$ were varied from NSs to NCs with changing the reaction temperature in the range 110-180 °C. Further, bulk powder and crystalline ingot of $Cs_3Bi_2I_9$ were also synthesized following mechanochemical grinding and LAG at ambient condition and vacuum-sealed tube solid-state melting. Mechanochemical solid state grinding was an inexpensive, solvent free, and room temperature synthetic process. Possible quantum confinement effect was observed for the ultrathin 2D NPLs of $Cs_3Bi_2I_9$, which is confirmed by the blue shift in the absorption edge. However, the large surface area for the 2D NPLs gives rise to surface defects that in turn resulted in long-lived photo blinking of the NPLs with good fluorescence properties, indicating high photostability of the product, which is investigated by super resolution fluorescence microscopy.

3.2.5. References

1. S. Chen and G. Shi, *Adv. Mater.*, 2017, **29**, 1605448.

2. T. A. Berhe, W. N. Su, C. H. Chen, C. J. Pan, J. H. Cheng, H. M. Chen, M. C. Tsai, L. Y. Chen, A. A. Dubale and B. J. Hwang, *Energy Environ. Sci.*, 2016, **9**, 323.

3. U. Thakur, U. Kwon, M. M. Hasan, W. Yin, D. Kim, N. Y. Ha, S. Lee, T. K. Ahn and H. J. Park, *Sci. Rep.*, 2016, **6**, 35994.

4. A. Swarnkar, V. K. Ravi and A. Nag, *ACS Energy Lett.*, 2017, **2**, 1089.

5. J. Pal, S. Manna, A. Mondal, S. Das, K. V. Adarsh and A. Nag, *Angew. Chem., Int. Ed.*, 2017, **56**, 14187.

6. F. Giustino and H. J. Snaith, *ACS Energy Lett.*, 2016, **1**, 1233.

7. N. K. Noel, S. D. Stranks, A. Abate, C. Wehrenfennig, S. Guarnera, A. A. Haghighirad, A. Sadhanala, G. E. Eperon, S. K. Pathak, M. B. Johnston, L. M. Petrozza and H. J. Snaith, *Energy Environ. Sci.*, 2014, **7**, 3061.

8. T. Krishnamoorthy, H. Ding, C. Yan, W. L. Leong, T. Baikie, Z. Zhang, M. Sherburne, S. Li, M. Asta, N. Mathews and S. G. Mhaisalkar, *J. Mater. Chem. A*, 2015, **3**, 23829.

9. F. Hao, C. C. Stoumpos, D. H. Cao, R. P. H. Chang and M. G. Kanatzidis, *Nat. Photonics*, 2014, **8**, 489.

10. Y. Zhang, J. Liu, Z. Wang, Y. Xue, Q. Ou, L. Polavarapu, J. Zheng, X. Qi and Q. Bao, *Chem. Commun.*, 2016, **52**, 13637.

11. L. Polavarapu, B. Nickel, J. Feldmann and A. S. Urban, *Adv. Energy Mater.*, 2017, **7**, 1700267.

12. Y. Tong, F. Ehrat, W. Vanderlinden, C. Cardenas-Daw, J. K. Stolarczyk, L. Polavarapu and A. S. Urban, *ACS Nano*, 2016, **10**, 10936.

13. Y. Zhang, J. Yin, M. R. Parida, G. H. Ahmed, J. Pan, O. M. Bakr, J. L. Brédas and O. F. Mohammed, *J. Phys. Chem. Lett.*, 2017, **8**, 3173.

14. X. Huang, S. Huang, P. Biswas and R. Mishra, *J. Phys. Chem. C*, 2016, **120**, 28924.

15. X. W. Tong, W. Y. Kong, Y. Y. Wang, J. M. Zhu, L. B. Luo and Z. H. Wang, *ACS Appl. Mater. Interfaces*, 2017, **9**, 18977.

16. M. Pazoki, M. B. Johansson, H. Zhu, P. Broqvist, T. Edvinsson, G. Boschloo and E. M. J. Johansson, *J. Phys. Chem. C*, 2016, **120**, 29039.

17. Y. Hu, S. Zhang, X. Miao, L. Su, F. Bai, T. Qiu, J. Liu and G. Yuan, *Adv. Mater. Interfaces*, 2017, **4**, 1700131.

18. M. B. Johansson, H. Zhu and E. M. J. Johansson, *J. Phys. Chem. Lett.*, 2016, **7**, 3467.

19. K. M. McCall, C. C. Stoumpos, S. S. Kostina, M. G. Kanatzidis and B. W. Wessels, *Chem. Mater.*, 2017, **29**, 4129.

20. B. Ghosh, B. Wu, H. K. Mulmudi, C. Guet, K. Weber, T. C. Sum, S. G. Mhaisalkar and N. Mathews, *ACS Appl. Mater. Interfaces*, 2018, **10**, 35000.

21. Z. Ma, S. Peng, Y. Wu, X. Fang, X. Chen, X. Jia, K. Zhang, N. Yuan, J. Ding and N. Dai, *Phys. B*, 2017, **526**, 136.

22. K. H. Hong, J. Kim, L. Debbichi, H. Kim and S. H. Im, *J. Phys. Chem. C*, 2017, **121**, 969.

23. J. Pal, A. Bhunia, S. Chakraborty, S. Manna, S. Das, A. Dewan, S. Datta and A. Nag, *J. Phys. Chem. C*, 2018, **122**, 10643.

24. M. Leng, *Adv. Funct. Mater.*, 2018, **28**, 1704446.

25. Y. Lou, M. Fang, J. Chen and Y. Zhao, *Chem. Commun.*, 2018, **54**, 3779.

26. P. Pal, S. Saha, A. Banik, A. Sarkar and K. Biswas, *Chem. Eur. J*, 2018, **24**, 1811.

27. Y. Bekenstein, B. A. Koscher, S. W. Eaton, P. Yang and A. P. Alivisatos, *J. Am. Chem. Soc.*, 2015, **137**, 16008.

28. J. A. Sichert, Y. Tong, N. Mutz, M. Vollmer, S. Fischer, K. Z. Milowska, R. García Cortadella, B. Nickel, C. Cardenas-Daw, J. K. Stolarczyk, A. S. Urban and J. Feldmann, *Nano Lett.*, 2015, **15**, 6521.

29. A. Pan, B. He, X. Fan, Z. Liu, J. J. Urban, A. P. Alivisatos, L. He and Y. Liu, *ACS Nano*, 2016, **10**, 7943.

30. J. S. Son, X. D. Wen, J. Joo, J. Chae, S. i. Baek, K. Park, J. H. Kim, K. An, J. H. Yu, S. G. Kwon, S. H. Choi, Z. Wang, Y. W. Kim, Y. Kuk, R. Hoffmann and T. Hyeon, *Angew. Chem., Int. Ed.*, 2009, **48**, 6861.

31. B. Yang, J. Chen, F. Hong, X. Mao, K. Zheng, S. Yang, Y. Li, T. Pullerits, W. Deng and K. Han, *Angew. Chem., Int. Ed.*, 2017, **56**, 12471.

32. Y. Tian, A. Merdasa, M. Peter, M. Abdellah, K. Zheng, C. S. Ponseca, T. Pullerits, A. Yartsev, V. Sundström and I. G. Scheblykin, *Nano Lett.*, 2015, **15**, 1603.

33. S. Seth, N. Mondal, S. Patra and A. Samanta, *J. Phys. Chem. Lett.*, 2016, **7**, 266.

PART 4

Ultralow Thermal Conductivity of Layered Metal Halide Perovskites

Chapter 4.1

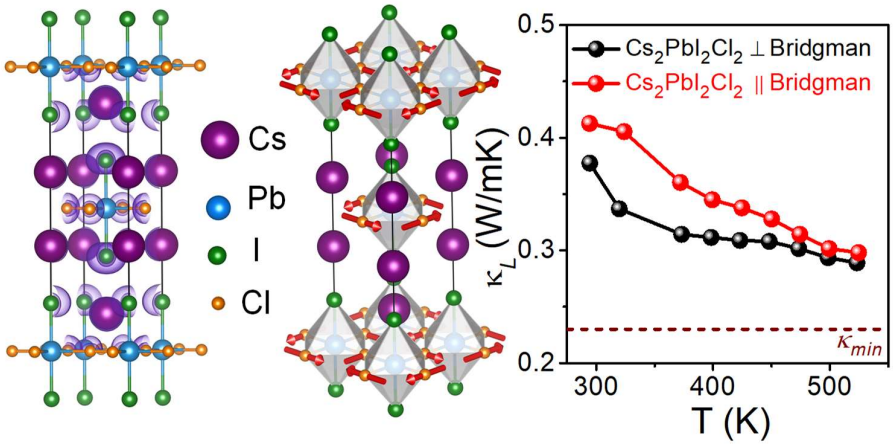

Intrinsically Ultralow Thermal Conductivity in Ruddlesden-Popper 2D Perovskite $Cs_2PbI_2Cl_2$: Localized Anharmonic Vibrations and Dynamic Octahedral Distortions

Chapter 4.1

Intrinsically Ultralow Thermal Conductivity in Ruddlesden-Popper 2D Perovskite $Cs_2PbI_2Cl_2$: Localized Anharmonic Vibrations and Dynamic Octahedral Distortions[†]

Summary

Fundamental understanding of the correlation between chemical bonding and lattice dynamics in intrinsically low thermal conductive crystalline solids is important to thermoelectrics, thermal barrier coating, and more recently to photovoltaics. Two-dimensional (2D) layered halide perovskites have recently attracted widespread attention in optoelectronics and solar cells. In this chapter, we discover intrinsically ultralow lattice thermal conductivity (κ_L) in the single crystal of all-inorganic layered Ruddlesden–Popper (RP) perovskite, $Cs_2PbI_2Cl_2$, synthesized by the Bridgman method. We have measured the anisotropic κ_L value of the $Cs_2PbI_2Cl_2$ single crystal and observed an ultralow κ_L value of ∼0.37–0.28 W/mK in the temperature range of 295–523 K when measured along the crystallographic c-axis. First-principles density functional theory (DFT) analysis of the phonon spectrum uncovers the presence of soft (frequency ∼18–55 cm^{-1}) optical phonon modes that constitute relatively flat bands due to localized vibrations of Cs and I atoms. A further low energy optical mode exists at ∼12 cm^{-1} that originates from dynamic octahedral rotation around Pb caused by anharmonic vibration of Cl atoms induced by a $3s^2$ lone pair. We provide experimental evidence for such low energy optical phonon modes with low-temperature heat capacity and temperature-dependent Raman spectroscopic measurements. The strong anharmonic coupling of the low energy optical modes with acoustic modes causes damping of heat carrying acoustic phonons to ultrasoft frequency (maximum ∼37 cm^{-1}). The combined effect of soft elastic layered structure, abundance of low energy optical phonons, and strong acoustic–optical phonon coupling results in an intrinsically ultralow κ_L value in the all-inorganic layered RP perovskite $Cs_2PbI_2Cl_2$.

[†]**P. Acharyya,** T. Ghosh, K. Pal, K. Kundu, K. S. Rana, J. Pandey, A. Soni, U. V. Waghmare and K. Biswas, *J. Am. Chem. Soc.,* 2020**, 142**, 15595-15603.

4.1.1. Introduction

Effective utilization and management of thermal energy are crucial to thermoelectrics,[1, 2] photovoltaics,[3-5] optoelectronics,[6, 7] and thermal barrier coatings.[8] Thermal transport progressively turns out to be essential in photovoltaics as their lifetime and performance are influenced by the temperature gradients developed in the devices.[9, 10] Crystalline solids with intrinsically low thermal conductivity (κ) are required, such as to achieve hot-phonon bottleneck in photovoltaics,[11, 12] and high performance in thermoelectrics.[1, 13] This leads to a wide-scale search for new low thermal conductive crystalline materials, and subsequently, develop a fundamental understanding of their chemical bonding and lattice dynamics.[14] Recently, innovative strategies have been developed to achieve low thermal conductivity in crystalline solids such as all-scale hierarchical nanostructuring,[15, 16] rattling,[17-19] lattice anharmonicity,[20-25] liquid-like ions,[26, 27] ferroelectric instability induced phonon softening.[28] However, most of these studies are based on heavy metal chalcogenides, skutterudites, and clathrates.[14, 17, 20, 29, 30]

Metal halide perovskites have recently attracted wide attention for important applications including solar cells and optoelectronics due to their outstanding physical and chemical properties, such as large carrier diffusion lengths, absorption coefficients, defect tolerance and high charge carrier mobilities.[31-34] While the lattice vibrations of these perovskites have been investigated with primary focus on their influence on the electronic and optoelectronic properties,[35-37] thermal transport properties subjected to a temperature gradient have been rarely explored.[38] Recently, few experimental and theoretical studies of the phonon transport in halide perovskites have appeared, but most of them have been carried out for the organic-inorganic hybrid materials which exhibit soft lattice expectedly due to the presence of organic cations.[39-46]

The investigations of phonon transport (thermal conductivity) in all-inorganic halide perovskites, which exhibit improved stability over their organic-inorganic hybrid counterpart, is rather rare.[47-50] The difference in thermal transport properties between organic-inorganic hybrid perovskites and the conventional all-inorganic $CsPbX_3$ (X = I, Br) arises due to distinctly different dynamics of the organic and inorganic cations.[43, 51] Recently, ultralow thermal conductivity in the range of 0.38-0.45 W/mK for three dimensional (3D) all-inorganic halide perovskite nanowires ($CsSnI_3$, and $CsPbX_3$) has been reported, which is attributed to the rattling of Pb/Sn-X clusters.[47] Fenwick et al.

reported similar thermal conductivity values for mixed $CsSnI_{3-x}Cl_x$ perovskite thin films.[48] However, such phonon transport investigations have been mainly carried out in 3D all-inorganic halide perovskites.

In contrast, while two-dimensional (2D) perovskites have created sensation in photovoltaics and optoelectronics,[52, 53] the phonon transport studies along with the fundamental understanding of lattice dynamics of these 2D layered all-inorganic perovskites are lacking. 2D Ruddlesden-Popper (RP) perovskites have recently gained widespread attention for their distinctive properties of large exciton binding energy, strong quantum confinement effect and enhanced stability.[54-57] The formula of Cs-Pb-X based RP perovskite is to be $Cs_{n+1}Pb_nX_{3n+1}$, where the n layers of $CsPbX_3$ unit are separated by an extra CsX layer. For example, the crystal structure of RP phase of $Cs_2PbI_2Cl_2$ (n =1) adopts the K_2NiF_4-type structure. The single-layer RP structure (n = 1) is composed of the corner-shared $[PbI_2Cl_4]^{4-}$ octahedral unit, in which the Cl and I atoms occupying the in-plane bridging and out-of-plane apical sites, respectively (see Figure 4.1.1a).[57]

In this chapter, we have demonstrated intrinsically ultralow lattice thermal conductivity (κ_L) of ~ 0.37-0.28 W/mK in the 295-523 K temperature range in a single crystal of layered Ruddlesden-Popper (RP) perovskite, $Cs_2PbI_2Cl_2$, synthesized by Bridgman method. We have measured an anisotropic ultralow κ_L along perpendicular and parallel to the Bridgman growth direction. An intriguing lattice dynamics in $Cs_2PbI_2Cl_2$ is noticed due to its anisotropic chemical bonding with co-existing mixed ionic (weak) and covalent (strong) bonding. Our first-principles density functional theoretical (DFT) calculations reveal that ns^2 lone pair induced anharmonic low energy vibration (~12 cm^{-1}) of Cl atoms dynamically distorts the octahedra around the Pb atoms. Moreover, the acoustic phonon modes strongly overlap with the localized vibrations of Cs and I atoms originating from weak chemical bonding and electrostatic repulsions of the lone pairs. The presence of such low energy optical phonon modes constituting flat bands that induce localized vibrations has been further experimentally confirmed from the low-temperature heat capacity and temperature dependent Raman spectroscopy. DFT calculations further reveal that the layered $Cs_2PbI_2Cl_2$ has exceptionally low bulk and shear moduli that causing low acoustic phonon frequency (maximum frequency ~37 cm^{-1}), which is one of the lowest among various low thermal conductive crystalline materials. The damped

acoustic phonon modes and strong acoustic-optical phonon mode coupling result in an ultralow κ_L value in all-inorganic 2D RP perovskite, $Cs_2PbI_2Cl_2$.

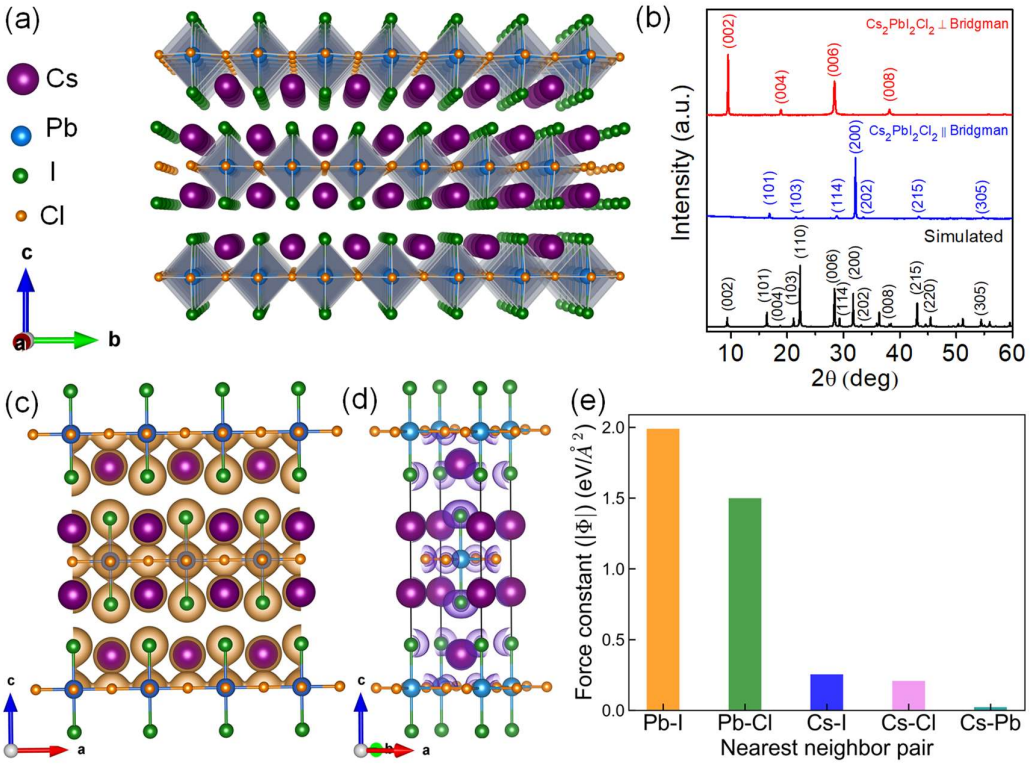

Figure 4.1.1. *(a) Crystal structure of the 2D Ruddlesden−Popper (RP) halide perovskite $Cs_2PbI_2Cl_2$. (b) Room-temperature XRD pattern of Bridgman grown $Cs_2PbI_2Cl_2$ cut in different directions. Iso-surfaces of the DFT calculated (c) total charge density and (d) electron localization function (ELF) visualized at an iso-surface value of 0.85 on a scale of 0−1. (e) Second-order interatomic force constants (IFC, Φ) for the nearest neighbor atom pairs in $Cs_2PbI_2Cl_2$.*

4.1.2. Methods

Materials. Cesium (I) chloride (CsCl, 99.9%, Sigma Aldrich) and lead (II) iodide (PbI_2, 99.9%, Sigma Aldrich) were used without further purification.

Bridgman crystal growth. $Cs_2PbI_2Cl_2$ single crystal was grown in a Bridgman furnace. $Cs_2PbI_2Cl_2$ was synthesized by melting stoichiometric amount of CsCl and PbI_2 in a 10 mm quartz tube sealed under a high vacuum of 10^{-6} Torr. In order to grow the large single crystal (Figure 4.1.2), first, the starting materials were heated to 923 K for 48 hrs. The

melt was then pulled in a temperature gradient from 773 K to 623 K at a speed of 0.77 mm/hr. Finally, the sample was slowly cooled to room temperature in 96 h.

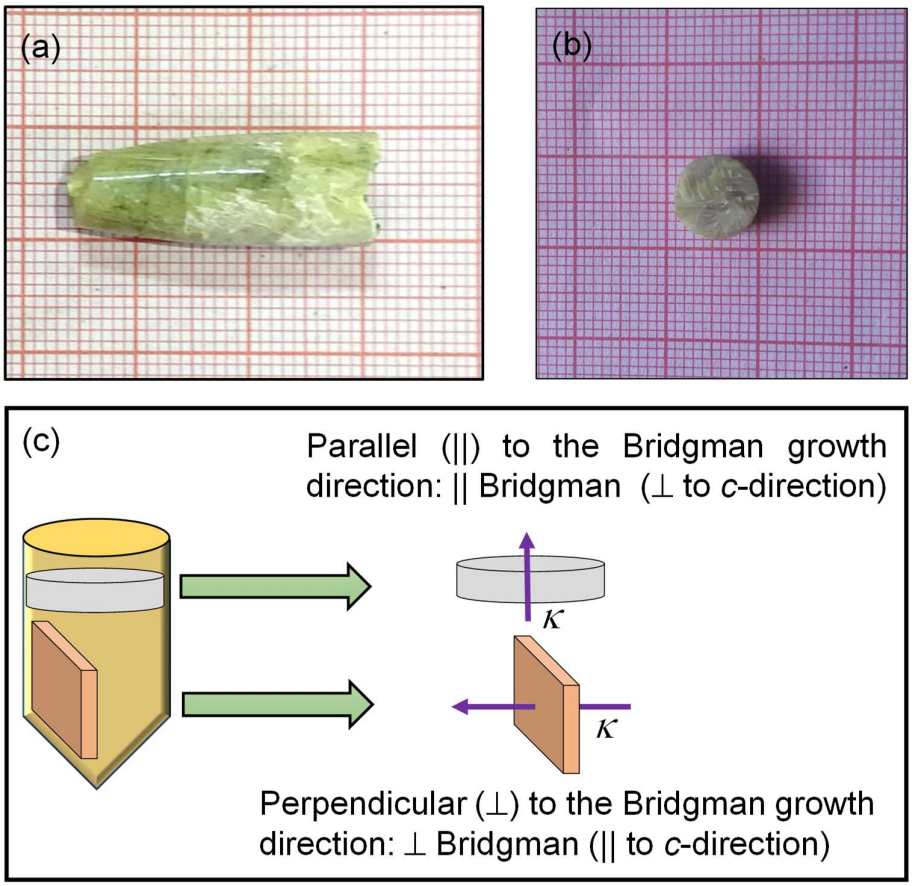

Figure 4.1.2. *(a) Photograph of $Cs_2PbI_2Cl_2$ Bridgman grown crystal. The high quality of the $Cs_2PbI_2Cl_2$ sample after cutting is shown in (b). (c) A schematic exhibiting the Bridgman grown $Cs_2PbI_2Cl_2$ single crystal was cut for thermal conductivity measurement.*

X-ray diffraction (XRD). Room temperature XRD pattern of $Cs_2PbI_2Cl_2$ was collected in Bruker D8 diffractometer using Cu Kα radiation (λ= 1.5406 Å). Synchrotron powder X-ray diffraction data was collected from finely ground powder using a synchrotron X-ray beam of λ = 0.7749 Å, at BL-18B (Indian beamline), Photon Factory, KEK, Tsukuba, Japan. The energy of the beam was set by a Si (111) double crystal monochromator and analyzed with standard Si (640b NIST). All the measurements were performed in

Bragg−Brentano geometry with a divergence slit (300 μm), an anti-scattering slit (350 μm), and a receiving slit (300 μm). Rietveld refinement of synchrotron powder X-ray diffraction data was performed using Fullprof program.

Thermal conductivity. Thermal diffusivity, D, was measured using laser flash diffusivity technique in Netzsch LFA-457 instrument in the temperature range of 295-523 K. Typical square (~8 x 8 mm^2) and coin (~8 mm diameter) shaped samples of thickness ~1.9 mm were used for the measurement of thermal transport properties. Then, thermal conductivity (κ) was estimated using the relation, $\kappa = D \times C_p \times \rho$, where ρ is the density of the sample and C_p is the specific heat. The obtained density of the single crystal is ~97.4 % of the theoretical density. We have used the Dulong – Petit C_p (0.21 J/g/K) for the estimation of thermal conductivity.

Calculation of minimum thermal conductivity (κ_{min}).

Minimum lattice thermal conductivity, κ_{min} in the Cahill's Model[58] can be expressed as,

$$\kappa_{min} = \frac{1}{2}\left(\frac{\pi}{6}\right)^{1/3} k_B V^{-2/3}(v_l + 2v_t)$$

where k_B is the Boltzmann constant, V is the average volume per atom, ν_t and ν_l are the transverse and longitudinal sound velocities, respectively. The estimated values of ν_t and ν_l for $Cs_2PbI_2Cl_2$ from phonon dispersion (DFT calculated) are 1360 m/s and 2460 m/s, respectively.

Heat capacity measurement. Low-temperature heat capacity (C_p) of $Cs_2PbI_2Cl_2$ was measured in a Physical Property Measurement System (PPMS) in the temperature range of 2-25 K.

Raman spectroscopy. The Raman spectroscopy measurements are done in collaboration with Prof. Ajay Soni, IIT Mandi, India. Raman spectroscopic measurements were performed using Jobin-Yvon Horiba LabRAM HR evolution Raman spectrometer in backscattering geometry with 1800 gr/mm grating and Peltier cooled CCD detector.

Ultra-low frequency filters were used to detect the vibrational modes close to Rayleigh line. Temperature-dependent Raman measurements were performed using close cycle cryostat (Montana Instruments, USA) in the range of 100 K - 300 K, using 532 nm laser excitation (0.75 mW power) and 10 seconds of acquisition time. All the spectra were baseline corrected, normalized, and fitted with the Lorentzian function.

Optical spectroscopy. The optical bandgap was recorded using a PerkinElmer, Lambda-900 UV/Vis/near-IR spectrometer in reflectance mode within the range of 250-800 nm. The absorption data (α/S) of $Cs_2PbI_2Cl_2$ was estimated from reflectance data using Kubelka–Munk equation; $\alpha/S = (1-R)^2/(2R)$; where R, α, and S denote reflectance, absorption, and scattering coefficients, respectively.

Field emission scanning electron microscopy (FESEM). FESEM images were taken using ZEISS Gemini SEM – Field Emission Scanning Electron Microscope.

Thermogravimetric analysis (TGA). TGA experiments were carried out using a 2 STAR TGA instrument. Powdered samples were heated in the temperature range of 300 - 1273 K in N_2 atmosphere at a rate of 5 K/min.

Computational details. Theoretical calculations are done in collaboration with Prof. U. V. Waghmare, JNCASR, India. Density functional theory (DFT) calculations were performed using the Vienna Ab-initio Simulation Package (VASP) [59, 60] using the projector augmented wave (PAW)[61, 62] methods and VASP recommended potentials. We utilized the PBEsol[63] generalized gradient approximation (GGA)[64] to the exchange-correlation functional. We used a kinetic energy cut-off of 520 eV and k-point mesh of 10 × 10 × 10 for the relaxation of the cell parameters as well as static calculations. The optimized lattice parameters (a = b = 5.627 Å, c = 18.858 Å) agree well with the experimental values (a=b= 5.6512(1) Å, c= 18.973(1) Å). We calculated the phonon dispersion of $Cs_2PbCl_2I_2$ using the supercell method in Phonopy,[65] where the displaced configurations were generated using 2×2×2 supercell (containing 56 atoms) of the primitive unit cell (with seven atoms). For phonon calculations, we used 5×5×5 mesh of k-points while calculating the total enegies of the displaced configurations. We included

the LO-TO splitting arising from the long-range interactions while calculating the phonon dispersion and phonon density of states. The high-symmetry points in the Brillouin zone are taken from Setyawan's work.[66] We determined the mode Grüneisen parameters of $Cs_2PbCl_2I_2$ using a finite difference method where we have calculated the phonon frequencies of the compound at two different volumes ($1.02xV_0$ and $0.98xV_0$, V_0 being the equilibrium unit cell volume) and utilized the formula $\gamma_{qn} = - d\ln(\gamma_{qn})/d\ln(V)$ where γ_{qn} and V denote Grüneisen parameter and unit cell volume, respectively.

4.1.3. Results and Discussion

The tetragonal crystal structure of $Cs_2PbI_2Cl_2$ (Figure 4.1.1a; space group, I4/mmm) consists of corner sharing PbI_2Cl_4 octahedra forming the 2D layer. The layers are separated by the Cs^+ ions, which stabilizes the crystal structure by transferring its charge to the layers. We have analyzed the electronic charge density and their iso-surfaces using DFT to understand the local chemical bonding environment (Figure 4.1.1c). The overlapping charge clouds of Pb with I and Cl within the octahedra signify the presence of directed covalent bonding, which are formed by the sharing of electrons between the Pb and the two halide (I and Cl) atoms. On the other hand, the absence of covalent bonding for Cs^+ ions are evident from their non-overlapping charge spheres, which interact with rest of the lattice through ionic interactions. This mixed ionic and covalent bonding interactions (i.e. bonding hierarchy) give rise to a large difference in the bond strengths between the cations (Cs, Pb) and anions (Cl, I), which is evident from the DFT calculated inter-atomic force constants (IFCs) (Figure 4.1.1e). IFCs of nearest neighbor Pb-I and Pb-Cl pairs have the highest values of 1.9 eV/Å^2 and 1.5 eV/Å^2, respectively, indicating their stronger bonding. On the other hand, the small value of IFCs for the nearest neighbor Cs-I (0.3 eV/Å^2) and Cs-Cl (0.2 eV/Å^2) pairs imply the weak interactions of Cs atoms in the lattice. Moreover, the analysis of the electron localization function (ELF) (Figure 4.1.1d) reveals the presence of $3s^2$ and $5s^2$ lone pairs around Cl and I atoms, respectively. Interestingly, our analysis based on orbital resolved density of states (Figure 4.1.3) and ELF (Figure 4.1.4) shows that the partially hybridized $6s^2$ lone pair of Pb is weakly localized below the Fermi level. The disparate bond-strengths, large mass difference between the constituent atoms and the electrostatic repulsions arising from the

lone pairs are expected to give rise to an intriguing anharmonic lattice dynamics in $Cs_2PbI_2Cl_2$.

A high-quality single crystal of $Cs_2PbI_2Cl_2$ was grown using Bridgman method (see Figure 4.1.2a-b and experimental method). Room temperature XRD pattern of the different directional cut of the single crystal exhibits oriented growth of the crystal planes

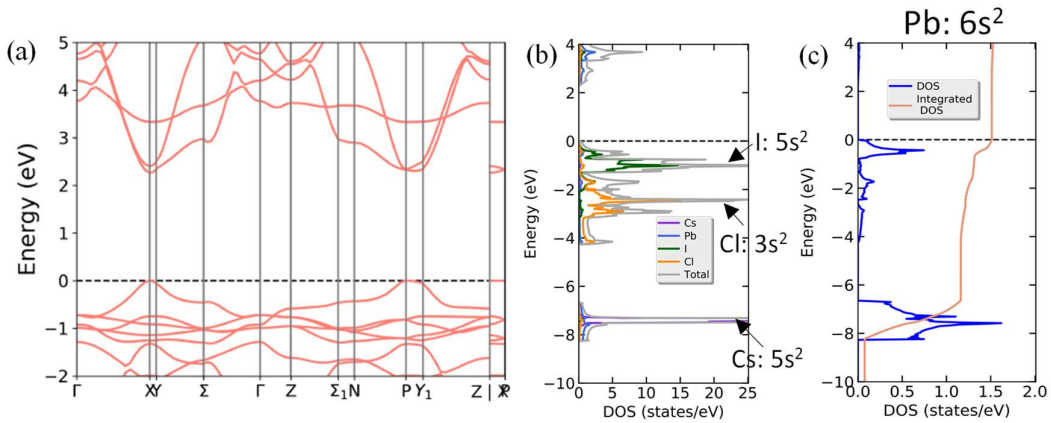

Figure 4.1.3. *(a) Electronic structure (without SOC) and (b) atom resolved electronic density of state (DOS) of $Cs_2PbI_2Cl_2$, and (c) DOS and integrated DOS of 6s states of Pb.*

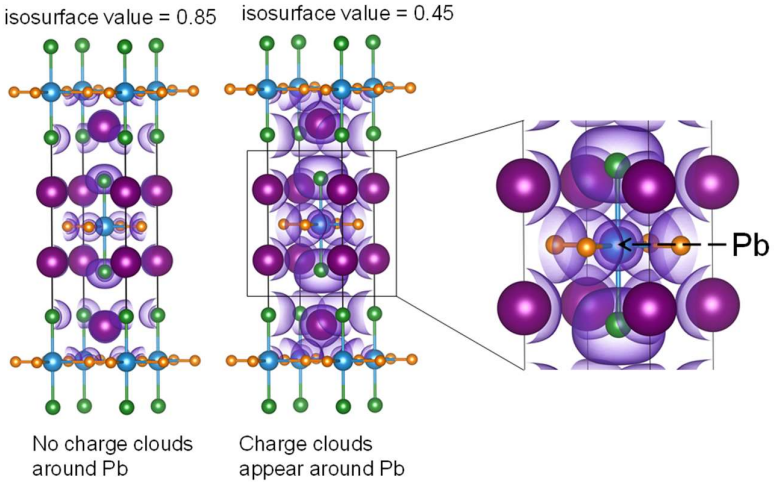

Figure 4.1.4. *Electronic localization function (ELF) of $Cs_2PbI_2Cl_2$ visualized at different values of the iso-surfaces. Cs, I, Pb and Cl atoms are denoted by the violet, green, blue and orange spheres, respectively.*

both for perpendicular and parallel to the Bridgman growth directions (Figure 4.1.1b). The 2D layers stack along perpendicular to the Bridgman growth direction. Further, room

temperature XRD pattern (Figure 4.1.5a; λ = 1.5406 Å) of the finely grounded powder of the single crystal exhibits high purity and all the peaks could be indexed based on the tetragonal structure (space group, I4/mmm). The obtained lattice parameters from the Rietveld refinement of synchrotron PXRD (λ = 0.7749 Å) pattern are a = b = 5.6512(1) Å, c = 18.973(1) Å (Figure 4.1.5b, and Table 4.1.1). Electronic absorption spectra exhibit an absorption edge at 3.06 eV along with a small kink near the absorption edge (Figure 4.1.5c), which can be ascribed to excitonic absorption as reported previously.[57] Field emission scanning electron microscopy (FESEM), energy dispersive X-ray (EDX) analysis and elemental colour mapping of the Bridgman grown $Cs_2PbI_2Cl_2$ single crystal indicate high quality of the synthesized crystal (Figure 4.1.6). Further, the EDX elemental colour mapping confirms the uniform distribution of the constituent Cs, Pb, I and Cl elements in the sample. Thermogravimetric analysis (TGA) exhibit that $Cs_2PbI_2Cl_2$ is thermally stable up to 793 K (Figure 4.1.5d).

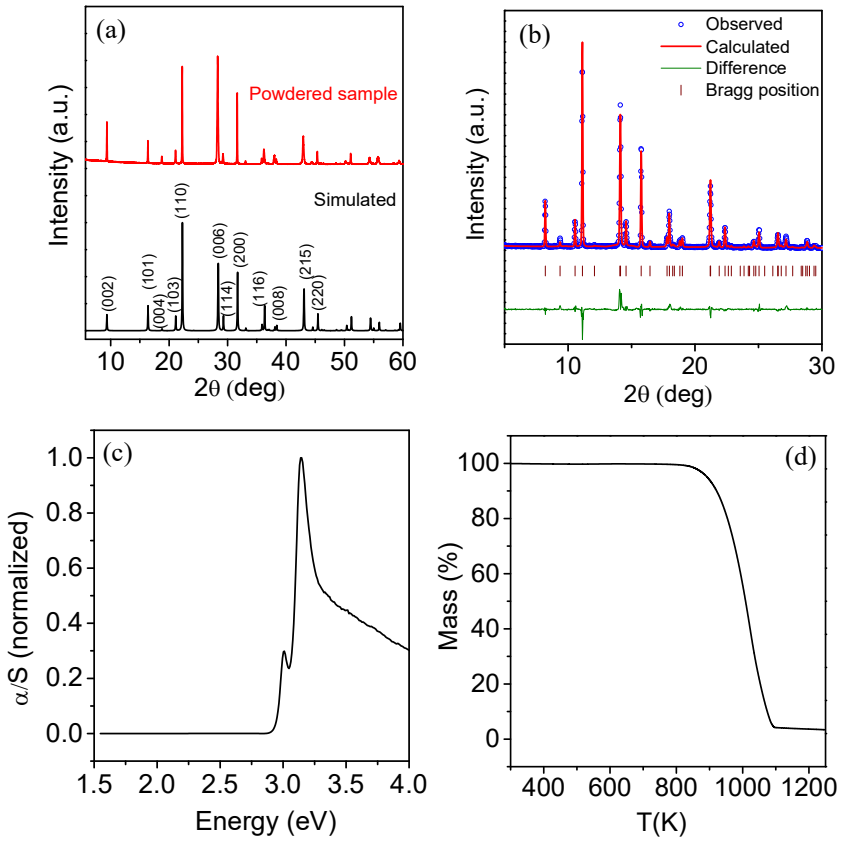

Figure 4.1.5. *(a) XRD pattern from finely grounded powder of the $Cs_2PbI_2Cl_2$ single crystal. (b) Rietveld refinement of the synchrotron (λ = 0.7749 Å) PXRD data and (c) optical absorption spectra of $Cs_2PbI_2Cl_2$. (d) TGA profile of $Cs_2PbI_2Cl_2$ in N_2 atmosphere.*

Table 4.1.1. *Reitveld refinement parameters of $Cs_2PbI_2Cl_2$.*

Space group: I 4/mmm; a=b= 5.6512(1) Å, c= 18.973(1) Å, $\alpha = \beta = \gamma = 90^0$; $\chi^2 = 5.99$					
Atom	**x**	**y**	**z**	**Occupancy**	**U_{iso}(Å^2)**
Pb	0.500	0.500	0.500	1	0.055
Cs	0.000	0.000	0.3712(4)	1	0.078
I	0.500	0.500	0.6684(3)	1	0.090
Cl	0.500	0.000	0.500	1	0.092

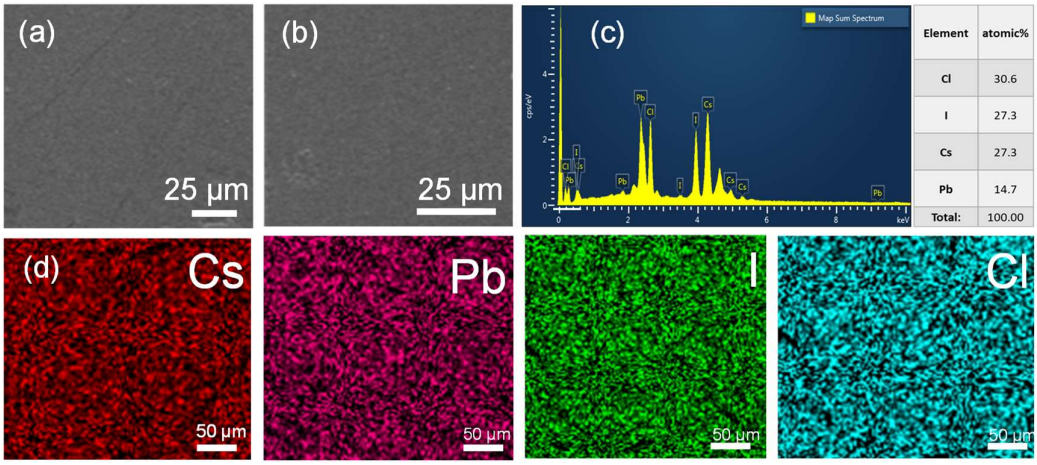

Figure 4.1.6. *(a, b) FESEM for Bridgman grown $Cs_2PbI_2Cl_2$ with corresponding EDAX spectra in (c). (d) EDAX elemental color mapping for Cs, Pb, I and Cl for the area in (a).*

We have measured anisotropic thermal conductivity of $Cs_2PbI_2Cl_2$ single crystal along perpendicular (⊥) and parallel (||) to the Bridgman growth directions (see schematic in Figure 4.1.2c). Perpendicular (⊥) to the Bridgman growth direction coincides with the crystallographic c-axis of $Cs_2PbI_2Cl_2$. Thermal conductivity of $Cs_2PbI_2Cl_2$ single crystal

(Figure 4.1.7a) decreases with increasing temperature, similar to typical crystalline materials. The room temperature thermal conductivity of $Cs_2PbI_2Cl_2$ along perpendicular (⊥) and parallel (||) to the Bridgman growth directions are 0.37 and 0.41 W/mK, respectively. Lower thermal conductivity along perpendicular (⊥) to the Bridgman growth direction (along the crystallographic c-axis; see Figure 4.1.2c) is due to the stacking of layers along c-axis in $Cs_2PbI_2Cl_2$. A comparison of thermal conductivity of $Cs_2PbI_2Cl_2$ with other state-of-the-art low thermal conductive crystalline materials and 3D all-inorganic halide perovskites are also shown in Figure 4.1.7b and Figure 4.1.8, respectively. The resistivity of $Cs_2PbI_2Cl_2$ is in the range >100 MΩ-cm. This high resistivity is expected because of the highly insulating nature of $Cs_2PbI_2Cl_2$ (bandgap of ~ 3.06 eV). Thus, electrical contribution (κ_{el}) in the total thermal conductivity is negligible and the thermal transport of $Cs_2PbI_2Cl_2$ is primarily dominated by the lattice contribution (κ_L). The thermal conductivity value along perpendicular (⊥) to the Bridgman growth direction is ~0.28 W/mK at 523 K, which is close to the theoretical minimum of lattice thermal conductivity, κ_{min} ~ 0.23 W/mK calculated using Cahill's Model[58] (for details, see method). The ultralow κ_L of $Cs_2PbI_2Cl_2$ is similar to various intrinsically ultralow thermal conductive state-of-the-art heavy metal chalcogenides such as Tl_3VSe_4 (~ 0.30 W/mK at 300 K),[20] SnSe (~ 0.46-0.68 W/mK at 300 K),[24] and $AgCrSe_2$ (~ 0.20 W/mK at 300 K).[67]

We have measured low temperature (2-25 K) heat capacity (C_p) to comprehend the experimentally observed ultralow thermal conductivity of $Cs_2PbI_2Cl_2$ and found that Debye model does not fully account for the observed temperature variation of C_p (Figure 4.1.7c). Subsequently, we attempted to fit the low-temperature C_p data using Debye-Einstein model:[18, 25]

$$\frac{C_p}{T} = \gamma + \beta T^2 + \sum_n \left(A_n \left(\theta_{E_n}\right)^2 . (T^2)^{-3/2} . \frac{e^{\theta_{E_n}/T}}{\left(e^{\theta_{E_n}/T} - 1\right)^2} \right)$$

in which γ is the Sommerfeld coefficient which accounts for the electronic contribution. $\beta = C(12\pi^4 N_A k_B/5) \cdot (\Theta_D)^{-3}$ signifies the lattice contribution, where N_A, k_B and Θ_D are the Avogadro's number, Boltzmann constant and Debye temperature, respectively and C is defined as, $C = 1 - \sum_n A_n/3NR$, where N represents the number of atoms per formula

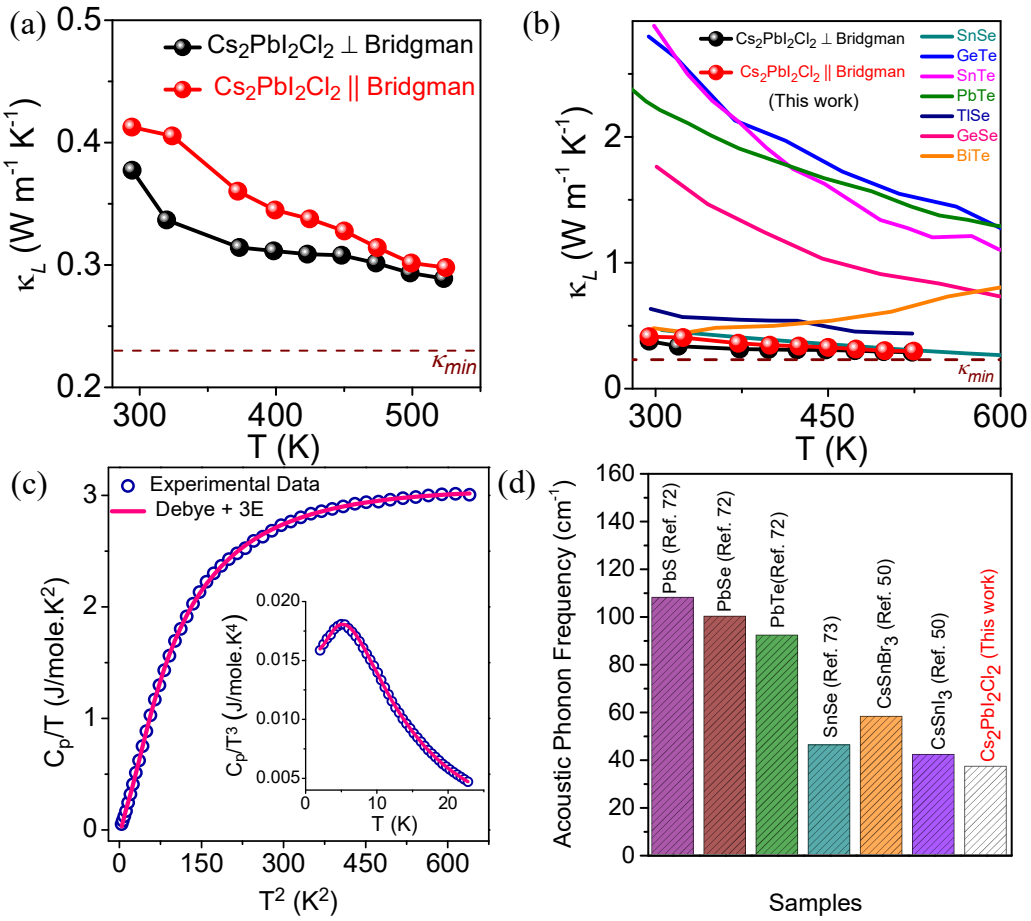

Figure 4.1.7. *(a) Temperature-dependent lattice thermal conductivity (κ_L) of $Cs_2PbI_2Cl_2$ measured parallel (∥) and perpendicular (⊥) to the Bridgman growth directions. (b) Comparison of temperature-dependent thermal conductivity of the Bridgman-grown $Cs_2PbI_2Cl_2$ single crystal with well-known ultralow thermal conductive crystalline materials. References in the plot are SnSe,[24] GeTe,[68] SnTe,[1] PbTe,[69] TlSe,[19] GeSe,[70] and BiTe.[71] (c) Low-temperature Cp/T versus T^2 plot of $Cs_2PbI_2Cl_2$ and fit with Debye−Einstein model. Inset shows the Cp/T^3 versus T plot exhibiting a Boson-like peak in low-temperature Cp. (d) Comparison of acoustic phonon frequency $Cs_2PbI_2Cl_2$ with well-known low thermal conductive heavy metal chalcogenides[72, 73] and 3D all-inorganic halide perovskites.[50]*

unit and R denote the universal gas constant (R = 8.314 J mol^{-1}K^{-1}). The third term in equation 1 describes the contributions of Einstein oscillators corresponding to the localized vibrations, where θ_{E_n} is the Einstein temperature for the nth mode. We find a good fit of the low-temperature C_p data of $Cs_2PbI_2Cl_2$ using Debye-Einstein model with

three Einstein modes of θ_{E_1} = 19 K (13 cm^{-1}), θ_{E_2} = 45 K (31 cm^{-1}) and θ_{E_3} = 88 K (61 cm^{-1}) (Figure 4.1.7c and Table 4.1.2). These low-frequency Einstein modes can be attributed to the localized vibrations of halides atoms (Cl and I) in $Cs_2PbI_2Cl_2$ (Figure 4.1.9a, b; discussed in the next paragraph). The obtained Debye temperature is 109 K, which is significantly lower compared to the Debye temperature of well-known low thermal conductive materials like PbTe (164 K), SnSe (142 K) etc.[25] The corresponding sound velocity (v_a) of $Cs_2PbI_2Cl_2$, derived using the following equation[74]:

$$\Theta_D = \frac{h}{k_B}\left(\frac{3N}{4\pi V}\right)^{1/3} v_a$$

where h is Plank's constant, is 1284 ms^{-1}. Such low sound velocity corroborates the experimentally observed ultralow thermal conductivity of $Cs_2PbI_2Cl_2$. Moreover, we observed a broad Boson-like peak in the C_p/T^3 vs. T plot (inset of Figure 4.1.7c), similar to various other low thermal conducting materials like heavy metal chalcogenides,[19, 20] skutterudites[17] and clathrates.[29] This peak originates from the contribution in C_p from excess optical phonon density of states due to the localized low energy vibrations.[29]

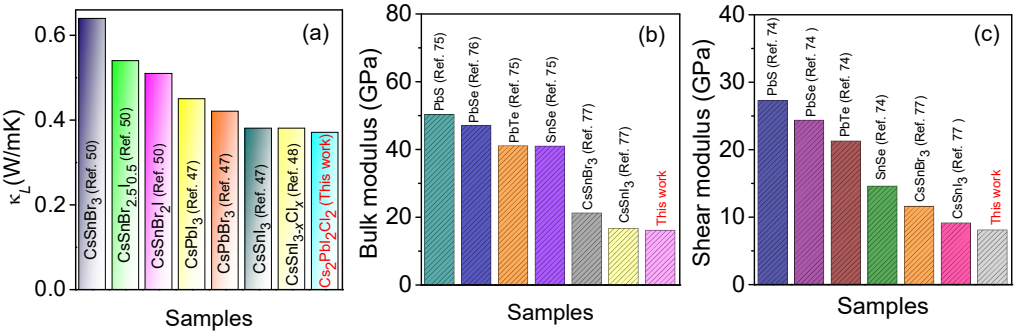

Figure 4.1.8. *(a) Comparison of room temperature lattice thermal conductivity of $Cs_2PbI_2Cl_2$ with previously reported various 3D all-inorganic halide perovskites.[47, 48, 50] Comparison of our DFT calculated (b) bulk modulus and (c) shear modulus of $Cs_2PbI_2Cl_2$ with several well-known low thermal conductive metal chalcogenides[74-76] and 3D all inorganic metal halide perovskites.[77]*

In order to understand the experimentally observed ultralow thermal conductivity and the origin of localized vibrations, we determined the phonon spectrum of $Cs_2PbI_2Cl_2$ using DFT finite-displacement method with the inclusion of LO-TO splitting. Calculated phonon dispersion (Figure 4.1.9a) contains soft acoustic phonon modes with a frequency

below 37 cm^{-1}. Frequencies of acoustic phonons of $Cs_2PbI_2Cl_2$ are lower than that of other low thermal conductive heavy metal chalcogenides and 3D all-inorganic halides perovskite (Figure 4.1.7d). This is reflected in its calculated bulk and shear moduli (16 GPa and 8 GPa, respectively) revealing its soft elastic nature associated with the layered structure of $Cs_2PbI_2Cl_2$. The bulk and shear moduli of $Cs_2PbI_2Cl_2$ are comparatively lower than that of the low thermal conductive crystalline heavy metal chalcogenides and other 3D all-inorganic halide perovskites (Figure 4.1.8b,c). Consequently, it exhibits rather low sound velocities along the different directions in the Brillouin zone (Table 4.1.3). We further find numerous low-energy optical phonon branches (< 55 cm^{-1}) with minimal dispersions (Figure 4.1.9a). Such flat, dispersion-less phonon bands permit localized vibrational modes with vanishingly low group velocities. With a notable overlap in frequencies of acoustic phonons, their strong coupling with acoustic waves give numerous channels of phonon scattering .[78-80] The soft layered structure together with the flat bands of low-energy optical modes and strong acoustic-optical phonon mode coupling pave the way towards the intrinsically ultralow lattice thermal conductivity in $Cs_2PbI_2Cl_2$.

Table 4.1.2. *Parameters obtained from fitting of low-temperature C_p/T vs. T^2 data of $Cs_2PbI_2Cl_2$ using Debye - Einstein model with 3 Einstein oscillators.*

Parameter	Value
γ (J/mole.K^2)	0.012
θ_D (K)	109
θ_{E1} (K)	19
θ_{E2} (K)	45
θ_{E3} (K)	88

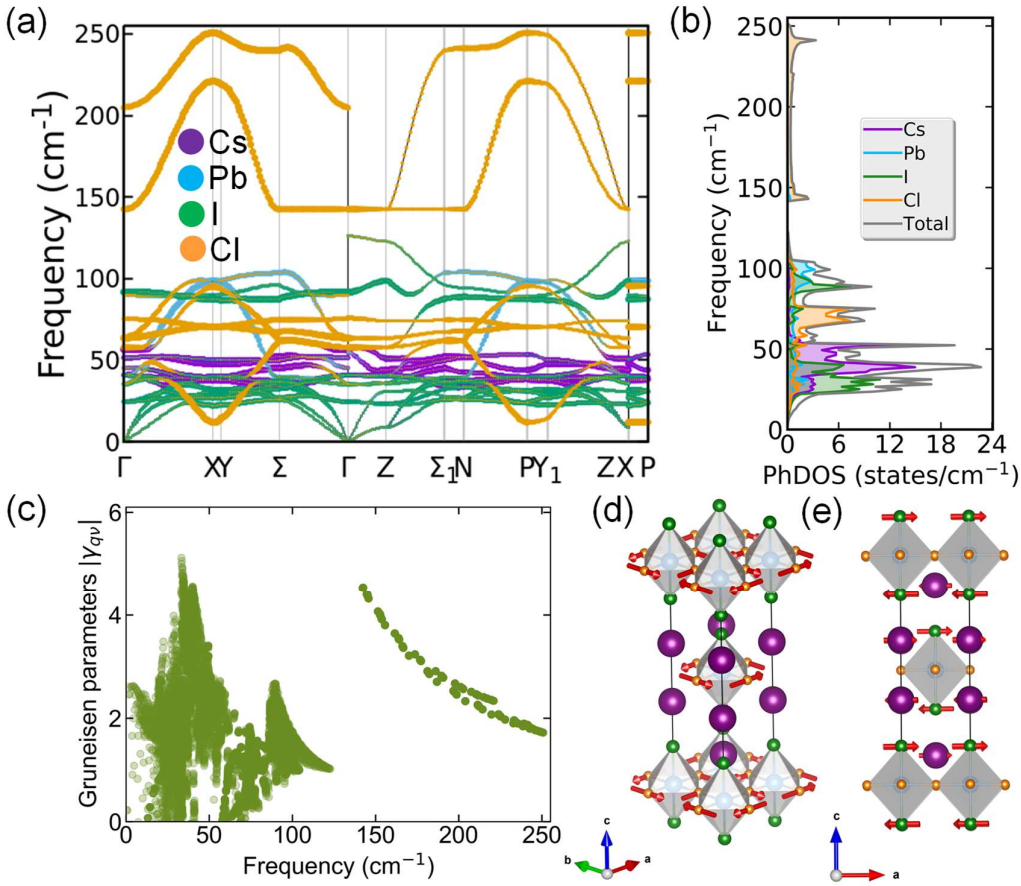

Figure 4.1.9. *(a) Atom-resolved phonon dispersion, (b) phonon density of states, (c) mode Grüneisen parameters of $Cs_2PbI_2Cl_2$. Eigenvectors of the (d) lowest frequency (ω = 12 cm^{-1}) phonon mode at X point which involves vibration of only Cl atoms on equatorial plane of the octahedra and (e) phonon mode at Γ point which involves vibration of I atoms (ω= 25 cm^{-1}). Cs, I, Pb and Cl atoms are denoted by the violet, green, blue, and orange spheres, respectively.*

The atom-resolved phonon dispersion (Figure 4.1.9a) shows that the low-frequency optical branches in the range 18 cm^{-1} < ω < 40 cm^{-1} arise mainly from the vibrations of the I atoms, while the phonon branches lying in the range of 25 cm^{-1} < ω < 55cm^{-1} are from the vibrations of the Cs atoms, which partially overlap with the former in the frequency range of 25 cm^{-1} < ω < 40 cm^{-1}. Hybridization or interactions between these two groups of phonons is evident in the atom-resolved phonon density of states (Figure 4.1.9b). The low energy vibrations of Cs atoms arise from the fact that the Cs atoms are weakly bonded (ionic) to the lattice, whereas the soft vibrations of I atoms

originates from the electrostatic repulsions of lone pairs around the anionic species. Interestingly, the lowest energy (12 cm^{-1}) optical phonon branches that appears along the X-Y and P-Y_1 directions have predominant Cl characters, which involves the dynamic rotation of the octahedra around Pb. We have visualized the eigenvectors of two low-energy optical phonon modes (i.e., 12 cm^{-1} at X point and 25 cm^{-1} at Γ point) in the conventional unit cell in Figure 4.1.9d and 9e. While the mode (Figure 4.1.9d) at X point involve dynamic rotations of PbX_6 octahedra with displacements of Cl atoms, the mode (Figure 4.1.9e) at Γ point involves dynamic octahedral tilts with displacements of I atoms. The octahedral tilting at 25 cm^{-1} (see Figure 4.1.9e) induces inter-layer sliding which is corresponding to soft shear waves.

Table 4.1.3. *Sound velocities along different directions in the Brillouin zone and average sound velocity of $Cs_2PbI_2Cl_2$.*

Directions	Sound velocity (m/s)			
	LA	TA1	TA2	Average
Γ-X	2396	1707	1204	1769
Γ–Σ	2785	1198	1198	1727
Γ-Z	2060	642	642	1114
Overall	2460	1360	1360	1460

The contributions of Pb atoms to the phonon branches (Figures 4.1.9a and 4.1.9b) are dispersed in a wide energy window of the phonon spectra, which is expected because of its strong bonding (covalent) with halogens in the compound. Soft phonon modes in a crystalline compound typically exhibit strong anharmonicity.[81] To quantify its strength, we have calculated the mode Grüneisen parameters $\gamma_{q\upsilon}$ (Figure 4.1.9c), which clearly show strong coupling between the acoustic and low-energy phonons corresponding to PbX_6 dynamic rotations and tilts. As the phonon scattering rates inversely proportional to the phonon lifetime[82] and increase with the inverse square of $\gamma_{q\upsilon}$[83], the phonons in $Cs_2PbI_2Cl_2$ have short lifetimes, and hence an ultralow κ_L

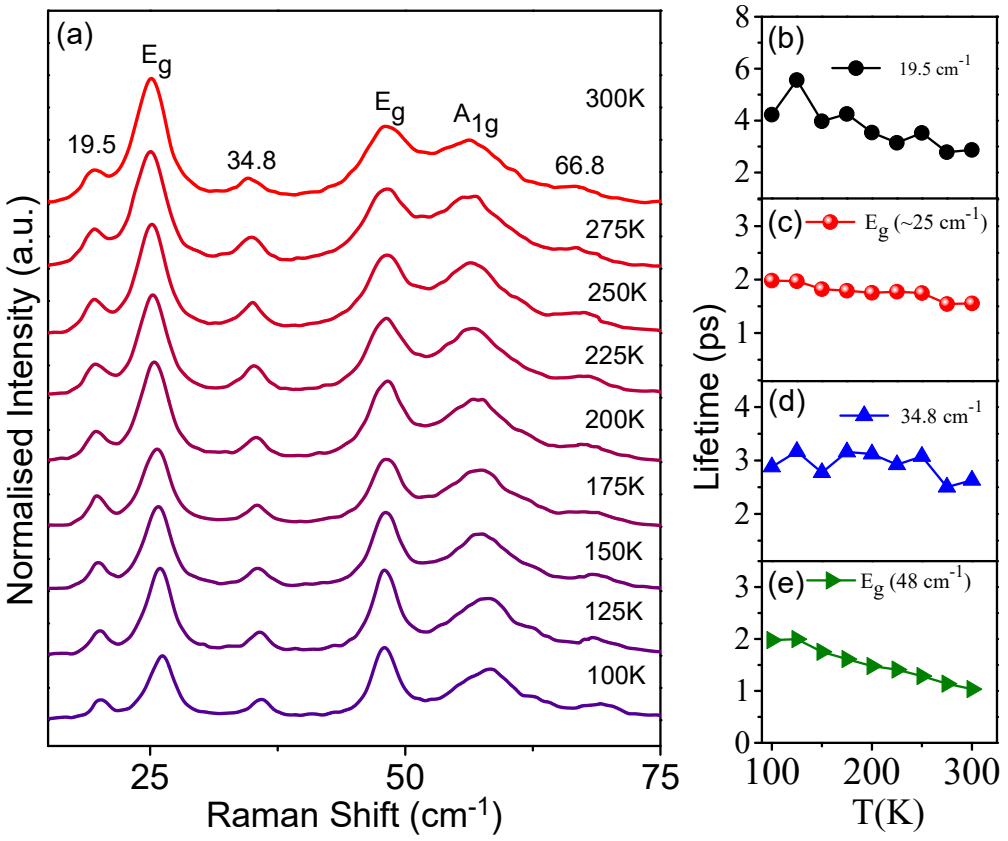

Figure 4.1.10. *(a) Temperature dependent Raman spectra of $Cs_2PbI_2Cl_2$ in the 100 -300 K range. (b-e) Temperature variation of phonon lifetime for various modes.*

From the Raman spectra of $Cs_2PbI_2Cl_2$ in the temperature range of 100 – 300 K, shown in Figure 4.1.10a, we confirm vibrational modes at ~ 20, 25, 35, 48, 57 and 67 cm^{-1} at 300 K. The modes at ~ 25 cm^{-1} and ~ 48 cm^{-1} have been assigned to E_g symmetry, while the mode at ~ 57 cm^{-1} has A_{1g} symmetry according to the theoretical analysis of Γ point phonon modes (see visualization of the Eigen modes at Γ point in Figure 4.1.11a). A careful examination of atom resolved phonon dispersion (Figure 4.1.9a) suggests that the low energy modes generally involve the vibration of halide atoms giving PbX_6 octahedral tilts. Additional Raman modes observed at ~ 20 cm^{-1}, 35 cm^{-1} and 67 cm^{-1} appear possibly due to structural disorder associated with local structural distortions. Such local structural distortions effectively cause doubling of the periodic unit cell, folding back the X and Z points of the Brillouin zone to Γ point. From our DFT results, we identify the modes at ~20 cm^{-1} and ~35 cm^{-1} to be associated with the twisting of axial Pb-I bonds in the PbI_2Cl_4 octahedra at X-point and Z- point as shown in Figures 4.1.11b

and 11c. The mode at 67 cm^{-1} involves out of plane vibration of Cl atoms as shown in Figure 4.1.11b and 11c. The phonon lifetime ($\tau_i = \frac{1}{2\pi(FWHM)_i}$) estimated from full width at half-maximum (FWHM) also decreases with increase in temperature from 100 K to 300 K for all the modes (Figure 4.1.10b-e).[82] The estimated phonon lifetimes are in the range of 0.5 to 4 ps, which are comparable to those of complex chalcogenides and clathrates reported earlier.[82,84] The small phonon lifetime and its further decrease with increasing temperature suggest significant increase in phonon scattering with temperature and thereby, explains the ultralow κ_L of $Cs_2PbI_2Cl_2$.

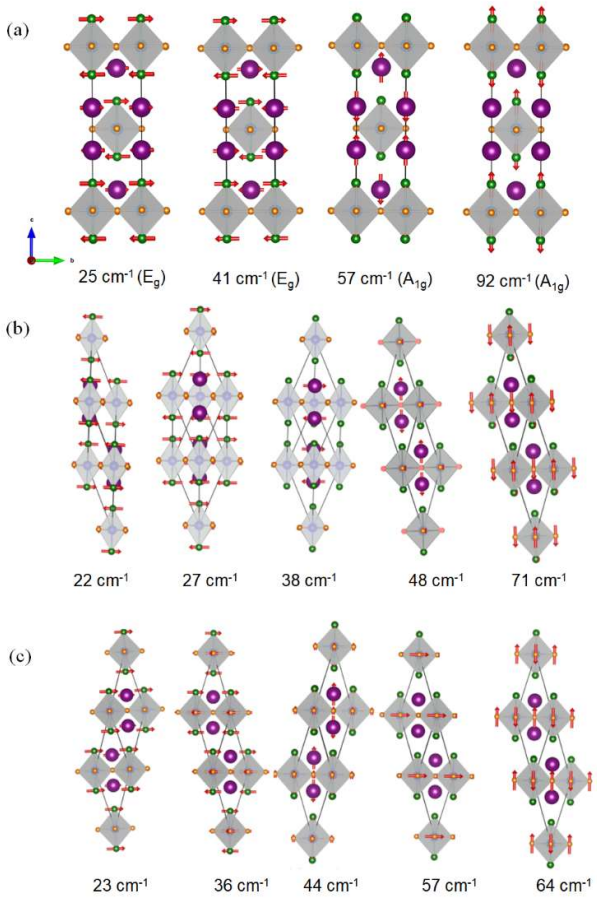

Figure 4.1.11. *Phonon modes of $Cs_2PbI_2Cl_2$ at (a) Γ point (b) X point and (c) Z point. Cs, I, Pb and Cl atoms are denoted by the violet, green, blue and orange spheres, respectively.*

4.1.4. Conclusions

In summary, we have demonstrated intrinsically ultralow thermal conductivity in the Bridgman grown single crystal of an all-inorganic 2D RP halide perovskite, $Cs_2PbI_2Cl_2$. Thermal conductivity of $Cs_2PbI_2Cl_2$ single crystal varies in the range ~0.37-0.28 W/mK in 295-523 K temperature range when measured perpendicular to the Bridgman growth direction. The heterogeneous bonding environment in $Cs_2PbI_2Cl_2$ due to the presence mixed covalent and ionic bonding results in numerous low energy localized optical phonon modes. The lowest energy optical phonon mode at ~12 cm^{-1} is associated with dynamic rotation of the PbX_6 octahedra. Flat phonon bands at low frequencies also support localized dynamic distortions comprising rotations and tilts of PbX_6 octahedra. Strong anharmonic coupling of these low frequency optical phonons with acoustic phonons results in very short phonon lifetime (0.5 - 4 ps). The ultra-soft acoustic phonon modes originating from a soft elastic layered structure of low bulk and shear moduli along with strong acoustic-optical phonon mode coupling result in intrinsically ultralow lattice thermal conductivity in $Cs_2PbI_2Cl_2$. The intriguing phonon transport properties with lone pairs induced dynamic octahedral rotations/tilts and anharmonic lattice dynamics in $Cs_2PbI_2Cl_2$ indicate the possible existence of novel thermal transport behavior in a plethora of low dimensional halide perovskites.

4.1.5. References

1. G. Tan, L.-D. Zhao and M. G. Kanatzidis, *Chem. Rev.*, 2016, **116**, 12123.

2. J. R. Sootsman, D. Y. Chung and M. G. Kanatzidis, *Angew. Chem., Int. Ed.*, 2009, **48**, 8616.

3. M. A. Green and S. P. Bremner, *Nat. Mater.*, 2017, **16**, 23.

4. M. M. Lee, J. Teuscher, T. Miyasaka, T. N. Murakami and H. J. Snaith, *Science*, 2012, **338**, 643.

5. I. Chung, B. Lee, J. He, R. P. H. Chang and M. G. Kanatzidis, *Nature*, 2012, **485**, 486.

6. T. Sadi, I. Radevici and J. Oksanen, *Nat. Photonics*, 2020, **14**, 205.

7. P. Santhanam, D. J. Gray and R. J. Ram, *Phys. Rev. Lett.*, 2012, **108**, 097403.

8. N. P. Padture, M. Gell and E. H. Jordan, *Science*, 2002, **296**, 280.

9. E. Skoplaki and J. A. Palyvos, *Sol. Energy*, 2009, **83**, 614.

10. G. Divitini, S. Cacovich, F. Matteocci, L. Cinà, A. Di Carlo and C. Ducati, *Nat. Energy*, 2016, **1**, 15012.

11. J. Yang, X. Wen, H. Xia, R. Sheng, Q. Ma, J. Kim, P. Tapping, T. Harada, T. W. Kee, F. Huang, Y.-B. Cheng, M. Green, A. Ho-Baillie, S. Huang, S. Shrestha, R. Patterson and G. Conibeer, *Nat. Commun.*, 2017, **8**, 14120.

12. Y. Yang, D. P. Ostrowski, R. M. France, K. Zhu, J. van de Lagemaat, J. M. Luther and M. C. Beard, *Nat. Photonics*, 2016, **10**, 53.

13. J. He and T. M. Tritt, *Science*, 2017, **357**, eaak9997.

14. M. K. Jana and K. Biswas, *ACS Energy Lett.*, 2018, **3**, 1315.

15. K. Biswas, J. He, I. D. Blum, C.-I. Wu, T. P. Hogan, D. N. Seidman, V. P. Dravid and M. G. Kanatzidis, *Nature*, 2012, **489**, 414.

16. G. Tan, F. Shi, S. Hao, L.-D. Zhao, H. Chi, X. Zhang, C. Uher, C. Wolverton, V. P. Dravid and M. G. Kanatzidis, *Nat. Commun.*, 2016, **7**, 12167.

17. X. Shi, J. Yang, J. R. Salvador, M. Chi, J. Y. Cho, H. Wang, S. Bai, J. Yang, W. Zhang and L. Chen, *J. Am. Chem. Soc.*, 2011, **133**, 7837.

18. M. K. Jana, K. Pal, A. Warankar, P. Mandal, U. V. Waghmare and K. Biswas, *J. Am. Chem. Soc.*, 2017, **139**, 4350.

19. M. Dutta, S. Matteppanavar, M. V. D. Prasad, J. Pandey, A. Warankar, P. Mandal, A. Soni, U. V. Waghmare and K. Biswas, *J. Am. Chem. Soc.*, 2019, **141**, 20293.

20. S. Mukhopadhyay, D. S. Parker, B. C. Sales, A. A. Puretzky, M. A. McGuire and L. Lindsay, *Science*, 2018, **360**, 1455.

21. L.-D. Zhao, G. Tan, S. Hao, J. He, Y. Pei, H. Chi, H. Wang, S. Gong, H. Xu, V. P. Dravid, C. Uher, G. J. Snyder, C. Wolverton and M. G. Kanatzidis, *Science*, 2016, **351**, 141.

22. W. He, D. Wang, H. Wu, Y. Xiao, Y. Zhang, D. He, Y. Feng, Y.-J. Hao, J.-F. Dong, R. Chetty, L. Hao, D. Chen, J. Qin, Q. Yang, X. Li, J.-M. Song, Y. Zhu, W. Xu, C. Niu, X. Li, G. Wang, C. Liu, M. Ohta, S. J. Pennycook, J. He, J.-F. Li and L.-D. Zhao, *Science*, 2019, **365**, 1418.

23. O. Delaire, J. Ma, K. Marty, A. F. May, M. A. McGuire, M. H. Du, D. J. Singh, A. Podlesnyak, G. Ehlers, M. D. Lumsden and B. C. Sales, *Nat. Mater.*, 2011, **10**, 614.

24. L.-D. Zhao, S.-H. Lo, Y. Zhang, H. Sun, G. Tan, C. Uher, C. Wolverton, V. P. Dravid and M. G. Kanatzidis, *Nature*, 2014, **508**, 373.

25. M. Samanta, K. Pal, P. Pal, U. V. Waghmare and K. Biswas, *J. Am. Chem. Soc.*, 2018, **140**, 5866.

26. H. Liu, X. Shi, F. Xu, L. Zhang, W. Zhang, L. Chen, Q. Li, C. Uher, T. Day and G. J. Snyder, *Nat. Mater.*, 2012, **11**, 422.

27. B. Li, H. Wang, Y. Kawakita, Q. Zhang, M. Feygenson, H. L. Yu, D. Wu, K. Ohara, T. Kikuchi, K. Shibata, T. Yamada, X. K. Ning, Y. Chen, J. Q. He, D. Vaknin, R. Q. Wu, K. Nakajima and M. G. Kanatzidis, *Nat. Mater.*, 2018, **17**, 226.

28. A. Banik, T. Ghosh, R. Arora, M. Dutta, J. Pandey, S. Acharya, A. Soni, U. V. Waghmare and K. Biswas, *Energy Environ. Sci.*, 2019, **12**, 589.

29. T. Takabatake, K. Suekuni, T. Nakayama and E. Kaneshita, *Rev. Mod. Phys.*, 2014, **86**, 669.

30. M. K. Jana, K. Pal, U. V. Waghmare and K. Biswas, *Angew. Chem., Int. Ed.*, 2016, **55**, 7792.

31. J. Burschka, N. Pellet, S.-J. Moon, R. Humphry-Baker, P. Gao, M. K. Nazeeruddin and M. Grätzel, *Nature*, 2013, **499**, 316.

32. G. Xing, N. Mathews, S. Sun, S. S. Lim, Y. M. Lam, M. Grätzel, S. Mhaisalkar and T. C. Sum, *Science*, 2013, **342**, 344.

33. Z.-K. Tan, R. S. Moghaddam, M. L. Lai, P. Docampo, R. Higler, F. Deschler, M. Price, A. Sadhanala, L. M. Pazos, D. Credgington, F. Hanusch, T. Bein, H. J. Snaith and R. H. Friend, *Nat. Nanotechnol.*, 2014, **9**, 687.

34. G. Xing, N. Mathews, S. S. Lim, N. Yantara, X. Liu, D. Sabba, M. Grätzel, S. Mhaisalkar and T. C. Sum, *Nat. Mater.*, 2014, **13**, 476.

35. J. S. Manser, J. A. Christians and P. V. Kamat, *Chem. Rev.*, 2016, **116**, 12956.

36. K. M. McCall, C. C. Stoumpos, S. S. Kostina, M. G. Kanatzidis and B. W. Wessels, *Chem. Mater.*, 2017, **29**, 4129.

37. A. D. Wright, C. Verdi, R. L. Milot, G. E. Eperon, M. A. Pérez-Osorio, H. J. Snaith, F. Giustino, M. B. Johnston and L. M. Herz, *Nat. Commun.*, 2016, **7**, 11755.

38. M. A. Haque, S. Kee, D. R. Villalva, W.-L. Ong and D. Baran, *Adv. Sci.*, 2020, **7**, 1903389.

39. G. A. Elbaz, W.-L. Ong, E. A. Doud, P. Kim, D. W. Paley, X. Roy and J. A. Malen, *Nano Lett.*, 2017, **17**, 5734.

40. H. Ma, C. Li, Y. Ma, H. Wang, Z. W. Rouse, Z. Zhang, C. Slebodnick, A. Alatas, S. P. Baker, J. J. Urban and Z. Tian, *Phys. Rev. Lett.*, 2019, **123**, 155901.

41. B. Li, Y. Kawakita, Y. Liu, M. Wang, M. Matsuura, K. Shibata, S. Ohira-Kawamura, T. Yamada, S. Lin, K. Nakajima and S. Liu, *Nat. Commun.*, 2017, **8**, 16086.

42. S.-Y. Yue, X. Zhang, G. Qin, J. Yang and M. Hu, *Phys. Rev. B*, 2016, **94**, 115427.

43. Y. Wang, R. Lin, P. Zhu, Q. Zheng, Q. Wang, D. Li and J. Zhu, *Nano Lett.*, 2018, **18**, 2772.

44. A. Pisoni, J. Jaćimović, O. S. Barišić, M. Spina, R. Gaál, L. Forró and E. Horváth, *J. Phys. Chem. Lett.*, 2014, **5**, 2488.

45. A. Z. C. Ashutosh Giri, Alessandro Mattoni, Kiumars Aryana, Depei; Zhang, X. H., Seung-Hun Lee, Joshua J. Choi, Patrick E. Hopkins, *Nano Lett.*, 2020, **20**, 3331.

46. M. A. Haque, A. N. Gandi, R. Mohanraman, Y. Weng, B. Davaasuren, A.-H. Emwas, C. Combe, D. Baran, A. Rothenberger, U. Schwingenschlögl, H. N. Alshareef, S. Dong and T. Wu, *Adv. Funct. Mater.*, 2019, **29**, 1809166.

47. W. Lee, H. Li, A. B. Wong, D. Zhang, M. Lai, Y. Yu, Q. Kong, E. Lin, J. J. Urban, J. C. Grossman and P. Yang, *Proc. Natl. Acad. Sci. U. S. A.* , 2017, **114**, 8693.

48. T. Liu, X. Zhao, J. Li, Z. Liu, F. Liscio, S. Milita, B. C. Schroeder and O. Fenwick, *Nat. Commun.*, 2019, **10**, 5750.

49. F. Qian, M. Hu, J. Gong, C. Ge, Y. Zhou, J. Guo, M. Chen, Z. Ge, N. P. Padture, Y. Zhou and J. Feng, *J. Phys. Chem. C*, 2020, **124**, 11749.

50. H. Xie, S. Hao, J. Bao, T. J. Slade, G. J. Snyder, C. Wolverton and M. G. Kanatzidis, *J. Am. Chem. Soc.*, 2020, **142**, 9553.

51. T. Hata, G. Giorgi and K. Yamashita, *Nano Lett.*, 2016, **16**, 2749.

52. L. Mao, C. C. Stoumpos and M. G. Kanatzidis, *J. Am. Chem. Soc.*, 2019, **141**, 1171.

53. S. Chen and G. Shi, *Adv. Mater.*, 2017, **29**, 1605448.

54. H. Tsai, W. Nie, J.-C. Blancon, C. C. Stoumpos, R. Asadpour, B. Harutyunyan, A. J. Neukirch, R. Verduzco, J. J. Crochet, S. Tretiak, L. Pedesseau, J. Even, M. A. Alam, G. Gupta, J. Lou, P. M. Ajayan, M. J. Bedzyk, M. G. Kanatzidis and A. D. Mohite, *Nature*, 2016, **536**, 312.

55. X. Gao, X. Zhang, W. Yin, H. Wang, Y. Hu, Q. Zhang, Z. Shi, V. L. Colvin, W. W. Yu and Y. Zhang, *Adv. Sci.*, 2019, **6**, 1900941.

56. Z. Xu, M. Chen and S. F. Liu, *J. Phys. Chem. C*, 2019, **123**, 27978.

57. J. Li, Q. Yu, Y. He, C. C. Stoumpos, G. Niu, G. G. Trimarchi, H. Guo, G. Dong, D. Wang, L. Wang and M. G. Kanatzidis, *J. Am. Chem. Soc.*, 2018, **140**, 11085.

58. D. G. Cahill, S. K. Watson and R. O. Pohl, *Phys. Rev. B*, 1992, **46**, 6131.

59. G. Kresse and J. Furthmüller, *Comput. Mater. Sci.*, 1996, **6**, 15.

60. G. Kresse and J. Furthmüller, *Phys. Rev. B*, 1996, **54**, 11169.

61. P. E. Blöchl, *Phys. Rev. B*, 1994, **50**, 17953.

62. G. Kresse and D. Joubert, *Phys. Rev. B*, 1999, **59**, 1758.

63. J. P. Perdew, K. Burke and M. Ernzerhof, *Phys. Rev. Lett.*, 1996, **77**, 3865.

64. J. P. Perdew, A. Ruzsinszky, G. I. Csonka, O. A. Vydrov, G. E. Scuseria, L. A. Constantin, X. Zhou and K. Burke, *Phys. Rev. Lett.*, 2008, **100**, 136406.

65. A. Togo and I. Tanaka, *Scr. Mater.*, 2015, **108**, 1.

66. W. Setyawan and S. Curtarolo, *Comput. Mater. Sci.*, 2010, **49**, 299.

67. F. Gascoin and A. Maignan, *Chem. Mater.*, 2011, **23**, 2510.

68. S. Roychowdhury, M. Samanta, S. Perumal and K. Biswas, *Chem. Mater.*, 2018, **30**, 5799.

69. L.-D. Zhao, V. P. Dravid and M. G. Kanatzidis, *Energy Environ. Sci.*, 2014, **7**, 251.

70. S. Roychowdhury, T. Ghosh, R. Arora, U. V. Waghmare and K. Biswas, *Angew. Chem., Int. Ed.*, 2018, **57**, 15167.

71. M. Samanta, K. Pal, U. V. Waghmare and K. Biswas, *Angew. Chem. Int. Ed.*, 2020, **59**, 4822.

72. Y. Zhang, X. Ke, C. Chen, J. Yang and P. R. C. Kent, *Phys. Rev. B*, 2009, **80**, 024304.

73. J. Carrete, N. Mingo and S. Curtarolo, *Appl. Phys. Lett.*, 2014, **105**, 101907.

74. Y. Xiao, C. Chang, Y. Pei, D. Wu, K. Peng, X. Zhou, S. Gong, J. He, Y. Zhang, Z. Zeng and L.-D. Zhao, *Phys. Rev. B*, 2016, **94**, 125203.

75. Y. Yu, M. Cagnoni, O. Cojocaru-Mirédin and M. Wuttig, *Adv. Funct. Mater.*, 2020, **30**, 1904862.

76. E. A. Albanesi, C. M. I. Okoye, C. O. Rodriguez, E. L. Peltzer y Blanca and A. G. Petukhov, *Phys. Rev. B*, 2000, **61**, 16589.

77. M. Shakil, A. Akram, I. Zeba, R. Ahmad, S. S. A. Gillani and M. A. Gadhi, *Mater. Res. Express*, 2020, **7**, 025513.

78. K. Pal, Y. Xia, J. He and C. Wolverton, *Chem. Mater.*, 2019, **31**, 8734.

79. K. Pal, X. Hua, Y. Xia and C. Wolverton, *ACS Appl. Energy Mater.*, 2020, **3**, 2110.

80. Y. Xia, K. Pal, J. He, V. Ozoliņš and C. Wolverton, *Phys. Rev. Lett.*, 2020, **124**, 065901.

81. S. Acharya, J. Pandey and A. Soni, *Appl. Phys. Lett.*, 2016, **109**, 133904.

82. J. Pandey, S. Mukherjee, D. Rawat, S. Athar, K. S. Rana, R. C. Mallik and A. Soni, *ACS Appl. Energy Mater.*, 2020, **3**, 2175.

83. D. T. Morelli, V. Jovovic and J. P. Heremans, *Phys. Rev. Lett.*, 2008, **101**, 035901.

84. T. Tadano, Y. Gohda and S. Tsuneyuki, *Phys. Rev. Lett.*, 2015, **114**, 095501.

Chapter 4.2

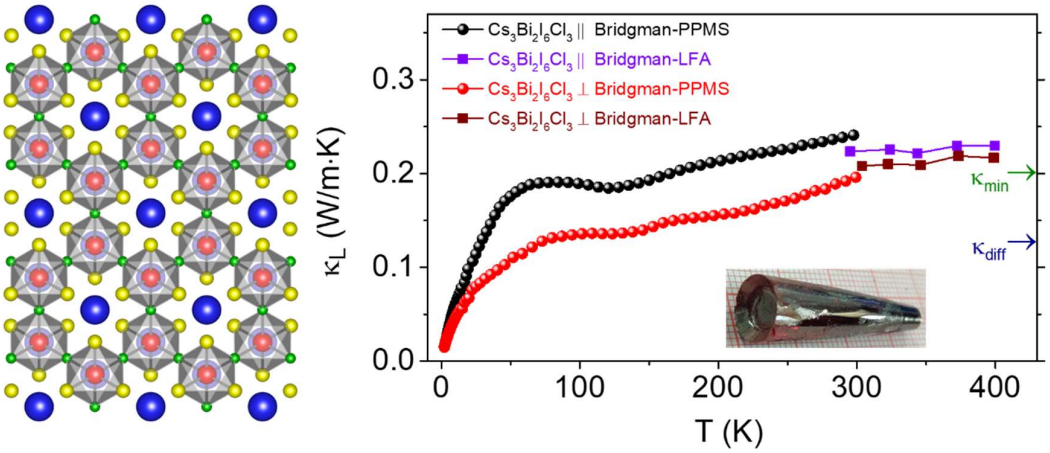

Glass-like Thermal Conductivity in Single Crystal of Layered Halide Perovskite $Cs_3Bi_2I_6Cl_3$

Chapter 4.2

Glass-like Thermal Conductivity in Single Crystal of Layered Halide Perovskite $Cs_3Bi_2I_6Cl_3$[†]

Summary

As the periodic atomic arrangement of a crystal is made to a disorder or glassy-amorphous system by destroying the long-range order, the value of lattice thermal conductivity, κ_L, decreases, and its fundamental characteristics changes. Disordered atomic arrangement severely limits the phonon mean free path in a material, however, it can also have deteriorating effect on the charge carrier transport. Therefore, the realization of ultralow and unusual glass-like κ_L in a crystalline material is challenging but it holds the key to many applications like in thermoelectrics and thermal barrier coatings. Herein, we demonstrate an ultralow value (~0.20 W/m·K at room temperature) and glass-like temperature dependence (2-400 K range) of κ_L in a large single crystal of layered halide perovskite, $Cs_3Bi_2I_6Cl_3$. Soft acoustic phonons with low cut-off frequency (20 cm^{-1}) are responsible for the low sound velocity in $Cs_3Bi_2I_6Cl_3$ and makes the structure elastically soft with low bulk and shear moduli. While a strong anharmonicity originates from the low energy and localized rattling-like vibration of Cs atoms, synchrotron X-ray pair-distribution function analysis evidences the presence of a local structural distortion in the Bi-halide octahedra. We demonstrate that the hierarchical chemical bonding and low energy vibrations from selective sublattice in the crystalline inorganic halide perovskites open an exciting platform for thermal transport research, which is intriguing from lattice dynamical aspects as well as have potential applications.

[†]**P. Acharyya,** T. Ghosh, K. Pal, K. S. Rana, M. Dutta, D. Swain, M. Etter, A. Soni, U. V. Waghmare, and K. Biswas. *Manuscript submitted.*

4.2.1. Introduction

Quantized normal modes of lattice vibration, called phonons, are the primary carrier of thermal energy in the crystalline insulators. The strength of phonon scattering, which blocks the propagation of thermal energy, vary from material to material depending on the intrinsic (chemical bonding and crystal structure) and extrinsic (solid solution point defects, nano/microstructures, etc.) parameters. Crystalline materials at both extreme end of ultrahigh or ultralow lattice thermal conductivity (κ_L) are technologically relevant to numerous applications[1]: while low thermal conductive materials are beneficial for thermoelectrics[2, 3] and thermal barrier coatings,[4] high thermal conductive materials are needed for heat transmission and dissipation.[5]

According to kinetic theory $\kappa_L = 1/3 C_v v_g l_{ph}$, where C_v is the volumetric heat capacity, v_g is the phonon group velocity, and l_{ph} is the phonon mean free path. Materials have low κ_L either because of comprising strong phonon scattering centers (e.g., strong lattice anharmonicity,[6-9] rattling dynamics,[10-12] excess disorder,[13, 14] hierarchical nanostructuring[15]) and/or because of low v_g due to soft chemical bonding and heavy atomic masses.[16] The wave nature of phonons, however, sets an intrinsic limit to the lower value of κ_L (κ_{min}): l_{ph} cannot be lower than the half of the wavelength ($\lambda/2$: λ is the phonon wavelength) or the interatomic spacing (a) of the lattice. In crystalline insulators, κ_L decreases with increasing temperature above the Debye temperature (θ_D) and κ_{min} is asymptotically reached in the highly anharmonic regime at high temperatures ($T >> \theta_D$). As the strength of anharmonicity increases, and/or the unit cell becomes large and complex, and/or disorder increases the temperature regime at which $\kappa_L \sim \kappa_{min}$ decreases.[16, 17] Disorder is particularly notorious in limiting l_{ph}: in fact, in amorphous materials and glasses, where the long-range periodicity of a crystal lattice is destroyed, $l_{ph} \sim \lambda/2$ (or, $l_{ph} \sim a$) is the highest frequency and the only remaining well-defined available phonon mode throughout the entire temperature range. This limit is also often called the glass-limit. Thermal conductivity of amorphous materials and glasses then has significantly lower value compared to their crystalline counterparts, and it slowly increases with increasing temperature with asymptotic limit of κ_{min}, in drastic contrary to the crystalline insulators.[18, 19]

Crystalline materials in which κ_L reaches this glass-limit and exhibit *glass-like* temperature variation of κ_L ($\kappa_L(T)$) is extremely important for a variety of applications such as in thermoelectrics. Previously glass-like κ_L has been observed in crystalline materials when they comprise large and complex unit cell,[20-22] incorporates large amount of disorder[23] and nanostructures,[24, 25] or have specially designed layered modules.[9] However, the presence of disorder is often unwarranted as it deteriorates charge carrier transport. The challenge is then how to realize glassy κ_L in a crystalline material, in the absence of impurity and disorder. Such materials would not only be fascinating from the perspective of chemical bonding and lattice dynamics but would have immense technological importance.

In this work, we demonstrate such glassy thermal conductivity in a large single crystal and high symmetry (space group: *P*-3*m*1) structure of all-inorganic metal halide perovskite $Cs_3Bi_2I_6Cl_3$. Recently, metal halide perovskites have received unprecedented attention because of their fascinating physical and chemical properties.[26-28] The outstanding electronic and optoelectronic properties and their application are however, found to be greatly affected by their lattice vibrations (phonons).[29, 30] Investigations of thermal conductivity of these halide perovskites are essential for application as it influences their stability, operating lifetime of a device and long-term device performance.[31, 32] Although the influence of lattice vibrations on electronic and optical transitions is to some extent explored, thermal transport properties of halide perovskites in presence of a temperature gradient are still in its infancy.[33, 34] Only a handful of studies have been carried out investigating thermal conductivity of these halide perovskites,[35-37] particularly, for the all-inorganic halide perovskites.[38-41]

Herein, we have demonstrated ultralow lattice thermal conductivity (κ_L) in a Bridgman grown large single crystal of layered $Cs_3Bi_2I_6Cl_3$ perovskite. The κ_L value is found to be 0.20 W/m·K and 0.22 W/m·K at room temperature when measured perpendicular and parallel to the Bridgman growth directions, respectively. The temperature (2-400 K) dependence of κ_L, both for the parallel and perpendicular to the Bridgman growth directions, exhibit the behavior similar to that of amorphous materials and glasses. At very low temperature (<10 K), temperature dependence of κ_L in $Cs_3Bi_2I_6Cl_3$ is strongly deviates from the typical T^3 dependence of crystalline materials. Secondly in the intermediate temperature range, the temperature dependence of κ_L lacks

the peak found in typical crystalline materials. Rather, it exhibits a flat plateau in the temperature range (40-150 K), and then a gradual increase with temperature approaching the glass limit. First-principles density functional theory (DFT) calculations of the harmonic interatomic force constant clearly reveal the large difference in bond stiffness of Bi-I/Cl and Cs-I/Cl, and demonstrate very soft elastic moduli, corroborating our experimentally measured low sound velocity in $Cs_3Bi_2I_6Cl_3$. In accordance, its phonon dispersion exhibits soft acoustic phonons with a rather low cut-off frequency (20 cm^{-1}) and reveals abundance of weakly dispersive low energy optical phonon modes below 60 cm^{-1}, which have been further verified using low temperature heat capacity (2-50 K) and temperature dependent (4-300 K) Raman measurements. Synchrotron X-ray pair distribution function (PDF) analysis revealed the presence of a local structural distortion in the Bi-halide octahedra of $Cs_3Bi_2I_6Cl_3$ which resulted in local symmetry breaking and large anharmonicity. Thereby, the combined presence of soft crystalline lattice, low energy optical phonons and high lattice anharmonicity results in low phonon lifetime and consequently in an ultralow and glass-like temperature dependence of κ_L in $Cs_3Bi_2I_6Cl_3$.

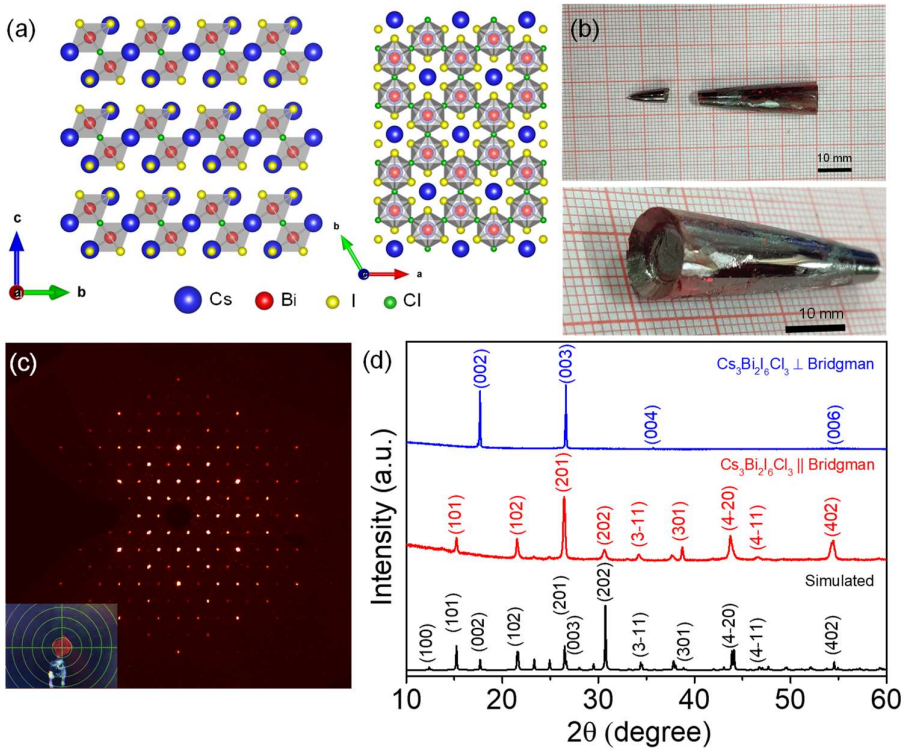

Figure 4.2.1. *(a) Crystal structure of the <111> oriented layered halide perovskite $Cs_3Bi_2I_6Cl_3$. (b) Optical photographs of Bridgman grown $Cs_3Bi_2I_6Cl_3$ single crystal. (c) Laue diffraction spots (along c direction) from the $Cs_3Bi_2I_6Cl_3$ single crystal. Inset shows*

photograph of a broken piece of single crystal specimen mounted on the sample holder. (d) Room temperature XRD pattern of $Cs_3Bi_2I_6Cl_3$ single crystal cut along parallel and perpendicular to the Bridgman growth direction.

4.2.2. Methods

Materials. Caesium (I) chloride (CsCl, 99.9%, Sigma Aldrich) and Bismuth (III) iodide (BiI_3, 99.998%, Sigma Aldrich) were used for synthesis without further purification.

Bridgman crystal growth. Single crystal of $Cs_3Bi_2I_6Cl_3$ was grown using a Bridgman furnace. In order to grow a large single crystal, stoichiometric amount of CsCl (2.0989 g) and BiI_3 (4.9011 g) were sealed in a 10 mm conical quartz tube under high vacuum (10^{-6} Torr). The ampule was kept at 750 ^oC for 48 hrs and the ampule was then moved through a temperature gradient from 600 ^oC to 480 ^oC at a speed of 1 mm/hr. Finally, the sample was slowly cooled to room temperature in 120 hrs.

Single crystal X-ray diffraction (SCXRD). Data were collected at room temperature (298 K) using a Bruker D8 VENTURE diffractometer equipped with a PHOTON detector and graphite-monochromatic Mo-Kα radiation (λ = 0.71073 Å, 50 kV, 1 mA). APEX III software was used to collect, reduce, and integrate the raw data. The structure solution was obtained from SHELXS and refined by using SHELXL included in the WinGX suite.[42-44] The crystallographic details are given in Table 4.2.1. The single crystal data are solved in collaboration with Dr. Diptikanta Swain, ICT, India.

Powder X-ray diffraction (PXRD). Room temperature XRD patterns of $Cs_3Bi2I_6Cl_3$ for two different directions (parallel and perpendicular to the Bridgman growth direction) were collected on a Bruker D8 diffractometer using Cu Kα radiation (λ= 1.5406 Å). Synchrotron powder X-ray diffraction data was collected from finely ground powder using a synchrotron X-ray beam of λ = 0.7762 Å, at BL-18B (Indian beamline), Photon Factory, KEK, Tsukuba, Japan. A Si (111) double crystal monochromator was used to set the energy of the beam and analyzed with standard Si (640b NIST). The measurement was performed in Bragg−Brentano geometry with an anti-scattering slit (350 μm), a divergence slit (300 μm), and a receiving slit (300 μm). Reitveld refinement of synchrotron powder X-ray diffraction data was performed using the Fullprof program.[45]

Thermal conductivity. First, large single crystal was cut in perpendicular and parallel to Bridgman growth direction by a diamond wire saw (Diamond wire saw 3500 premium) to measure the thermal conductivity. Thermal conductivity measurement was carried out in the temperature range of 2-400 K. The low temperature thermal conductivity (2-300 K) was measured for a rectangular bar shaped specimen with dimensions of ~2 x 2 x 8 mm^3 using a physical properties measurement system (DynaCool PPMS, Quantum Design). Above room temperature (300-400 K), thermal diffusivity, *D*, was measured by laser flash diffusivity technique using a Netzsch LFA-457 instrument. Typical square (~8 x 8 mm^2) and coin (~8 mm diameter) shaped samples of thickness less than 2 mm were used for the measurement of thermal transport properties above room temperature and thermal conductivity (κ) was estimated using the relation, $\kappa = D \times C_p \times \rho$, where ρ is the density of the sample and C_p is the specific heat. The obtained density of the single crystal is ~98 % of the theoretical density. We have used the Dulong–Petit C_p (0.21 J/g/K) for the estimation of thermal conductivity in the 300-400 K range.

Sound velocity measurement. The longitudinal (v_l) and transverse (v_t) sound velocities were measured using disc-shaped and square-shaped samples, respectively, with an Epoch 650 Ultrasonic Flaw Detector (Olympus) instrument with the transducer frequency of 5 MHz. The minimum lattice thermal conductivity (κ_{min}) was then calculated using the Cahill's Model[23]:

$$\kappa_{min} = 1.21\mathrm{n}^{2/3} k_B \frac{1}{3}(v_l + 2v_t) \dots\dots\dots\dots\dots\dots (1)$$

We have calculated the diffuson mediated thermal conductivity (κ_{diff}) using the formula below[46]:

$$\kappa_{diff} = 0.76\mathrm{n}^{2/3} k_B \frac{1}{3}(v_l + 2v_t) \dots\dots\dots\dots\dots\dots (2)$$

where k_B is the Boltzmann constant and n is the number density of atoms.

Poisson ratio (ν_p) and the Grüneisen parameter (γ) were calculated using equations below (see Table 4.2.2)[47]:

$$\nu_p = \frac{1-2(v_t/v_l)^2}{2-2(v_t/v_l)^2} \ldots\ldots\ldots\ldots\ldots\ldots (2)$$

$$\gamma = \frac{3}{2}.\frac{1+\nu_p}{2-3\nu_p} \ldots\ldots\ldots\ldots\ldots\ldots\ldots\ldots (3)$$

Further, the average sound velocity (v_a) was also estimated from the Debye temperature (Θ_D) using the following equation[48]:

$$\Theta_D = \frac{h}{k_B}\left(\frac{3N}{4\pi V_u}\right)^{1/3} v_a$$

where h is Planck's constant, N is the number of atoms in a unit cell, V_u is the unit-cell volume.

The estimated average sound velocity (v_a) was determined to be ~ 1200 m/s which is close to the experimental value (Table 4.2.2).

Heat capacity measurement. Low-temperature heat capacity (C_p) of $Cs_3Bi_2I_6Cl_3$ was measured in a Physical Property Measurement System (PPMS, DynaCool) in the temperature range of 2-200 K.

Raman spectroscopy. The Raman spectroscopy measurements are done in collaboration with Prof. Ajay Soni, IIT Mandi, India. Horiba Jobin-Yvon LabRAM HR evolution Raman spectrometer was used for Raman measurements in back scattering geometry with excitation laser 785 nm (1.58 eV) and 633 nm (1.96 eV), large working distance 50 x objective, grating 1800 lines/mm and Peltier cooled CCD detector. The temperature dependent (4-300 K) Raman study was conducted by using Montana cryostat through unpolarized excitation laser 785 nm laser and power ~0.80 mW. All the observed spectra were baseline corrected, normalized with respect to the intense peak (59 cm^{-1}) and fitted with the Lorentzian function.

Optical spectroscopy. PerkinElmer, Lambda-900 UV/Vis/near-IR spectrometer was used to measure the optical bandgap in reflectance mode within the range of 250-800 nm.

The absorption data (α/S) of $Cs_3Bi_2I_6Cl_3$ was estimated from reflectance data using Kubelka–Munk equation; $\alpha/S = (1-R)^2/(2R)$; where R, α, and S denote reflectance, absorption and scattering coefficients, respectively.

Field emission scanning electron microscopy (FESEM) in back-scattered electron (BSE). FESEM-BSE images were taken using ZEISS Gemini SEM – Field Emission Scanning Electron Microscope.

Thermogravimetric analysis (TGA). TGA experiments were carried out using a 2 STAR TGA instrument. Powdered samples were heated in the temperature range of 300-1247 K in N_2 atmosphere at a rate of 5 K/min.

Synchrotron X-ray Pair Distribution Function (X-PDF). Samples were finely ground with an agate mortar pestle and then filled in capillary of 0.6 mm diameter for performing synchrotron X-ray PDF measurements. Both ends of capillaries were sealed using an adhesive. A Perkin Elmer XRD1621 area detector was used to record the diffraction data. To subtract the background, data sets of empty capillaries were collected. A dark measurement prior to each data collection was done and Lanthanum Hexaboride (LaB_6) was taken as a standard for calibration. The wavelength of the beam was fixed at 0.20742 Å. The data was taken at the P02.1 beamline of PETRA III, DESY, Germany.[49]

G(r) defines the probability of finding nearest neighbor bonding at a certain distance *r* in the material, G(r) was obtained via Fourier transformation of the scattering structure function, F(Q)[50]

$$G(r) = \frac{2}{\pi}\int_{\mathrm{Qmin}}^{\infty} \mathrm{F(Q)\ sinQr\ dQ}$$

where Q represents the momentum transfer of the scattering particle. F(Q) is obtained from the scattering data and is related to the structure function S(Q) as F(Q) = Q[S(Q)-1]. Initial data reduction was done using DAWN[51] and PDFgetX3[52] software. The processing parameters used for the data conversion are: Q_{min} = 0.0 Å $^{-1}$, Q_{max} = 21.5 Å $^{-1}$, r_{min} = 1.0 Å and r_{max} = 30 Å.

Simulation of the experimental PDF data was done using the PDFgui[53] software. The data at 300 K was initially modelled using a *P*-3*m*1 model. The refinement parameters were the scale, linear atomic correlation factor, lattice parameters, and the

thermal displacement values. For positional refinements of each atom, the allowed positions were refined along with the aforementioned parameters. The *r* value of the experimental data was taken from 2 – 30 Å for the simulation. The first peak of the G(r) *vs. r* plot represents the nearest atom-atom correlation, the second peak corresponds to second nearest atom-atom distances and so on. The PDF measurements are done at beamline P02.1, PETRA III, DESY, Germany, in collaboration with Dr. Martin Etter.

Computational details. Theoretical calculations are done in collaboration with Prof. U. V. Waghmare, JNCASR, India. We performed first-principles density functional theory (DFT) calculations using the Vienna Ab-initio Simulation Package (VASP) [54, 55] with potentials derived using the projector augmented wave (PAW) [56, 57] method. We used the following potentials in our calculations: Cs ($5s^2$ $5p^6$ $6s^1$), Bi ($5d^{10}$ $6s^2$ $6p^3$), Cl ($3s^2$ $3p^5$) and I ($5s^2$ $5p^5$). The exchange-correlation energies of the electron were approximated using the PBEsol[58] functional within the generalized gradient approximation (GGA).[59] The kinetic energy cut-off was set to 520 eV and a k-point mesh of 9 × 9 × 7 was used for the relaxation of the cell parameters. The optimized lattice parameters (a= 8.18 Å, c= 9.93 Å) agree well with the experimentally values (a= 8.24 Å, c= 10.03 Å). The relaxed structure retains the hexagonal space group (*P*-3*m*1, No. 164). The Brillouin zone (BZ) for this unit cell is shown in Figure 4.2.2a. We calculated the harmonic phonon dispersion of $Cs_3Bi_2I_6Cl_3$ using the finite-displacement method as implemented in the Phonopy[60] code, where the displaced configurations were generated using a 2×2×2 supercell (containing 112 atoms) of the primitive unit cell that has 14 atoms. For phonon calculations, we used a 4×4×4 k-point mesh for the calculation of the forces. The calculated phonon dispersion exhibits quite a few imaginary phonon branches, which is common in the family of inorganic halide perovskites.[61] The imaginary phonon mode at Γ exhibits a double-well potential energy surface. To stabilize these imaginary phonons, we nudged the atoms in the primitive unit cell with the eigenvectors of the imaginary phonon mode (-19 cm^{-1}) at the Γ point in the Brillouin zone and relaxed the crystal structure of the unit cell which lowers the symmetry to triclinic (space group: *P*1, No.1). The relaxed structure was then utilized to calculate the harmonic phonon dispersion, phonon density of states and mode Grüneisen parameter. The BZ for this triclinic unit cell is shown in Figure 4.2.2b. Most of the imaginary phonon modes got stabilized in the

phonon dispersion of the relaxed structure. We determined the mode Grüneisen parameters of $Cs_3Bi_2I_6Cl_3$ using a finite difference method, where we have calculated the phonon frequencies of the compound at two different volumes ($1.02V_0$ and $0.98V_0$, V_0 being the equilibrium unit cell volume) and utilized the formula $\gamma_{qv} = -\frac{dln\ _{qv}}{dlnV}$, where γ_{qv}, V and ω_{qv} denote Grüneisen parameter, unit cell volume, and frequency of a phonon mode at wavevector q for branch ν, respectively. To estimate the elastic properties of $Cs_3Bi_2I_6Cl_3$, we calculated its bulk (B) and shear (G) moduli using Voigt's formula[62] utilizing the elastic tensor obtained from VASP. We have analyzed the chemical bonding of the compound using the crystal orbital Hamilton population (COHP) method the LOBSTER code.[63, 64]

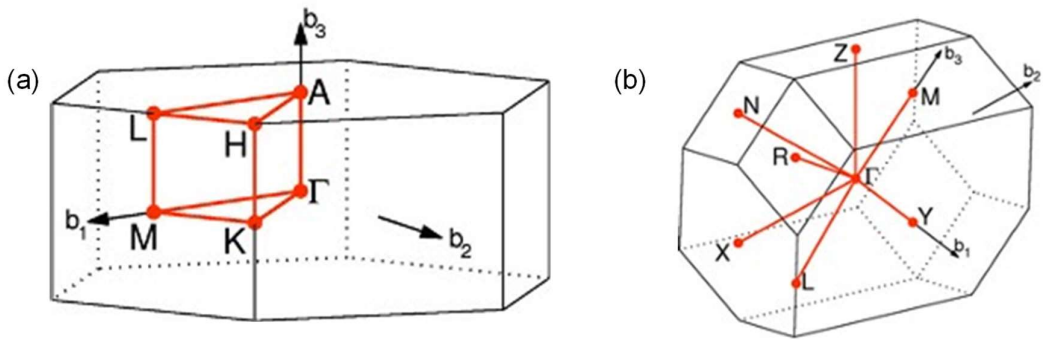

Figure 4.2.2. *Brillouin zones of the (a) hexagonal and (b) triclinic unit cells of $Cs_3Bi_2I_6Cl_3$, with high-symmetry points. Figures are taken from reference.*[65]

4.2.3. Results and Discussion

$Cs_3Bi_2I_6Cl_3$ (space group: *P*-3*m*1) is a member in the <111> oriented layered halide perovskites family and it is isostructural to $Cs_3Bi_2Br_9$ and α-$Cs_3Sb_2I_9$.[66-68] Each octahedra of $Cs_3Bi_2I_6Cl_3$ comprises three capping iodine atoms that terminates the bilayers and three bridging chlorine atoms that connects the octahedra to adjacent opposite layers, thereby forming a layered structure with 2D connectivity (Figure 4.2.1a). The bridging Cl atoms in $Cs_3Bi_2I_6Cl_3$ makes it a 2D structure when compared to 0D $Cs_3Bi_2I_9$ which are devoid of such Cl atoms.[66, 68]

Large single crystal of $Cs_3Bi_2I_6Cl_3$ (Figure 4.2.1b; for details see experimental section) has been synthesized using a Bridgman furnace. The crystal structure of $Cs_3Bi_2I_6Cl_3$ is solved and refined using single crystal X-ray diffraction at room

temperature (Table 4.2.1). Figure 4.2.1c exhibits the typical Laue diffraction spots collected from the $Cs_3Bi_2I_6Cl_3$ single crystal at room temperature. The laboratory XRD (Cu Kα) patterns of $Cs_3Bi_2I_6Cl_3$ crystal, measured at room temperature for both parallel and perpendicular cut to the Bridgman growth directions, is shown in Figure 4.2.1d. The crystallographic *c*-axis is perpendicular to the Bridgman growth direction, i.e., the stacking direction of the layers is perpendicular to the Bridgman growth direction. The room temperature synchrotron (λ = 0.7762 Å) powder XRD pattern of the finely ground sample could be also indexed with the trigonal space group (*P*-3*m*1) as shown in Figure 4.2.3. The obtained lattice parameters *a* = *b* = 8.2438(3) Å and *c* =10.0337(6) Å, from the Rietveld refinement, also agree well with the lattice parameters obtained from our single crystal XRD data (see Table 4.2.1).[66]

Table 4.2.1. *Single crystal data and structure refinement for $Cs_3Bi_2I_6Cl_3$ at 295(2) K.*

Empirical formula	$Cs_3Bi_2I_6Cl_3$
Formula weight	1684.44 g/mol
Temperature	295 (2) K
Wavelength	0.71073 Å
Crystal System	Trigonal
Space group	*P*-3*m*1
Unit cell dimensions	a = 8.2985(10) Å; α = 90°
	b = 8.2985(10) Å; β = 90°
	c = 10.1591(18) Å; γ = 120°
Volume	605.88(18) $Å^3$
Z	1
Calculated density	4.617 g/cm^3
F(000)	700
Crystal size	0.19×0.18×0.12 mm^3
$\theta_{min,max}$	2.005, 25.448
$h_{min,max}$ $k_{min,max}$ $l_{min,max}$	-10, 10 -9, 10 -12, 11

Absorption coefficient	26.896 mm^{-1}
Reflections collected	3914
Unique reflections/ No. parameters	458/19
Goodness-of-fit	1.087
Final R indices (I>2σ (I))	R_{obs} = 0.0728, wR_{obs} = 0.1732
R indices (all data)	R_{all} = 0.1006, wR_{all} = 0.1885
CCDC Number	2150864

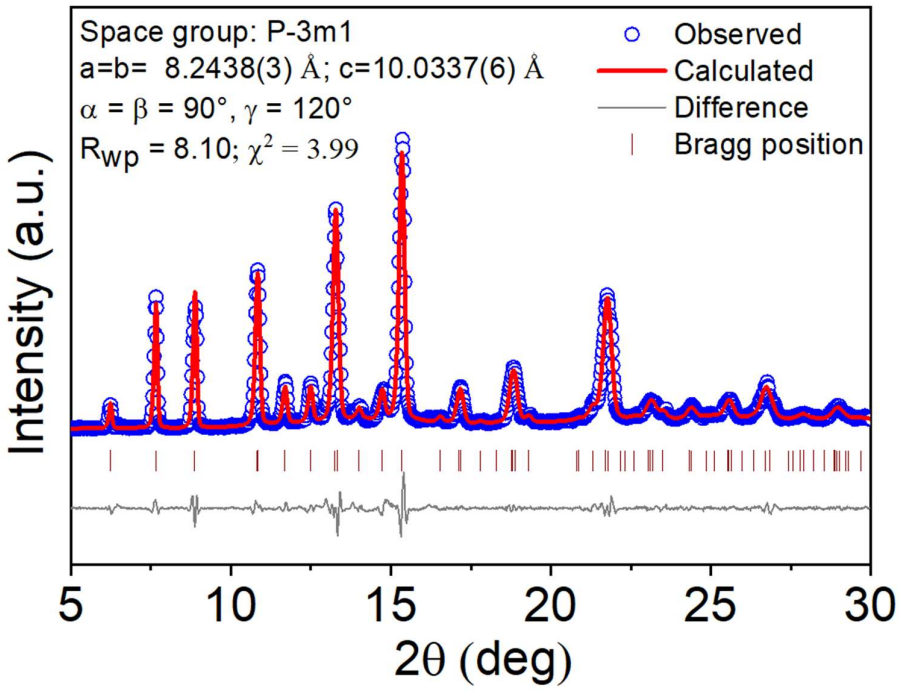

Figure 4.2.3. *Rietveld refinement of the synchrotron (λ = 0.7762 Å) PXRD data of* $Cs_3Bi_2I_6Cl_3$.

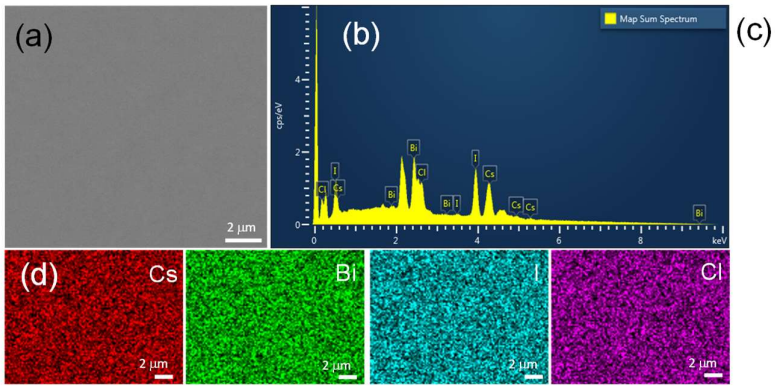

(c)

Element	Wt%	At%
Cs	25.12	23.8
Bi	24.04	14.5
I	46.65	46.2
Cl	4.20	15.12
Total:	100.00	100.00

Figure 4.2.4. *FESEM-BSE image for the Bridgman grown $Cs_3Bi_2I_6Cl_3$ single crystal with corresponding energy-dispersive X-ray (EDX) spectra in (b). (c) weight and atomic percentage of Cs, Bi, I and Cl atoms. (d) EDX elemental color mapping for Cs, Bi, I and Cl for the area in (a).*

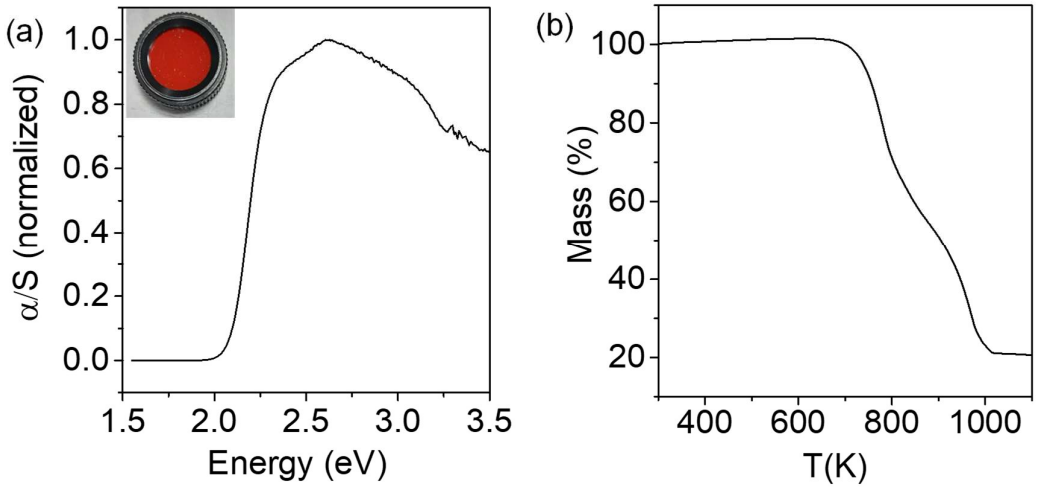

Figure 4.2.5 *(a) Optical absorption spectra and (b) TGA profile of $Cs_3Bi_2I_6Cl_3$.*

Back-scattered electron (BSE) imaging in field emission scanning electron microscope (FESEM), energy dispersive X-ray (EDX) spectra and elemental color mapping with EDX (Figure 4.2.4) show the homogeneous nature of the sample with uniform distribution of the compositional elements (Cs, Bi, I and Cl). Optical absorption study reveals an insulating nature of $Cs_3Bi_2I_6Cl_3$ with the absorption edge at ~2.0 eV (Figure 4.2.5a). Thermal gravimetric analysis (TGA) further ensures that the compound is thermally stable up to 673 K, after which it starts to decompose due to sublimation of BiI_3 (melting point of BiI_3 is 681 K) as depicted in Figure 4.2.5b.

Thermal conductivity of $Cs_3Bi_2I_6Cl_3$ in the temperature range of 2-400 K along parallel (∥) and perpendicular (⊥) to the Bridgman growth direction is shown in Figure 4.2.6a. While in the 2-300 K temperature range, the thermal conductivity is measured using a DynaCool physical property measurement system (PPMS), the thermal conductivity is measured using a laser flash apparatus (LFA 457) in the 300-400 K range (Figure 4.2.6a). Because of the highly insulating nature of the sample with band gap ~ 2.0 eV (Figure 4.2.5a), the total thermal conductivity has a negligible contribution from the charge carriers and, thus, can be considered nearly equal to the lattice thermal conductivity (κ_L). κ_L exhibits a lower value for the entire measured temperature range along the ⊥ to Bridgman growth direction (i.e., ∥ to the crystallographic *c*-direction) when compared to that of the ∥ to Bridgman growth direction (i.e. ⊥ to the *c*-direction). This observed thermal anisotropy is because of the stacking of 2D $[Bi_2I_6Cl_3]^{3-}$ layers along the crystallographic *c*-direction.

We observed several intriguing features in the experimentally measured thermal conductivity of $Cs_3Bi_2I_6Cl_3$ in the 2 to 400 K range. The κ_L at 300 K along ⊥ and ∥ to the Bridgman directions has ultralow values ~0.20 W/m·K and ~0.22 W/m·K, respectively, which are close to the theoretical minimum value of κ_L, κ_{min} = 0.19 W/m·K estimated using Cahill's model (Table 4.2.2).[23] The estimated value of κ_{min} (i.e., κ_{diff}) according to the diffuson model proposed by Agne et al.[18] is 0.12 W/m·K for $Cs_3Bi_2I_6Cl_3$ (Table 4.2.2).

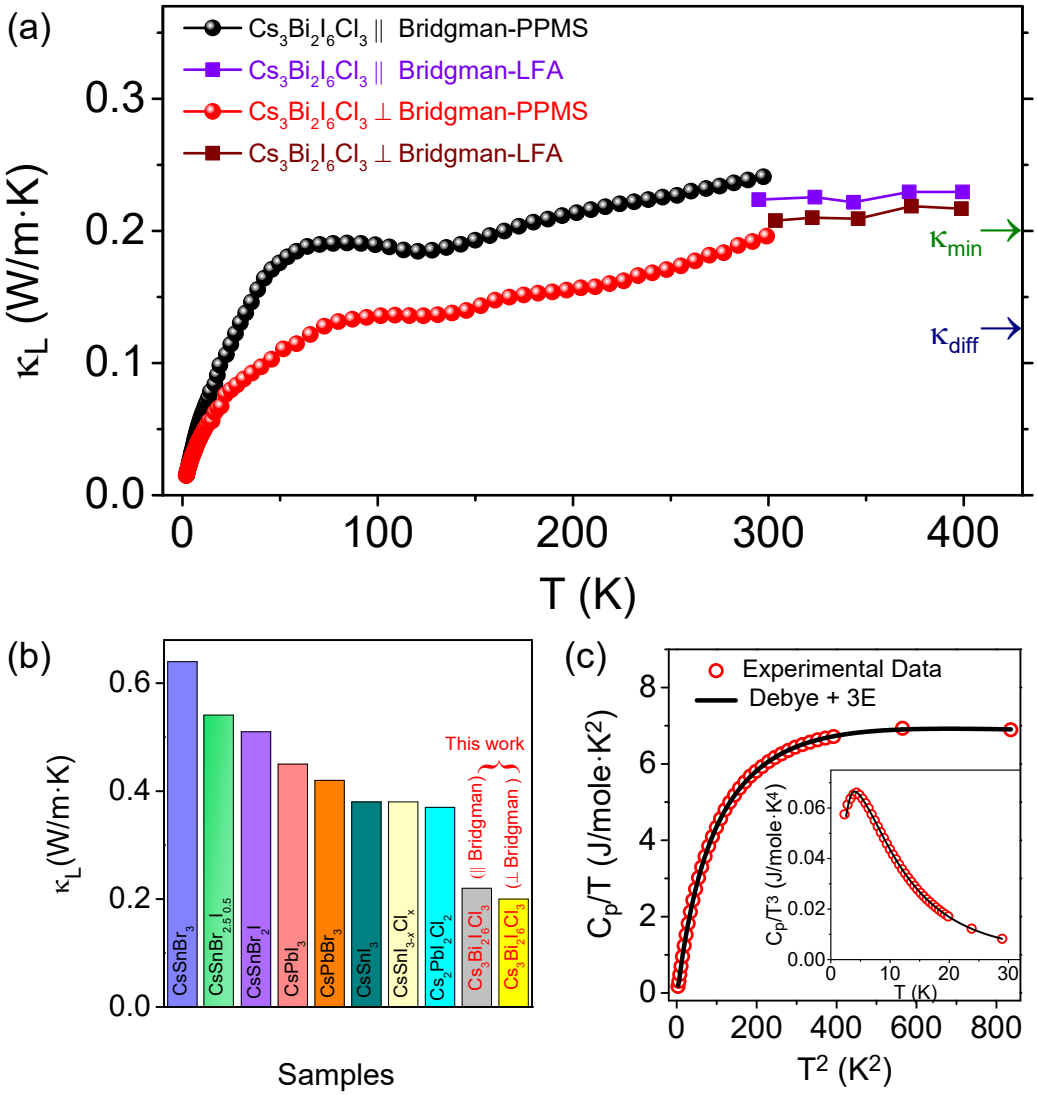

Figure 4.2.6. *(a) Temperature dependent lattice thermal conductivity (κ_L) of $Cs_3Bi_2I_6Cl_3$ along parallel (||) and perpendicular (⊥) to the Bridgman growth directions measured both by PPMS (2-300 K) and LFA (300-400 K). (b) Comparison of room temperature κ_L of $Cs_3Bi_2I_6Cl_3$ single crystal with well-known ultralow thermal conductive all-inorganic halide perovskites.[38-41] (c) Low-temperature C_p/T vs. T^2 plot of $Cs_3Bi_2I_6Cl_3$ and fit with Debye-Einstein model. Inset shows C_p/T^3 vs. T plot exhibiting boson-like peak in low-temperature C_p.*

Table 4.2.2. *Experimental sound velocities, minimum thermal conductivity (κ_{min}), diffuson thermal conductivity (κ_{diff}), Poisson ratio (ν_p) and Grüneisen parameters (γ) of $Cs_3Bi_2I_6Cl_3$.*

Sample	Longitudinal sound velocity (m/s)	Transverse sound velocity (m/s)	Avg. sound velocity (m/s)	κ_{min} (W/mK)	κ_{diff} (W/mK)	ν_p	γ
$Cs_3Bi_2I_6Cl_3$ ($\perp$ Bridgman)	2116	954	1076	0.18	0.11	0.37	2.3
$Cs_3Bi_2I_6Cl_3$ ($\parallel$ Bridgman)	2136	1028	1156	0.19	0.12	0.35	2.1

The measured room temperature value of κ_L of $Cs_3Bi_2I_6Cl_3$ is lower compared to that of the other all-inorganic metal-halide perovskites (Figure 4.2.6b). Moreover, layered compounds generally exhibit highly anisotropic thermal conductivity between the in-plane and out-of-plane directions (Figure 4.2.7a). However, $Cs_3Bi_2I_6Cl_3$ exhibits weak anisotropy with ratio of ~1.10 (based on LFA data) between κ_L values along $\parallel$ and $\perp$ to the Bridgman growth directions at 300 K due to the low anisotropy in the measured sound velocities between the in-plane and out-of-plane direction, which have average values of ~1155 m/s and ~1075 m/s along the $\parallel$ and $\perp$ to Bridgman growth directions, respectively (Table 4.2.2). The interlayer separation (~3.57 Å) is shorter than the expected van der Waals distance (~3.96 Å, van der Waals radius of iodine is ~1.98 Å), but longer than the covalent bonding (~2.78 Å, covalent radius of iodine is ~1.39 Å). Although the structure resembles the 2D materials without any overlapping charge cloud, weak interlayer interaction exists and results in a weak thermal anisotropy in $Cs_3Bi_2I_6Cl_3$.[66] A similar weak anisotropic thermal conductivity has also been reported recently for an organic-inorganic hybrid perovskite BA_2PbI_4 crystal, in which preferential alignment of the organic chains between two inorganic layers along the out-of-plane direction lowers the

anisotropy.[69] The third and most significant observation is the unusual glass-like temperature dependence of κ_L of $Cs_3Bi_2I_6Cl_3$ despite its crystalline structure and measurement of thermal conductivity using a single crystal specimen. Crystalline materials generally exhibit an ~T^3 dependent κ_L at low temperature, followed by a peak after which κ_L decreases following a T^{-1} dependence due to Umklapp scattering and finally reaches a temperature independent κ_{min} value when the phonon mean free path becomes of the order of interatomic distance.[23] However, unlike typical crystalline materials, the temperature dependence of κ_L of $Cs_3Bi_2I_6Cl_3$ largely deviates from a T^3 (Figure 4.2.7b) dependence at low temperature. The temperature dependence of κ_L of $Cs_3Bi_2I_6Cl_3$ also lacks crystalline-like peak in the intermediate temperature range. Rather, we observed a plateau region (40-150 K) in the temperature dependence of κ_L of $Cs_3Bi_2I_6Cl_3$, which is also typically observed in amorphous materials and glasses.[17, 19] After the plateau, a weakly increasing and then nearly constant κ_L was observed at high temperatures that approaches the glass limit.

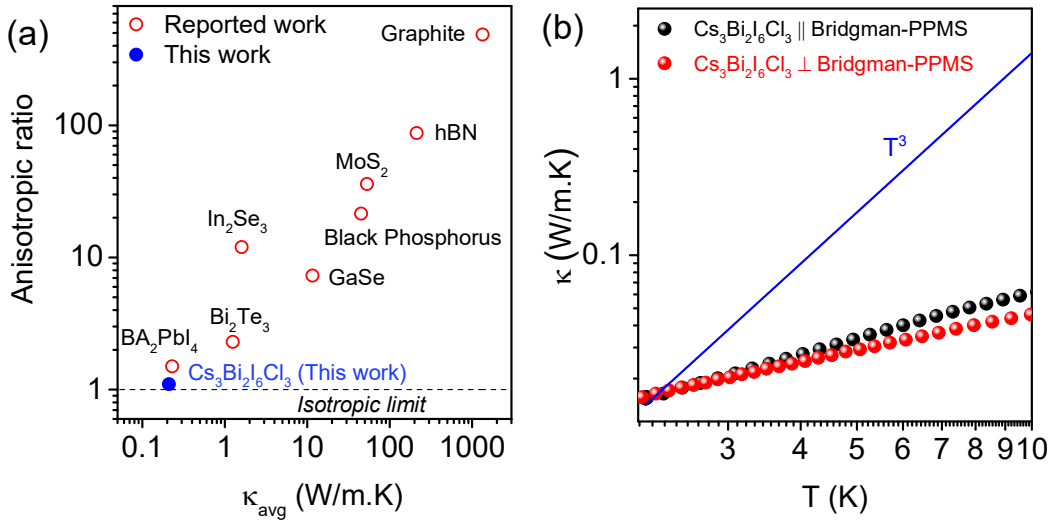

Figure 4.2.7. *(a) Comparison plot of anisotropic ratio (defined as $\kappa_L(\perp c)/\kappa_L(||c)$ vs. average thermal conductivity ($\kappa_{avg} = [\kappa_L(\perp c)+\kappa_L(||c)]/2$) of $Cs_3Bi_2I_6Cl_3$ single crystals with other layered single crystals at room temperature. References in the plot are graphite,[70] hexagonal boron nitride (hBN),[71] MoS_2,[72] black phosphorus,[73] In_2Se_3,[74] GaSe,[70] Bi_2Te_3,[75] and BA_2PbI_4.[69] (b) Low temperature thermal conductivity (<10 K) of $Cs_3Bi_2I_6Cl_3$ largely deviates from T^3 dependency.*

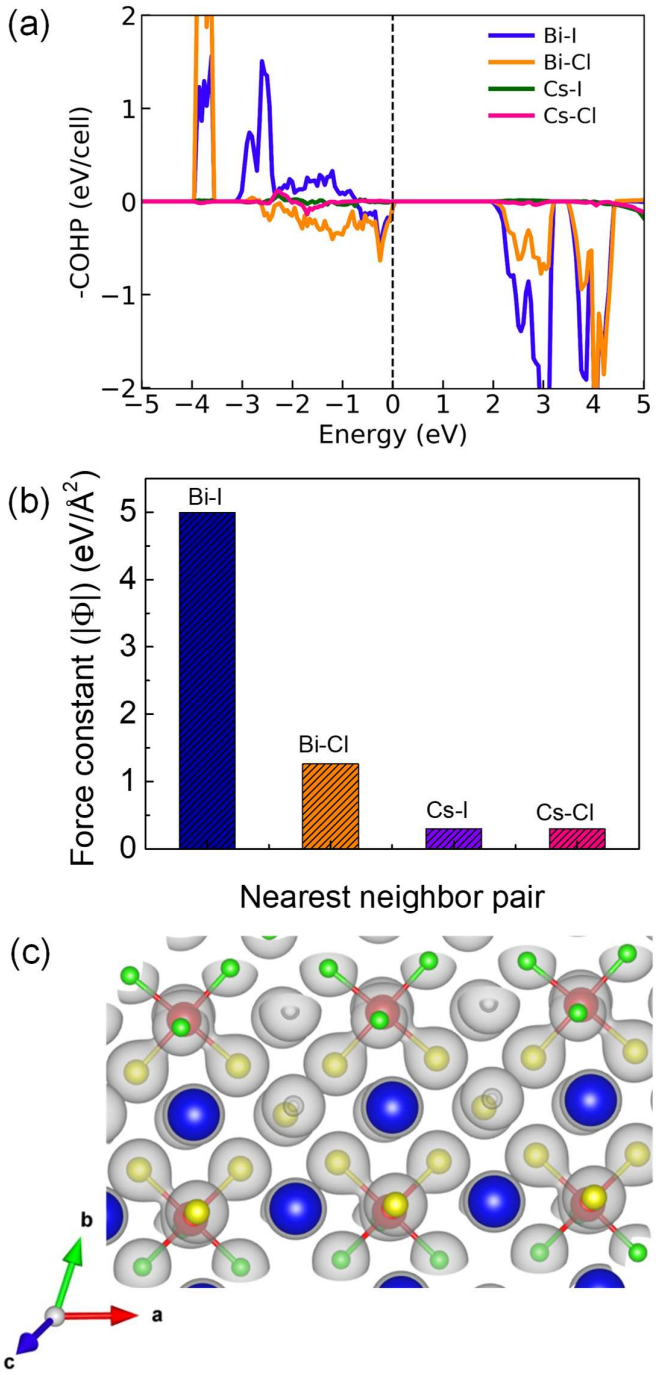

Figure 4.2.8 *(a) Crystal orbital Hamiltonian population (COHP) analysis of $Cs_3Bi_2I_6Cl_3$. Positive and negative values in the y-axis indicate bonding and anti-bonding states, respectively. (b) Harmonic interatomic force constants for the nearest neighbor atom pairs in $Cs_3Bi_2I_6Cl_3$. (c) Total charge-density plot in the supercell of $Cs_3Bi_2I_6Cl_3$, where iso-surfaces of charge-density are shown in light gray color. Cs, Bi, I, and Cl atoms are denoted by the blue, red, yellow, and green spheres, respectively.*

We performed first-principles DFT calculations for analysis of chemical bonding, crystal structure and lattice dynamics of $Cs_3Bi_2I_6Cl_3$ to understand its ultralow thermal conductivity. We have performed crystal orbital Hamilton population (COHP)[63, 64] analysis (Figure 4.2.8a) using wavefunctions obtained from DFT. COHP is a method which partitions electronic energy of bands into pairwise orbital or atomic interactions, identifying their chemical character as bonding, anti-bonding or non-bonding.[63, 64] Figure 4.2.8a shows sharp anti-bonding peaks (near -0.2 eV) just below the Fermi level (E_f) associated with Bi-Cl and Bi-I interactions. Below -0.75 eV however, Bi-I interactions have a bonding character whereas Bi-Cl interactions maintain anti-bonding character down to -2 eV below E_f. Such filled anti-bonding states in the valance band just below the Fermi level soften the lattice, leading to low sound velocities. On the other hand, Cs-I and Cs-Cl interactions show nearly vanishing COHP characters, indicating no covalency and primarily ionic interaction between them. Analysis of harmonic interatomic force constants (IFCs) clearly reveals the large difference in bond stiffness of Bi-Cl/I and Cs-Cl/I bonds (Figure 4.2.8b) with the Bi-I bond being the strongest (force constant, $|\Phi|$ = 5.0 eV/Å^2) followed by the Bi-Cl bond stiffness ($|\Phi|$ = 1.5 eV/Å^2). The disparity in interactions of Cl and I with the metal atoms (Bi and Cs) gives rise to a bonding hierarchy that helps in suppressing κ_L in the compound.[76] Chemical interactions between different species can also be rationalized by charge density analysis as shown in Figure 4.2.8c on a supercell of the crystal structure of $Cs_3Bi_2I_6Cl_3$. It is seen that the charge clouds of Bi and I strongly overlap, confirming their strong covalent bonding. On the other hand, charge clouds of Cl do not have any overlap with that of Bi, signifying their weaker interaction. Thus, the presence of bonding hierarchy and antibonding states induced lattice softening are expected to give rise to strong lattice anharmonicity in the crystal structure of $Cs_3Bi_2I_6Cl_3$.

Our calculated harmonic phonon dispersion of $Cs_3Bi_2I_6Cl_3$ exhibits multiple imaginary phonon branches (computational method, and Figure 4.2.9a) which is common in the family of halide perovskites.[61] The imaginary phonon mode (-18 cm^{-1}) at Γ exhibits a double-well potential energy surface (Figure 4.2.9b). To stabilize the structure, we nudged the atoms along the eigenvectors of this imaginary phonon mode at Γ and relaxed the crystal structure. Calculated phonon dispersion for this relaxed structure of $Cs_3Bi_2I_6Cl_3$ exhibits a weakly unstable (-12 cm^{-1}) phonon branch with negligible

dispersion (Figure 4.2.10a). Phonon dispersion of $Cs_3Bi_2I_6Cl_3$ also exhibits notably soft acoustic phonon modes with cut-off frequencies below 20 cm^{-1} (Figure 4.2.10c) in all directions of the Brillouin zone, responsible for soft elastic moduli and low speeds of sound (Table 4.2.2). Calculated bulk and shear moduli of $Cs_3Bi_2I_6Cl_3$ are 14.4 GPa and 6.7 GPa, respectively, which are lower than the corresponding values of most other materials exhibiting ultralow κ_L (Figure 4.2.11). These are the properties relevant to the origin of the ultralow κ_L of $Cs_3Bi_2I_6Cl_3$.

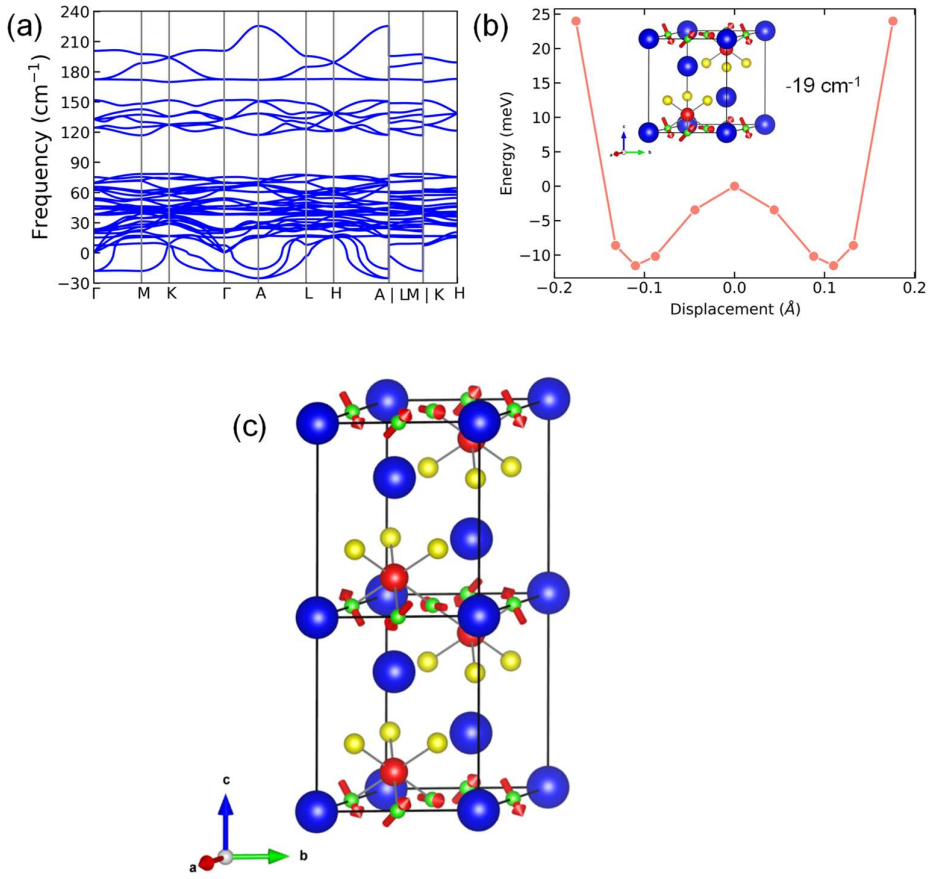

Figure 4.2.9. *(a) Phonon dispersion of the original primitive unit cell of $Cs_3Bi_2I_6Cl_3$ and (b) the double-well potential energy of the imaginary phonon mode at Γ point that appear at -19 cm^{-1}. Inset shows the visualization of the eigenvector. (c) The visualization of the eigenvector of the lowest frequency (-25 cm^{-1}) phonon mode at A-point in a 1x1x2 supercell. Transverse acoustic (TA) phonons hybridize with the lowest frequency torsional phonon modes (-25 cm^{-1}) at the A-point strongly suppressing TA phonons and reducing the speed of sound. Cs, Bi, I, and Cl atoms are denoted by the blue, red, yellow, and green spheres, respectively.*

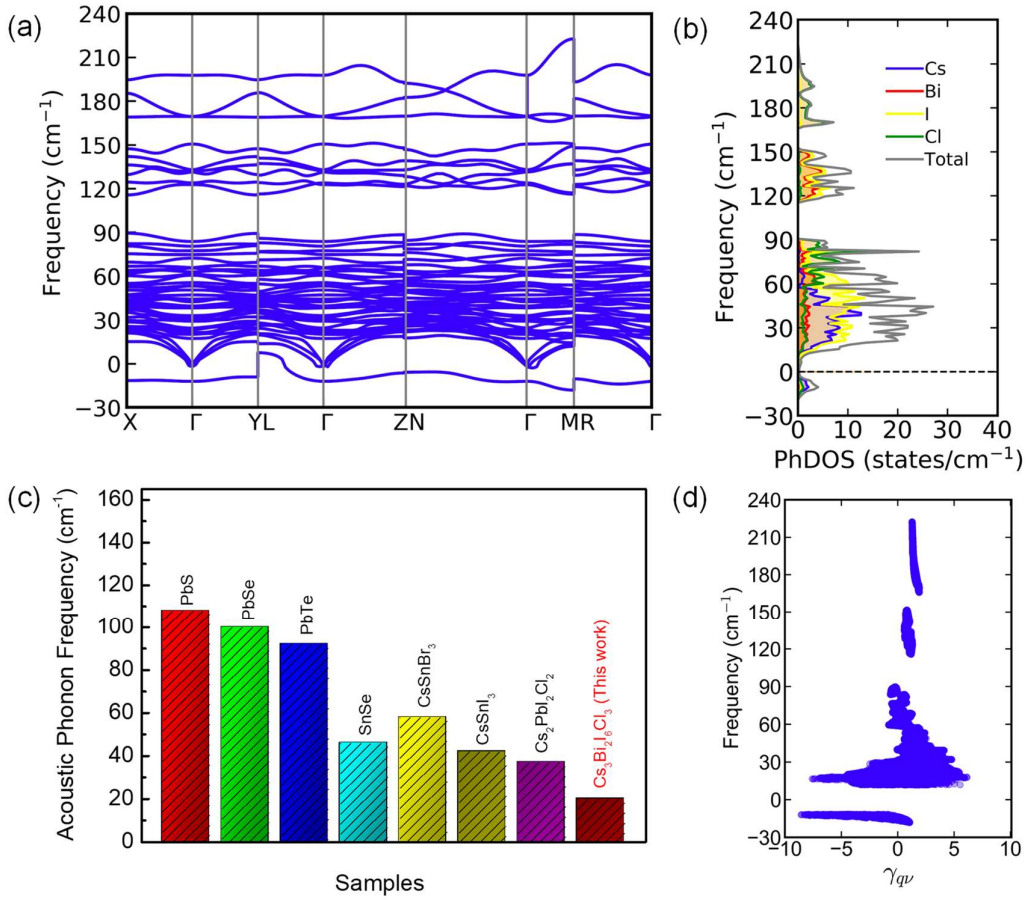

Figure 4.2.10. *(a) Phonon dispersion, (b) atom-resolved phonon density of states of $Cs_3Bi_2I_6Cl_3$. The phonon dispersion exhibits several nearly dispersion-less phonon branches around 40 cm^{-1} including the one that appear near -12 cm^{-1}. These phonon branches are primarily due to the weakly bonded Cs atoms which show rattling like vibrations. (c) Comparison of acoustic phonon frequency of $Cs_3Bi_2I_6Cl_3$ with well-known low thermal conductive heavy metal chalcogenides and 3D all-inorganic halide perovskites.*[40, 41, 77, 78] *(d) Calculated mode Grüneisen parameters of $Cs_3Bi_2I_6Cl_3$.*

The phonon dispersion (Figure 4.2.10a) exhibits multiple low-energy optical phonon branches with high density below 90 cm^{-1}. Interestingly, the phonon branch with unstable phonons with frequency ~ -12 cm^{-1} is rather weakly dispersive and bears similarities to a branch of phonons with rattling atoms.[40, 79, 80] The potential energy landscapes of the atoms in $Cs_3Bi_2I_6Cl_3$ shows that the Cs atoms have the shallowest potential energy surface in all the direction compare to other atoms (Bi, I, and Cl) in the crystal structure signifying their rattling-like dynamics (Figure 4.2.12). The phonon

dispersion (Figure 4.2.10a) and phonon-density of states (Figure 4.2.10b) reveal that unstable modes primarily involve vibrations of Cs atoms. The analysis of participation ratio (PR)[81] of the phonon modes (Figure 4.2.13) reveals that the unstable phonon modes (near -12 cm^{-1}) have low values of PR (~0.2-0.3), indicating their localization which is characteristic of rattling phonon modes.[18c] The atom-resolved phonon density of states (PhDOS) (Figure 4.2.10b) also reveals that the contributions of the Cs vibrations are mostly localized in a narrow energy window centered around 40 cm^{-1}. Because of similar atomic masses of Cs and I, we also observe contributions of iodine atoms to phonon bands centered around 40 cm^{-1} but due to the strong bonding of I they are dispersed over the relatively broader frequency range. Due to the high density of phonons at low energies (~40 cm^{-1}), they can give rise to numerous phonon-scattering processes that can strongly suppress κ_L.[79, 82, 83] Further analysis shows that the torsional mode distorts the soft $[BiCI_{6/2}I_3]^{3-}$ octahedra due to presence of smaller size of Cl at bridging position, making the crystal structure more flexible and elastically soft (Figure 4.2.9).[84, 85]

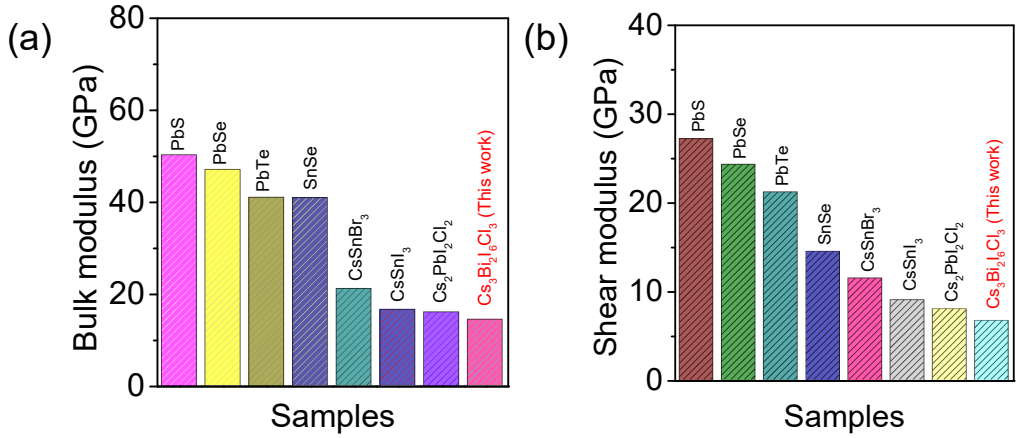

Figure 4.2.11*. Comparison of the DFT calculated (a) bulk modulus[41, 86-88] and (b) shear modulus[41, 48, 88] of $Cs_3Bi_2I_6Cl_3$ with several well-known low thermal conductive metal chalcogenides and other all-inorganic metal halide perovskites.*

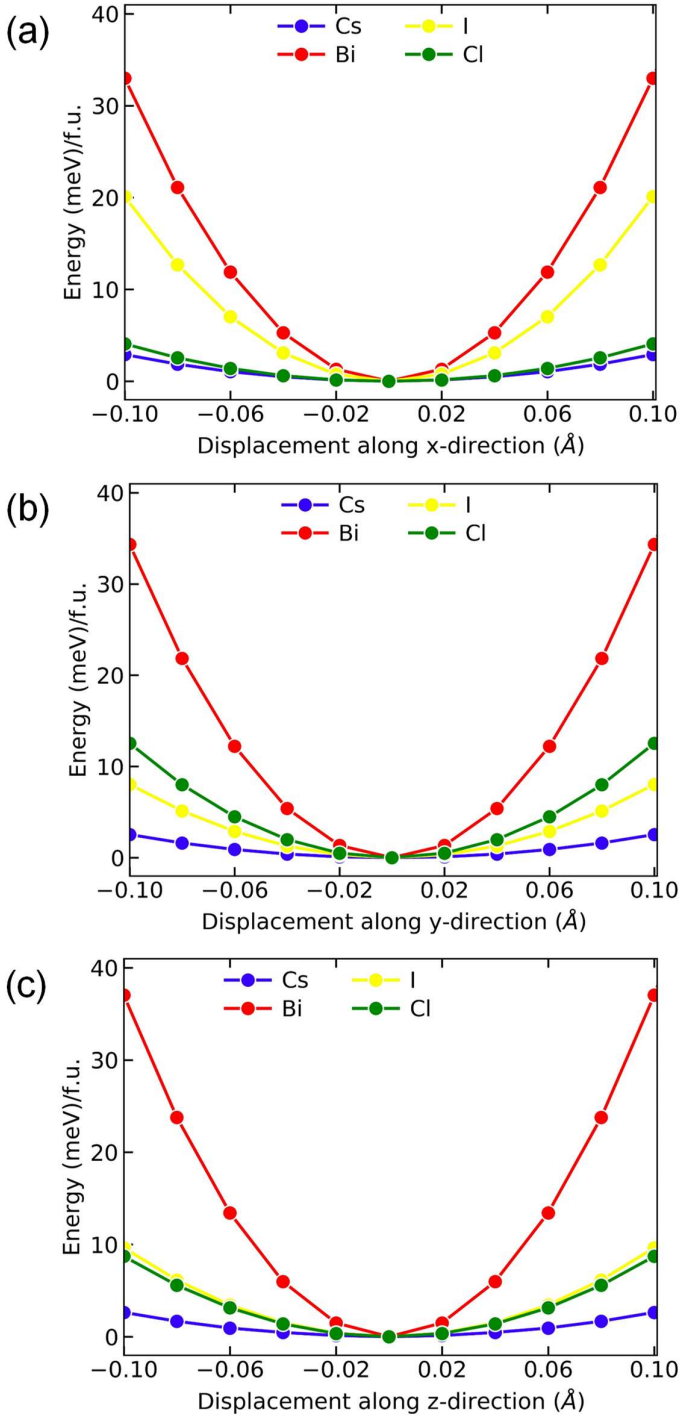

***Figure 4.2.12**. Potential energy vs. displacement plot of $Cs_3Bi_2I_6Cl_3$ along (a) x-direction, (b) y-direction and (c) z-direction.*

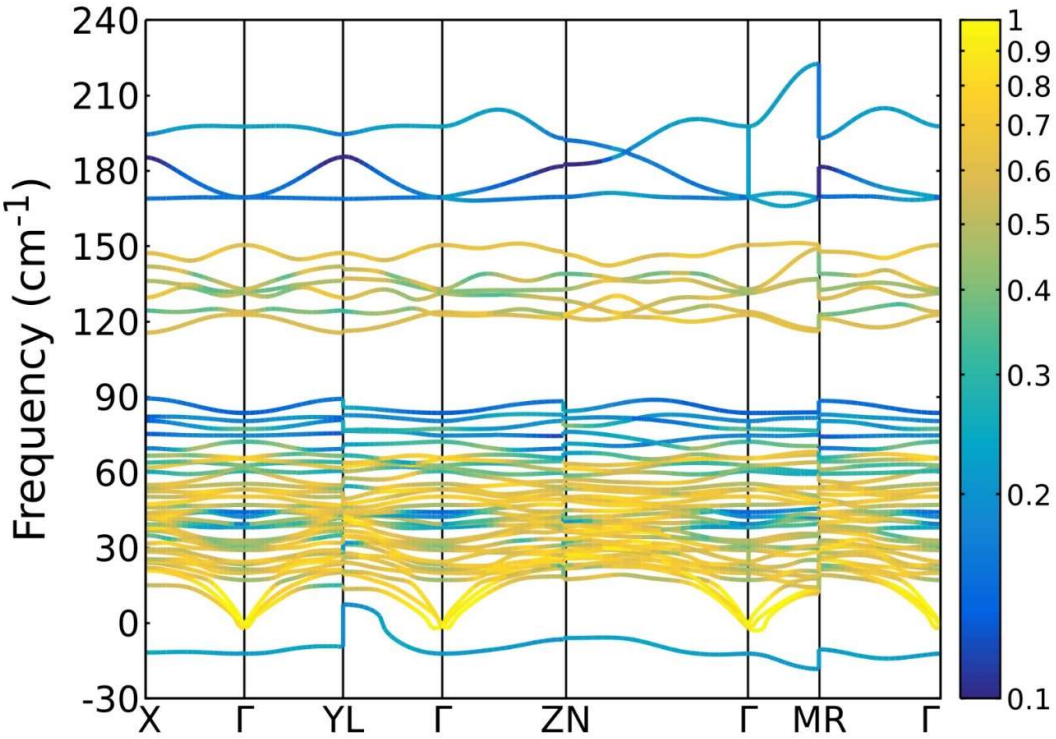

Figure 4.2.13. *Calculated participation ratio (PR)[81] for the phonon modes of $Cs_3Bi_2I_6Cl_3$. Lower value (~0-0.3) of PR indicates more localized phonon modes. Blue and yellow colour indicates lowest and highest value of PR.*

$Cs_3Bi_2I_6Cl_3$ possesses low elastic moduli (Figure 4.2.11), which indicate the softness of its structure, resulting in soft phonon frequencies that generally possess strong anharmonicity. To quantify anharmonicity of the phonon modes in $Cs_3Bi_2I_6Cl_3$, we estimated mode Grüneisen parameters (γ_{qv}) (Figure 4.2.10d), which are notably large (>> 1) for the acoustic and low-energy optical phonons. The estimated average Grüneisen parameter from experimental sound velocities is to be ~2.3 (Table 4.2.2). Since phonon scattering rates (inversely proportional to phonon lifetimes) vary inversely with square of γ_{qv},[89] large values of γ_{qv} limits κ_L to an ultralow in $Cs_3Bi_2I_6Cl_3$.

We have carried out low temperature heat capacity (2-200 K) measurements to understand the ultralow κ_L in $Cs_3Bi_2I_6Cl_3$ (Figure 4.2.14). The plot of C_p/T vs. T^2 can be well fitted using a combined Debye-Einstein model rather than only a Debye model in the temperature range of 2-30 K (Figure 4.2.6c). The Debye model is not sufficient to fit the experimental low temperature heat capacity data of $Cs_3Bi_2I_6Cl_3$ due to the presence

of weakly dispersive low energy optical phonon modes which correspond to independent or nearly independent atomic vibrations similar to Einstein oscillators. Thus, we included several Einstein oscillators, and the combined Debye-Einstein model can be expressed as[90, 91]:

$$\frac{C_p}{T} = \gamma + \beta T^2 + \sum_n \left(A_n (\theta_{E_n})^2 . (T^2)^{-3/2} . \frac{e^{\theta_{E_n}/T}}{\left(e^{\theta_{E_n}/T} - 1\right)^2} \right)$$

The coefficient of the first term on the right-hand side in the equation is the Sommerfeld coefficient γ which represents the electronic contribution and the coefficient for the second term, β, depicts the lattice contribution. The third term in the equation represents contributions from the Einstein oscillators corresponding to the localized lattice vibrations where the A_n is the prefactor and θ_{E_n} is the Einstein temperature of the n^{th} Einstein oscillator mode. We have observed a good fit using this combined Debye-Einstein model with three Einstein modes of θ_{E_1}= 19.2 K (13.3 cm^{-1}), θ_{E_2}= 40.9 K (28 cm^{-1}) and, θ_{E_3}= 76.9 K (53.4 cm^{-1}) (Figure 4.2.6c, Table 4.2.3). These low energy Einstein modes can be attributed to the localized vibration of Cs and I atoms (Figure 4.2.15).

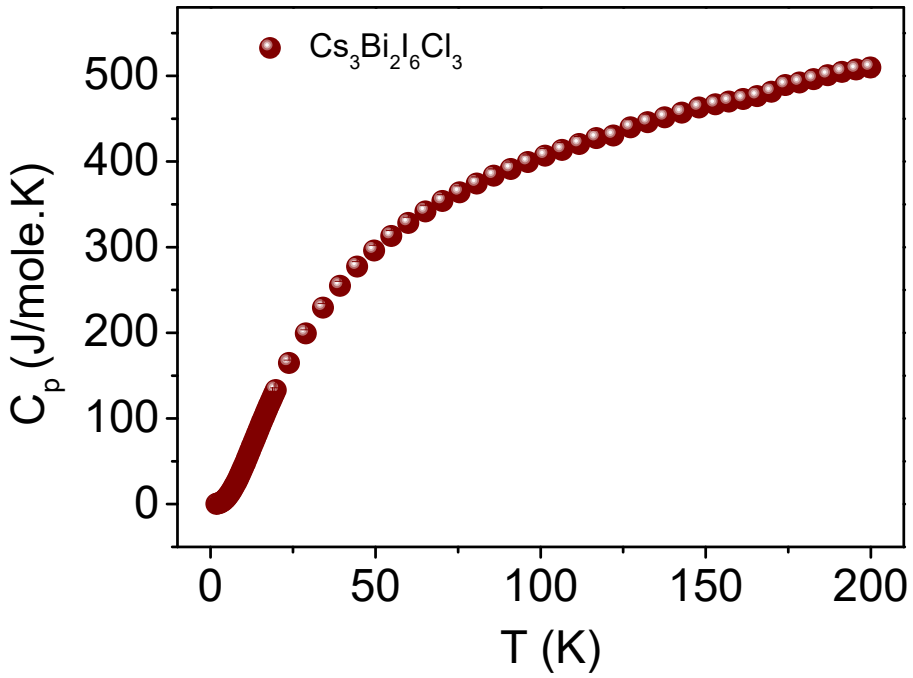

Figure 4.2.14. *Low temperature heat capacity (C_p) of $Cs_3Bi_2I_6Cl_3$.*

Table 4.2.3. *Parameters obtained from the fitting of low-temperature C_p/T vs. T^2 data of $Cs_3Bi_2I_6Cl_3$ using a Debye-Einstein model with three Einstein oscillators.*

Parameter	Value
γ (J/mole.K^2)	0.15926
θ_D (K)	82
θ_{E1} (K)	19.2
θ_{E2} (K)	40.9
θ_{E3} (K)	76.9

The fit of C_p/T^3 vs. T data (inset of Figure 4.2.6c) shows the presence of a boson-like peak similar to that observed in disordered glasses[92-94] which signifies excess phonon density of states contributed by the localized and low frequency optical phonons.[95] The obtained Debye temperature (Θ_D) is 82 K which is estimated using the relation $\beta = C(12\pi^4 N_A k_B/5) \cdot (\Theta_D)^{-3}$ where C can be defined as , $C = 1 - \sum_n A_n/3NR$, (N = number of atoms/ formula unit and R = 8.314 J mol^{-1}K^{-1}, universal gas constant) and N_A, and k_B are the Avogadro's number, and Boltzmann constant respectively. The Debye temperature is lower compared to the state-of-the-art low thermal conductive materials such as SnSe (142 K) and PbTe (164 K).[48]

The occurrence of low-lying optical phonon modes is further verified by temperature dependent Raman spectroscopy. Figure 4.2.17a shows the temperature dependent (4-300 K) Raman spectra in the range 30-180 cm^{-1}, where eleven Raman active modes have been observed with two major peaks positioned at ~58 and ~150 cm^{-1} with

785 nm laser. From group theoretical analysis, A_{1g} and E_g are the two possible Raman mode symmetries (Figure 4.2.15). Most of the peaks in the Raman spectra originate from the terminal and bridging symmetric and asymmetric stretching motion of Bi-X (X = Cl and I) bonding.[66, 96] We have observed four low frequency Raman active modes in the range 35-75 cm^{-1} with a weak mode positioned at ~48 cm^{-1} (A_{1g}), a highest intensive bending mode at ~58 cm^{-1} (E_g), ~63 cm^{-1} (E_g) and ~75 cm^{-1} (A_{1g}). Moreover, a symmetrical and an asymmetrical stretching modes are observed at ~147 cm^{-1} (A_{1g}) and ~132 cm^{-1} (E_g) due to vibration of octahedra at 300 K (see visualization of the Eigen modes at the Γ point in Figure 4.2.15) using a 785 nm laser.[22a] We have also observed a Raman active mode at ~38 cm^{-1} (E_g) using 633 nm laser (Figure 4.2.15, 4.2.16b).

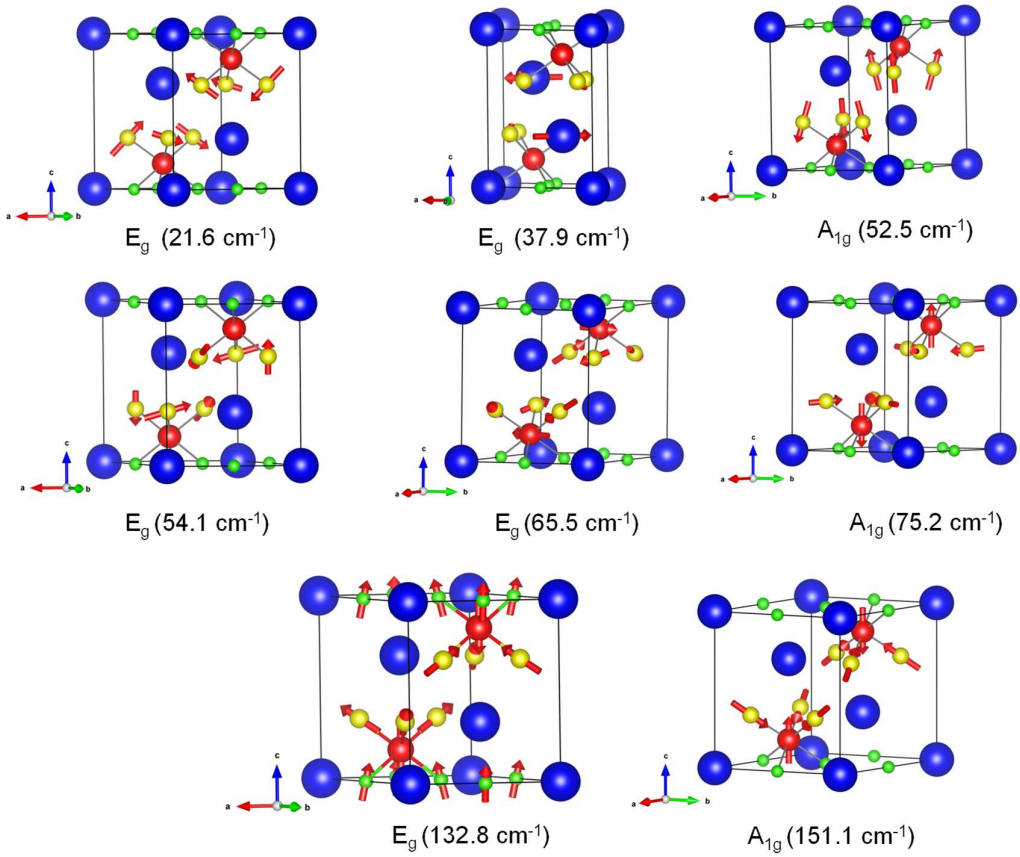

Figure 4.2.15. *Eigenvector visualizations of Raman active modes at Γ-point of $Cs_3Bi_2I_6Cl_3$. Cs, Bi, I, and Cl atoms are denoted by the blue, red, yellow, and green spheres, respectively.*

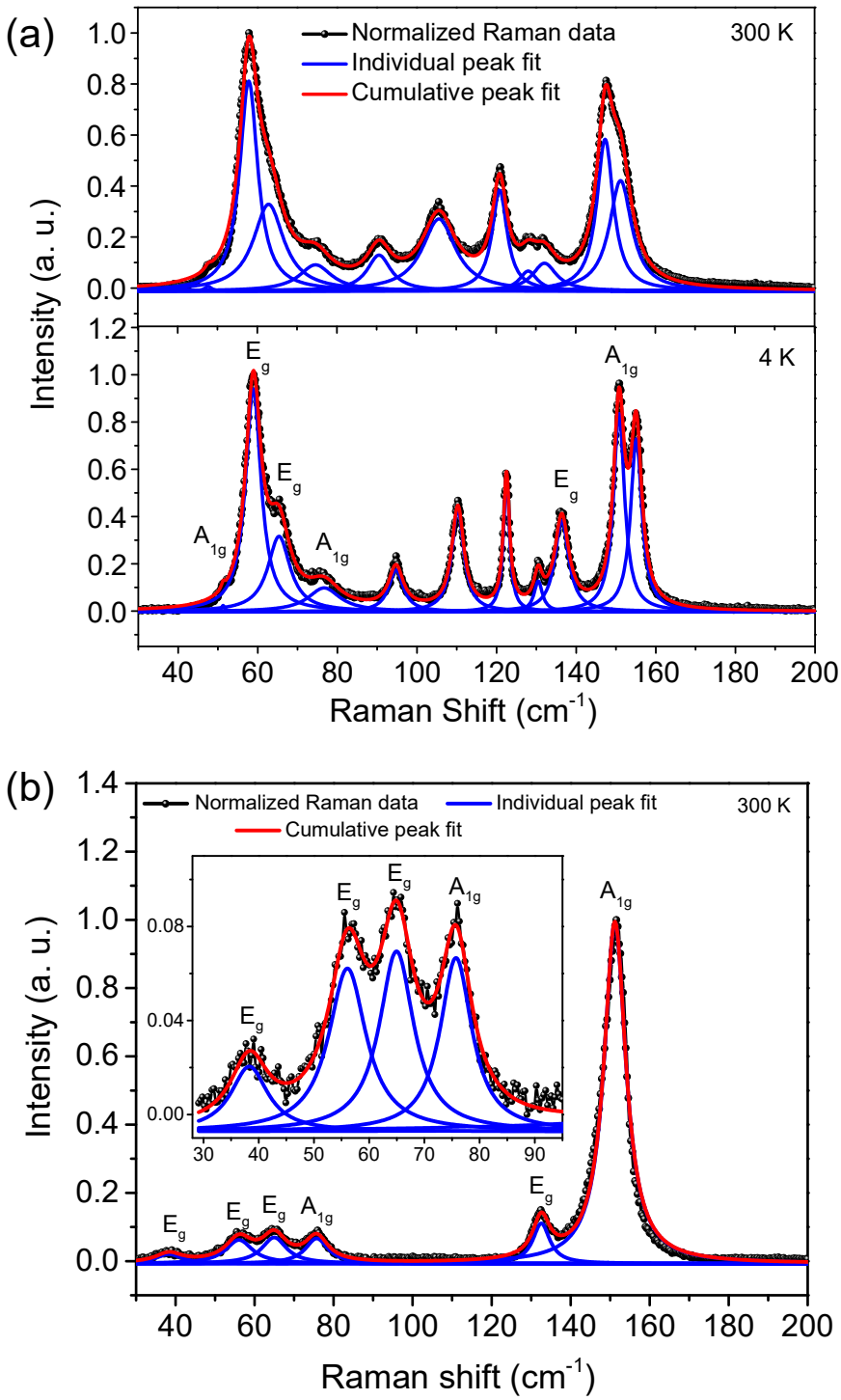

Figure 4.2.16. *(a) Raman spectra of $Cs_3Bi_2I_6Cl_3$ at 4 K and 300 K using 785 nm laser. (b) Room temperature Raman spectra of $Cs_3Bi_2I_6Cl_3$ using 633 nm laser.*

While a distinct signature of all the eleven Raman active modes is present throughout the measured temperature range, a gradual red shift in all the peaks and merging of few of the peaks has been seen with increasing temperature (Figure 4.2.17a). The integrated intensity (Figure 4.2.18a) and FWHM (Figure 4.2.18b) of the Raman peaks increase with increasing temperature indicating that the phonon population increases and the scattering process intensifies, respectively, as shown in Figure 4.2.18. We have estimated the phonon lifetime (τ_i) for the Raman active modes by $\tau_i = \frac{1}{2\pi\, FWHM_i}$, where $FWHM_i$ is the full-width-half-maxima of the observed peaks.[97] The calculated τ_i is of the order of pico-seconds (ps) and decreases with increasing temperature (Figure 4.2.17b), which reflects strong phonon scattering processes increasing with temperature. Furthermore, there are five unassigned Raman modes at 91, 106, 121, 128, and 151 cm^{-1} (at 300 K), which arise probably due to the presence of a local structural distortion in $Cs_3Bi_2I_6Cl_3$ single crystal.

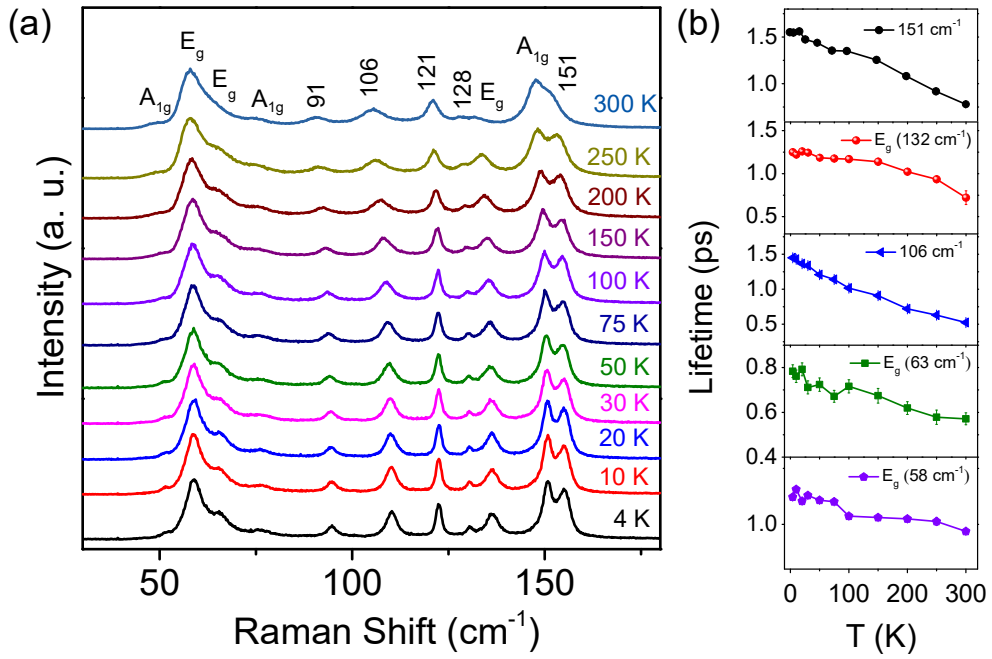

Figure 4.2.17. *(a) Temperature dependent Raman spectra and (b) temperature variation of phonon lifetime for various modes of* $Cs_3Bi_2I_6Cl_3$.

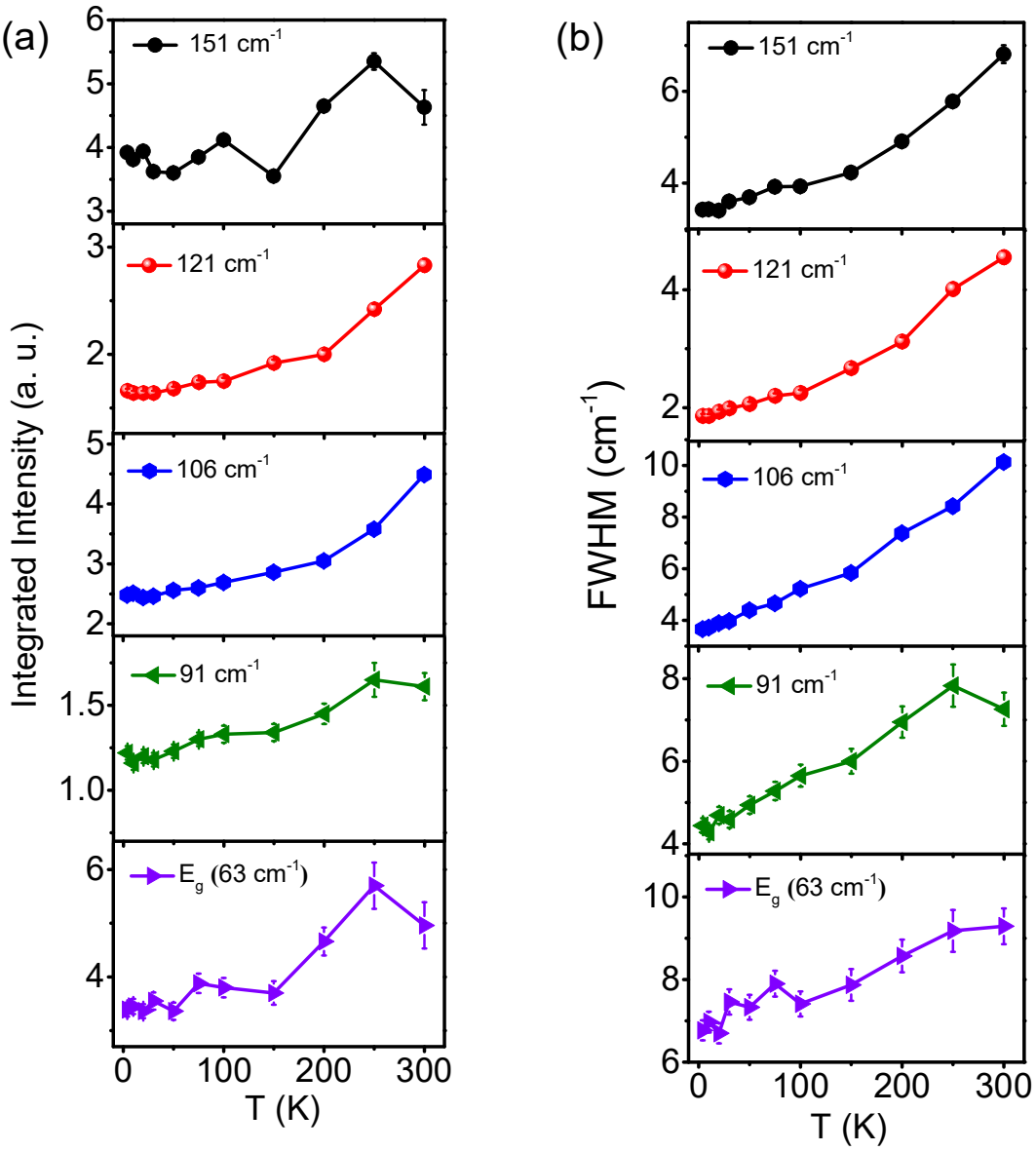

Figure 4.2.18. *Temperature-dependent (a) integrated intensity and (b) FWHM of different Raman peaks of* $Cs_3Bi_2I_6Cl_3$.

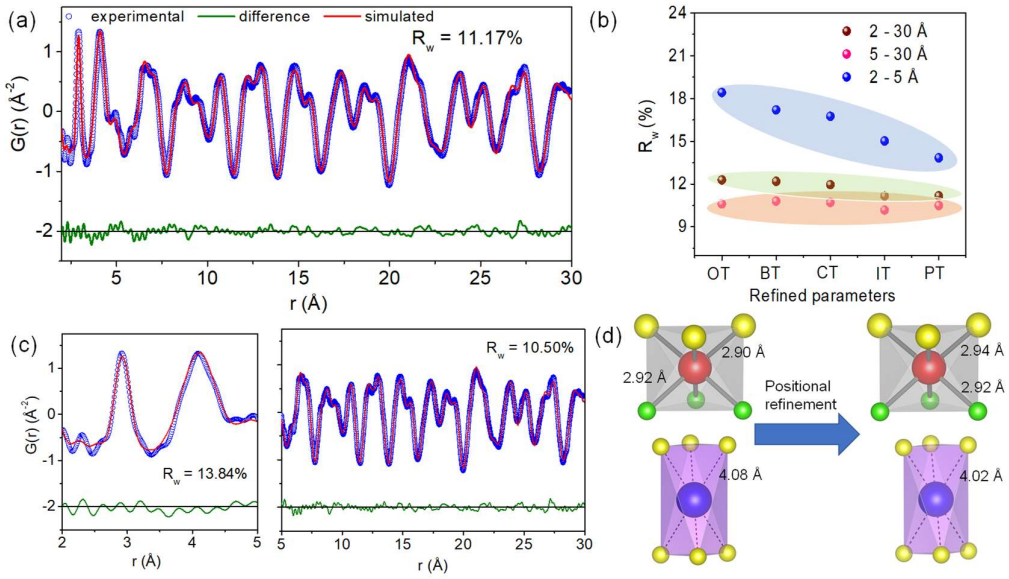

Figure 4.2.19. *a) Room temperature synchrotron X-ray PDF data fitted using P-3m1 space group (ambient crystal structure) with all atom positions and thermal parameters refinement. (b) Goodness of fit (R_w) vs. refinement parameters, where OT: only thermal parameters; BT: bismuth position and thermal parameters, CT: caesium position and thermal parameters, IT: iodine position and thermal parameters and PT: all atomic positions and thermal parameters, are refined. (c) Fitting of local (2-5 Å) and average structural peaks (5-30 Å) for the synchrotron X-ray PDF data of $Cs_3Bi_2I_6Cl_3$ at 300 K using distorted model. (d) Illustration of the bismuth and caesium halide octahedra in $Cs_3Bi_2I_6Cl_3$ exhibiting change in bond lengths upon refinement of local structural peaks of synchrotron PXRD data at 300 K. Cs, Bi, I, and Cl atoms are denoted by the blue, red, yellow, and green spheres, respectively.*

Soft elastic lattice and low speed of sounds, abundance of low energy optical phonon modes and a large anharmonicity rationalize the intrinsic ultralow κ_L in $Cs_3Bi_2I_6Cl_3$. However, the archetypal glass-like temperature dependence of κ_L in single crystalline $Cs_3Bi_2I_6Cl_3$ with well-ordered atomic arrangement is still ambiguous. Such observation of glass-like temperature dependence of κ_L is known for a very few crystalline materials, which originated either because structural disorder such as in $(KCl)_{1-x}(KBr)_x$[23] and YSZ (yttrium stabilized zirconia),[98] rattling vibration in filled skutterudites (such as $CoSb_3$)[99] and off-centering of guest in intermetallic clathrates (such as $Sr_8Ga_{16}Ge_{30}$),[100, 101] modular bonding anisotropy in $Bi_4O_4SeCl_2$[9] and a nanoscale

superstructure in $AgSbTe_2$.[24] The presence of strong anharmonicity in $Cs_3Bi_2I_6Cl_3$ is already evident from the Grüneisen parameter estimated from experimentally measured sound velocity and first-principles based calculations. Moreover, the temperature dependent Raman spectra contain several unassigned peaks which indicates towards the possible presence of a local structural distortion in $Cs_3Bi_2I_6Cl_3$, which would further amplify the phonon scattering strength and probably provide a glass-like temperature dependence of κ_L. To verify this, we have carried out room temperature synchrotron X-ray pair distribution function (PDF) analysis of $Cs_3Bi_2I_6Cl_3$. X-ray PDF is a total scattering technique and gives simultaneous information for both the local and average crystal structure of a material.[102] Figure 4.2.19a shows the X-ray PDF data of $Cs_3Bi_2I_6Cl_3$ at room temperature which is fitted using the trigonal crystal structure (space group *P*-3*m*1). The peaks below (r < 5 Å) provide information about the local structure whereas the peaks above 5 Å describe the average structure of $Cs_3Bi_2I_6Cl_3$ (Figure 4.2.19a). When the X-ray PDF data is refined by tuning only the thermal parameters (OT), we observed that the average structure can be well described within this model as indicative from its goodness of fit R_w = 0.12 (Figure 4.2.19b). However, the corresponding fit to the local structure (r < 5.0 Å) with this structural model is quite poor as evident with high R_w = 0.18 (Figure 4.2.20b). Systematic refinement of atomic positional parameters improves the local structural fitting; however, the best fit is obtained when the positional parameters of all the atoms are refined simultaneously along with their thermal parameter (denoted as PT). The local fit improves significantly to 0.13 for PT as compared to 0.18 for OT (Figure 4.2.19b). R_w value for the average structure (r = 5.0 – 30 Å) remains almost identical in all the cases. The Bi-Cl bond distance is 2.92 Å whereas Bi-I bond distance is 2.90 Å (Figure 4.2.19d) in the global structure which is unusual because Cl is more electronegative than I. The local structural refinement leads to Bi-Cl and Bi-I bond distance 2.92 Å and 2.94 Å, respectively, with a goodness-of fit of 0.13 (Figure 4.2.19c) leading to a local structural distortion $[BiCI_{6/2}I_3]^{3-}$ octahedra. The second peak ~ 4 Å in Figure 4.2.19a corresponds to the Cs and I nearest neighbour correlation. The Cs-I distance is also found to change from 4.08 to 4.02 Å with no notable off-centering of Cs from its parent position. The presence of a bonding anomaly in the Bi-halide octahedra leads to the local structural distortion which lowers the local structural symmetry and might be the reason why we observe unassigned extra Raman modes. This local structural

disorder further enhances the phonon scattering in $Cs_3Bi_2I_6Cl_3$. Therefore, the combined presence of soft elastic crystal structure, large anharmonic phonon modes and local structural distortion can be attributed to the experimentally observed ultralow and glass-like temperature dependence of κ_L.

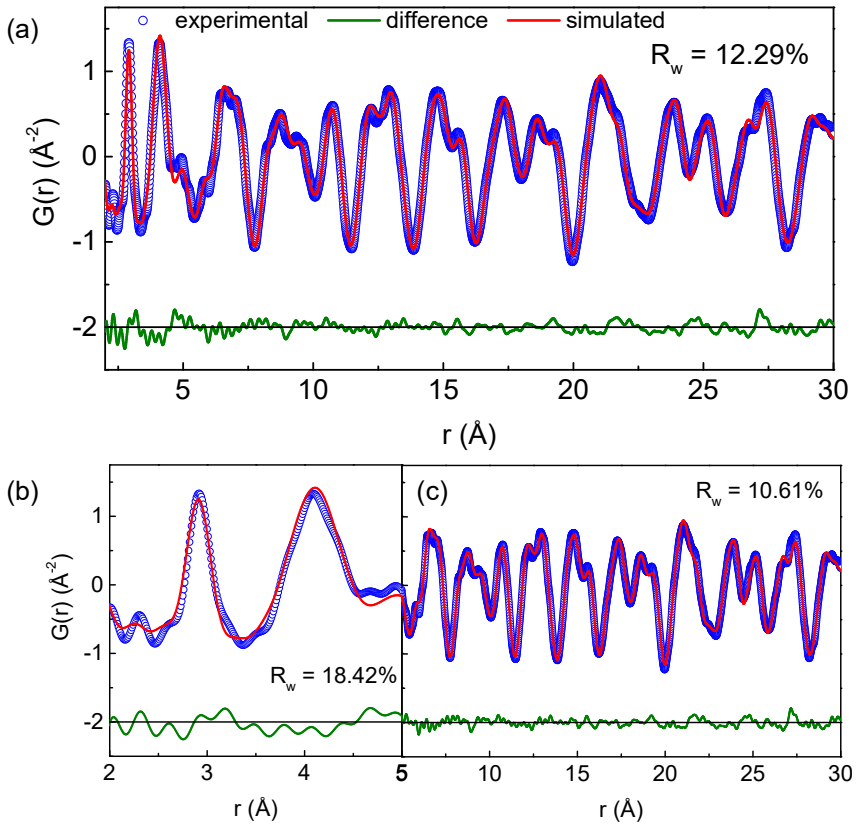

Figure 4.2.20. *(a) Synchrotron X-ray PDF data along with fitting data only with thermal parameter refinement of $Cs_3Bi_2I_6Cl_3$. (b) Fitting of local structure (2-5 Å) and (c) average structure (5-30 Å) of $Cs_3Bi_2I_6Cl_3$ using only thermal parameters refinement.*

4.2.4. Conclusions

In summary, we have demonstrated an ultralow lattice thermal conductivity (κ_L) and its glass-like temperature dependence in the 2-400 K range for a Bridgman grown single crystal of 2D all-inorganic halide perovskites $Cs_3Bi_2I_6Cl_3$. The measured κ_L at room temperature along $\perp$ and || to the Bridgman directions are ultralow values of ~0.20 W/m·K and ~0.22 W/m·K, respectively. The soft elastic layered structure results in a very low

cut-off frequencies (20 cm^{-1}) of the acoustic phonons and hence low speeds of sound. Moreover, chemical bonding hierarchy results in an abundance of weakly dispersive low energy optical phonon modes which includes a torsional motion of $[BiI_3Cl_3]^{3-}$ octahedra and localized anharmonic rattling like vibrations of Cs atoms bonded weakly to lattice. Soft acoustic phonons, abundance of low energy optical phonons and high lattice anharmonicity result in strong phonon scattering and ultra-short phonon lifetimes (0.5-1 ps at 300 K). A local structural distortion is evidenced in the Bi-halide octahedra of $Cs_3Bi_2I_6Cl_3$ by synchrotron X-ray PDF. Localized anharmonic vibrations and local structural distortion result in a glass-like temperature dependence of κ_L in $Cs_3Bi_2I_6Cl_3$. This intriguing phonon transport with an ultralow κ_L and its unusual glass-like temperature dependence in a single crystal of all-inorganic halide perovskite demonstrate rich interplay between chemical bonding and lattice dynamics which could be useful in various optoelectronic and thermoelectric applications.

4.2.5. References

1. X. Qian, J. Zhou and G. Chen, *Nat. Mater.*, 2021, **20**, 1188.

2. G. Tan, L.-D. Zhao and M. G. Kanatzidis, *Chem. Rev.*, 2016, **116**, 12123.

3. G. J. Snyder and E. S. Toberer, *Nat. Mater.*, 2008, **7**, 105.

4. N. P. Padture, M. Gell and E. H. Jordan, *Science*, 2002, **296**, 280.

5. F. Tian, B. Song, X. Chen, K. Ravichandran Navaneetha, Y. Lv, K. Chen, S. Sullivan, J. Kim, Y. Zhou, T.-H. Liu, M. Goni, Z. Ding, J. Sun, G. Udalamatta Gamage Geethal Amila, H. Sun, H. Ziyaee, S. Huyan, L. Deng, J. Zhou, J. Schmidt Aaron, S. Chen, C.-W. Chu, Y. Huang Pinshane, D. Broido, L. Shi, G. Chen and Z. Ren, *Science*, 2018, **361**, 582.

6. S. Mukhopadhyay, D. S. Parker, B. C. Sales, A. A. Puretzky, M. A. McGuire and L. Lindsay, *Science*, 2018, **360**, 1455.

7. L.-D. Zhao, S.-H. Lo, Y. Zhang, H. Sun, G. Tan, C. Uher, C. Wolverton, V. P. Dravid and M. G. Kanatzidis, *Nature*, 2014, **508**, 373.

8. C. Chang, M. Wu, D. He, Y. Pei, C.-F. Wu, X. Wu, H. Yu, F. Zhu, K. Wang, Y. Chen, L. Huang, J.-F. Li, J. He and L.-D. Zhao, *Science*, 2018, **360**, 778.

9. D. Gibson Quinn, T. Zhao, M. Daniels Luke, C. Walker Helen, R. Daou, S. Hébert, M. Zanella, S. Dyer Matthew, B. Claridge John, B. Slater, W. Gaultois Michael, F. Corà, J. Alaria and J. Rosseinsky Matthew, *Science*, 2021, **373**, 1017.

10. M. Dutta, M. Samanta, T. Ghosh, D. J. Voneshen and K. Biswas, *Angew. Chem., Int. Ed.*, 2021, **60**, 4259.

11. M. Christensen, A. B. Abrahamsen, N. B. Christensen, F. Juranyi, N. H. Andersen, K. Lefmann, J. Andreasson, C. R. H. Bahl and B. B. Iversen, *Nat. Mater.*, 2008, **7**, 811.

12. X. Shi, J. Yang, J. R. Salvador, M. Chi, J. Y. Cho, H. Wang, S. Bai, J. Yang, W. Zhang and L. Chen, *J. Am. Chem. Soc.*, 2011, **133**, 7837.

13. C. Chiritescu, G. Cahill David, N. Nguyen, D. Johnson, A. Bodapati, P. Keblinski and P. Zschack, *Science*, 2007, **315**, 351.

14. B. Jiang, Y. Yu, J. Cui, X. Liu, L. Xie, J. Liao, Q. Zhang, Y. Huang, S. Ning, B. Jia, B. Zhu, S. Bai, L. Chen, J. Pennycook Stephen and J. He, *Science*, 2021, **371**, 830.

15. K. Biswas, J. He, I. D. Blum, C.-I. Wu, T. P. Hogan, D. N. Seidman, V. P. Dravid and M. G. Kanatzidis, *Nature*, 2012, **489**, 414.

16. M. Dutta, D. Sarkar and K. Biswas, *Chem. Commun.*, 2021, **57**, 4751.

17. M. Beekman and D. G. Cahill, *Cryst. Res.Tech.*, 2017, **52**, 1700114.

18. M. T. Agne, R. Hanus and G. J. Snyder, *Energy Environ. Sci.*, 2018, **11**, 609.

19. C. Kittel, *Phys. Rev.*, 1949, **75**, 972.

20. J. L. Cohn, G. S. Nolas, V. Fessatidis, T. H. Metcalf and G. A. Slack, *Phys. Rev. Lett.*, 1999, **82**, 779.

21. A. Weathers, J. Carrete, J. P. DeGrave, J. M. Higgins, A. L. Moore, J. Kim, N. Mingo, S. Jin and L. Shi, *Phys. Rev. B*, 2017, **96**, 214202.

22. Z. Liu, W. Zhang, W. Gao and T. Mori, *Energy Environ. Sci.*, 2021, **14**, 3579.

23. D. G. Cahill, S. K. Watson and R. O. Pohl, *Phys. Rev. B*, 1992, **46**, 6131.

24. S. Roychowdhury, T. Ghosh, R. Arora, M. Samanta, L. Xie, K. Singh Niraj, A. Soni, J. He, V. Waghmare Umesh and K. Biswas, *Science*, 2021, **371**, 722.

25. J. Ma, O. Delaire, A. F. May, C. E. Carlton, M. A. McGuire, L. H. VanBebber, D. L. Abernathy, G. Ehlers, T. Hong, A. Huq, W. Tian, V. M. Keppens, Y. Shao-Horn and B. C. Sales, *Nat. Nanotechnol.*, 2013, **8**, 445.

26. W. Zhang, G. E. Eperon and H. J. Snaith, *Nat. Energy*, 2016, **1**, 16048.

27. Q. A. Akkerman, G. Rainò, M. V. Kovalenko and L. Manna, *Nat. Mater.*, 2018, **17**, 394.

28. J. S. Manser, J. A. Christians and P. V. Kamat, *Chem. Rev.*, 2016, **116**, 12956.

29. A. D. Wright, C. Verdi, R. L. Milot, G. E. Eperon, M. A. Pérez-Osorio, H. J. Snaith, F. Giustino, M. B. Johnston and L. M. Herz, *Nat. Commun.*, 2016, **7**, 1.

30. K. Miyata, L. Atallah Timothy and X. Y. Zhu, *Sci. Adv.*, **3**, e1701469.

31. E. Skoplaki and J. A. Palyvos, *Sol. Energy*, 2009, **83**, 614.

32. G. Divitini, S. Cacovich, F. Matteocci, L. Cinà, A. Di Carlo and C. Ducati, *Nat. Energy*, 2016, **1**, 1.

33. L. M. Herz, *J. Phys. Chem. Lett.*, 2018, **9**, 6853.

34. M. A. Haque, S. Kee, D. R. Villalva, W.-L. Ong and D. Baran, *Adv. Sci.*, 2020, **7**, 1903389.

35. H. Ma, C. Li, Y. Ma, H. Wang, Z. W. Rouse, Z. Zhang, C. Slebodnick, A. Alatas, S. P. Baker and J. J. Urban, *Phys. Rev. Lett.*, 2019, **123**, 155901.

36. B. Li, Y. Kawakita, Y. Liu, M. Wang, M. Matsuura, K. Shibata, S. Ohira-Kawamura, T. Yamada, S. Lin, K. Nakajima and S. Liu, *Nat. Commun.*, 2017, **8**, 16086.

37. A. Gold-Parker, P. M. Gehring, J. M. Skelton, I. C. Smith, D. Parshall, J. M. Frost, H. I. Karunadasa, A. Walsh and M. F. Toney, *Proc. Natl. Acad. Sci. U.S.A.*, 2018, **115**, 11905.

38. W. Lee, H. Li, A. B. Wong, D. Zhang, M. Lai, Y. Yu, Q. Kong, E. Lin, J. J. Urban, J. C. Grossman and P. Yang, *Proc. Natl. Acad. Sci. U. S. A.* , 2017, **114**, 8693.

39. T. Liu, X. Zhao, J. Li, Z. Liu, F. Liscio, S. Milita, B. C. Schroeder and O. Fenwick, *Nat. Commun.*, 2019, **10**, 5750.

40. H. Xie, S. Hao, J. Bao, T. J. Slade, G. J. Snyder, C. Wolverton and M. G. Kanatzidis, *J. Am. Chem. Soc.*, 2020, **142**, 9553.

41. P. Acharyya, T. Ghosh, K. Pal, K. Kundu, K. Singh Rana, J. Pandey, A. Soni, U. V. Waghmare and K. Biswas, *J. Am. Chem. Soc.*, 2020, **142**, 15595.

42. G. Sheldrick, *Acta. Cryst.* , 2008, **64**, 112.

43. G. Sheldrick, *Acta. Cryst.* , 2015, **71**, 3.

44. L. Farrugia, *J. Appl. Cryst.*, 1999, **32**, 837.

45. J. Rodríguez-Carvajal, *Physica B Condens. Matter*, 1993, **192**, 55.

46. M. T. Agne, R. Hanus and G. J. Snyder, *Energy Environ. Sci.*, 2018, **11**, 609.

47. L.-D. Zhao, J. He, D. Berardan, Y. Lin, J.-F. Li, C.-W. Nan and N. Dragoe, *Energy Environ. Sci.*, 2014, **7**, 2900.

48. Y. Xiao, C. Chang, Y. Pei, D. Wu, K. Peng, X. Zhou, S. Gong, J. He, Y. Zhang, Z. Zeng and L.-D. Zhao, *Phys. Rev. B*, 2016, **94**, 125203.

49. A.-C. Dippel, H.-P. Liermann, J. T. Delitz, P. Walter, H. Schulte-Schrepping, O. H. Seeck and H. Franz, *J. Synchrotron Rad.*, 2015, **22**, 675.

50. T. Proffen, S. J. L. Billinge, T. Egami and D. Louca, *Z. Kristallogr. Cryst. Mater.* , 2003, **218**, 132.

51. M. Basham, J. Filik, M. T. Wharmby, P. C. Y. Chang, B. El Kassaby, M. Gerring, J. Aishima, K. Levik, B. C. A. Pulford, I. Sikharulidze, D. Sneddon, M. Webber, S. S. Dhesi, F. Maccherozzi, O. Svensson, S. Brockhauser, G. Naray and A. W. Ashton, *J. Synchrotron Rad.*, 2015, **22**, 853.

52. P. Juhas, T. Davis, C. L. Farrow and S. J. L. Billinge, *J. Appl. Crystallogr.*, 2013, **46**, 560.

53. C. L. Farrow, P. Juhas, J. W. Liu, D. Bryndin, E. S. Božin, J. Bloch, T. Proffen and S. J. L. Billinge, *J. Phys. Condens. Matter*, 2007, **19**, 335219.

54. G. Kresse and J. Furthmüller, *Comput. Mater. Sci.*, 1996, **6**, 15.

55. G. Kresse and J. Furthmüller, *Phys. Rev. B*, 1996, **54**, 11169.

56. P. E. Blöchl, *Phys. Rev. B*, 1994, **50**, 17953.

57. G. Kresse and D. Joubert, *Phys. Rev. B*, 1999, **59**, 1758.

58. J. P. Perdew, A. Ruzsinszky, G. I. Csonka, O. A. Vydrov, G. E. Scuseria, L. A. Constantin, X. Zhou and K. Burke, *Phys. Rev. Lett.*, 2008, **100**, 136406.

59. J. P. Perdew, K. Burke and M. Ernzerhof, *Phys. Rev. Lett.*, 1996, **77**, 3865.

60. A. Togo and I. Tanaka, *Scr. Mater.*, 2015, **108**, 1.

61. R. X. Yang, J. M. Skelton, E. L. da Silva, J. M. Frost and A. Walsh, *J. Chem. Phys.*, 2020, **152**, 024703.

62. J. F. Nye, *Physical properties of crystals: Their representation by tensors and matrices*, Oxford University Press, 1957.

63. V. L. Deringer, A. L. Tchougréeff and R. Dronskowski, *J. Phys. Chem. A*, 2011, **115**, 5461.

64. R. Dronskowski and P. E. Bloechl, *J. Phys. Chem.*, 1993, **97**, 8617.

65. W. Setyawan and S. Curtarolo, *Comput. Mater. Sci.*, 2010, **49**, 299.

66. K. M. McCall, C. C. Stoumpos, O. Y. Kontsevoi, G. C. B. Alexander, B. W. Wessels and M. G. Kanatzidis, *Chem. Mater.*, 2019, **31**, 2644.

67. K. K. Bass, L. Estergreen, C. N. Savory, J. Buckeridge, D. O. Scanlon, P. I. Djurovich, S. E. Bradforth, M. E. Thompson and B. C. Melot, *Inorg. Chem.*, 2017, **56**, 42.

68. K. Kundu, P. Acharyya, K. Maji, R. Sasmal, S. S. Agasti and K. Biswas, *Angew. Chem., Int. Ed.*, 2020, **59**, 13093.

69. C. Li, H. Ma, T. Li, J. Dai, M. A. J. Rasel, A. Mattoni, A. Alatas, M. G. Thomas, Z. W. Rouse, A. Shragai, S. P. Baker, B. J. Ramshaw, J. P. Feser, D. B. Mitzi and Z. Tian, *Nano Lett.*, 2021, **21**, 3708.

70. R. McKinney, P. Gorai, E. S. Toberer and V. Stevanovic̀, *Chem. Mater.*, 2019, **31**, 2048.

71. P. Jiang, X. Qian, R. Yang and L. Lindsay, *Phys. Rev. Mater.*, 2018, **2**, 064005.

72. P. Jiang, X. Qian, X. Gu and R. Yang, *Adv. Mater.*, 2017, **29**, 1701068.

73. H. Jang, J. D. Wood, C. R. Ryder, M. C. Hersam and D. G. Cahill, *Adv. Mater.*, 2015, **27**, 8017.

74. C.-L. Hsin, J.-H. Huang, P. Spiewak, Ł. Ciupiński and S.-W. Lee, *Appl. Surf. Sci.*, 2019, **494**, 867.

75. L. Ainsworth, *Proc. Phys. Soc. B*, 1956, **69**, 606.

76. W. Lai, Y. Wang, D. T. Morelli and X. Lu, *Adv. Funct. Mater.*, 2015, **25**, 3648.

77. Y. Zhang, X. Ke, C. Chen, J. Yang and P. R. C. Kent, *Phys. Rev. B*, 2009, **80**, 024304.

78. J. Carrete, N. Mingo and S. Curtarolo, *Appl. Phys. Lett.*, 2014, **105**, 101907.

79. M. K. Jana, K. Pal, U. V. Waghmare and K. Biswas, *Angew. Chem., Int. Ed.*, 2016, **55**, 7792.

80. W. Qiu, L. Xi, P. Wei, X. Ke, J. Yang and W. Zhang, *Proc. Natl. Acad. Sci. U.S.A.*, 2014, **111**, 15031.

81. S. Pailhès, H. Euchner, V. M. Giordano, R. Debord, A. Assy, S. Gomès, A. Bosak, D. Machon, S. Paschen and M. de Boissieu, *Phys. Rev. Lett.*, 2014, **113**, 025506.

82. K. Pal, Y. Xia, J. Shen, J. He, Y. Luo, M. G. Kanatzidis and C. Wolverton, *npj Comput. Mater.*, 2021, **7**, 1.

83. M. Dutta, K. Pal, U. V. Waghmare and K. Biswas, *Chem. Sci.*, 2019, **10**, 4905.

84. Y. Fu, D. J. Singh, W. Li and L. Zhang, *Phys. Rev. B*, 2016, **94**, 075122.

85. L. Ji, H.-Y. Hsu, J. C. Lee, A. J. Bard and E. T. Yu, *Nano Lett.*, 2018, **18**, 994.

86. Y. Yu, M. Cagnoni, O. Cojocaru-Mirédin and M. Wuttig, *Adv. Funct. Mater.*, 2020, **30**, 1904862.

87. E. A. Albanesi, C. M. I. Okoye, C. O. Rodriguez, E. L. Peltzer y Blanca and A. G. Petukhov, *Phys. Rev. B*, 2000, **61**, 16589.

88. M. Shakil, A. Akram, I. Zeba, R. Ahmad, S. S. A. Gillani and M. A. Gadhi, *Mater. Res. Express*, 2020, **7**, 025513.

89. D. T. Morelli, V. Jovovic and J. P. Heremans, *Phys. Rev. Lett.*, 2008, **101**, 035901.

90. M. K. Jana, K. Pal, A. Warankar, P. Mandal, U. V. Waghmare and K. Biswas, *J. Am. Chem. Soc.*, 2017, **139**, 4350.

91. M. Samanta, K. Pal, P. Pal, U. V. Waghmare and K. Biswas, *J. Am. Chem. Soc.*, 2018, **140**, 5866.

92. W. Schirmacher, G. Diezemann and C. Ganter, *Phys. Rev. Lett.*, 1998, **81**, 136.

93. H. Shintani and H. Tanaka, *Nat. Mater.*, 2008, **7**, 870.

94. T. S. Grigera, V. Martín-Mayor, G. Parisi and P. Verrocchio, *Phys. Rev. Lett.*, 2001, **87**, 085502.

95. X. Su, N. Zhao, S. Hao, C. C. Stoumpos, M. Liu, H. Chen, H. Xie, Q. Zhang, C. Wolverton, X. Tang and M. G. Kanatzidis, *Adv. Funct. Mater.*, 2019, **29**, 1806534.

96. K. M. McCall, C. C. Stoumpos, S. S. Kostina, M. G. Kanatzidis and B. W. Wessels, *Chem. Mater.*, 2017, **29**, 4129.

97. J. Pandey, S. Mukherjee, D. Rawat, S. Athar, K. S. Rana, R. C. Mallik and A. Soni, *ACS Appl. Energy Mater.*, 2020, **3**, 2175.

98. P. K. Schelling and S. R. Phillpot, *J. Am. Ceram. Soc.*, 2001, **84**, 2997.

99. B. C. Sales, D. Mandrus, B. C. Chakoumakos, V. Keppens and J. R. Thompson, *Phys. Rev. B*, 1997, **56**, 15081.

100. T. Takabatake, K. Suekuni, T. Nakayama and E. Kaneshita, *Rev. Mod. Phys.*, 2014, **86**, 669.

101. S. Christensen, M. S. Schmøkel, K. A. Borup, G. K. H. Madsen, G. J. McIntyre, S. C. Capelli, M. Christensen and B. B. Iversen, *J. Appl. Phys.*, 2016, **119**, 185102.

102. T. Egami and S. J. L. Billinge, *Underneath the Bragg peaks: structural analysis of complex materials*, Elsevier, 2003.

Chapter 4.3

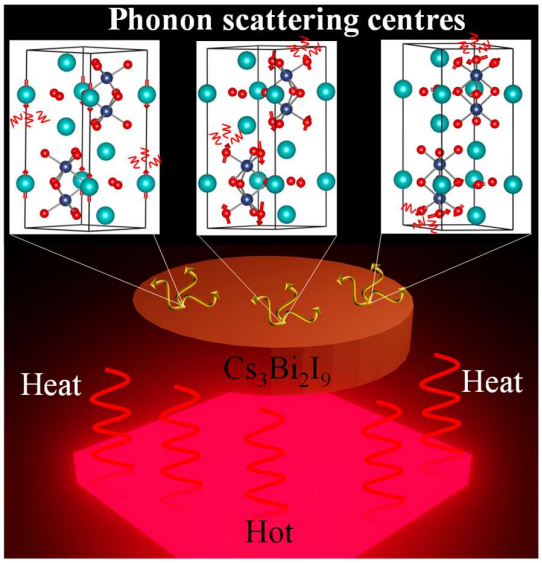

Elastic Softness and Localized Vibration Induced Intrinsically Ultra-low Thermal Conductivity in $Cs_3Bi_2I_9$

Chapter 4.3

Elastic Softness and Localized Vibration Induced Intrinsically Ultra-low Thermal Conductivity in $Cs_3Bi_2I_9$[†]

Summary

Recently, halide perovskites have begun to receive fascination for future cost-effective thermoelectrics beyond the optoelectronic and photovoltaic devices. The promising research accomplishment of perovskite thermoelectrics was mainly recognized by the achievement of their ultra-low thermal conductivity. However, the advancement towards this field has been restricted because of the exploitation of unstable organic cation and/or toxic lead (Pb). These require extensive search for Pb-free all-inorganic perovskites accompanied by the fundamental understanding on their lattice dynamics and low thermal conductivity. In this chapter, we have studied the thermal transport properties of zero-dimensional perovskite, $Cs_3Bi_2I_9$, which exhibited lattice thermal conductivity (κ_L) of ~ 0.20 W/m.K at room temperature. First-principles density functional theory (DFT) calculations reveals the presence of very soft dispersion-less optical phonon modes originating from the presence of bonding heterogeneity, double octahedral rotation, and torsional vibration of $[Bi_2I_9]^{3-}$ octahedra in $Cs_3Bi_2I_9$. These low-lying optical phonons strongly interact with the heat carrying acoustic modes with a very short phonon lifetime (~ 1 ps), leading to softening of the acoustic modes (ω_{max} =15 cm^{-1}). Further, we have experimentally verified the presence of low-lying optical phonon modes via low temperature heat capacity, temperature-dependent Raman spectroscopy and X-ray pair distribution function (PDF) analysis. The presence of ultra-soft acoustic modes, numerous low energy phonon modes, and strong lattice anharmonicity (γ = 2.32) leads to the ultralow κ_L in $Cs_3Bi_2I_9$.

[†]**P. Acharyya,** K. Pal, A. Ahad, D. Sarkar, K. S. Rana, M. Dutta, M. Etter, A. Soni, and K. Biswas. *Manuscript under preparation.*

4.3.1. Introduction

Metal halide perovskites with three-dimensional (3D) structure have appeared as a novel class of semiconductors with enthralling properties for example tunable bandgap, high absorption coefficient, narrow emission line-width, high photoluminescence quantum yield, long charge diffusion lengths and superior charge-carrier mobility.[1-5] In consequence of these outstanding properties, these materials have initiated a perception in wide-ranging field of applications from photovoltaics to optoelectronics.[4, 6-8] Notwithstanding the progressive investigations and flexible applications, the instability against light, heat, and moisture together with the toxicity of lead (Pb) turned out to be detrimental for practical applications of the Pb-based organic-inorganic hybrid perovskites.[9, 10] Reduction of electronic dimensionality and exchange by inorganic cations have been renowned as compelling strategies for resolving the aforementioned issues.[11-16] Thus, the exploration of *all-inorganic* and environmentally benign Pb-free low-dimensional halide perovskites is imperative for advancing this research arena.[8, 17] In recent times, the low dimensional perovskites experienced a remarkable consideration for their tunable electrical and optical properties owing to the quantum and dielectric confinement effects with enriched photo- and thermal stability.[11, 13-15] With these rationales, they have been exploited not only in the light-emitting devices but also in energy harvesting applications.[7] Furthermore, the multifunctional nature of halide perovskites unfolds their diverse applications.[18-22] For example, the ultralow thermal conductivity values together with reasonable charge carrier tunability and mobility directed to the prediction of these materials as probable candidates for forthcoming thermoelectrics.[22-24] Earlier, several approaches (e.g., point defect, rattling, ferroelectric instability, lattice anharmonicity and so forth) have been implemented to achieve low thermal conductivity,[25-31] which is convenient for multipurpose applications resembling thermal barrier coatings, thermal management in electronic devices, and thermoelectrics.[32-37] However, most of the strategies are executed in metal chalcogenides, skutterudites, and clathrate compounds.[38-43]

Low dimensional materials are well-known for efficient thermoelectric as phonons are effectively scattered, resulting in low lattice thermal conductivity.[44, 45] Lately, a few experimental and theoretical reports have appeared on the low-dimensional halide perovskites, which exhibited very low lattice thermal conductivity.[46-49] For

example, Tian's group studied the thermal conductivity of two-dimensional (2D) hybrid butylammonium lead iodide (BA_2PbI_4) and 0D $(CH_3NH_3)_3Bi_2I_9$ crystals.[46, 47] The in-plane and out-of-plane thermal conductivity of 2D BA_2PbI_4 displayed an ultralow thermal conductivity (below 0.3 W/m.K), which was attributed to the low phonon group velocities, and short phonon lifetimes.[46] Whereas the room temperature thermal conductivity of $(CH_3NH_3)_3Bi_2I_9$ is 0.23 ± 0.02 W/m.K. The strong acoustic-optical coupling leads to a small phonon lifetimes resulting a ultralow thermal conductivity in $(CH_3NH_3)_3Bi_2I_9$.[47] To overcome the instability issue of hybrid perovskites, Biswas' group investigated the thermal conductivity of 2D Pb-based Ruddlesden-Popper perovskite $Cs_2PbI_2Cl_2$ single crystal recently, which exhibited very low lattice thermal conductivity of 0.37 W/m.K at 300 K due to the presence of numerous low-frequency optical phonon mode in addition to the dynamic rotation of PbX_6 octahedra and strongly hybridized with the acoustic phonon modes.[48] Further, to get rid of the Pb toxicity, Kanatzidis and co-workers reported the low lattice thermal conductivity (0.32 W/m.K at 550 K) of $CsSnBrI_2$ perovskite.[50] However, such systems may also suffer from the stability issue due to the presence of Sn(II), which can be readily oxidized to the stable Sn(IV) state at ambient condition.[51, 52] However, all these studies encounter the familiar problems of either the presence of unstable organic or inorganic Sn(II) cations or the toxic Pb. Therefore, the quest for a stable *all-inorganic* low-dimensional Pb-free halide perovskites and understanding their phonon transport mechanisms and relationship with the crystal structure are important to develop novel and efficient eco-friendly materials for prospective thermoelectric applications.

In this chapter, we have studied for the first time the thermal transport properties of 0D Pb-free metal halide perovskite $Cs_3Bi_2I_9$. It exhibits ultralow lattice thermal conductivity (κ_L) of ~ 0.20 W/m.K in the temperature range of 30-523 K. Low temperature thermal conductivity study shows the crystalline like thermal conductivity with a well-defined peak which gradually decrease with increase in temperature (5-30 K) due to phonon scattering, which becomes temperature independent at high temperature regime (30-523 K) as it reaches to the minimum thermal conductivity (κ_{diff}) estimated using diffuson model.[53] The presence of the bonding heterogeneity (ionic as well as covalent bonding), the rattling-like motion of the Cs atoms and octahedral distortion creates substantial lattice anharmonicity in the crystal. Moreover, the heat carrying

acoustic phonon modes are strongly coupled with the localized vibrations of Cs atom which originate from the weaker chemical bond (ionic bond) in the lattice. Density functional theory (DFT) reveals the very low bulk and shear moduli that lead to significantly low acoustic phonon frequency (ω_{max} ~15 cm^{-1}). Further, the presence of dispersion-less low-lying optical phonon modes are well characteristics by low-temperature heat capacity (C_p) data, temperature dependent Raman spectroscopy and X-ray pair distribution function (PDF) analysis. We propose that the presence of low-lying optical phonon modes affect the acoustic phonons of comparable energies especially with transverse vibration and leads to the suppression of thermal conductivity to an ultra-low value. Additionally, the ultrasoft elasticity, and large anharmonicity in the structure support the ultralow κ_L in *all-inorganic* Pb-free $Cs_3Bi_2I_9$ perovskite.

4.3.2. Methods

Materials. Caesium (I) iodide (CsI, 99.9%, Sigma Aldrich) and bismuth (III) iodide (BiI_3, 99.998%, Sigma Aldrich) were used without further purification.

Synthesis of $Cs_3Bi_2I_9$. Polycrystalline $Cs_3Bi_2I_9$ is synthesized by reaction of stoichiometric amount of CsI and BiI_3 (3:2) in a quartz ampoules. The tube is sealed under high vacuum (~ 10^{-6} Torr) and slowly heated to 1023 K and kept it for 24 hours followed by slow cooling to room temperature over 48 hours. The obtained ingots are ground into fine powders and sintered by Spark Plasma Sintering (SPS) under a pressure of 50 MPa at 593 K for 5 min under high vacuum to obtain fully dense pellet (~2 mm thickness and 10 mm diameter) with 98% theoretical density and kept the samples inside the desiccator.

X-ray diffraction (XRD). The room temperature powder XRD pattern of $Cs_3Bi_2I_9$ using a synchrotron X-ray beam of $\lambda = 0.7762$ Å, at BL-18B (Indian beamline), Photon Factory, KEK, Tsukuba, Japan. The measurement is performed in Bragg−Brentano geometry with an anti-scattering slit (350 μm), a divergence slit (300 μm), and a receiving slit (300 μm).

Optical spectroscopy. The Optical band gap of $Cs_3Bi_2I_9$ is measured in PerkinElmer, Lambda-900 UV/Vis/near-IR spectrometer in the reflectance mode within the range of 250-800 nm. The absorption data (α/S) of $Cs_3Bi_2I_9$ is anticipated from reflectance data

using Kubelka–Munk equation: $\alpha/S = (1-R)^2/(2R)$; where R, α, and S represent reflectance, absorption and scattering coefficients, respectively.

Field emission scanning electron microscopy (FESEM). FESEM images of $Cs_3Bi_2I_9$ are taken using Apreo 2S, SEM, thermoscientific microscope.

Thermogravimetric analysis (TGA). TGA experiment is conducted using a 2 STAR TGA instrument. The powdered sample of $Cs_3Bi_2I_9$ is heated in the temperature range of 300-1021 K in N_2 atmosphere at a rate of 5 K/ min.

Thermal conductivity. Thermal conductivity measurement is carried out in the temperature range of 2-523 K. The low temperature thermal conductivity (2-300 K) was measured for a rectangular bar shaped specimen with dimensions of ~2 x 2 x 8 mm^3 using a physical properties measurement system (PPMS, DynaCool, Quantum Design). Above room temperature (300-523 K), thermal diffusivity, *D*, is measured by laser flash diffusivity technique using a Netzsch LFA-457 instrument. Typical coin (~10 mm diameter) shaped samples of thickness ~1.86 mm is used for the measurement of thermal transport properties above room temperature and thermal conductivity (κ) is estimated using the relation, $\kappa = D \times C_p \times \rho$, where ρ is the density of the sample and C_p is the specific heat. The obtained density is ~98 % of the theoretical density. We have used the Dulong – Petit C_p (0.178 J/g/K) for the estimation of thermal conductivity.

Heat capacity measurement. Low-temperature heat capacity (C_p) of $Cs_3Bi_2I_9$ is measured in a PPMS, DynaCool, Quantum Design in the temperature range of 2-50 K.

Sound Velocity Measurement. The longitudinal (ν_l) and transverse (ν_t) sound velocities were measured using disc-shaped samples with an Epoch 650 Ultrasonic Flaw Detector (Olympus) instrument with the transducer frequency of 5 MHz. The minimum lattice thermal conductivity was then calculated using the diffusive thermal conductivity[53]:

$$\kappa_{diff} \approx 0.76 k_B \mathrm{n}^{\frac{2}{3}} \frac{1}{3}(v_l + 2v_t) \qquad (1)$$

where k_B is the Boltzmann constant and n is the number density of atoms. Poisson ratio (ν_p) and the Grüneisen parameter (γ) are calculated using below equations (see Table 4.3.2)[54]:

$$\nu_p = \frac{1 - 2(v_t/v_l)^2}{2 - 2(v_t/v_l)^2} \quad (2)$$

$$\gamma = \frac{3}{2}.\frac{1 + \nu_p}{2 - 3\nu_p} \quad (3)$$

Further, the average sound velocity (v_a) was also estimated from the Debye temperature (Θ_D) using the following equation[55]:

$$\Theta_D = \frac{h}{k_B}\left(\frac{3N}{4\pi V_u}\right)^{1/3} v_a \quad (4)$$

where h is Planck's constant, N is the number of atoms in a unit cell, V_u is the unit-cell volume.

Raman spectroscopy. Room temperature Raman spectroscopy of $Cs_3Bi_2I_9$ was conducted via Horiba Jobin-Yvon LabRAM HR evolution Raman spectrometer with excitation laser 633 nm, 50xLWD objective, 1800 lines/mm grating and Peltier cooled CCD detector in the back scattering configuration. Ultra-low frequency filter was used to observed the low frequency Raman active modes. Further, low laser power density ($\leq$ ~ 10 μW) were used to obtain all the Raman spectra. All the spectra are baseline corrected, normalized, and fitted through the Lorentzian function. The room temperature Raman spectroscopy measurements are done in collaboration with Prof. Ajay Soni, IIT Mandi, India.

Temperature dependent Raman spectroscopy measurements (100-300 K) are carried out with a Renishaw spectrometer. The excitation wavelength of the laser is 785 nm.

Computational details. All first-principles density functional theory (DFT) calculations are performed using the Vienna Ab-initio Simulation Package (VASP)[56, 57] utilizing the projector augmented-wave (PAW) [58, 59] potentials for Cs ($5s^2\ 5p^6\ 6s^1$), Bi ($5d^{10}\ 6s^2\ 6p^3$), and I ($5s^2\ 5p^5$). We used the PBEsol[60] exchange-correlation energy functional in our calculations. The kinetic energy cut-off is set to 350 eV and a k-point mesh of 9 × 9 × 4

is used for the relaxation of the cell parameters. The optimized lattice parameters (a= 8.32 Å, c= 22.23 Å) agree well with the experimentally reported values (a= 8.40 Å, c= 21.18 Å).[61] Phonon dispersion of $Cs_3Bi_2I_9$ is calculated using Phonopy[62] code which uses a finite-displacement method for determining the second-order harmonic interatomic force constants (IFCs). We used 3×3×1 supercells (252 atoms) of the primitive unit cell containing 28 atoms for generating the displaced configurations and the calculations of the forces in DFT. Due to the large size of the supercell, we performed Γ point calculations to get the forces on the atoms. The calculated harmonic phonon dispersion exhibits weak imaginary phonon frequencies appearing around Γ and A points. The presence of imaginary phonon frequencies is common in the family of inorganic halide perovskites[63] due to their structural instability in high symmetry structure at low temperature. To stabilize these imaginary phonons, we nudged the atoms in the primitive unit cell with the eigenvectors of the strongest imaginary phonon mode (-9.6 cm^{-1}) which appears at Γ in the Brillouin zone and relaxed the crystal structure of the distorted unit cell. This negative phonon mode exhibits a double-well potential energy surface with a very shallow depth of the well. The relaxed unit cell (henceforth, we call it the distorted structure) lowers its symmetry, which is then utilized to calculate the phonon dispersion in which most of the imaginary phonon modes (including the mode at Γ) got stabilized. We determined the mode Grüneisen parameters of $Cs_3Bi_2I_9$ using a finite difference method, where we have calculated the phonon frequencies of the compound at two different volumes ($1.02V_0$ and $0.98V_0$, V_0 being the equilibrium unit cell volume) and utilized the formula $\gamma_{qv} = -\frac{dln\omega_{qv}}{dlnV}$, where γ_{qv}, V and ω_{qv} denote Grüneisen parameter, unit cell volume, and frequency of a phonon mode at wavevector q for branch ν, respectively. We calculated the bulk (B) and shear (G) moduli of $Cs_3Bi_2I_9$ using Voigt's formula[64] utilizing the elastic tensor obtained from VASP. We have analyzed the chemical bonding of the compound using the crystal orbital Hamilton population method using the LOBSTER code.[65, 66] Theoretical calculations are done in collaboration with Dr. Koushik Pal, Northwestern University, USA.

Synchrotron X-ray Pair Distribution Function (X-PDF).

Samples are finely ground with agate mortar pestle and then filled in capillary of 0.6 mm diameter for performing synchrotron X-ray PDF. Both ends of capillaries are sealed using

adhesive. Perkin Elmer image plate detector is used to record the diffraction data. To subtract the background, data sets of empty capillaries is performed. Dark measurement prior to each data collection is done and Lanthanum Hexaboride (LaB_6) is taken as standard for calibration. The wavelength of the beam is fixed at 0.20742 Å. The data was taken at the P02.1 beamline of PETRA III, DESY, Germany.[67]

G(r) defines the probability of finding nearest neighbor bonding at a certain distance r in the material, is obtained via Fourier transformation of the scattering structure function, F(Q)[68]

$$G(r) = \frac{2}{\pi}\int_{\mathrm{Qmin}}^{\infty} \mathrm{F(Q)\ sinQr\ dQ}$$

where Q represents the momentum transfer of the scattering particle. F(Q) is obtained from the scattering data and is related to the structure function S(Q) as F(Q) = Q[S(Q)-1]. Initial data reduction is done using DAWN[69] and PDFgetx3[70] software. The processing parameters used for the data conversion are: Q_{min} = 0.22 Å^{-1} , Q_{max} = 20.2 Å^{-1} , r_{min} = 0 Å and r_{max} = 30 Å.

Simulation of the experimental PDF data was done using PDFgui[71] software. The data at 300 K initially modelled using a *P*6$_3$/*mmc* model. The refinement parameters were the scale, linear atomic correlation factor, lattice parameter, and the thermal displacement values. The *r* value of the experimental data was taken from 2.2 – 30 Å for the simulation. The first peak of the G(r) *vs. r* plot represents the nearest atom -atom correlation, the second peak corresponds to second nearest atom-atom distances and so on. The PDF measurements are done at beamline P02.1, PETRA III, DESY, Germany, in collaboration with Dr. Martin Etter.

4.3.3. Results and Discussion

$Cs_3Bi_2I_9$ is a member of <111>-oriented perovskite where two octahedra (BiI_6) connected to each other to form a face sharing dimer $[Bi_2I_9]^{3-}$.[52] These dimers are electrostatically isolated from each other and form a 0D molecular salt crystal structure of $Cs_3Bi_2I_9$ (Figure 4.3.1a). The crystal structure of $Cs_3Bi_2I_9$ possesses a hexagonal symmetry (space group *P*6$_3$/*mmc*).[8, 72, 73] The coulombic repulsion between the two Bi^{3+} cations in a face-sharing octahedra lead to a significant elongation (*l'* > *l,* where *l'* = 3.19 Å, *l* = 2.95 Å) of Bi-I bonds (Figure 4.3.1c), resulting in significant weakening of the bond-strength according to Pauling's third rule.[74]

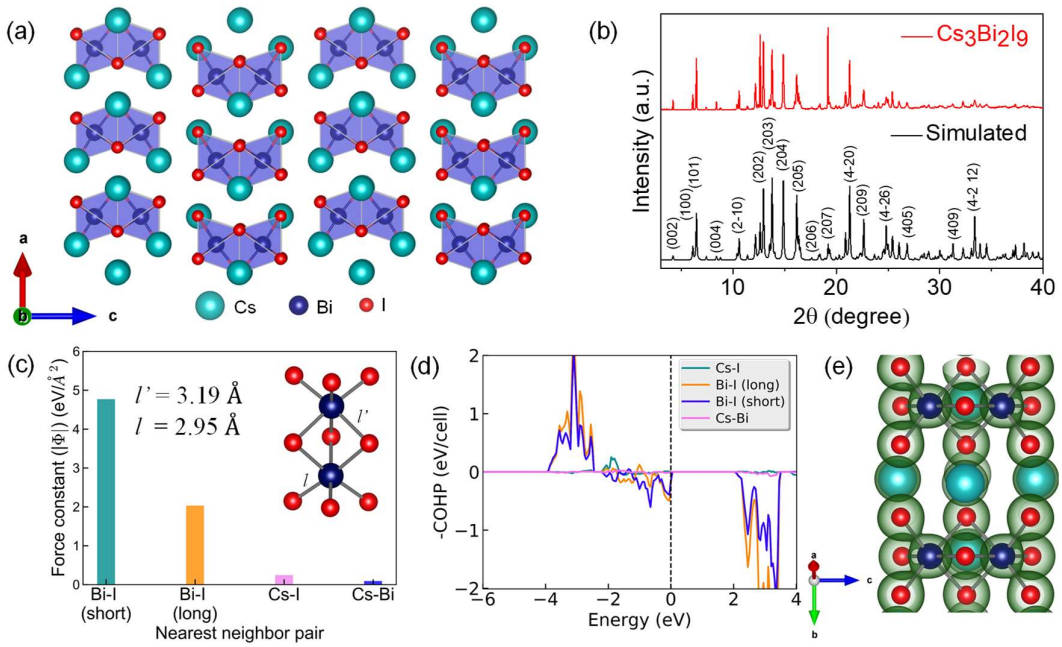

Figure 4.3.1. *(a) Crystal structure of zero-dimensional (0D) $Cs_3Bi_2I_9$ viewed along crystallographic b-direction. (b) Room temperature powder XRD (λ= 0.7762 Å) pattern of $Cs_3Bi_2I_9$ (space group $P6_3/mmc$). (c) Harmonic interatomic force constants for the nearest neighbor atom pair in the crystal structure of $Cs_3Bi_2I_9$. Bi-I (short) and Bi-I (long) denote the shortest (l) and longest (l') Bi-I bonds in the face-sharing BiI_6 octahedra (i.e., Bi_2I_9 unit). (d) Crystal orbital Hamiltonian population (COHP) analysis of $Cs_3Bi_2I_9$. Positive and negative values in the y-axis indicate bonding and anti-bonding states, respectively. (e) Total charge-density plot of $Cs_3Bi_2I_9$, where iso-surfaces of charge-density are shown in green color. Cs, Bi, and I atoms are denoted by the cyan, blue, and red spheres, respectively.*

Our analysis indeed reveals that the absolute values of the interatomic force constants (IFCs) associated with the longer (*l'*) Bi-I bond (2.03 eV/Å^2) is much smaller than that of the shorter (*l*) bond (4.77 eV/Å^2). To understand the chemical bonding in this compound, we have performed the Crystal orbital Hamiltonian population (COHP)[66, 75] analysis using the wavefunctions obtained from our DFT calculations. Figure 4.3.1d shows anti-bonding states below the Fermi level for Bi-I interactions, that extends up to -2 eV. On the other hand, the Cs-I bond shows nearly vanishing non-bonding interactions, indicating that Cs atoms do not form directional covalent bonds with I atoms. The presence of filled anti-bonding and non-bonding states further weaken the bond-strength

in a material which cause ultrasoft elasticity in this compound (discussed later). Analysis of the harmonic IFCs also clearly reveal the large difference in bond strengths between the shorter (*l*) Bi-I bond, longer (*l'*) Bi-I bond, and Cs-I bond (Figure 4.3.1c), signifying the disparate interactions between the cations and the halides, establishing a strong bonding heterogeneity in this compound at the atomic scale. The chemical interactions between different species can also be rationalized by charge density analysis as shown in Figure 4.3.1e, which shows an overlapping charge cloud along the short Bi-I bonds and nearly non-overlapping charge clouds along the long Bi-I bonds, signifying a strong covalent bonding along with shorter Bi-I bonds, but a weaker one along the longer Bi-I bonds. On the other hand, the charges around Cs do not have any connectivity with the other atoms and remain almost spherical. Non-overlapping charge clouds between atoms indicate the absence of strong covalent-like bonding interactions. The unequal bond lengths ($l \neq l'$) in the face-sharing octahedra around Bi atoms i.e., $[Bi_2I_9]^{3-}$ strongly distort the coordination environments around the cations due to strong coulombic repulsion between the two Bi^{3+} cations, and which is expected to exhibit induce strong anharmonic effects on the lattice dynamics in $Cs_3Bi_2I_9$.

High quality polycrystalline $Cs_3Bi_2I_9$ is synthesized by high temperature solid-state melting reaction (see experimental section for details). The room temperature Synchrotron powder X-ray diffraction (PXRD) exhibits high purity of the sample, and all the peaks are well matched with the hexagonal crystal structure of $Cs_3Bi_2I_9$ as demonstrated in Figure 4.3.1b. The optical bandgap of $Cs_3Bi_2I_9$ is measured at room temperature using UV-Vis diffuse reflectance spectroscopy. The absorption spectra demonstrate an absorption edge at ~2 eV along with the excitonic transition near 2.6 eV as reported earlier (Figure 4.3.2a).[72, 76] Field emission scanning electron microscopy (FESEM) images show the high quality of the as-synthesized $Cs_3Bi_2I_9$ samples (Figure 4.3.3a-d). The elemental colour mapping shows the distribution of Cs, Bi and I elements is uniform in $Cs_3Bi_2I_9$ sample (Figure 4.3.3e). Thermogravimetric analysis (TGA) shows that the $Cs_3Bi_2I_9$ sample is thermally stable up to 700 K as shown in Figure 4.3.2b.

We have measured the thermal conductivity of $Cs_3Bi_2I_9$ in the temperature range of 2-523 K which is well below the decomposition temperature of the sample (~700 K).

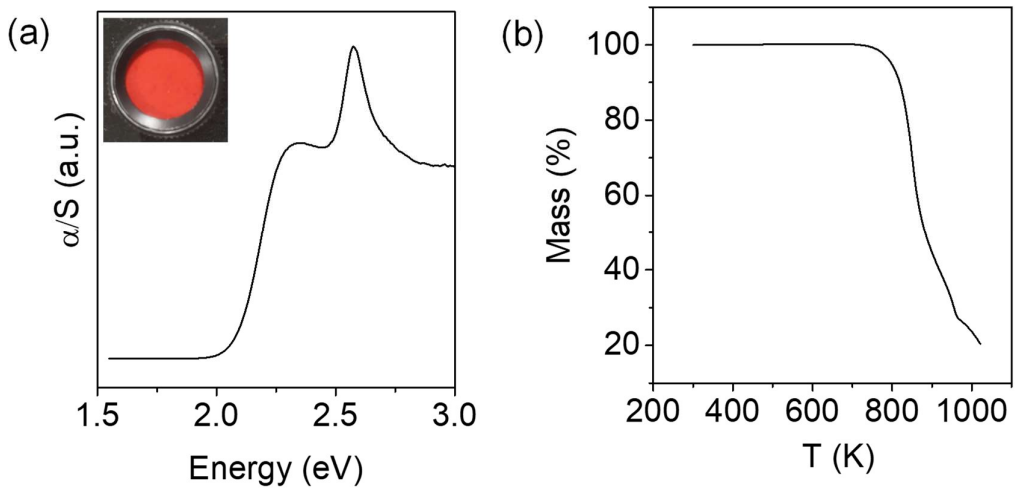

Figure 4.3.2. *(a) Optical absorption spectra of $Cs_3Bi_2I_9$. Inset shows the photograph of powder $Cs_3Bi_2I_9$ sample.*(b) TGA profile of $Cs_3Bi_2I_9$ in N_2 atmosphere.

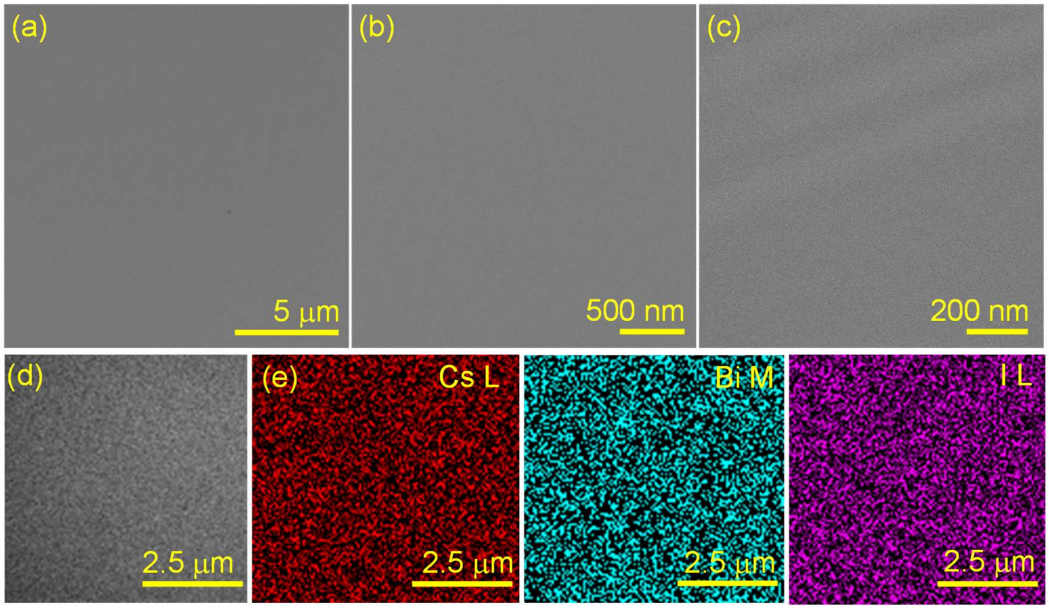

Figure 4.3.3. *(a-c) FESEM images of $Cs_3Bi_2I_9$ at different magnification. (e) Elemental colour mapping for Cs, Bi, and I for the area in (d).*

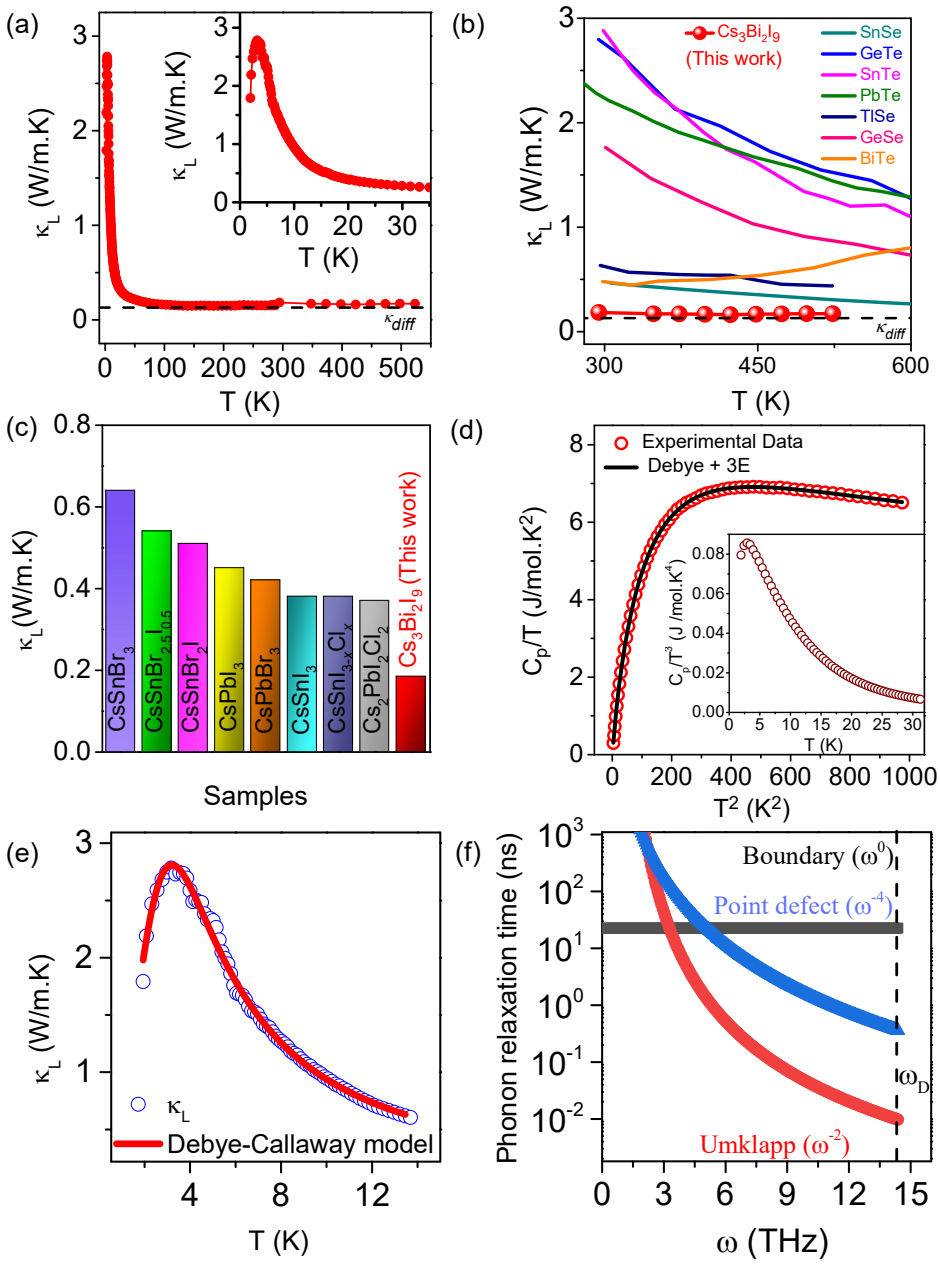

Figure 4.3.4. *(a) Temperature dependent lattice thermal conductivity (κ_L) of $Cs_3Bi_2I_9$. (b) Comparison of κ_L with state-of-the-art low thermal conductive (b) metal chalcogenides[77-83] and (c) room temperature metal halide perovskites.[48, 50, 84, 85] (d) Low temperature C_p/T vs. T^2 plot of $Cs_3Bi_2I_9$ and fit with the Debye – Einstein model. Inset shows the presence of boson like peak in C_p/T^3 vs. T plot. (e) Low temperature κ_L below the temperature independent region. Red solid line showing the fitting to the data with the Debye-Callaway model. (f) Calculated phonon relaxation time, for different scattering mechanism involved in the lattice thermal conductivity, as a function of frequency.*

The high resistivity (> 100 MΩ-cm) of the sample is anticipated due to the high band gap of $Cs_3Bi_2I_9$ (~ 2 eV; Figure 4.3.2). Thus, electronic contribution (κ_{ele}) to total thermal conductivity (κ) is negligible and the k is governed by lattice thermal conductivity (κ_L) solely. At low temperature (below 3 K), the κ_L increases with increasing in temperature and exhibits a "peak-shaped" at 3 K (Figure 4.3.4a). The κ_L value of $Cs_3Bi_2I_9$ is 2.8 W/m.K at 3 K which gradually decrease to ~ 0.20 W/m.K at 30 K mainly due to phonon-phonon Umklapp scattering (discussed later) and becomes independent of temperature at high temperature regime (30-523 K) as it reaches to the diffuson thermal conductivity (κ_{diff}) limit of 0.13 W/m.K.[53] The thermal conductivity value of $Cs_3Bi_2I_9$ (~ 0.20 W/m.K) at room temperature is extremely low compared to the well-known low thermal conductive metal chalcogenides[28, 40, 77-83, 86] and metal halide perovskites (Figure 4.3.4b, c).[48, 50, 84, 85, 87]

To comprehend the experimentally observed ultralow κ_L in $Cs_3Bi_2I_9$, we have measured the low temperature (2-50 K) heat capacity (C_p) (Figure 4.3.5). The C_p/T *vs.* T^2 plot (Figure 4.3.4d) can be well fitted by Debye-Einstein model using the following equation:[42, 88]

$$\frac{C_p}{T} = \gamma + \beta T^2 + \sum_n \left(A_n \left(\theta_{E_n}\right)^2 . (T^2)^{-3/2} . \frac{e^{\theta_{E_n}/T}}{\left(e^{\theta_{E_n}/T} - 1\right)^2} \right)$$

where γ (Sommerfeld constant) denotes the electronic contribution. The second term in the equation, $\beta = C(12\pi^4 N_A k_B/5) \cdot (\Theta_D)^{-3}$ is defined as lattice contribution, where N_A, k_B and θ_D are Avogadro number, Boltzmann constant, and Debye temperature respectively. The parameter C is described as $C = 1 - \sum_n A_n/3NR$, where N, and R denote the number of atoms per formula unit and universal gas constant respectively. The third term in the equation consists of Einstein oscillator mode where A_n and θ_{E_n} are the prefactor and Einstein temperature of the n^{th} Einstein oscillator mode. Figure 4.3.4d shows the Debye + 3 Einstein model fits well compared to the only Debye model and the corresponding $\theta_D, \theta_{E_1}, \theta_{E_2}$, and θ_{E_3} are 107 K, 17 K (12 cm^{-1}), 38 K (26 cm^{-1}) and 71 K (49 cm^{-1}) respectively (Table 4.3.1). The low energy Einstein modes can be attributed to the localized rattling-like vibration of the Cs atoms (12 cm^{-1}; E_{2g}), octahedral distortion (38 cm^{-1},51 cm^{-1}; E_{1g}) as evident from the eigenvector visualizations at Γ-point (Figure 4.3.6). The obtained Debye temperature (107 K) is significantly low compared to the

well-known low thermal conductive materials like PbSe (190 K), PbTe (164 K) and SnSe (142 K)[55] and the corresponding average sound velocity (v_a) is 1288 m/s obtained from the following equation:[55]

$$\Theta_D = \frac{h}{k_B}\left(\frac{3N}{4\pi V}\right)^{1/3} v_a$$

where h, N and V are the plank constant, number of atoms in a unit cell, and unit-cell volume respectively. The derived sound velocity matches well with the measured average sound velocity of 1297 m/s (Table 4.3.2). Such a low sound velocity indicates the soft bonding interaction in the crystal structure which inhibits the heat propagation, result in an ultralow κ_L in $Cs_3Bi_2I_9$. Moreover, the very low θ_D reveals that low temperature is sufficient (< 4.8 K) to activate all the phonons. It justifies the appearance of thermal conductivity peak at low temperature (~0.05 Θ_D or ~ 4.8 K)[89] which further demonstrate the early activation of phonon-phonon scattering.

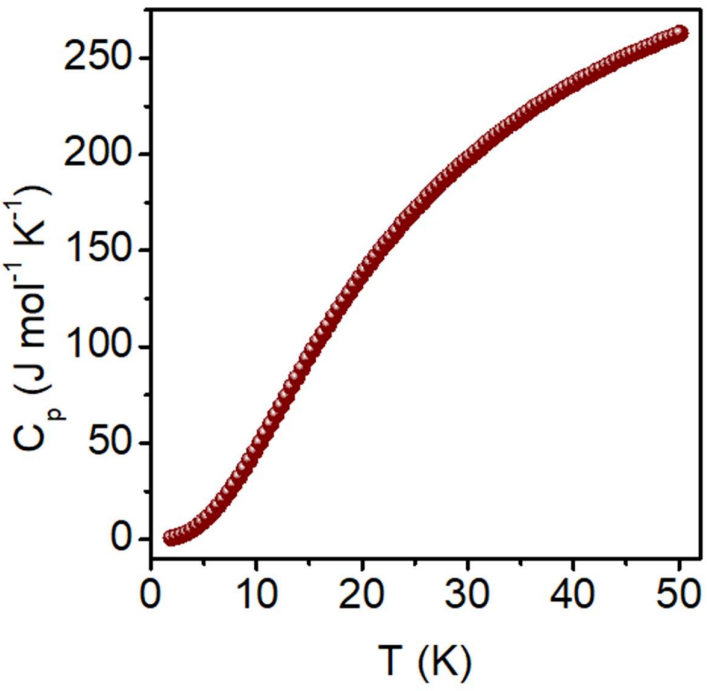

Figure 4.3.5*. Low temperature heat capacity (C_p) of $Cs_3Bi_2I_9$ sample.*

Figure 4.3.4d inset shows the presence of boson peak in C_p/T^3 *vs.* T plot. The presence of boson peak at low temperature signifies the presence of strong coupling between heat

carrying acoustic modes with low-lying optical phonon,[90] resulting in an ultralow κ_L in $Cs_3Bi_2I_9$. The appearance of boson peak in reduced specific heat (C_p/T^3) is heavily associated with the excess vibrational density of states due to low energy phonons and it is found to be responsible for softening the heat carrying acoustic phonons.[39]

Table 4.3.1. *Parameters obtained from fitting of low-temperature C_p/T vs. T^2 data of $Cs_3Bi_2I_9$ using Debye - Einstein model with three Einstein Oscillators.*

Parameter	Value
γ (J/mol.K^2)	0.22
θ_D (K)	107
θ_{E1} (K)	17 (12 cm^{-1})
θ_{E2} (K)	38 (26 cm^{-1})
θ_{E3} (K)	71 (49 cm^{-1})

These low energy optical phonon modes can affect the acoustic modes phonons of comparable energies through strong coupling. Generally, the transverse acoustic (TA) phonons exhibit low energies and are dominant at low temperatures, thus, they can be more strongly affected by the low energy localized phonon modes available in a compound. It is proposed for glasses that the boson peak frequency (ω_{BP}) can be the Ioffe-Regel (IR) limit (ω_{TA}^{IR}) for TA phonons and higher frequency phonon modes above this limit cannot propagate.[91] It is also observed that the TA phonon can be suppressed by intrinsically distorted lattice, resulting in low thermal conductivity.[92]. In some cases, the boson peak occurs at a van Hove singularity at which band flattering ($d\omega/dk=0$) takes place due to hybridization of acoustic and optical phonon branches that manifest as an avoided crossing feature[93] and hence it is the limit of phonon propagation.[94] Plausibly, in

our present case the occurrence of boson peak and thermal conductivity maximum at the same temperature explains the suppression of the TA modes below the peak due to flattening of the low-lying TA branch. As a result, only longitudinal acoustic (LA) phonons become primarily available to propagate heat which also attains minimum mean free path after scattering. Hence, the thermal conductivity becomes ultralow and temperature independent (~ 0.20 W/m.K). The calculated phonon dispersion of $Cs_3Bi_2I_9$ (Figure 4.3.7a) clearly shows the presence of a strong coupling between the TA phonon and an optical phonon mode at a small negative phonon frequency (-3 cm^{-1}) at A point, that severely suppresses the frequency of TA phonon and their propagation in the lattice.

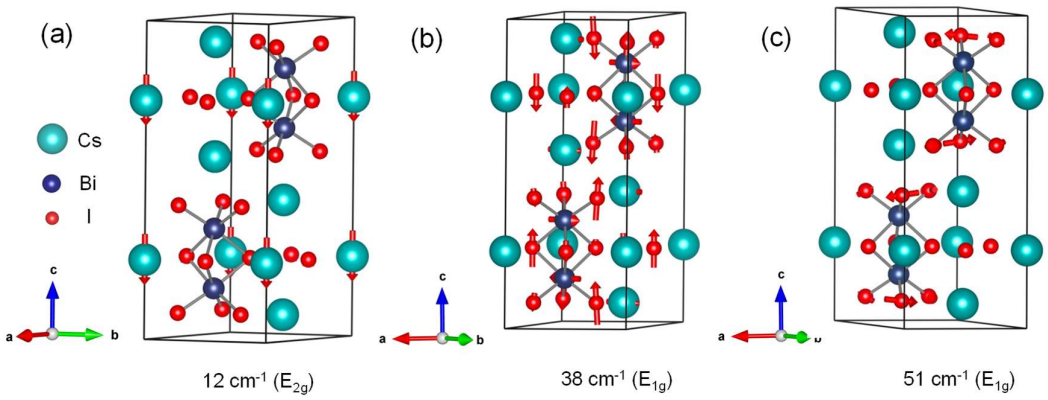

Figure 4.3.6. *Eigenvector visualizations of few Raman active modes at G-point of primitive unit cell of* $Cs_3Bi_2I_9$.

To better understand the role of different scattering mechanism involved in the thermal conductivity we have fitted the data using Debye-Callaway model,[95] given as

$$\kappa_L(x) = \frac{k_B}{2\pi^2 v_a}\left(\frac{k_B T}{\hbar}\right)^3 \int_0^{\frac{\theta_D}{T}} \frac{x^4 e^x}{\tau_{ph}^{-1}(e^x - 1)^2} dx$$

where, $x = \frac{\hbar\omega}{k_B T}$, (ω represents the phonon angular frequency), τ_{ph} is the phonon scattering relaxation time and $\hbar$ is the reduced Planck constant. This model contains possible phonon scattering effects as per Matthiessen's rule in the forms of different relaxation rates.[96] Among them the boundary scattering must include to model the low temperature range while other remains valid for moderate to high temperature.[97-101] The overall scattering rate can be expressed as $\tau_{ph}^{-1} = \tau_B^{-1} + \tau_D^{-1} + \tau_U^{-1}$ where τ_B, τ_D and τ_U are the relaxation times associated with the boundary ($\tau_B = \frac{v_a}{L}$), point defect ($\tau_D = A\omega^4$)

and Umklapp $\left(\tau_U = B\omega^2 T e^{\frac{-\theta_D}{mT}}\right)$ scatterings, respectively, where *m* is the dimension less constant (7.6), *L* is the grain size (24 μm), parameters *A* (10.1 x 10^{-41} s^3), *B* (4.72 x 10^{-16} s K^{-1}), have been used for fitting and these parameters are in the order of well-studied compounds.[102] From the trends of phonon relaxation times, it is evident that the Umklapp scattering (intrinsic) is the dominant for the reduction of thermal conductivity as compared to point defect scattering (extrinsic) as shown in Figure 4.3.4e, f.[103]

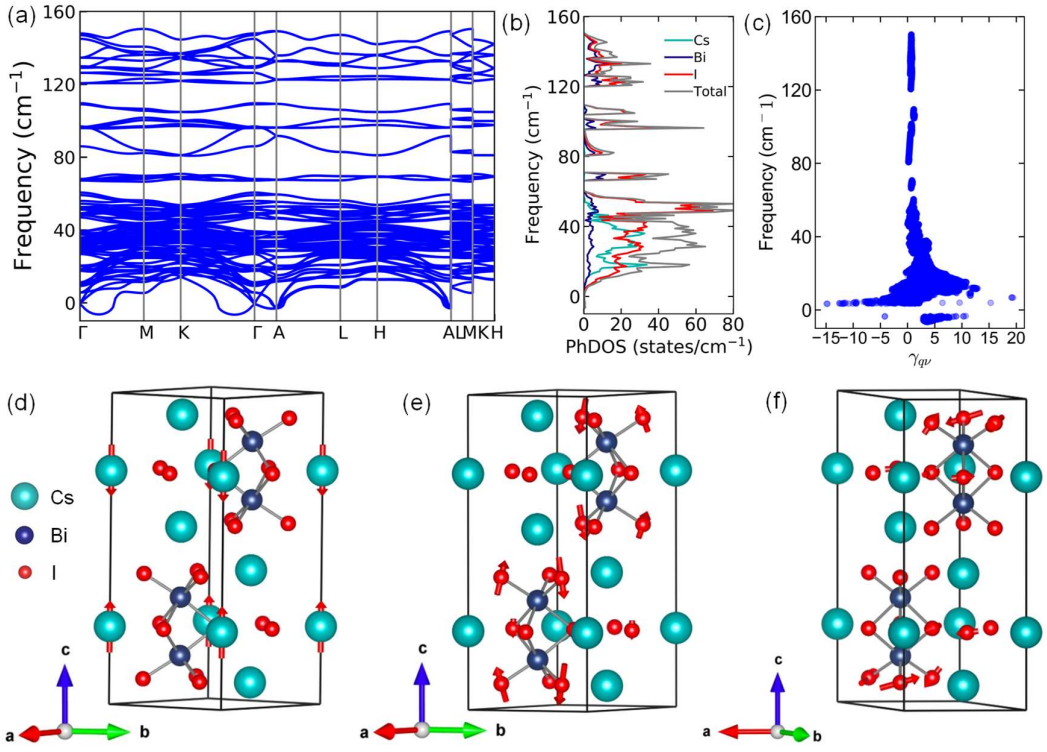

Figure 4.3.7*. (a) Harmonic phonon dispersion, (b) atom-resolved phonon density of states, and (c) mode Grüneisen parameters of $Cs_3Bi_2I_9$. A sharp peak appears at 18 cm^{-1} in (b) which signifies the strong localization of the phonon modes due to the rattling-like vibrations of the Cs cations. Phonon mode at Γ point which involves the (d) rattling like vibration of Cs cation (ω = 18 cm^{-1}), (e) double octahedral rotation (ω= 38 cm^{-1}), (f) torsion mode which involves the rotation of non-bridged I atoms (ω = 52.5 cm^{-1}). The red arrow on the atoms indicates the direction of movement.*

We have performed the analysis of phonon dispersion to understand the origin of ultralow κ_L in $Cs_3Bi_2I_9$. The calculated phonon dispersion (Figure 4.3.7a) for the $Cs_3Bi_2I_9$ exhibits very soft acoustic phonon modes with frequency below 15 cm^{-1} in all directions

in the Brillouin zone that give rise to soft elastic moduli and low sound velocities. The frequency of acoustic phonon modes is significantly lower compared to the well-known low thermal conductive metal chalcogenides and all-inorganic halide perovskites (Figure 4.3.8a). The low value of acoustic phonon mode frequency is reflected in the DFT-calculated bulk and shear moduli (10.9 GPa and 1.3 GPa, respectively) of $Cs_3Bi_2I_9$, which are among the lowest in crystalline compounds (Figure 4.3.8b,c). Such low values of elastic moduli reveal the soft crystal structure and the presence of very low-energy optical phonon modes are anticipated to give rise to a strong anharmonicity in the $Cs_3Bi_2I_9$.

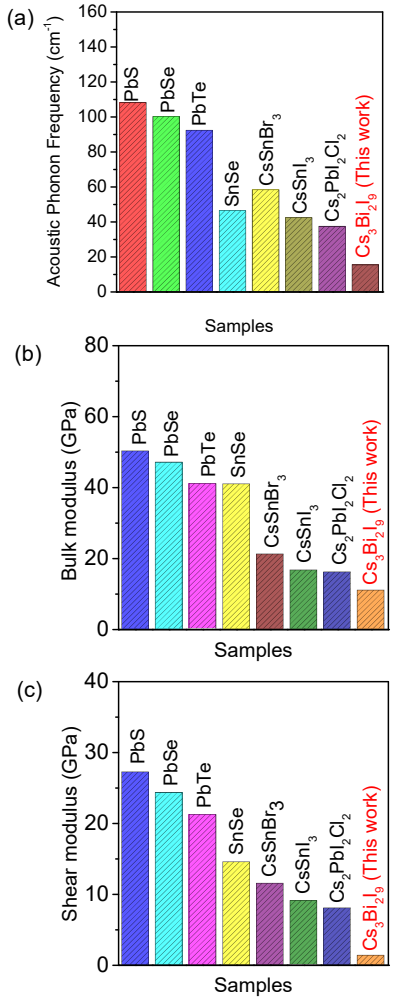

Figure 4.3.8. *(a) Comparison of maximum cut-off of the acoustic phonon frequency of $Cs_3Bi_2I_9$ with well-known low thermal conductive heavy metal chalcogenides*[104, 105] *and all-inorganic halide perovskites.*[48, 50] *Comparison of our DFT calculated (b) bulk modulus and (c) shear modulus of $Cs_3Bi_2I_9$ with several well-known low thermal conductive metal chalcogenides*[55, 106, 107] *and 3D all inorganic metal halide perovskites.*[48, 108]

To quantify the anharmonicity in the system we have estimated the mode Grüneisen parameter (γ_{qv}). Figure 43.7c shows the very high γ_{qv} value ($\gamma_{qv} >> 1$) for the heat carrying acoustic and low-lying optical phonon modes. The calculated average γ_{qv} from the experimental sound velocity is 2.32 ($\gamma_{qv} > 1$) (Table 4.3.2), which is very high. The phonon scattering rates (inversely proportional to the phonon lifetimes) increase with the inverse square of γ_{qv}.[109] Hence, strong phonon-scattering is expected in this compound, that leads to the ultralow κ_L in $Cs_3Bi_2I_9$.

Table 4.3.2. *Experimental sound velocities, diffuson thermal conductivity (κ_{diff}), Poisson ratio (ν_p) and Grüneisen parameters (γ) of $Cs_3Bi_2I_9$.*

Longitudinal sound velocity (m/s)	**Transverse sound velocity (m/s)**	**Average sound velocity (m/s)**	**κ_{diff} (W/m.K)**	**ν_p**	**γ**
2541	1150	1297	0.13	0.37	2.32

Furthermore, Figure 4.3.7a also exhibits several low-energy (< 60 cm^{-1}) optical phonon branches with very small dispersions that are densely packed along with some weak imaginary phonon modes (~ -6 cm^{-1}) appearing in the vicinity of Γ and A points. The phonon density of states (Figure 4.3.7b) reveal that these dispersion-less phonon branches give rise to the strong localization of the phonon modes at low energies. It is interesting to note that a sharp peak appears at 18 cm^{-1} in the density of states, which signify the presence of the rattling-like vibration of the Cs atoms in the crystal structure of $Cs_3Bi_2I_9$, that are loosely bound and can scatter the heat carrying phonon quite effectively (Figure 4.3.7d). The participation ratio (PR) analysis of the phonon modes reveals very low values of PR (~ 0.1) of the phonon modes at 18 cm^{-1} (Figure 4.3.9), signifying the strongly localized vibrations that is the hallmark of rattling phonons. The eigen vector visualization at Γ-point (Figure 4.3.7e, f) demonstrate the presence of the octahedral distortion in $Cs_3Bi_2I_9$. Figure 4.3.7e demonstrates the double octahedral rotation whereas Figure 4.3.7f shows the presence of torsion mode which involves the

rotation of non-bridged I atoms. Thus, the presence of double octahedral rotation (ω = 38 cm^{-1}) and torsion mode (ω = 51 cm^{-1}) strongly perturbs the $Bi_2I_9^{3-}$ molecular salt which substantially creates octahedral distortion in the system and induces strong lattice anharmonicity in the system,[48, 110] resulting in substantial phonon scattering. Thus, weak bonds due the presence of face-sharing polyhedral, filled anti-bonding and non-bonding states, soft elasticity, low speed of sounds, localized low-energy phonon modes, large anharmonicity, and suppression of transverse acoustic modes rationalize the experimental observation of ultralow κ_L in $Cs_3Bi_2I_9$ system.

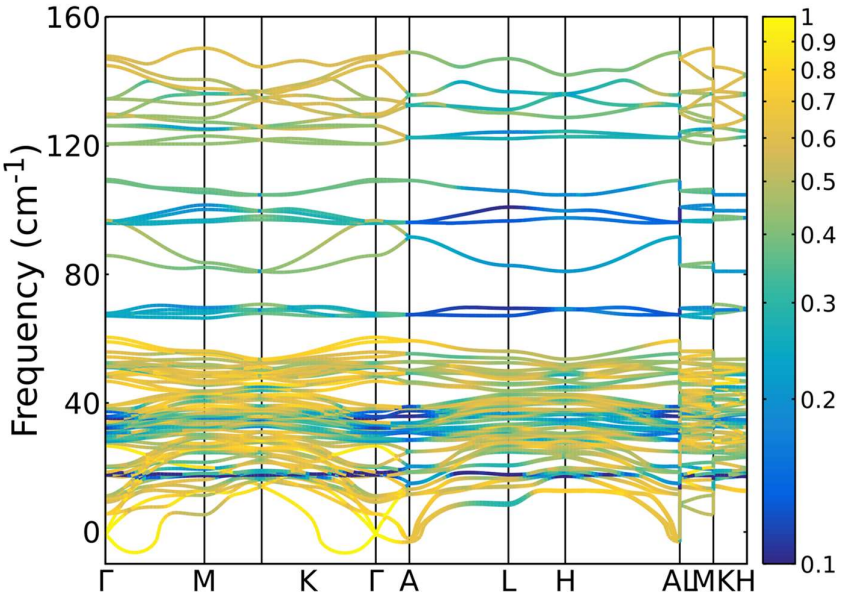

Figure 4.3.9. *Calculation of participation ratio (PR)[111] for the phonon modes of $Cs_3Bi_2I_9$. A localized phonon branch appears at 18 cm^{-1} and possesses very low values of PR (~ 0.1), signifying rattling-like vibration of the loosely bound Cs cations.*

The Raman spectroscopy shows the presence of total 10 Raman active modes in the range of 25-170 cm^{-1} including 5 low lying overlapped modes below 70 cm^{-1}, with an excitation wavelength 633 nm as shown in Figure 4.3.10a. According to the theoretical and group theory analysis A_{1g}, E_{1g}, and E_{2g} are the possible Raman active mode symmetry (space group $P6_3/mmc$, point group D_{6h}). All the observed modes are well matched with the theoretical calculation and earlier reports of $Cs_3Bi_2I_9$ where the vibrational modes are primarily resulting from the vibration of $[Bi_2I_9]^{3-}$ anions.[72, 112] We observed low frequency

Raman active modes at ~ 34 (E_{1g}), 42 (A_{1g}), 48 (E_{1g}), 58 (A_{1g}) and 63 cm^{-1} (E_{1g}) for $Cs_3Bi_2I_9$. The E_{1g} mode at 34 cm^{-1} is lattice vibrational mode, which largely involved the vibration of Cs atom and vibration of $[Bi_2I_9]^{3-}$ anions as seen from the atom projected DOS (Figure 4.3.7b), whereas the rest of low frequency modes are due to bending and stretching motion of Bi-I bond in Cs3Bi_2I_9.[72, 113] Furthermore, we have observed two modes at 90 (E_{2g}; asymmetric) and 105 cm^{-1} (A_{1g}; symmetric) due to bridged Bi–I stretching, and three modes at 120 (E_{1g}; asymmetric), 127 (E_{2g}; asymmetric) and 147 cm^{-1} (A_{1g}; symmetric) due to terminal Bi−I stretching in the $[Bi_2I_9]^{3-}$ anion.

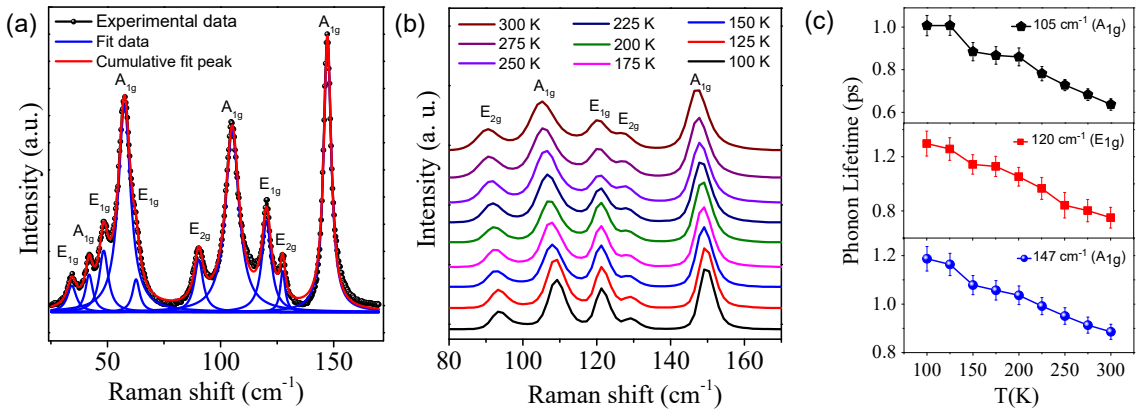

Figure 4.3.10. *(a) Fitted Raman spectra of $Cs_3Bi_2I_9$ at 300 K using 633 nm excitation wavelength. (b) Temperature dependent Raman spectra of $Cs_3Bi_2I_9$ using 785 nm excitation wavelength. (c) Phonon lifetime of few Raman active modes in the temperature range 100-300 K.*

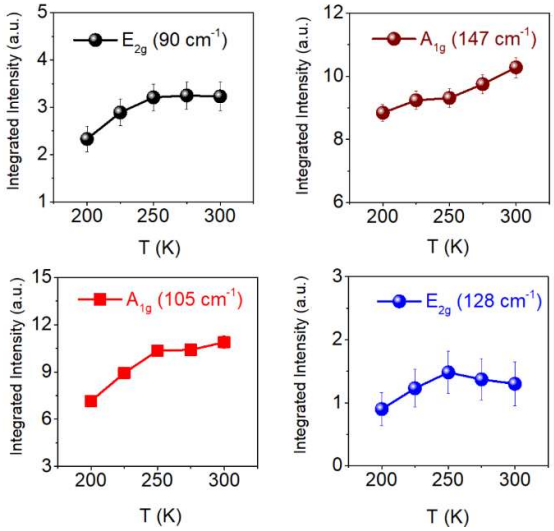

Figure 4.3.11. *Temperature-dependent integrated intensity of the Raman peaks of $Cs_3Bi_2I_9$.*

Temperature dependent Raman spectra of $Cs_3Bi_2I_9$ (Figure 4.3.10b) represents the shifting of spectra towards red region and increased integrated intensity (phonon populations) from 200 - 300 K as shown in Figure 4.3.11. We have also estimated the temperature dependent phonon lifetime (τ_i) by $\tau_i = \frac{1}{2\pi\, FWHM_i}$, where $FWHM_i$ is the full-width at half-maxima of active modes.[114] The estimated τ_i is of the order of pico-seconds (ps) and decreasing with the increase in the temperature (Figure 4.3.10c) signifying the strong phonon scattering processes, which ultimately leads to ultralow κ_L in $Cs_3Bi_2I_9$.

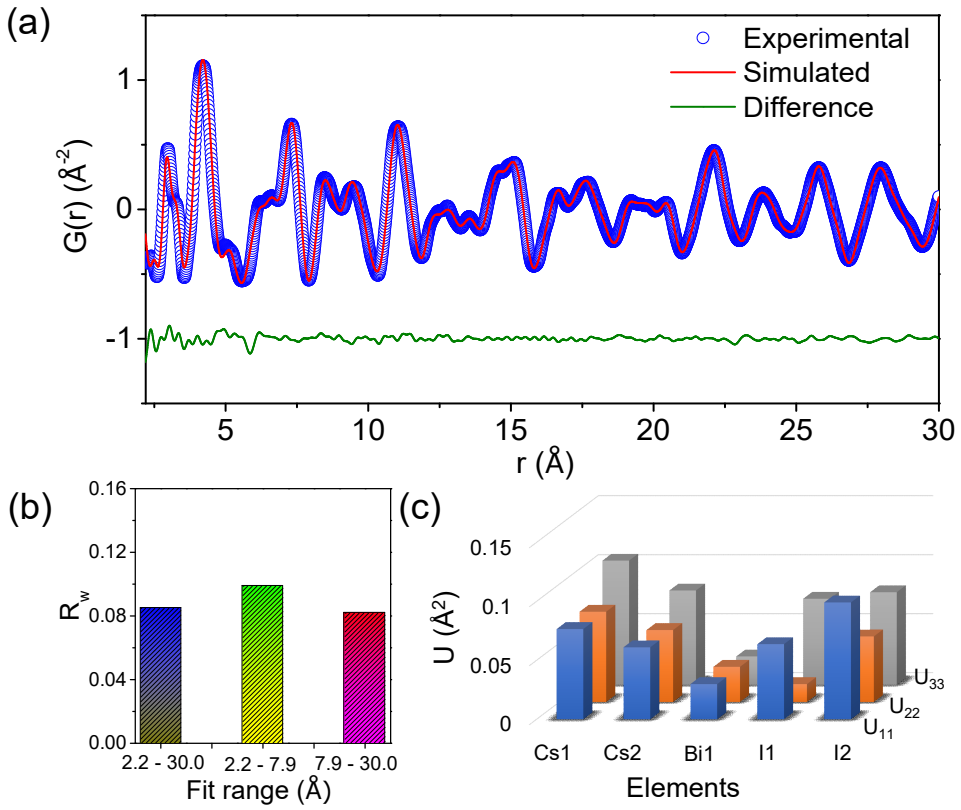

Figure 4.3.12. *(a) X-ray pair distribution function (PDF) of $Cs_3Bi_2I_9$, simulated using the hexagonal $P6_3/mmc$ space group at 300 K. (b) Goodness of fit (R_w) values for different fit range. (c) Thermal displacement parameter (U) values for the individual atoms in $Cs_3Bi_2I_9$. U_{11}, U_{22} and U_{33} are U values along x, y and z-direction respectively. All data are at 300 K.*

Further we have performed pair distribution function (PDF) analysis to understand the bonding environment and atomic vibration in $Cs_3Bi_2I_9$ system. PDF is a total scattering technique which provides simultaneous information of the structure in both

local and global length scales.[115] The experimental PDF data (shown in blue open circles) at 300 K shows excellent agreement when simulated with the hexagonal $P6_3/mmc$ space group (shown in red line) thus confirming the phase purity of this material and is in line with the PXRD observation (Figure 4.3.12a). The goodness of fit (R_w) is found to be 0.085 for the whole range fitting (i.e., r = 2.2- 30.0 Å), further validating the excellent match between the experimental and the simulated data. To gain the insights into the local and average environment of $Cs_3Bi_2I_9$, we have divided the PDF plot into two parts: the low r region (r = 2.2 – 7.9 Å), indicative of the local environment in $Cs_3Bi_2I_9$ and the high r region (r = 7.9 – 30.0 Å), indicative of the average structure. The refinement of the local and average structure gave R_w values of 0.099 and 0.082 respectively, suggesting that there is no significant deviation in the local structure as compared to the average one at room temperature (Figure 4.3.12b) by keeping the parameters constant as obtained for the whole range fitting (i.e., r = 2.2 – 30.0 Å).

However, the thermal displacement parameters of $Cs_3Bi_2I_9$ at room temperature reveals that Cs vibrates with a high magnitude compared to other atoms. Cs1, which consists of bridged I (I1) shows U values of 0.076 Å^2 (U_{11}), 0.076 Å^2 (U_{22}), and 0.105 Å^2 (U_{33}) along x, y and z-axis, respectively (Figure 4.3.12c). Cs2, which contains terminal I (I2) has U values of 0.061 Å^2, 0.061 Å^2 and 0.079 Å^2 along x, y and z-axis respectively. The bridging I (I1) with U values 0.063 Å^2, 0.015 Å^2 and 0.072 Å^2 along x, y, and z-axis respectively, signify that the vibrations are enhanced along the x-z direction, which could lead to a double octahedral rotation along that direction as observed from theoretical calculation (Figure 4.3.7e). Similarly, terminal I (I2) has U values of 0.099 Å^2, 0.055 Å^2 and 0.078 Å^2 along x, y, and z-axis respectively. This signifies the vibrations of I2, are predominantly in the along x-z direction. Bi has low U values of 0.029 Å^2, 0.029 Å^2.and 0.024 Å^2 along x, y, and z-axis respectively, which infers that Bi has much stronger interaction with its surrounding atoms, in agreement with our theoretical analysis. While the enhanced I vibrations can be related to the octahedral distortion as observed through eigenvector visualizations (Figure 4.3.7e, f), enhanced Cs vibrations indicates their rattling nature which induces low energy flat optical phonon modes (Figure 4.3.7d, Figure 4.3.9) influencing the heat transport via phonon scattering.

4.3.4 Conclusions

In summary, we have demonstrated that Pb-free 0D $Cs_3Bi_2I_9$ halide perovskite exhibits intrinsically ultralow κ_L. The room temperature κ_L is ~ 0.20 W/m.K which is significantly lower compared to the reported crystalline materials. The presence of bonding heterogeneity and elastic softness give rise to low-frequency acoustic and abundant low-energy optical phonon modes. The optical phonon mode at Γ (ω= 18 cm^{-1}) is associated with the anharmonic rattling of Cs^+ ions. Along with the rattling-like vibration, the presence of double octahedral rotation and torsion modes strongly perturbs the $Bi_2I_9^{3-}$ molecular salt which substantially creates octahedral distortion and induces a strong lattice anharmonicity in the system es evidenced in the experimentally derived large Grüneisen parameter ~ 2.32. The phonon dispersion for the relaxed structure of $Cs_3Bi_2I_9$ exhibits very soft acoustic phonon modes (ω_{max}= 15 cm^{-1}) in all directions in the Brillouin zone that give rise to soft elastic moduli which is appreciably lower compared to the well-known low thermal conductive metal chalcogenides and all-inorganic halide perovskites. Furthermore, the phonon dispersion exhibits strong hybridization between the low-energy optical and acoustic phonon modes that leads to very short phonon lifetime of ~ 1 ps as determined from the Raman measurements. Thus, the soft crystal structure, strong anharmonicity along with hybridization of acoustic-optical phonon modes leads to the ultralow κ_L in $Cs_3Bi_2I_9$. This finding establishes a new benchmark for the thermal transport properties of Pb-free low-dimensional metal halides, paving the way for the development of novel and efficient thermal energy management materials.

4.3.5. References

1. C. C. Stoumpos and M. G. Kanatzidis, *Acc. Chem. Res.*, 2015, **48**, 2791.

2. J. S. Manser, J. A. Christians and P. V. Kamat, *Chem. Rev.*, 2016, **116**, 12956.

3. Q. A. Akkerman, G. Rainò, M. V. Kovalenko and L. Manna, *Nat. Mat.*, 2018, **17**, 394.

4. X.-K. Liu, W. Xu, S. Bai, Y. Jin, J. Wang, R. H. Friend and F. Gao, *Nat. Mater.*, 2021, **20**, 10.

5. A. Dey, J. Ye, A. De, E. Debroye, S. K. Ha, E. Bladt, A. S. Kshirsagar, Z. Wang, J. Yin, Y. Wang, L. N. Quan, F. Yan, M. Gao, X. Li, J. Shamsi, T. Debnath, M. Cao, M. A. Scheel, S. Kumar, J. A. Steele, M. Gerhard, L. Chouhan, K. Xu, X.-g. Wu, Y. Li, Y. Zhang, A. Dutta, C. Han, I. Vincon, A. L. Rogach, A. Nag, A. Samanta, B. A. Korgel, C.-J. Shih, D. R. Gamelin, D. H. Son, H. Zeng, H. Zhong, H. Sun, H. V. Demir, I. G. Scheblykin, I. Mora-Seró, J. K. Stolarczyk, J. Z. Zhang, J. Feldmann, J. Hofkens, J. M. Luther, J. Pérez-Prieto, L. Li, L. Manna, M. I. Bodnarchuk, M. V. Kovalenko, M. B. J. Roeffaers, N. Pradhan, O. F. Mohammed, O. M. Bakr, P. Yang, P. Müller-Buschbaum, P. V. Kamat, Q. Bao, Q. Zhang, R. Krahne, R. E. Galian, S. D. Stranks, S. Bals, V. Biju, W. A. Tisdale, Y. Yan, R. L. Z. Hoye and L. Polavarapu, *ACS Nano*, 2021, **15**, 10775.

6. S. D. Stranks and H. J. Snaith, *Nat. Nanotech.*, 2015, **10**, 391.

7. W. Zhang, G. E. Eperon and H. J. Snaith, *Nat. Energy*, 2016, **1**, 16048.

8. P. Acharyya, K. Kundu and K. Biswas, *Nanoscale*, 2020, **12**, 21094.

9. J. Li, H.-L. Cao, W.-B. Jiao, Q. Wang, M. Wei, I. Cantone, J. Lü and A. Abate, *Nat. Commun.*, 2020, **11**, 310.

10. P. Su, Y. Liu, J. Zhang, C. Chen, B. Yang, C. Zhang and X. Zhao, *J. Phys. Chem. Lett.*, 2020, **11**, 2812.

11. H. Tsai, W. Nie, J.-C. Blancon, C. C. Stoumpos, R. Asadpour, B. Harutyunyan, A. J. Neukirch, R. Verduzco, J. J. Crochet, S. Tretiak, L. Pedesseau, J. Even, M. A. Alam, G. Gupta, J. Lou, P. M. Ajayan, M. J. Bedzyk, M. G. Kanatzidis and A. D. Mohite, *Nature*, 2016, **536**, 312.

12. L. Etgar, *Energy Environ. Sci.*, 2018, **11**, 234.

13. L. Mao, C. C. Stoumpos and M. G. Kanatzidis, *J. Am. Chem. Soc.*, 2019, **141**, 1171.

14. I. C. Smith, E. T. Hoke, D. Solis-Ibarra, M. D. McGehee and H. I. Karunadasa, *Angew. Chem., Int. Ed.*, 2014, **53**, 11232.

15. M. D. Smith, B. A. Connor and H. I. Karunadasa, *Chem. Rev.*, 2019, **119**, 3104.

16. Y. Zhou and Y. Zhao, *Energy Environ. Sci.*, 2019, **12**, 1495.

17. W. Ke and M. G. Kanatzidis, *Nat. Commun.*, 2019, **10**, 965.

18. S. Park, W. J. Chang, C. W. Lee, S. Park, H.-Y. Ahn and K. T. Nam, *Nat. Energy*, 2016, **2**, 16185.

19. C. Gu and J.-S. Lee, *ACS Nano*, 2016, **10**, 5413.

20. Y. C. Kim, K. H. Kim, D.-Y. Son, D.-N. Jeong, J.-Y. Seo, Y. S. Choi, I. T. Han, S. Y. Lee and N.-G. Park, *Nature*, 2017, **550**, 87.

21. A. K. Jena, A. Kulkarni and T. Miyasaka, *Chem. Rev.*, 2019, **119**, 3036.

22. S. Hu, Z. Ren, A. B. Djurišić and A. L. Rogach, *ACS Energy Lett.*, 2021, **6**, 3882.

23. M. A. Haque, S. Kee, D. R. Villalva, W.-L. Ong and D. Baran, *Adv. Sci.*, 2020, **7**, 1903389.

24. Y. Zhou, J. Wang, D. Luo, D. Hu, Y. Min and Q. Xue, *Nano Energy*, 2022, **94**, 106949.

25. J. He, L.-D. Zhao, J.-C. Zheng, J. W. Doak, H. Wu, H.-Q. Wang, Y. Lee, C. Wolverton, M. G. Kanatzidis and V. P. Dravid, *J. Am. Chem. Soc.*, 2013, **135**, 4624.

26. M. Dutta, M. Samanta, T. Ghosh, D. J. Voneshen and K. Biswas, *Angew. Chem., Int. Ed.*, 2021, **60**, 4259.

27. D. Sarkar, T. Ghosh, S. Roychowdhury, R. Arora, S. Sajan, G. Sheet, U. V. Waghmare and K. Biswas, *J. Am. Chem. Soc.*, 2020, **142**, 12237.

28. D. Gibson Quinn, T. Zhao, M. Daniels Luke, C. Walker Helen, R. Daou, S. Hébert, M. Zanella, S. Dyer Matthew, B. Claridge John, B. Slater, W. Gaultois Michael, F. Corà, J. Alaria and J. Rosseinsky Matthew, *Science*, 2021, **373**, 1017.

29. Y. Luo, Z. Ma, S. Hao, S. Cai, Z.-Z. Luo, C. Wolverton, V. P. Dravid, J. Yang, Q. Yan and M. G. Kanatzidis, *J. Am. Chem. Soc.*, 2022, **144**, 1445.

30. B. Jiang, Y. Yu, J. Cui, X. Liu, L. Xie, J. Liao, Q. Zhang, Y. Huang, S. Ning, B. Jia, B. Zhu, S. Bai, L. Chen, J. Pennycook Stephen and J. He, *Science*, 2021, **371**, 830.

31. Y. Xiao, L. Xu, T. Hong, H. Shi, S. Wang, X. Gao, X. Ding, J. Sun and L.-D. Zhao, *Energy Environ. Sci.*, 2022, **15**, 346.

32. P. Padture Nitin, M. Gell and H. Jordan Eric, *Science*, 2002, **296**, 280.

33. X. Qian, J. Zhou and G. Chen, *Nat. Mater.*, 2021, **20**, 1188.

34. T. Sadi, I. Radevici and J. Oksanen, *Nat. Photonics*, 2020, **14**, 205.

35. P. Santhanam, D. J. Gray and R. J. Ram, *Phys. Rev. Lett.*, 2012, **108**, 097403.

36. Q. Yan and M. G. Kanatzidis, *Nat. Mater.*, 2021, DOI: 10.1038/s41563-021-01109-w, 10.1038/s41563.

37. S. Roychowdhury, T. Ghosh, R. Arora, M. Samanta, L. Xie, K. Singh Niraj, A. Soni, J. He, V. Waghmare Umesh and K. Biswas, *Science*, 2021, **371**, 722.

38. M. K. Jana and K. Biswas, *ACS Energy Lett.*, 2018, **3**, 1315.

39. M. Dutta, D. Sarkar and K. Biswas, *Chem. Commun.*, 2021, **57**, 4751.

40. B. Sun, S. Niu, R. P. Hermann, J. Moon, N. Shulumba, K. Page, B. Zhao, A. S. Thind, K. Mahalingam, J. Milam-Guerrero, R. Haiges, M. Mecklenburg, B. C. Melot, Y.-D. Jho, B. M. Howe, R. Mishra, A. Alatas, B. Winn, M. E. Manley, J. Ravichandran and A. J. Minnich, *Nat. Commun.*, 2020, **11**, 6039.

41. X. Shi, J. Yang, J. R. Salvador, M. Chi, J. Y. Cho, H. Wang, S. Bai, J. Yang, W. Zhang and L. Chen, *J. Am. Chem. Soc.*, 2011, **133**, 7837.

42. T. Takabatake, K. Suekuni, T. Nakayama and E. Kaneshita, *Rev. Modern Phys.*, 2014, **86**, 669.

43. S. Christensen, M. S. Schmøkel, K. A. Borup, G. K. H. Madsen, G. J. McIntyre, S. C. Capelli, M. Christensen and B. B. Iversen, *J. Appl. Phys.*, 2016, **119**, 185102.

44. M. S. Dresselhaus, G. Chen, M. Y. Tang, R. G. Yang, H. Lee, D. Z. Wang, Z. F. Ren, J. P. Fleurial and P. Gogna, *Adv. Mater.*, 2007, **19**, 1043.

45. L. D. Hicks and M. S. Dresselhaus, *Phys. Rev. B*, 1993, **47**, 16631.

46. C. Li, H. Ma, T. Li, J. Dai, M. A. J. Rasel, A. Mattoni, A. Alatas, M. G. Thomas, Z. W. Rouse, A. Shragai, S. P. Baker, B. J. Ramshaw, J. P. Feser, D. B. Mitzi and Z. Tian, *Nano Lett.*, 2021, **21**, 3708.

47. H. Ma, C. Li, Y. Ma, H. Wang, Z. W. Rouse, Z. Zhang, C. Slebodnick, A. Alatas, S. P. Baker, J. J. Urban and Z. Tian, *Phys. Rev. Lett.*, 2019, **123**, 155901.

48. P. Acharyya, T. Ghosh, K. Pal, K. Kundu, K. Singh Rana, J. Pandey, A. Soni, U. V. Waghmare and K. Biswas, *J. Am. Chem. Soc.*, 2020, **142**, 15595.

49. Y.-K. Jung, I. T. Han, Y. C. Kim and A. Walsh, *NPJ Comput. Mater.*, 2021, **7**, 51.

50. H. Xie, S. Hao, J. Bao, T. J. Slade, G. J. Snyder, C. Wolverton and M. G. Kanatzidis, *J. Am. Chem. Soc.*, 2020, **142**, 9553.

51. A. Swarnkar, V. K. Ravi and A. Nag, *ACS Energy Lett.*, 2017, **2**, 1089.

52. F. Giustino and H. J. Snaith, *ACS Energy Lett.*, 2016, **1**, 1233.

53. M. T. Agne, R. Hanus and G. J. Snyder, *Energy Environ. Sci.*, 2018, **11**, 609.

54. L.-D. Zhao, J. He, D. Berardan, Y. Lin, J.-F. Li, C.-W. Nan and N. Dragoe, *Energy Environ. Sci.*, 2014, **7**, 2900.

55. Y. Xiao, C. Chang, Y. Pei, D. Wu, K. Peng, X. Zhou, S. Gong, J. He, Y. Zhang, Z. Zeng and L.-D. Zhao, *Phys. Rev. B*, 2016, **94**, 125203.

56. G. Kresse and J. Furthmüller, *Comput. Mater. Sci.*, 1996, **6**, 15.

57. G. Kresse and J. Furthmüller, *Phys. Rev. B*, 1996, **54**, 11169.

58. P. E. Blöchl, *Phys. Rev. B*, 1994, **50**, 17953.

59. G. Kresse and D. Joubert, *Phys. Rev. B*, 1999, **59**, 1758.

60. J. P. Perdew, A. Ruzsinszky, G. I. Csonka, O. A. Vydrov, G. E. Scuseria, L. A. Constantin, X. Zhou and K. Burke, *Phys. Rev. Lett.*, 2008, **100**, 136406.

61. B. Chabot and E. Parthe, *Acta Crystallogr. B*, 1978, **34**, 645.

62. A. Togo and I. Tanaka, *Scr. Mater.*, 2015, **108**, 1.

63. Z. Ma, Z. Shi, C. Qin, M. Cui, D. Yang, X. Wang, L. Wang, X. Ji, X. Chen, J. Sun, D. Wu, Y. Zhang, X. J. Li, L. Zhang and C. Shan, *ACS Nano*, 2020, **14**, 4475.

64. J. F. Nye, *Physical properties of crystals: their representation by tensors and matrices*, Oxford university press, 1985.

65. R. Dronskowski and P. E. Bloechl, *J. Phys. Chem.*, 1993, **97**, 8617.

66. V. L. Deringer, A. L. Tchougréeff and R. Dronskowski, *J. Phys. Chem. A*, 2011, **115**, 5461.

67. A.-C. Dippel, H.-P. Liermann, J. T. Delitz, P. Walter, H. Schulte-Schrepping, O. H. Seeck and H. Franz, *J. Synchrotron Rad.*, 2015, **22**, 675.

68. T. Proffen, S. J. L. Billinge, T. Egami and D. Louca, *Z. Kristallogr. Cryst. Mater.*, 2003, **218**, 132.

69. M. Basham, J. Filik, M. T. Wharmby, P. C. Y. Chang, B. El Kassaby, M. Gerring, J. Aishima, K. Levik, B. C. A. Pulford, I. Sikharulidze, D. Sneddon, M. Webber, S. S. Dhesi, F. Maccherozzi, O. Svensson, S. Brockhauser, G. Naray and A. W. Ashton, *J. Synchrotron Rad.*, 2015, **22**, 853.

70. P. Juhas, T. Davis, C. L. Farrow and S. J. L. Billinge, *J. Appl. Crystallogr.*, 2013, **46**, 560.

71. C. L. Farrow, P. Juhas, J. W. Liu, D. Bryndin, E. S. Božin, J. Bloch, T. Proffen and S. J. L. Billinge, *J. Phys. Condens. Matter*, 2007, **19**, 335219.

72. K. M. McCall, C. C. Stoumpos, S. S. Kostina, M. G. Kanatzidis and B. W. Wessels, *Chem. Mater.*, 2017, **29**, 4129.

73. A. Sarkar, P. Acharyya, R. Sasmal, P. Pal, S. S. Agasti and K. Biswas, *Inorg. Chem.*, 2018, **57**, 15558.

74. L. Pauling, *J. Am. Chem. Soc.*, 1929, **51**, 1010.

75. R. Dronskowski and P. E. Bloechl, *J. Phys. Chem.*, 1993, **97**, 8617.

76. V. F. Machulin, F. V. Motsnyi, O. M. Smolanka, G. S. Svechnikov and E. Y. Peresh, *Low Temp. Phys.*, 2004, **30**, 964.

77. M. Dutta, S. Matteppanavar, M. V. D. Prasad, J. Pandey, A. Warankar, P. Mandal, A. Soni, U. V. Waghmare and K. Biswas, *J. Am. Chem. Soc.*, 2019, **141**, 20293.

78. S. Roychowdhury, T. Ghosh, R. Arora, U. V. Waghmare and K. Biswas, *Angew. Chem., Int. Ed.*, 2018, **57**, 15167.

79. S. Roychowdhury, M. Samanta, S. Perumal and K. Biswas, *Chem. Mater.*, 2018, **30**, 5799.

80. G. Tan, L.-D. Zhao and M. G. Kanatzidis, *Chem. Rev.*, 2016, **116**, 12123.

81. L.-D. Zhao, V. P. Dravid and M. G. Kanatzidis, *Energy Environ. Sci.*, 2014, **7**, 251.

82. L.-D. Zhao, S.-H. Lo, Y. Zhang, H. Sun, G. Tan, C. Uher, C. Wolverton, V. P. Dravid and M. G. Kanatzidis, *Nature*, 2014, **508**, 373.

83. M. Samanta, K. Pal, U. V. Waghmare and K. Biswas, *Angew. Chem., Int. Ed.*, 2020, **59**, 4822.

84. W. Lee, H. Li, A. B. Wong, D. Zhang, M. Lai, Y. Yu, Q. Kong, E. Lin, J. J. Urban, J. C. Grossman and P. Yang, *Proc. Natl. Acad. Sci. U. S. A*, 2017, **114**, 8693.

85. T. Liu, X. Zhao, J. Li, Z. Liu, F. Liscio, S. Milita, B. C. Schroeder and O. Fenwick, *Nat. Commun.*, 2019, **10**, 5750.

86. S. Mukhopadhyay, S. Parker David, C. Sales Brian, A. Puretzky Alexander, A. McGuire Michael and L. Lindsay, *Science*, 2018, **360**, 1455.

87. Y. Wang, R. Lin, P. Zhu, Q. Zheng, Q. Wang, D. Li and J. Zhu, *Nano Lett.*, 2018, **18**, 2772.

88. I. K. Dimitrov, M. E. Manley, S. M. Shapiro, J. Yang, W. Zhang, L. D. Chen, Q. Jie, G. Ehlers, A. Podlesnyak, J. Camacho and Q. Li, *Phys. Rev. B*, 2010, **82**, 174301.

89. V. G. Plekhanov, *Introduction to Isotopic Materials Science*, Springer, 2018.

90. X. Su, N. Zhao, S. Hao, C. C. Stoumpos, M. Liu, H. Chen, H. Xie, Q. Zhang, C. Wolverton, X. Tang and M. G. Kanatzidis, *Adv. Funct. Mater.*, 2019, **29**, 1806534.

91. H. Shintani and H. Tanaka, *Nat. Mater.*, 2008, **7**, 870.

92. X. Li, P.-F. Liu, E. Zhao, Z. Zhang, T. Guidi, M. D. Le, M. Avdeev, K. Ikeda, T. Otomo, M. Kofu, K. Nakajima, J. Chen, L. He, Y. Ren, X.-L. Wang, B.-T. Wang, Z. Ren, H. Zhao and F. Wang, *Nat. Commun.*, 2020, **11**, 942.

93. E. Duval, A. Mermet and L. Saviot, *Phys. Rev. B*, 2007, **75**, 024201.

94. M. Baggioli, B. Cui and A. Zaccone, *Phys. Rev. B*, 2019, **100**, 220201.

95. J. Callaway, *Phys. Rev.*, 1959, **113**, 1046.

96. J. S. Dugdale and Z. S. Basinski, *Phys. Rev.*, 1967, **157**, 552.

97. C. J. Glassbrenner and G. A. Slack, *Phys. Rev.*, 1964, **134**, A1058.

98. M. G. Holland, *Phys. Rev.*, 1963, **132**, 2461.

99. M. Samanta and K. Biswas, *J. Am. Chem. Soc.*, 2017, **139**, 9382.

100. X. Shi, Y. Pei, G. J. Snyder and L. Chen, *Energy Environ. Sci.*, 2011, **4**, 4086.

101. M. Jin, J. Liang, P. Qiu, H. Huang, Z. Yue, L. Zhou, R. Li, L. Chen and X. Shi, *J. Phys. Chem. Lett.*, 2021, **12**, 8246.

102. G. A. Slack and S. Galginaitis, *Phys. Rev.*, 1964, **133**, A253.

103. H. Xie, X. Su, S. Hao, C. Zhang, Z. Zhang, W. Liu, Y. Yan, C. Wolverton, X. Tang and M. G. Kanatzidis, *J. Am. Chem. Soc.*, 2019, **141**, 18900.

104. Y. Zhang, X. Ke, C. Chen, J. Yang and P. R. C. Kent, *Phys. Rev. B*, 2009, **80**, 024304.

105. J. Carrete, N. Mingo and S. Curtarolo, *Appl. Phys. Lett.*, 2014, **105**, 101907.

106. Y. Yu, M. Cagnoni, O. Cojocaru-Mirédin and M. Wuttig, *Adv. Funct. Mater.* , 2020, **30**, 1904862.

107. E. A. Albanesi, C. M. I. Okoye, C. O. Rodriguez, E. L. Peltzer y Blanca and A. G. Petukhov, *Phys. Rev. B*, 2000, **61**, 16589.

108. M. Shakil, A. Akram, I. Zeba, R. Ahmad, S. S. A. Gillani and M. A. Gadhi, *Mater. Res. Express*, 2020, **7**, 025513.

109. D. T. Morelli, V. Jovovic and J. P. Heremans, *Phys. Rev. Lett.*, 2008, **101**, 035901.

110. Y. Fu, D. J. Singh, W. Li and L. Zhang, *Phys. Rev. B*, 2016, **94**, 075122.

111. S. Pailhès, H. Euchner, V. M. Giordano, R. Debord, A. Assy, S. Gomès, A. Bosak, D. Machon, S. Paschen and M. de Boissieu, *Phys. Rev. Lett.*, 2014, **113**, 025506.

112. V. V. Olegh, O. G. Victor, V. K. Stepan, V. M. Fedir, P. Eugen Yu and A. T. Volodymyr, 1998.

113. J. Laane and P. W. J. I. C. Jagodzinski, *Inorg. Chem.*, 1980, **19**, 44.

114. J. Pandey, S. Mukherjee, D. Rawat, S. Athar, K. S. Rana, R. C. Mallik and A. Soni, *ACS Appl. Energy Mater.*, 2020, **3**, 2175.

115. T. Egami and S. J. Billinge, *Underneath the Bragg peaks: structural analysis of complex materials*, Elsevier, Amsterdam, 2003.

PART 5

Dielectric, Magnetic, and Thermochromic Properties of Complex Metal Halides

Chapter 5.1

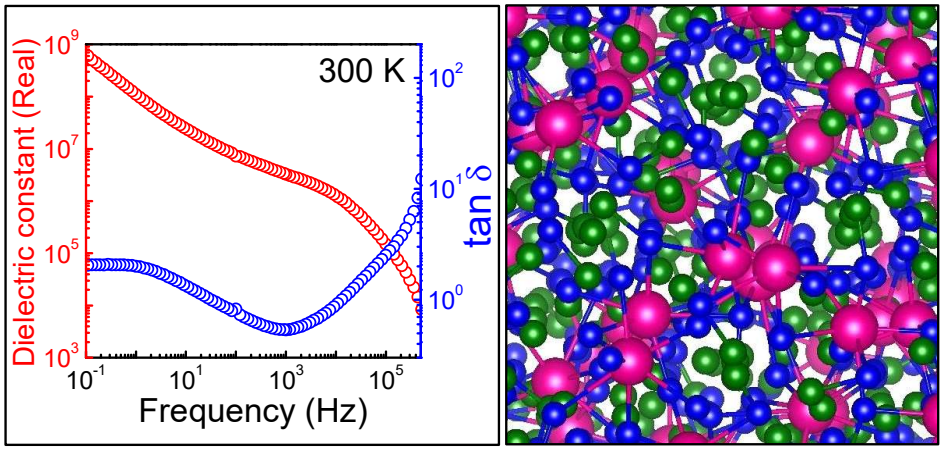

Broadband Colossal Dielectric Constant in the Superionic Halide $RbAg_4I_5$: Role of Inter-cluster Ag^+ Diffusion

Chapter 5.1

Broadband Colossal Dielectric Constant in the Superionic Halide $RbAg_4I_5$: Role of Inter-cluster Ag^+ Diffusion†

Summary

Materials with ultrahigh dielectric constants and a low value of dielectric loss are important for energy storage and electronic devices. Traditionally, high dielectric constant is found in ferroelectric complex oxides, but they exhibit high dielectric loss as well. In this chapter, a broadband colossal dielectric constant in a superionic halide, $RbAg_4I_5$, with a low dielectric loss is presented. The real part of the dielectric constant, ε', increases by 10^2 orders of magnitude as $RbAg_4I_5$ goes through a superionic transition at 121 K. At room temperature, $\varepsilon' > 10^6$ in the frequency range 10^{-1} to 10^4 Hz with a low dielectric loss, which ranges between 2.03 and 0.53. The maximum of ε' reaches a colossal value of 6.4×10^8 at 0.1 Hz at 300 K. The molecular dynamics simulation reveals the presence of Ag^+ clusters with a broad size distribution. The intercluster diffusion of Ag^+ causes significant instantaneous charge separation and a consequent large fluctuation in the dipole moments. The fluctuating dipoles, in turn, result in the colossal dielectric constant in $RbAg_4I_5$.

†**P. Acharyya,** T. Ghosh, S. Matteppanavar, R. K. Biswas, P. Yanda, S. R. Varanasi, D. Sanyal, A. Sundaresan, S. K. Pati and K. Biswas. *J. Phys. Chem. C*, 2020, **124**, 9802-9809.

5.1.1. Introduction

The development of materials with colossal dielectric constant (CDC) is an integral part of advancing the modern electronics, sensors, and energy storage devices.[1-6] Traditionally, high dielectric constant is associated with ferroelectric oxides across their paraelectric to ferroelectric transition, where $\varepsilon' \sim 10^3$-10^4 can be easily achieved.[7-12] Recently, few complex oxides have also emerged as non-ferroelectric high dielectric constant materials where high ε' arises either from polarization relaxation and polar fluctuations in nano-size domains or from Maxwell-Wagner polarization in the grain-boundaries.[13-18] One of the most notable examples is the double-perovskite $CaCu_3Ti_4O_{12}$ (CCTO) in which CDC with $\varepsilon' \sim 10^4$-10^5 has been achieved over a broad temperature and frequency range, although the exact origin of such CDC in CCTO is still under debate.[19-22] However, most of these oxides have a high dielectric loss, tan δ, as well. Low dimensional systems with charge density wave also show high dielectric constant; however, the associated tan δ is high.[23, 24] Recently, another intriguing category of materials, called superionic conductors, are emerging as high dielectric constant materials with low tan δ.[25-27] The perovskite oxide superionic conductor $Rb_2Ti_2O_5$ exhibited a dielectric constant $\varepsilon' \sim 10^9$ at 0.01 Hz at 300 K.[25]

Superionic conductors are the solid materials with high ionic conductivity ($\sigma > 10^{-3}$ S/cm; while in ordinary solid $\sigma \sim 10^{-8}$ S/cm).[28, 29] For example, the room temperature ionic conductivity of the superionic compounds $Rb_2Ti_2O_5$ and $RbAg_4I_5$ are $\sim 10^{-3}$ S/cm and ~ 0.2 S/cm, respectively.[25, 30] Such high ionic conductivity is, in general, thought to be detrimental to achieving CDC in a material. One of the requirements of observing CDC in superionic conductors is that the material must have very low electronic conductivity. For example, $Rb_2Ti_2O_5$ has room temperature electronic conductivity $\sim 10^{-8}$ S/cm.[25] The room temperature electronic conductivity of the present $RbAg_4I_5$ is $\sim 10^{-9}$ S/cm, which satisfies the required condition.[31, 32] Superionicity in a material is induced when highly disordered cation sites are present along with polar states.[33] The polar states are created by the charge transfer due to ion migrations to the interstices. Consequently, these ionic migrations may create dipoles in the lattice which is probably important to have high dielectric constant. $RbAg_4I_5$ exhibits a complex crystal structure[34-36] with a

large number of Ag^+ present in the lattice which migrates to the interstitial positions in its superionic phase and therefore, $RbAg_4I_5$ is expected to show CDC.

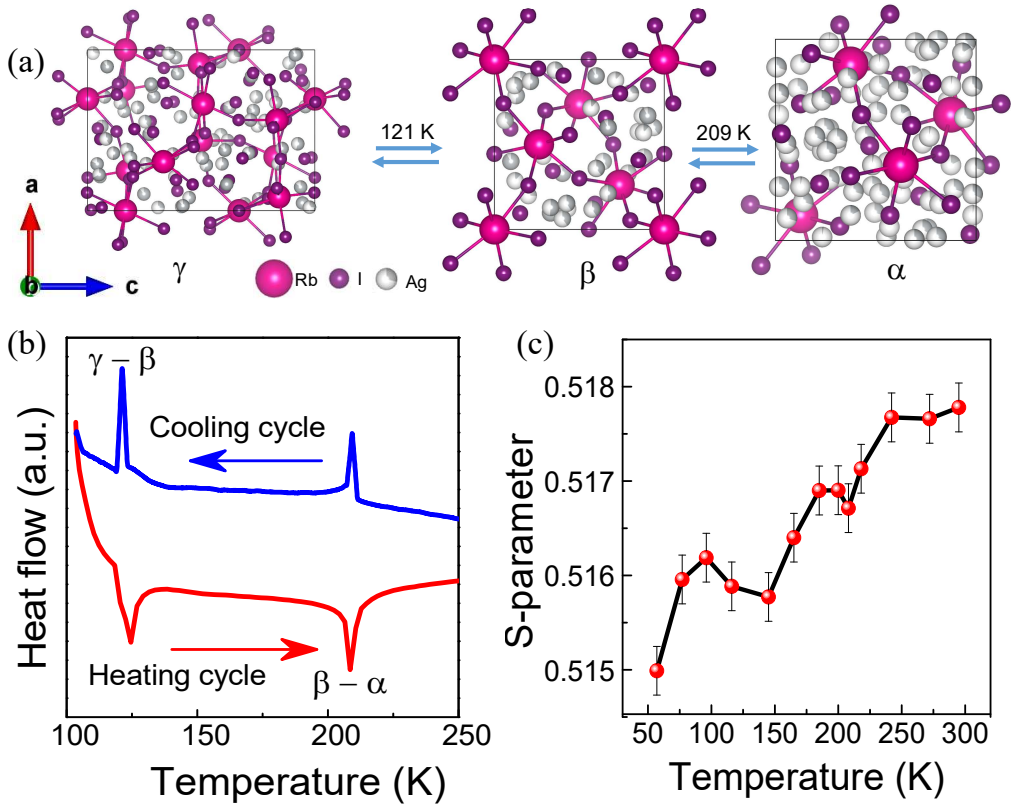

Figure 5.1.1. *(a) Cubic α-phase, rhombohedral β-phase and trigonal γ-phase of $RbAg_4I_5$. (b) DSC signal showing the structural phase transitions in $RbAg_4I_5$. (c) Temperature dependence of the S-parameter obtained from PAL spectroscopy.*

In this chapter, we have demonstrated a broadband CDC with a low dielectric loss in superionic $RbAg_4I_5$, which is synthesized by a facile solvent-free mechanochemical synthesis at room temperature. The presence of two structural phase transitions with decreasing temperature: α (cubic, space group $P4_332$; Figure 5.1.1a) → β (rhombohedral, space group R32; Figure 5.1.1a) at 209 K and β → γ (trigonal, space group P321; Figure 5.1.1a) at 121 K has been confirmed *via* temperature dependent powder X-ray diffraction (PXRD) and differential scanning calorimetry (DSC). The temperature dependent positron annihilation lifetime (PAL) spectroscopy and coincidence Doppler broadening

(CDB) spectra evidence the presence of charged vacancies associated with the diffusion of Ag^+. We have shown that ε' increases by 10^2 order in magnitude as $RbAg_4I_5$ goes through the γ → β superionic phase transition from the low temperature side and ε' reaches a giant value ~ 6.4 x 10^8 at 0.1 Hz in the room temperature superionic α phase. The molecular dynamics (MD) simulation showed charge density fluctuation within Ag^+ clusters because of intercluster Ag^+ diffusion. This causes fluctuation in the instantaneous dipole moments associated with Ag^+ clusters and results in the experimentally observed CDC in the room temperature superionic phase of $RbAg_4I_5$.

5.1.2. Methods

A. Experimental section

Starting materials. Rubidium (I) iodide (RbI, 99.5%) and silver (I) iodide (AgI, 99.999%) were purchased from Sigma Aldrich and used without further purification during synthesis.

Method of synthesis. For $RbAg_4I_5$ synthesis, 939 mg of AgI (4 mmol) and 212.4 mg (1 mmol) of RbI were taken as a precursor in a mortar pestle. The precursors were mechanically ground and mixed thoroughly in the mortar pestle for about two hours in inert condition (N_2 filled glove bag).

The following scheme is implemented to synthesize high quality polycrystals of $RbAg_4I_5$:

$$RbI + 4\,AgI \xrightarrow{\text{Mechanochemistry}} RbAg_4I_5$$

The polycrystalline pellets of $RbAg_4I_5$ (Figure 5.1.2) were obtained thorough spark plasma sintering (SPS) using a SPS211-LX, Dr. Sinter Lab SPS machine. SPS was carried out at 120 °C under an applied pressure of 50 MPa for 20 min. The SPS-processed sample was polished and used for PAL spectroscopy and dielectric measurements.

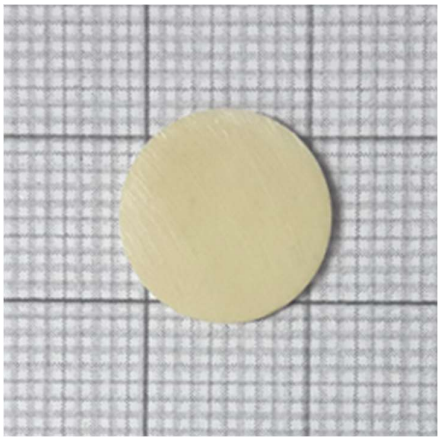

Figure 5.1.2. *Typical picture of the SPS processed pellet specimen of $RbAg_4I_5$.*

Powder X-ray diffraction (PXRD). Rigaku Smart Lab X-ray diffractometer equipped with Cu Kα (wavelength = 1.54059 Å) X-ray source was used to acquire the temperature-dependent PXRD patterns of as-synthesized $RbAg_4I_5$ at 80, 180, and 300 K.

Differential scanning calorimetry (DSC). Finely ground powder samples were used for DSC measurements, in which the data were collected in a wide temperature range from 100 K to 300 K by using a METTLER TOLEDO differential scanning calorimeter (DSC 822 e) at fixed heating/cooling rate of 1 K/min.

Positron annihilation life-time (PAL) and coincidence Doppler broadening (CDB) spectroscopy. The PAS measurements are done in collaboration with Dr. Dirtha Sanyal of VECC, Kolkata. The PAL spectrometer was measured by the standard fast γ–γ coincidence technique by utilizing two BaF_2 ultrafast scintillators coupled with XP2020Q photomultiplier tube. About 10 μCi ^{22}NaCl positron emitting source sealed in a thin mylar foil has been sandwiched between the two identical pellets of $RbAg_4I_5$ sample. The specific experimental set-up can be found in earlier report.[37] The acquired life-time spectrum has been deconvoluted to reveal the lifetime values by the computer programme PATFIT-88,[38] after considering proper source correction.

An HPGe detector was exploited for the detection of the Doppler broadening, originated from the positron annihilation γ-ray of 511 keV. An energy resolution of 1.15

from ^{85}Sr at 514 keV possess an efficiency equivalent to 12% (model number PGC 1216sp of DSG, Germany). The details of the experimental setup are described in earlier report.[39]

The CDB spectroscopic method was employed to recognize either the chemical features of defect or the potential rationale for the enhancement in *S*-parameter. The CDB experiments were carried out by using two analogous HPGe detectors of 12% efficiency with the model number PGC 1216sp of DSG, Germany. The peak to background for the present CDB set-up with ± ΔE selection is better than 105:1. Detail of the experimental set-up is depicted in earlier report.[39]

S-parameter can be designated as the ratio of the counts within the energy range of |511 keV – E| ≤ 0.85 keV to the total counts within the energy range of |511 keV–E| ≤ 4.25 keV under the photopeak of 511 keV.

I-V measurement. The room temperature I-V curve of $RbAg_4I_5$ (Figure 5.1.3) was measured using a rectangular bar of dimension ~ 2 X 2 X 8 mm, which has been obtained after polishing a SPS processed pellet specimen, in a ULVAC-RIKO ZEM-3 instrument.

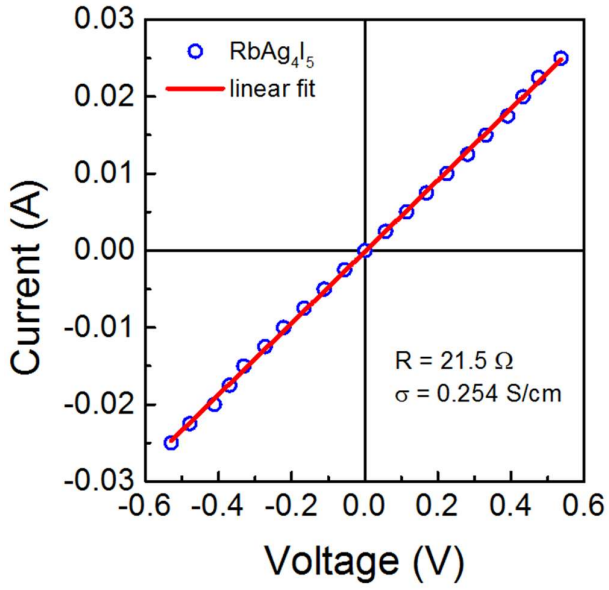

Figure 5.1.3. *Room temperature I-V curve of $RbAg_4I_5$. The obtained room temperature electrical conductivity is $\sigma \sim 0.254$ S/cm.*

Dielectric measurements. The temperature dependent dielectric measurements are done in collaboration with Prof. A. Sundaresan, JNCASR, India. The temperature and frequency dependent dielectric properties were determined in a physical property measurement system (PPMS, Quantum Design, USA) using the Agilent E4980A LCR meter within the frequency range of 20 Hz-200 kHz. The room temperature dielectric properties were obtained using a Solartron 1260A impedance analyser from the frequency of 0.1 Hz to 500 kHz. These measurements were conducted in the parallel plate geometry, in which Pelco high performance silver paste from TED PELLA was coated on either side of the disk-shaped pellet sample.

B. **Theoretical section.** The theoretical calculations are done in collaboration with Prof. S. K. Pati, JNCASR, India.

Molecular dynamics (MD) simulation. The interactions between Ag^+-Ag^+, Ag^+-I^-, Ag^+-Rb^+ and I^--I^- have been modeled using Vashista-Rahman (VR) potential.[40]

$$\phi_{ab}^{VR} = \frac{Z_a Z_b e^2}{r_{ab}} + \frac{A(\sigma_a+\sigma_b)^{n_{ab}}}{r_{ab}^{n_{ab}}} - \frac{w_{ab}}{r_{ab}^6} - \frac{(\alpha_a Z_b^2+\alpha_b Z_a^2)/2}{r_{ab}^4} \quad (1)$$

where r_a, r_b, and r_{ab} are the positions of the ions a and b, and the distance between them, respectively. A is the repulsive strength; σ_a, σ_b are the ionic radii; α_a, α_b are the electronic polarizabilities; and Z_a, Z_b are the fractional charges on the ions a and b, respectively. Electronic polarizabilities of Ag^+ and Rb^+ have been taken to be zero since they are relatively smaller in size than I^-. n_{ab} is the degree of hardness of the repulsive interaction between the ions a and b.

The interaction between Rb^+-Rb^+ and Rb^+-I^- have been modeled with Born-Mayer potential:[40]

$$\phi_{ab}^{BM} = \frac{Z_a Z_b e^2}{r_{ab}} + B_{ab} e^{-\gamma r_{ab}} - \frac{C_{ab}}{r_{ab}^6} - \frac{D_{ab}}{r_{ab}^8} \quad (2)$$

where, the first and second terms emerged from the Coulomb interactions between two point charges and the overlap between the outer shell electrons of corresponding ions, respectively. Furthermore, the third and fourth terms are appeared due to the van der Waals interactions. The parameters related to the above-mentioned interaction potentials have been extracted from the work of Tahara and Fukami.[40]

We have taken the crystal structure of α-$RbAg_4I_5$ as our starting configuration, and the unit cell has been replicated 3 times in each direction to form a larger cubic simulation box. The simulation box contains 2560 atoms in total. MD simulations were performed in NPT ensemble at ambient conditions for about 3 ns to obtain an equilibrated volume of the simulation cell. A time step of 1 fs was used in the velocity form of Verlet integrator. We implemented the simulation in the microcanonical (NVE) ensemble for about 3 ns to equilibrate the system at 298 K. After achieving the equilibration, further MD simulation has been executed for 10 ns during which the trajectories have been stored at every 10 fs. In order to calculate the electrostatic interactions, Ewald summation technique has been utilized. All the interactions were truncated using a cut-off distance of 1.8 nm. Periodic boundary conditions were employed in all directions in order to ensure that there are no surface effects at the boundaries.

Connectivity analysis and cluster size estimation. Further to study the ordering arrangement of Ag^+ ions, connectivity analysis was carried out on the equilibrated atomic configurations procured from the MD simulations. In the connectivity analysis, we considered that the neighboring atoms formed cluster of various sizes within the first correlation length corresponding to the first peak position in $g_{ab}(r)$. The dimensions of such cluster sizes are estimated by the number of ions present in the cluster within the first peak in the radial distribution function. The size distributions of these clusters were estimated by considering an average of 25 atomic configurations, each of which was obtained after consecutive 2000 MD time steps.

Diffusion coefficient calculation. To further validate our results, we investigated the dynamical properties of Ag^+, which correspond to the time correlation functions. These functions are further associated with the values obtained at different time scales (t), by assuming the system is in equilibrium as well as independent of the choice of origin. The time evolution of ionic configurations in the simulation cell was implemented to calculate the physical quantity equivalent to the ionic transport properties, which is as follows. The following equation of mean square displacement (MSD) can be expressed as;

$$< r_a^2(t) >= \frac{1}{N_a}\sum_{i_a=1}^{N_a} < \left|r_{i_a}(t) - r_{i_a}(0)\right|^2 > \qquad (3)$$

where, the total number of *a*-type ions can be denoted by the N_a term. We notice that the diffusive behavior of Ag^+ is more prominent compared to all other types of ions. Once MSD is calculated, the diffusion coefficient (*D*) can be estimated from the linear regime in the MSD curve of Ag^+ ions at $t \rightarrow \infty$, i.e.

$$D = \lim_{t\to\infty} \frac{r_a^2(t)}{6t} \quad (4)$$

Dipole moment calculation. The dipole moment (M) of component x at time step *t* of a molecular dynamics simulation trajectory is calculated by the expression[41]:

$$M_{x,t} = \sum_{k=1}^{N} q_k r_{k,t} \quad (5)$$

where, $r_k, N,$ and q_k are the position coordinate of the atom *k*, the total number of atoms in the simulation box, and the charges, respectively. It is important to mention that the calculation of the dipole moment relied on the choice of the basis of coordinate system. For our model, the dipole moment was evaluated in respect of the center of mass of the system. The static dielectric constant of a material follows the expression[42]:

$$\epsilon = \frac{<M^2>-<M>^2}{3V\varepsilon_0 k_B T} + 1 \quad (6)$$

where, V, k_B, ε_0, and T are the volume of the supercell, the Boltzmann constant, the permittivity of free space, and the absolute temperature, respectively.

5.1.3. Results and Discussion

$RbAg_4I_5$ is a well-known prototypical superionic conductor with very high ionic conductivity of ~ 0.2 S/cm at room temperature.[30] The room temperature superionic phase (α-phase) has a complex cubic crystal structure with four $RbAg_4I_5$ unit in the unit cell.[34-36] Three types of crystallographically nonequivalent sites are present for Ag^+: one eight-fold (Ag-c sites) and two 24-fold sets (Ag-I and Ag-II sites). The superionicity in $RbAg_4I_5$ arises from the fast diffusion of Ag^+ (diffusion coefficient ~ 10^{-6} cm^2 s^{-1}) in a β-Mn type rigid iodide sublattice.[34-36, 43, 44] The iodide substructure contains 56 iodide tetrahedra in which 16 Ag^+ are randomly distributed in the interstitial positions. The tetrahedral framework is arranged in such a fashion that they create a network of passageways for the diffusions of Ag^+. The room temperature cubic α-phase of $RbAg_4I_5$ is preceded by two structural phase transitions with decreasing temperature: a weakly first order α → β

phase transition at 209 K and a first order β → γ phase transition at 121 K.[35, 45-48] Remarkably, the iodide substructure remains almost intact, suffering only minor distortions to accommodate the partial ordering of Ag^+ at specific sites, across all these phase transitions.[35] The partial ordering of Ag^+ in the β phase restricts the movement of Ag^+ along the crystallographic *c*-axis, which decreases the ionic conductivity. Interestingly, Ag^+ remains partially disordered in the lowest temperature γ phase; however, the Ag^+ ionic diffusion occurs only within isolated clusters.[36]

Here, we have carried out a facile solvent-free mechanochemical synthesis of $RbAg_4I_5$ at room temperature (see details in experimental section). The presence of two sharp peaks in the DSC signal (Figure 5.1.1b) confirms the presence of two structural phase transitions at 209 K and 121 K in the mechanochemically synthesized $RbAg_4I_5$. The temperature dependent PXRD patterns at 300 K, 180 K and 80 K are shown in Figure 5.1.4. The Rietveld refinements of the temperature dependent PXRD patterns confirm

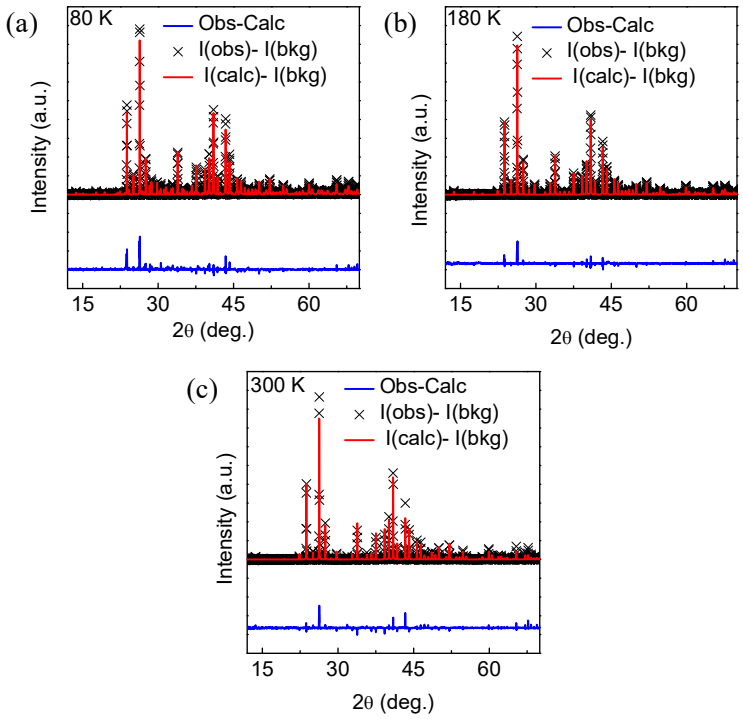

Figure 5.1.4. *Rietveld refinement of the PXRD patterns at (a) 80 K, (b) 180 K and (c) 300 K corresponding to the low-temperature trigonal γ-phase, mid-temperature rhombohedral β-phase and room temperature cubic α-phase, respectively, of the superionic halide* $RbAg_4I_5$.

the room temperature cubic (space group $P4_332$), mid-temperature rhombohedral (space group R32), and low-temperature trigonal (space group P321) structures corresponding to the α, β, and γ phase, respectively. The two superionic α and β phases are differentiated only by a small distortion in the iodide sublattice. The obtained crystal structure parameters (Table 5.1.1-5.1.4) for the all three phases agree well with the previous reports.

Table 5.1.1. *Crystal structure parameters of $RbAg_4I_5$ obtained from the Rietveld refinements of temperature dependent PXRD patterns.*

Phases	γ- $RbAg_4I_5$	β- $RbAg_4I_5$	α- $RbAg_4I_5$
Space group	P 3_1 2 1	R 3 2	P 4_3 3 2
Temperature	80 K	180 K	300 K
Cell parameter	a= b= 15.8536(5) Å c= 19.411(1) Å α= β= 90° γ = 120°	a = b = c = 11.24419(7) Å α = β = γ = 90.061° (2)	a = b = c = 11.23510(6) Å α= β= γ = 90°
χ^2	9.85	4	3.4225

Table 5.1.2. *Atomic parameters of γ-$RbAg_4I_5$ obtained from the Rietveld refinements of PXRD patterns at 80 K*.

		x	y	z	Occ.	U_{iso}
1.	Rb1	0.436(4)	0.436(4)	0.50000	1.000	0.122(6)
2.	Rb2	0.913(4)	0.664(4)	0.492(2)	1.000	0.122(6)

3.	Rb3	0.695(5)	0.695(5)	0.00000	1.000	0.122(6)
4.	I1	0.397(3)	0.185(3)	0.467(2)	1.000	0.097(2)
5.	I2	0.163(2)	0.885(3)	0.462(2)	1.000	0.097(2)
6.	I3	0.432(2)	0.925(3)	0.460(2)	1.000	0.097(2)
7.	I4	0.980(3)	0.857(3)	0.272(2)	1.000	0.097(2)
8.	I5	0.489(3)	0.811(2)	0.288(2)	1.000	0.097(2)
9.	I6	0.555(2)	0.364(3)	0.277(2)	1.000	0.097(2)
10.	I7	0.888(3)	0.564(3)	0.336(2)	1.000	0.097(2)
11.	I8	0.794(3)	0.00000	0.33333	1.000	0.097(2)
12.	I9	0.860(3)	0.860(3)	0.50000	1.000	0.097(2)
13.	I10	0.482(2)	0.678(2)	0.517(2)	1.000	0.097(2)
14.	I11	0.674(3)	0.670(2)	0.652(2)	1.000	0.097(2)
15.	Ag1	0.613(3)	0.284(3)	0.478(3)	0.57(4)	0.088(2)
16.	Ag2	0.328(3)	0.708(3)	0.505(2)	0.59(5)	0.088(2)
17.	Ag3	0.561(4)	0.642(4)	0.780(3)	0.52(4)	0.088(2)
18.	Ag4	0.643(2)	0.35(3)	0.625(2)	0.82(4)	0.088(2)
19.	Ag5	0.958(6)	0.978(6)	0.643(4)	0.26(4)	0.088(2)
20.	Ag6	0.476(5)	0.623(5)	0.271(3)	0.85(4)	0.088(2)
21.	Ag7	0.775(4)	0.564(4)	0.283(3)	0.67(4)	0.088(2)
22.	Ag8	0.788(2)	0.836(3)	0.279(2)	1.000	0.088(2)
23.	Ag9	0.030(2)	0.926(3)	0.4193(2)	0.89(4)	0.088(2)
24.	Ag10	0.584(3)	0.292(3)	0.4086(3)	0.54(4)	0.088(2)
25.	Ag11	0.554(4)	0.528(4)	0.2530(4)	0.41(4)	0.088(2)

Table 5.1.3. *Atomic parameters of β-$RbAg_4I_5$ obtained from the Rietveld refinements of PXRD patterns at 180 K.*

		x	y	z	Occ.	U_{iso}
1.	Rb1	0.50000	0.737(2)	0.263(2)	1.000	0.156(4)
2.	Rb2	0.00000	0.00000	0.00000	1.000	0.156(4)
3.	Ag1	0.153(4)	0.881(3)	0.425(3)	0.41(3)	0.189(3)
4.	Ag2	0.801(2)	0.801(2)	0.801(2)	0.25(3)	0.189(3)
5.	Ag3	0.937(3)	0.600(4)	0.359(4)	0.4(2)	0.189(3)
6.	Ag4	0.400(2)	0.330(2)	0.097(2)	0.920(2)	0.189(3)
7.	Ag5	0.331(4)	0.129(4)	0.788(3)	0.511(2)	0.189(3)

8.	Ag6	0.122(9)	0.286(8)	0.431(8)	0.112(2)	0.189(3)
9.	I1	0.259(1)	0.946(1)	0.200(2)	1.000	0.135(1)
10.	I2	0.152(1)	0.095(1)	0.593(1)	1.000	0.135(1)
11.	I3	0.00000	0.444(2)	0.556(2)	1.000	0.135(1)
12.	I4	0.50000	0.300(1)	0.700(1)	1.000	0.135(1)
13.	I5	0.656(1)	0.656(1)	0.656(1)	1.000	0.135(1)

Table 5.1.4. *Atomic parameters of α-$RbAg_4I_5$ obtained from the Rietveld refinements of PXRD patterns at 300 K.*

		x	y	z	Occ.	U_{iso}
1.	Rb1	0.12500	0.12500	0.12500	1.000	0.182(5)
2.	Ag1	0.62500	0.62500	0.62500	0.17(2)	0.246(5)
3.	Ag2	0.318(4)	0.318(4)	0.318(4)	0.16(1)	0.246(5)
4.	Ag3	0.12500	0.26700(4)	0.983(4)	0.024(9)	0.246(5)
5.	Ag4	0.303(3)	0.48300(5)	0.269(4)	0.326(8)	0.246(5)
6.	Ag5	0.558(5)	0.38900(5)	0.244(5)	0.301(7)	0.246(5)
7.	I1	0.4700(7)	0.4700(7)	0.4700(7)	1.000	0.148(2)
8.	I2	0.12500	0.6789(6)	0.5711(6)	1.000	0.148(2)

The diffusion of Ag^+ creates charged vacancies in the system, which has been experimentally probed using PAL and CDB spectroscopy. The fitting of PAL spectra at 300 K (Figure 5.1.5a) yields a short lifetime 180 ± 2 ps of 20 ± 1 % intensity and a longer component 341 ± 5 ps with 80 ± 1 % intensity. The positron trapped in a cation defect elapses for a longer time.[49] Therefore, the short lifetime component (180 ± 2 ps) has been assigned to the free annihilation of positrons, while the longer lifetime component (341 ± 5 ps) has been assigned to the positron annihilation at the vacancy sites.[49] The high intensity of the positron annihilation lifetime component at the vacancy sites indicates the strong ionic character of the material as these charged vacancies are created due to the diffusions of Ag^+. The ionic conductivity of $RbAg_4I_5$ increases with increasing temperature due to increased diffusions of the Ag^+.[43, 44] As a result, charged vacancies also increase and this is reflected in the gradual increase of the Doppler broadening

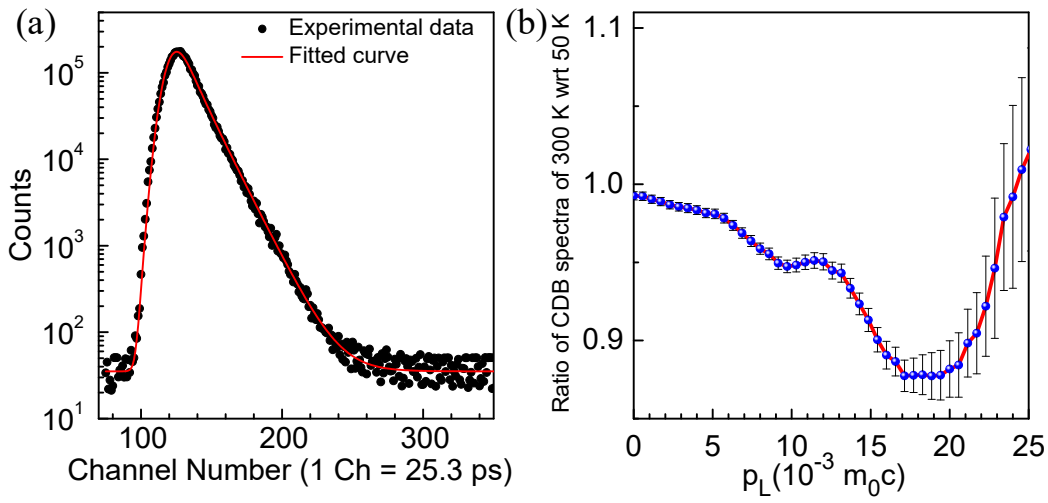

Figure 5.1.5. *(a) Typical positron annihilation lifetime (PAL) spectra at room temperature and (b) the area normalized ratio curve of the coincidence Doppler broadening (CDB) spectra at 300 K with respect to 50 K CDB spectra for the $RbAg_4I_5$ sample.*

S-parameter with increasing temperature (Figure 5.1.1c). Two anomalies corresponding to the γ → β and β → α phase transitions with increasing temperature are also evident in the temperature variation of *S*-parameter. The area normalized ratio curve of the CDB spectra at 300 K with respect to the 50 K CDB spectra (Figure 5.1.5b) shows a broad dip at the momentum value ~ 19×10^{-3} m_oc. The corresponding energy value is 92 eV which is very close to the binding energy of the 4s electron of Ag. This indicates that the positrons are less annihilating with the core electrons of the Ag^+ at 300 K.

The experimentally measured temperature variations of dielectric constant (ε') and dielectric loss (tan δ) at different frequencies ranging between 1 kHz to 200 kHz are shown in Figure 5.1.6. The presence of two phase transitions, γ → β and β → α, with increasing temperature is evident from the temperature variations of ε' and tan δ. From the low temperature side, ε' steeply increased by 10^1 - 10^2 order in magnitude at the first order superionic γ → β phase transition. For example, ε' at 1 kHz increases from 16.5 at 110 K to 3096 at 125 K. Correspondingly, tan δ exhibits a peak which shifts to higher temperature with increasing frequency. ε' continues to increase gradually after the

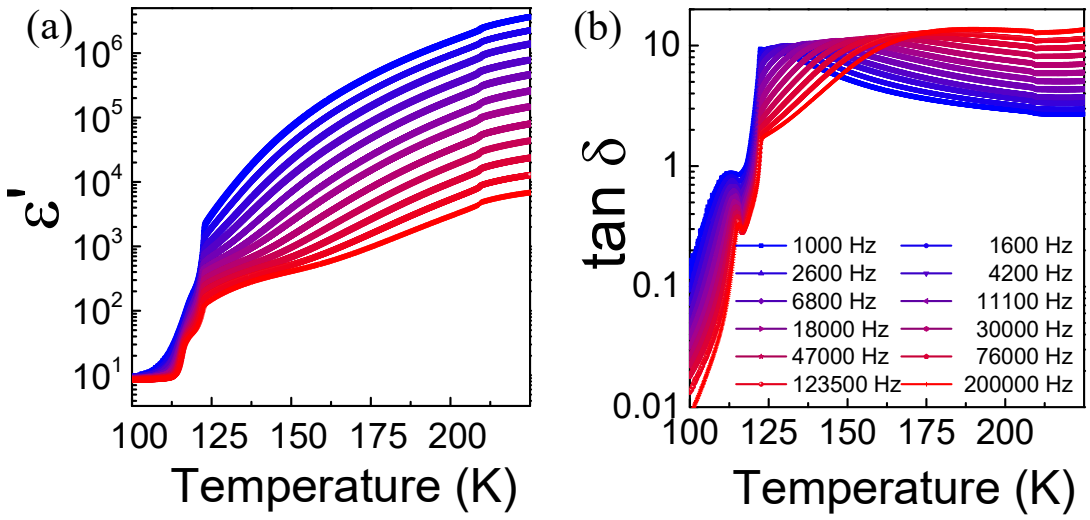

Figure 5.1.6. *Temperature and frequency dependences of (a) dielectric constant (ε') and (b) dielectric loss (tan δ) for $RbAg_4I_5$.*

superionic γ → β phase transition with increasing temperature except for a weak anomaly across the first order β → α phase transition at 209 K. $RbAg_4I_5$ emerges to the superionic phase at the first structural transition (γ → β at ~121 K) therefore, dielectric constant changes drastically across this transition. However, $RbAg_4I_5$ is already in the superionic regime when the second phase transition (β → α) occurs at ~209 K and, as a result, the change in dielectric response is not as dramatic as the one observed across the first structural transition (γ → β) at ~121 K.

The experimentally obtained frequency dependence of the dielectric constant (ε') at 150 K and 300 K corresponding to the superionic β and α phases, respectively, is shown in Figure 5.1.7a. At 300 K, ε' have a broadband colossal value > 10^6 in the frequency range 10^{-1} – 10^4 Hz with the maximum value reaching ~ 6.4 x 10^8 at 0.1 Hz. The corresponding dielectric loss (tan δ) in the frequency range 10^{-1} – 10^4 varies between 2.03 to 0.53, which is low (Figure 5.1.7b). Ag^+ diffusion dominates the transport behavior of $RbAg_4I_5$ at 300 K. For such diffusion dominated behavior, *log*|Z| (|Z| is the impedance magnitude) varies linearly with *log f* in the low frequency region and have a slope -1/2 or -1/4.[50] This linear relationship between *log*|Z| and *log f* is evident in the low frequency

region at room temperature (Figure 5.1.7c). The obtained slope is -0.234(2) in the frequency region 1 Hz to 0.1 Hz. Furthermore, the Nyquist plot (Figure 5.1.7d) also show linear relationship between the real and imaginary parts of impedance, Z' and Z'', respectively, in the low frequency region indicating the diffusion dominated behavior.

The observed dielectric properties of $RbAg_4I_5$ can also be reconciled with the universal dielectric response (UDR) as put forwarded by A. K. Jonscher.[51, 52] According to the Jonscher's theory, dielectric response of most materials follows a universal pattern, which in the frequency domain can be expressed as: (i) the frequency dependence of the imaginary part of complex susceptibility (χ) follows a sublinear power law, i.e., $\chi''(\omega) \propto \omega^{n-1}$ with $0 < n < 1$ and (ii) the ratio $\chi''(\omega)/\chi'(\omega)$ is constant and independent of frequency. In case of ionic conductors, n has low values so that the exponent (n-1) is close to unity, which is often called as low frequency dispersion (LFD). The frequency dependences of room temperature $\chi''(\omega)$ and $\chi''(\omega)/\chi'(\omega)$ are shown in Figures 5.1.7e,f, respectively, which evidence that LFD of $RbAg_4I_5$ is in accordance with UDR with $n \sim 0.2$.

MD simulation was carried out in order to understand the origin of the experimentally observed broadband CDC behavior in the superionic $RbAg_4I_5$. The calculated partial radial pair distribution function $g_{ab}(r)$, which has been defined as $g_{ab}(r) = \frac{N_{ab}(r)}{4\pi r^2 \Delta r \rho_b}$ where $N_{ab}(r)$ is the number of b-type ions at a distance between r and $r+\Delta r$ from the central a-type ion and ρ_b is the mean number density of the b-type ions, from the equilibrated atomic configuration in the MD simulation cell at 298 K is shown in Figure 5.1.8a. The partial radial distribution functions calculated from our model match reasonably well with other previous studies.[40, 42] The first sharp peak in $g_{ab}(r)$ for the I^--I^- pair ~ 4.28 Å and a deep minimum ~ 5.76 Å (Figure 5.1.8a) correspond to the first coordination between I^--I^- pair and indicate the structural ordering of I^-. Further, the presence of well-defined second and third peak ~ 7.30 Å and ~ 8.60 Å, respectively, in

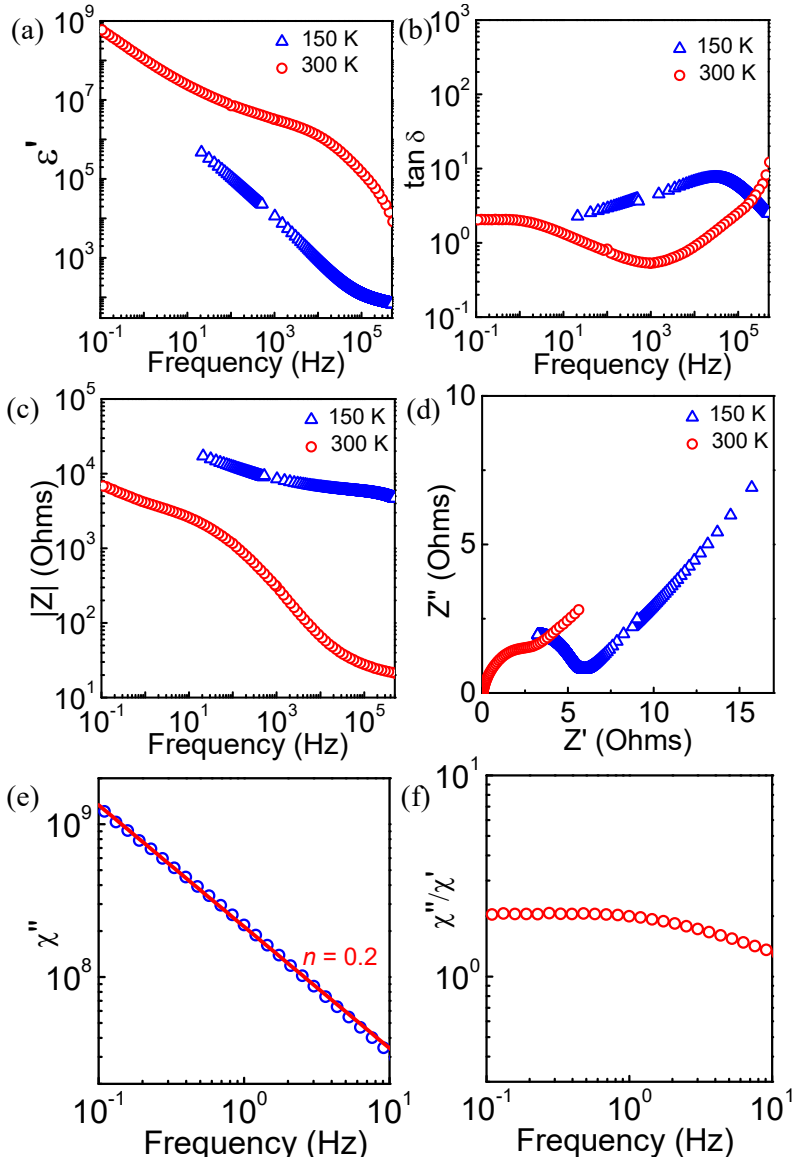

Figure 5.1.7. *Frequency dependences of (a) dielectric constant (ε'), (b) dielectric loss (tan δ), (c) |Z| and (d) Nyquist plots at 150 K and 300 K. Room temperature (e) χ''(ω) and (f) χ''(ω)/χ'(ω) exhibiting the universal dielectric response according to Jonscher's theory.*

$g_{ab}(r)$ indicates the long-range ordering of I^-. The presence of first sharp peak in the $g_{ab}(r)$ corresponding to the first neighbor coordination for the Ag^+-I^- pair ~ 2.62 Å (Figure 5.1.9a) further indicates the ordered arrangement of I^- around the Ag^+ throughout the solid. The first peak in $g_{ab}(r)$ for Rb^+-I^- pair ~ 3.30 Å (Figure 5.1.9a) is also sharp, but the magnitude is lower than that of the Ag^+-I^- pair which suggests that a greater number of Ag^+ are present in the surrounding of I^- than Rb^+. This particular arrangement formed by I^- enforces Ag^+ to come close to each other and make a collection of Ag^+ as a cluster. A similar signature is observed in the $g_{ab}(r)$ for the Ag^+-Ag^+ pair (Figure 5.1.8a). Instead of a complete randomness, $g_{ab}(r)$ for the Ag^+-Ag^+ pair shows a broad peak ~ 4.10 Å corresponding to the nearest neighbor coordination, however, the long range coordination peaks, such as for the second and third coordinations, are not well defined which indicate clustering of Ag^+. Ag^+ accumulation within the network of channel created by the I^- and the formation

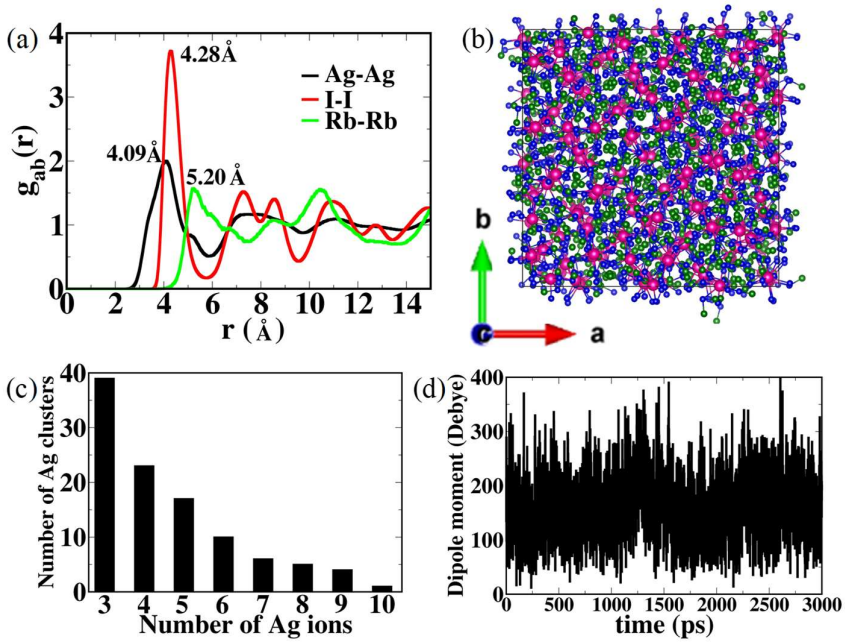

Figure 5.1.8. *(a) Partial radial pair distribution function $g_{ab}(r)$ vs. the radial distance r between Ag^+-Ag^+, Rb^+-Rb^+ and I^--I^-, and (b) snapshot of the $RbAg_4I_5$ supercell obtained from MD simulation at 298 K; Ag green, Rb magenta and I blue. (c) Histogram showing distribution of Ag cluster. (d) Fluctuation in dipole moments at 298 K.*

of Ag^+ clusters are evident from the snapshot of the $RbAg_4I_5$ supercell obtained from MD simulation (Figure 5.1.8b and Figure 5.1.9b). Rb^+, due to their large size, facilitate smooth conduction pathways for the Ag^+ to hop from one cluster to another, which consequently results in the high diffusion coefficient. The calculated diffusion coefficient 0.383 x 10^{-5} cm^2/sec (see Methods for the diffusion coefficient calculation) agrees well with the experimental reports.[43] This inter-cluster ionic diffusion leads to a broad size distribution of the clusters (Figure 5.1.8c) and large charge separations which, in turn, lead to large fluctuations in the instantaneous dipole moments in the range between 25 and 300 Debye (see Methods for dipole moment calculation) (Figure 5.1.8d). Consequently, these large fluctuating dipole moments result in the high dielectric constant as observed in the experiment.

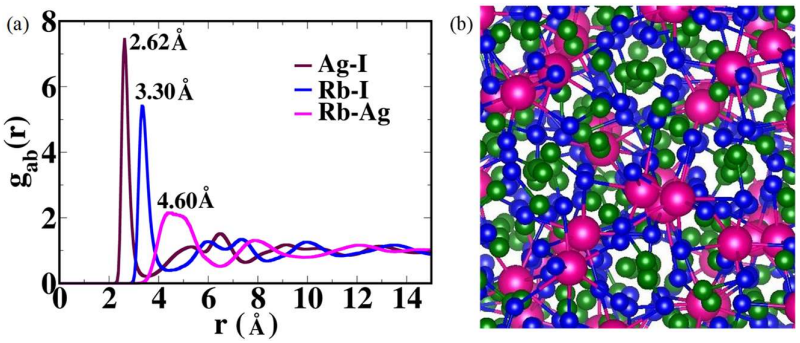

Figure 5.1.9. *(a) Partial radial pair distribution function $g_{ab}(r)$ vs. the radial distance r for the Ag^+-I^-, Rb^+-I^- and Rb^+-Ag^+ pairs , and (b) the zoomed version of the snapshot of the $RbAg_4I_5$ supercell obtained from MD simulation at 298 K. Ag atoms are green, Rb atoms are magenta and I atoms are represented in blue color.*

5.1.4. Conclusions

In conclusions, we have demonstrated an extremely high room temperature ε' in the superionic halide $RbAg_4I_5$ which reaches a maximum value ~ 6.4 x 10^8 at 0.1 Hz. This colossal ε' persists over a wide frequency range along with low dielectric loss. The frequency dependence of impedance indicates that ionic diffusion has the dominating contribution, which results in such a giant ε'. MD simulation further established that this colossal ε' arises due to inter-cluster Ag^+ diffusion which causes a large charge separation and an associated fluctuation in the instantaneous dipole moments. The observed

broadband colossal ε' in this non-oxide superionic solid opens up new opportunities in dielectric investigations and structure-property relationship in new halides.[53]

5.1.5. References

1. A. I. Kingon, J. P. Maria and S. K. Streiffer, *Nature*, 2000, **406**, 1032.

2. Y. Wang, W. Jie, C. Yang, X. Wei and J. Hao, *Adv. Funct. Mater.*, 2019, **29**, 1808118.

3. K. Yim, Y. Yong, J. Lee, K. Lee, H. H. Nahm, J. Yoo, C. Lee, C. Seong Hwang and S. Han, *NPG Asia Mater.*, 2015, **7**, e190.

4. X. Hao, *J. Adv. Dielectr.*, 2013, **03**, 1330001.

5. F. Palumbo, C. Wen, S. Lombardo, S. Pazos, F. Aguirre, M. Eizenberg, F. Hui and M. Lanza, *Adv. Funct. Mater.*, 2020, **30**, 1900657.

6. J. I. Roscow, C. R. Bowen and D. P. Almond, *ACS Energy Lett.*, 2017, **2**, 2264.

7. B. G. Kim, S. M. Cho, T. Y. Kim and H. M. Jang, *Phys. Rev. Lett.*, 2001, **86**, 3404.

8. C. Pecharromán, F. Esteban-Betegón, J. F. Bartolomé, S. López-Esteban and J. S. Moya, *Adv. Mater.*, 2001, **13**, 1541.

9. Y. Yan, J. E. Zhou, D. Maurya, Y. U. Wang and S. Priya, *Nat. Commun.*, 2016, **7**, 13089.

10. J. Yu, T. Ishikawa, Y. Arai, S. Yoda, M. Itoh and Y. Saita, *Appl. Phys. Lett.*, 2005, **87**, 252904.

11. Z. Wang, X. M. Chen, L. Ni and X. Q. Liu, *Appl. Phys. Lett.*, 2007, **90**, 022904.

12. J. H. Haeni, P. Irvin, W. Chang, R. Uecker, P. Reiche, Y. L. Li, S. Choudhury, W. Tian, M. E. Hawley and B. Craigo, *Nature*, 2004, **430**, 758.

13. S. Sarkar, P. K. Jana, B. K. Chaudhuri and H. Sakata, *Appl. Phys. Lett.*, 2006, **89**, 212905.

14. J. Wu, C. W. Nan, Y. Lin and Y. Deng, *Phys. Rev. Lett.*, 2002, **89**, 217601.

15. S. Krohns, P. Lunkenheimer, C. Kant, A. V. Pronin, H. B. Brom, A. A. Nugroho, M. Diantoro and A. Loidl, *Appl. Phys. Lett.*, 2009, **94**, 122903.

16. T. Park, Z. Nussinov, K. R. A. Hazzard, V. A. Sidorov, A. V. Balatsky, J. L. Sarrao, S. W. Cheong, M. F. Hundley, J. S. Lee and Q. X. Jia, *Phys. Rev. Lett.*, 2005, **94**, 017002.

17. W. Hu, Y. Liu, R. L. Withers, T. J. Frankcombe, L. Norén, A. Snashall, M. Kitchin, P. Smith, B. Gong and H. Chen, *Nat. Mater.*, 2013, **12**, 821.

18. J. Liu, C. G. Duan, W. G. Yin, W. N. Mei, R. W. Smith and J. R. Hardy, *Phys. Rev. B: Condens. Matter Mater. Phys.*, 2004, **70**, 144106.

19. T. B. Adams, D. C. Sinclair and A. R. West, *Adv. Mater.*, 2002, **14**, 1321.

20. P. Lunkenheimer, R. Fichtl, S. G. Ebbinghaus and A. Loidl, *Phys. Rev. B: Condens. Matter Mater. Phys.*, 2004, **70**, 172102.

21. M. A. Subramanian, D. Li, N. Duan, B. A. Reisner and A. W. Sleight, *J. Solid State Chem.*, 2000, **151**, 323.

22. A. P. Ramirez, M. A. Subramanian, M. Gardel, G. Blumberg, D. Li, T. Vogt and S. M. Shapiro, *Solid State Commun.*, 2000, **115**, 217.

23. D. Staresinic, P. Lunkenheimer, J. Hemberger, K. Biljakovic and A. Loidl, *Phys. Rev. Lett.*, 2006, **96**, 046402.

24. G. Blumberg, P. Littlewood, A. Gozar, B. S. Dennis, N. Motoyama, H. Eisaki and S. Uchida, *Science*, 2002, **297**, 584.

25. R. Federicci, S. Hole, A. F. Popa, L. Brohan, B. Baptiste, S. Mercone and B. Leridon, *Phys. Rev. Mater.*, 2017, **1**, 032001.

26. M. M. Ahmad and K. Yamada, *Appl. Phys. Lett.*, 2007, **91**, 052912.

27. M. M. Ahmad, Y. Yamane and K. Yamada, *J. Appl. Phys.*, 2009, **106**, 074106.

28. F. A. Karamov, *Superionic conductors: heterostructures and elements of functional electronics based on them*, 2008.

29. J. B. Boyce and B. A. Huberman, *Phys. Rep.*, 1979, **51**, 189.

30. B. B. Owens and G. R. Argue, *Science*, 1967, **157**, 308.

31. A. Boris and S. I. Bredikhin, *Solid State Ionics*, 1990, **40-41**, 269.

32. S. Bredikhin, V. N. Bondarev, A. V. Boris, P. V. Pikhitsa and W. Weppner, *Solid State Ionics*, 1995, **81**, 19.

33. N. S. Lidorenko, V. E. ZiI'bervarg and E. L. Nagaev, *Sov. Phys. JETP*, 1980, **51**, 89.

34. S. Geller, *Science*, 1967, **157**, 310.

35. S. Geller, *Phys. Rev. B: Condens. Matter Mater. Phys.*, 1976, **14**, 4345.

36. K. Funke, R. D. Banhatti, D. Wilmer, R. Dinnebier, A. Fitch and M. Jansen, *J. Phys. Chem. A*, 2006, **110**, 3010.

37. A. Sarkar, M. Chakrabarti, S. K. Ray, D. Bhowmick and D. Sanyal, *J. Phys.: Condens. Matter*, 2011, **23**, 155801.

38. P. Kirkegaard, N. J. Pedersen and M. Eldroup, Report of Riso National Lab (Riso-M2740), 1989.

39. H. Luitel, D. Sanyal, N. Gogurla and A. Sarkar, *J. Mater. Sci.*, 2017, **52**, 7615.

40. S. Tahara and T. Fukami, *J. Phys. Soc. Jpn.*, 2015, **84**, 024602.

41. S. Floros, M. Liakopoulou-Kyriakides, K. Karatasos and G. E. Papadopoulos, *Eur. Biophys. J.*, 2015, **44**, 599.

42. S. Matsunaga, *J. Phys.: Conf. Ser.*, 2009, **144**, 012011.

43. H. Looser, M. Mali, J. Roos and D. Brinkmann, *Solid State Ionics*, 1983, **9–10**, 1237.

44. G. G. Bentle, *J. Appl. Phys.*, 1968, **39**, 4036.

45. F. L. Lederman, M. B. Salamon and H. Peisl, *Solid State Commun.*, 1976, **19**, 147.

46. D. Brinkmann, W. Freudenreich, H. Arend and J. Roos, *Solid State Commun.*, 1978, **27**, 133.

47. D. A. Gallagher and M. V. Klein, *Phys. Rev. B: Condens. Matter Mater. Phys.*, 1979, **19**, 4282.

48. R. Vargas and G. W. Coronel, *Solid State Ionics*, 1995, **81**, 69.

49. J. Dhar, S. Sil, A. Dey, P. P. Ray and D. Sanyal, *J. Phys. Chem. Lett.*, 2017, **8**, 1745.

50. M. Sharon, *An introduction to the physics and electrochemistry of semiconductors: fundamentals and applications*, 2016.

51. A. K. Jonscher, *Nature*, 1977, **267**, 673.

52. A. K. Jonscher, *J. Phys. D: Appl. Phys.*, 1999, **32**, R57.

53. A. Mohanty, D. Swain, S. Govinda, T. N. G. Row and D. D. Sarma, *ACS Energy Lett.*, 2019, **4**, 2045.

Chapter 5.2

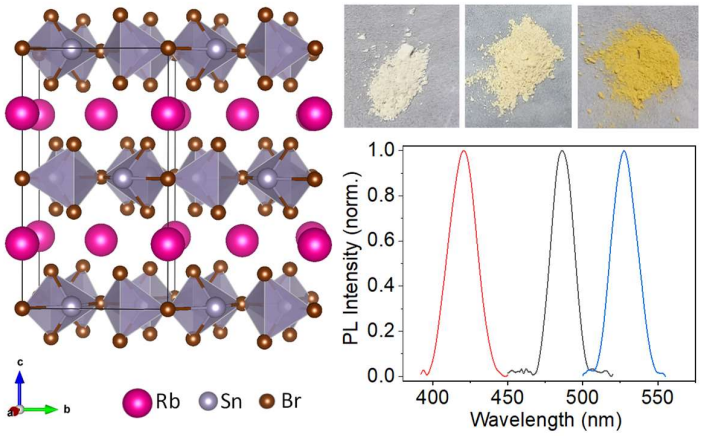

Pb-free Layered All-Inorganic Metal Halides, $RbSn_2Br_5$: Mechanochemical Synthesis, Band Gap Tuning, Optical and Dielectric Properties

Chapter 5.2

Pb-free Layered All-Inorganic Metal Halides, $RbSn_2Br_5$: Mechanochemical Synthesis, Band Gap Tuning, Optical and Dielectric Properties[†]

Summary

Recently, two-dimensional (2D) layered metal halide perovskites stimulate substantial attention in photovoltaics and optoelectronics. Nevertheless, one of the main hurdles to their commercialization is the Pb toxicity. Although challenging, the emergence of Sn(II)-based halides considered as a most favourable environmentally benign substitute to Pb based material. In this chapter, we investigate the optical and dielectric properties of 2D Pb-free all-inorganic metal halide, $RbSn_2Br_5$, which is synthesized by all-solid state mechanochemistry. The material exhibited a band gap of ~3.20 eV with room-temperature photoluminescence (PL) centered at ~2.51 eV. The Raman spectroscopic investigation demonstrated distinct vibrational modes related to the Sn-Br bond from 2D polymeric $[Sn_2Br_5]_n^{n-}$ layer units. The thermal stability indicated that the material is stable up to ~205 ^0C. An excitonic absorption with high exciton binding energy is perceived for ultrasonic treated toluene-dispersed solution of $RbSn_2Br_5$. Enhanced PL intensity with red-shifted and broad emission line were demonstrated at 77 K than the room-temperature emission. The charge-carrier recombination took place from the band-edge states and intrinsic defect sites (shallow states) at both temperatures. Further, the halide mixing strategy is applied to tune the band gap (2.68-3.36 eV) and PL emission (2.31-2.58 eV) by synthesizing $RbSn_2Br_3Cl_2$ and $RbSn_2Br_4I$. Finally, the dielectric measurement of $RbSn_2Br_5$ was carried out as a function of temperature (4-300 K), which exhibited a strong frequency dependence.

[†]K. Kundu, P. Dutta, **P. Acharyya,** and K. Biswas. *Mater. Res. Bull.,* 2021, **140**, 111339-111348.

5.2.1. Introduction

Recently, *all-inorganic* metal halide perovskites showed great promises in optoelectronics and photovoltaics due to their exceptional properties, which include narrow photoluminescence (PL) line-width, high PL quantum yield, superior stability, enriched defect tolerance, and suitably tuned band gap energy.[1-6] However, the principal focus was dedicated mainly toward lead (Pb)-based *all-inorganic* analogues.[7-11] which suffers shortcoming due to the inherent toxicity of Pb, and therefore, restricts their applications.[12, 13] As a consequence, extensive research efforts have been dedicated toward advancing Pb-free halide perovskites in terms of their synthesis, stabilities, optical and electronic properties.[2, 14-16] Among all alternatives, tin (Sn)-based halides are considered as favourable replacements of Pb-based metal halides both in optoelectronic and photovoltaic devices because of their environmentally benign nature.[17, 18] Nonetheless, only a handful reports are available on the *all-inorganic* $CsSnX_3$-type materials,[19-21] which offer inferior stability due to their affinity toward oxidation from +2 to +4 state. Thus, boosting the stability of Sn-based metal halide perovskites becomes a vital assignment.

Such issues can be ruled out by introducing two-dimensional (2D) layered perovskites, which have common composition of $A'_2A_{n-1}B_nX_{3n+1}$, wherein A′ is a bulky organic spacer cation separating inorganic octahedral layers, *A* represents small organic cation, and *n* denotes the number of octahedral layers.[22-24] These layered halides exhibited promising layer-dependent optical properties, large exciton binding energy, tunable and wider band gap, PL intermittency, and improved stability, which expanded their applications in solar cells, light emitting diodes (LEDs), and thermoelectrics.[25-29] Most of the recent investigations were focused on the synthesis and characterization of hybrid organic-inorganic Sn-based metal halides,[30-37] in contrast their *all-inorganic* equivalents are rarely explored. Recently, *all-inorganic* Sn-based mixed halides ($Cs_2SnCl_2I_2$, $Cs_{2.38}Rb_{1.62}Sn_3Cl_8I_2$ and $Cs_8Sn_6Br_{13}I_7$) were discovered with 2D layered crystal structures by Kanatzidis's group,[38] and Kovalenko's group.[30] In view of these, it is essential to develop Sn-based 2D alternatives of toxic Pb, which will be advantageous in terms of the optical properties, improved stabilities and so on.

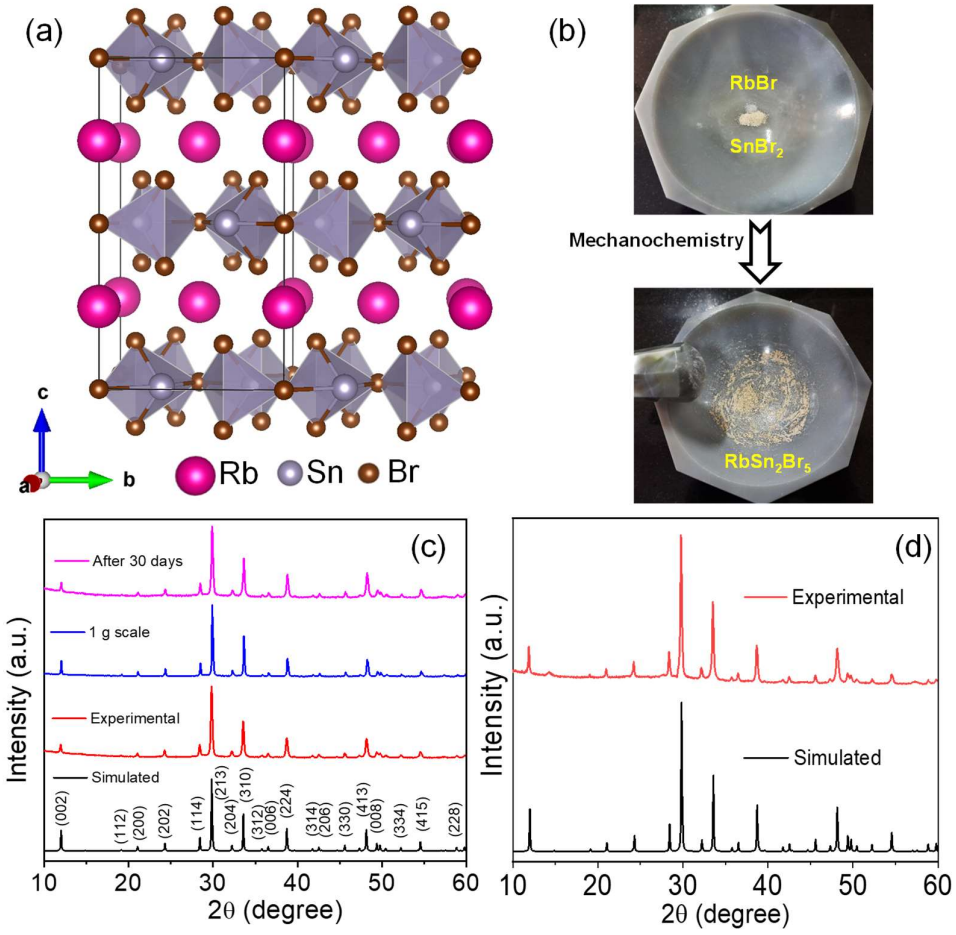

Figure 5.2.1. *a) Crystal structure of $RbSn_2Br_5$, b) Pictorial representation of mechanochemical synthesis, and c) PXRD patterns of as-synthesized $RbSn_2Br_5$ powders, in 1 gm scale and keeping it after 30 days in ambient condition. d) PXRD pattern of $RbSn_2Br_5$ sample precipitated after ultrasonication in toluene.*

In this chapter, we report all-solid state mechanochemical synthesis of 2D layered Pb-free metal halide, $RbSn_2Br_5$, and its mixed halide counterparts, $RbSn_2Br_3Cl_2$ and $RbSn_2Br_4I$. The all-solid state methodology is organic solvent-free, cost-effective, and scalable to achieve ~1 g for each reaction of pure crystalline metal halides. The crystal structure of $RbSn_2Br_5$ can be visualized as the layered lattice involving 2D polymeric $[Sn_2Br_5]_n^{n-}$ layer units and separated by Rb ions (Figure 5.2.1a). The stability studies of $RbSn_2Br_5$ powders exhibited no sign of degradation after keeping at ambient environments for 30 days and it is thermally stable up to ~205 ^{0}C. The Raman spectral

investigation of as-synthesized powders displayed distinct modes at low frequency regions corresponding to the Sn-Br bond vibrations from 2D polymeric $[Sn_2Br_5]_n^{n-}$ layer units. We have studied the optical properties of as-synthesized materials by solid-state UV-Vis absorption and PL spectroscopic techniques, which showed an optical band gap of ~3.20 eV along with a PL emission centered at ~2.51 eV. We have extended the investigation to explore the optical properties and charge-carrier recombination dynamics both at 298 K and 77 K using toluene-dispersed solution of $RbSn_2Br_5$ after prolonged ultrasonication. The excitonic recombinations occurred through the band-edge states and intrinsic defect sites (shallow states) at both temperature with average life-times in the range of few nanoseconds. The optical band gap (2.68-3.36 eV) and PL emission (2.31 eV to 2.58 eV) were further tuned by adjusting the halide composition in $RbSn_2Br_5$ by synthesizing $RbSn_2Br_3Cl_2$ and $RbSn_2Br_4I$. Finally, the dielectric measurement of $RbSn_2Br_5$ was carried out as a function of temperature (4-300 K).

5.2.2. Methods

Reagents. Rubidium bromide (RbBr, 99.6% trace metals basis, Sigma-Aldrich), rubidium iodide (RbI, 99.9% trace metals basis, Sigma-Aldrich), tin (II) bromide ($SnBr_2$, Sigma Aldrich), tin (II) chloride ($SnCl_2$, anhydrous, powder, ≥ 99.99% trace metals basis, Sigma-Aldrich), and toluene (ACS reagent, ≥ 99.5%, Sigma-Aldrich) were used for the synthesis and characterization without further purification.

Synthesis of $RbSn_2Br_5$ by mechanochemistry. In a representative synthesis, 82.69 mg (0.5 mmol) and 278.52 mg (1.0 mmol) of RbBr and $SnBr_2$, respectively at 1:2 stoichiometric ratio were taken in a mortar pestle and ground mechanically for 2 h at ambient atmosphere. Similarly, the mixed halide analogues (e.g., $RbSn_2Br_3Cl_2$ and $RbSn_2Br_4I$) were also synthesized mechanochemically.

Ultrasonication. Bulk powders were dispersed in toluene and then sonicated by an ultrasonic probe (VCX 750, Sonics & Materials INC.; 20 kHz frequency; 700 W power) for 1 hour to achieve homogeneous dispersion for further investigations.

Powder X-ray diffraction (PXRD). A Rigaku Smart Lab diffractometer was utilized to collect the PXRD patterns of all samples at room temperature using Cu Kα radiation (λ = 1.5406 Å) with accelerating voltage of 40 kV and current of 30 mA.

Raman spectroscopy. Raman spectroscopic measurement of bulk $RbSn_2Br_5$ powder samples was performed by Renishaw InVia Raman spectrometer with a Leica upright microscope using a precise laser excitation source. Before sample measurement, a silicon standard (520.5 cm^{-1}) was applied as a reference standard to calibrate the Raman instrument. The spectrum was monitored with 10 sec of exposure time and 5 accumulations with a collection optics of 50X objective.

Transmission electron microscopy (TEM). A JEOL (JEM3010) instrument was employed to acquire the TEM images.

Thermogravimetric analysis (TGA). A 2 STAR TGA instrument was utilized for the TGA measurements of bulk sample. Powder samples were heated in the temperature range of 50-800 °C at a rate of 5 °C min^{-1} under N_2 atmosphere (40 mL min^{-1}).

Electronic spectroscopy. UV-vis absorption spectra were recorded using a PerkinElmer, Lambda-900 UV/vis/near-IR spectrometer. To estimate the optical band gap of the solid state sample, diffuse reflectance measurements were carried out in 250 nm to 800 nm range in the reflectance mode. Absorption (α/S) values were evaluated from the reflectance data by employing the Kubelka-Munk equation: $\alpha/S = (1-R)^2/2R$, wherein α is the absorption, R and S are the reflectance, and scattering coefficients, respectively. From α/S vs. wavelength (in nm) plot, the energy band gap was procured by extrapolating the linear region. Electronic absorption spectrum was also monitored for the ultrasonic treated toluene-dispersed solution of bulk $RbSn_2Br_5$ samples. The solid state and solution phase (ultrasonic dispersion in toluene) emission and excitation spectra were measured by a PerkinElmer LS 55 luminescence spectrometer at different temperatures (25-85 ^{0}C).

Low-temperature photoluminescence (PL). Edinburgh FLS1000 spectrofluorometer was implemented for low-temperature PL measurements at 77 K using a vacuum liquid-nitrogen cryostat.

PL life-time measurements. The time-resolved decay plots were collected by using Edinburgh FLS1000 spectrofluorometer coupled with EPL-405 laser (wavelength 405 nm ± 10 nm, maximum average power 5 mW) at 298 K and 77 K.

Dielectric measurement. Temperature and frequency dependent dielectric permittivity (ε) of the studied sample was measured by an Impedance Analyzer (Solartron SI 1260) attached to a 4 K closed cycle refrigerator (Advanced Research Systems, Inc.). A Lakeshore 335 temperature controller was used to control the temperature of the system and measure the temperature. A polished thin rectangular-shaped sample was used for this dielectric measurement. Thin layer of silver paste on either side of the two polished surfaces was used as electrodes. All the dielectric data were recorded during heating.

5.2.3. Results and Discussion

In order to synthesize bulk polycrystalline powders of $RbSn_2Br_5$, RbBr and $SnBr_2$ as precursors were used, where the molar ratio of RbBr and $SnBr_2$ is fixed at 1:2 for all-solid state mechanochemical grinding (Scheme 5.2.1).

Scheme 5.2.1. *Mechanochemical synthesis of $RbSn_2Br_5$.*

$$RbBr + SnBr_2 \xrightarrow{Mechanochemistry} RbSn_2Br_5$$

Initially, we have taken a stoichiometric amount of starting precursors (herein, RbBr and $SnBr_2$) in a mortar, and subsequently, performed mechanochemical grinding at ambient environments. To confirm a thorough transformation of the starting precursors to the final products, the powders were ground constantly for 2 hours. The visual appearance of starting reagents along with the final products were displayed in Figure

5.2.1b. This method has been utilized to yield up to ~1 g of solid state pure phase powders. Finally, a fixed amount of mechanochemically ground powder (~15 mg) was dispersed in 10 ml of toluene and exposed to the ultrasonication, which produced a homogeneous dispersion after 1 hour of sonication.

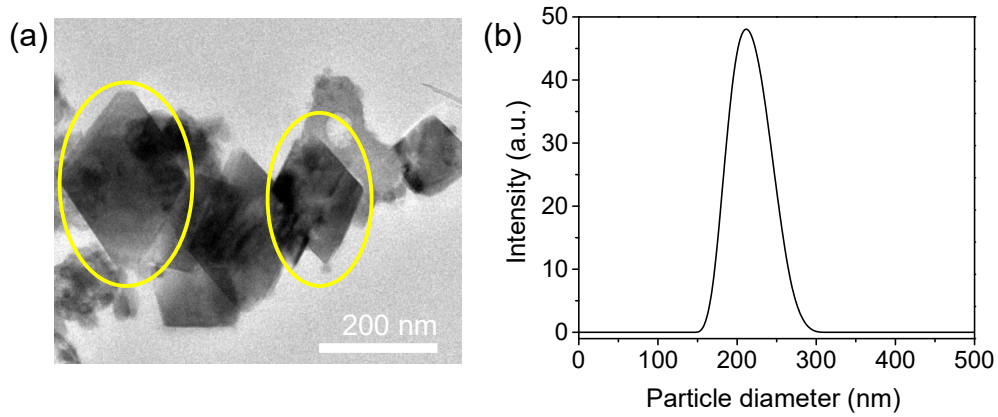

Figure 5.2.2. *a) TEM image of ultrasonically treated toluene dispersed $RbSn_2Br_5$. b) Particle size distribution by DLS measurement for toluene dispersed $RbSn_2Br_5$.*

The PXRD patterns of mechanochemically ground powders of $RbSn_2Br_5$ and corresponding precipitates from its toluene-dispersed solution were matched with the tetragonal phase of $RbSn_2Br_5$ (space group of *I*4*/mcm*), which specify the formation of pure phase $RbSn_2Br_5$ (Figure 5.2.1c and Figure 5.2.1d, respectively). The peak emerged at $2\theta = 11.98°$ for $RbSn_2Br_5$ designates the existence of (002) plane, which is a typical peak of 2D layered material (e.g., $CsPb_2Br_5$).[39] The demonstration of crystal structure for $RbSn_2Br_5$ is provided in Figure 5.2.1a, wherein the layered lattice comprising of 2D polymeric $[Sn_2Br_5]_n^{n-}$ layer units is isolated by Rb^+ ions. Two bridging Br atoms in the plane of polymeric network and two terminal Br atoms above and below the network plane are located to the adjacent Sn atom. Also, the bridging Br atoms are enclosed by the two Rb and four Sn atoms at the axial and equatorial positions, respectively, as described by Grimes and co-workers previously.[40]

The morphology of ultrasonic treated toluene-dispersed $RbSn_2Br_5$ solution is examined by TEM techniques. The TEM images of nanoparticles obtained after prolonged ultrasonication of bulk powders are presented in Figures 5.2.2a. Further, dynamic light scattering (DLS) measurement has been utilized to probe the particle size

distribution of toluene-dispersed solution after ultrasonication, which exhibited an average particle size of ~200 nm, as represented in Figure 5.2.2b.

The Raman spectroscopic measurements were performed using 633 and 830 nm laser excitations at room temperature to identify the distinctive vibrational modes of layered $RbSn_2Br_5$. The dominant vibrational signatures are arose from the $[Sn_2Br_5]_n^{n-}$ unit, as illustrated in Figure 5.2.3a. After careful monitoring up to 2000 cm^{-1} region, no vibrational bands were appeared above 300 cm^{-1}. In $RbSn_2Br_5$, the distinctive Raman bands at 190, 151, and 108 cm^{-1} were entitled to the $\nu(A_{1g})$, $\nu(E_g)$ and $\delta(F_{2g})$ modes, respectively. The $\nu(A_{1g})$ and $\nu(E_g)$ modes were assigned to the symmetric and asymmetric Sn-Br bond stretching, respectively, whereas the $\delta(F_{2g})$ mode is represented as the Br-Sn-Br asymmetric bending. All the assignments of these vibrational modes are in good agreement with the previous literature.[41]

The thermal and environmental stabilities of as-synthesized polycrystalline powders of $RbSn_2Br_5$ have been examined by the TGA and PXRD measurements. The observation from the TGA measurements is presented in Figure 5.2.3b, which revealed a two-step weight loss events as a function of temperature. The thermal degradation of material started at ~205 ^{0}C along with a foremost weight loss at ~380 ^{0}C. The first weight loss at ~205 ^{0}C is perhaps due to the partial sublimation of lower melting $SnBr_2$, whereas the second major weight loss associated with the melting event of RbBr at higher temperature and probable disintegration of the inorganic framework. Therefore, the consequential analysis suggest that bulk $RbSn_2Br_5$ is thermally stable up to ~205 ^{0}C. Likewise, mechanochemically grounded 2D $CsPb_2Br_5$ and thin film of $(4Tm)_2SnI_4$ (where, 4Tm represents a class of π-conjugated oligothiophene ligand) reported to exhibit thermal stability up to 195 °C and 180 °C, respectively from TGA measurement.[34, 42] Furthermore, Figure 5.2.1c represents the PXRD patterns of $RbSn_2Br_5$, which was examined after exposure of bulk powder sample to the ambient laboratory environments for 30 days. Interestingly, no sign of decomposition or the appearance of new phases is evidenced, which certainly imply decent environmental stability of $RbSn_2Br_5$.

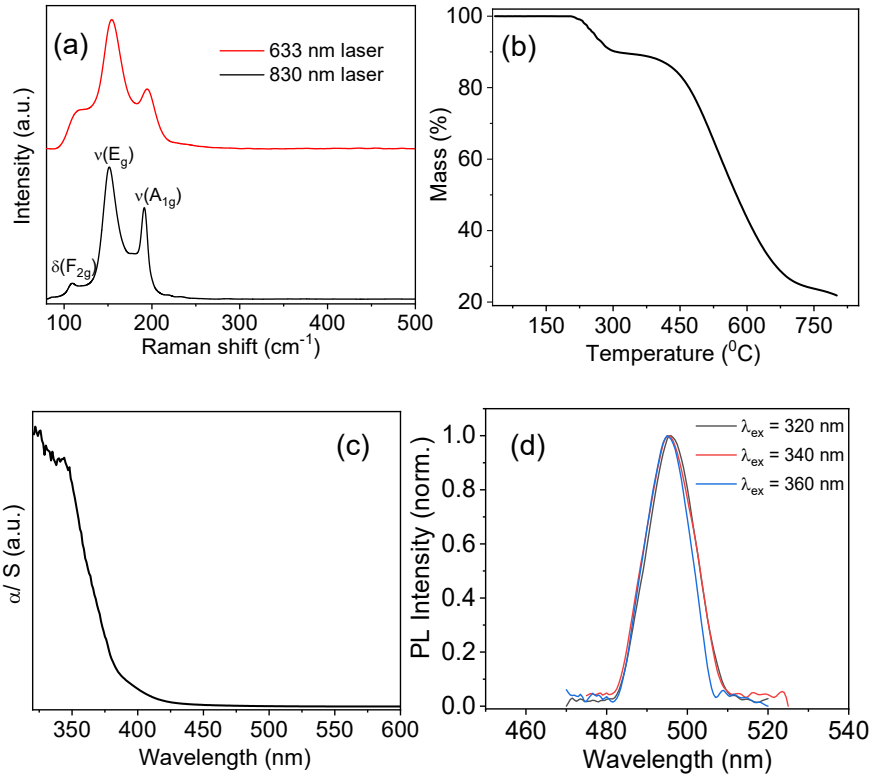

Figure 5.2.3. *a) Raman spectra, b) thermogravimetric analysis (TGA), c) solid-state UV/Vis absorption (α/S), and d) PL spectra at different excitation wavelengths of* $RbSn_2Br_5$ *at 298 K.*

We have studied optical properties of $RbSn_2Br_5$ using UV-Vis absorption and PL spectroscopic tools accompanied by the time-resolved PL spectroscopy. In order to extract the band gap of $RbSn_2Br_5$ powder, the solid state UV-vis diffuse reflectance spectra were collected, and successively, using the Kubelka-Munk equation, the reflectance values were transformed into absorbance values (discussed in experimental section). The band gap of $RbSn_2Br_5$ is extracted from the onset of the absorption spectrum (Figure 5.2.3c), which is observed to be ~386 nm (~3.20 eV). Practically unaltered emission line appeared at ~ 495 nm (~2.51 eV) under different excitation wavelength, which is evidenced from the solid-state room-temperature PL spectra (Figure 5.2.3d).

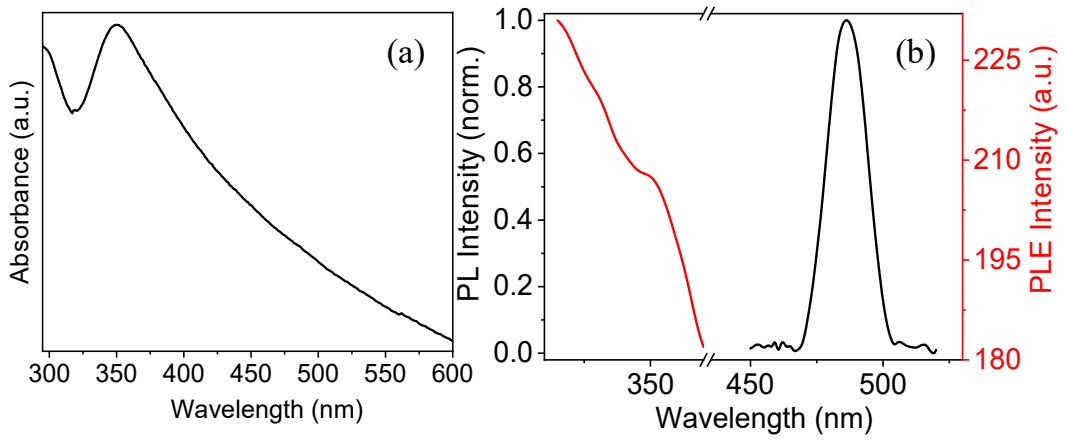

Figure 5.2.4. *a) Optical absorption, b) PL excitation (PLE), and PL emission spectra of ultrasonically dispersed $RbSn_2Br_5$ in toluene at 298 K.*

The photophysical properties of ultrasonic treated $RbSn_2Br_5$ solution in toluene were explored by the absorbance and PL measurements both at room-temperature (298 K) and cryogenic temperature (77 K). An excitonic peak centered at ~349 nm can be noticed in the absorption spectrum (Figure 5.2.4a) at room temperature, which is a distinctive characteristics of layered metal halides. Such features arise mainly from the dielectric and quantum confinements between the inorganic well and barrier of layered structures, which provide firmly bound excitons.[43, 44] It is essential to emphasize that a long absorption tail widened up to ~600 nm is manifested in toluene-dispersed $RbSn_2Br_5$ solution, which is common in Pb-free materials.[45-48] Such a long tail in this material suggests the involvement of sub-bandgap states during electronic transition.[45, 47] The PL excitation (PLE) and PL spectra of toluene-dispersed $RbSn_2Br_5$ solution at 298 K are demonstrated in Figure 5.2.4b. A peak-like feature at around 350 nm was detected in the PLE spectra, when examined at λ_{em}^{max} and analogous with the position of excitonic peak in absorption spectrum. Furthermore, a PL band centered at ~485 nm has been appeared for toluene-dispersed $RbSn_2Br_5$ with a narrow line-width of ~17 nm (Figure 5.2.4b). The PL spectrum also unveiled large Stokes shift (~0.99 eV) and minimal overlap with the PLE spectrum, which efficiently avoid the self-absorption.

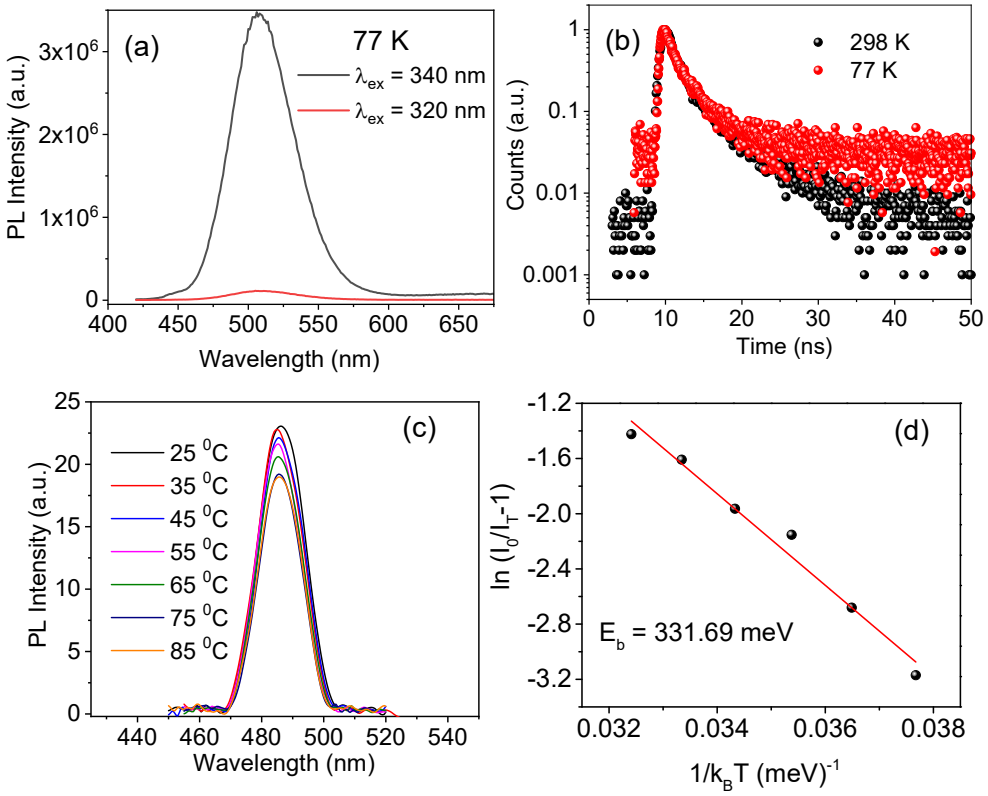

Figure 5.2.5. *a) PL spectra as a function of excitation wavelengths at 77 K, and b) comparative PL decay profile of toluene dispersed $RbSn_2Br_5$ at 298 K and 77 K. c) Temperature-dependent PL spectra of $RbSn_2Br_5$. d) The Arrhenius-type plot for extracting exciton binding energy (E_b).*

The PL emission measurement at cryogenic temperature (77 K) was also performed for toluene-dispersed $RbSn_2Br_5$ solution at different excitation wavelengths. Figure 5.2.5a presents an emission spectra centered at 507 nm with relatively broad line-width of 52 nm. For all PL spectra at 77 K, we deconvoluted the plots into two contributions (Figure 5.2.6), representing the lower-wavelength and higher-wavelength contributions as the exciton peak and the supplementary path that results in spectral broadening, respectively (i.e., free and bound excitons).[49]

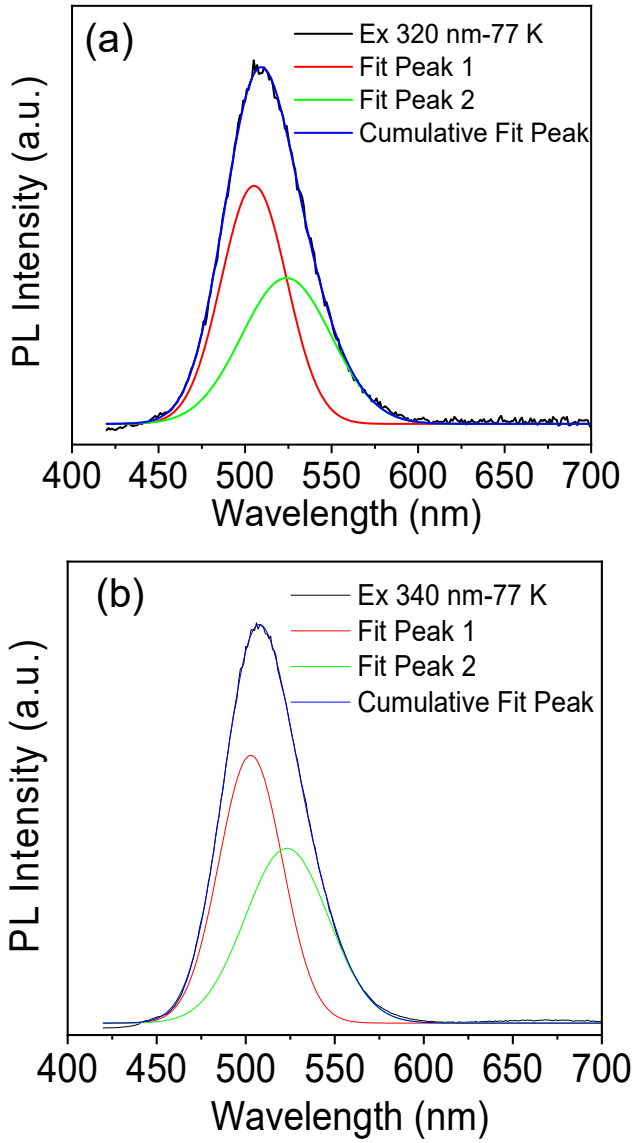

Figure 5.2.6. *Deconvoluted PL spectra of $RbSn_2Br_5$ at 77 K with different excitation wavelength of a) 320 nm, and b) 340 nm.*

Time-correlated single photon counting (TCSPC) technique was employed to monitor the PL decays in ultrasonic treated toluene-dispersed $RbSn_2Br_5$ solution. The PL decays monitored at λ_{em}^{max} under 405 nm laser excitation are presented in Figure 5.2.5b. To comprehend the dynamics of excitonic recombinations in $RbSn_2Br_5$, we have

performed the measurement at both room-temperature and 77 K. The plots for the respective PL decay can be fitted following the biexponential model;

$$A(t) = A_1 e^{-t/\tau_1} + A_2 e^{-t/\tau_2}$$

The estimated average life-time (τ_{avg}) is extracted from following equation;

$$\tau = (A_1\tau_1^2 + A_2\tau_2^2) / (A_1\tau_1 + A_2\tau_2)$$

Herein, the PL amplitudes and PL life-time components are A_1, A_2 and τ_1, τ_2, respectively.[50] At both temperature, solution-processed $RbSn_2Br_5$ displays two dissimilar PL decay routes with few nanoseconds of life-time (Table 5.2.1) similar to the earlier reported Sn-based perovskite nanocrystals.[51] The PL decay at room-temperature produces two life-times: τ_1 (1.418 ns) and τ_2 (6.443 ns), respectively, with marginally comparable contribution from both the components. On the other hand, the life-time components along with the relative contributions at 77 K are found to be τ_1 = 1.324 ns (43%) and τ_2 = 4.303 ns (57%). The faster-decaying PL originate from the band-edge states, whereas the slower decay one may be attributable to the recombinations from state just below the band-edge (i.e., shallow state) or the intrinsic defect sites.[51, 52]

Table 5.2.1. *The PL decay life-times and relative amplitudes of $RbSn_2Br_{5-y}X_y$ (X = Cl or I and y = 2 or 1, respectively) at 298 and 77 K.*

Sample	T (K)	τ_1 (ns)	A_1	τ_2 (ns)	A_2	τ_{avg} (ns)
$RbSn_2Br_5$	298	1.418	0.507	6.443	0.492	5.514
	77	1.324	0.433	4.303	0.567	3.737
$RbSn_2Br_3Cl_2$	298	1.787	0.561	7.526	0.439	6.191
$RbSn_2Br_4I$	298	0.782	0.242	3.858	0.758	3.671

The temperature-induced PL measurement was performed at 25-85 ^{0}C range to access the photo-stability of ultrasonic treated toluene-dispersed $RbSn_2Br_5$ solution. Figure 5.2.5c reveals only a ~18% drop in PL intensity at 85 ^{0}C compared to its initial

value at 25 ^{0}C, which implies a superior photo-stability of $RbSn_2Br_5$. It is anticipated that the thermally activated charge carrier trapping is responsible for such PL intensity trend with increasing temperature.[50] The reduction in PL intensity at higher temperature is a consequence of the excitons thermal dissociation and successive decrease in their population.[53, 54] The following equation has been utilized for the variation of temperature-induced PL intensity;[50, 55]

$$I(T) = {I_0}\Big/{1 + Aexp({-E_b}/{k_BT})}$$

The E_b and k_B signify the excitonic binding energy, and the Boltzmann constant, respectively, whereas I(T) and I_0 are the integrated PL intensities at 85 ^{0}C and 25 ^{0}C, respectively. Figure 5.2.5d illustrates the linear relationship of logarithm of [I_0/I(T)-1] *versus* 1/k_BT, which offers the assessment of E_b consistent with the Arrhenius-type of equation.[56, 57] The E_b of 2D $RbSn_2Br_5$ was estimated to be 331.69 meV, which is comparable to the earlier reported layered hybrid perovskite.[58, 59] The calculated E_b of $RbSn_2Br_5$ is perceived to be superior than Sn-based 3D $CsSnX_3$,[60] and other Sn-based 2D hybrid perovskites (PEA_2SnI_4 and TEA_2SnI_4).[61] This result certainly pointed out that the PL emission in $RbSn_2Br_5$ is mostly initiated from the radiative recombination of excitons owing to such high E_b.[62]

To tune the optical band gap, we have carried out the compositional changes through halide mixing in $RbSn_2Br_5$. We have synthesized the mixed halide materials (for example, $RbSn_2Br_3Cl_2$ and $RbSn_2Br_4I$) by solid-state mechanochemical grinding. The schemes for their synthesis have been offered herein;

Scheme 5.2.2. *Mechanochemical synthesis of $RbSn_2Br_{5-y}X_y$ (X = Cl or I and Y = 2 or 1, respectively).*

$$RbBr + SnCl_2 + SnBr_2 \xrightarrow{Mechanochemistry} RbSn_2Br_3Cl_2$$

$$RbI + 2SnBr_2 \xrightarrow{Mechanochemistry} RbSn_2Br_4I$$

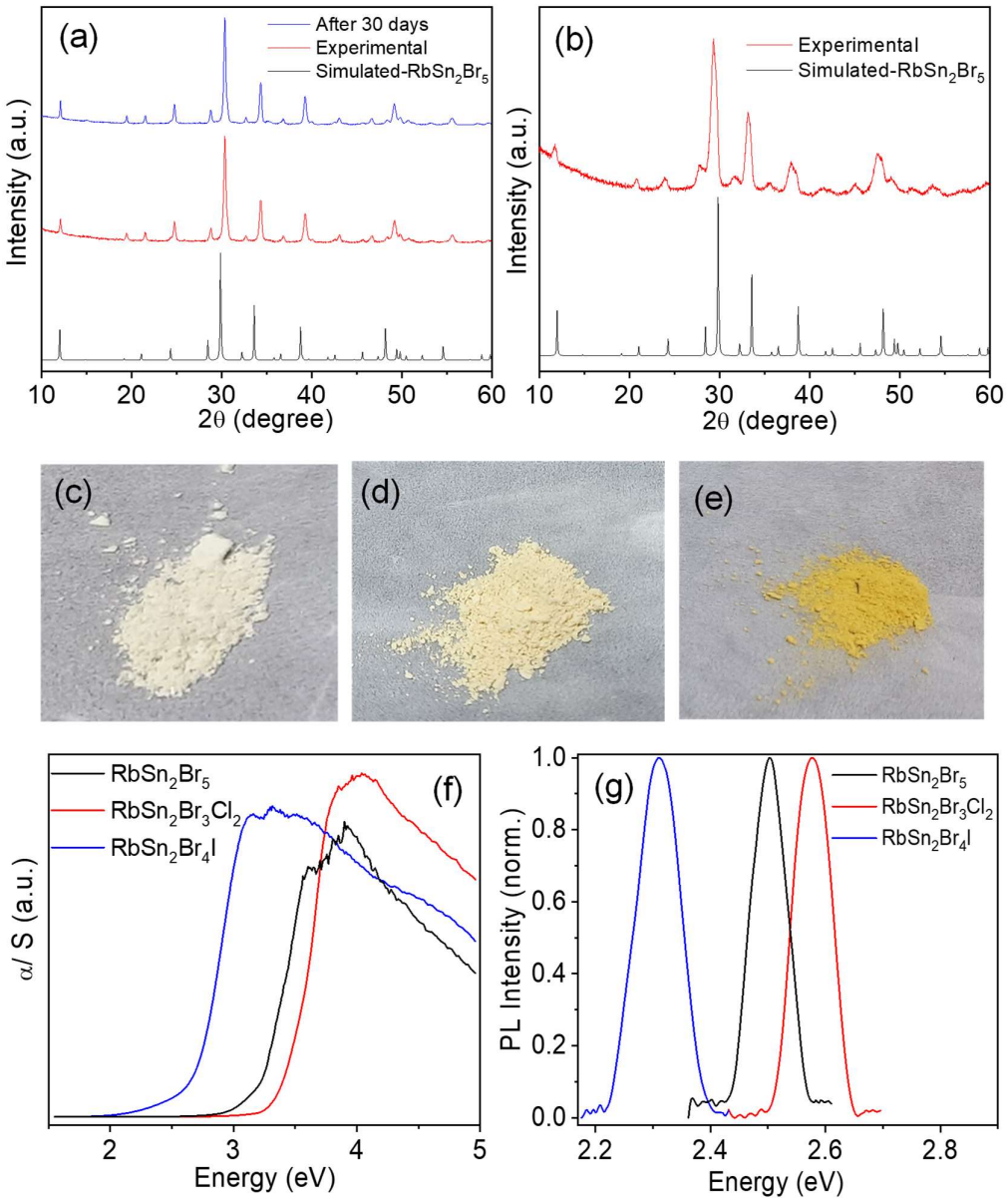

Figure 5.2.7. *PXRD pattern of as-synthesized a) $RbSn_2Br_3Cl_2$, and b) $RbSn_2Br_{54}I$ powders synthesized by mechanochemistry. Visual appearance of as-synthesized c) $RbSn_2Br_3Cl_2$, d) $RbSn_2Br_5$, and e) $RbSn_2Br_4I$ powders by mechanochemistry. f) Solid-state UV/Vis absorption (α/S) spectra, and g) PL spectra of $RbSn_2Br_3Cl_2$, $RbSn_2Br_5$, and $RbSn_2Br_4I$ powders at 298 K.*

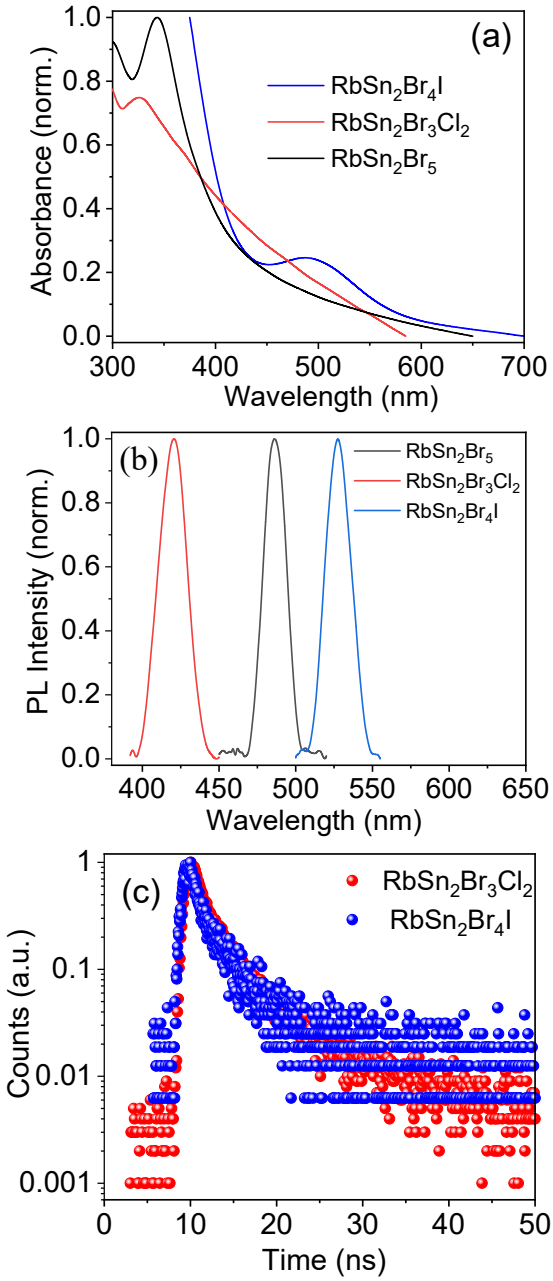

Figure 5.2.8. *Comparative a) optical absorption, b) PL spectra, and c) PL decay profile of toluene dispersed $RbSn_2Br_3Cl_2$ and $RbSn_2Br_4I$ at 298 K.*

The PXRD patterns, shown in Figures 5.2.7a-b for the as-synthesized $RbSn_2Br_3Cl_2$ and $RbSn_2Br_4I$ powders display analogous peak features to the simulated pattern (i.e., tetragonal phase with space group of *I4/mcm*), however, the pattern is slightly

right-shifted or left-shifted depending on their mixed halide compositions. Partial substitution of Br with the smaller Cl or larger I atoms shrinks or expands the unit cell, respectively, which results in a shift of diffraction peaks toward higher or lower angles, respectively. Photographic appearance of phase-pure bulk powders of mixed halide systems under day light is shown in Figures 5.2.7c-e, which changes from white to deep yellowish with halide composition from Cl to I. The solid-state optical properties of $RbSn_2Br_3Cl_2$ and $RbSn_2Br_4I$ bulk powders have been explored. Tuning of the optical band gap energy can be evidenced across the range of 2.68-3.36 eV by changing the halide compositions (Figure 5.2.7f), whereas the solid-state PL maxima shifts from 2.31 eV to 2.58 eV upon partial substitution of Br with I and Cl in $RbSn_2Br_5$, respectively (Figure 5.2.7g). The shift in PL spectra with halide substitutions takes place as a result of the band gap tuning wherein the valence band maximum (VBM) of Sn-based halide perovskites is largely involved Sn *s* and halide *p* orbitals, and the conduction band minimum (CBM) is primarily derived from the Sn *p* orbitals.[63]

Finally, the bulk powders of $RbSn_2Br_3Cl_2$ and $RbSn_2Br_4I$ were ultrasonically treated in toluene to achieve homogeneous dispersion and studied their solution-phase steady-state and time-resolved optical properties. Absorbance and PL measurements of toluene-dispersed solution revealed the appearance of excitonic peaks at 326 nm and 493 nm, while the narrow and single-peak emission lines centered at 421 nm and 527 nm for $RbSn_2Br_3Cl_2$ and $RbSn_2Br_4I$, respectively (see, Figure 5.2.8a and Figure 5.2.8b, respectively). The time-resolved PL measurements are conducted to acquire insight into the excitonic recombination dynamics upon halide mixing in $RbSn_2Br_5$. With partial substitution of Br by Cl and I, the average life-times (τ_{avg}) are found to be increased and decreased, respectively (Table 5.2.1). Such trend in life-times for mixed halide composition is observed earlier for $CsSnX_3$ and $(PEA)_2PbX_4$ systems.[51, 59]

Figures 5.2.9a and b represent the temperature-dependent (4-300 K) real (ε') and imaginary (ε'') part of dielectric permittivity for $RbSn_2Br_5$ measured at different selective frequencies, respectively. The value of ε' is found to be small and remains almost constant up to T = 230 K and then it increases sharply with the increase in temperature and shows strong frequency dispersion. This type of dielectric behaviour is related to the thermally excited relaxation mechanism.[64, 65] The strong frequency dependence of the dielectric

constant for the present sample is also clearly observed from the Figures 5.2.9c and d, where dielectric constant is plotted as a function of frequency for some constant temperatures. At a particular temperature, the value of dielectric constant decreases with the increase of frequency, which is a common feature observed in most of the dielectric materials.[66, 67] The maximum value of ε' is found to be 70 at room temperature in presence of 100 Hz frequency. Temperature and frequency dependent dielectric loss tangent (tan δ) of the present sample was also recorded. The obtained value of tanδ is found to be less than 1 in the measured temperature and frequency range (see Figures 5.2.10a and b).

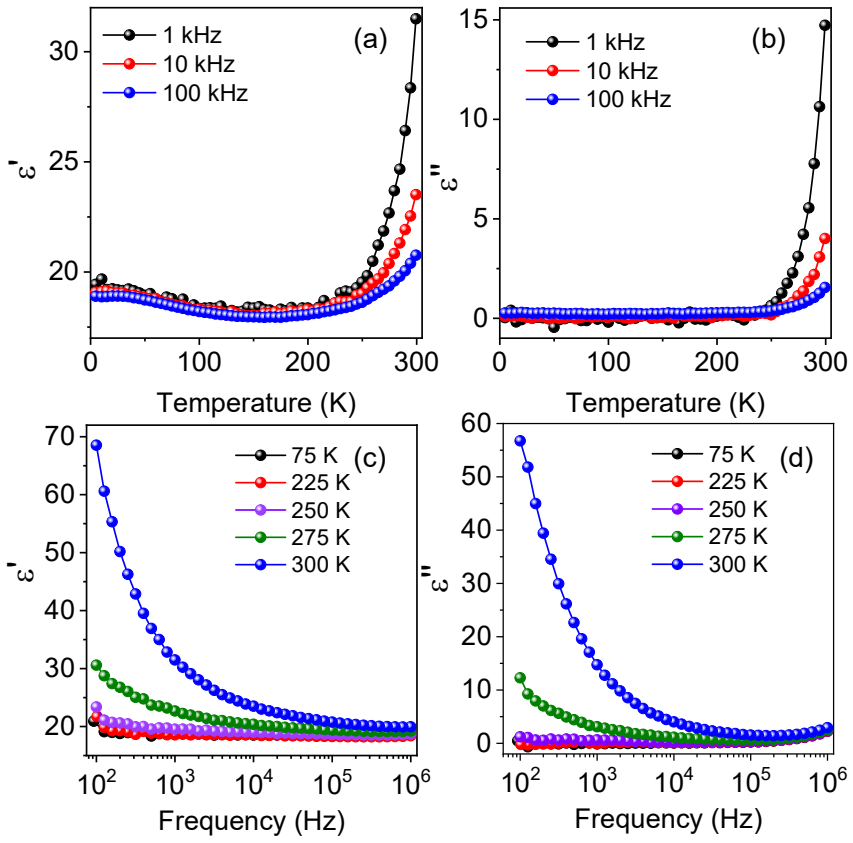

Figure 5.2.9. *Temperature dependent a) real, b) imaginary part of dielectric permittivity for the $RbSn_2Br_5$ sample measured at different selective frequencies. c) Real, d) imaginary part of dielectric permittivity as a function of frequency at several fixed temperatures.*

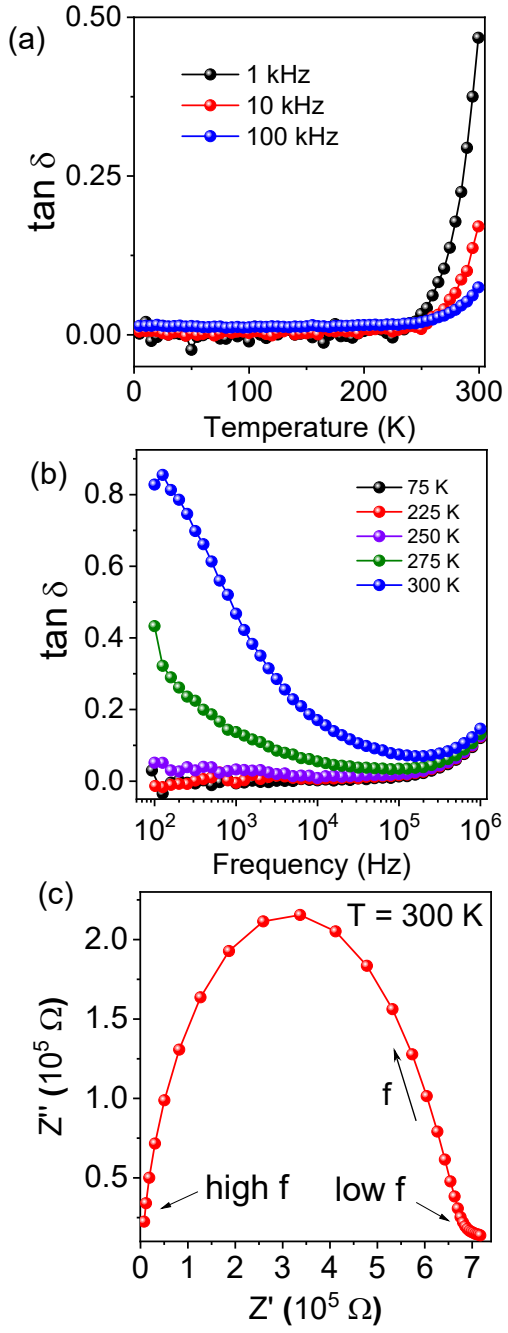

Figure 5.2.10. *a) Temperature and b) frequency dependences of the dielectric loss (tan δ) for the $RbSn_2Br_5$ sample. c) Nyquist plot between imaginary (Z'') and real (Z') part of impedence at room-temperature.*

Impedance spectroscopy is an effective and important tool to understand the electrical response of dielectric samples.[68] Figure 5.2.10c shows the Nyquist plot (Cole-Cole plot) between imaginary (Z'') and real (Z') part of impedence in the frequncy range 100 Hz to 1 MHz at room-temperature. Usually, one observes two semi-circular arcs in the case of electrically inhomogeneous system. Semi-circular arc at the high frequency side represents the contribution of grain, on the other hand the low frequency side semi-circular arc corresponds to the contribution of grain boundary and sample-electrode.[68] Here, we have observed only one semicircle, which indicates that the main contribution is coming from the grain.[69]

5.2.4. Conclusions

In summary, we have synthesized bulk powders of Pb-free layered *all-inorganic* $RbSn_2Br_5$ by solid-state mechanochemical grinding, which exhibited a band gap of ~3.20 eV accompanied by a room-temperature PL emission centered at ~2.51 eV. Distinct vibrational modes were appeared in Raman spectroscopic measurements at low frequency region from the vibrations of Sn-Br bond from polymeric $[Sn_2Br_5]_n^{n-}$ layer. Interestingly, this Sn(II)-based layered material displayed reasonable thermal stability up to ~205 ^{0}C along with the absence of any secondary phase after keeping it at ambient environments for 30 days. The absorption and PL spectral analysis of ultrasonically treated toluene-dispersed solution of $RbSn_2Br_5$ revealed a sharp excitonic peak at ~349 nm with high exciton binding energy of 331.69 meV. A red-shifted and broaden emission line with enhanced intensity were evidenced at 77 K in comparison to the room-temperature emission. The life-time measurements at both temperature pointed out the occurrence of excitonic recombinations through the band edge states and intrinsic defect sites (shallow states) with few nanoseconds of average life-times. Further, we undertook the halide mixing approach in $RbSn_2Br_5$ to tune the band gap (2.68-3.36 eV) and PL emission (2.31-2.58 eV) by mechanochemically synthesizing $RbSn_2Br_3Cl_2$ and $RbSn_2Br_4I$. All the mixed halide materials exhibited excitonic absorption and the narrow emission peaks. Finally, we have investigated the dielectric properties of $RbSn_2Br_5$ at 4-300 K temperature range. The dielectric behaviour of $RbSn_2Br_5$ is related to the thermally excited relaxation

mechanism with a strong frequency dependence and the main contribution in impedance comes from the grain.

5.2.5. References

1. L. Protesescu, S. Yakunin, M. I. Bodnarchuk, F. Krieg, R. Caputo, C. H. Hendon, R. X. Yang, A. Walsh and M. V. Kovalenko, *Nano Lett.*, 2015, **15**, 3692.

2. Q. Fan, G. V. Biesold-McGee, J. Ma, Q. Xu, S. Pan, J. Peng and Z. Lin, *Angew. Chem. Int. Ed.*, 2020, **59**, 1030.

3. Y. Wu, X. Li and H. Zeng, *ACS Energy Lett.*, 2019, **4**, 673.

4. C. C. Stoumpos and M. G. Kanatzidis, *Acc. Chem. Res.*, 2015, **48**, 2791.

5. A. Swarnkar, W. J. Mir and A. Nag, *ACS Energy Lett.*, 2018, **3**, 286.

6. J. Shamsi, Z. Dang, P. Ijaz, A. L. Abdelhady, G. Bertoni, I. Moreels and L. Manna, *Chem. Mater.*, 2018, **30**, 79.

7. Q. A. Akkerman, G. Rainò, M. V. Kovalenko and L. Manna, *Nat. Mater.*, 2018, **17**, 394.

8. N. Pradhan, *J. Phys. Chem. Lett.*, 2019, **10**, 5847.

9. A. Dutta, R. K. Behera, P. Pal, S. Baitalik and N. Pradhan, *Angew. Chem. Int. Ed.*, 2019, **58**, 5552.

10. V. K. Ravi, G. B. Markad and A. Nag, *ACS Energy Lett.*, 2016, **1**, 665.

11. A. Dutta, R. K. Behera, S. K. Dutta, S. Das Adhikari and N. Pradhan, *J. Phys. Chem. Lett.*, 2018, **9**, 6599.

12. Q. Zhang and Y. Yin, *ACS Cent. Sci.*, 2018, **4**, 668.

13. A. Babayigit, A. Ethirajan, M. Muller and B. Conings, *Nat. Mater.*, 2016, **15**, 247.

14. A. Koliogiorgos, S. Baskoutas and I. Galanakis, *Comput. Mater. Sci.*, 2017, **138**, 92.

15. A. Koliogiorgos, S. Baskoutas and I. Galanakis, *Comput. Condens. Matter*, 2018, **14**, 161.

16. J. Wang, J. Dong, F. Lu, C. Sun, Q. Zhang and N. Wang, *J. Mater. Chem. A*, 2019, **7**, 23563.

17. F. Hao, C. C. Stoumpos, D. H. Cao, R. P. H. Chang and M. G. Kanatzidis, *Nat. Photonics*, 2014, **8**, 489.

18. W. Ke, C. C. Stoumpos and M. G. Kanatzidis, *Adv. Mater.*, 2019, **31**, 1803230.

19. M. Coduri, T. A. Strobel, M. Szafrański, A. Katrusiak, A. Mahata, F. Cova, S. Bonomi, E. Mosconi, F. De Angelis and L. Malavasi, *J. Phys. Chem. Lett.*, 2019, **10**, 7398.

20. T.-B. Song, T. Yokoyama, S. Aramaki and M. G. Kanatzidis, *ACS Energy Lett.*, 2017, **2**, 897.

21. B. Li, R. Long, Y. Xia and Q. Mi, *Angew. Chem. Int. Ed.*, 2018, **57**, 13154.

22. L. Mao, C. C. Stoumpos and M. G. Kanatzidis, *J. Am. Chem. Soc.*, 2019, **141**, 1171.

23. P. Acharyya, K. Kundu and K. Biswas, *Nanoscale*, 2020, **12**, 21094.

24. X. Li, J. M. Hoffman and M. G. Kanatzidis, *Chem. Rev.*, 2021, **121**, 2230.

25. F. Zhang, H. Lu, J. Tong, J. J. Berry, M. C. Beard and K. Zhu, *Energy Environ. Sci.*, 2020, **13**, 1154.

26. A. S. R. Bati, M. Batmunkh and J. G. Shapter, *Adv. Energy Mater.*, 2020, **10**, 1902253.

27. J. Jagielski, S. Kumar, W.-Y. Yu and C.-J. Shih, *J. Mater. Chem. C*, 2017, **5**, 5610.

28. P. Acharyya, T. Ghosh, K. Pal, K. Kundu, K. Singh Rana, J. Pandey, A. Soni, U. V. Waghmare and K. Biswas, *J. Am. Chem. Soc.*, 2020, **142**, 15595.

29. K. Kundu, P. Acharyya, K. Maji, R. Sasmal, S. S. Agasti and K. Biswas, *Angew. Chem. Int. Ed.*, 2020, **59**, 13093.

30. O. Nazarenko, M. R. Kotyrba, S. Yakunin, M. Wörle, B. M. Benin, G. Rainò, F. Krumeich, M. Kepenekian, J. Even, C. Katan and M. V. Kovalenko, *Chem. Mater.*, 2019, **31**, 2121.

31. V. V. Nawale, T. Sheikh and A. Nag, *J. Phys. Chem. C*, 2020, **124**, 21129.

32. F. Li, Y. Xie, Y. Hu, M. Long, Y. Zhang, J. Xu, M. Qin, X. Lu and M. Liu, *ACS Energy Lett.*, 2020, **5**, 1422.

33. L. Lanzetta, J. M. Marin-Beloqui, I. Sanchez-Molina, D. Ding and S. A. Haque, *ACS Energy Lett.*, 2017, **2**, 1662.

34. Y. Gao, Z. Wei, P. Yoo, E. Shi, M. Zeller, C. Zhu, P. Liao and L. Dou, *J. Am. Chem. Soc.*, 2019, **141**, 15577.

35. A. Wang, Y. Guo, Z. Zhou, X. Niu, Y. Wang, F. Muhammad, H. Li, T. Zhang, J. Wang, S. Nie and Z. Deng, *Chem. Sci.*, 2019, **10**, 4573.

36. X. Zhang, C. Wang, Y. Zhang, X. Zhang, S. Wang, M. Lu, H. Cui, S. V. Kershaw, W. W. Yu and A. L. Rogach, *ACS Energy Lett.*, 2019, **4**, 242.

37. L. Romani, A. Bala, V. Kumar, A. Speltini, A. Milella, F. Fracassi, A. Listorti, A. Profumo and L. Malavasi, *J. Mater. Chem. C*, 2020, **8**, 9189.

38. J. Li, C. C. Stoumpos, G. G. Trimarchi, I. Chung, L. Mao, M. Chen, M. R. Wasielewski, L. Wang and M. G. Kanatzidis, *Chem. Mater.*, 2018, **30**, 4847.

39. P. Acharyya, P. Pal, P. K. Samanta, A. Sarkar, S. K. Pati and K. Biswas, *Nanoscale*, 2019, **11**, 4001.

40. I. Abrahams, J. D. Donaldson, S. Grimes, G. Valle and S. Calogero, *Polyhedron*, 1986, **5**, 1593.

41. G. Yuan, S. Huang, S. Qin, X. Wu, H. Ding and A. Lu, *Eur. J. Inorg. Chem.*, 2019, **2019**, 2524.

42. P. Pal, S. Saha, A. Banik, A. Sarkar and K. Biswas, *Chem. Eur. J.*, 2018, **24**, 1811.

43. J. Li, Q. Yu, Y. He, C. C. Stoumpos, G. Niu, G. G. Trimarchi, H. Guo, G. Dong, D. Wang, L. Wang and M. G. Kanatzidis, *J. Am. Chem. Soc.*, 2018, **140**, 11085.

44. E. R. Dohner, A. Jaffe, L. R. Bradshaw and H. I. Karunadasa, *J. Am. Chem. Soc.*, 2014, **136**, 13154.

45. B. Yang, J. Chen, F. Hong, X. Mao, K. Zheng, S. Yang, Y. Li, T. Pullerits, W. Deng and K. Han, *Angew. Chem. Int. Ed.*, 2017, **56**, 12471.

46. J. Pal, S. Manna, A. Mondal, S. Das, K. V. Adarsh and A. Nag, *Angew. Chem. Int. Ed.*, 2017, **56**, 14187.

47. B. Yang, J. Chen, S. Yang, F. Hong, L. Sun, P. Han, T. Pullerits, W. Deng and K. Han, *Angew. Chem. Int. Ed.*, 2018, **57**, 5359.

48. B. Yang, X. Mao, F. Hong, W. Meng, Y. Tang, X. Xia, S. Yang, W. Deng and K. Han, *J. Am. Chem. Soc.*, 2018, **140**, 17001.

49. W. G. Delmas, E. T. Vickers, A. C. DiBenedetto, C. Lum, I. N. Hernandez, J. Z. Zhang and S. Ghosh, *J. Phys. Chem. Lett.*, 2020, **11**, 7886.

50. W. Lv, X. Tang, L. Li, L. Xu, M. Li, R. Chen and W. Huang, *J. Phys. Chem. C*, 2019, **123**, 24313.

51. T. C. Jellicoe, J. M. Richter, H. F. J. Glass, M. Tabachnyk, R. Brady, S. E. Dutton, A. Rao, R. H. Friend, D. Credgington, N. C. Greenham and M. L. Böhm, *J. Am. Chem. Soc.*, 2016, **138**, 2941.

52. N. K. Noel, S. D. Stranks, A. Abate, C. Wehrenfennig, S. Guarnera, A.-A. Haghighirad, A. Sadhanala, G. E. Eperon, S. K. Pathak, M. B. Johnston, A. Petrozza, L. M. Herz and H. J. Snaith, *Energy Environ. Sci.*, 2014, **7**, 3061.

53. C. Zhang, J. Duan, F. Qin, C. Xu, W. Wang and J. Dai, *J. Mater. Chem. C*, 2019, **7**, 10454.

54. R. Roccanova, A. Yangui, G. Seo, T. D. Creason, Y. Wu, D. Y. Kim, M.-H. Du and B. Saparov, *ACS Mater. Lett.*, 2019, **1**, 459.

55. M. Leng, Y. Yang, Z. Chen, W. Gao, J. Zhang, G. Niu, D. Li, H. Song, J. Zhang, S. Jin and J. Tang, *Nano Lett.*, 2018, **18**, 6076.

56. M. a. Mączka, M. Ptak, A. Gągor, D. Stefańska, J. K. Zaręba and A. Sieradzki, *Chem. Mater.*, 2020, **32**, 1667.

57. G. Xiong, L. Yuan, Y. Jin, H. Wu, Z. Li, B. Qu, G. Ju, L. Chen, S. Yang and Y. Hu, *Adv. Opt. Mater.*, 2020, **8**, 2000779.

58. I. Neogi, A. Bruno, D. Bahulayan, T. W. Goh, B. Ghosh, R. Ganguly, D. Cortecchia, T. C. Sum, C. Soci, N. Mathews and S. G. Mhaisalkar, *ChemSusChem*, 2017, **10**, 3765.

59. R. Chakraborty and A. Nag, *J. Phys. Chem. C*, 2020, **124**, 16177.

60. L.-y. Huang and W. R. L. Lambrecht, *Phys. Rev. B*, 2013, **88**, 165203.

61. Z. Wang, F. Wang, B. Zhao, S. Qu, T. Hayat, A. Alsaedi, L. Sui, K. Yuan, J. Zhang, Z. Wei and Z. a. Tan, *J. Phys. Chem. Lett.*, 2020, **11**, 1120.

62. P. Cheng, L. Sun, L. Feng, S. Yang, Y. Yang, D. Zheng, Y. Zhao, Y. Sang, R. Zhang, D. Wei, W. Deng and K. Han, *Angew. Chem. Int. Ed.*, 2019, **58**, 16087.

63. B. M. Benin, D. N. Dirin, V. Morad, M. Wörle, S. Yakunin, G. Rainò, O. Nazarenko, M. Fischer, I. Infante and M. V. Kovalenko, *Angew. Chem. Int. Ed.*, 2018, **57**, 11329.

64. G. Catalan, D. O'Neill, R. M. Bowman and J. M. Gregg, *Appl. Phy. Lett.*, 2000, **77**, 3078.

65. D. K. Pradhan, P. Misra, V. S. Puli, S. Sahoo, D. K. Pradhan and R. S. Katiyar, *J. Appl. Phys.*, 2014, **115**, 243904.

66. D. K. Pradhan, R. N. P. Choudhary, C. Rinaldi and R. S. Katiyar, *J. Appl. Phys.*, 2009, **106**, 024102.

67. P. Acharyya, T. Ghosh, S. Matteppanavar, R. K. Biswas, P. Yanda, S. R. Varanasi, D. Sanyal, A. Sundaresan, S. K. Pati and K. Biswas, *J. Phys. Chem. C*, 2020, **124**, 9802.

68. S. Kumari, N. Ortega, A. Kumar, S. P. Pavunny, J. W. Hubbard, C. Rinaldi, G. Srinivasan, J. F. Scott and R. S. Katiyar, *J. Appl. Phys.*, 2015, **117**, 114102.

69. S. Mukherjee, S. Chatterjee, S. Rayaprol, S. D. Kaushik, S. Bhattacharya and P. K. Jana, *J. Appl. Phys.*, 2016, **119**, 134103.

Chapter 5.3

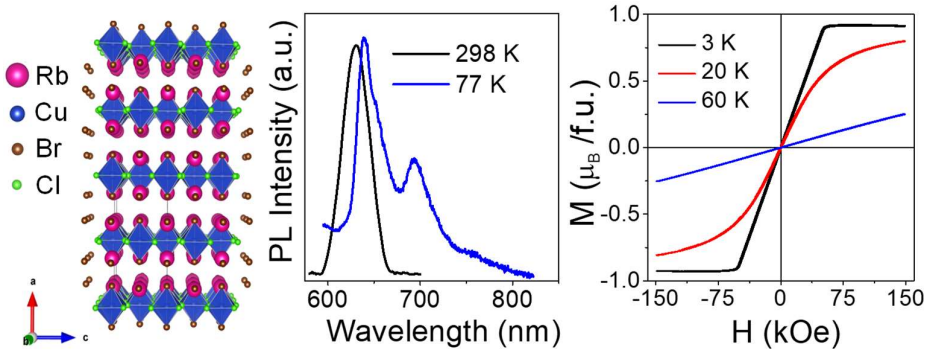

Mechanochemical Synthesis, Optical and Magnetic Properties of Pb-free Ruddlesden-Popper type Layered $Rb_2CuCl_2Br_2$ Perovskite

Chapter 5.3

Mechanochemical Synthesis, Optical and Magnetic Properties of Pb-free Ruddlesden-Popper type Layered $Rb_2CuCl_2Br_2$ Perovskite[†]

Summary

2D layered Ruddlesden-Popper (RP) perovskites gained significant attention owing to their unique optoelectronic properties and ultralow thermal conductivity, however, in comparison to the hybrid Pb-based RP phases, their Pb-free all-inorganic analogues are rarely explored. In this chapter, we demonstrate the optical and magnetic properties of Pb-free RP-type layered $Rb_2CuCl_2Br_2$, which was synthesized by liquid-assisted mechanochemistry at ambient temperature and pressure. The dark brown coloured material displayed band gap of ~1.88 eV accompanied by a room-temperature photoluminescence (PL) at ~1.97 eV. Moreover, Raman scattering at low-frequency region from $[CuCl_4Br_2]^{4-}$ unit; and reasonable thermal and environmental stabilities were manifested. The $Rb_2CuCl_2Br_2$ exhibited an excitonic absorption which is characteristics of layered perovskites accompanied by high exciton binding energy. Large Stokes-shifted PL emission, negligible self-absorption, and fast charge carrier life-times were evidenced for $Rb_2CuCl_2Br_2$. Low-temperature (77 K) measurement revealed red-shifted and intense dual emission in contrast to the room-temperature emission. Finally, temperature dependent magnetization measurement indicates a paramagnetic to antiferromagnetic (AFM) transition at ~16.1 K in $Rb_2CuCl_2Br_2$, primarily related to the inter-layer AFM exchange interaction. Competition between the inter-layer AFM interaction and the intra-layer ferromagnetic interaction determines the nature of magnetic ground state in $Rb_2CuCl_2Br_2$.

[†]K. Kundu, P. Dutta, **P. Acharyya,** and K. Biswas. *J. Phys. Chem. C*, 2021, **125**, 4720–4729.

5.3.1. Introduction

Recently, two dimensional (2D) layered Ruddlesden-Popper (RP) halide perovskites have expanded extensive considerations as potential candidates for high performance optoelectronic devices.[1-5] The chemical compositions of such RP phases are $(A')_2(A)_{n-1}B_nX_{3n+1}$ (n = 1, 2, 3, 4 … and so on), where A′, A, B, and X represent large aromatic or aliphatic alkylammonium spacer cation [e.g., 2-phenylethylammonium (PEA), *n*-butylammonium (*n*-BA) etc.], monovalent organic or inorganic cation [$CH_3NH_3^+$ (MA^+), $HC(NH_2)_2^+$ (FA^+), Cs^+ etc.], divalent metal cation (Pb^{2+} or Sn^{2+}), and halide anion, respectively.[6] The 2D RP perovskite crystal can be represented as the insertion of *n* layers of $[MX_6]^{4-}$ octahedral sheets in between the two layers of large organic spacer cations, which induces natural multiple-quantum-well structures. Here, the inorganic slabs and organic layers act as the potential "wells" and "barriers", respectively.[7] The recent emergence of 2D RP phases is attributed to their unique properties, such as strong quantum confinement effect, large exciton binding energy, and improved stability than their 3D counterparts.[4, 6] Moreover, diverse choice of the number of layers, organic cations, and metal halides results in the variation of crystal structures and optical properties of 2D RP perovskites with tunable bandgap and enhanced quantum efficiency. These 2D RP perovskites turn out to be attractive in the fields of photovoltaics, field-effect transistors, photodetection, and light-emitting diodes.[8-11]

In spite of their speedy progress, the significant challenges including the long-term stability and presence of toxic Pb are the concerns for their applications.[12] To date, most of the reports on 2D RP phases are associated with the Pb-based materials,[1-3, 13-21] while few investigations are directed toward their "Pb-free" analogues.[22-24] Additionally, popular strategy to design 2D RP phases is mostly focused on the organic-inorganic hybrid perovskites, but limited attention has been offered to their *all-inorganic* counterparts. Recently, *all-inorganic* RP phases assure to display better robust nature than the hybrid materials.[25] Further, interchanging the organic spacer layer with inorganic rock-salt layer will provide reasonable interaction between adjacent perovskite layers, which may offer fascinating properties distinct from both the electronically uncoupled hybrid RP phases and conventional 3D perovskites.[26] So far, reported *all-inorganic* RP halide phases are $Cs_2PbI_2Cl_2$, $Cs_2SnI_2Cl_2$, Cs_2CdCl_4, and $Cs_3Cd_2Cl_7$, some of which

showed stimulating optoelectronic and ultra-low thermal conductivity along with enhanced solar cell efficiency and stabilities.[25, 27-35] Recently, transition metals (Fe^{2+}, Zn^{2+}, and Cu^{2+}) have appealed pronounced attention for replacement of toxic Pb in halide perovskites.[31, 36] Cu-based materials are mainly attractive due to their flexible and tunable structures resulting from the Jahn-Teller effect of Cu^{2+}, improved stability under ambient conditions, and high absorption co-efficient in wide-ranging visible regions.[37] Recently, few reports were appeared regarding the synthesis, structural information, specific heat measurement, and electronic properties of 2D *all-inorganic* Cu^{2+}-based halide perovskites,[38-40] however, lacking of detail optical studies. In general, the Cu^{2+}-based 2D layered analogues are interesting due to their fascinating magnetic properties.[41-45]

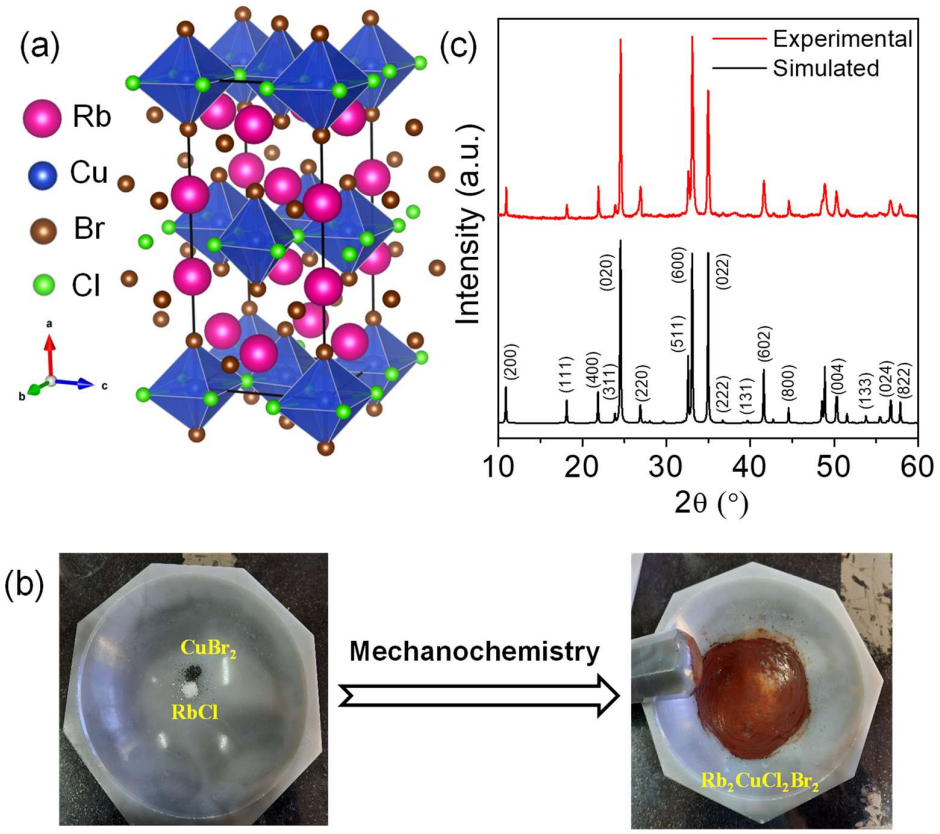

Figure 5.3.1. *a) Crystal structure of $Rb_2CuCl_2Br_2$, b) Visual appearances of mechanochemical synthesis, and c) PXRD pattern of $Rb_2CuCl_2Br_2$ powders synthesized by mechanochemistry.*

In this chapter, bulk polycrystalline powders of Pb-free RP-type phase of $Rb_2CuCl_2Br_2$ were synthesized by liquid-assisted mechanochemical grinding and their optical and magnetic properties have been investigated. We have avoided the use of excess organic solvent and the synthesis is scalable to yield large quantity (~ 1g) of pure crystalline *all-inorganic* layered RP-type halides. The crystal structure of $Rb_2CuCl_2Br_2$ can be designated as a distorted K_2NiF_4 structure, in which the octahedra are distorted (see Figure 5.3.1a). Solid-state UV-Vis absorption and photoluminescence (PL) spectroscopic measurements have been performed to investigate the optical properties of as-synthesized powders. The dark brown-coloured material displayed band gap of ~1.88 eV accompanied by a room-temperature emission at ~1.97 eV. Further, we have explored the optical properties and carrier recombination dynamics of $Rb_2CuCl_2Br_2$ at both room-temperature and cryogenic temperature (77 K). A red-shifted dual emission with enhanced intensity was evidenced at 77 K in comparison to the room-temperature emission. The layered $Rb_2CuCl_2Br_2$ exhibited favourable environmental and thermal stabilities as evident from the powder X-ray diffraction, thermogravimetric analysis, and high-temperature PL measurements. Finally, the magnetic measurement of $Rb_2CuCl_2Br_2$ showed a paramagnetic to antiferromagnetic (AFM) transition at ~16.1 K.

5.3.2. Methods

Reagents. Rubidium (I) chloride [RbCl, ReagentPlus®, ≥99.0% (metals basis), Sigma-Aldrich], copper (II) bromide ($CuBr_2$, 99.999% trace metals basis, Sigma Aldrich), *N,N*-dimethyl formamide (DMF, ACS reagent, ≥99.8%, Sigma-Aldrich), chloroform ($CHCl_3$, ReagentPlus®, ≥99.8%, Sigma-Aldrich), and toluene ($C_6H_5CH_3$, ACS reagent, ≥99.5%, Sigma-Aldrich) were used for the synthesis and characterization without further purification.

Synthesis of $Rb_2CuCl_2Br_2$ by mechanochemistry. In a typical synthesis, 157.2 mg (1.3 mmol) of RbCl and 145.18 mg (0.65 mmol) of $CuBr_2$ were taken at 2:1 stoichiometric ratio in a mortar pestle with few drops of DMF. The mixtures were ground mechanically for 2 h in a N_2-filled glove bag.

Powder X-ray diffraction (PXRD). The PXRD patterns of all samples were collected using a using a Rigaku Smart Lab diffractometer using Cu Kα radiation (λ = 1.5406 Å) with accelerating voltage 40 kV and current 30 mA at room temperature.

Raman spectroscopy. The Raman Spectra were collected by Jobin-Yvon Horiba LabRAM HR evolution Raman spectrometer in backscattering geometry with 1800 gr/mm grating and Peltier cooled CCD detector using the excitation source of 514.5 nm (green laser) and 10 sec of acquisition time.

Thermogravimetric analysis (TGA). TGA experiments were carried out using a 2 STAR TGA instrument. Powder samples were heated at a rate of 5 °C min^{-1} in N_2 atmosphere (40 mL min^{-1}) throughout a temperature range of 50-750 °C.

Optical spectroscopy. UV-vis absorption spectra were recorded using a PerkinElmer, Lambda-900 UV/vis/near-IR spectrometer. To estimate the optical band gap in the solid state sample, diffuse reflectance measurements were carried out in 250 nm to 800 nm range in the reflectance mode. Absorption (α/S) data were calculated from reflectance data by using the Kubelka-Munk equation: $\alpha/S = (1 - R)^2/(2R)$, in which R is the reflectance, α and S are the absorption and scattering coefficients, respectively. The energy band gap was derived from α/S vs. wavelength (in nm) plot by extrapolating the linear region. Electronic absorption spectroscopy is also performed in the solution phase. The emission and excitation spectra were recorded on PerkinElmer LS 55 luminescence spectrometer in the solid state and in solution phase (disperse either in toluene or chloroform) at different temperatures (25-85 ^{0}C). The emission and excitation spectra were recorded in solution phase at different excitation and emission wavelengths, respectively.

Low-temperature photoluminescence (PL) measurements. Low-temperature PL measurements were performed using Edinburgh FLS1000 spectrofluorometer at 77 K using a vacuum liquid-nitrogen cryostat.

Photoluminescence (PL) life-time measurements. Edinburgh FLS1000 spectrofluorometer coupled with EPL-510 picosecond pulsed diode laser (wavelength 510 nm ± 10 nm, maximum average power 5 mW) was employed to collect time-resolved decay plots at 298 K and 77 K.

Magnetic measurements. The temperature (T) and magnetic field (H) dependent dc-magnetization (M) of the powder sample was carried out by using a vibrating sample magnetometer attached with the commercial cryogen-free high magnetic field system from Cryogenic Ltd., U.K.

5.3.3. Results and Discussion

To synthesize $Rb_2CuCl_2Br_2$, we have used RbCl and $CuBr_2$ as precursors (Scheme 1). The molar ratio of RbCl and $CuBr_2$ in $Rb_2CuCl_2Br_2$ is 2:1, which essentially decide the mole ratio of the starting reagents for mechanochemical grinding (Scheme 5.3.1).

Scheme 5.3.1. *Mechanochemical synthesis of $Rb_2CuCl_2Br_2$.*

$$2RbCl + CuBr_2 \xrightarrow{Mechanochemistry} Rb_2CuCl_2Br_2$$

Typically, a stoichiometric quantity of RbCl and $CuBr_2$ is taken in a mortar and pestle; and ground mechanically in presence of few drops of DMF in a N_2-filled glove bag for 2 hours at ambient temperature. The white colour of RbCl and greenish brown colour of $CuBr_2$ converted to dark brown colour product upon DMF-assisted grinding (Figure 5.3.1b). This process yielded up to 1 g pure solid-state powder.

The PXRD patterns of as-synthesized $Rb_2CuCl_2Br_2$ by mechanochemical grinding method was matched with the orthorhombic phase of $Rb_2CuCl_2Br_2$ (space group *Cmca*), which clearly indicate the formation of pure phase $Rb_2CuCl_2Br_2$ (Figure 5.3.1c). The peak appeared at $2\theta = 10.87°$ indicates the presence of the (200) plane for $Rb_2CuCl_2Br_2$, which is the representative peak of layered material. The crystal structure of $Rb_2CuCl_2Br_2$ is presented in Figure 5.3.1a, which can be designated as a deformation of the K_2NiF_4 ($A_{n+1}B_nX_{3n+1}$ RP phase, n = 1) structure, wherein the octahedra are distorted. As a result of the deformation, the structure becomes orthorhombic (space group *Cmca*) rather than

tetragonal.[41] The structure of K_2NiF_4 is comprising of 2D slab of NiF_2 layers, separated by two KF layers, in which stronger intra-layer interaction is evident than the inter-layer interaction. Therefore, this type of structure could display the characteristics of 2D magnetic systems. When the halogen atoms in the K_2NiF_4 type structure are partially substituted by larger and more polarizable ones, then the larger halogen prefers the apical sites. Similarly, in corner sharing $[CuCl_4Br_2]^{4-}$ octahedra of $Rb_2CuCl_2Br_2$, the Cl lies in the equatorial plane of octahedron, whereas the Br resides at the axial sites.[41] The Rb^+ cations are disseminated between the layers of the structure. Accordingly, the $Rb_2CuCl_2Br_2$ crystallizes in the $(NH_4)_2CuCl_4$ structure, which is a deformed K_2NiF_4 structure.[41, 46]

The thermal stability of as-synthesized $Rb_2CuCl_2Br_2$ has been monitored by TGA. Figure 5.3.2a illustrates a two-step weight loss events as a function of temperature, which start at ~202 ^{0}C accompanied by the major weight loss at ~597 ^{0}C. At lower temperature, the first weight loss is probably due to the partial sublimation of lower melting point $CuBr_2$, whereas the major second weight loss at higher temperature associated with the melting event of RbCl and decomposition of compound. Thus, the resulting measurements designate that $Rb_2CuCl_2Br_2$ possesses thermal stability up to ~200 ^{0}C, which is found to be significantly higher than its analogues hybrid materials, $MA_2CuCl_2Br_2$ and $MA_2CuCl_{0.5}Br_{3.5}$ (140 °C and 120 °C, respectively).[47] Other reported hybrid Cu(II)-based perovskites, $C_6H_4NH_2CuBr_2I$ and $(C_6H_5CH_2NH_3)_2CuBr_4$ also revealed lower thermal stability than the RP-type $Rb_2CuCl_2Br_2$,[48, 49] which further validates the enhanced thermal stability of *all-inorganic* 2D perovskites. The photoluminescence (PL) of the sample was noticed to be unaltered after being kept at ambient environment and monitored consecutively up to 30 days (Figure 5.3.3a), which also suggests toward high environmental stability.

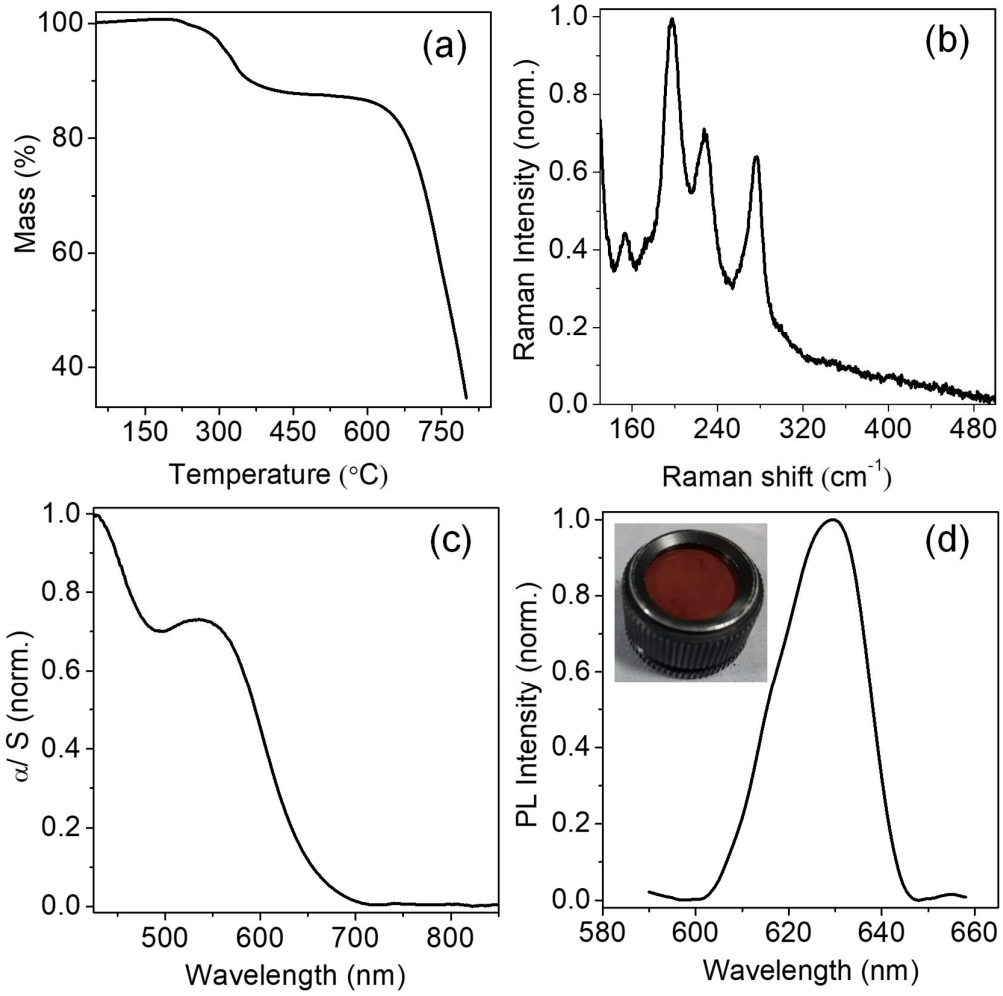

Figure 5.3.2. *a) Thermogravimetric analysis (TGA), b) Raman spectra, c) Solid-state UV/Vis absorption (α/S), and d) PL spectra of $Rb_2CuCl_2Br_2$ (inset shows the photograph of dark brown coloured powder).*

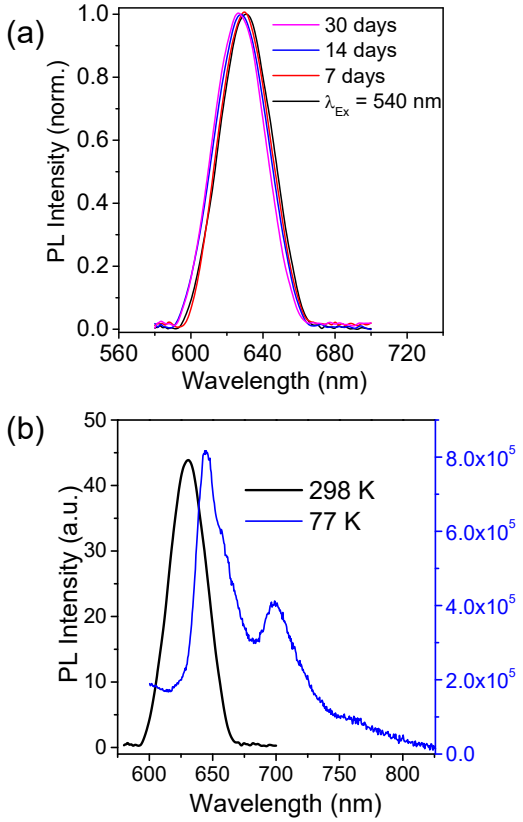

Figure 5.3.3. *a) PL spectra of $Rb_2CuCl_2Br_2$ with gradual interval up to 30 days at 298 K. b) Comparative PL spectra of $Rb_2CuCl_2Br_2$ at 298 K and 77 K.*

To ascertain the characteristic vibrational modes of the RP-type $Rb_2CuCl_2Br_2$, the Raman spectroscopic studies were carried out using 514.5 nm laser excitation at room temperature (Figure 5.3.2b). The major vibrational signatures are appeared from the $[CuCl_4Br_2]^{4-}$ octahedra. Interestingly, no vibrational modes were evidenced above 300 cm^{-1} after careful measurement up to 2000 cm^{-1}. In $[CuCl_4Br_2]^{4-}$ unit, the Cl^- and Br^- ions occupy the equatorial and axial sites of the corner-shared octahedron, respectively. In $Rb_2CuCl_2Br_2$, the Raman modes at 276 and 228 cm^{-1} were designated to the symmetric [$\upsilon_1(A_1g)$] and asymmetric [$\upsilon_3(B_1g)$] Cu-Cl_{eq} stretching, respectively. While, the other two Raman modes at 197 and 153 cm^{-1} were originated from the symmetric and asymmetric Cu-Br_{ax} stretching, respectively. The Raman spectral assignments of $Rb_2CuCl_2Br_2$ are in

good agreement with previous vibrational spectroscopic studies of Cu(II)-based chloride and bromide materials by Stepakova et al.[50]

Investigations of the optical properties of $Rb_2CuCl_2Br_2$ were carried out both in solid state and solution phase by steady-state UV-Vis absorption and PL spectroscopic techniques along with time-resolved PL spectroscopy. To estimate the optical band gap of bulk $Rb_2CuCl_2Br_2$ powder sample, we have collected the solid state UV-vis diffuse

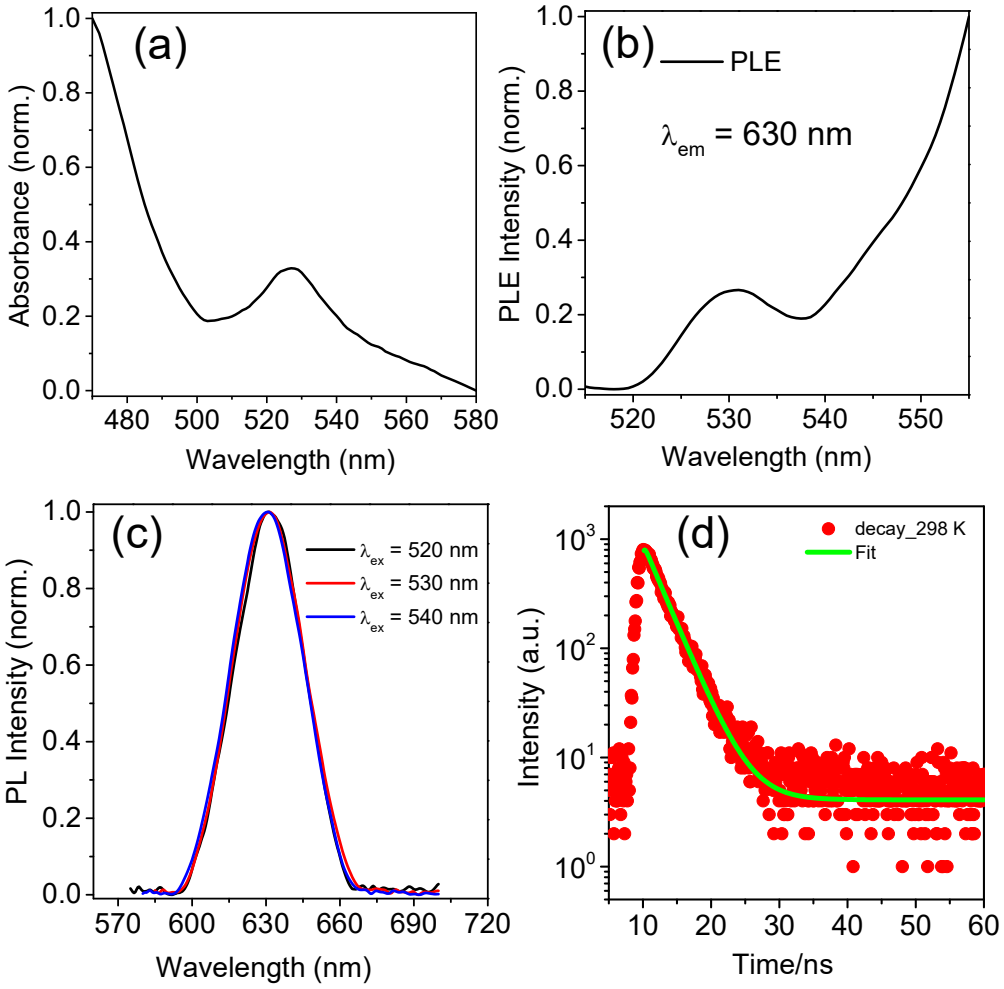

Figure 5.3.4*. a) Optical absorption, b) PL excitation (PLE), c) PL spectra, and d) PL decay profile of $Rb_2CuCl_2Br_2$ dispersed in $CHCl_3$ at 298 K.*

reflectance spectra, and subsequently, the reflectance data were converted into absorbance by applying the Kubelka-Munk equation (discussed in method). The band gap

of $Rb_2CuCl_2Br_2$ is deduced from the onset of the absorption spectrum by extrapolating the linear region, which is found to be ~657 nm (~1.88 eV) (Figure 5.3.2c). The solid-state PL spectra of $Rb_2CuCl_2Br_2$ at room-temperature display emission centred at ~ 629 nm (~1.97 eV) (Figure 5.3.2d). Interestingly, previously reported Cu^{2+}-based layered double perovskite, $Cs_4CuSb_2Cl_{12}$ showed a direct band gap of ~1.0 eV without any detectable emission at room-temperature.[51, 52]

Subsequently, the optical properties of $Rb_2CuCl_2Br_2$ dispersed in chloroform are investigated through the absorbance and PL measurements at 298 K. The absorption spectra display an excitonic peak at ~530 nm (Figure 5.3.4a). This excitonic absorption peak is a typical feature of layered perovskites owing to the quantum and dielectric confinement between the inorganic barrier and inorganic well.[25, 53] However, the relatively weak nature of excitonic peak is due to the reduced dielectric mismatch between inorganic barrier and inorganic well in *all-inorganic* perovskites than the long-chain organic barriers in hybrid perovskites.[25] Figures 5.3.4b-c demonstrate the PL excitation (PLE) and PL spectra of solution dispersed $Rb_2CuCl_2Br_2$, respectively, at 298 K. A PLE peak around 530 nm (Figure 5.3.4b) was measured, when monitored at λ_{em}^{max} (~630 nm) and consistent with the corresponding excitonic feature in the absorption spectra. Under different excitation wavelengths (520-540 nm), a PL band centered at ~630 nm has been appeared for solution dispersed $Rb_2CuCl_2Br_2$ (Figure 5.3.4c). The PL spectrum with a line-width of ~34 nm exhibited a large Stokes shift of ~100 nm (~1.19 eV) and minimal overlap with the absorption spectrum. Such large Stokes shift evidenced herein is probably due to the stabilization of the distorted excited state, as observed earlier for layered perovskite.[53]

We have also performed PL measurement at cryogenic temperature (77 K). Figure 5.3.5a represents the PL emission of $Rb_2CuCl_2Br_2$ at different excitation wavelength. At 77 K, a narrower PL band centered at 640 nm is appeared along with an additional relatively broader peak near 695 nm, which are separated by 55 nm (~150 meV). The low-energy second peak observed at low temperature is due to the bound excitonic emission, which generally originated from the intrinsic defect sites just below the band-edge (such as shallow trap states).[54-56] Such low temperature-induced dual emission is earlier reported for several low-dimensional halide perovskite systems, such as,

$(MA)_2CuCl_4$, Cu-doped Cs_2ZnBr_4, $Cs_3Sb_2I_9$, $(C_4H_9NH_3I)_2(PbI_2)$, $(PEA)_2PbX_4$, and $(PEA)_2CsSn_2I_7$.[54, 56-60] During the temperature elevation from 77 to 298 K, the high energy emission band remains at the expense of low energy band. This event implies that with increasing temperature, the trapped excitons acquire sufficient thermal energy to overcome the energy barrier between two emitting excited states and finally emerge as one asymmetric emission at 298 K.[58] To further verify the two sub-peak analysis, the room temperature PL spectra are fitted with the two-Gaussian peak function, which is nicely separated into two bands at 627 and 644 nm (Figure 5.3.5d). This result suggests that the presence of two emission centres at both temperatures,[56] but the bands are well separated at 77 K. Further, an increase in PL intensity along with a red-shifted emission at 77 K than the emission at 298 K (Figure 5.3.3b) is evidenced, which is also consistent with the previous reports for $(C_4H_9NH_3I)_2(PbI_2)$, and Cs_3BiBr_6.[54, 61]

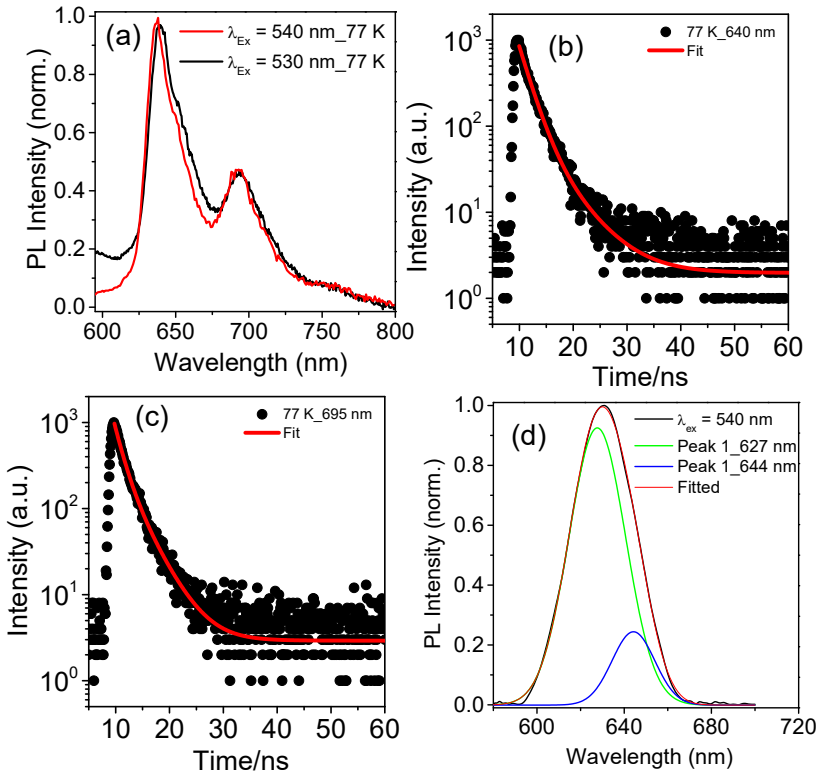

Figure 5.3.5. *a) PL spectra of $Rb_2CuCl_2Br_2$ at 77 K under different excitation wavelength. PL decay profiles of $Rb_2CuCl_2Br_2$ at 77 K, monitored b) at 640 nm, and c) 695 nm. (d) Deconvoluted room-temperature PL spectra of $Rb_2CuCl_2Br_2$.*

Time-resolved PL spectra *via* time-correlated single photon counting (TCSPC) technique were collected to understand the exciton recombination dynamics in $Rb_2CuCl_2Br_2$. The PL decay curve under 510 nm laser excitation of solution dispersed $Rb_2CuCl_2Br_2$ at 298 K is shown in Figure 5.3.4d, which was monitored at the λ_{em}^{max} of 630 nm. The decay curve is fitted according to the biexponential model;

$$A(t) = A_1 e^{-t/\tau_1} + A_2 e^{-t/\tau_2}$$

The average life-time (τ_{avg}) can be estimated by following equation;

$$\tau = (A_1{\tau_1}^2 + A_2{\tau_2}^2) \Big/ (A_1\tau_1 + A_2\tau_2)$$

In these equations, A_1 and A_2 are the PL amplitudes, whereas τ_1 and τ_2 are the PL life-time components.[62] The nature of the biexponential decay in $Rb_2CuCl_2Br_2$ implies the participation of two dissimilar de-excitation ways during the exciton recombination events; the recombination through radiative way of primarily generated exciton on light absorption, and the non-radiative way involving the excitons and defects.[62] The room-temperature PL decay gives rise to two life-times: τ_1 (0.166 ± 0.05 ns) and τ_2 (2.922 ± 0.21 ns), respectively, with superior contribution from the shorter-lived component (79%) over the longer-lived (21%) component (see, Table 5.3.1). The shorter-lived life-time can be ascribed to the excitonic recombination, whereas the longer-lived constituent could be associated with the defect-assisted recombination.[7, 63, 64] The major contribution of shorter-lived component suggests that the PL of $Rb_2CuCl_2Br_2$ sample is typically controlled by the radiative recombination of excitons, which further supported from the estimated large exciton binding energy (discussed later).[63, 64] The calculated average life-time (τ_{avg}) of bulk $Rb_2CuCl_2Br_2$ is found to be 2.417 ns, which is similar with the other RP single crystal $Cs_2PbI_2Cl_2$,[25] Cs_2PdBr_6 microcrystals,[65] and RP $(PEA)_2PbI_4$ crystal.[14]

Table 5.3.1. *The PL decay life-time and relative amplitudes of $Rb_2CuCl_2Br_2$ samples at 298 and 77 K.*

Monitored at λ_{em} (nm)	T (K)	τ_1 (ns)	A_1	τ_2 (ns)	A_2	τ_{avg} (ns)
630	298	0.166 ± 0.05	0.79	2.922 ± 0.21	0.21	2.417
640	77	1.962 ± 0.14	0.75	5.340 ± 0.27	0.25	3.574
695		1.447 ± 0.16	0.49	3.633 ± 0.19	0.51	3.029

Relatively shorter carrier lifetimes in sub-ns time scale are also reported for RP hybrid $(BA)_2(MA)_2Sn_3I_{10}$ (~0.39 ns) and $(BA)_2(MA)_3Sn_4I_{13}$ (~0.61 ns) thin films.[22] The differences in PL decay with variation in temperature and emission wavelength are minor (Table 5.3.1), which may be attributed to the progressive fluctuation of emission phenomenon and the contribution from near band-edge states or shallow trap states.[66] Such minor variations in life-time as a function of temperature and emission wavelength are also evidenced earlier for other 2D perovskite systems.[60, 66-68]

To understand the mechanism of excitonic recombination, we further performed the time-resolved PL measurement of $Rb_2CuCl_2Br_2$ at 77 K. The dynamics of PL decay monitored at both emission peaks (~640 and 695 nm) are illustrated in Figures 5.3.5b, c in which both emission decays were fitted by biexponential model (Table 5.3.1). At λ^{max}_{em} of 640 nm, the life-times are found to be τ_1 = 1.962 ± 0.14 ns (75%) and τ_2 = 5.340 ± 0.27 ns (25%), and at the λ^{max}_{em} of 695 nm, the life-times are τ_1 = 1.447 ± 0.16 ns (49%) and τ_2 = 3.633 ± 0.19 ns (51%). The average PL life-times of both the emissions (3.574 and 3.029 ns at 640 and 695 nm, respectively) are comparable. The comparable PL life-times possibly rule out the existence of emission from the deep level defect states, which usually

have a longer life-time scale (≥ 100 ns). Such analogous life-time components with dual emissions are earlier reported for 2D layered hybrid perovskites.[60, 67] Yang and co-workers[69] stated analogous optical features of single-crystalline 2D $(C_4H_9NH_3)_2PbBr_4$, where the material exhibited single emission at 298 K, and conversely, red-shifted highly intense double emission with bi-exponentially fitted short carrier life-time at 6 K.

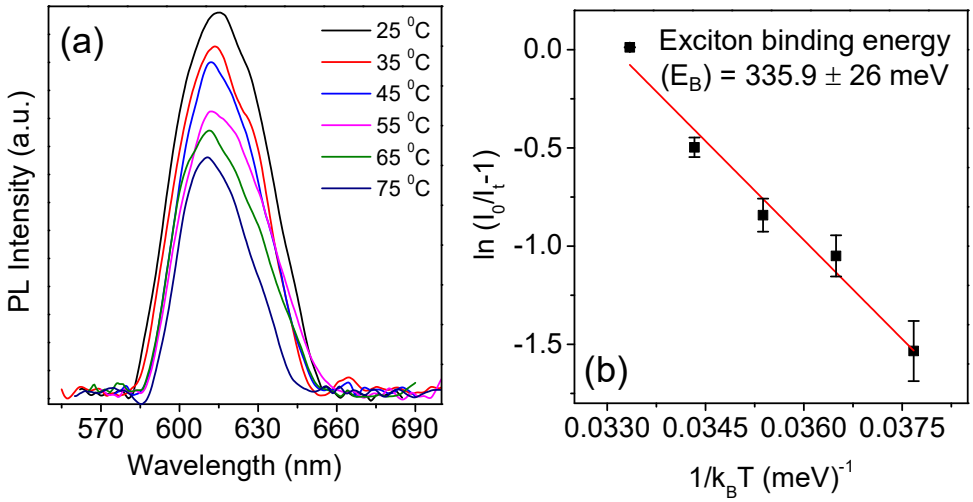

Figure 5.3.6. *a) Temperature-dependent PL spectra of $Rb_2CuCl_2Br_2$. b) The Arrhenius-type plot for extracting the exciton binding energy (E_B).*

The photostability of $Rb_2CuCl_2Br_2$ was also studied by measuring the temperature-dependent PL in the range of 25-85 ^{0}C. The sample shows a reduction in PL intensity with increase in temperature owing to the thermally activated trapping of charge carrier (Figure 5.3.6a).[62] At higher temperature, the quenched PL intensity results from the thermal dissociation of excitons (i.e., electron-hole pairs) and subsequent reduction in the exciton population.[70, 71] The temperature-dependent integrated PL intensity was fitted according to the following equation;[7, 62]

$$I(T) = {I_0}/{1 + Aexp({-E_b}/{k_B T})}$$

Wherein, I_0 and I(T) are the integrated PL intensities at a specified temperature (herein, 25 ^{0}C and 85 ^{0}C, respectively), and A is a constant. The E_b and k_B represent the exciton binding energy, and the Boltzmann constant, respectively. The linear correlation of logarithm of $[I_0/I(T)-1]$ *versus* $1/k_BT$ (Figure 5.3.6b) provides the estimation of E_b according to the Arrhenius-type equation.[72, 73] The E_b of $Rb_2CuCl_2Br_2$ was found to be 335.9 ± 26 meV, which is comparable to the earlier reported layered hybrid perovskite,[60, 74] and other Cu-based perovskites.[75, 76] Such high E_b of $Rb_2CuCl_2Br_2$ complied that the PL emission is predominantly originated from the excitonic recombination, which accelerates the radiative recombination.[77] However, the estimated E_b of $Rb_2CuCl_2Br_2$ is much larger than the *all-inorganic* 3D perovskite materials.[62, 70] The superior E_b of 2D layered perovskites compared to that in 3D perovskites emerges from the spatial confinement of charge carriers, which is the characteristics of low-dimensional structures.[60, 78]

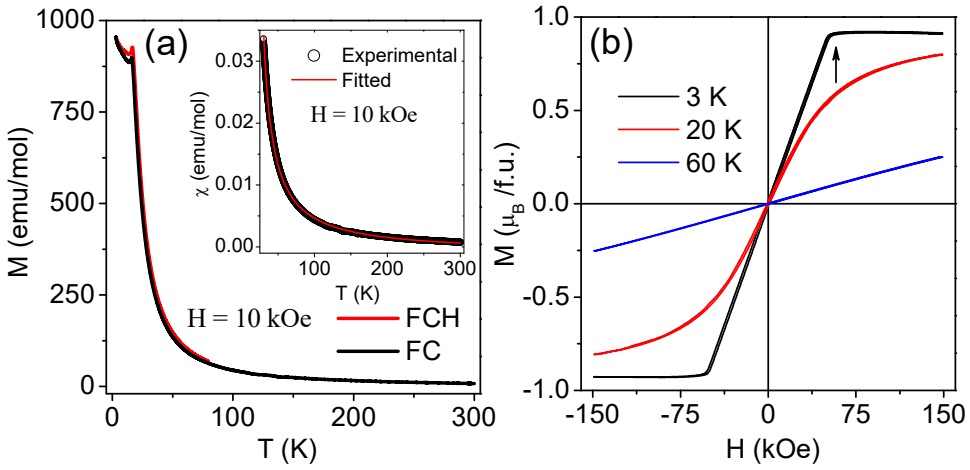

Figure 5.3.7. *a) Magnetization (M) versus temperature (T) data recorded in field cooling (FC) and field-cooled heating (FCH) protocols at 10 kOe of applied magnetic field (H). Inset shows the T dependent magnetic susceptibility (χ = M/H) data fitted with the modified Curie-Weiss law; and b) isothermal M(H) curves recorded at different constant temperatures.*

Magnetic properties of $Rb_2CuCl_2Br_2$ sample have been investigated. Figure 5.3 9a shows the dc-magnetization (M) versus temperature (T) data recorded in presence of 10 kOe applied magnetic field (H) in the T range of 3 K to 300 K. The measurements were

performed in two different protocols; field cooling (FC) and field-cooled heating (FCH). In FC mode, the data were recorded during cooling in presence of applied magnetic field and the subsequent heating data were collected in FCH mode. The M(T) data start to increase with the decrease of temperature and eventually show a peak like feature at around 16.1 K. This magnetic ordering is related to the antiferromagnetic (AFM) transition.[41] A close observation reveals that there is a small thermal hysteresis between FC and FCH data at around the AFM transition temperature (T_N). This type of hysteresis is generally observed in materials having structural (crystal or magnetic) phase transition.[79] In this case the origin of this hysteresis is not clear yet. The T_N for the present system is sensitive to the external magnetic field. With the increase of applied magnetic field the T_N decreases to lower temperature at a rate of around dT_N/dH = -0.1 K/kOe. It is important to mention that the T_N measured in present system is higher than the previously reported value of Rb_2CuCl_4 (T_N = 13.7 K).[41] Inset of Figure 5.3.7a depicts the T dependent magnetic susceptibility (χ = M/H) data in the temperature range 30 K to 300 K. The χ(T) data obey the modified Curie-Weiss law; $\chi(T) = \frac{C}{T-\theta_p} + \chi_0$, where C, θ_p and χ_0 are Curie constant, Curie temperature, and temperature-independent part of the magnetic susceptibility, respectively. From the fitting, we have obtained C = 0.4727 (5) emu-K/mol, θ_p = 16.90 (2) K and χ_0 = -0.00104 (4) emu/mol. The positive value of θ_p indicates the presence of ferromagnetic (FM) interactions in the studied system. The experimental effective paramagnetic moment (p_{eff}) is found to be 1.94 μ_B/f.u. The expected value of p_{eff} for the present sample is 1.73 μ_B/f.u. (taking spin-only value for S = 1/2 of Cu^{2+}). Thus, the experimental value of p_{eff} is quite close to the expected one.

To shed more light on the magnetic states of the sample, we have also recorded the isothermal M versus H data in presence of ±150 kOe applied field at different constant temperatures (Figure 5.3.7b). All the M-H isotherms were recorded in a thermally demagnetised state. Linear behaviour of M(H) data at T = 60 K indicates that the sample is in paramagnetic state. On the other hand, M(H) at 3 K is found to be linear up to H = 60 kOe with sharply increasing value of M. This is a clear indication of AFM state. Interestingly, the M(H) curve starts to saturate on further application of H. The critical field (H_c) for saturation is found to be 60.2 kOe and marked by an arrow, as shown in Figure 5.3.7b. This observed H_c value of $Rb_2CuCl_2Br_2$ relatively higher than that of the

Rb_2CuCl_4 (H_c value was 17 kOe).[41] The saturation magnetic moment (M_s) is 0.91 μ_B/f.u. The magnetic moment of free Cu^{2+} ion is μ (= gS) = 1.05 μ_B (by taking the average gyromagnetic factor, g = 2.1 and S = 1/2).[80] In present case, the M_s value is slightly less than the magnetic moment of free Cu^{2+} ion. It is worth mentioning here that neutron diffraction study performed on Rb_2CuCl_4 by Aguado et al, indicates that the magnetic moment of copper at 1.5 K is 0.84 (5) μ_B.[45] In the $Rb_2CuCl_2Br_2$, there are two types of magnetic interactions: the intra-layer Cu-Cu interactions are FM in nature, whereas the inter-layer interactions are AFM type.[45] Below the critical field H_c, the inter-layer interaction dominates over the intra-layer interaction and as a results the system shows AFM nature. On the other hand, above H_c the intra-layer FM interaction overcomes the inter-layer AFM interaction. Mention must be made that magnetic properties of the $Rb_2CuCl_2Br_2$ is interesting compared to the previously reported Cu-based layered double perovskite such as $Cs_4CuSb_2Cl_{12}$,[52] where the AFM ordering is missing.

5.3.4. Conclusions

In summary, bulk powders and crystalline ingot of Pb-free *all-inorganic* RP-type layered $Rb_2CuCl_2Br_2$ were synthesized using liquid-assisted mechanochemistry. A band gap of ~1.88 eV along with a PL emission at ~1.97 eV at room-temperature were demonstrated for the dark brown-coloured material. Layered $Rb_2CuCl_2Br_2$ was further identified by the intense Raman scattering, which revealed distinctive Cu-X bond vibrations from $[CuCl_4Br_2]^{4-}$ unit at the low-frequency region. Additionally, this material showed reasonable thermal, environmental, and photo-stabilities. The absorption and PL spectral analysis of solution dispersed $Rb_2CuCl_2Br_2$ revealed a sharp excitonic peak with high exciton binding energy of ~336 meV and large Stokes shifted emission with shorter carrier life-time at room-temperature. A dual PL emission with enhanced intensity was achieved at 77 K. Finally, we have investigated the magnetic properties of $Rb_2CuCl_2Br_2$ through temperature and field dependent magnetic measurements. The material exhibits a paramagnetic to AFM transition at around 16.1 K, which primarily depends on the AFM exchange interaction present between the two layers. The AFM transition temperature is found to be sensitive to the applied external magnetic field. The competition between the inter-layer AFM interaction and the intra-layer FM interaction played a vital role to

govern the magnetic ground state of $Rb_2CuCl_2Br_2$. Such 2D layered magnetic system could be beneficial for spintronic-based device applications.

5.3.5. References

1. J. Xi, I. Spanopoulos, K. Bang, J. Xu, H. Dong, Y. Yang, C. D. Malliakas, J. M. Hoffman, M. G. Kanatzidis and Z. Wu, *J. Am. Chem. Soc.*, 2020, **142**, 19705.

2. H. Tsai, W. Nie, J.-C. Blancon, C. C. Stoumpos, R. Asadpour, B. Harutyunyan, A. J. Neukirch, R. Verduzco, J. J. Crochet, S. Tretiak, L. Pedesseau, J. Even, M. A. Alam, G. Gupta, J. Lou, P. M. Ajayan, M. J. Bedzyk, M. G. Kanatzidis and A. D. Mohite, *Nature*, 2016, **536**, 312.

3. C. C. Stoumpos, D. H. Cao, D. J. Clark, J. Young, J. M. Rondinelli, J. I. Jang, J. T. Hupp and M. G. Kanatzidis, *Chem. Mater.*, 2016, **28**, 2852.

4. S. Kahmann, E. K. Tekelenburg, H. Duim, M. E. Kamminga and M. A. Loi, *Nat. Commun.*, 2020, **11**, 2344.

5. D. Pan, Y. Fu, N. Spitha, Y. Zhao, C. R. Roy, D. J. Morrow, D. D. Kohler, J. C. Wright and S. Jin, *Nat. Nanotech.*, 2021, **16**, 159.

6. X. Gao, X. Zhang, W. Yin, H. Wang, Y. Hu, Q. Zhang, Z. Shi, V. L. Colvin, W. W. Yu and Y. Zhang, *Adv. Sci.*, 2019, **6**, 1900941.

7. M. Leng, Y. Yang, Z. Chen, W. Gao, J. Zhang, G. Niu, D. Li, H. Song, J. Zhang, S. Jin and J. Tang, *Nano Lett.*, 2018, **18**, 6076.

8. F. Liu, L. Wang, J. Wang, F. Wang, Y. Chen, S. Zhang, H. Sun, J. Liu, G. Wang, Y. Hu and C. Jiang, *Adv. Funct. Mater.*, 2020, **30**, 2005662.

9. Y. Zheng, T. Niu, X. Ran, J. Qiu, B. Li, Y. Xia, Y. Chen and W. Huang, *J. Mater. Chem. A*, 2019, **7**, 13860.

10. B. Sun, Y. Xu, Y. Chen and W. Huang, *APL Mater.*, 2020, **8**, 040901.

11. X. Tian, Y. Zhang, R. Zheng, D. Wei and J. Liu, *Sustain. Energy Fuels*, 2020, **4**, 2087.

12. A. S. R. Bati, M. Batmunkh and J. G. Shapter, *Adv. Energy Mater.*, 2020, **10**, 1902253.

13. H. Ren, S. Yu, L. Chao, Y. Xia, Y. Sun, S. Zuo, F. Li, T. Niu, Y. Yang, H. Ju, B. Li, H. Du, X. Gao, J. Zhang, J. Wang, L. Zhang, Y. Chen and W. Huang, *Nat. Photonics*, 2020, **14**, 154.

14. J. Yin, R. Naphade, L. Gutiérrez Arzaluz, J.-L. Brédas, O. M. Bakr and O. F. Mohammed, *ACS Energy Lett.*, 2020, **5**, 2149.

15. H. Lai, B. Kan, T. Liu, N. Zheng, Z. Xie, T. Zhou, X. Wan, X. Zhang, Y. Liu and Y. Chen, *J. Am. Chem. Soc.*, 2018, **140**, 11639.

16. I. Spanopoulos, I. Hadar, W. Ke, Q. Tu, M. Chen, H. Tsai, Y. He, G. Shekhawat, V. P. Dravid, M. R. Wasielewski, A. D. Mohite, C. C. Stoumpos and M. G. Kanatzidis, *J. Am. Chem. Soc.*, 2019, **141**, 5518.

17. H. Esmaielpour, V. R. Whiteside, S. Sourabh, G. E. Eperon, J. T. Precht, M. C. Beard, H. Lu, B. K. Durant and I. R. Sellers, *J. Phys. Chem. C*, 2020, **124**, 9496.

18. N. Ashari-Astani, F. Jahanbakhshi, M. Mladenović, A. Q. M. Alanazi, I. Ahmadabadi, M. R. Ejtehadi, M. I. Dar, M. Grätzel and U. Rothlisberger, *J. Phys. Chem. Lett.*, 2019, **10**, 3543.

19. Y. Fu, X. Jiang, X. Li, B. Traore, I. Spanopoulos, C. Katan, J. Even, M. G. Kanatzidis and E. Harel, *J. Am. Chem. Soc.*, 2020, **142**, 4008.

20. S. Silver, Q. Dai, H. Li, J.-L. Brédas and A. Kahn, *Adv. Energy Mater.*, 2019, **9**, 1901005.

21. C. M. Raghavan, T.-P. Chen, S.-S. Li, W.-L. Chen, C.-Y. Lo, Y.-M. Liao, G. Haider, C.-C. Lin, C.-C. Chen, R. Sankar, Y.-M. Chang, F.-C. Chou and C.-W. Chen, *Nano Lett.*, 2018, **18**, 3221.

22. D. H. Cao, C. C. Stoumpos, T. Yokoyama, J. L. Logsdon, T.-B. Song, O. K. Farha, M. R. Wasielewski, J. T. Hupp and M. G. Kanatzidis, *ACS Energy Lett.*, 2017, **2**, 982.

23. L. Ma, M.-G. Ju, J. Dai and X. C. Zeng, *Nanoscale*, 2018, **10**, 11314.

24. E. T. McClure, A. P. McCormick and P. M. Woodward, *Inorg. Chem.*, 2020, **59**, 6010.

25. J. Li, Q. Yu, Y. He, C. C. Stoumpos, G. Niu, G. G. Trimarchi, H. Guo, G. Dong, D. Wang, L. Wang and M. G. Kanatzidis, *J. Am. Chem. Soc.*, 2018, **140**, 11085.

26. Y. Yu, D. Zhang and P. Yang, *Nano Lett.*, 2017, **17**, 5489.

27. J. Li, C. C. Stoumpos, G. G. Trimarchi, I. Chung, L. Mao, M. Chen, M. R. Wasielewski, L. Wang and M. G. Kanatzidis, *Chem. Mater.*, 2018, **30**, 4847.

28. C. F. Holder, J. Fanghanel, Y. Xiong, I. Dabo and R. E. Schaak, *Inorg. Chem.*, 2020, **59**, 11688.

29. Z. Xu, M. Chen and S. F. Liu, *J. Phys. Chem. C*, 2019, **123**, 27978.

30. P. Acharyya, T. Ghosh, K. Pal, K. Kundu, K. Singh Rana, J. Pandey, A. Soni, U. V. Waghmare and K. Biswas, *J. Am. Chem. Soc.*, 2020, **142**, 15595.

31. P. Acharyya, K. Kundu and K. Biswas, *Nanoscale*, 2020, **12**, 21094.

32. Q. A. Akkerman, E. Bladt, U. Petralanda, Z. Dang, E. Sartori, D. Baranov, A. L. Abdelhady, I. Infante, S. Bals and L. Manna, *Chem. Mater.*, 2019, **31**, 2182.

33. A. Dutta, R. K. Behera, S. Deb, S. Baitalik and N. Pradhan, *J. Phys. Chem. Lett.*, 2019, **10**, 1954.

34. S. Yang, W. Liu, Y. Han, Z. Liu, W. Zhao, C. Duan, Y. Che, H. Gu, Y. Li and S. Liu, *Adv. Energy Mater.*, 2020, **10**, 2002882.

35. L.-Y. Pan, Y.-F. Ding, Z.-L. Yu, Q. Wan, B. Liu and M.-Q. Cai, *J. Power Sources*, 2020, **451**, 227732.

36. M. D. Smith, B. A. Connor and H. I. Karunadasa, *Chem. Rev.*, 2019, **119**, 3104.

37. Q. Li, S. Li, K. Wang, Z. Quan, Y. Meng and B. Zou, *J. Phys. Chem. Lett.*, 2017, **8**, 500.

38. Arramel, A. Xie, X. Yin, C. S. Tang, A. D. Fauzi, X. Chi, C. Diao, M. F. Sahdan, M. D. Birowosuto, C. Dang, A. Rusydi and A. T. S. Wee, *ACS Appl. Mater. Interfaces*, 2020, **12**, 4114.

39. N. Krüger, S. Belz, F. Schossau, A. A. Haghighirad, P. T. Cong, B. Wolf, S. Gottlieb-Schoenmeyer, F. Ritter and W. Assmus, *Cryst. Growth Des.*, 2010, **10**, 4456.

40. U. Tutsch, O. Tsyplyatyev, M. Kuhnt, L. Postulka, B. Wolf, P. T. Cong, F. Ritter, C. Krellner, W. Aßmus, B. Schmidt, P. Thalmeier, P. Kopietz and M. Lang, *Phys. Rev. Lett.*, 2019, **123**, 147202.

41. H. T. Witteveen, *Physica*, 1974, **71**, 204.

42. F. Yamada, T. Ono, H. Tanaka and J.-i. Yamaura, *J. Phys. Soc. Japan*, 2007, **76**, 014708.

43. N. van Well, K. Foyevtsova, S. Gottlieb-Schönmeyer, F. Ritter, R. S. Manna, B. Wolf, M. Meven, C. Pfleiderer, M. Lang, W. Assmus, R. Valentí and C. Krellner, *Phys. Rev. B*, 2015, **91**, 035124.

44. S. V. Streltsov and D. I. Khomskii, *Phys. Rev. B*, 2012, **86**, 035109.

45. F. Aguado, F. Rodríguez, R. Valiente, A. Señas and I. Goncharenko, *J. Condens. Matter Phys.*, 2004, **16**, 1927.

46. H. T. Witteveen, D. L. Jongejan and V. Brandwijk, *Mater. Res. Bull.*, 1974, **9**, 345.

47. D. Cortecchia, H. A. Dewi, J. Yin, A. Bruno, S. Chen, T. Baikie, P. P. Boix, M. Grätzel, S. Mhaisalkar, C. Soci and N. Mathews, *Inorg. Chem.*, 2016, **55**, 1044.

48. X. Li, X. Zhong, Y. Hu, B. Li, Y. Sheng, Y. Zhang, C. Weng, M. Feng, H. Han and J. Wang, *J. Phys. Chem. Lett.*, 2017, **8**, 1804.

49. X. Li, B. Li, J. Chang, B. Ding, S. Zheng, Y. Wu, J. Yang, G. Yang, X. Zhong and J. Wang, *ACS Appl. Energy Mater.*, 2018, **1**, 2709.

50. L. V. Stepakova, M. Y. Skripkin, L. V. Chernykh, G. L. Starova, L. Hajba, J. Mink and M. Sandström, *J. Raman Spectrosc.*, 2008, **39**, 16.

51. B. Vargas, E. Ramos, E. Pérez-Gutiérrez, J. C. Alonso and D. Solis-Ibarra, *J. Am. Chem. Soc.*, 2017, **139**, 9116.

52. N. Singhal, R. Chakraborty, P. Ghosh and A. Nag, *Chem. Asian J.*, 2018, **13**, 2085.

53. E. R. Dohner, A. Jaffe, L. R. Bradshaw and H. I. Karunadasa, *J. Am. Chem. Soc.*, 2014, **136**, 13154.

54. X. Wu, M. T. Trinh, D. Niesner, H. Zhu, Z. Norman, J. S. Owen, O. Yaffe, B. J. Kudisch and X. Y. Zhu, *J. Am. Chem. Soc.*, 2015, **137**, 2089.

55. S. M. Lee, C. J. Moon, H. Lim, Y. Lee, M. Y. Choi and J. Bang, *J. Phys. Chem. C*, 2017, **121**, 26054.

56. H. Shen, J. Li, H. Wang, J. Ma, J. Wang, H. Luo and D. Li, *J. Phys. Chem. Lett.*, 2019, **10**, 7.

57. M. A. Naradipa, A. Xie, Arramel, X. Yin, C. S. Tang, M. F. Sahdan, T. C. Asmara, C. Dang, M. D. Birowosuto, A. T. S. Wee and A. Rusydi, *J. Phys. Chem. C*, 2020, **124**, 14272.

58. P. Cheng, L. Feng, Y. Liu, D. Zheng, Y. Sang, W. Zhao, Y. Yang, S. Yang, D. Wei, G. Wang and K. Han, *Angew. Chem., Int. Ed.*, 2020, **59**, 21414.

59. A. Singh, N.-C. Chiu, K. M. Boopathi, Y.-J. Lu, A. Mohapatra, G. Li, Y.-F. Chen, T.-F. Guo and C.-W. Chu, *ACS Appl. Mater. Interfaces*, 2019, **11**, 35088.

60. R. Chakraborty and A. Nag, *J. Phys. Chem. C*, 2020, **124**, 16177.

61. Y. Tang, L. Gomez, M. van der Laan, D. Timmerman, V. Sebastian, C.-C. Huang, T. Gregorkiewicz and P. Schall, *J. Mater. Chem. C*, 2021, **9**, 158.

62. W. Lv, X. Tang, L. Li, L. Xu, M. Li, R. Chen and W. Huang, *J. Phys. Chem. C*, 2019, **123**, 24313.

63. M. Leng, Z. Chen, Y. Yang, Z. Li, K. Zeng, K. Li, G. Niu, Y. He, Q. Zhou and J. Tang, *Angew. Chem., Int. Ed.*, 2016, **55**, 15012.

64. M. Leng, Y. Yang, K. Zeng, Z. Chen, Z. Tan, S. Li, J. Li, B. Xu, D. Li, M. P. Hautzinger, Y. Fu, T. Zhai, L. Xu, G. Niu, S. Jin and J. Tang, *Adv. Funct. Mater.*, 2018, **28**, 1704446.

65. L. Zhou, J.-F. Liao, Z.-G. Huang, X.-D. Wang, Y.-F. Xu, H.-Y. Chen, D.-B. Kuang and C.-Y. Su, *ACS Energy Lett.*, 2018, **3**, 2613.

66. K. Kundu, P. Acharyya, K. Maji, R. Sasmal, S. S. Agasti and K. Biswas, *Angew. Chem., Int. Ed.*, 2020, **59**, 13093.

67. V. V. Nawale, T. Sheikh and A. Nag, *J. Phys. Chem. C*, 2020, **124**, 21129.

68. E. R. Dohner, E. T. Hoke and H. I. Karunadasa, *J. Am. Chem. Soc.*, 2014, **136**, 1718.

69. L. Dou, A. B. Wong, Y. Yu, M. Lai, N. Kornienko, S. W. Eaton, A. Fu, C. G. Bischak, J. Ma, T. Ding, N. S. Ginsberg, L.-W. Wang, A. P. Alivisatos and P. Yang, *Science*, 2015, **349**, 1518.

70. C. Zhang, J. Duan, F. Qin, C. Xu, W. Wang and J. Dai, *J. Mater. Chem. C*, 2019, **7**, 10454.

71. R. Roccanova, A. Yangui, G. Seo, T. D. Creason, Y. Wu, D. Y. Kim, M.-H. Du and B. Saparov, *ACS Mater. Lett.*, 2019, **1**, 459.

72. M. a. Mączka, M. Ptak, A. Gągor, D. Stefańska, J. K. Zaręba and A. Sieradzki, *Chem. Mater.*, 2020, **32**, 1667.

73. G. Xiong, L. Yuan, Y. Jin, H. Wu, Z. Li, B. Qu, G. Ju, L. Chen, S. Yang and Y. Hu, *Adv. Opt. Mater.*, 2020, **8**, 2000779.

74. I. Neogi, A. Bruno, D. Bahulayan, T. W. Goh, B. Ghosh, R. Ganguly, D. Cortecchia, T. C. Sum, C. Soci, N. Mathews and S. G. Mhaisalkar, *ChemSusChem*, 2017, **10**, 3765.

75. T. D. Creason, A. Yangui, R. Roccanova, A. Strom, M.-H. Du and B. Saparov, *Adv. Opt. Mater.*, 2020, **8**, 1901338.

76. R. Lin, Q. Zhu, Q. Guo, Y. Zhu, W. Zheng and F. Huang, *J. Phys. Chem. C*, 2020, **124**, 20469.

77. P. Cheng, L. Sun, L. Feng, S. Yang, Y. Yang, D. Zheng, Y. Zhao, Y. Sang, R. Zhang, D. Wei, W. Deng and K. Han, *Angew. Chem., Int. Ed.*, 2019, **58**, 16087.

78. X. Zhao, G. Niu, J. Zhu, B. Yang, J.-H. Yuan, S. Li, W. Gao, Q. Hu, L. Yin, K.-H. Xue, E. Lifshitz, X. Miao and J. Tang, *J. Phys. Chem. Lett.*, 2020, **11**, 1873.

79. S. C. Das, K. Mandal, P. Dutta, S. Pramanick and S. Chatterjee, *Phys. Rev. B*, 2019, **100**, 024409.

80. R. J. H. Wong, R. D. Willett and J. E. Drumheller, *J. Chem. Phys.*, 1981, **74**, 6018.

Chapter 5.4

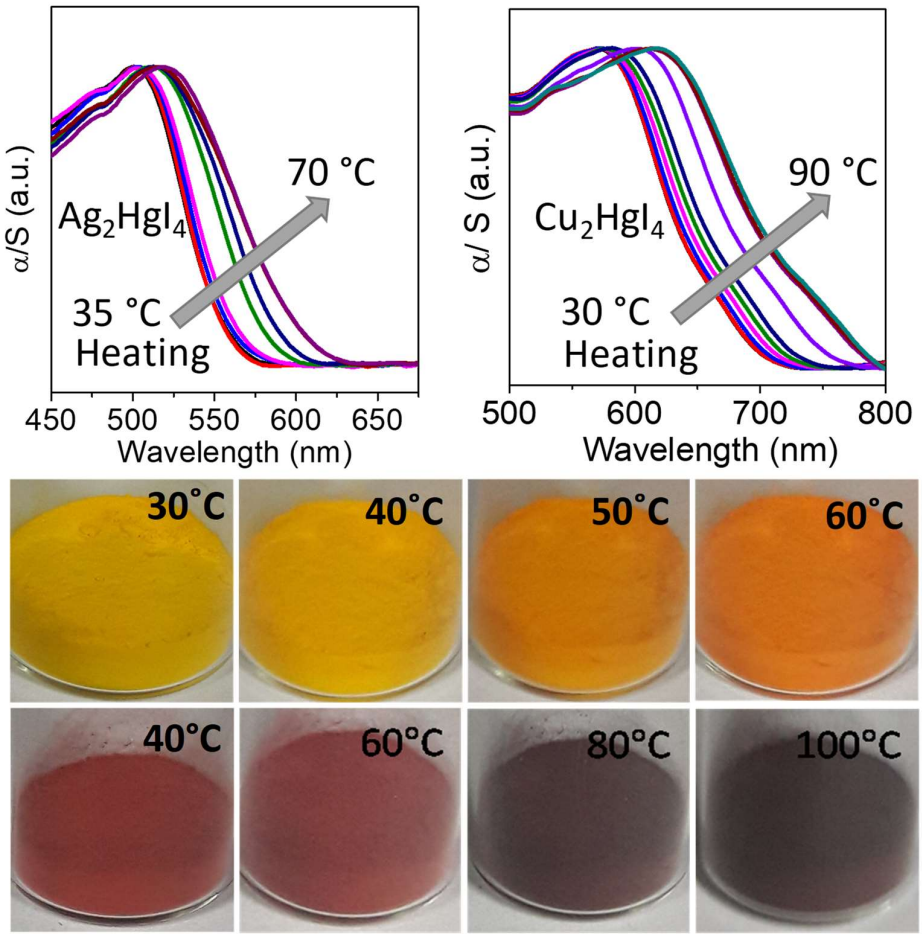

Mechanochemical Synthesis and Temperature-dependent Optical Properties of Thermochromic $(Ag_{1-x}Cu_x)_2HgI_4$

Chapter 5.4

Mechanochemical synthesis and temperature dependent optical properties of thermochromic $(Ag_{1-x}Cu_x)_2HgI_4$[†]

Summary

Thermochromic materials are generally synthesized via high-temperature melting reaction or solution-based synthesis. In this chapter, all-inorganic thermochromic compounds $(Ag_{1-x}Cu_x)_2HgI_4$ were synthesized by solvent-free simple and scalable mechanochemical grinding at room temperature. Temperature-dependent electronic absorption spectroscopy along with DSC analysis confirmed the thermochromic events in these materials, and the phase transition temperature varied with solid solution compositions. The photoluminescence (PL) spectra are red-shifted with the increase in the Cu content in $(Ag_{1-x}Cu_x)_2HgI_4$ (x=0–1).

[†] K. Maji,* **P. Acharyya,*** P. Satapathy, S. K. Prasad, and K. Biswas. *Chem. Asian J.* 2019, **14**, 4641-4644. *(*contributed equally)*

5.4.1. Introduction

The investigation of physical and chemical responses of organic and inorganic materials to external stimuli is an eminent area of scientific research. The responses can be induced by applying temperature, pressure, electric field, magnetic field or by light irradiation which leads to various effects like thermochromic, electrochromic/ferroelectric, ferromagnetic and photochromic respectively.[1, 2] Thermochromic materials have attracted considerable attention in various practical applications such as temperature display,[3] smart window,[4, 5] colour textile,[6] and photovoltaics.[7] Thermochromism refers to a phenomenon in which a material changes its colour in a response to change in temperature.[8] The primary reason of such temperature dependent transformation of inorganic compounds can be attributed to the changes in crystalline phase, ligand geometry or coordination number around the metal center.[8, 9]

Conventionally, inorganic thermochromic materials are synthesized either by high temperature melting reaction[10-12] or via solution phase reaction.[9, 13-15] While the prerequisite for a melting reaction lies in attaining considerably higher temperatures, the major bottleneck for solution based pathway is the unwanted precipitation as impurities and use of toxic and expensive solvents.[9] Hence, the common rationale would be to design an alternative route for synthesizing thermochromic materials which would be devoid of any aforementioned drawbacks. Mechanochemical synthesis technique attracted wide attention in modern synthetic chemistry for its simplicity, reproduciblity, cost effectiveness and environment friendly.[16, 17]

Mechanochemical route was introduced in the early 19th century by Faraday to reduce AgCl to metallic Ag using reducing agent like Zn, Cu, Sn or Fe by simply grinding in a mortar and pestle.[18] Recently, mechanochemical synthesis is shown to be a popular technique to synthesize metal-organic frameworks (MOFs) and covalent organic frameworks (COFs).[19-23] Recently, organic-inorganic hybrid perovskite halides[24-28] and all-inorganic halide perovskites[29-31] were also synthesized using this route. Hence, it would be important to synthesize thermochromic materials via mechanochemical synthesis which will be a good addition to the thermochromic research fields. Ag_2HgI_4 and Cu_2HgI_4 are well known thermochromic materials for decades.[32, 33] These materials

by virtue of possessing mobile Ag^+ and Cu^+ cations at the tetrahedral site of the crystal structure show high ionic conductivity value albeit at higher temperatures.[34]

In this chapter, we have synthesized $(Ag_{1-x}Cu_x)_2HgI_4$ (where $0 \leq x \leq 1$) via solvent free, simple, and scalable mechanochemical grinding at room temperature and investigated the structural and optical properties by varying the Cu concentration and temperature. Temperature dependent solid state diffuse reflectance spectroscopy confirmed the thermochromic behavior of these materials. Differential scanning calorimetry (DSC) shows that the phase transition temperature passes through a minimum at 36 °C when $x = 0.5$ in $(Ag_{1-x}Cu_x)_2HgI_4$. A noticeable red shift in the photoluminescence (PL) spectra is detected with increase in the Cu content in $(Ag_{1-x}Cu_x)_2HgI_4$ and falls within the two extremities (i.e., $x = 0$ and 1).

5.4.2. Methods

Reagents. Silver (I) Iodide (AgI, 99.999%, Sigma Aldrich), copper (I) Iodide (CuI, 99.5%, Sigma Aldrich) and mercury (II) Iodide (HgI_2, 99.99%, Sigma Aldrich) were used for the synthesis purpose without any further purification.

Synthesis. In a typical synthesis of Ag_2HgI_4, 113.6 mg (0.25 mmol) of HgI_2 and 117.38 mg (0.5 mmol) of AgI were taken in a mortar pestle, kept in a N_2 filled glove bag, mixed and ground mechanically for about 2 hours. The pale yellow colour of AgI and red color of HgI_2 converted orange-red (colour of Ag_2HgI_4) upon mechanical grinding. Whereas for the synthesis of Cu_2HgI_4, 2:1 molar ratio of CuI and HgI_2 were taken (i.e. 380.9 mg of CuI and 454.4 mg of HgI_2) and the same procedure as for Ag_2HgI_4 was followed. For the synthesis of other samples, the amounts of starting materials are given in the following table:

Samples	***Molar ratio***	***Weight taken (mg)***		
		AgI	*CuI*	*HgI_2*
$(Ag_{0.75}Cu_{0.25})_2HgI_4$	1.5:0.5:1	352.2	95.2	454.4
$AgCuHgI_4$	1:1:1	58.7	47.6	113.6

$(Ag_{0.25}Cu_{0.75})_2HgI_4$	0.5:1.5:1	117.4	285.7	454.4

Powder X-ray diffraction. The powder X-ray Diffraction pattern of all the samples were collected on a Bruker D8 difractometer by using Cu Kα (λ=1.5406 Å) at room temperature.

Thermal analysis. Thermal analysis was performed by Differential Scanning Calorimetry (DSC) using TA DSCQ2000 instrument. The sample was heated at the rate of 2°C per min. in N_2 (40 mL per min.) at the temperature range of 30 °C to 150 °C.

Optical properties. Diffuse reflectance measurement was carried out to estimate the optical band gap in the range of 250 nm to 800 nm by using Perkin-Elmer Lambda 900 UV/Vis/Near-IR spectrometer in reflectance mode. From the reflectance data, we calculated absorption data (α/S) by using Kubelka-Munk equation: $\alpha/S = (1-R)^2 / (2R)$ where R is reflectance α is absorption and S is scattering coefficient. The optical band gaps were obtained from α/S vs wavelength (nm) plots. Variable temperature measurements of the diffuse reflectance were performed by placing the sample inside a homemade heating block with a wide optical window. The actual sample temperatures were measured using a laser-based IR thermometer (Fluke 59A). The temperature dependent measurements are done in collaboration with Prof. S. K. Prasad, CeNS, India.

The emission spectra were obtained by using Perkin-Elmer LS 55 Luminescence spectrometer in the solid state. Luminescence spectra of the solid samples were recorded at the different excitation wavelength.

5.4.3. Results and Discussion

β-Ag_2HgI_4 and *β*-Cu_2HgI_4 have a body centered tetragonal crystal structure with space group *I-4* and *I-42m,* respectively at ambient temperature, in which Hg and I form covalently bonded corner sharing tetrahedra at the corners as well as in the middle of the unit cell. Ag^+ and Cu^+ cations occupy the tetrahedral voids (Figure 5.4.1a, b).[34-36] These structure can be derived from chalcopyrite ($Cu_2Fe_2S_4$) by re-arranging four Ag/Cu and two Hg atoms over the eight cationic sites.[34] *β*-Ag_2HgI_4 further undergoes a phase

transition from tetragonal to cubic structures at 50 ºC where the cubic structure is of the disordered cubic zinc blend type (space group; *F4-3m*).[13, 34] In the cubic phase, the cations (Hg^{2+} and Ag^{+}) randomly occupy the tetrahedral voids within an anionic (I^{-}) rigid face centered cubic sublattice (Figure 5.4.1c).[34] The rapid hopping of the Ag^{+} within these tetrahedral voids enables this α-cubic to show superionicity at high temperatures. On the other hand, Cu_2HgI_4 also exhibits equivalent cubic crystal structure above 70 ºC. They are isomorphous in nature and formation of the solid solution is preferred due to similar lattice constant.[37]

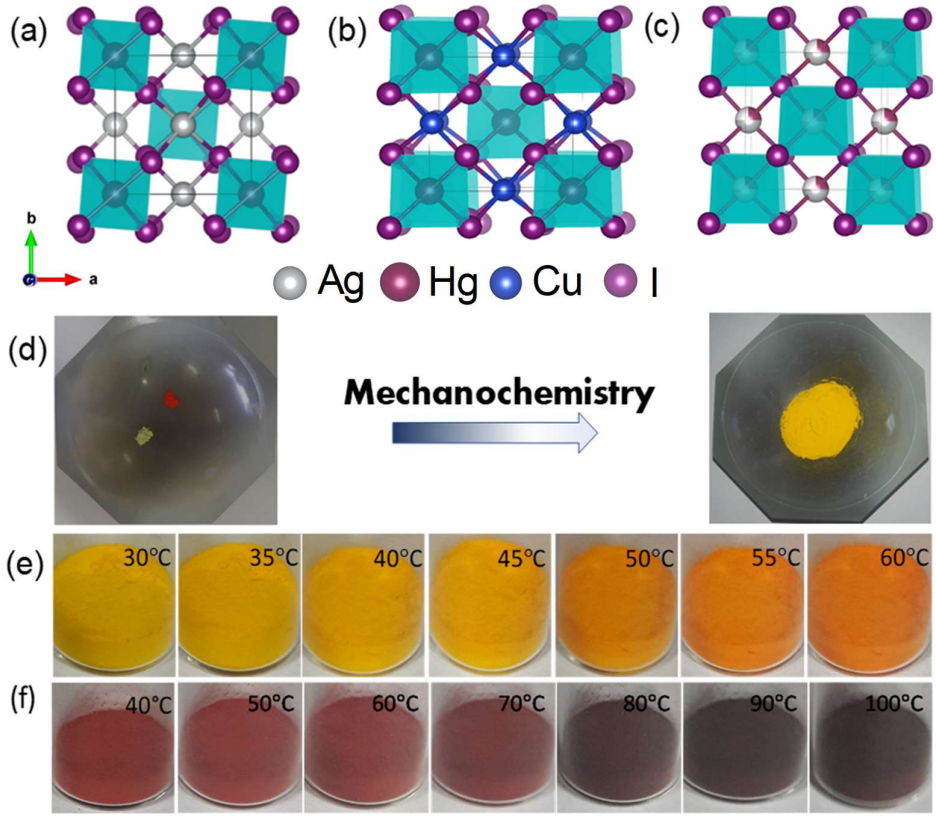

Figure 5.4.1. *Crystal structure of (a) β-Ag_2HgI_4, (b) β-Cu_2HgI_4, and (c) α-Ag_2HgI_4. (d) Mechanochemical synthesis of Ag_2HgI_4 from AgI and HgI_2. Colour changes for (e) Ag_2HgI_4 and (f) Cu_2HgI_4 as a function of temperature.*

Mechanochemical synthetic route is a simple and efficient technique to synthesize $(Ag_{1-x}Cu_x)_2HgI_4$ without using any sophisticated and expensive instruments. To synthesize these compositions, a general scheme is followed:

$$2(1\text{-}x)\,AgI + 2x\,CuI + HgI_2 \xrightarrow{\text{Mechanochemistry}} (Ag_{1-x}Cu_x)_2HgI_4$$

It is notable that the mole ratio of the starting precursors is decided via elementary balancing the reaction, wherein, the formation of one mole of $(Ag_{1-x}Cu_x)_2HgI_4$ would mean that the molar ratio of the precursors, i.e., AgI, CuI, and HgI_2 are in the ratio of 2(1-*x*):2*x*:1 (where: $x = 0$ - 1). In a typical synthesis of Ag_2HgI_4, AgI and HgI_2 were mixed at 2:1 molar ratio of and ground mechanochemically using a mortar and pestle for about 2 hours in a N_2 filled glove bag. While the formation of the product starts within the first few minutes of grinding, it takes around 2 hours to complete the reaction which is noticeable from its distinct color change to deep yellow (Ag_2HgI_4) from red HgI_2 and pale yellow AgI precursors (Figure 5.4.1d). We have synthesized $(Ag_{1-x}Cu_x)_2HgI_4$ compounds (where $x = 0$, 0.25, 0.5, 0.75 and 1) by only changing the molar ratio of AgI, CuI, and HgI_2 using the above synthetic procedure.

Figure 5.4.2a shows the powder X-ray diffraction (PXRD) pattern of all the compounds with general formula $(Ag_{1-x}Cu_x)_2HgI_4$ (where x = 0 to 1). The PXRD patterns of the compounds Ag_2HgI_4 and Cu_2HgI_4 could be indexed with the simulated pattern for the space groups *I-4* and *I-42m,* respectively without the presence of any other impurity phases within the detection limit of PXRD. As the concentration of Cu increases in $(Ag_{1-x}Cu_x)_2HgI_4$, PXRD peaks indicated in Figure 5.4.2a are shifted towards the right side. This emphasized the decrease in the lattice constant as the size of the Cu^+ (77 pm) ions are less than that of Ag^+ (115 pm) which was further verified by Vegard's law plot (Figure 5.4.3). These results confirmed the formation of the solid solution at room temperature. The structural phase transition temperature of Ag_2HgI_4 and Cu_2HgI_4 are 50 °C and 70 °C, respectively.[13] We have measured the phase transition temperature using differential scanning calorimetry (DSC) technique for $(Ag_{1-x}Cu_x)_2HgI_4$ at $x = 0.25$, 0.5 and 0.75 which are found to be 39.5 °C, 36°C and 59 °C, respectively (Figure 5.4.2b). Figure 5.4.2c shows the change in phase transition temperatures of $(Ag_{1-x}Cu_x)_2HgI_4$ (x = 0 - 1) as a function of Cu concentration. The phase transition temperature passes through a minimum and in case of $AgCuHgI_4$, the phase transition temperature reaches minima at 35.9 ºC. Careful DSC analysis provides an extra hump at around 42 °C along with the peak 36 °C for

$AgCuHgI_4$ (x = 0.5) in the DSC plot which indicates the phase separation (Figure 5.4.2b) with high Cu concentration of 50 mol%.

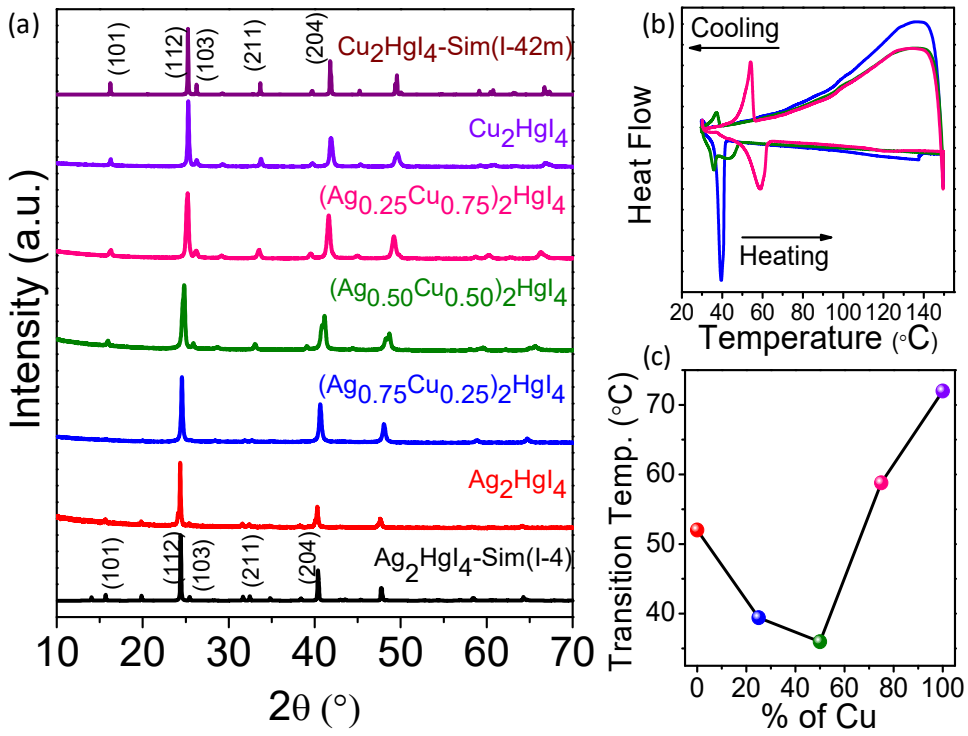

Figure 5.4.2. *(a) PXRD patterns for Cu doped Ag_2HgI_4. (b) DSC curves for $(Ag_{1-x}Cu_x)_2HgI_4$. (c) Transition temperature vs. concentration of Cu in $(Ag_{1-x}Cu_x)_2HgI_4$.*

With increase in temperature from 30 °C to 60 °C, the yellow coloured Ag_2HgI_4 started turning to orange-red due to thermochromism. This initial transformation from yellow to orange-red takes place at around 40 °C (Figure 5.4.1e). This colour change is reversible, as it returns into its initial yellow colour when the compound is cooled down (Figure 5.4.4). Similarly, red coloured Cu_2HgI_4 transformed to brownish black with increasing temperature and turned back to red upon cooling (Figure 5.4.1f and Figure 5.4.4). The colour change in $(Ag_{1-x}Cu_x)_2HgI_4$ with temperature is mainly attributed to the structural phase transition.[9]

Temperature dependent diffuse reflectance spectroscopy further confirmed the thermochromic behavior in these materials. The absorption spectrum shows a continuous absorption edge shift in the range of 555-600 nm for Ag_2HgI_4 (Figures 5.4.5a,b) with increasing the temperature. In case of Cu_2HgI_4, the absorption edge shifts in the range 690-795 nm (Figure 5.4.5c,d) with increasing the temperature from 30 to 90 °C . On the cooling cycle, the band edge is shifted to lower wavelength, as shown in Figures 5.4.5b and 5.4.5d, which confirmed that the transition is reversible in nature.

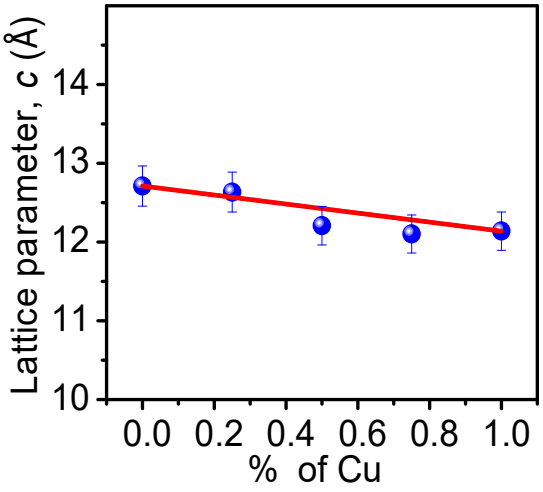

Figure 5.4.3. *Lattice parameter c of* $(Ag_{1-x}Cu_x)_2HgI_4$ *as a function of the Cu doped, x. The solid line shows the linear decrease of lattice parameter c according to Vegard's law.*

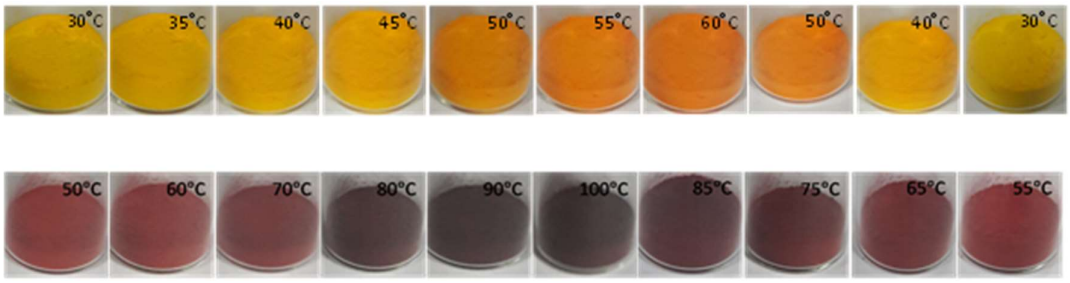

Figure 5.4.4. *Reversible color change of* Ag_2HgI_4 *(up) and* Cu_2HgI_4 *(down) with temperature.*

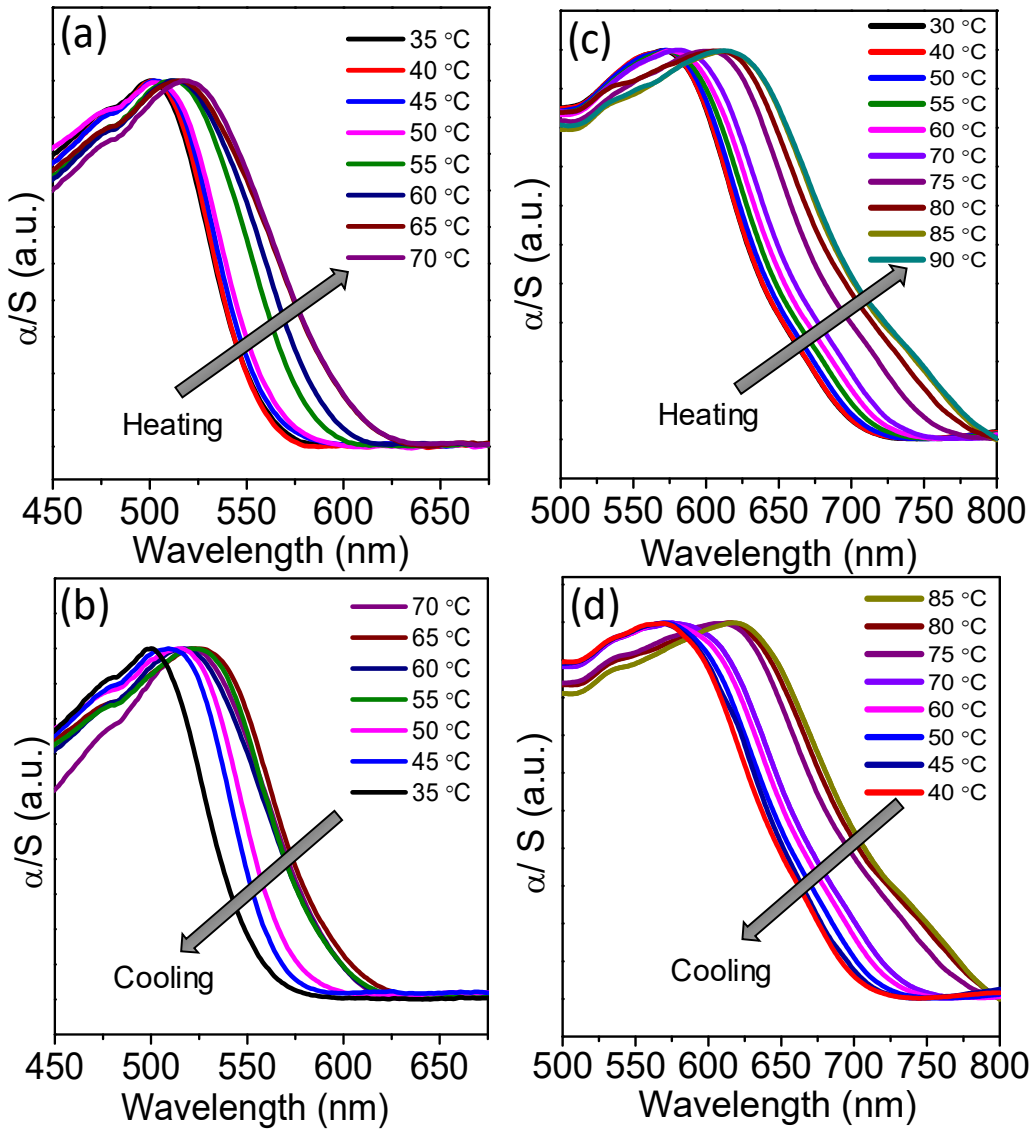

Figure 5.4.5. *Solid state electronic absorption (α/S) on the heating cycle (a, c) and on the cooling cycle (b, d) of Ag_2HgI_4 and Cu_2HgI_4, respectively.*

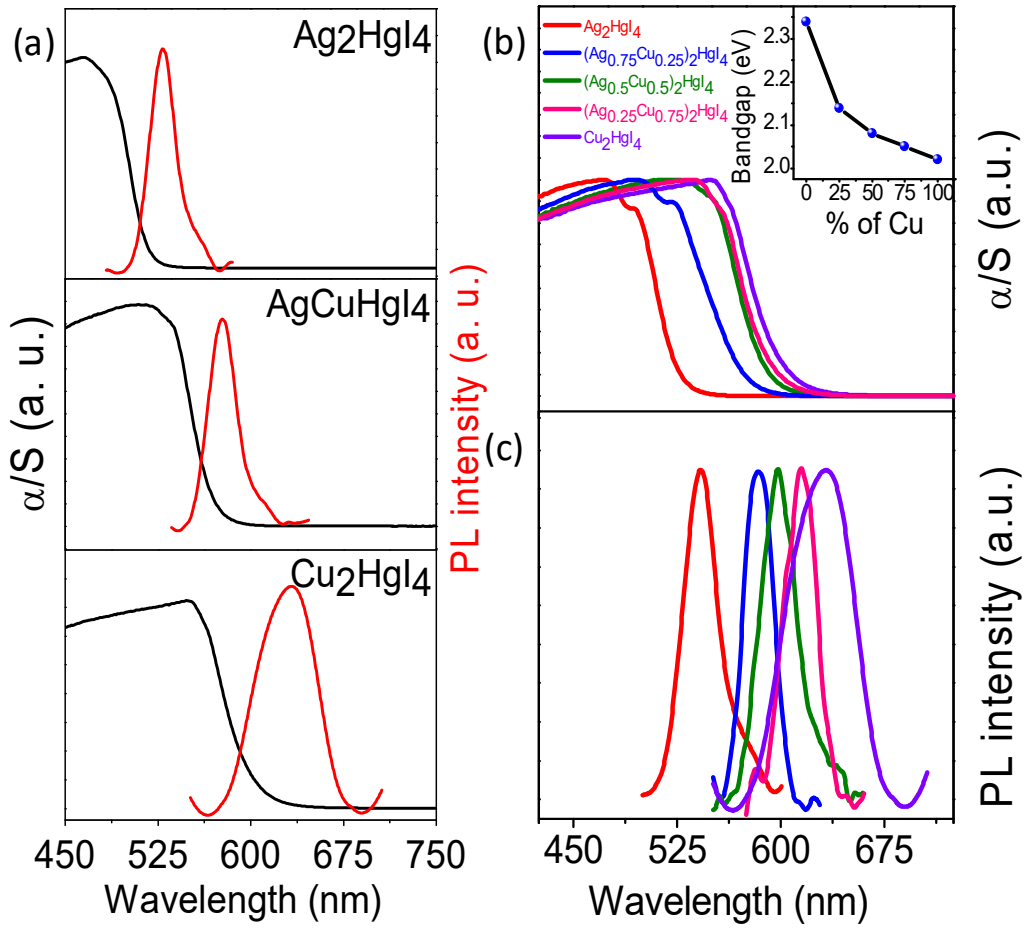

Figure 5.4.6. *(a) Solid-state electronic absorption (α/S) (black) and PL (red) spectra of Ag_2HgI_4, AgCuHgI4 and Cu_2HgI_4 respectively. (b) electronic absorption (α/S), band gap vs. different Cu content plot (inset).and (c) PL spectra of Cu alloyed Ag_2HgI_4.*

Optical properties were further investigated via electronic absorption and photoluminescence (PL) spectra in the solid state at room temperature (Figure 5.4.6 and Figure 5.4.7). For Ag_2HgI_4, the absorption edge appears at 530 nm (2.34 eV), whereas the PL band emerges with a maximum at 542 nm when excited at 400 nm. Similarly, the absorption edge appears at 600 nm (2.02 eV) and PL band with a maximum at 633 nm with an excitation wavelength of 480 nm occur for Cu_2HgI_4, (Figure 5.4.6a). For $AgCuHgI_4$, the absorption edge and PL band appears at 592 nm (2.07 eV) and 600 nm (excited at 440 nm) (Figure 5.4.6a). For $x = 0.25$ and 0.75, the absorption edge appears at

574 nm (2.14 eV) and 583 nm (2.04 eV), respectively, whereas PL band arises at 594 nm (excited at 430 nm) and 615 nm (excited at 450 nm), respectively (Figure 5.4.7). Figure 5.4.6b shows the red shift of the absorption edge and decrease of the band gap with increasing Cu content in $(Ag_{1-x}Cu_x)_2HgI_4$. With increasing Cu concentration $(Ag_{1-x}Cu_x)_2HgI_4$ the PL band maxima are red shifted as well (Figure 5.4.6c).

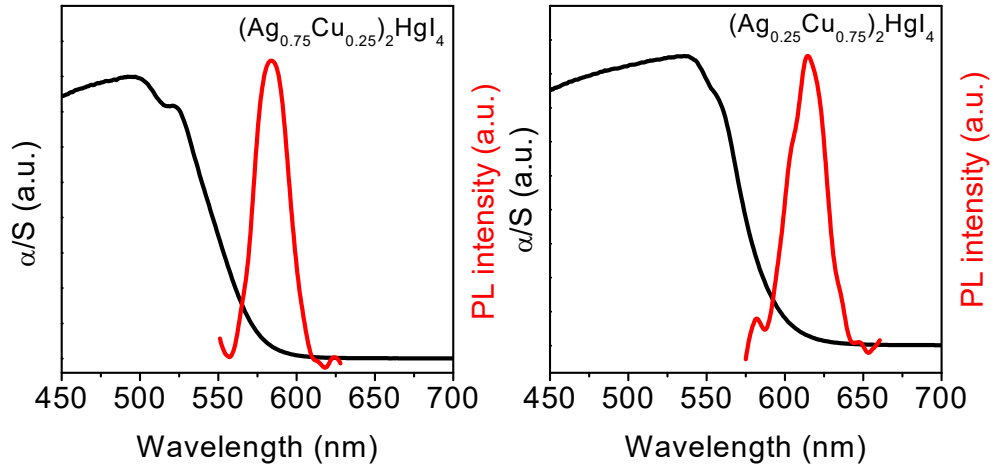

Figure 5.4.7. *Solid-state UV/Vis absorption (α/S) (black) and PL (red) spectra of (a) $(Ag_{0.75}Cu_{0.25})_2HgI_4$ and (b) $(Ag_{0.25}Cu_{0.75})_2HgI_4$.*

5.4.4. Conclusions

In conclusions, we have synthesized Ag_2HgI_4, Cu_2HgI_4 and their solid solutions via solvent free and scalable mechanochemical grinding at room temperature for the first time. We have demonstrated the colour change of $(Ag_{1-x}Cu_x)_2HgI_4$ (x = 0 - 1) with the change in temperature, which is further confirmed by temperature dependent diffuse reflectance spectroscopy at solid state. Mechanochemical grinding is energy and cost efficient, scalable and less time-consuming procedure compared to other well studied synthetic procedures like solid state melting reactions or solution-based methods. We believe that the current reaction technique will serve as a paradigm for large-scale synthesis of thermochromic materials.

5.4.5. References

1. P. Kiri, G. Hyett and R. Binions, *Adv. Mater. Lett.*, 2010, **1**, 86.

2. T. Taniguchi, H. Sato, Y. Hagiwara, T. Asahi and H. Koshima, *Commun. Chem.*, 2019, **2**, 1.

3. L. Liu, S. Peng, W. Wen and P. Sheng, *Appl. Phys. Lett.*, 2007, **90**, 213508.

4. Y. Gao, H. Luo, Z. Zhang, L. Kang, Z. Chen, J. Du, M. Kanehira and C. Cao, *Nano Energy*, 2012, **1**, 221.

5. L. S. Long and H. Ye, *Sci. Rep.*, 2014, **4**.

6. M. A. Chowdhury, M. Joshi and B. S. Butola, *J. Eng. Fibers Fabr.*, 2014, **9**, 107.

7. J. Lin, M. Lai, L. Dou, C. S. Kley, H. Chen, F. Peng, J. Sun, D. Lu, S. A. Hawks and C. Xie, *Nat. Mater.*, 2018, **17**, 261.

8. J. H. Day, *Chem. Rev.*, 1968, **68**, 649.

9. F. Soofivand and M. Salavati-Niasari, *J. Mol. Liq.*, 2018, **252**, 112.

10. N. Saba and A. Ahmad, *J. Adv. Electrochem.*, 2016, **2**, 45.

11. D. K. Nguyen, H. Lee and I.-T. Kim, *Materials*, 2017, **10**, 476.

12. B. G. Ravi, S. Ramasamy and N. Baskaran, *J. Mater. Sci. Lett.*, 1993, **12**, 464.

13. A. M. Sukeshini and K. Hariharan, *Solid State Commun.*, 1991, **78**, 85.

14. K. W. Browall and J. S. Kasper, *J. Solid State Chem.*, 1975, **15**, 54.

15. T. A. Hameed, I. M. E. Radaf and G. B. Sakr, *Appl. Phys. A*, 2018, **124**, 684.

16. R. E. Morris and S. L. James, *Angew. Chem., Int. Ed.*, 2013, **52**, 2163.

17. S. L. James, C. J. Adams, C. Bolm, D. Braga, P. Collier, T. Friščić, F. Grepioni, K. D. M. Harris, G. Hyett, W. Jones, A. Krebs, J. Mack, L. Maini, A. G. Orpen, I. P. Parkin, W. C. Shearouse, J. W. Steed and D. C. Waddell, *Chem. Soc. Rev.*, 2012, **41**, 413.

18. C. N. R. Rao and K. Biswas, *Essentials of inorganic materials synthesis*, John Wiley & Sons, 2015.

19. W. Yuan, T. Friščić, D. Apperley and S. L. James, *Angew. Chem., Int. Ed.*, 2010, **49**, 3916.

20. T. Friščić, I. Halasz, P. J. Beldon, A. M. Belenguer, F. Adams, S. A. J. Kimber, V. Honkimäki and R. E. Dinnebier, *Nat. Chem.*, 2013, **5**, 66.

21. T. Friščić, *Chem. Soc. Rev.*, 2012, **41**, 3493.

22. C. Xu, S. De, A. M. Balu, M. Ojeda and R. Luque, *Chem. Commun.*, 2015, **51**, 6698.

23. B. P. Biswal, S. Chandra, S. Kandambeth, B. Lukose, T. Heine and R. Banerjee, *J. Am. Chem. Soc.*, 2013, **135**, 5328.

24. A. D. Jodlowski, A. Yépez, R. Luque, L. Camacho and G. de Miguel, *Angew. Chem., Int. Ed.*, 2016, **55**, 14972.

25. A. Jana, M. Mittal, A. Singla and S. Sapra, *Chem. Commun.*, 2017, **53**, 3046.

26. D. Prochowicz, M. Franckevičius, A. M. Cieślak, S. M. Zakeeruddin, M. Grätzel and J. Lewiński, *J. Mater. Chem. A*, 2015, **3**, 20772.

27. Z.-Y. Zhu, Q.-Q. Yang, L.-F. Gao, L. Zhang, A.-Y. Shi, C.-L. Sun, Q. Wang and H.-L. Zhang, *J. Phys. Chem. Lett.*, 2017, **8**, 1610.

28. V. A. Hintermayr, A. F. Richter, F. Ehrat, M. Döblinger, W. Vanderlinden, J. A. Sichert, Y. Tong, L. Polavarapu, J. Feldmann and A. S. Urban, *Adv. Mater.*, 2016, **28**, 9478.

29. P. Pal, S. Saha, A. Banik, A. Sarkar and K. Biswas, *Chem. Eur. J*, 2018, **24**, 1811.

30. A. Sarkar, P. Acharyya, R. Sasmal, P. Pal, S. S. Agasti and K. Biswas, *Inorg. Chem.*, 2018, **57**, 15558.

31. Y. El Ajjouri, V. S. Chirvony, N. Vassilyeva, M. Sessolo, F. Palazon and H. J. Bolink, *J. Mater. Chem. C*, 2019, **7**, 6236.

32. H. R. C. Jaw, M. M. Mooney, T. Novinson, W. C. Kaska and J. I. Zink, *Inorg. Chem.*, 1987, **26**, 1387.

33. K. Funke, *Prog. Solid State Chem.*, 1976, **11**, 345.

34. S. Hull and D. A. Keen, *J. Phys. Condens. Matter*, 2000, **12**, 3751.

35. K. W. Browall, J. S. Kasper and H. Wiedemeier, *J. Solid State Chem.*, 1974, **10**, 20.

36. S. Hull and D. A. Keen, *J. Phys. Condens. Matter*, 2001, **13**, 5597.

37. L. Suchow and P. H. Keck, *J. Am. Chem. Soc.*, 1953, **75**, 518.

PART 6

High Performance Germanium Telluride-based Thermoelectrics

Chapter 6.1

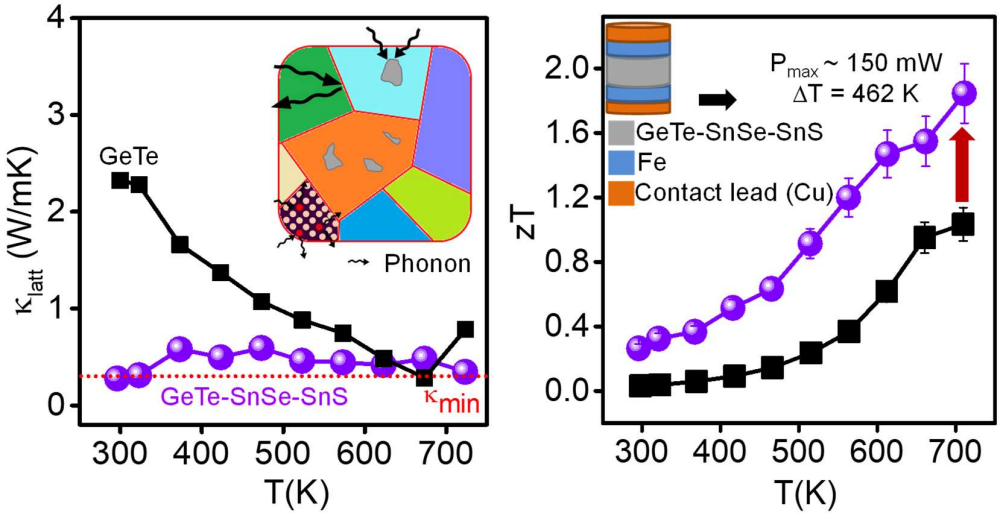

Ultralow Thermal Conductivity, Enhanced Mechanical Stability and High Thermoelectric Performance in $(GeTe)_{1-2x}(SnSe)_x(SnS)_x$

Chapter 6.1

Ultralow Thermal Conductivity, Enhanced Mechanical Stability and High Thermoelectric Performance in $(GeTe)_{1-2x}(SnSe)_x(SnS)_x$[†]

Summary

Thermoelectric (TE) energy conversion demands high performance crystalline inorganic solids that exhibit ultralow thermal conductivity, high mechanical stability and good TE device properties. Pb-free germanium telluride (GeTe) based material has recently attracted significant attention in TE power generation in mid temperatures, but pristine GeTe possesses significantly higher lattice thermal conductivity (κ_{latt}) compared to that of its theoretical minimum (κ_{min}) of ~ 0.3 W/mK. In this chapter, we have demonstrated the reduction of κ_{latt} of $(GeTe)_{1-2x}(SnSe)_x(SnS)_x$ very near to its κ_{min}. $(GeTe)_{1-2x}(SnSe)_x(SnS)_x$ system behaves as coexistence of point defect rich solid solution and phase separation. Initially, the addition of equimolar SnSe and SnS in the GeTe reduces the κ_{latt} by effective phonon scattering owing to excess point defects and rich microstructures. In the second step, introduction of Sb doping leads additional phonon scattering centers and optimizes the p-type carrier concentration. Notably, 10 mol% Sb-doped $(GeTe)_{0.95}(SnSe)_{0.025}(SnS)_{0.025}$ exhibits ultralow κ_{latt} of ~ 0.30 W/mK at 300 K. Subsequently, 10 mol% Sb-doped $(GeTe)_{0.95}(SnSe)_{0.025}(SnS)_{0.025}$ exhibits high TE figure of merit (zT) of ~1.9 at 710 K. The high-performance sample exhibit Vickers microhardness (mechanical stability) value of ~194 H_V that is significantly higher compared to the pristine GeTe and other state-of-art thermoelectric materials. Further, we have achieved a high output power, ~ 150 mW for the temperature difference of 462 K, in single leg TE device based on 10 mol% Sb-doped $(GeTe)_{0.95}(SnSe)_{0.025}(SnS)_{0.025}$.

[†]**P. Acharyya**, S. Roychowdhury, M. Samanta and K. Biswas, ***J. Am. Chem. Soc.*** 2020, **142**, 20502–20508.

6.1.1. Introduction

Thermoelectric materials and devices are important for energy conversion and utilization as they can convert waste heat to electricity. The dimensionless figure of merit (zT) determines the performance of thermoelectric materials, which is defined as, $zT = \sigma S^2T/\kappa_{tot}$, where, σ, S, κ_{tot}, and T are electrical conductivity, Seebeck coefficient, total thermal conductivity, and absolute temperature, respectively.[1-6] Significant efforts were attempted to improve the thermoelectric performance by optimizing both the Seebeck coefficient and/or the thermal conductivity to enhance the zT.[7-13] The aforementioned parameters such as electrical conductivity, Seebeck coefficient and electrical thermal conductivity are interrelated with the electronic structure of a particular material and thus, cannot be optimized independently.[1, 2] Lattice thermal conductivity (κ_{latt}) is the only parameter, which can be tailored independently.[13] Thus, an effective way to maximize the zT of a material is to control the κ_{latt}.

Recently, GeTe have been considered as high-performance thermoelectric material for power generation in the mid temperature range (600-900 K) as an alternative of PbTe.[14-19] Moreover, GeTe is unique from other members of IV-VI family because it possesses a rhombohedral crystal structure (space group $R3m$) at room temperature, which is a ferroelectric phase. The main disadvantage with pristine GeTe is its high carrier concentration originating from intrinsic Ge vacancy, resulting high electrical conductivity (~ 8500 S/cm), low Seebeck coefficient (~ 30 μV/ K) and high total thermal conductivity (~ 8 W/mK) rendering maximum zT of ~ 0.9 in pristine GeTe at 720 K.[20] However, the last couple of year, we have seen a radical enhancement in thermoelectric performances of GeTe, facilitated by the innovation of several novel strategies and material design methodologies.[16, 21-26]

At room temperature, κ_{latt} of GeTe is ~ 2.5 W/mK which is substantially higher compared to its minimum lattice thermal conductivity (κ_{min} ~ 0.3 W/mK).[27] Thermodynamics of a system governs the material's properties, which can dramatically influence the thermoelectric properties of inorganic solids. Entropy engineering is one of the powerful strategies to improve the thermoelectric performance.[28, 29] κ_{latt} of GeTe has been significantly reduced by alloying with multiple elements which create significant

disorder thereby enhanced phonon scattering.[29, 30] Pseudo-ternary system can exhibit significant reduction of κ_{latt} compared to pseudo-binary system due to entropy driven enhanced disorder.[30, 31] With this motivation, we thought to examine the impact of equimolar substitution of SnSe and SnS in a GeTe rich system, which might decrease the κ_{latt} efficiently due to large sets of disorder in both cation (Ge/Sn) and anion (Te/Se/S) sites. While investigating such a complex system, $(GeTe)_{1-2x}(SnSe)_x(SnS)_x$, few important questions arise e.g. (a) is the material $(GeTe)_{1-2x}(SnSe)_x(SnS)_x$ a phase separated system or forms solid solution? (b) if it is a phase separated system, then what is the minimum miscibility concentration of SnSe/SnS in GeTe? (c) More interestingly, can they also behave as coexistence of solid solutions and phase separation? and (d) How the κ_{latt} and over-all thermoelectric performance of the system will be influenced by all the above factors?

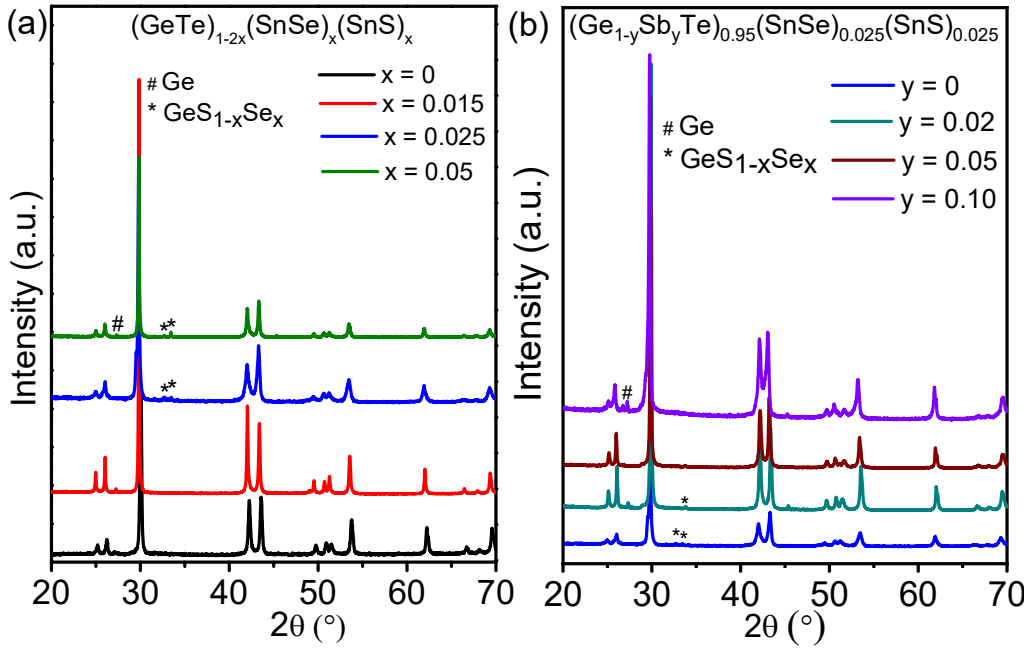

***Figure 6.1 1**. Powder X-ray diffraction pattern of (a) $(GeTe)_{1-2x}(SnSe)_x(SnS)_x$ (x = 0 - 0.05) samples and (b) $(Ge_{1-y}Sb_yTe)_{0.95}(SnSe)_{0.025}(SnS)_{0.025}$ samples (y = 0 – 0.10) samples.*

In this chapter, we demonstrate an ultralow κ_{latt}, high thermoelectric performance, and high mechanical stability in Sb doped GeTe-rich $(GeTe)_{1-2x}(SnSe)_x(SnS)_x$ system. The realization of ultralow κ_{latt} and high zT is achieved *via* two successive stages.

Initially, the addition of SnSe and SnS (each of 2.5 mol%) in GeTe reduces the κ_{latt} due to phonon scattering because of enhanced point defects and microstructures. Further, introduction of Sb doping introduces additional phonon scattering center and optimizes the *p*-type carrier concentration. As a result, 10 mol % Sb-doped $(GeTe)_{0.95}(SnSe)_{0.025}(SnS)_{0.025}$ sample exhibits ultralow κ_{latt} of ~ 0.34 W/mK accompanied by the zT of ~1.9 at 710 K. The ultralow κ_{latt} is attributed due to the phonon scattering in Sb-doped $(GeTe)_{1-2x}(SnSe)_x(SnS)_x$ primarily by (a) excess solid solution point defects and (b) grain boundaries and micron size precipitates, thereby κ_{latt} reaches nearly to the κ_{min} of GeTe (0.3 W/m.K). Moreover, the measured Vickers microhardness (mechanical stability) value of high-performance sample is ~194 H_V, that is higher compared to pristine GeTe (~145 H_V). Motivated by the high zT and enhanced mechanical stability, we have constructed single-leg based thermoelectric device and achieved a high output power, ~ 150 mW for the temperature difference of 462 K, for 10 mol % Sb-doped $(GeTe)_{0.95}(SnSe)_{0.025}(SnS)_{0.025}$ sample.

6.1.2. Methods

Reagents. Germanium (Sigma Aldrich 99.999%), tin (Alfa Aesar 99.999%), antimony (Alfa Aesar 99.9999%), tellurium (Alfa Aesar 99.999 %), selenium (Alfa Aeser 99.9999%), and sulfur (Alfa Aesar 99.9999%) were used for synthesis without further purification.

Synthesis. High quality polycrystalline ingots of $(GeTe)_{1-2x}(SnSe)_x(SnS)_x$ (x=0-5 %) were synthesized by mixing appropriate ratio of starting element of Ge, Sn, Te, Se, and S in a quartz tube. The tubes were sealed under high vacuum (10^{-6} Torr) and slowly heated to 723 K over 12 h and then heated up to 1223 K over 5 h, soaked for 6 h and finally cooled down to room temperature over 10 h. Similar reaction procedure were followed for Sb doped samples.

Further we have studied the thermoelectric properties of spark plasma sintering (SPS) processed samples for the best performed sample. The ingot samples crushed and ground to fine powders using a mortar and pestle. The powders were then loaded into a

graphite die (~10 mm diameter) and the die assembly into a spark plasma sintering system (SPS211-LX, Dr. Sinter Lab). The sintering system was first evacuated to 10^{-3} Torr. The temperature of the SPS chamber was held at room temperature for the first 1 min and the axial pressure was increased to 50 MPa. Then the temperature was increased to 350 °C in 5 min, followed by 450 °C in 2 min with a constant pressure of 50 MPa. For the next 5 min, the temperature and pressure were held at 450 °C and 50 MPa, respectively under vacuum, and then slowly decreased to ambient conditions in 10 min. The SPS-processed cylindrical-shaped sample (10 mm diameter and 10 mm height) was further cut and polished for electrical and thermal transport measurement.

Powder X-ray diffraction. Powder X-ray diffraction for all the samples were recorded using a PANalytical empyrean diffractometer with Cu Kα1 radiation.

Band Gap Measurement. The optical band gaps of all the powered samples were measured using the diffuse reflectance mode in an FT-IR Bruker IFS 66 V/S spectrometer in the wavenumber range 4000−400 cm^{-1}. Absorption (α/Λ) value were calculated from measured reflectance data using the Kubelka−Munk equation: $\alpha/\Lambda = (1 - R)^2/(2R)$, where α, Λ and R are the absorption, scattering coefficient and reflectance respectively.

Field Emission Scanning Electron Microscopy (FESEM). Backscattered FESEM imaging and EDAX were performed using NOVA NANO SEM 600 (FEI, Germany) operated at 15 KV.

Electrical transport. Electrical conductivity and Seebeck coefficients of all the samples (2X2X8 mm^3) were measured simultaneously under a helium atmosphere in an ULVAC-RIKO ZEM-3 instrument from room temperature to 723 K. Electrical transport and thermal condctivity are measured in same direction.

Hall measurement. The carrier concentration of all the samples where measured under variable magnetic field of 0−0.57 T with dc supply of 100 mA at room temperature in the setup developed by Excel Instruments.

Thermal transport. Thermal diffusivity (D) of the samples (~ 2 mm thickness) were measured in a Netzsch LFA-457 instrument in the temperature range 300−723 K under a nitrogen atmosphere. The total thermal conductivity (κ_{total}) was calculated using the formula $\kappa_{total} = D \times \rho \times C_p$ where ρ is the density of the sample and C_p is the heat capacity of the sample. Here we have used Dulong−Petit's C_p value to calculate the κ_{total} of all the samples.

Microhardness. The microhardness was measured in a Zwick Roell zhu 2.5 microhardness instrument using the diamond indenter on the Vickers hardness scale. 2 N force was applied, and the indent was kept for 10 s for the measurement. Vickers hardness ($kg \cdot f/mm^2$) values of the samples were determined by the equation $H_v = 1.854 \times L/(2d)^2$, where L is the indentation load and 2d is the diagonal length of the indentation.

Preparation of single-leg thermoelement and measurement of its power generating properties. Typically, fabrication of the single-leg thermoelement involves consolidation of the melt grown $(Ge_{0.90}Sb_{0.10}Te)_{0.95}(SnSe)_{0.025}(SnS)_{0.025}$ powder along with the end layers of Cu/Fe using SPS (Dr. Sinter Lab. SPS21Lx) at 500 ºC with 50 MPa for 5 min under vacuum. The arrangement of different layers in the fabricated single-leg $(Ge_{0.90}Sb_{0.10}Te)_{0.95}(SnSe)_{0.025}(SnS)_{0.025}$ based thermoelement can be described as Cu/Fe/$(Ge_{0.90}Sb_{0.10}Te)_{0.95}(SnSe)_{0.025}(SnS)_{0.025}$ /Fe/Cu. Typical dimension of the fabricated cylinder shape thermoelement is of 8 mm diameter and 9 mm length. Power generation properties of the fabricated $(Ge_{0.90}Sb_{0.10}Te)_{0.95}(SnSe)_{0.025}(SnS)_{0.025}$ thermoelement was estimated by mini-PEM module testing system (Advance Riko).[32-34]

6.1.3. Results and Discussion

High quality $(GeTe)_{1-2x}(SnSe)_x(SnS)_x$ (x = 0 - 0.05) samples are synthesized by high temperature vacuum sealed tube melting (see Method). Room temperature powder X-ray diffraction (PXRD) pattern of $(GeTe)_{1-2x}(SnSe)_x(SnS)_x$ (x = 0 - 0.05) in Figure 6.1.1a could be indexed based on the rhombohedral phase of GeTe (space group *R*3*m*). However, weak diffraction peaks of the $GeS_{1-x}Se_x$ (space group *Pbnm*) secondary phase at higher concentration of SnSe and SnS ($x \geq 0.025$) was observed in the PXRD patterns (Figure

6.1.1a). We also observe very weak diffraction peak for Ge as well. Simultaneous substitution of SnSe and SnS (with lower concentration) in GeTe shifts the Bragg peaks towards lower angle (2θ) because of the increase in the lattice parameter. The initial increase in the lattice parameter for $(GeTe)_{1-2x}(SnSe)_x(SnS)_x$ samples is indicating towards the incorporation of the Sn (118 pm) in the position of Ge (87 pm) in GeTe.

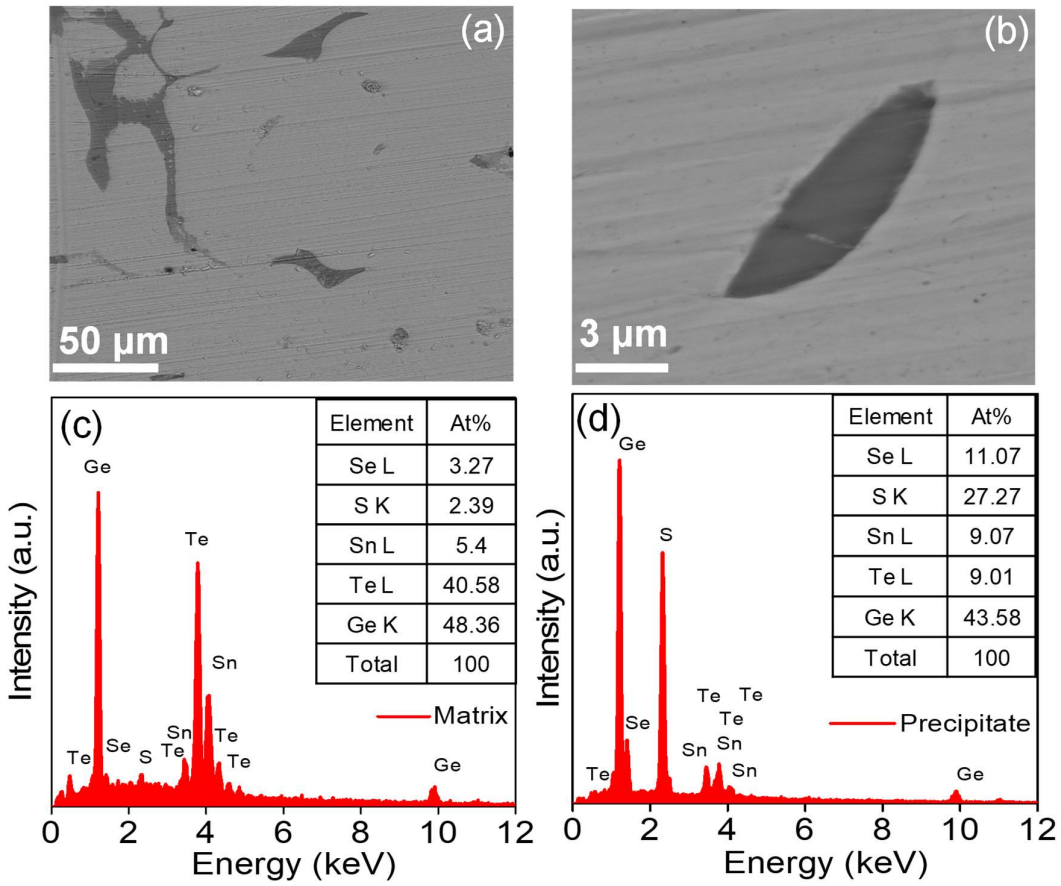

Figure 6.1.2. *(a)-(b) BSE-FESEM images of $(GeTe)_{0.95}(SnSe)_{0.025}(SnS)_{0.025}$ sample. EDS spectra taken from both (c) matrix and (d) precipitate. Inset in (c) and (d) show the elemental composition.*

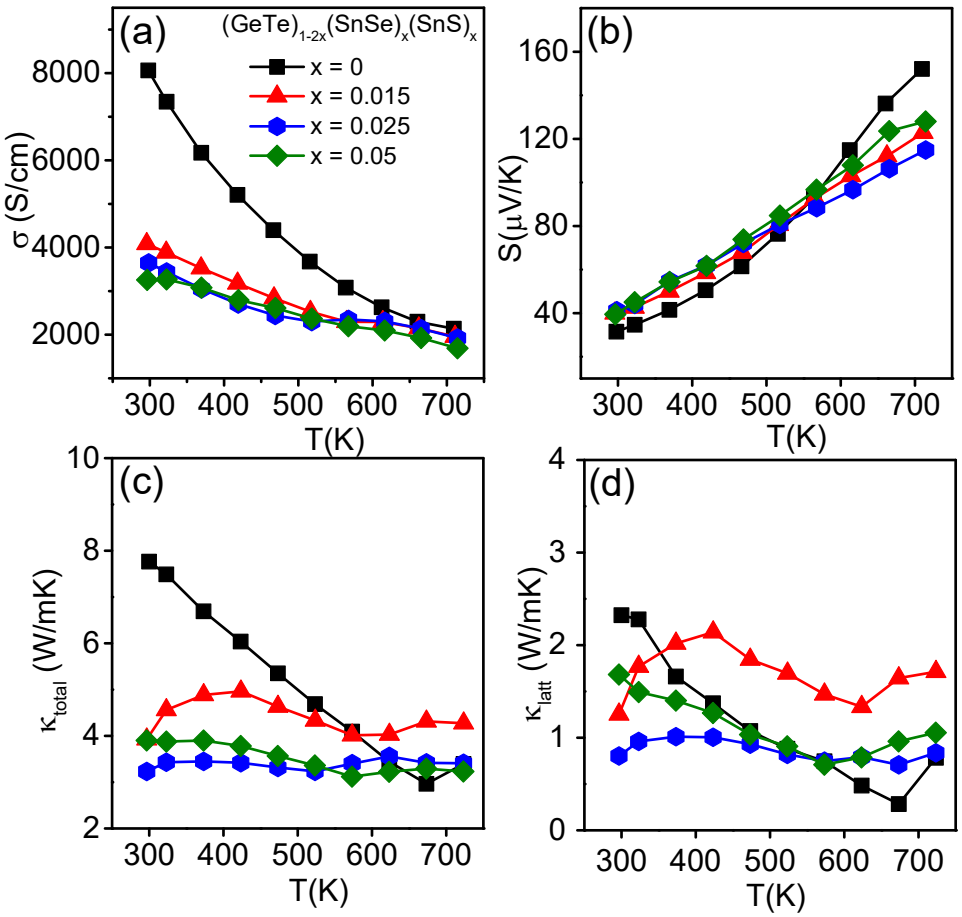

Figure 6.1.3. *Temperature dependent (a) electrical conductivity (σ), (b) Seebeck coefficient (S), (c) total thermal conductivity (κ_{total}) and (d) lattice thermal conductivity (κ_{latt}) for $(GeTe)_{1-2x}(SnSe)_x(SnS)_x$ (x = 0 - 0.05) samples.*

To analyze microstructure compositions of $(GeTe)_{1-2x}(SnSe)_x(SnS)_x$, the BSE - FESEM (backscattered electron imaging - field emission scanning electron microscopy) and EDS (energy dispersive spectroscopy) measurements are performed (Figure 6.1.2). Figure 6.1.2a and 2b represent the BSE-FESEM micrograph of $(GeTe)_{1-2x}(SnSe)_x(SnS)_x$ (x = 0.025) sample. We have observed the presence of micrometer sized (2-20 μm) precipitate with dark contrast in the light contrast matrix. EDS analysis confirms the composition of both matrix (Figure 6.1.2c) along with the existence of precipitate (Figure 6.1.2d). The matrix is $Ge_{1-x}Sn_xTe$ rich whereas the dark contrast precipitates observed in

BSE-FESEM are $GeS_{1-x}Se_x$ rich. After careful investigation of the structure and microstructure of $(GeTe)_{1-2x}(SnSe)_x(SnS)_x$, we conclude that the system behaves as solid solution initially with the lower concentration of SnSe and SnS. With increasing the SnSe and SnS concentration ($x \geq 0.025$), the material displays the coexistence of point-defect rich solid solution and phase separation with micron sized precipitates.

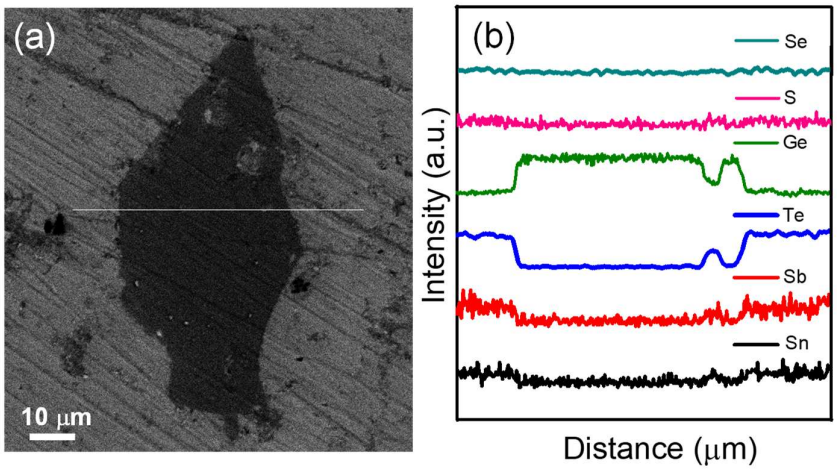

Figure 6.1.4. *(a) BSE-FESEM images of $(Ge_{0.90}Sb_{0.10}Te)_{0.95}(SnSe)_{0.025}(SnS)_{0.025}$ sample. (b) EDS line scans (white line in a) along the precipitate of $(Ge_{0.90}Sb_{0.10}Te)_{0.95}(SnSe)_{0.025}(SnS)_{0.025}$ sample.*

Figure 6.1.3 represents the thermoelectric transport properties of the $(GeTe)_{1-2x}(SnSe)_x(SnS)_x$ (x = 0 - 0.05) samples as a function of temperature in the range of 300-723 K. The temperature dependent electrical conductivity (σ) of all the samples exhibits the typical behavior of the degenerate semiconductor. The electrical conductivity of pristine GeTe decreases with the substitution of SnSe and SnS. Typically, the room temperature σ decreases from ~ 8062 S/cm for GeTe to ~ 3645 S/cm for $(GeTe)_{0.95}(SnSe)_{0.025}(SnS)_{0.025}$ sample (Figure 6.1.3a). We have measured the room temperature carrier concentration ($n = 1/eR_H$; where R_H and e are the Hall coefficient, and electronic charge respectively) for all the samples from the Hall measurement (Table 6.1.1). Positive Hall co-efficient for all samples indicating the holes are major carrier at all compositions. Interestingly, initially the *p*-type carrier concentration of GeTe decreasing with substitution of SnSe and SnS due to decrease in intrinsic Ge vacancy. Further, the *p*-type carrier concentrations for $(GeTe)_{1-2x}(SnSe)_x(SnS)_x$ are nearly

unchanged with increasing the SnSe and SnS concentration (Table 6.1.1) as the iso-valent nature of the substitutions. All $(GeTe)_{1-2x}(SnSe)_x(SnS)_x$ samples exhibit slightly higher Seebeck coefficient compared to the pristine GeTe sample in 300-570 K range. The Seebeck coefficients in $(GeTe)_{1-2x}(SnSe)_x(SnS)_x$ samples remain nearly unchanged with the increasing the SnSe and SnS concentration (Figure 6.1.3b). Typically, the Seebeck value for all $(GeTe)_{1-2x}(SnSe)_x(SnS)_x$ sample is to be ~ 40 μV/K at room temperature, which again validates the existence of a comparable *p*-type carrier concentration in $(GeTe)_{1-2x}(SnSe)_x(SnS)_x$ (x = 0.015-0.05).

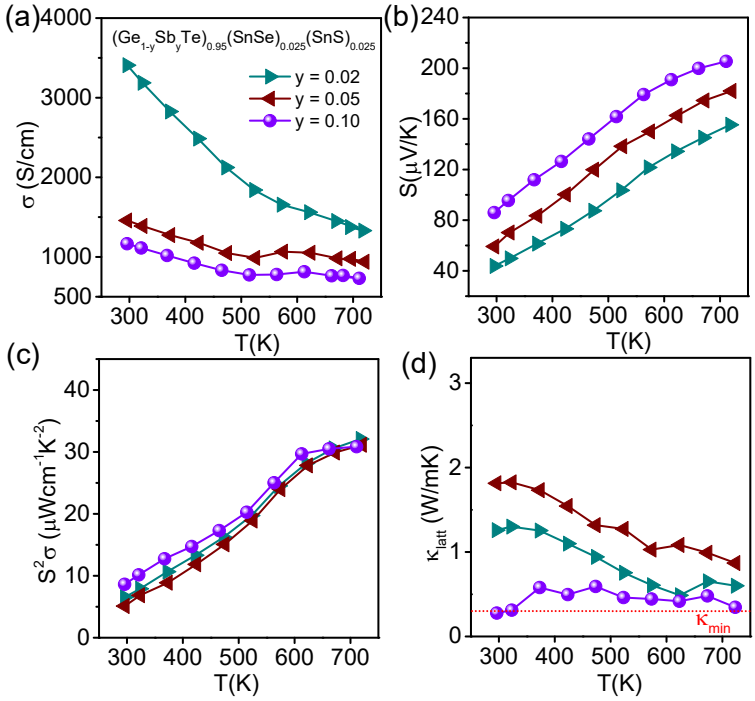

Figure 6.1.5. *Temperature dependent (a) electrical conductivity (σ), (b) Seebeck coefficient (S), (c) power factor (σS^2), and (d) lattice thermal conductivity (κ_{latt}) for $(Ge_{1-y}Sb_yTe)_{0.95}(SnSe)_{0.025}(SnS)_{0.025}$ (y = 0.02 – 0.10) samples.*

Temperature-dependent total thermal conductivity (κ_{tot}) for $(GeTe)_{1-2x}(SnSe)_x(SnS)_x$ (x = 0 - 0.05) samples decreases with the increase in SnSe and SnS contents (Figure 6.1.3c) near room temperature. The κ_{tot} of pristine GeTe is found to be decreased from ~ 7.76 W/mK at room temperature to ~ 3.4 W/mK at 710 K. Typically, $(GeTe)_{0.95}(SnSe)_{0.025}(SnS)_{0.025}$ sample exhibits κ_{tot} value of ~ 3.23 W/mK at 300 K. Figure

6.1.3d represents the κ_{latt} for all the samples obtained by subtracting the electronic contribution from κ_{tot} by using Wiedemann-Franz's law, $\kappa_{el} = L\sigma T$. Temperature-dependent Lorenz number, L for all the samples were obtained based on fitting the respective temperature-dependent Seebeck value.[30] The substitution of SnSe and SnS in GeTe enormously decreases the κ_{latt} in the temperature range of 300-500 K than the pristine GeTe sample (Figure 6.1.3d). Typically, $(GeTe)_{0.95}(SnSe)_{0.025}(SnS)_{0.025}$ sample shows κ_{latt} value of ~ 0.80 W/mK at 300 K and ~ 0.83 W/mK at 723 K. The $(GeTe)_{1-2x}(SnSe)_x(SnS)_x$ samples possess extensive solid solution point defects and micron size (~2-20 μm) $GeS_{1-x}Se_x$ rich precipitates. The interface of the matrix and micron size precipitates may have several defects and dislocations which can effectively scatter the heat carrying phonons. Thus, the reduction of κ_{latt} can be attributed to the significant scattering of the heat carrying phonon via the point defect mass fluctuations and microstructures.

The obtained κ_{latt} value in $(GeTe)_{0.95}(SnSe)_{0.025}(SnS)_{0.025}$ sample (0.80 W/mK) is still higher than κ_{min} of GeTe, thus it is leaving the room for further reduction of κ_{latt} to realize even higher zT values. Hence, in the next step, we have alloyed Sb in $(GeTe)_{0.95}(SnSe)_{0.025}(SnS)_{0.025}$ sample to optimize the p-type carrier concentration and decrease the κ_{latt} further. We have synthesized $(Ge_{1-y}Sb_yTe)_{0.95}(SnSe)_{0.025}(SnS)_{0.025}$ (y = 0 – 0.10) samples mainly by the vacuum sealed tube melting reaction and we have also performed spark plasma sintering (SPS) for the best performed sample. However, we observe very weak diffraction peak of Ge along with main peaks of GeTe in the PXRD pattern of $(Ge_{1-y}Sb_yTe)_{0.95}(SnSe)_{0.025}(SnS)_{0.025}$ (Figure 6.1.1b), which is generally observed in GeTe based samples.[30] We have not observed second phase peak of $GeS_{1-x}Se_x$ in higher concentration Sb doped samples, which probably indicates the solubility of SnSe/SnS increases with Sb doping in GeTe.

We have performed BSE-FESEM and EDS to get better insight into the microstructure of $(Ge_{0.90}Sb_{0.10}Te)_{0.95}(SnSe)_{0.025}(SnS)_{0.025}$ sample (Figure 6.1.4). We have observed the presence of micrometer size (~10-30 μm) precipitates with dark contrast in the light contrast matrix (Figure 6.1.4a). Further, EDS line scanning on both the matrix and precipitate verifies the presence of Sb in the matrix (Figure 6.1.4) which have an important role in tailoring the carrier concentration of

$(Ge_{0.90}Sb_{0.10}Te)_{0.95}(SnSe)_{0.025}(SnS)_{0.025}$ to optimize its thermoelectric performance. The precipitate is Ge rich.

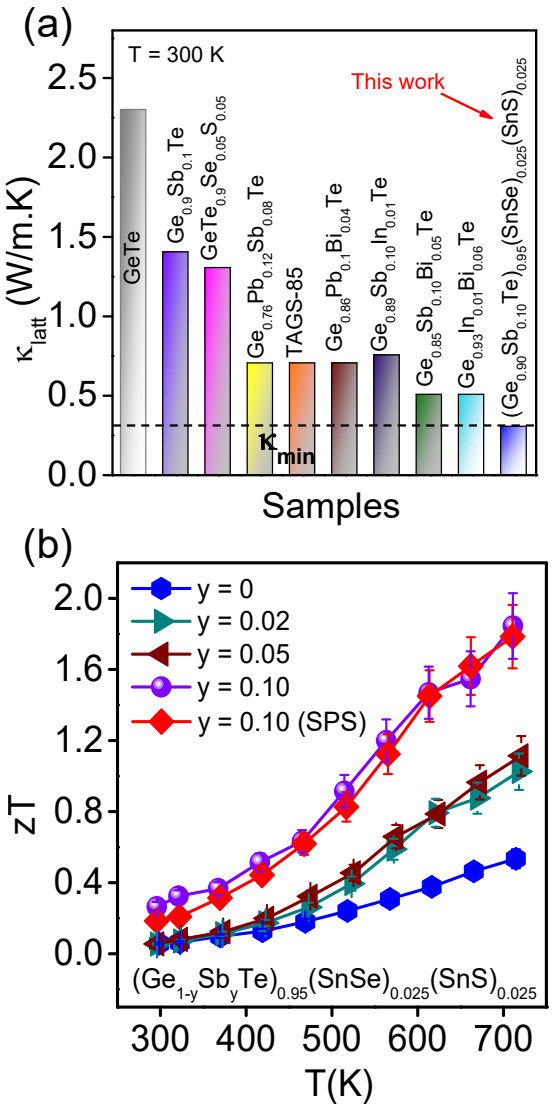

Figure 6.1.6. *(a) Comparison of the present lattice thermal conductivity (κ_{latt}) with that of the other previously reported GeTe-based samples.*[17, 20, 30, 35-38] *(b) Temperature dependent thermoelectric figure of merit (zT) for $(Ge_{1-y}Sb_yTe)_{0.95}(SnSe)_{0.025}(SnS)_{0.025}$ (y = 0 – 0.10) samples.*

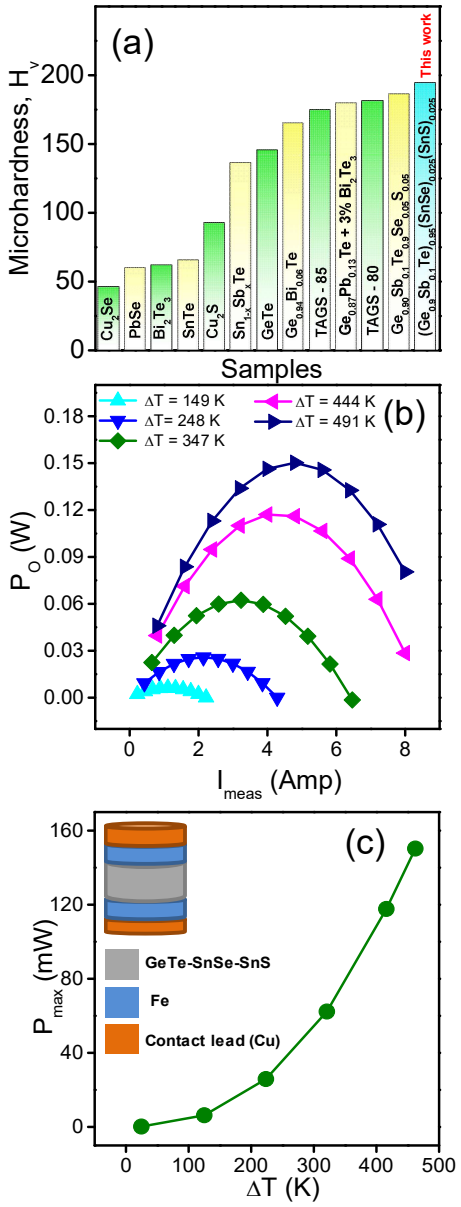

Figure 6.1.7. *(a) Comparison of Vickers microhardness value (H_v) of $(Ge_{0.90}Sb_{0.10}Te)_{0.95}(SnSe)_{0.025}(SnS)_{0.025}$ sample with other state-of-the-art thermoelectric materials.[30, 36, 39-43] Variation of (b) output power (P_O) as a function of measured current (I_{meas}) at different ΔT and (c) maximum obtainable power (P_{max}) as a function of temperature difference (ΔT) of single leg GeTe-SnSe-SnS based device.*

The electrical conductivities for $(Ge_{1-y}Sb_yTe)_{0.95}(SnSe)_{0.025}(SnS)_{0.025}$ (y = 0.02 – 0.10) samples are found to be decreased with increase in temperature as well as the increasing amount of Sb in the 300-723 K temperature range (Figure 6.1.5a). Substitution of Sb^{3+} in place Ge^{2+} decreases the electrical conductivity because of the substantial reduction in p-type carrier concentrations for all the samples (Table 6.2.2). Typically, the room temperature σ decreases from ~ 3645 S/cm for $(GeTe)_{0.95}(SnSe)_{0.025}(SnS)_{0.025}$ to ~ 1165 S/cm for $(Ge_{0.90}Sb_{0.10}Te)_{0.95}(SnSe)_{0.025}(SnS)_{0.025}$ sample. Seebeck coefficients, S, as a function of temperature for $(Ge_{1-y}Sb_yTe)_{0.95}(SnSe)_{0.025}(SnS)_{0.025}$ (y = 0.02 – 0.10) samples are presented in Figure 6.1.5b. Seebeck coefficients for $(Ge_{1-y}Sb_yTe)_{0.95}(SnSe)_{0.025}(SnS)_{0.025}$ samples are considerably higher than the undoped $(GeTe)_{1-2x}(SnSe)_x(SnS)_x$ sample over the whole range of temperature (Figure 6.1.3b and 5b).

Table 6.1.1. *Carrier concentration and mobility of $(GeTe)_{1-2x}(SnSe)_x(SnS)_x$ (x = 0-0.05) samples at 300 K:*

Sample	Carrier Concentration (n) x 10^{20} (cm^{-3})	Mobility ($cm^2v^{-1}s^{-1}$)
GeTe	8.6	58.5
$(GeTe)_{0.97}(SnSe)_{0.015}(SnS)_{0.015}$	4.9	51.9
$(GeTe)_{0.95}(SnSe)_{0.025}(SnS)_{0.025}$	4.5	50.5
$(GeTe)_{0.90}(SnSe)_{0.05}(SnS)_{0.05}$	4.1	49.5

Table 6.1.2. *Carrier concentration of $(Ge_{1-y}Sb_yTe)_{0.95}(SnSe)_{0.025}(SnS)_{0.025}$ (y = 0.02–0.10) samples at 300 K:*

Sample	Carrier Concentration(n) x 10^{20} (cm^{-3})
$(Ge_{0.98}Sb_{0.02}Te)_{0.95}(SnSe)_{0.025}(SnS)_{0.025}$	2.82
$(Ge_{0.95}Sb_{0.05}Te)_{0.95}(SnSe)_{0.025}(SnS)_{0.025}$	2.0
$(Ge_{0.90}Sb_{0.10}Te)_{0.95}(SnSe)_{0.025}(SnS)_{0.025}$	0.85

Typically, Seebeck value for $(Ge_{0.90}Sb_{0.10}Te)_{0.95}(SnSe)_{0.025}(SnS)_{0.025}$ sample is ~ 86 μV/K at room temperature which further increases to 205 μV/K at 710 K. This increase of Seebeck coefficient values with increasing the Sb concentration could be attributed to reduction of *p*-type carrier concentration (Table 6.2.2).

Power factor, σS^2 as a function of temperature for $(Ge_{1-y}Sb_yTe)_{0.95}(SnSe)_{0.025}(SnS)_{0.025}$ (y = 0.02 – 0.10) samples are presented in Figure 6.1.5c. Sb doped samples exhibit higher power factor compared to the undoped $(GeTe)_{1-2x}(SnSe)_x(SnS)_x$ sample over the measured temperature range because of optimal electrical conductivity and relatively high Seebeck coefficient (Figure 6.1.5a and 5b). Typically, the σS^2 value for $(Ge_{0.90}Sb_{0.10}Te)_{0.95}(SnSe)_{0.025}(SnS)_{0.025}$ sample is found to be ~ 8.6 μW/cm·K^2 at room-temperature, which further rises to ~ 31 μW/cm·K^2 at 710 K.

Figure 6.1.5d represents the κ_{latt} for $(Ge_{1-y}Sb_yTe)_{0.95}(SnSe)_{0.025}(SnS)_{0.025}$ samples (y = 0.02 – 0.10) samples obtained by subtracting the electronic contribution from κ_{tot} by using Wiedemann-Franz's law. Substitution of Sb in $(GeTe)_{0.95}(SnSe)_{0.025}(SnS)_{0.025}$ decreases the κ_{latt} immensely than that of the $(GeTe)_{0.95}(SnSe)_{0.025}(SnS)_{0.025}$ sample in the measured temperature range (Figure 6.1.5d). Typically, $(Ge_{0.90}Sb_{0.10}Te)_{0.95}(SnSe)_{0.025}(SnS)_{0.025}$ sample shows the κ_{latt} value of ~ 0.30 W/mK at 300 K which is smaller than the previously reported GeTe based samples (Figure 6.1 6a) and it reached to the theoretical minimum thermal conductivity of GeTe (0.3 W/mK).[17, 20, 28, 30, 35-38, 44] $(Ge_{0.90}Sb_{0.10}Te)_{0.95}(SnSe)_{0.025}(SnS)_{0.025}$ sample have widespread solid solutions point defects and micron size Ge rich precipitates (Figure 6.1.4). Substitution Sb in the $(GeTe)_{0.95}(SnSe)_{0.025}(SnS)_{0.025}$ sample further enhances solubility of SnSe and SnS in GeTe, which increases the point defects in the system originating from Ge/Sn/Sb and Te/Se/S substitution disorder that resulting in the huge reduction of κ_{latt} in $(Ge_{0.90}Sb_{0.10}Te)_{0.95}(SnSe)_{0.025}(SnS)_{0.025}$.

The zT as a function of temperature for $(Ge_{1-y}Sb_yTe)_{0.95}(SnSe)_{0.025}(SnS)_{0.025}$ (y = 0 – 0.10) samples is presented in Figure 6.1.6b. $(Ge_{0.90}Sb_{0.10}Te)_{0.95}(SnSe)_{0.025}(SnS)_{0.025}$ sample exhibits the highest zT of ~1.9 at 710 K which is significantly higher than that of pristine GeTe. We have further performed SPS processing of $(Ge_{0.90}Sb_{0.10}Te)_{0.95}(SnSe)_{0.025}(SnS)_{0.025}$ which also show similar zT vs T behavior (Figure 6.1.6b).

Apart from high zT, the thermoelectric materials should have good mechanical stability for the device fabrication. We have carried out Vickers microhardness test for Sb doped-$(GeTe)_{1-2x}(SnSe)_x(SnS)_x$ sample in order to measure its mechanical strength. The microhardness value for Sb doped-$(GeTe)_{1-2x}(SnSe)_x(SnS)_x$ sample is found to be ~194 H_v (kgf/mm^2), which is superior than that of the pristine GeTe (~145 H_v) and the other state-of-the-art thermoelectric materials (Figure 6.1.7a).[30, 36, 39-43] This enhanced mechanical stability can be attributed to the reduction of Ge vacancy after Sb substitution in $(GeTe)_{1-2x}(SnSe)_x(SnS)_x$, enhanced solid solutions and rich microstructures, which block the propagation of cracks.

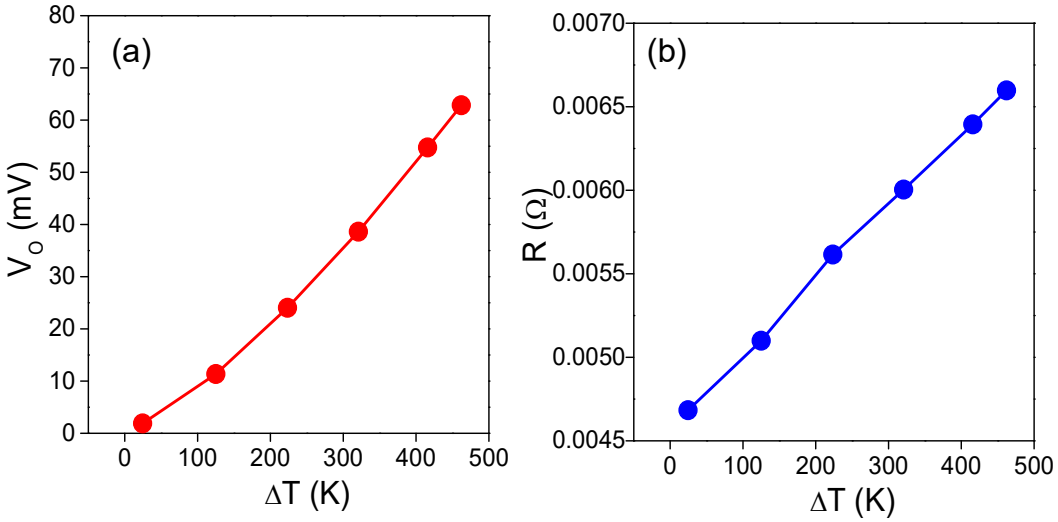

Figure 6.1.8. *(a) Open circuit voltage (V_O) and (b) resistance (R) of single-leg GeTe-SnSe-SnS based thermo-element as a function of temperature difference (ΔT), where cold side temperature (T_C) is ~ 298 K.*

We have studied the power conversion characteristics of the fabricated single leg $(Ge_{0.90}Sb_{0.10}Te)_{0.95}(SnSe)_{0.025}(SnS)_{0.025}$ thermoelectric device (Figure 6.1.7b, c). Figure 6.1.8 represents variation of open circuit voltage (V_O) and resistance (R) of fabricated thermoelement as a function of temperature difference (ΔT), where $\Delta T = T_{hot} - T_{cold}$, with T_{cold} = 298 K. Fabricated thermoelement shows maximum V_O of ~ 63 mV at ΔT = 462 K (Figure 6.1.8a). Figure 6.1.8b shows that the resistance of the device increases with ΔT which is the characteristic features of a degenerate semiconductor. However, the total resistance of the fabricated device is higher than that of the material because of contact

resistance at each of the interfaces in the fabricated device.[33, 44-46] Figure 6.1.7b shows output power (P_O) of the device as a function of measured current, I_{meas}. Maximum power output (P_{max}) at a particular ΔT is obtained when the external load resistance matches with internal resistance (R) of the $(Ge_{0.90}Sb_{0.10}Te)_{0.95}(SnSe)_{0.025}(SnS)_{0.025}$ thermoelement.[33] Figure 6.1.7c shows P_{max} as a function of ΔT and the device shows significantly high P_{max} ~ 150 mW at ΔT = 462 K, which makes the system useful for the power generation applications at the mid-temperature range.

6.1.4. Conclusions

We have achieved ultralow κ_{latt}, high thermoelectric performance, and high mechanical stability in Sb doped GeTe-rich $(GeTe)_{1-2x}(SnSe)_x(SnS)_x$ system through the two step approaches. To minimize the complexity in $(GeTe)_{1-2x}(SnSe)_x(SnS)_x$ system, here we have limited our study to GeTe rich compositions with an equimolar fraction of SnSe and SnS (x = 0 - 5 mol%). Substitution of SnSe and SnS at lower concentration in GeTe unveils the existence of solid-solution, whereas coexistence of solid solution and phase separation of $GeS_{1-x}Se_x$ rich precipitates in $Ge_{1-x}Sn_xTe$ rich matrix is evidenced in $(GeTe)_{1-2x}(SnSe)_x(SnS)_x$ system with $x \geq 0.025$. 10 mol % Sb-doped $(GeTe)_{0.95}(SnSe)_{0.025}(SnS)_{0.025}$ sample exhibits ultralow κ_{latt} of ~ 0.34 W/mK and zT of ~1.9 at 710 K. Moreover, the measured Vickers microhardness value of the high-performance sample is ~194 H_V, which is higher compared to pristine GeTe (~145 H_V). For the temperature difference of 462 K, we achieved a high output power of ~ 150 mW, in single leg p-type TE module of $(Ge_{0.90}Sb_{0.10}Te)_{0.95}(SnSe)_{0.025}(SnS)_{0.025}$. Hence, the present results should motivate further structural and thermoelectric investigations in the various compositions of $(GeTe)_{1-2x}(SnSe)_x(SnS)_x$ system for the potential utilization in mid temperature Pb-free power generation applications.

6.1.5. References

1. G. Tan, L.-D. Zhao and M. G. Kanatzidis, *Chem. Rev.*, 2016, **116**, 12123.

2. J. R. Sootsman, D. Y. Chung and M. G. Kanatzidis, *Angew. Chem. Int. Ed.*, 2009, **48**, 8616.

3. C. Chang, M. Wu, D. He, Y. Pei, C.-F. Wu, X. Wu, H. Yu, F. Zhu, K. Wang, Y. Chen, L. Huang, J.-F. Li, J. He and L.-D. Zhao, *Science*, 2018, **360**, 778.

4. Y. K. Lee, Z. Luo, S. P. Cho, M. G. Kanatzidis and I. Chung, *Joule*, 2019, **3**, 719.

5. J. He, M. G. Kanatzidis and V. P. Dravid, *Materials Today*, 2013, **16**, 166.

6. Y. Xiao and L.-D. Zhao, *Science*, 2020, **367**, 1196.

7. J. P. Heremans, V. Jovovic, E. S. Toberer, A. Saramat, K. Kurosaki, A. Charoenphakdee, S. Yamanaka and G. J. Snyder, *Science*, 2008, **321**, 554.

8. Q. Zhang, B. Liao, Y. Lan, K. Lukas, W. Liu, K. Esfarjani, C. Opeil, D. Broido, G. Chen and Z. Ren, *Proc. Natl. Acad. Sci. U. S. A.*, 2013, **110**, 13261.

9. Y. Pei, X. Shi, A. LaLonde, H. Wang, L. Chen and G. J. Snyder, *Nature*, 2011, **473**, 66.

10. A. Banik, U. S. Shenoy, S. Anand, U. V. Waghmare and K. Biswas, *Chem. Mater.*, 2015, **27**, 581.

11. K. Biswas, J. He, I. D. Blum, C.-I. Wu, T. P. Hogan, D. N. Seidman, V. P. Dravid and M. G. Kanatzidis, *Nature*, 2012, **489**, 414.

12. B. Poudel, Q. Hao, Y. Ma, Y. Lan, A. Minnich, B. Yu, X. Yan, D. Wang, A. Muto, D. Vashaee, X. Chen, J. Liu, M. S. Dresselhaus, G. Chen and Z. Ren, *Science*, 2008, **320**, 634.

13. M. K. Jana and K. Biswas, *ACS Energy Lett.*, 2018, **3**, 1315.

14. S. Perumal, S. Roychowdhury and K. Biswas, *J. Mater. Chem. C*, 2016, **4**, 7520.

15. W.-D. Liu, D.-Z. Wang, Q. Liu, W. Zhou, Z. Shao and Z.-G. Chen, *Adv. Energy Mater.*, 2020, **10**, 2000367.

16. S. Roychowdhury, M. Samanta, S. Perumal and K. Biswas, *Chem. Mater.*, 2018, **30**, 5799.

17. J. Li, X. Zhang, Z. Chen, S. Lin, W. Li, J. Shen, I. T. Witting, A. Faghaninia, Y. Chen, A. Jain, L. Chen, G. J. Snyder and Y. Pei, *Joule*, 2018, **2**, 976.

18. X. Zhang, Z. Bu, S. Lin, Z. Chen, W. Li and Y. Pei, *Joule*, 2020, **4**, 986.

19. Y. Gelbstein, J. Davidow, S. N. Girard, D. Y. Chung and M. Kanatzidis, *Adv. Energy Mater.*, 2013, **3**, 815.

20. S. Perumal, S. Roychowdhury, D. S. Negi, R. Datta and K. Biswas, *Chem. Mater.*, 2015, **27**, 7171.

21. S. Roychowdhury and K. Biswas, *Chem*, 2018, **4**, 939.

22. M. Hong, W. Lyv, M. Li, S. Xu, Q. Sun, J. Zou and Z.-G. Chen, *Joule*, 2020, **4**, 2030.

23. Z. Zheng, X. Su, R. Deng, C. Stoumpos, H. Xie, W. Liu, Y. Yan, S. Hao, C. Uher, C. Wolverton, M. G. Kanatzidis and X. Tang, *J. Am. Chem. Soc.*, 2018, **140**, 2673.

24. D. Wu, L.-D. Zhao, S. Hao, Q. Jiang, F. Zheng, J. W. Doak, H. Wu, H. Chi, Y. Gelbstein, C. Uher, C. Wolverton, M. Kanatzidis and J. He, *J. Am. Chem. Soc.*, 2014, **136**, 11412.

25. F. Fahrnbauer, D. Souchay, G. Wagner and O. Oeckler, *J. Am. Chem. Soc.*, 2015, **137**, 12633.

26. T. Rosenthal, M. N. Schneider, C. Stiewe, M. Döblinger and O. Oeckler, *Chem. Mater.*, 2011, **23**, 4349.

27. M. Samanta, S. Roychowdhury, J. Ghatak, S. Perumal and K. Biswas, *Chem. Eur. J.* , 2017, **23**, 7438.

28. L. Hu, Y. Zhang, H. Wu, J. Li, Y. Li, M. McKenna, J. He, F. Liu, S. J. Pennycook and X. Zeng, *Adv. Energy Mater.*, 2018, **8**, 1802116.

29. Y. Qiu, Y. Jin, D. Wang, M. Guan, W. He, S. Peng, R. Liu, X. Gao and L.-D. Zhao, *J. Mater. Chem. A*, 2019, **7**, 26393.

30. M. Samanta and K. Biswas, *J. Am. Chem. Soc.*, 2017, **139**, 9382.

31. S. Roychowdhury, R. K. Biswas, M. Dutta, S. K. Pati and K. Biswas, *ACS Energy Lett.*, 2019, **4**, 1658.

32. H. Kunioka, A. Yamamoto, T. Iida and H. Obara, *Appl. Phys. Express*, 2017, **10**, 095801.

33. R. Chetty, Y. Kikuchi, Y. Bouyrie, P. Jood, A. Yamamoto, K. Suekuni and M. Ohta, *J. Mater. Chem. C*, 2019, **7**, 5184.

34. X. Hu, M. R. Barnett and A. Yamamoto, *J. Alloys Compd.*, 2015, **649**, 1060.

35. X. Zhang, J. Li, X. Wang, Z. Chen, J. Mao, Y. Chen and Y. Pei, *J. Am. Chem. Soc.*, 2018, **140**, 15883.

36. J. Davidow and Y. Gelbstein, *J. Electron. Mater.*, 2013, **42**, 1542.

37. S. Perumal, P. Bellare, U. S. Shenoy, U. V. Waghmare and K. Biswas, *Chem. Mater.*, 2017, **29**, 10426.

38. M. Hong, Z.-G. Chen, L. Yang, Y.-C. Zou, M. S. Dargusch, H. Wang and J. Zou, *Adv. Mater.*, 2018, **30**, 1705942.

39. S. Perumal, S. Roychowdhury and K. Biswas, *Inorg. Chem. Front.*, 2016, **3**, 125.

40. L.-D. Zhao, B.-P. Zhang, J.-F. Li, M. Zhou, W.-S. Liu and J. Liu, *J. Alloys Compd.*, 2008, **455**, 259.

41. A. Banik, B. Vishal, S. Perumal, R. Datta and K. Biswas, *Energy Environ. Sci.*, 2016, **9**, 2011.

42. M. S. Darrow, W. B. White and R. Roy, *J. Mater. Sci.*, 1969, **4**, 313.

43. L. Zhao, X. Wang, F. Y. Fei, J. Wang, Z. Cheng, S. Dou, J. Wang and G. J. Snyder, *J. Mater. Chem. A*, 2015, **3**, 9432.

44. S. Perumal, M. Samanta, T. Ghosh, U. S. Shenoy, A. K. Bohra, S. Bhattacharya, A. Singh, U. V. Waghmare and K. Biswas, *Joule*, 2019, **3**, 2565.

45. A. Singh, S. Bhattacharya, C. Thinaharan, D. K. Aswal, S. K. Gupta, J. V. Yakhmi and K. Bhanumurthy, *J. Phys. D: Appl. Phys.*, 2008, **42**, 015502.

46. P. Jood, M. Ohta, A. Yamamoto and M. G. Kanatzidis, *Joule*, 2018, **2**, 1339.

Chapter 6.2

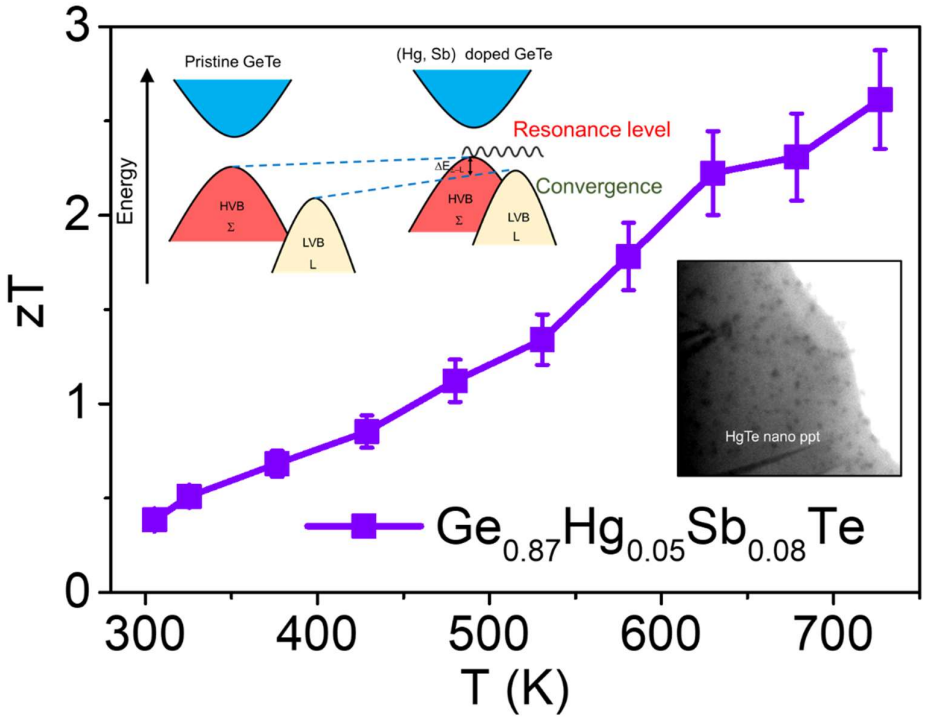

Synergistic Effect of Electronic and Micro-structure Modulation by Hg and Sb co-doping in GeTe Lead to a High zT of 2.6

Chapter 6.2

Synergistic Effect of Electronic and Micro-structure Modulation by Hg and Sb co-doping in GeTe Lead to a High zT of 2.6[†]

Summary

GeTe and its derivatives have recently attracted wide attention as promising thermoelectric materials. The principle challenge in optimizing the thermoelectric figure of merit, zT, is the low Seebeck coefficient (S) and high thermal conductivity of GeTe. Here, we report a high zT of 2.6 at 727 K in Hg and Sb codoped GeTe samples along with significant cyclable temperature stability through simultaneous enhancement in Seebeck coefficient and reduction of thermal conductivity. Further we have achieved high output power of 160 mW in a single-leg thermoelectric generator for the temperature difference of 464 K. Hg and Sb play a distinct but complementary role in terms of modulating the electronic structure and scatter the heat carrying acoustic phonon modes. Hg doping markedly reduces the lattice thermal conductivity due to the presence of nano precipitates of HgTe in GeTe matrix. Hg doping enhanced the S by valance band convergent near Fermi level (E_F), additionally, as we introduce Hg in GeTe, a very flat (localized) mid-gap electronic impurity state emerges touching the conduction band. Additional Sb doping results in a downward shift in the conduction band minimum energy. As a result, localized state lies closer to the E_F compared to Hg doped GeTe samples and consequently, the distortion in the electronic density of states near E_F increases and significantly enhances the S which is confirmed with first-principles density functional theory calculations and Pisarenko plot considering two valance band model.

[†]**P. Acharyya**, M. Samanta, R. Arora, T. Ghosh, R. S. Roy, U. K. Gautam, U.V. Waghmare and K. Biswas, *Manuscript under preparation.*

6.2.1. Introduction

The growing energy demand and environmental sustainability have sparked extensive research into alternate sustainable energy resources and energy harvesting systems. Thermoelectric (TE) technology has been considered a promising alternative to meet the challenges of global energy dilemma.[1] Thermoelectric power generation involves direct conversion of waste heat into electricity without emitting any toxic gases, thereof ensures environmental sustainability.[2-4] The performance of a TE material is determined by the dimensionless figure of merit (zT) which is defined as $zT = \frac{\sigma S^2}{\kappa}.T$, where σ is the electrical conductivity, S is the Seebeck coefficient, κ is the total thermal conductivity at absolute temperature T.[1, 5-7] κ in a crystalline solids is mainly carried out by lattice-vibrations (phonons) and free carriers of the system, thus κ has the contribution from both the electrical thermal conductivity (κ_{ele}) and lattice thermal conductivity (κ_{lat}).[8, 9] Inter-dependency between various thermoelectric parameters σ, S and κ makes it extremely challenging to tune one TE parameter independently which limits the overall TE performance.[6] Over the decades the better understanding of structure-properties relationship in TE materials leads to discover innovative strategies to design an efficient thermoelectric materials via reduction of κ_{lat} by solid solution point defects,[10] all-scale hierarchical meso- and nanostructuring,[11] lattice anharmonicity,[12] and boosting the power factor ($S^2\sigma$) by electronic structure modulation.[13, 14]

In recent years GeTe and its derivatives have shown great promise as efficient p-type TE materials for mid temperature power generation. GeTe undergoes a ferroelectric transition from rhombohedral phase (*R*3*m*, low symmetry, ferroelectric phase) to high symmetric cubic phase (Fm-3m, paraelectric phase) at 700 K. The pristine GeTe is a p-type degenerate semiconductor with a very high hole carrier concertation (~10^{21} cm^{-3}) at room temperature due to the presence of intrinsic Ge vacancies result in a high σ ~ 8000 S/cm, κ ~ 8 W/m.K (due to high κ_e) and low S ~ 30 μV/K. As a result, GeTe exhibits limited TE performance at room temperature and maximum zT is ~ 0.9 at 723 K.[15] Underlying pathways to boost TE performance of GeTe is to enhance the Seebeck coefficient by electronic structure modulation and reduce the κ_{lat} by defect/microstructure engineering.[14, 16] Typically, the Seebeck coefficient of GeTe can be improved via valance

band convergence,[17-20] slight symmetry reduction,[21, 22] introducing Rashba effect,[23, 24] and formation of resonance level near fermi level.[25, 26] Whereas κ_{lat} contribution in κ can be suppressed via solid solution point defects,[19, 27-29] micro-/nanostructuring[30-32] which can effectively scatter the heat carrying acoustic phonon modes.[16, 33] Although, several notable strategies are implemented in recent days to design high TE performance in GeTe-based system but single leg GeTe-based TE device is not so much explored so far.[34-37]

The isovalent doping in Ge sites in GeTe system which can modulate the electronic as well as the microstructure of the system, are found be effective in order to improve the TE performance of GeTe.[18, 24, 38, 39] For instance, Sn^{2+} doped in GeTe system shows Rashba effect, leading to the band convergence and a high power factor.[24] Similarly Pb^{2+} doping in GeTe forms PbTe nano-precipitates in the GeTe matrix which sustainably decrease the thermal conductivity and enhanced the Seebeck coefficient.[40] Among all the isovalent dopant, Hg doping in MTe (M=Pb, Sn) system is considered as an effective dopant to achieve high TE performance.[41-43] In the SnTe system, Hg alloying decreases the energy gap between the valance band result in band convergence that improves the Seebeck coefficient,[41] whereas in PbTe upon HgTe alloying, reduces the κ_{lat} significantly.[42] In spite of GeTe belongs to the same IV-VI metal telluride family,[15] Hg doping is not studied so far. In this work, we have studied the role of Hg doping in GeTe system, followed by Sb doping which leads to record high TE performance in Hg and Sb co-doped GeTe system. Motivated by high zT, we have further constructed single leg GeTe-based TE device.

In this chapter, we have discussed the role of Hg and Sb doping in GeTe system with a record high thermoelectric performance. The role of Hg and Sb are distinct but complementary in terms of modulating the electronic structure and scatter the heat carrying acoustic phonon modes. Introduction of Hg into GeTe leads to a very flat (localized) mid-gap electronic impurity state emerges touching the conduction band. Further, the electronic structure of GeTe is modified by Hg results in multiple maxima in valence band within a narrow energy range of the valence band maximum and consequent valence band convergence. The enhanced Seebeck coefficient in Hg doped GeTe system arises due the valance band convergence as confirmed by the electronic structure as well as the Pisarenko plot. Further the low κ_{lat} is mainly attributed due to the presence of HgTe

nano precipitates, confirmed by microscopic analysis. With the additional Sb doping to tune the carrier concentration of the Hg doped GeTe system. The electronic structure reveals that formation of resonance level in the co-doping sample and consequently, the distortion in the electronic DOS near E_F increases. This is reflected in the Pisarenko analysis of the room temperature Seebeck coefficient, which indicates higher effective mass of the heavy hole valence band in case of Hg and Sb co-doped GeTe and accounts for a huge enhancement in Seebeck coefficient. The enhanced power factor and low thermal conductivity leads to peak zT of 2.6 at 723 K in $Ge_{0.87}Hg_{0.05}Sb_{0.08}Te$ sample. Furthermore, we have studied TE power generating properties of the single leg TE device of $Ge_{0.87}Hg_{0.05}Sb_{0.08}Te$ sample and we have obtained a high output power of 160 mW for the temperature difference of 464 K. With this high zT over a wide temperature range, we calculated device thermoelectric figure of merit (ZT_{dev}) ~ 1.23 for a $Ge_{0.87}Hg_{0.05}Sb_{0.08}Te$ sample in the temperature range from room temperature to 727 K.

6.2.2. Methods

Reagents. Germanium (Ge, strategic metal investments Ltd., 99.999%), mercury (Hg, Ranbaxy laboratories Ltd., 99.5%), antimony (Sb, Alfa Aesar 99.9999%), tellurium (Te, strategic metal investments Ltd., 99.99 %) was used for synthesis without further purification.

Synthesis. High quality polycrystalline $Ge_{1-x}Hg_xTe$ (x=0-0.05) were prepared by mixing the appropriate amount of Ge, Hg and Te in a carbon coated quartz tube. The tubes were sealed under high vacuum (~10^{-6} Torr) and slowly heated to 1223 K over 12 hr., soaked for 10 hr. and finally cooled down to room temperature over 15 hr. Similar reaction profile is used for Sb doped $Ge_{1-x}Hg_xTe$ (x=0-0.05) samples.

The samples were then crushed and ground to fine powders and loaded into the 10 mm diameter graphite die for sintering (Spark Plasma Sintering system, SPS211-LX, Dr. Sinter Lab). The sintering system was first evacuated to ~10^{-3} Torr. at room temperature and the axial pressure was increased to 50 MPa. Then the temperature was increased to 450 ^oC in 7 min and hold for 5 min at a constant pressure of 50 MPa and then slowly decreased to ambient conditions in 10 min. The SPS-processed cylindrical-shaped

sample (10 mm diameter and 3 mm height) was further cut and polished for electrical and thermal transport measurement.

Powder X-ray diffraction (PXRD). Room temperature PXRD measurements of finely ground samples were recorded on Rigaku SmartLab SE diffractometer using Cu Kα (λ= 1.54059 Å) radiation.

Field Emission Scanning Electron Microscopy (FESEM). Backscattered FESEM imaging and EDAX were performed using FESEM-ZEISS Gemini 500 controlled at 20 KV.

Transmission Electron Microscopy (TEM). The TEM imaging was performed using a JEOL (JEM3010) TEM instrument (200 kV accelerating voltage) fitted with a Gatan CCD camera. The TEM images of $Ge_{0.87}Hg_{0.05}Sb_{0.08}Te$ were recorded with JEOL JEM-F200.

Electronic properties. Electrical conductivity (σ) and Seebeck coefficient (S) were simultaneously measured under He-atmosphere from 290 K up to 723 K using ULVAC-RIKO S3 ZEM-3 instrument. Rectangular bar shaped samples of dimension 8 mm x 2 mm x 2 mm were used for the measurements. The thermoelectric figure of merit (zT) has an error of 10%.

Hall Measurements. The hall measurement for all the samples was performed in home build set up under a varying magnetic field of 0.0 – 1.0 T in 100 mA current at room temperature.

Thermal conductivity. The thermal diffusivity, D, was measured between 290 K and 723 K using laser flash diffusivity technique in Netzsch LFA-457 instrument. A coin shaped SPS'ed pellets with 10 mm diameter and less than 2 mm thickness were used for thermal transport measurement. Total thermal conductivity (κ_{tot}) was estimated using the relation, κ = D x Cp x ρ, where ρ is the density (> 97%) and C_p is the heat capacity. Lattice

thermal conductivity (κ_{lat}) is extracted by subtracting electronic thermal conductivity (κ_{el}) from total thermal conductivity. κ_{el} is calculated using the Wiedemann Franz law, $\kappa_{el} = L\sigma T$, where σ is the electrical conductivity and L is the temperature dependent Lorenz number obtained by fitting the Seebeck coefficient to the reduced chemical potential.[11]

Preparation of single-leg thermoelement and measurement of its power generating properties. Typically, fabrication of the single-leg thermoelement involves consolidation of the melt grown $Ge_{0.87}Hg_{0.05}Sb_{0.08}Te$ powder along with the end layers of Cu/Fe using SPS (Dr. Sinter Lab. SPS21Lx) at 500 ºC with 50 MPa for 5 min under vacuum. The arrangement of the fabricated single-leg is Cu/Fe/$Ge_{0.87}Hg_{0.05}Sb_{0.08}Te$/Fe/Cu. Typical dimension of the fabricated cylinder shape thermoelement is of 10 mm diameter and 9 mm length. Power generation properties of the fabricated Cu/Fe/$Ge_{0.87}Hg_{0.05}Sb_{0.08}Te$/Fe/Cu thermoelement was estimated by mini-PEM module testing system (Advance Riko).[44-46]

Computational details. The DFT calculation are done in collaboration with Prof. Umesh. V. Waghmare, JNCASR, India. Our first-principles calculations within density functional theory (DFT) are based on QUANTUM ESPRESSO Package (QE)[47] and projector augmented wave (PAW) potentials.[48] Electronic exchange and correlation energy was treated within a generalized gradient approximated (GGA)[49] functional with Perdew, Burke, and Ernzerhof (PBE) method parametrization.[50] Electronic wave functions and charge density were represented using plane wave basis sets truncated at cut-off energies of 45 Ry and 360 Ry respectively such as to ensure convergence of the computed energy within less than 10^{-6} Ry atom^{-1}. The discontinuity in occupation numbers of electronic states was smeared with broadening temperature of k_BT = 0.003 Ry in the Fermi-Dirac distribution function.

We determined electronic structure of GeTe, $(Ge_{0.92}Hg_{0.08})Te_1$, and $(Ge_{0.84}Hg_{0.08}Sb_{0.08})Te_1$ in R3m structure at optimized lattice parameters. We adopted a 2 × 2 × 1 supercell of hexagonal unit of GeTe in the calculations of rhombohedral phases, including the ones with group IIB dopant Hg and group VB dopant Sb. Structural parameters i.e., both cell parameters and atomic positions were fully optimized to reduce

the residual forces acting on atoms below 10^{-3} Ry $Bohr^{-1}$. Our estimates of lattice parameters of GeTe in its rhombohedral structure (hexagonal unit) are a=b=4.23 Å, c=10.89 Å, which agree within the typical GGA errors with experimental lattice parameters (a=b=4.22 Å, c=10.56 Å).[51] Electronic spectrum was determined at Bloch vectors along high symmetry lines (Γ - M - K - Γ - A - L - H - A - L - M - K - H) in the Brillouin zone of rhombohedral lattice. Our estimates of lattice parameters of the rhombohedral structure of $(Ge_{0.92}Hg_{0.08})Te_1$, and $(Ge_{0.84}Hg_{0.08}Sb_{0.08})Te_1$ constructed in hexagonal setting are a=b=4.22 Å, c=10.78 Å and a=b=4.24 Å, c=10.75 Å respectively. We assessed effects of spin-orbit coupling (SOC) through comparison of electronic structures calculated with and without using fully relativistic and scalar relativistic potentials respectively.[52] Linear responses to electric field and to G point atomic displacements were computed using density functional linear response (called as density functional perturbation theory)[53] as implemented in the QE package.

6.2.4. Results and Discussion

The polycrystalline $Ge_{1-x}Hg_xTe$ (x= 0-0.05) samples are synthesized via solid state melting reaction in a quartz tube under high vacuum of ~10^{-6} Torr (see method). Figure 6.2.1a shows the room temperature powder X-ray diffraction (PXRD) of $Ge_{1-x}Hg_xTe$ (x= 0-0.05) which could be indexed with rhombohedral crystal structure (space group *R*3*m*) of GeTe. The weak reflection in the PXRD (marked as "*" in Figure 6.2.1a) corresponds to the presence of thermodynamically driven Ge precipitates in the system which is well supported by earlier reports.[17, 34] Along with this Ge precipitates, there are an additional reflections in the PXRD which corresponds to HgTe (space group *F*-43*m*, marked as "#" in Figure 6.2.1a). PXRD pattern also confirms the solubility limit of Hg in the GeTe is very low (~1 mol%) similar to Hg doped SnTe and PbTe systems.[41, 42] The high intense peak of GeTe (2θ ~ 29°) shifted to lower angle as the size of the Hg^{2+} (ionic radius 110 pm) is larger than Ge^{2+} (ionic radius 87 pm).

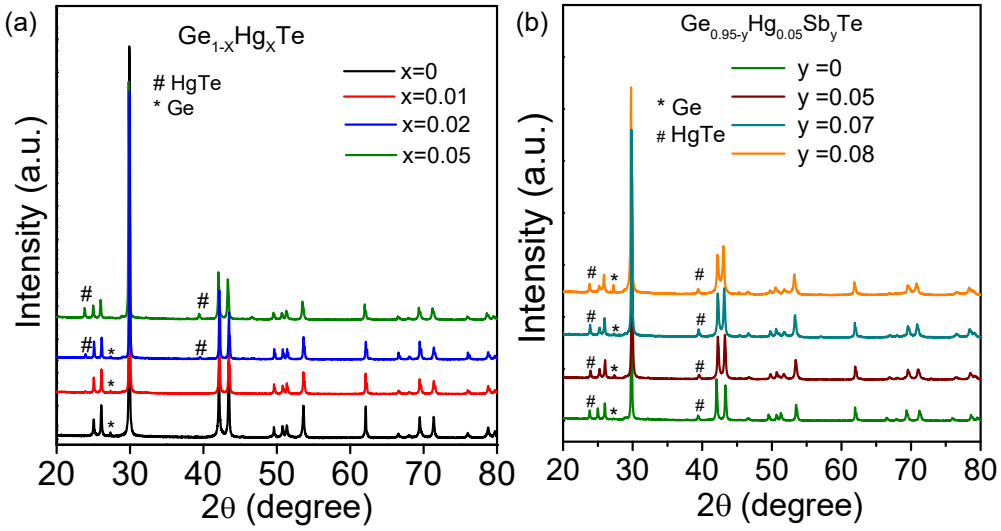

Figure 6.2.1. *Powder X-ray diffraction pattern of (a) $Ge_{1-x}Hg_xTe$ (x= 0-0.05) samples and (b) $Ge_{0.95-y}Hg_{0.05}Sb_yTe$ (x= 0-0.08).*

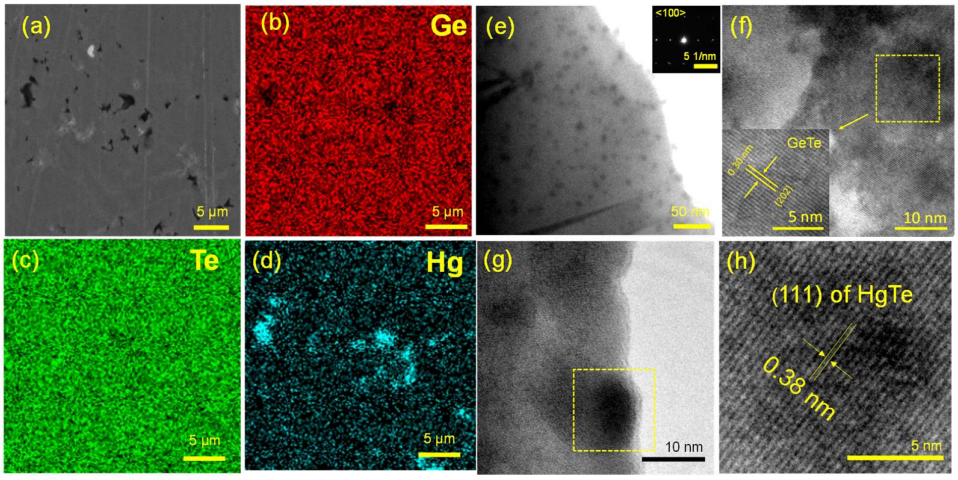

Figure 6.2.2. *(a) BSE-FESEM image of $Ge_{0.95}Hg_{0.05}Te$, (b-d) EDAX elemental color mapping for Ge, Te, and Hg for the area in (a). (e) TEM image of $Ge_{0.95}Hg_{0.05}Te$ where nanoprecipitate of HgTe are well distributed, SAED pattern of $Ge_{0.95}Hg_{0.05}Te$ along <100> direction inset of (e). (f-h) HR-TEM image of $Ge_{0.95}Hg_{0.05}Te$ samples, inset of (f) shows the d-spacing of GeTe, (h) the enlarged view of box region in (g).*

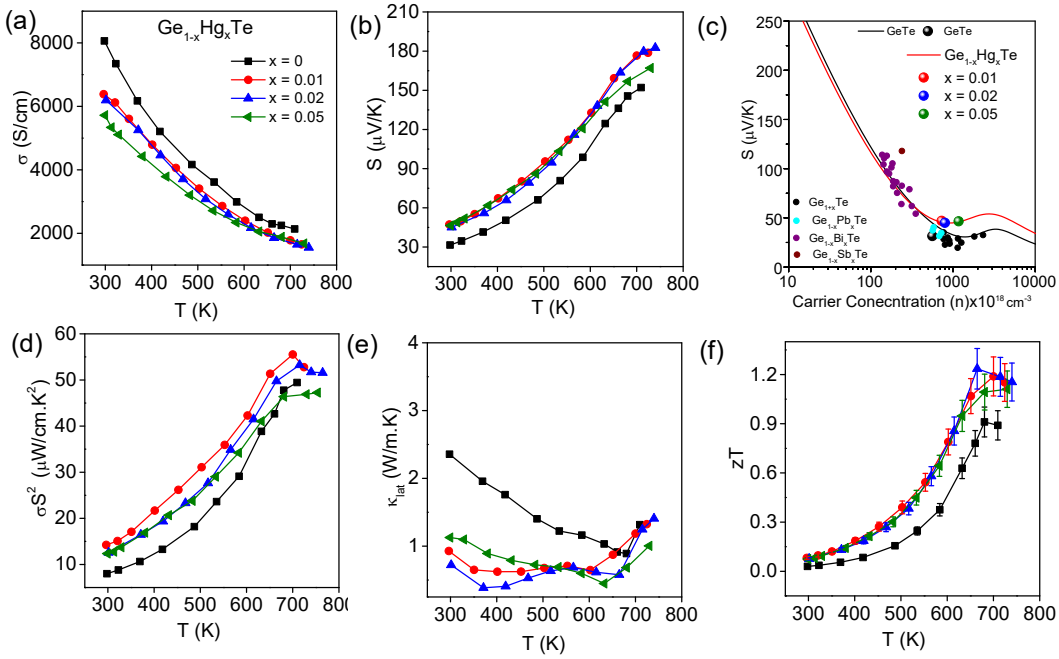

Figure 6.2.3. *Temperature dependent (a) electrical conductivity (σ), (b) Seebeck coefficient (S), (c) Pisarenko plot along with the previously reported GeTe-based materials[19, 21], (d) power factor, (e) lattice thermal conductivity (k_{lat}), and (f) figure of merit (zT) for $Ge_{1-x}Hg_xTe$ (x=0-0.05).*

Figure 6.2.2 represents the microstructure and nanostructure of $Ge_{0.95}Hg_{0.05}Te$ sample. The back scattered electron (BSE) - field emission scanning electron microscope (FESEM) shows the presence of HgTe micro precipitates of ~ 1 μm with dark contrast in the light contrast matrix of GeTe (Figure 6.2.2a-d). The colour mapping of individual elements shows the presence of Hg in the matrix as well as the precipitate (Figure 6.2.2d). The presence of Hg micro-precipitate is also evident from the PXRD pattern of $Ge_{0.95}Hg_{0.05}Te$ (Figure 6.2.1a). Figure 6.2.2e shows the transmission electron microscopy (TEM) image of $Ge_{0.95}Hg_{0.05}Te$ sample where HgTe nanoprecipitates (~ 10 nm) are randomly distributed over the GeTe matrix. The selected area electron diffraction (SAED) is shown inset of Figure 6.2.2e, which confirms the high crystalline nature. HR-TEM analysis shows the d-spacing of the matrix is matched with (202) plane of GeTe (Figure 2f) whereas the nanoprecipitates are Hg reach and corresponds to the (111) plane of cubic HgTe (space group *F*-43*m*) as shown in Figure 6.2.2h. The presence of micro precipitate

(~ 1 μm) and nano precipitate (5-10 nm) form a hierarchical microstructure which is established as an effective strategy to scatter the heat carrying acoustic phonon modes and thus reduces κ_{lat} effectively in $Ge_{0.95}Hg_{0.05}Te$ sample.[11, 54]

Table 6.2.1. *Carrier concentration, and carrier mobility of Hg and Sb doping in GeTe.*

Samples	Carrier Conc. x 10^{20} cm^{-3}	Mobility (cm^2/ V.s)
GeTe	5.60	58.5
$Ge_{0.99}Hg_{0.01}Te$	7.27	54.8
$Ge_{0.98}Hg_{0.02}Te$	7.98	48.4
$Ge_{0.95}Hg_{0.05}Te$	11.7	30.5
$Ge_{0.90}Hg_{0.05}Sb_{0.05}Te$	3.21	35.4
$Ge_{0.88}Hg_{0.05}Sb_{0.07}Te$	2.35	30.5
$Ge_{0.87}Hg_{0.05}Sb_{0.08}Te$	2.03	23.6

Figure 6.2.3 represents the thermoelectric properties of $Ge_{1-x}Hg_xTe$ (x= 0-0.05) samples. Figure 3a shows the electrical conductivity (σ) of Hg doped GeTe samples. The σ of the all the samples decreases with increasing temperature similar to typical degenerate semiconductor. The room temperature σ of GeTe sample is 8062 S/cm and decrease to 2137 S/cm at 709 K (Figure 6.2.3a). The σ of the all the Hg doped samples decreases compared to pristine GeTe. Typically, the room temperature σ decreases from 8062 S/cm for GeTe to 5719 S/cm for $Ge_{0.95}Hg_{0.05}Te$ sample (Figure 6.2.3a) is because of the reduction in mobility due to point defect carrier scattering (Table 6.2.1). The Seebeck coefficient of the all the (x= 0-0.05) samples shows the positive value over the entire temperature region indicating p-type conduction. The Seebeck coefficient of all the Hg-doped samples increases compared to the pristine GeTe as shown in Figure 6.2.3b.

The room temperature Seebeck coefficient of GeTe is 30 μV/K, increases to 46 μV/K for $Ge_{0.95}Hg_{0.05}Te$ sample despite of enhancement of the hole carrier density (Table 6.2.1). To comprehend the high Seebeck coefficient, we have compared the room temperature S with *n* plot with the well-established Pisarenko plot considering two valance band model.[21, 55, 56] In the two-valance band model, the total Seebeck coefficient has the contribution from both the heavy hole valance band (S_{hh}) and light hole valance band (S_{lh}). The heavy hole valance band is considered as non-parabolic with a non-parabolicity factor k_BT/Eg (Eg is the band gap), while the light hole valance band far below the Fermi level is considered as parabolic. The values of acoustic deformation potentials are taken from the literature.[56] The pristine GeTe exactly fall on the Pisarenko plot whereas all the doped samples are far higher than the theoretical predication as shown in Figure 6.2.3c which arises due to the valanced band convergence similar to Sb doped GeTe system.[19] We examined the existence of the valance band convergence through detail density function theory (DFT). We simulated electronic structure of $(Ge_{0.92}Hg_{0.08})Te_1$ by replacing one of the Ge atoms with Hg atom in the 2x2x1 supercell of hexagonal GeTe (Figure 6.2.4a, d). We find that introduction of Hg in GeTe lattice changes its electronic structure drastically (Figure 6.2.4b, e). The valence band maximum in rhombohedral $(Ge_{0.92}Hg_{0.08})Te_1$ occurs at A point and the electronic bands along the Γ-A-L-H directions exhibit multiple maxima within a narrow energy range of the valence band maximum (within a small energy range of 0.10-0.20 eV below the primary valence band maximum), which facilitate the contribution from the secondary valence bands to electronic transport with rising temperature. High Seebeck coefficient of Hg doped GeTe also arises from strong electronic structure modulations and convergence of multiple valence bands caused by Hg-doping: the energy differences between VB1 and VB2 reduces by 90 meV and that between VB1 and VB3 reduces by 91 meV, resulting in enhanced thermoelectric response of $(Ge_{0.92}Hg_{0.08})Te_1$. As a result, we have obtained high Seebeck coefficient which leads to high power factor in $Ge_{1-x}Hg_xTe$ (x= 0.01-0.05) over the entire temperature range (Figure 6.2.3d).

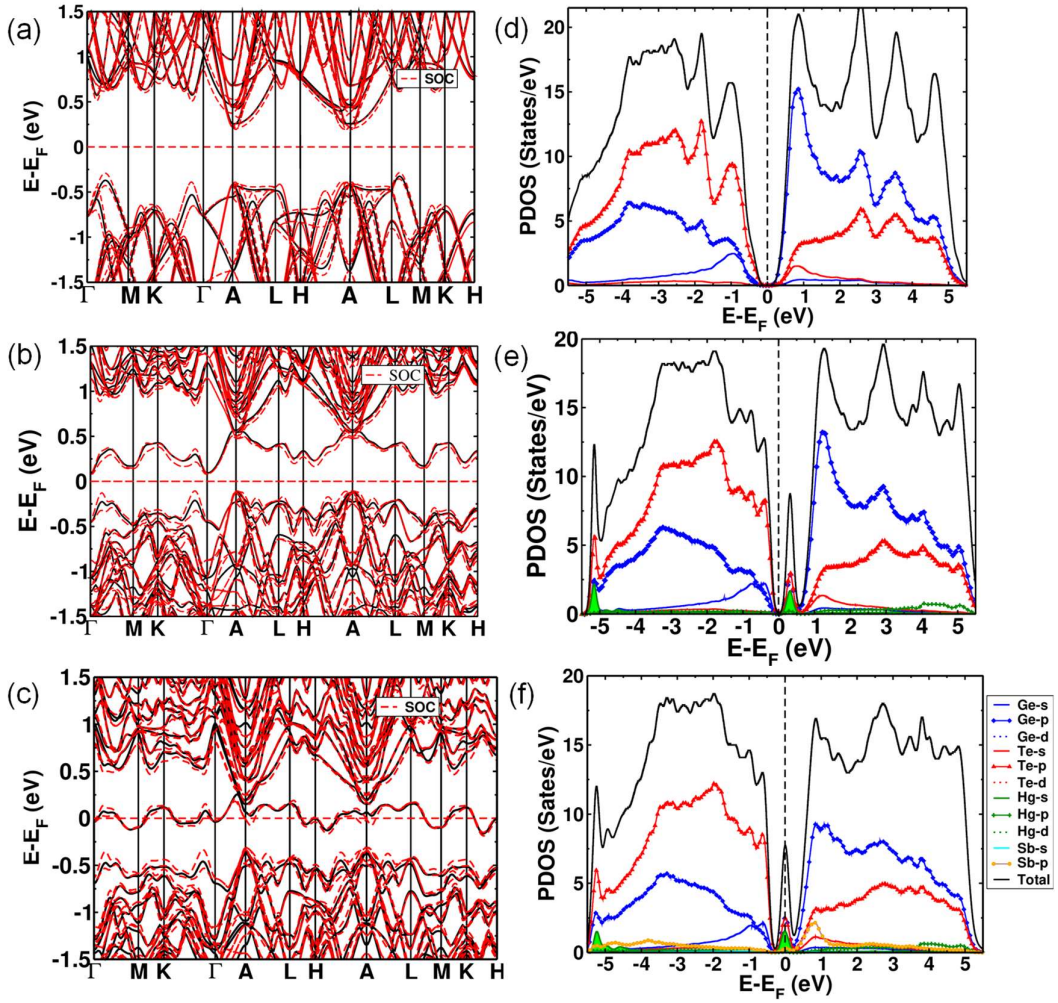

Figure 6.2.4. *Electronic structure of rhombohedral a) GeTe, b) $(Ge_{0.92}Hg_{0.08})Te_1$, and c) $(Ge_{0.84}Hg_{0.08}Sb_{0.08})Te_1$ calculated at the theoretical lattice constant with the inclusion of spin-orbit coupling (SOC) (red line) and without SOC (black lines); the effects of SOC are evident in the electronic structure. Electronic density of states (DOS) and projected density of states (PDOS) of GeTe (d), $(Ge_{0.92}Hg_{0.08})Te_1$ (e), and $(Ge_{0.84}Hg_{0.08}Sb_{0.08})Te_1$ (f), obtained without including spin-orbit coupling. $(Ge_{0.92}Hg_{0.08})Te_1$ and $(Ge_{0.84}Hg_{0.08}Sb_{0.08})Te_1$ shows a sharp peak in DOS near E_F, i.e., the presence resonant level.*

Additionally, as we introduce Hg in GeTe, a very flat (localized) mid-gap electronic impurity state emerges touching the conduction band (Figure 6.2.4b). Due to zone-folding, the uppermost valence band of $Ge_{12}Te_{12}$ is 4-fold degenerate at Γ (see Figure 6.2.4b). When Hg is doped in GeTe, its degeneracy is lifted and the 4-fold degenerate

band splits into 2 sets of doubly degenerate band at Γ (see Figure 6.2.4b) and a localized flat band[20, 21] touching the conduction at A is observed and since it is not near the Fermi level, thus that impurity states do not affect any thermoelectric performance of Hg doped GeTe samples. The formation of valence band degeneracy reflected in the increased room temperature Seebeck coefficient. Such a distinct feature has been observed previously in doped and co-doped systems of SnTe and GeTe, with In, Zn and Cd as dopants.[23-26]

The temperature dependent κ_{lat} of $Ge_{1-x}Hg_xTe$ (x= 0-0.05) samples are shown in Figure 6.2.3e. The substantial decrease in the κ_{lat} compared to the GeTe is due to the point defect phonon scattering as well as the presence of HgTe nanoprecipitates in the GeTe matrix (Figure 6.2.2). The room temperature κ_{lat} of GeTe is ~ 2.5 W/m.K which is reduces to ~ 1 W/m.K for $Ge_{1-x}Hg_xTe$ (x= 0.01-0.05) samples (Figure 6.2.3e). The low κ_{lat} along with high power factor (Figure 6.2.3d) leads to the high thermoelectric figure of merit (zT) of ~ 1.2 in $Ge_{1-x}Hg_xTe$ (x= 0.01-0.05) samples as shown in Figure 6.2.3f.

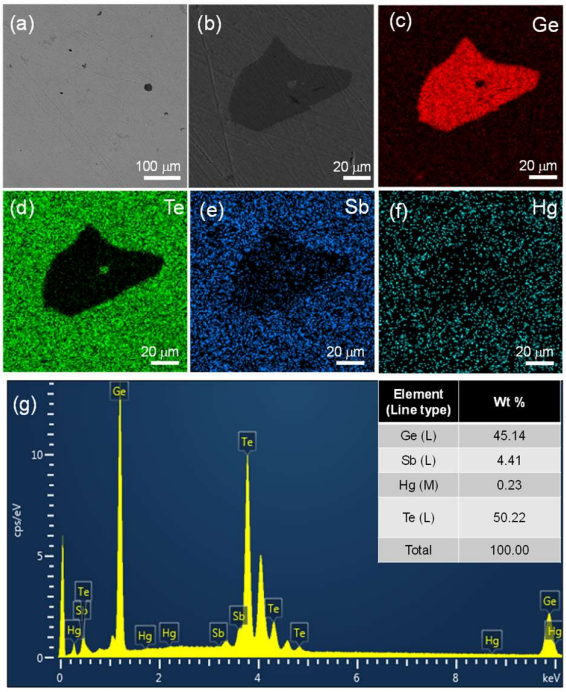

Figure 6.2.5. *(a-b) BSE-FESEM image of $Ge_{0.87}Hg_{0.05}Sb_{0.08}Te$, (c-f) EDAX elemental color mapping for Ge, Te, Hg and Sb for the area in (b) with corresponding EDAX spectra in (g).*

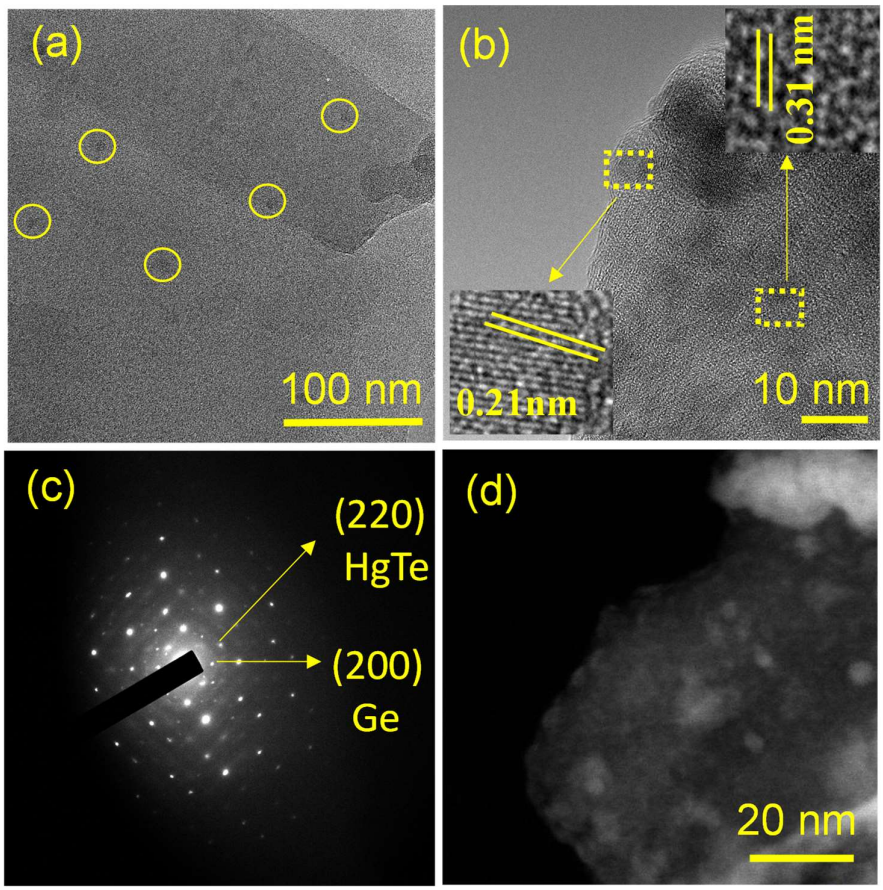

Figure 6.2.6. *(a) TEM image (b) HRTEM image, inset shows the lattice fringe spacing corresponding to HgTe (0.21 nm) and Ge (0.31 nm), (c) SAED pattern (d) HAADF-STEM image of* $Ge_{0.87}Hg_{0.05}Sb_{0.08}Te$.

Further we have doped Sb in $Ge_{0.95}Hg_{0.05}Te$ for optimizing the carrier concentration to achieve high TE performance in co-doped system. The polycrystalline $Ge_{0.95-y}Hg_{0.05}Sb_yTe$ (y= 0-0.08) samples are synthesized similar to $Ge_{1-x}Hg_xTe$ (x= 0-0.05) samples. Figure 6.2.1b represents the room temperature PXRD pattern of $Ge_{0.95-y}Hg_{0.05}Sb_yTe$ (y= 0-0.08) samples. The very weak reflection in PXRD denotes the presence of Ge precipitates present in the system, however HgTe micro-precipitate found to be dissolved in the presence Sb dopant. Further, BSE-FESEM shows the presence of Ge micro-precipitate (~ 50 μm) as shown in Figure 6.2.5. TEM analysis shows the presence of very few HgTe nano-precipitate as shown in Figure 6.2.6. HR-TEM and

SAED analysis exhibits the presence of HgTe nano-precipitate with d-spacing of 0.21 nm corresponds to the (220) plane in the GeTe matrix (d spacing of 0.31 nm) as shown in Figure 6.2.6b, c.

The electronic structure of $(Ge_{0.84}Hg_{0.08}Sb_{0.08})Te_1$ reveals formation of resonance level in the co-doping sample (Figure 6.2.4c, f) which lies closer to the Fermi energy compared to $(Ge_{0.92}Hg_{0.08})Te_1$ and consequently, the distortion in the electronic DOS near E_F increases. Stronger electronegative character of Sb compared to Ge and the donor nature of Sb dopant results in a downward shift in the CBM energy. Sb^{3+} substitution in place of Ge^{2+} acts as a donor dopant and increases the n-type carrier concentration which is also evident from the projected density of states (PDOS), where the contribution of Sb p-orbital to the states at the CB edge of $(Ge_{0.84}Hg_{0.08}Sb_{0.08})Te_1$ increases considerably. This is reflected in the Pisarenko analysis of the room temperature Seebeck coefficient, which indicates higher effective mass of the heavy hole valence band in case of Hg and Sb co-doped GeTe. Sb has almost no effect on the total DOS near E_F. The co-doping of Sb and Hg in GeTe leads to distinct but complementary contributions to modulations in electronic structure of GeTe, and hence results in high thermoelectric performance.

Figure 6.2.7 shows the TE properties of $Ge_{0.95-y}Hg_{0.05}Sb_yTe$ (y= 0-0.08) samples. Temperature dependent σ shows the reduction of the σ value throughout the temperature range. Typical σ value of $Ge_{0.95}Hg_{0.05}Te$ is 2137 S/cm which is reduced to 1000 S/cm for $Ge_{0.87}Hg_{0.05}Sb_{0.08}Te$ at room temperature as depicted in Figure 6.2.7a. The Seebeck coefficient drastically increases to 150 μV/K for $Ge_{0.87}Hg_{0.05}Sb_{0.08}Te$ from 46 μV/K for $Ge_{0.95}Hg_{0.05}Te$. The large enhancement of the Seebeck coefficient is mainly due to reduction of the carrier concentration (Table 6.2.1) because of the donor dopant nature of Sb^{3+} over Ge^{2+} sites. Moreover, the high effective mass of heavy hole valance band of the co-doped GeTe samples indicates that the distortion in the electronic density of states (DOS) by forming the resonance level close to the fermi level which is confirmed through our detail electronic structure (Figure 6.2.4).

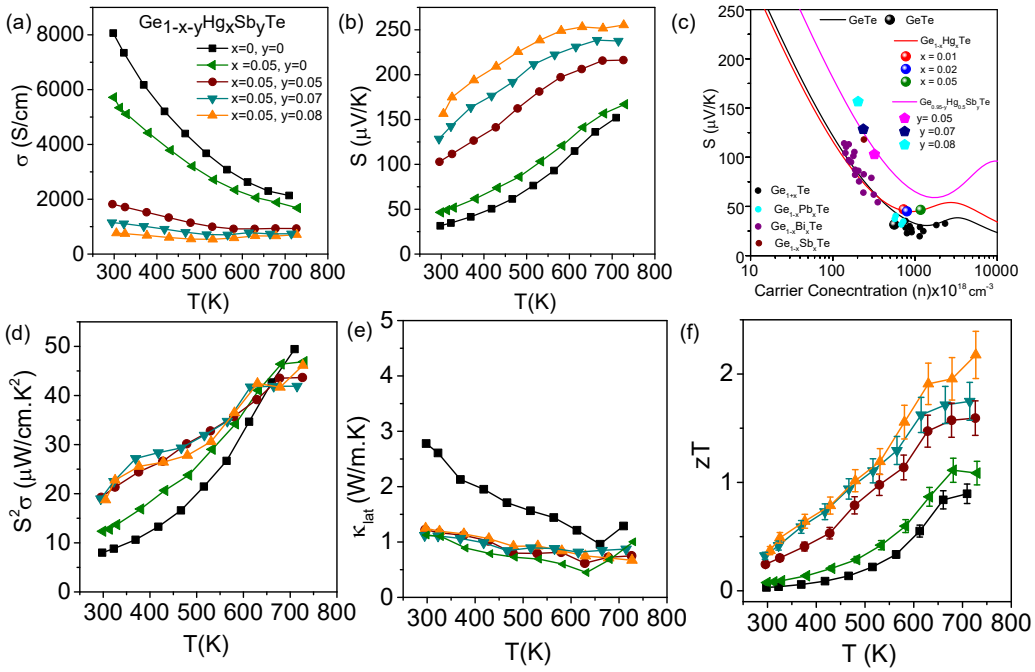

Figure 6.2.7. *Temperature dependent (a) electrical conductivity (σ), (b) Seebeck coefficient (S), (c) Pisarenko plot along with the previously reported GeTe-based materials,[19, 21] (d) power factor, (e) lattice thermal conductivity (k_{lat}) and (f) figure of merit (zT) for $Ge_{0.95-y}Hg_{0.05}Sb_yTe$ (y= 0-0.08).*

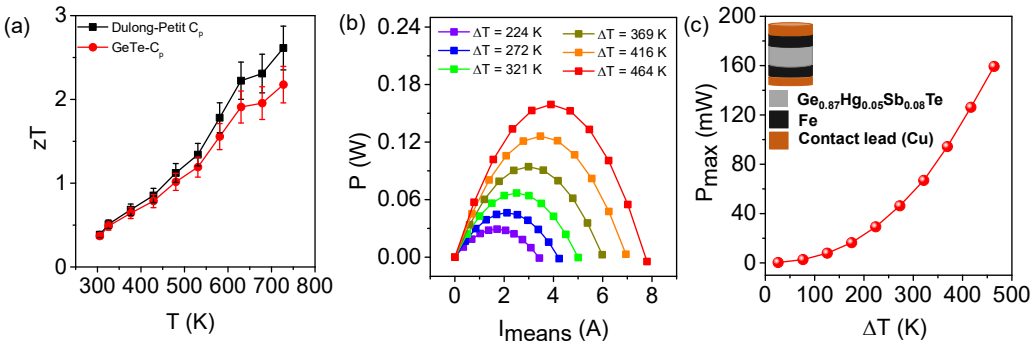

Figure 6.2.8. *Temperature dependent figure of merit (zT) of $Ge_{0.87}Hg_{0.05}Sb_{0.08}Te$ using Dulong-Petit heat capacity (Cp), pristine GeTe Cp. Variation of (b) output power (P) as a function of measured current (I_{meas}) at different temperature difference (ΔT) and (c)*

maximum obtainable power (P_{max}) as a function of ΔT of single leg $Ge_{0.87}Hg_{0.05}Sb_{0.08}Te$ based device.

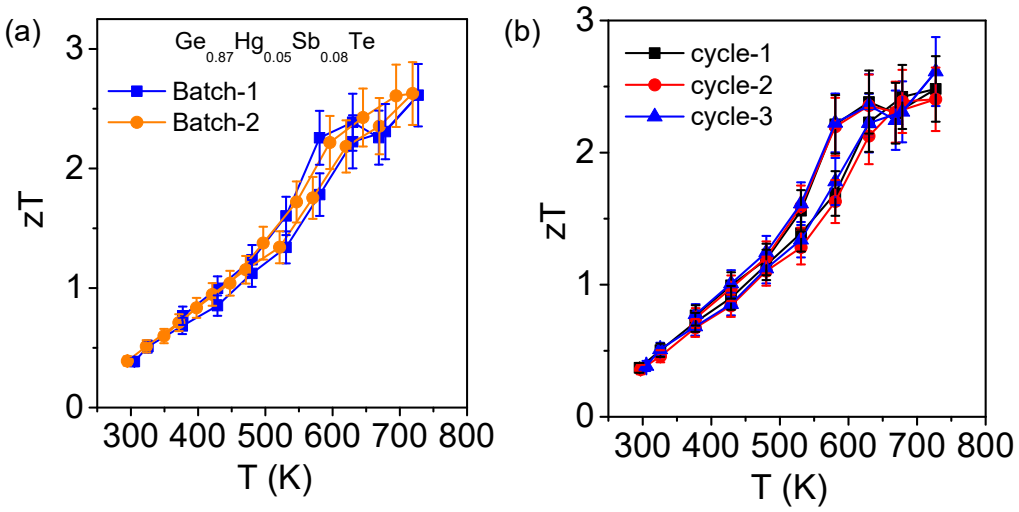

Figure 6.2.9. *zT of $Ge_{0.87}Hg_{0.05}Sb_{0.08}Te$ sample is reversible and reproducible over different (a) batch and (b) temperature cycles.*

The κ_{lat} for the co-doped samples is very much similar to Hg doped GeTe samples which signify that Sb doping in $Ge_{0.95}Hg_{0.05}Te$ samples have minimal effects on thermal transport properties as shown in Figure 6.2.7e rather it effects the electronic properties of GeTe samples. The enhanced Seebeck coefficient leads to the high-power factor of 46 $\mu W/cm.K^2$ at 729 K in $Ge_{0.87}Hg_{0.05}Sb_{0.08}Te$. As a result of high-power factor and low κ_{lat} leads to peak zT of 2.2 at 727 K (Figure 6.2.7d) whereas zT of 2.6 is achieved using Dulong-petit C_p as shown in Figure 6.2.8a. The sample is highly reproducible as well as reversible over different cycles as well as different batches as shown in Figure 6.2.9. Motived by the high zT, we have fabricated the single leg device of $Ge_{0.87}Hg_{0.05}Sb_{0.08}Te$ samples (see method) using diffusion barrier (Fe) and contact layers (Cu) as demonstrated in Figure 6.2.8b, c. The open circuit voltage (V_0) as a function of temperature range (ΔT) is shown in Figure 6.2.10a**.** The V_o increases with increase in ΔT due the increase in the Seebeck coefficient at higher temperature and reaches to maximum value of 80 mV at ΔT of 464 K. Figure 6.2.10b shows the resistance (R) of the fabricated $Ge_{0.87}Hg_{0.05}Sb_{0.08}Te$

thermoelements increases with increasing ΔT as a characteristic feature of degenerate semiconductors. The output power as a function of current (I_{means}) is shown in Figure 6.2.8b. The output power increase with increasing ΔT and reaches to maximum power (P_{max}) when external load matches with the internal resistance.[44] We have achieved a P_{max} of 160 mW at 464 K (Figure 6.2.8c) which can be useful for mid temperature power generation application. With this high zT over a wide temperature range, we calculated device thermoelectric figure of merit (ZT_{dev})[57] ~ 1.23 for a $Ge_{0.87}Hg_{0.05}Sb_{0.08}Te$ sample in the temperature range from room temperature to 727 K.

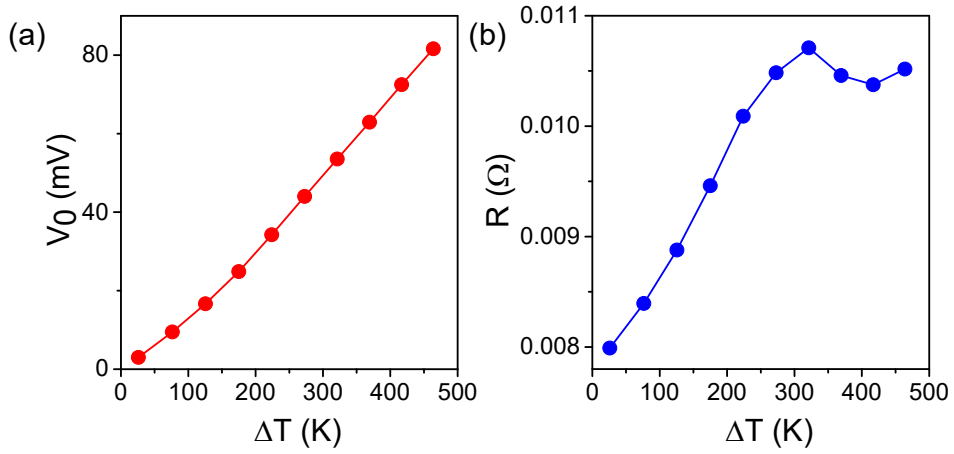

Figure 6.2.10. *(a) Open circuit voltage (V_O) and (b) resistance (R) of single-leg $Ge_{0.87}Hg_{0.05}Sb_{0.10}Te$ based hermo-element as a function of temperature difference (ΔT), where cold side temperature (T_C) is ~ 298 K.*

6.2.4. Conclusions

In conclusion, we have demonstrated a very high zT of 2.6 at 727 K along with high ZT_{dev} of 1.23 in the temperature range of 300–727 K in Hg and Sb co-doped GeTe samples. The electronic structure of GeTe is modified substantially by Hg doping results in a formation of multiple maxima in VB within a narrow energy range of the valence band maximum and consequent valence band convergence. On the other hand, Sb doping in $Ge_{0.95}Hg_{0.05}Te$ leads to the formation of resonant states close to the Fermi level which consequently distorts DOS and accounts for the huge enhancement in Seebeck coefficient. The co-doping of Hg and Sb in GeTe leads to distinct but complementary

contributions to modulate the electronic structure and thermal transport of GeTe and hence results in high thermoelectric performance. The fabricated single-leg TE devices based on Hg and Sb co-doped GeTe shows very high output power of 160 mW for the temperature difference of 464 K.

6.2.5. References

1. G. Tan, L. D. Zhao and M. G. Kanatzidis, *Chem. Rev.*, 2016, **116**, 12123.

2. Q. Yan and M. G. Kanatzidis, *Nat. Mat.*, 2022, **21**, 503.

3. L.-D. Zhao, V. P. Dravid and M. G. Kanatzidis, *Energy Environ. Sci.*, 2014, **7**, 251.

4. Z.-H. Ge, L.-D. Zhao, D. Wu, X. Liu, B.-P. Zhang, J.-F. Li and J. He, *Mater. Today*, 2016, **19**, 227.

5. Y. Zheng, T. J. Slade, L. Hu, X. Y. Tan, Y. Luo, Z.-Z. Luo, J. Xu, Q. Yan and M. G. Kanatzidis, *Chem. Soc. Rev.*, 2021, **50**, 9022.

6. J. R. Sootsman, D. Y. Chung and M. G. Kanatzidis, *Angew. Chem., Int. Ed.*, 2009, **48**, 8616.

7. W. G. Zeier, A. Zevalkink, Z. M. Gibbs, G. Hautier, M. G. Kanatzidis and G. J. Snyder, *Angew. Chem. Int. Ed.*, 2016, **55**, 6826.

8. T. M. Tritt and M. A. Subramanian, *MRS Bull.*, 2006, **31**, 188.

9. M. Dutta, D. Sarkar and K. Biswas, *Chem. Commun.*, 2021, **57**, 4751.

10. B. Jiang, Y. Yu, J. Cui, X. Liu, L. Xie, J. Liao, Q. Zhang, Y. Huang, S. Ning, B. Jia, B. Zhu, S. Bai, L. Chen, S. J. Pennycook and J. He, *Science*, 2021, **371**, 830.

11. K. Biswas, J. He, I. D. Blum, C.-I. Wu, T. P. Hogan, D. N. Seidman, V. P. Dravid and M. G. Kanatzidis, *Nature*, 2012, **489**, 414.

12. L.-D. Zhao, S.-H. Lo, Y. Zhang, H. Sun, G. Tan, C. Uher, C. Wolverton, V. P. Dravid and M. G. Kanatzidis, *Nature*, 2014, **508**, 373.

13. S. Roychowdhury, T. Ghosh, R. Arora, M. Samanta, L. Xie, N. K. Singh, A. Soni, J. He, U. V. Waghmare and K. Biswas, *Science*, 2021, **371**, 722.

14. X. Zhang, Z. Bu, S. Lin, Z. Chen, W. Li and Y. Pei, *Joule*, 2020, **4**, 986.

15. S. Roychowdhury, M. Samanta, S. Perumal and K. Biswas, *Chem. Mater.*, 2018, **30**, 5799.

16. W.-D. Liu, D.-Z. Wang, Q. Liu, W. Zhou, Z. Shao and Z.-G. Chen, *Adv. Energy Mater.*, 2020, **10**, 2000367.

17. D. Wu, L.-D. Zhao, S. Hao, Q. Jiang, F. Zheng, J. W. Doak, H. Wu, H. Chi, Y. Gelbstein, C. Uher, C. Wolverton, M. Kanatzidis and J. He, *J. Am. Chem. Soc.*, 2014, **136**, 11412.

18. Z. Zheng, X. Su, R. Deng, C. Stoumpos, H. Xie, W. Liu, Y. Yan, S. Hao, C. Uher, C. Wolverton, M. G. Kanatzidis and X. Tang, *J. Am. Chem. Soc.*, 2018, **140**, 2673.

19. S. Perumal, S. Roychowdhury, D. S. Negi, R. Datta and K. Biswas, *Chem. Mater.*, 2015, **27**, 7171.

20. S. Perumal, P. Bellare, U. S. Shenoy, U. V. Waghmare and K. Biswas, *Chem. Mater.*, 2017, **29**, 10426.

21. J. Li, X. Zhang, Z. Chen, S. Lin, W. Li, J. Shen, I. T. Witting, A. Faghaninia, Y. Chen, A. Jain, L. Chen, G. J. Snyder and Y. Pei, *Joule*, 2018, **2**, 976.

22. S. Roychowdhury and K. Biswas, *Chem*, 2018, **4**, 939.

23. D. Di Sante, P. Barone, R. Bertacco and S. Picozzi, *Adv. Mater.*, 2013, **25**, 509.

24. M. Hong, W. Lyv, M. Li, S. Xu, Q. Sun, J. Zou and Z.-G. Chen, *Joule*, 2020, **4**, 2030.

25. L. Wu, X. Li, S. Wang, T. Zhang, J. Yang, W. Zhang, L. Chen and J. Yang, *NPG Asia Mater.*, 2017, **9**, e343.

26. M. Hong, Z.-G. Chen, L. Yang, Y.-C. Zou, M. S. Dargusch, H. Wang and J. Zou, *Adv. Mater.*, 2018, **30**, 1705942.

27. P. Acharyya, S. Roychowdhury, M. Samanta and K. Biswas, *J. Am. Chem. Soc.*, 2020, **142**, 20502.

28. M. Samanta and K. Biswas, *J. Am. Chem. Soc.*, 2017, **139**, 9382.

29. J. Li, Z. Chen, X. Zhang, Y. Sun, J. Yang and Y. Pei, *NPG Asia Mater.*, 2017, **9**, e353.

30. Y. Gelbstein, J. Davidow, S. N. Girard, D. Y. Chung and M. Kanatzidis, *Adv. Energy Mater.*, 2013, **3**, 815.

31. F. Fahrnbauer, D. Souchay, G. Wagner and O. Oeckler, *J. Am. Chem. Soc.*, 2015, **137**, 12633.

32. S. Perumal, S. Roychowdhury and K. Biswas, *Inorg. Chem. Front.*, 2016, **3**, 125.

33. S. Perumal, S. Roychowdhury and K. Biswas, *J. Mater. Chem. C*, 2016, **4**, 7520.

34. S. Perumal, M. Samanta, T. Ghosh, U. S. Shenoy, A. K. Bohra, S. Bhattacharya, A. Singh, U. V. Waghmare and K. Biswas, *Joule*, 2019, **3**, 2565.

35. Z. Bu, X. Zhang, B. Shan, J. Tang, H. Liu, Z. Chen, S. Lin, W. Li and Y. Pei, *Sci. Adv.*, **7**, eabf2738.

36. E. Hazan, O. Ben-Yehuda, N. Madar and Y. Gelbstein, *Adv. Energy Mater.*, 2015, **5**, 1500272.

37. T. Xing, Q. Song, P. Qiu, Q. Zhang, M. Gu, X. Xia, J. Liao, X. Shi and L. Chen, *Energy Environ. Sci.*, 2021, **14**, 995.

38. M. Hong, Y. Wang, W. Liu, S. Matsumura, H. Wang, J. Zou and Z.-G. Chen, *Adv. Energy Mater.*, 2018, **8**, 1801837.

39. J. Li, X. Zhang, X. Wang, Z. Bu, L. Zheng, B. Zhou, F. Xiong, Y. Chen and Y. Pei, *J. Am. Chem. Soc.*, 2018, **140**, 16190.

40. S. P. Li, J. Q. Li, Q. B. Wang, L. Wang, F. S. Liu and W. Q. Ao, *Solid State Sci.*, 2011, **13**, 399.

41. G. Tan, F. Shi, J. W. Doak, H. Sun, L.-D. Zhao, P. Wang, C. Uher, C. Wolverton, V. P. Dravid and M. G. Kanatzidis, *Energy Environ. Sci.*, 2015, **8**, 267.

42. K. Ahn, K. Biswas, J. He, I. Chung, V. Dravid and M. G. Kanatzidis, *Energy Environ. Sci.*, 2013, **6**, 1529.

43. X. J. Tan, H. Z. Shao, J. He, G. Q. Liu, J. T. Xu, J. Jiang and H. C. Jiang, *Phys. Chem. Chem. Phys.*, 2016, **18**, 7141.

44. R. Chetty, Y. Kikuchi, Y. Bouyrie, P. Jood, A. Yamamoto, K. Suekuni and M. Ohta, *J. Mater. Chem. C*, 2019, **7**, 5184.

45. X. Hu, M. R. Barnett and A. Yamamoto, *J. Alloys Compd.*, 2015, **649**, 1060.

46. H. Kunioka, A. Yamamoto, T. Iida and H. Obara, *Appl. Phys. Express*, 2017, **10**, 095801.

47. *Quantum-ESPRESSO is a community project for high-quality quantum-simulation software, based on density-functional theory, and coordinated by P. Giannozzi. See http://www. quantum-espresso.org.*

48. G. Kresse and D. Joubert, *Phys. Rev. B*, 1999, **59**, 1758.

49. X. Hua, X. Chen and W. A. Goddard, *Phys. Rev. B*, 1997, **55**, 16103.

50. J. P. Perdew, K. Burke and M. Ernzerhof, *Phys. Rev. Lett.*, 1996, **77**, 3865.

51. T. Chattopadhyay, J. X. Boucherle and H. G. vonSchnering, *J. Phys. C: Solid State Phys.*, 1987, **20**, 1431.

52. A. Dal Corso, *Comput. Mater. Sci.*, 2014, **95**, 337.

53. S. Baroni, S. de Gironcoli, A. Dal Corso and P. Giannozzi, *Rev. Mod. Phys.*, 2001, **73**, 515.

54. K. Biswas, J. He, Q. Zhang, G. Wang, C. Uher, V. P. Dravid and M. G. Kanatzidis, *Nat. Chem.*, 2011, **3**, 160.

55. Q. Zhang, B. Liao, Y. Lan, K. Lukas, W. Liu, K. Esfarjani, C. Opeil, D. Broido, G. Chen and Z. Ren, *Proc. Natl. Acad. Sci. U. S. A.*, 2013, **110**, 13261.

56. J. Li, X. Zhang, S. Lin, Z. Chen and Y. Pei, *Chem. Mater.*, 2017, **29**, 605.

57. G. J. Snyder and A. H. Snyder, *Energy Environ. Sci.*, 2017, **10**, 2280.

Part 7

Summary and Future Outlook

Part 7

Summary and Future Outlook[†]

7.1 Summary

This part summarizes the thesis. The work done in this thesis provides a systematic pathway to study the structure-property relationship in metal halides and chalcogenides. Metal halides and chalcogenides are the some of the important classes of materials with a rich structural diversity and plethora of diverse applications. In my Ph.D. work, we have implemented different synthetic route, such as hot injection method for synthesis of monodispersed nanocrystals, Bridgman method to grow large single crystals, mechanochemical grinding to synthesize bulk powder of complex metal halides, and high temperature melting reaction to grow high quality polycrystal metal chalcogenides. Further, we have studied their intrinsic properties, gained an in-depth understanding of their diverse structure, and established their structure-property relationship. Finally, we have probed their applicability in diverse fields, such as optical blinking and magnetic properties along with the dielectric response in metal halides, while thermoelectric application for metal chalcogenides.

Part 1 of the thesis provides a general introduction of metal halides and chalcogenides. I have discussed about the synthesis, structural diversity and different application of metal halides. On the other hand, metal chalcogenides having a vast compositional variety as well as diverse crystal structures exhibit remarkable physical and chemical properties, which designate them as emerging candidates for thermoelectric applications. Thermoelectric materials which can convert heat energy to electricity rely on crystalline inorganic solid-state compounds exhibiting low phonon transport without much inhibiting the electrical transport. Crystalline materials with low lattice thermal conductivity (κ_{lat}) provide an attractive paradigm as it helps in simplifying the complex

---

[†]*A part of this chapter is published in* **P. Acharyya,** K. Kundu, and K. Biswas, *Nanoscale* 2020, **12**, 21094-21117 (Review) and **P. Acharyya**, D. Sarkar, P. Dutta, and K. Biswas, Comprehensive Inorganic Chemistry III, Elsevier. *submitted* (Book Chapter), Ed. by Ram Seshadri & Serena Corr.

interrelated thermoelectric parameters and allows us to focus largely on improving the electronic properties.

Part 2 of my thesis involves the synthesis and characterization of 2D Pb-based metal halide-based perovskites. In chapter 2.1, we have presented the single pot solution-based transformation of tetragonal 2D $CsPb_2Br_5$ nanosheets (NSs) from orthorhombic 3D $CsPbBr_3$ nanocrystals (NCs).[1] Electronic structure calculation by Density functional theory (DFT) demonstrates the direct band gap nature of 3D $CsPbBr_3$, while the 2D $CsPb_2Br_5$ NSs exhibit indirect band gap, and thus not expected to show the photoluminescence (PL) phenomena. In spite of having indirect bandgap, as synthesized $CsPb_2Br_5$ NSs show bright green luminescence with a blue-shifted PL spectra in comparison to that of the $CsPbBr_3$ NCs. We investigated the origin of the luminescence property of $CsPb_2Br_5$, which was arising from the different amorphous lead bromide ammonium complexes present at the surface of this material, but not due to their indirect band gap nature. In chapter 2.2, we have discussed the formation of 2D nanoplates (NPs) of Ruddlesden-Popper (RP) phase of $Cs_2PbI_2Cl_2$ using benzoyl halides as halide source and subsequently, studied their optical properties both at cryogenic and room temperatures.[2] We have also shown the chemical transformation of 2D RP phase of $Cs_2PbI_2Cl_2$ for the first time to 3D $CsPbBr_3$ and 0D Cs_4PbCl_6 by adding $PbBr_2$ and $MnCl_2$ in solution at room temperature, respectively. Furthermore, Mn^{2+} was introduced as a dopant (up to 5 mol%) with partial replacement of Pb^{2+} in $Cs_2PbI_2Cl_2$ NCs and studied their optical properties. The Mn^{2+} doping in the $Cs_2PbI_2Cl_2$ NCs induced additional dopant emission band at 585 nm with prolonged lifetime in millisecond time scale.

Part 3 of my thesis offers the synthesis and PL blinking properties of 2D NSs of layered perovskites. In chapter 3.1, we have synthesized the 2D NSs and small NCs of $Cs_3Bi_2I_6Cl_3$ by hot-injection method for the first time.[3] The 2D NSs and NCs of $Cs_3Bi_2I_6Cl_3$ showed distinct optical properties and excitonic recombination dynamics, while the activation of shallow trap states was evidenced at cryogenic temperature. Finally, the fluorescence microscopy was employed to investigate the single-particle PL properties of 2D NSs and NCs of $Cs_3Bi_2I_6Cl_3$, both of which showed luminescence at green region along with the localized blinking events at millisecond time scale. In chapter 3.2, we have demonstrated the low-temperature colloidal synthesis of free-standing

ultrathin (~1.78 nm) few-layer (~2 layers) NPLs (300-600 nm lateral dimension) of $Cs_3Bi_2I_9$ and studied their optical properties.[4] The NSs (0.6-1.5 μm) and NCs of layered $Cs_3Bi_2I_9$ were also synthesized by varying the reaction temperature and subsequently, intriguing chemical insight to the formation mechanism was provided. Further, bulk powder and crystalline ingot of $Cs_3Bi_2I_9$ have also been synthesized by mechanochemistry, liquid-assisted grinding (LAG), and vacuum-sealed tube melting reaction. The single-particle fluorescence properties of $Cs_3Bi_2I_9$ NPLs was also investigated by super-resolution fluorescence microscopy, which revealed that the luminescence intensity of the NPLs is homogeneous and in the far-red region; importantly, the fluorescence blinking was in the millisecond time scale. The dispersive nature of the blinking kinetics indicated the existence of surface defects present on the large surface of the NPLs that trapped the excitons, which led to non-radiative recombination. These trapping sites could alternatively be activated and deactivated by the incident photons.

Part 4 involves the thermal conductivity measurements of layered metal halide perovskites. In chapter 4.1, we have demonstrated intrinsically ultralow lattice thermal conductivity (κ_{latt}) of ~ 0.37-0.28 W/mK in a single crystal of layered Ruddlesden-Popper (RP) perovskite, $Cs_2PbI_2Cl_2$, synthesized by Bridgman method at the 295-523 K temperature range.[5] An anisotropic ultralow κ_{latt} along perpendicular and parallel to the Bridgman growth direction was also determined. We have noticed an intriguing lattice dynamics in $Cs_2PbI_2Cl_2$ due to its anisotropic chemical bonding with co-existing mixed ionic (weak) and covalent (strong) bonding. The damped acoustic phonon modes and strong acoustic-optical phonon mode coupling resulted in an ultralow κ_L value in all-inorganic 2D RP perovskite, $Cs_2PbI_2Cl_2$. In chapter 4.2, we have also studied the thermal conductivity of $Cs_3Bi_2I_6Cl_3$. Surprisingly the single crystal of $Cs_3Bi_2I_6Cl_3$ exhibited ultralow as well as glass-like thermal conductivity in the temperature range of 2-400 K. The presence of local distortion in the Bi-octahedra makes a highly disorder $Cs_3Bi_2I_6Cl_3$ system, which is the primary reason for the glass-like thermal conductivity. While in chapter 4.3, we have discussed the thermal transport properties of 0D $Cs_3Bi_2I_9$ polycrystal samples, which exhibited thermal conductivity similar to the distinctive crystalline materials.

Part 5 involves the dielectric, magnetic, and thermochromic properties of complex metal halides. In chapter 5.1, we have demonstrated a broadband colossal dielectric constant (CDC) with a low dielectric loss in superionic $RbAg_4I_5$, which is synthesized by a facile solvent-free mechanochemical synthesis at room temperature.[6] The presence of two structural phase transitions with decreasing temperature: α (cubic, space group $P4_332$) → β (rhombohedral, space group R32) at 209 K and β → γ (trigonal, space group P321) at 121 K was confirmed *via* temperature dependent powder X-ray diffraction (PXRD) and differential scanning calorimetry (DSC). The temperature dependent positron annihilation lifetime (PAL) spectroscopy and coincidence Doppler broadening (CDB) spectra evidenced the presence of charged vacancies associated with the diffusion of Ag^+. We have shown that ε' increases by 10^2 order in magnitude as $RbAg_4I_5$ goes through the γ → β superionic phase transition from the low temperature side and ε' reaches a giant value of ~ 6.4 x 10^8 at 0.1 Hz in the room temperature superionic α phase. The molecular dynamics (MD) simulation showed charge density fluctuation within Ag^+ clusters because of the intercluster Ag^+ diffusion. This causes fluctuation in the instantaneous dipole moments associated with the Ag^+ clusters and results in the experimentally observed CDC in the room temperature superionic $RbAg_4I_5$ phase. In chapter 5.2, we have presented all-solid state mechanochemical synthesis of 2D layered Pb-free metal halide, $RbSn_2Br_5$, and its mixed halide counterparts, $RbSn_2Br_3Cl_2$ and $RbSn_2Br_4I$.[7] The Raman spectral investigation of as-synthesized powders displayed distinct modes at low frequency regions corresponding to the Sn-Br bond vibrations from 2D polymeric $[Sn_2Br_5]_n^{n-}$ layer units. We have studied the optical properties of as-synthesized materials by solid-state UV-Vis absorption and PL spectroscopic techniques, which showed an optical band gap of ~3.20 eV along with a PL emission centered at ~2.51 eV. We have extended the investigation to explore the optical properties and charge-carrier recombination dynamics both at 298 K and 77 K using toluene-dispersed $RbSn_2Br_5$ solution after prolonged ultrasonication. The excitonic recombinations occurred through the band-edge states and intrinsic defect sites (shallow states) at both temperature with average life-times of few nanoseconds. The optical band gap (2.68-3.36 eV) and PL emission (2.31 eV to 2.58 eV) were further tuned by adjusting the halide composition in $RbSn_2Br_5$ by synthesizing $RbSn_2Br_3Cl_2$ and $RbSn_2Br_4I$. Finally, the

dielectric measurement of $RbSn_2Br_5$ was carried out as a function of temperature (4-300 K). In chapter 5.3, bulk polycrystalline powders of Pb-free RP-type phase of $Rb_2CuCl_2Br_2$ were synthesized by liquid-assisted mechanochemical grinding and their optical and magnetic properties were investigated. The optical properties and carrier recombination dynamics of $Rb_2CuCl_2Br_2$ at both room-temperature and cryogenic temperature (77 K) were studied systematically.[8] A red-shifted dual emission with enhanced intensity was evidenced at 77 K in comparison to the room-temperature emission. Finally, the magnetic measurement of $Rb_2CuCl_2Br_2$ showed a paramagnetic to antiferromagnetic (AFM) transition at ~16.1 K. In chapter 5.4, we have discussed the thermochromic properties of as synthesized $(Ag_{1-x}Cu_x)_2HgI_4$ (where $0 \leq x \leq 1$). Temperature-dependent solid state diffuse reflectance spectroscopy confirmed the thermochromic behavior in these materials. The DSC study shows that the phase transition temperature passes through a minimum at 36 °C and at $x = 0.5$ in $(Ag_{1-x}Cu_x)_2HgI_4$. A noticeable red shift in the PL spectra is detected with increase in the Cu content in $(Ag_{1-x}Cu_x)_2HgI_4$ and falls within the two extremes (i.e., $x = 0$ and 1).[9]

Part 6 involves the thermoelectric performance of germanium telluride. In part 6.1 we demonstrated an ultralow κ_{lat}, high thermoelectric performance, and high mechanical stability in Sb doped GeTe-rich $(GeTe)_{1-2x}(SnSe)_x(SnS)_x$ system. The realization of ultralow κ_{latt} and high zT is achieved *via* two successive stages. Initially, the addition of SnSe and SnS (each of 2.5 mol%) in GeTe reduces the κ_{lat} due to phonon scattering because of enhanced point defects and microstructures. Further, introduction of Sb doping introduces additional phonon scattering center and optimizes the *p*-type carrier concentration. As a result, 10 mol % Sb-doped $(GeTe)_{0.95}(SnSe)_{0.025}(SnS)_{0.025}$ sample exhibits ultralow κ_{latt} of ~ 0.34 W/mK accompanied by the high zT of ~1.9 at 710 K.[10] The ultralow κ_{latt} is attributed due to the phonon scattering in Sb-doped $(GeTe)_{1-2x}(SnSe)_x(SnS)_x$ primarily by (a) excess solid solution point defects, and (b) grain boundaries and micron size precipitates, thereby κ_{latt} reaches nearly to the κ_{min} of GeTe (0.3 W/m.K). Moreover, the measured Vickers microhardness (mechanical stability) value of high-performance sample is found to be ~194 H_V, that is higher compared to pristine GeTe (~145 H_V). Motivated by the high zT and enhanced mechanical stability, we have constructed a single-leg based thermoelectric device and achieved a high output

power of ~ 150 mW for the temperature difference at 462 K for 10 mol % Sb-doped $(GeTe)_{0.95}(SnSe)_{0.025}(SnS)_{0.025}$ sample. In chapter 6.2, we unraveled the role of Hg and Sb doping in GeTe system with a record high thermoelectric performance. The role of Hg and Sb are distinct but complementary in terms of modulating the electronic structure and scatter the heat carrying acoustic phonon modes. The enhanced Seebeck coefficient in Hg doped GeTe system arises due to the valance band convergence. The low κ_{lat} is mainly attributed due to the presence of HgTe nano precipitates, which was confirmed by microscopic analysis. With the additional Sb doping, the carrier concentration of the Hg doped GeTe system was tuned. The co-doped samples introduce a localized state near the fermi level, which enhanced both the Seebeck coefficient and power factor. The enhanced power factor and low thermal conductivity in $Ge_{0.87}Hg_{0.05}Sb_{0.08}Te$ led to the maximum zT of 2.6 at 723 K. Furthermore, we have studied TE power generating properties of the single leg TE device of $Ge_{0.87}Hg_{0.05}Sb_{0.08}Te$ sample and obtained a high output power of 160 mW for the temperature difference of 464 K.

To summarize, the initial part of my thesis involved the synthesis and optical properties of various nanostructures of metal halide perovskites with vast structural diversity (part 2, and 3). Then, we have studied the thermal transport properties of low dimensional metal halide perovskites and presented an in-depth understanding of the origins of low thermal conductivity in these systems though theoretical calculations and supportive experimental methods (part 4).[11] Being an experimental inorganic chemist, we have also explored the solid-state mechanochemical synthetic route to synthesize complex metal halides and studied their different physical properties (optical, dielectric, magnetic and thermochromic) in part 5. Finally, we have demonstrated that how low κ_{latt} can be beneficial in realizing high thermoelectric performance in GeTe compounds (part 6).

7.2 Future Outlook

Metal Halides

Metal halide perovskites exhibit superior optical properties including tunable and high PL emission intensity, narrower emission line-widths, high PLQY, wide band gap range,

and distinctive excitonic properties in their 2D structural analogues.[12, 13] However, PL blinking properties of the 2D halide perovskite nanostructures are rarely studied, and thereby needed to be explored.[11] Recently, halide perovskites showed significant potential in displaying ultra-low thermal conductivity and decent thermoelectric performances.[14] We believe that the heavy metal based all-inorganic halide perovskites can be good contender for future thermoelectrics. Till now, few handful reports on the thermoelectric properties of 3D halide perovskites and thermal properties of 2D hybrid perovskites are reported. The family of 2D all-inorganic halide perovskites should exhibit promising thermoelectric properties due to their soft crystal structure, superior stability, and bond anharmonicity.

Largely, these halide perovskites are potential candidates for implementation in the solar cells, LED, lasers, and photodetectors and also, in photocatalytic CO_2 reduction reaction.[15] Hence, future of the 2D inorganic halide perovskites is bright and opens the new opportunity for optoelectronics, magnetism, thermoelectrics, and photocatalysis.

Germanium telluride

The research on GeTe has attracted significant attention from the material facet to the device stage owing to their superior thermal and mechanical stabilities. The main constraint for the improvement of thermoelectric performance of GeTe comes from its intrinsic high p-type carrier concentration, which needs to be solved. Recent studies showed that Sb is an effective dopant to solve this issue partly.[16] Interestingly, GeTe is the only material in the IV−VI family, which crystallizes in the rhombohedral structure at an ambient condition, having polar Ge and Te bonds. This resulted in the ferroelectricity in the structure, which has a strong influence on the transport properties.[17] Near the ferroelectric phase transition, the thermal conductivity decreases to its minimum value owing to the strong optic-acoustic phonon coupling. Thus, there is enormous room for further studies on the phase transition of GeTe to achieve the minimum thermal conductivity near the room temperature. Although remarkable efforts have been made to improve TE performance of materials in the last few decades, the progress of research on the high-performance TE device is still very slow. In spite of tremendous improvement of thermoelectric performances of p-type GeTe based materials, hardly any efforts have

been made to construct a device or module for the real-life application.[18] Moreover, the high mechanical strength (Vickers microhardness of ~209 H_V), and thermal stability of GeTe-based thermoelectric materials,[10, 16, 19] compared to other IV−VI chalcogenides such as PbTe/SnTe make them a suitable and potential candidates for device applications. Therefore, significant attention should be given to the GeTe based device fabrication.[20] Compatibility is another issue for fabrication of any thermoelectric module or devices. Better compatibility of any thermoelectric device or module demands both p- and n-type legs made of the same materials. Though, there are significant advances of the thermoelectric performance of p-type GeTe, hardly any n-type GeTe is known hitherto. High hole carrier concentration in GeTe makes it difficult to change the carrier type from p-type to n-type. So, new methods/strategies are required to develop high-performance n-type GeTe based materials.

7.3. References

1. P. Acharyya, P. Pal, P. K. Samanta, A. Sarkar, S. K. Pati and K. Biswas, *Nanoscale*, 2019, **11**, 4001.

2. P. Acharyya, K. Maji, K. Kundu and K. Biswas, *ACS Appl. Nano Mater.*, 2020, **3**, 877.

3. K. Kundu, P. Acharyya, K. Maji, R. Sasmal, S. S. Agasti and K. Biswas, *Angew. Chem., Int. Ed.*, 2020, **59**, 13093.

4. A. Sarkar, P. Acharyya, R. Sasmal, P. Pal, S. S. Agasti and K. Biswas, *Inorg. Chem.*, 2018, **57**, 15558.

5. P. Acharyya, T. Ghosh, K. Pal, K. Kundu, K. Singh Rana, J. Pandey, A. Soni, U. V. Waghmare and K. Biswas, *J. Am. Chem. Soc.*, 2020, **142**, 15595.

6. P. Acharyya, T. Ghosh, S. Matteppanavar, R. K. Biswas, P. Yanda, S. R. Varanasi, D. Sanyal, A. Sundaresan, S. K. Pati and K. Biswas, *J. Phys. Chem. C*, 2020, **124**, 9802.

7. K. Kundu, P. Dutta, P. Acharyya and K. Biswas, *Mater. Res. Bull.*, 2021, **140**, 111339.

8. K. Kundu, P. Dutta, P. Acharyya and K. Biswas, *J. Phys. Chem. C*, 2021, **125**, 4720.

9. K. Maji, P. Acharyya, P. Satapathy, S. K. Prasad and K. Biswas, *Chem. Asian J.*, 2019, **14**, 4641.

10. P. Acharyya, S. Roychowdhury, M. Samanta and K. Biswas, *J. Am. Chem. Soc.*, 2020, **142**, 20502.

11. P. Acharyya, K. Kundu and K. Biswas, *Nanoscale*, 2020, **12**, 21094.

12. W. Zhang, G. E. Eperon and H. J. Snaith, *Nat. Energy*, 2016, **1**, 16048.

13. Y. Chen, Y. Sun, J. Peng, J. Tang, K. Zheng and Z. Liang, *Adv. Mater.*, 2018, **30**, 1703487.

14. H. Xie, S. Hao, J. Bao, T. J. Slade, G. J. Snyder, C. Wolverton and M. G. Kanatzidis, *J. Am. Chem. Soc.*, 2020, **142**, 9553.

15. S. S. Bhosale, A. K. Kharade, E. Jokar, A. Fathi, S.-m. Chang and E. W.-G. Diau, *J. Am. Chem. Soc.*, 2019, **141**, 20434.

16. S. Perumal, S. Roychowdhury, D. S. Negi, R. Datta and K. Biswas, *Chem. Mater.*, 2015, **27**, 7171.

17. S. Roychowdhury, M. Samanta, S. Perumal and K. Biswas, *Chem. Mater.*, 2018, **30**, 5799.

18. E. Hazan, O. Ben-Yehuda, N. Madar and Y. Gelbstein, *Adv. Energy Mater.*, 2015, **5**, 1500272.

19. M. Samanta and K. Biswas, *J. Am. Chem. Soc.*, 2017, **139**, 9382.

20. Z. Bu, X. Zhang, B. Shan, J. Tang, H. Liu, Z. Chen, S. Lin, W. Li and Y. Pei, *Sci. Adv.*, **7**, eabf2738.

List of Publications (included in this Thesis)

1. **P. Acharyya,** T. Ghosh, K. Pal, K. S. Rana, M. Dutta, D. Swain, M. Etter, A. Soni, U. V. Waghmare, and K. Biswas (manuscript submitted).
2. **P. Acharyya,** K. Pal, A. Ahad, D. Sarkar, K. S. Rana, M. Dutta, M. Etter, A. Soni, and K. Biswas, (manuscript under preparation).
3. **P. Acharyya,** M. Samanta, R. Arora, T. Ghosh, R. S. Roy, U. K. Gautam, U.V. Waghmare and K. Biswas, (manuscript under preparation).
4. **P. Acharyya**, S. Roychowdhury, M. Samanta and K. Biswas, ***J. Am. Chem. Soc.*** 2020, 142, 20502–20508.
5. **P. Acharyya**, T. Ghosh, K. Pal, K. Kundu, K. S. Rana, J. Pandey, A. Soni, U. V. Waghmare, and K. Biswas, ***J. Am. Chem. Soc.*** 2020, *142*, 15595–15603.
6. K. Kundu,* **P. Acharyya**,* K. Maji, R. Sasmal, S. S Agasti, Kanishka Biswas, ***Angew. Chem. Int. Ed.*** 2020, *59*, 13093-13100. (*contributed equally)
7. **P. Acharyya**, T. Ghosh, S. Matteppanavar, R. K. Biswas, P. Yanda, S. R. Varanasi, D. Sanyal, A. Sundaresan, S. K. Pati, and K. Biswas, ***J. Phys. Chem. C*** 2020, 124, 9802–9809.
8. **P. Acharyya**, K. Kundu, and K. Biswas, ***Nanoscale*** 2020, *12*, 21094-21117.
9. **P. Acharyya**, K. Maji, K. Kundu, and K. Biswas, ***ACS Appl. Nano Mater.*** 2020, 3, 877–886.
10. K. Maji,* **P. Acharyya**,* P. Satapathy, S. K. Prasad, and K. Biswas, ***Chem. Asian J.*** 2019, *14*, 4641. (*contributed equally)
11. **P. Acharyya**, P. Pal, P. K. Samanta, A. Sarkar, S. K. Pati, and K. Biswas, ***Nanoscale*** 2019, *11*, 4001-4007.
12. A. Sarkar,* **P. Acharyya**,* R. Sasmal, P. Pal, S. S. Agasti, and K. Biswas, ***Inorg. Chem.*** 2018, 57, 15558–15565. (*contributed equally)
13. K. Kundu, P. Dutta, **P. Acharyya**, and K. Biswas, ***Mater. Res. Bull.*** 2021, *140*, 111339-111348.
14. K. Kundu, P. Dutta, **P. Acharyya**, and K. Biswas, ***J. Phys. Chem. C*** 2021, 125, 4720–4729.
15. **P. Acharyya**, D. Sarkar, P. Dutta, and K. Biswas, *"Metal Chalcogenide Materials: Synthesis, Structure and Properties",* Comprehensive Inorganic Chemistry III, Elsevier, *submitted* (Book Chapter) Ed. by Ram Seshadri & Serena Corr.

Biography

Paribesh Acharyya obtained his B.Sc. (2015) degree in Chemistry from Jadavpur University, India, and M.Sc. (2017) degree in Chemistry from Indian Institute of Technology Kharagpur, India. He is currently pursuing his Ph. D. under the guidance of Prof. Kanishka Biswas at New Chemistry Unit, Jawaharlal Nehru Centre for Advanced Scientific Research (JNCASR), Bangalore, India. His research areas focus on bulk and nanostructured metal halides and chalcogenides: synthesis, optical, dielectric, and thermoelectric properties. He is a recipient of the best poster prize at “In-House Symposium (2020), JNCASR, India”, and “ICONSAT, Kolkata, 2020”.